Chetan S. Mistry
S. Kishore Kumar
B. N. Raghunandan
Gullapalli Sivaramakrishna *Editors*

Proceedings of the National Aerospace Propulsion Conference

Springer

Lecture Notes in Mechanical Engineering

Series Editors

Fakher Chaari, National School of Engineers, University of Sfax, Sfax, Tunisia

Mohamed Haddar, National School of Engineers of Sfax (ENIS), Sfax, Tunisia

Young W. Kwon, Department of Manufacturing Engineering and Aerospace Engineering, Graduate School of Engineering and Applied Science, Monterey, CA, USA

Francesco Gherardini, Dipartimento di Ingegneria, Università di Modena e Reggio Emilia, Modena, Italy

Vitalii Ivanov, Department of Manufacturing Engineering Machine and Tools, Sumy State University, Sumy, Ukraine

Francisco Cavas-Martínez, Departamento de Estructuras, Universidad Politécnica de Cartagena, Cartagena, Murcia, Spain

Justyna Trojanowska, Poznan University of Technology, Poznan, Poland

Lecture Notes in Mechanical Engineering (LNME) publishes the latest developments in Mechanical Engineering - quickly, informally and with high quality. Original research reported in proceedings and post-proceedings represents the core of LNME. Volumes published in LNME embrace all aspects, subfields and new challenges of mechanical engineering. Topics in the series include:

- Engineering Design
- Machinery and Machine Elements
- Mechanical Structures and Stress Analysis
- Automotive Engineering
- Engine Technology
- Aerospace Technology and Astronautics
- Nanotechnology and Microengineering
- Control, Robotics, Mechatronics
- MEMS
- Theoretical and Applied Mechanics
- Dynamical Systems, Control
- Fluid Mechanics
- Engineering Thermodynamics, Heat and Mass Transfer
- Manufacturing
- Precision Engineering, Instrumentation, Measurement
- Materials Engineering
- Tribology and Surface Technology

Chetan S. Mistry · S. Kishore Kumar ·
B. N. Raghunandan · Gullapalli Sivaramakrishna
Editors

Proceedings of the National Aerospace Propulsion Conference

Editors
Chetan S. Mistry
Indian Institute of Technology Kharagpur
Kharagpur, West Bengal, India

S. Kishore Kumar
Gas Turbine Research Establishment
Bangalore, Karnataka, India

B. N. Raghunandan
Indian Institute of Science Bangalore
Bangalore, Karnataka, India

Gullapalli Sivaramakrishna
Gas Turbine Research Establishment
Bangalore, Karnataka, India

Preface

The second National Aerospace Propulsion Conference (NAPC-2018) is a biennial event being held since 2017. This conference is an amalgamation of the National Propulsion Conference (NPC) and National Conference on Air-Breathing Engines (NCABE) conferences. It was organized and hosted by the Indian Institute of Technology, Kharagpur between 17–19 December 2019.

These proceedings constitute about thirty-five percent of the research articles presented at the conference. All published papers were subjected to a rigorous refereeing process, which resulted in uniformly high quality.

The papers cover the state-of-the-art design and analysis of Gas Turbine Engine components like the compressor, turbine, combustor and afterburner, as well as systemic issues related to health monitoring, flow and structural dynamics and instrumentation. The contents also cover topics on Scramjets, Rockets and UAVs.

We owe our sincere gratitude and appreciation to all the members of the technical committee and reviewers. DRDO, ISRO HQ, AR and DB, DST, CSIR and TSI have supported as major contributors to the conference by providing necessary finances, and we duly acknowledge their support. We thank Mr. MZ Siddique, Director, GTRE, and Prof P P Chakraborty, Director, IIT Kharagpur, for their support and encouragement.

There are many others who have contributed to the publication of these proceedings whom we are unable to mention individually. We thank all of them.

Kharagpur, India	Chetan S. Mistry
Bangalore, India	S. Kishore Kumar
Bangalore, India	B. N. Raghunandan
Bangalore, India	Gullapalli Sivaramakrishna

Contents

About the Editors

Dr. Chetan S. Mistry is an Assistant Professor in the Department of Aerospace Engineering, IIT Kharagpur. He has 19 years' experience in teaching and research. He has his graduation in Mechanical Engineering from REC, Surat (Presently NIT-Surat). He received his Master's of Engineering in Turbo Machinery from NIT, Surat; Ph.D. from IIT Bombay. His Ph.D. thesis on "Experimental Investigation on the Performance of a Contra Rotating Fan Stage under Clean and Distorted Inflow Conditions" awarded with "Award for Excellence in Thesis Work", IIT Bombay in 2014. He is also a recipient of "ASME- IGTI-Young Engineer Travel Award" in 2013. His area of research are: design and performance augmentation strategies for turbomachines, experimental and CFD study of turbomachines, contra rotating axial flow turbomachines aerodynamics, electric propulsion as well as fluid mechanics & heat transfer, and experimental aerodynamics.

Dr. S. Kishore Kumar is currently a DRDO Fellow in Gas Turbine Research Establishment, DRDO. He was an AICTE-INAE Distinguished Visiting Professor from 2014-2016. He was formerly Scientist G & Associate Director heading CFD, Compressor, Turbine, Combustor, Afterburner, Heat Transfer and Secondary Air System Groups in GTRE. He was Program Director of Gas Turbine Enabling Technology (GATET) – A National Initiative of GTRE, DRDO from its inception to 2014. He has published over 100 papers in journals and conferences and edited five books related to aerospace technologies. He has guided twelve doctoral students. He is Vice Chairman of National Committee of Air Breathing Engines (NCABE). He is a Fellow of AeSI and Life Member of Combustion Institute, FMFP and CSI.

Prof. B. N. Raghunandan is a specialist in the area of Aerospace Propulsion and Combustion. During his long tenure at the Indian Institute of Science, he held many senior positions such as Dean, Faculty of Engineering and Chairman, Department of Aerospace Engineering. He has been active in promoting the area of Aerospace Propulsion and is currently serving as the Chairman, National Committee on Air Breathing Engines.

Gullapalli Sivaramakrishna is a Scientist in Gas Turbine Research Establishment, DRDO. After graduating from Osmania University in Mechanical Engineering, he did Post Graduation in I.C. Engines & Gas Turbines from NIT Warangal. He has 27 years of experience in CFD based Design & Development of Gas Turbine Combustion Systems. He was Deputy Program Director of a Gas Turbine Enabling Technology (GATET) – A National Initiative of GTRE, DRDO from its inception in 2009 till 2014; became Program Director of the same in the year 2014 and held the post till 2017. Through this initiative, he has pursued several technology development projects in various areas of relevance to bridge the technology gaps as well as to initiate research in emerging technology areas pertinent to gas turbines, in collaboration with academia and R&D institutions in India. He has authored about 35 technical publications in National & International Conferences and he is a recipient of National Science Day Award of DRDO.

Fans and Compressor

Understanding of an Effect of Plenum Volume of a Low Porosity Bend Skewed Casing Treatment on the Performance of Single-Stage Transonic Axial Flow Compressor

Darshan P. Pitroda, Dilipkumar Bhanudasji Alone, and Harish S. Choksi

Abstract The present study intends to improve the performance of transonic axial flow compressor stage and its operating range by implementing passive flow control technique, a Casing Treatment. A plenum chamber with two different volumes placed above the bend skewed slots was implemented. The objective was to understand the effect of plenum volume on the performance of transonic axial flow compressor retrofitted with bend skewed casing treatment. The porosity of the selected bend skewed casing treatment was 33%. A detailed steady-state CFD analysis has been carried out for the compressor operating at six different speeds. Axial location of the casing treatment above the rotor tip was chosen based upon the previous experiments reported in literature [1]. For the same axial location and porosity, plenum chamber depth was varied from zero depth to full plenum depth to understand effect of a plenum volume. The results were compared with baseline model with solid casing wall. Significant improvement in stall margin was observed at all rotational speeds. Minor deviation was observed in stage total pressure ratio with reduction in efficiency at design speed.

Keywords Casing treatment · Plenum chamber · Stall margin · Transonic compressor · Bend skewed slots · Tip flow

Nomenclature

AFCR	Axial Flow Compressor Research Facility
BLM	Base line model CSIR Council of Scientific and Industrial Research
CT	Casing Treatment

D. P. Pitroda · H. S. Choksi
Maharaja Sayajirao University, Gujarat, India
e-mail: darshanpitroda98@gmail.com

D. B. Alone (✉)
CSIR-National Aerospace Laboratories, Bangalore, Karnataka, India
e-mail: dilipbalone@nal.res.in

FP   Full Plenum
HP   Half Plenum
MMF   Maximum Mass Flow Rate N Rotational Speed, rpm
NAL   National Aerospace Laboratories
NP   No Plenum
NS   Near Stall
PE   Peak Efficiency
PS   Pressure Surface
SC   Solid Casing
SMI   Stall Margin Improvement
SS   Suction surface
TLV   Tip Leakage Vortex
m   Mass flow rate
π Pressure Ratio Corrected rotational speed $= \sqrt{\frac{N}{\theta}}$ (RPM) Corrected mass

        flow rate $= m_{\text{actual}} * \sqrt{\frac{\theta}{\delta}}$ (RPM)

1 Introduction

Transonic axial flow compressors are widely used today in aviation applications. The need for continuous improvement in performance of engines has pushed the operating limits of axial compressor. With limitation imposed on total operating weight, the compressor needs to work at higher per stage pressure ratio. It leads to higher flow turning and increased blade loading, requiring the compressor to operate at off-design conditions in critical situations. Axial compressor performs very efficiently at its design point. But at the off-design condition, its performance reduces drastically. The deterioration in performance is due to flow disturbances created by shock generation, tip leakage, and secondary flow, etc. Many attempts have been made to understand the flow physics at the tip gap of axial flow compressor and to find main reasons for stalling of the rotor blades [2–3]. Tip leakage vortex, shock-boundary layer interactions, and secondary flow are assumed to be main reasons behind the stall phenomena. The effect of shock and tip leakage vortex interaction has been reported by Sunder and Celestina [2]. Further experimental investigations revealed interaction between shock and tip leakage vortex. It caused high blockage in flow passage which is further grown downstream in circumferential and radial direction. As a result, flow with higher incidence angle was entering the rotor. Furthermore, investigation on blade-generated vortex due to different incidence angle was carried out by Beselt et al. [4] by analyzing the compressor cascade. At lower incidence angles vortex generated had enough energy to sustain while at higher incidence angles breakdown of vortex occurred. That leads to increased blockage downstream. The effect of tip gap between the blade tip and shroud in tip leakage vortex formation is significant. Thompson et al. [3] performed investigations on axial compressor

with stepped tip gaps and different clearance levels. Pressure ratio and efficiency of compressor dropped with increased clearance. At low clearance levels stepped tips were properly utilized by compressor and performance improved. The positioning of stepped tip gap relies on design of compressor.

To reduce or suppress the effect of these near tip flow phenomenon more attention has been given to end-wall treatments. Instead of solid casing in conventional rotor, implementation of grooved walls has proved beneficial. It extended operating range of axial compressor but at an expense of efficiency. Chen et al. [5] studied the effects of circumferential groove casing treatment (CGCT) on transonic compressor for three different tip clearance configurations. Stall was triggered by trailing edge vortex in no tip gap. For small tip gap configuration, it further mixed with tip leakage flow and triggered stall. At large tip gap, breakdown of tip leakage vortex triggered stall. Along with CGCTs, slotted casing treatments are also known to increase stall margin of compressor. Relationship between SMI and momentum flux near tip was provided by Ross et al. [6]. Linear variation in stall margin extension corresponding to tip clearance momentum flux was found in grooved slots with effect of grooves being additive.

Legras et al. [7] performed unsteady numerical analysis on compressor with slotted casing treatment. Bleeding of flow form downstream and re-injecting it upstream of the rotor leading edge pushed the tip leakage vortex downstream and increased stall margin. Performance improvement in compressor varied significantly with positioning of casing treatment. Relative axial positioning of casing treatment also affects its performance [8]. Depending on flow mechanisms of rotor, optimum location of casing treatment can provide much higher stall margin [1]. There is much literature available about effect of casing treatment on stabilizing tip flow. However, much less studies are performed on plenum chamber combined with casing treatment. Emmrich et al. [9, 10] performed one such simulation with plenum chamber to understand its stabilizing effect. It was found out that plenum chamber was the reason for continuous extraction of fluid from blade passage which relaxed tip clearance vortex and stabilized flow. More investigations on plenum chamber revealed its role in suppressing the adverse effect caused by CT [11]. Wang et al. noted detuning effect of plenum chamber on compressor which improved compressor performance at design point. Casing treatment had unsteady effects on the flow which induced oscillations in mass flow rates. Plenum chamber restrained these oscillations by connecting all slots in circumferential direction.

2   Flow Domain

Figure 1 shows schematic of axial flow compressor setup at AFCR-NAL. Co-ordinate data for rotor and stator blades at different span were obtained by contour measuring machine. Compressor stage specifications are provided in Table 1.

Professional modeling software was used thereafter to generate rotor and stator blade profiles. Figure 2 shows modeled rotor and stator blade profiles. Flow domain as
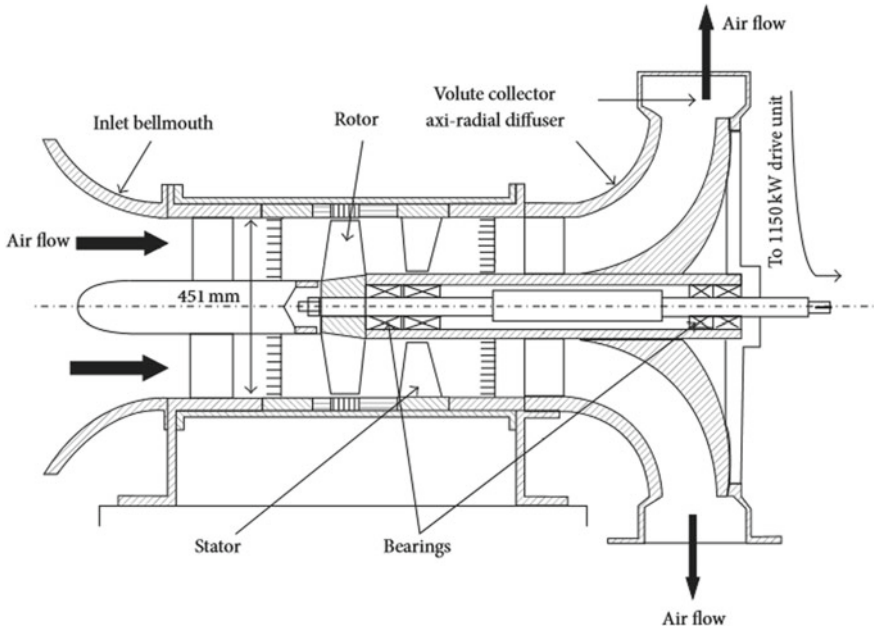
Fig. 1 Schematic axial flow compressor setup (Courtesy-AFCR NAL)

Table 1 Axial compressor design specifications

Design specifications	
No. of stages	1
Stage total pressure ratio	1.35
Corrected mass flow rate	23 kg/s
No. of rotor blades	21
No. of STATOR BLADES	18
Rotor Corrected Speed (RPM)	12930
Peak stage efficiency	86.38%
Relative Mach number (Tip)	1.15

shown in Fig. 3 was then generated for rotor and stator using blade-centric approach. In this approach, instead of modeling the whole compressor only flow for single blade is simulated assuming that flow is identical for all blades.

Flow domain was extended on both side of a blade by half a pitch of respective blades. Resulting sector was, therefore, 17.1428° for rotor and 20° for stator blade. Extension of domain on upstream of the rotor and downstream of stator was done about 2.5 times the chord length of respective blades.

Fig. 2 Rotor and stator geometry. (Courtesy: AFCR-NAL)

Rotor blade

Stator blade

Rotor

Stator

Inlet

Mixing plane interface

Outlet
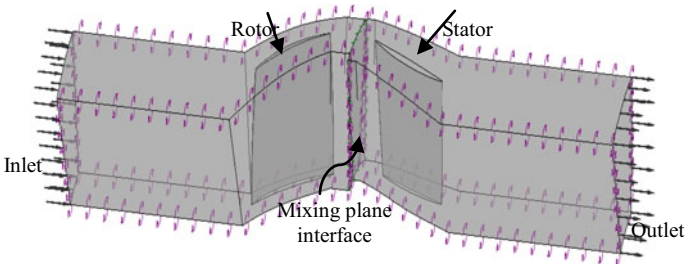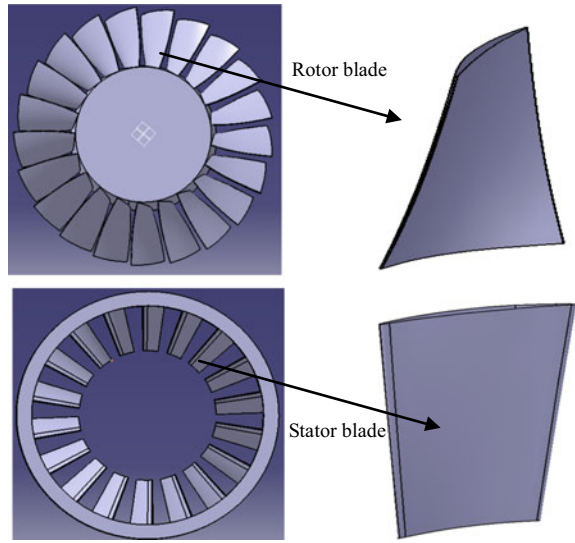
Fig. 3 Flow domain for base line model

2.1 Casing Treatment and Plenum Chamber Geometry

Bend skewed casing treatment retrofitted with plenum chamber was designed as per their profiles given in Fig. 4. Casing treatment is having bent rear section about 45° such that it follows the rotor blade tip stagger. Radial skewness of 45° is applied such that the flow emerging from the casing slots are in the opposite direction of the rotor rotation. As observed from experimental data maximum stall margin improvement was obtained for 40C placement of casing treatment. Hence, 40C location was further chosen for analysis. Two different plenum depth configurations were analyzed at same axial location of the treatment. Plenum depth was varied from half plenum to full plenum. The width of plenum chamber was equal to the axial length of casing treatment. Specifications of plenum chamber are defined in Table 2.
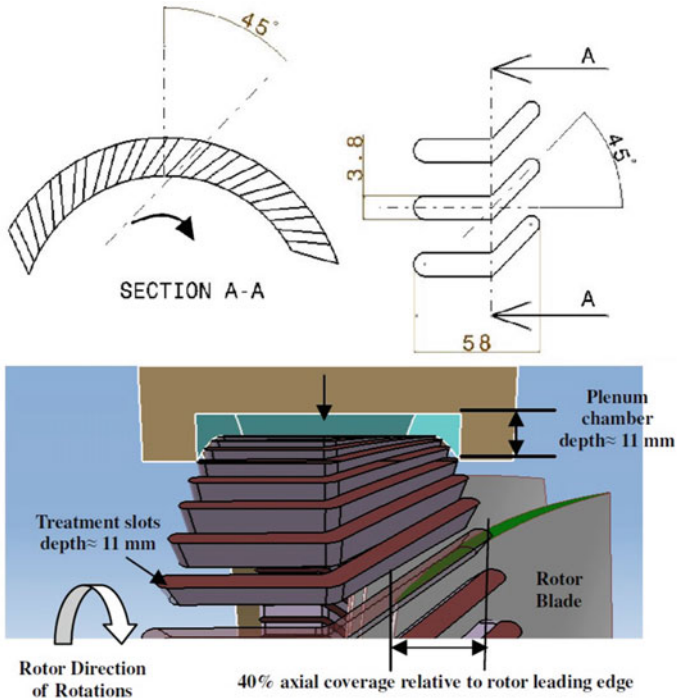
Fig. 4 Casing treatment configuration. (Courtesy-AFCR-NAL)

Table 2 Plenum chamber configuration

Casing treatment configuration	Radial depth of plenum chamber (mm)	Plenum chamber volume (m^3)
Half Plenum (HP)	5.5	457×10^{-6}
Full Plenum (FP)	11	926×10^{-6}

2.2 Domain Discretization

Structured hexahedral mesh with H-grid topology was used for both domains. Blocking strategy was used to discretize the domain. Domains were divided into blocks such that resulting mesh will follow the flow path. To maintain orthogonality of mesh and to capture boundary layer phenomenon O-grid with inflation layer was applied near the blade. Inflation layers were applied on all other walls with possibility of boundary layer formation. Nearly 120 grid points chordwise, 86 grid points circumferentially and 60 in radial direction were generated with tip gap discretized by 10 grid points. Figure 5 shows mesh distribution in rotor and stator blades.

Mesh size was calculated to be a total of about 1.4 million of which 0.8 million elements were used for rotor and 0.6 million for the stator. For casing treatment,
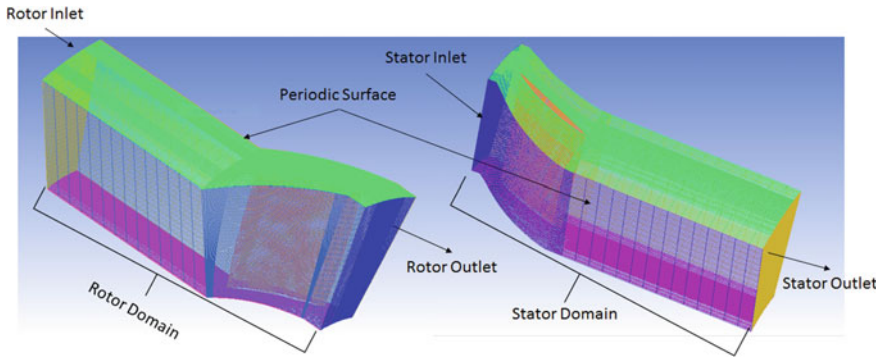
Fig. 5 Mesh distribution in base line model

5 slots were modeled which covered the whole shroud. Non-matching grids were generated near the interface which were then connected by GGI connection. Plenum chamber was modeled separately to completely overlap the casing geometry. All the domains were then imported and aligned properly in pre-processing software. Steady-state analysis was performed with air ideal gas as a fluid. Constant total pressure inlet and static pressure outlet with ambient temperature conditions were defined for flow domain as main boundary conditions. Average static pressure at outlet was varied up to stall point of the compressor. Numerical stall point was identified as a point where solution will diverge with subsequent iterations. Ambient pressure and temperature conditions were used for inlet. Turbulence was modeled using shear stress transport (SST K-ω) model. Solid walls were defined as adiabatic and no-slip condition was applied on them to obtain zero fluid velocity at walls. Conservative interface flux conditions were applied near all the interfaces. Mixing-plane method was used between the interfaces with frame changes.

3　Grid Validation

Grid independency study was carried out to establish numerical accuracy of the model. It validates that results obtained are independent of mesh element size and further refinement will not affect results significantly. Two grids as shown in Table 2, with 1.4 million and 1.8 million mesh elements were analyzed for this purpose (Table 3).

Table 3 Grid sizes used for numerical validation

Grid	Rotor elements	Stator elements	Total no. of elements
Grid A	818419	590495	1408914
Grid B	1023926	779913	1803839
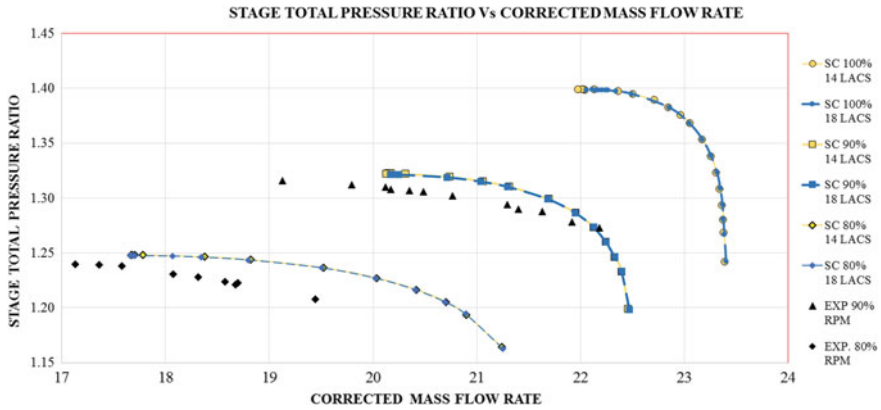
Fig. 6 Grid comparison charts (Corrected mass flow rate v/s stage total pressure ratio)
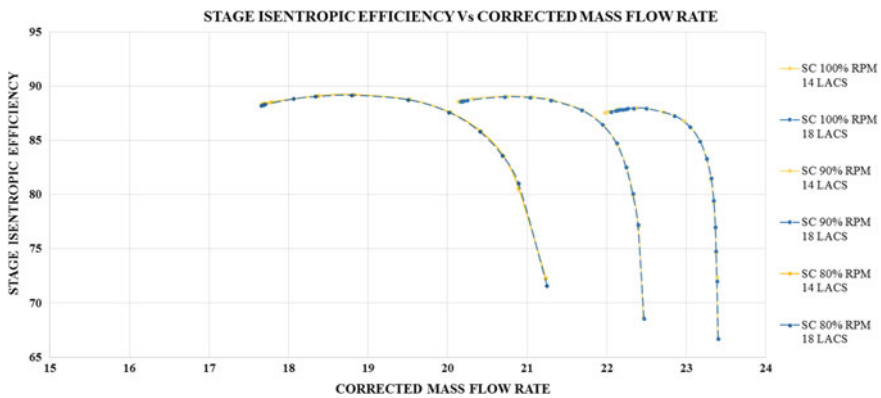
Fig. 7 Grid comparison charts (Corrected mass flow rate v/s isentropic efficiency)

Compressor performance parameters such as mass flow rate, isentropic efficiency, and total stage pressure ratio were noted down with the same boundary conditions and at three different speeds for comparison. Performance charts obtained for these grids are plotted in Figs. 6 and 7. Mesh with 1.4 million elements was then chosen for further investigation on account of less processing time and its adequate flow capturing capability.

4 Results and Discussion

Performance parameters for base line model (BLM) are derived and plotted in Figs. 6 and 7. For all cases, compressor is initially operated at lower back pressure which
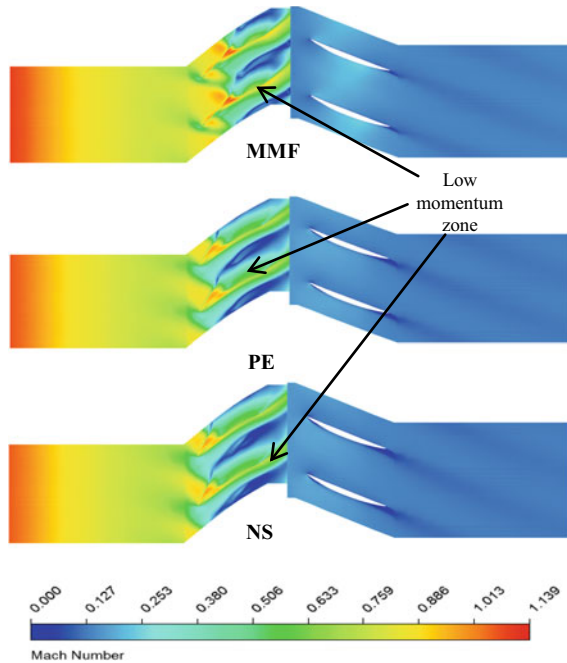
Fig. 8 Relative Mach number at 99.5% of span from hub at different operating conditions (100% RPM)

is then gradually increased until solution diverges. Near Stall (NS) condition is the condition just before the last point at which the solution converges. All the performance parameters are compared for 90 and 80% of rotation speed as experimental data is available at this speed. For contour mapping data at 100% speed is used as compressor operates in transonic region at this speed. Predicted choke mass flow rate (Corrected) by numerical method is about 22.181 kg/s which is in accordance with experimentally measured choke flow of 22.33 kg/s. Choking limit of compressor was predicted within 0.6% error. There was a slight discrepancy for stall limit as numerical approach predicted stall slightly early than experimental study. Isentropic efficiency is overestimated by simulation as flow is considered to be steady for simulation in contrast to the unsteady nature of flow in real. The total peak stage pressure ratio predicted by numerical simulation was 1.32 in agreement with the experimental peak stage pressure ratio of 1.316. To visualize the flow phenomena in blade passages contours at different locations are plotted for the solid casing. All the reference planes used for plotting contours are shown in Fig. 9. Relative Mach number contours are added for base line model at 98.5% span height for three different flow conditions—maximum mass flow, i.e., choke condition, peak efficiency, and near stall. With Increase in back pressure from MMF condition to NS condition as observed from Fig. 8, the shock shifts toward leading edge due to increased back pressure and growth in low momentum zone is also observed. Figure 10 indicates

blade to blade relative Mach number contour at near stall condition, for base line model at 99.5% span height plane drawn 0.5% from the tip.

A shock is observed at the leading edge of suction side which covers up to 20–30% of rotor chord length and half of the blade span at inlet in radial direction. Downstream of rotor large region is covered by low momentum zone. It virtually covers whole blade passage near tip circumferentially. The difference in pressure between pressure side and suction side near leading edge pushes fluid to suction side. This injected fluid interacts with shock as observed in Fig. 11 and vortex is generated near suction side, which further flows downstream at reduced speed. Static entropy contour at 98.5% span location reveals effect of vortex on flow entropy. After passing through shock wave, tip leakage vortex generates high entropy region near the trailing edge and disturbs streamlined flow. Radial extent of vortex further downstream near trailing edge is observed to be about 10–15% as depicted in Fig. 11. At 98.5% height from the hub from Fig. 12, it was observed that there is a high entropy region starting from the suction side leading edge of the rotor which travels toward the trailing edge of pressure side of adjacent blade indicating that a flow in region with high turbulence is
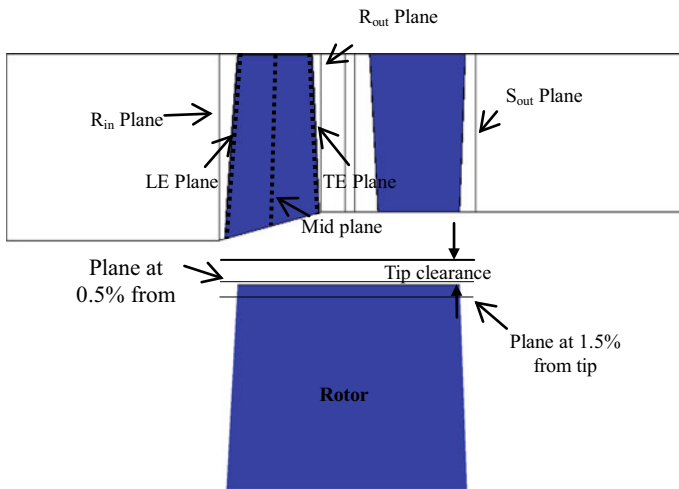
Fig. 9 Reference planes used for contour mapping
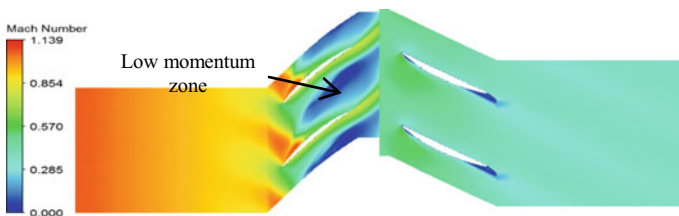
Fig. 10 Rel. Mach number distribution for NS condition at 99.5% span (100% RPM)
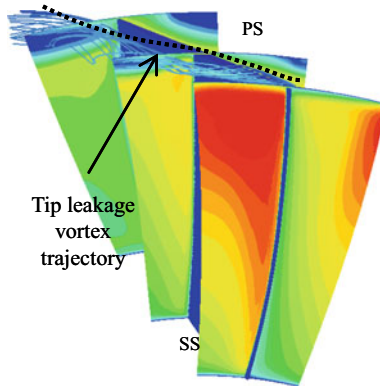
Fig. 11 Span wise Rel. Mach number distribution for NS condition (100% RPM)
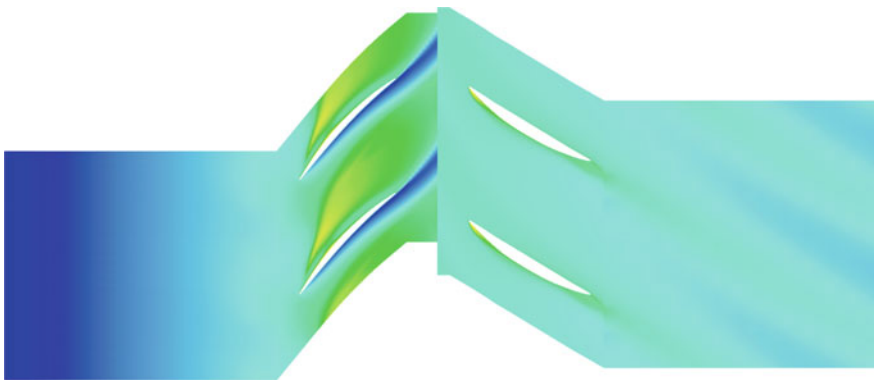
Fig. 12 Static Entropy contour at 98.5% span for SC at NS (100% RPM)

traveling along that path denoted as blade tip leading edge vortex. Blade tip leading edge vortex shown in Fig. 11 is tightly twisted in choke condition, but with increase in back pressure the twisting of the vortex is relaxed which blocks the incoming flow and leads to stall.

4.1 Effect of Casing Treatment

Figures 13, 14, 15, and 16 show the compressor performance chart with two different casing treatment configurations. Compressor peak efficiency dropped with increase in operating speeds, but stage pressure ratio increased. At lower speeds, compressor efficiency had shown marginal improvement over solid casing and there was high degradation in efficiency at 100% operating speed. The peak efficiency
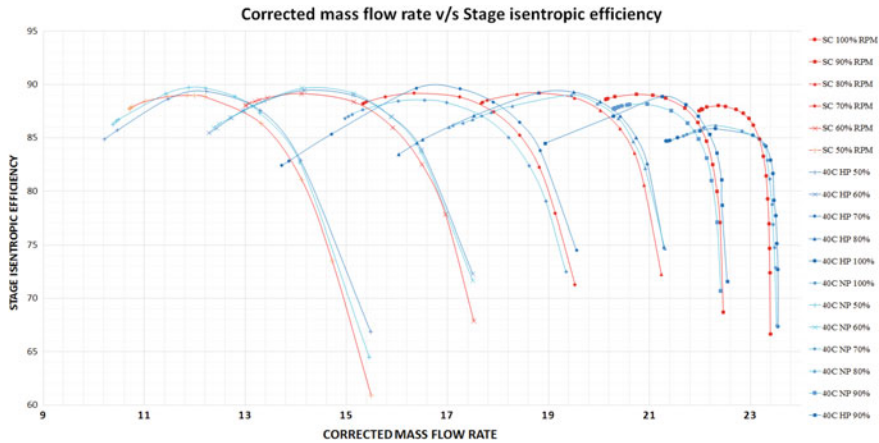
Fig. 13 Mass flow rate v/s Stage isentropic efficiency (40C HP)
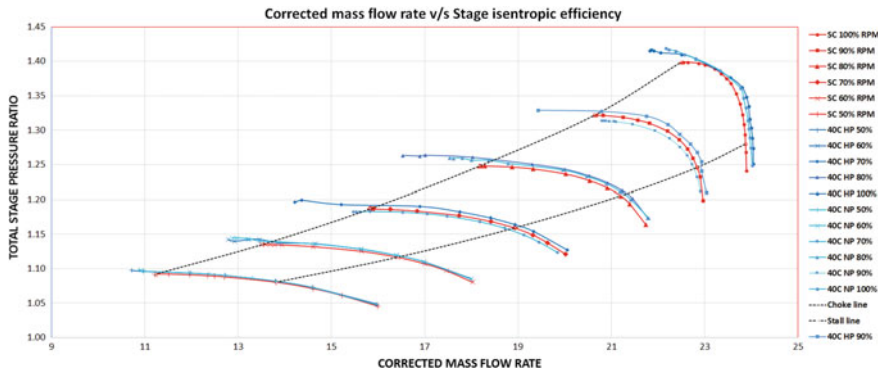
Fig. 14 Mass flow rate v/s Pressure ratio (40C HP)

for 100% speed with treatment configuration 40C FP was observed at 85.84% compared to 88.00% of solid casing at same speed. For same operating speed 40C HP configuration has peak efficiency of 85.86%. This loss in efficiency can be justified as increase in total operating volume due to increased plenum chamber depth of compressor annulus, Thus, compressor requires more work to deliver same outlet pressure. Only for lower operating speeds of 50 and 60%, 40C HP configuration has less improvement in efficiency compared to 40C FP. For remaining all operating speeds, 40C HP has lesser drop or higher improvement in efficiency compared to 40C FP. Comparison between peak efficiency of different configuration is as shown in Table 5. As shown in Fig. 15, highest total stage pressure ratio of 1.42 at a mass flow rate of 21.54 kg/s was noticed for 40C FP at 100% operating speed. For 40C HP configuration at same operating speed, peak total stage pressure ratio was observed to be 1.4165 at 21.35 kg/s. Pressure ratio at this condition was still higher than solid
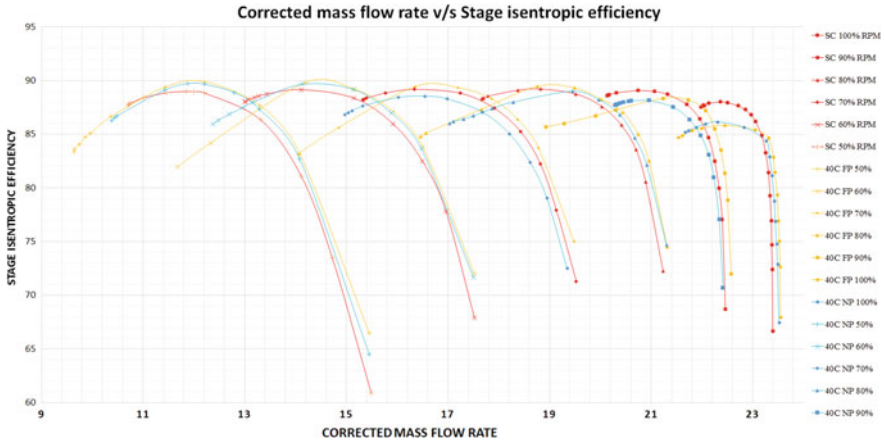
Fig. 15 Mass flow rate v/s Stage isentropic efficiency (40C FP)
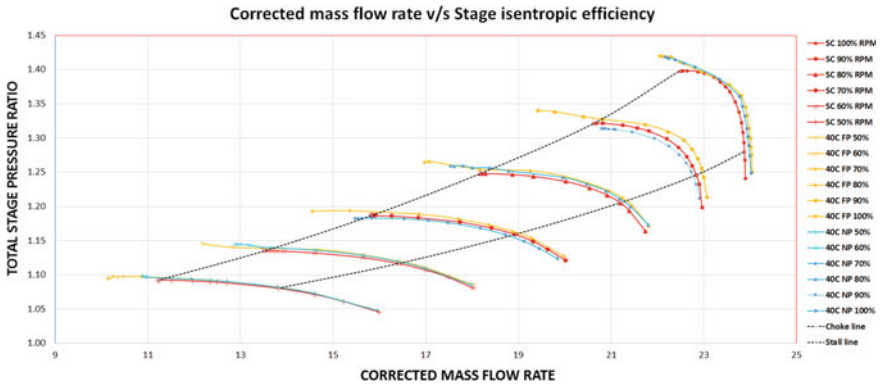
Fig. 16 Mass flow rate v/s Pressure ratio (40C FP)

casing peak total pressure ratio of 1.3987 at 22.08 kg/s mass flow rate. Stall margin improvements for 40C FP as shown in Table 4 were higher for 60% operating speed at 12.34 and 11. 59% at 50% operating speed. For 40C HP condition maximum stall margin improvement was observed at 70% operating speed of 13.47% and 11.55% at 80% operating speed. However, with increase in operating speed SMI reduces consequently for both configurations, with lowest SMI observed at 100% speed of 3.6% for 40C FP and 4.39% for 40C HP. Stall margin improvement was, however, still higher than the no plenum condition for which maximum SMI at 100% speed was 2.66%. Drop in peak efficiency was 1.85% for no plenum condition. Gradual decrement in isentropic stage efficiency is also evident from Table 5.

Compressor stall margin improvement was calculated from the equation below:

Table 4 SMI in compressor with casing treatment
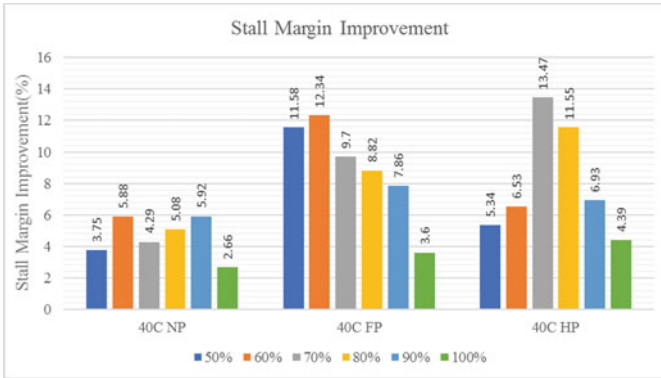
Table 5 PE drop in compressor with casing treatment
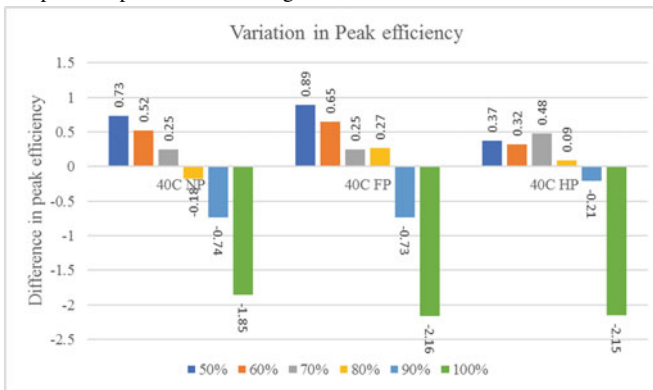
$$\text{Stall margin improvement (SMI) } (\%) = \left[\frac{\pi \text{max}_{CT} \, m_{\text{stall}, SC}}{\pi \text{max}_{, SC} \, m_{\text{stall}, CT}} - 1 \right] * 100$$

Casing treatment is designed such that flow emerging from rotor edge will have a smooth entry in the slots, and fluid from the slots would enter with swirl contrary to blade rotation. Fluid at high Mach number near tip enters the region above in casing and plenum chamber. Red patches are formed as shown in Fig. 17, where casing geometry is placed indicating flow suction in casing treatment. Shock intensity is reduced at this place. Patches formed can clearly be seen at 40C condition in Fig. 17. Instantaneous pressure rising immediately downstream of the shock is observed. Application of casing treatment has certainly reduced the low momentum zone by removing this low momentum fluid and re-injecting it with swirl. For same chord placement of CT, plenum volume has decreased low momentum zone significantly as more fluid is pushed in due to increase in volume available for flow circulation. This can be one of the factors for delay in stall and improvement in stall
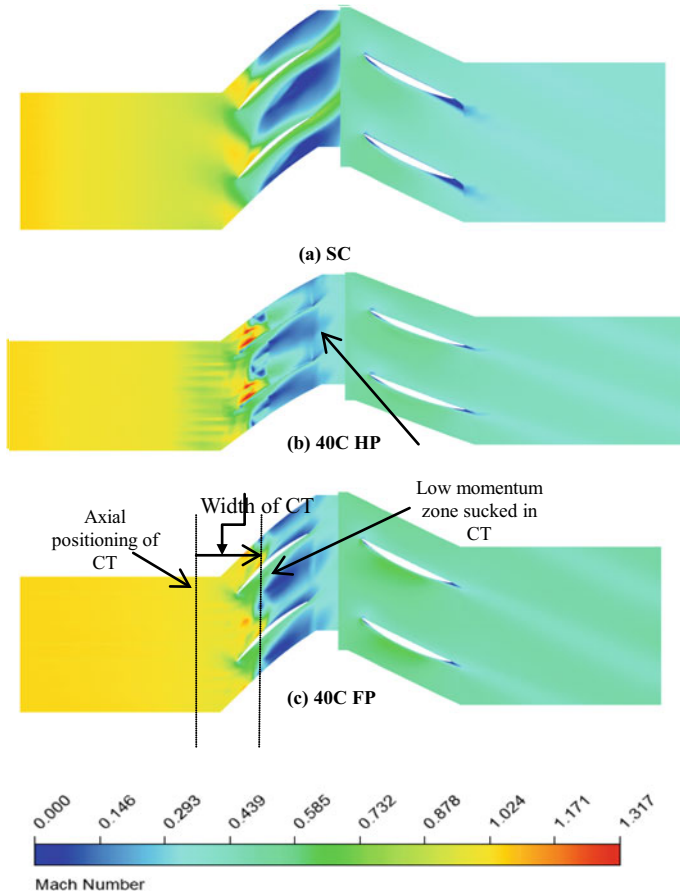
Fig. 17 Relative Mach number contours of casing treatment and solid casing at 98.5% span and NS condition (100% RPM)

margin. Figure 18 represents static entropy contours for solid casing and with casing treatment. In the casing affected region, mixing of flow increased entropy and total temperature in this region. With casing treatment applied on the compressor, there is fluid exchange between compressor and casing treatment. Flow emerging from the rotor and the returning flow from casing treatment are mixed and high entropy region is generated. Compared to half plenum condition, entropy near the casing affected region is reduced drastically for full plenum chamber configuration. This points to enhanced flow recirculation inside casing treatment due to increased depth of plenum chamber. Figure 19 shows categorization of flow inside slots depending on the patterns recognized by Wang et al. [11]. The axial co-ordinate a_0 represents the leading edge of rotor. Flow is classified based on position and velocity as follows.

Counter $(V_r > 0 \; \& \; V_z < 0, \; a < a_0)$
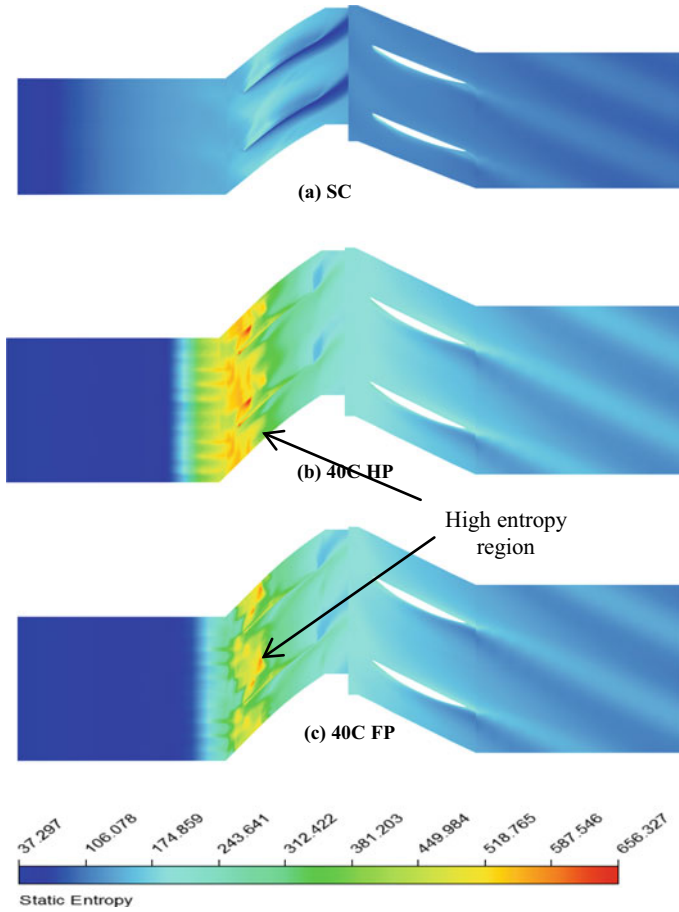
Fig. 18 Static entropy contours of casing treatment and solid casing at 99.5% span and NS condition (100% RPM)

Injection $(V_r < 0 \, \& \, V_z > 0, \, a < a_0)$
Depression $(V_r < 0 \, \& \, V_z < 0, \, a > a_0)$
Bleed $(V_r > 0 \, \& \, V_z < 0 \mid V_r > 0 \, \& \, V_z > 0, \, a > a_0)$

Inside casing slot, most favorable flow mechanisms are bleeding of flow from downstream and injecting flow back to upstream of the leading edge of rotor. Depression and counter flow has adverse effect on main flow due to upstream injection which is observed for suction side as shown in Fig. 20. The distribution of radial velocity in pitch-wise direction is plotted in Fig. 20. These contours were plotted at three different pitch-wise locations at suction side, pressure side, and at half pitch distance from pressure side. At pressure side, bleeding of fluid near the leading edge of the rotor is observed. After recirculation in casing, injection is observed. At middle plane tip, flow behavior is observed. Fluid is rushing from suction to pressure side and plenum,

Fig. 19 Flow categorization in casing slots
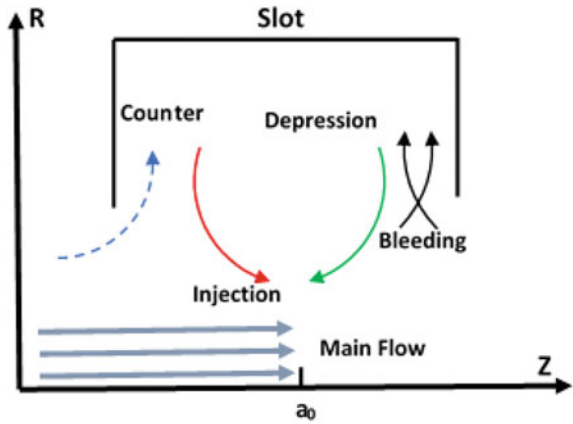
(i) Half pitch   **(ii) Pressure side**   **(iii) Suction side**
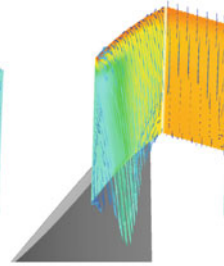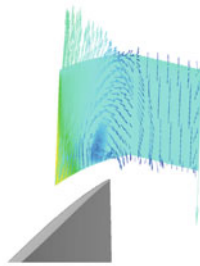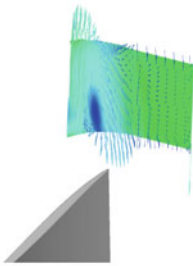
(a) 40C FP
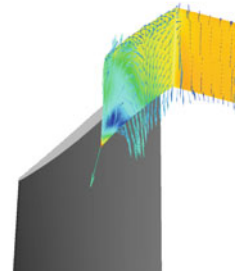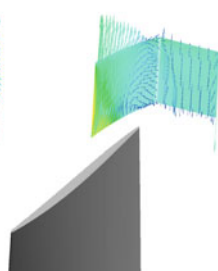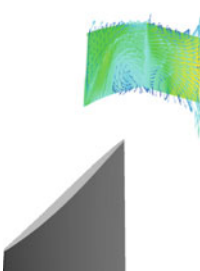
(b) 40C HP

Fig. 20 Radial velocity contours inside casing treatment at different pitch locations and NS condition (100% RPM)

fluid is further injected back to incoming flow upstream of rotor. At suction side, there is both injection and depression of fluid from CT. Apart from the bleeding counter flow entry of fluid is also observed. From velocity contour at half pitch it is clear that low momentum zone is sucked in by casing treatment as previously indicated in Fig. 17. Figure 21 shows radial distribution of velocity at three different streamwise locations, at leading edge, middle, and trailing edge of casing treatment. Here leading edge refers to the edge of CT which is first to encounter the incoming flow. Near the leading edge of rotor flow from small tip gap between rotor and shroud, casing treatment bleeds some amount of this flow and reinjects it near suction side which stabilizes the flow. At trailing edge, it is observed that flow from pressure side is recirculated in plenum and re-injected back into the suction side of adjacent blade, near the casing affected region. Blade loading diagram at 95 and 98.5% span height for Near shock occurred at 30% chord location. Placement of treatment at 40% chord length reduced the intensity of shock. Instead of sudden pressure rise, gradual increment is observed. As casing and plenum volume is directly placed above the shock region, it bleeds more fluid in it and pushes shock further downstream. Shock occurs after passing through the region below casing treatment. It is clearly
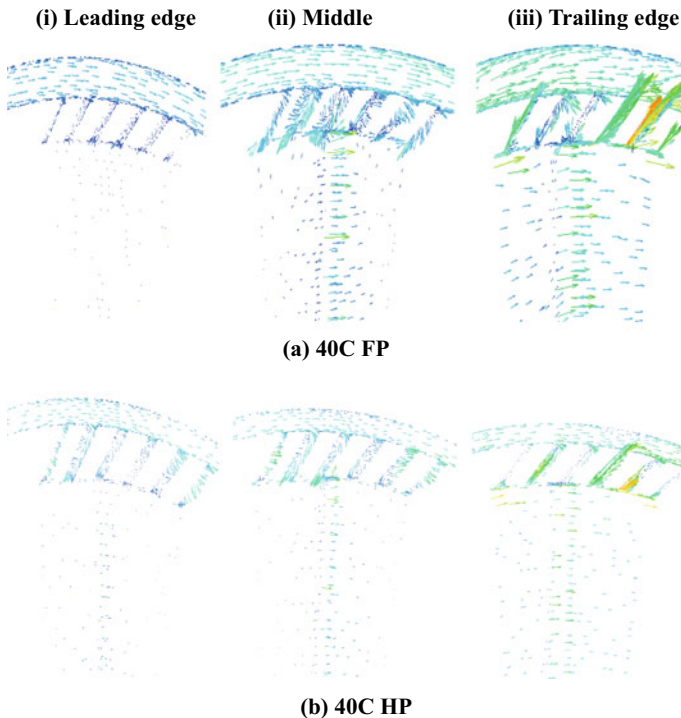
Fig. 21 Radial velocity contours inside casing treatment at different stream locations for NS condition (100% RPM)

indicated at 40% location as shock intensity reduces due to plenum volume implementation and more fluid will be pushed into the plenum. Blade loading at 98.5% is shown in Fig. 22. Compared to 95% there is higher pressure difference between suction and pressure side surface at 98.5% condition which is a driving force for tip leakage vortex formation. Placing the casing treatment at 40% chord smoothens the flow for that region and shock is pushed to downstream. After passing through shock, pressure rises evenly on suction surface, which indicates smooth flow lines after shock in configuration with casing treatment than solid casing. Static entropy distribution over hub to shroud region near leading edge of the rotor for near stall condition is plotted in Fig. 23. Flow has higher entropy due to flow recirculation
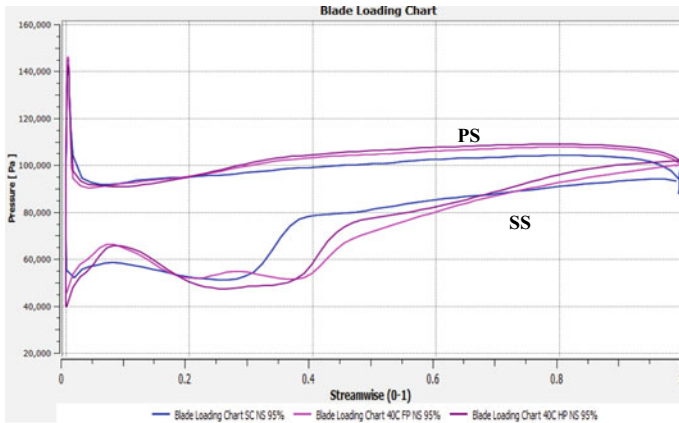
(a) 95%
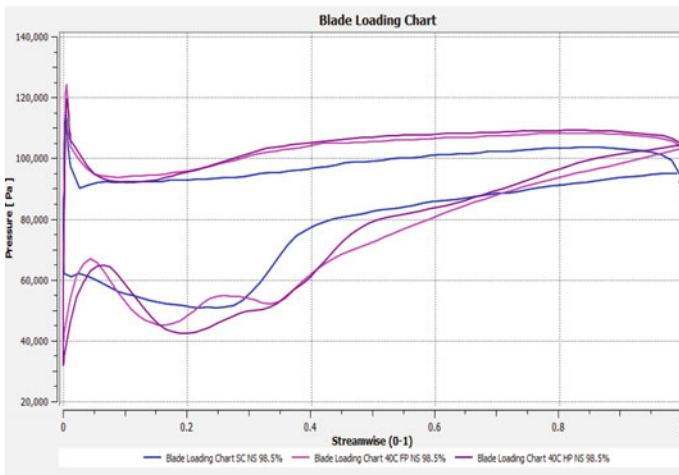
(b) 98.5%

Fig. 22   Blade loading chart at different span location (100% RPM)
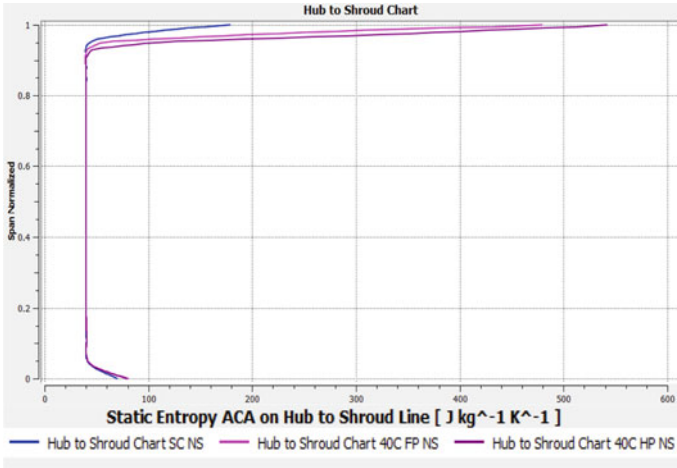
Fig. 23 Radial distribution of Static entropy at NS condition

and injection in CT affected region. Static entropy for treatment configuration was higher compared to the base line model. This was in evidence as already discussed due to mixing of casing fluid with the main flow. However, plenum depth does have impact in entropy as plenum volume provided more space for recirculation inside the casing. With increase in plenum chamber, space for flow recirculation increases and hence there is reduction in entropy. Total temperature distribution over hub to shroud has been plotted in Fig. 24. Chart is plotted at the leading edge of rotor. Total temperature at the tip location is higher in 40C FP compared to base line model, and this is due to mixing of fluid in the region due to presence of casing treatment. Hub
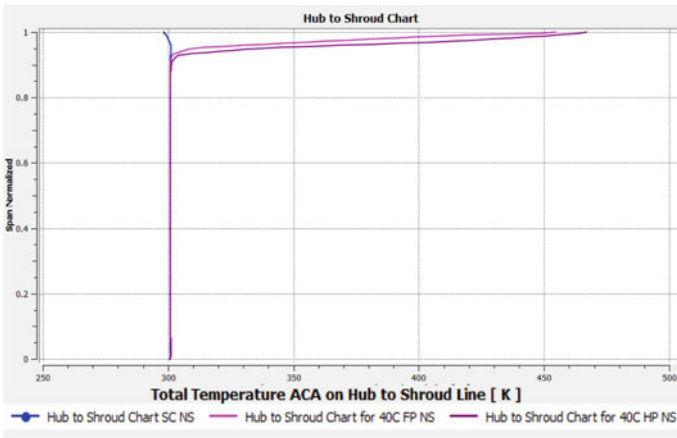
Fig. 24 Radial distribution of total temperature at NS (100% RPM)

to shroud contours as shown in Fig. 25 were extracted little upstream of rotor leading edge and downstream of stator and rotor trailing edges. Reference planes as shown in Fig. 9 were used for plotting. Blue region at the rotor outlet and stator outlet contour represents low-speed region after the blade. There is also boundary layer separation on suction side as indicated by blue low-speed region which is near suction side of blade. Plane upstream of rotor indicates the shape of shock formation. As seen in Fig. 25, bow shock is being generated in the rotor with higher intensity near tip region; this intensity gradually reduces toward hub. A strong bow shock observed in base line model is weakened by casing treatment configuration. Blue region near tip of the rotor outlet plane is a low-speed region generated due to blade tip vortex. This region covers almost about 10–15% rotor span height and 70–80% of blade passage near leading edge. To observe shock coverage from hub to shroud, distribution of relative Mach number at 100% speed, near leading edge of rotor has been plotted. These contours are plotted for full 360° revolution of the rotor. As observed before, casing is more effective for compressor operating at near stall condition. From Fig. 26, it is clear that in base line model shock coverage from shroud to hub is higher compared to casing treatment configuration. In 40% chord location coverage of shock from shroud to hub is reduced as compared to solid casing.

5   Conclusions

1. Stall margin was improved on application of all configurations of casing treatment fitted with plenum chamber.
2. Maximum stall margin improvement of 12.34% was observed for 40C FP casing treatment configuration at 50% rotational speed and 11.47% for 40C HP configuration at 70% operating speed.
3. There was a drop in peak efficiency of compressor at high rotational speeds. Maximum drop of 2.16% was observed at 100% rotational speed for 40C FP and 2.15% for 40C HP condition.
4. Minor improvement in peak efficiency was observed for both casing treatment configurations at lower rotational speeds.
5. Casing treatment smoothened the flow near the tip region by providing damping effect near tip region. This effect was enhanced by increase in plenum chamber volume as more space was allowed for flow recirculation.
6. Numerical results of the solid casing and casing treatment were agreed well with the experimental data.
7. A shock of bow shape was observed upstream of the rotor. Its intensity was reduced by casing and plenum configurations.
8. Location of shock was pushed downstream of the flow by casing treatment as casing removes the shock from the region directly below it.
9. Low momentum zone which was generated after shock was reduced by casing treatment.

(a) SC

(b) 40C HP

(c) 40C FP
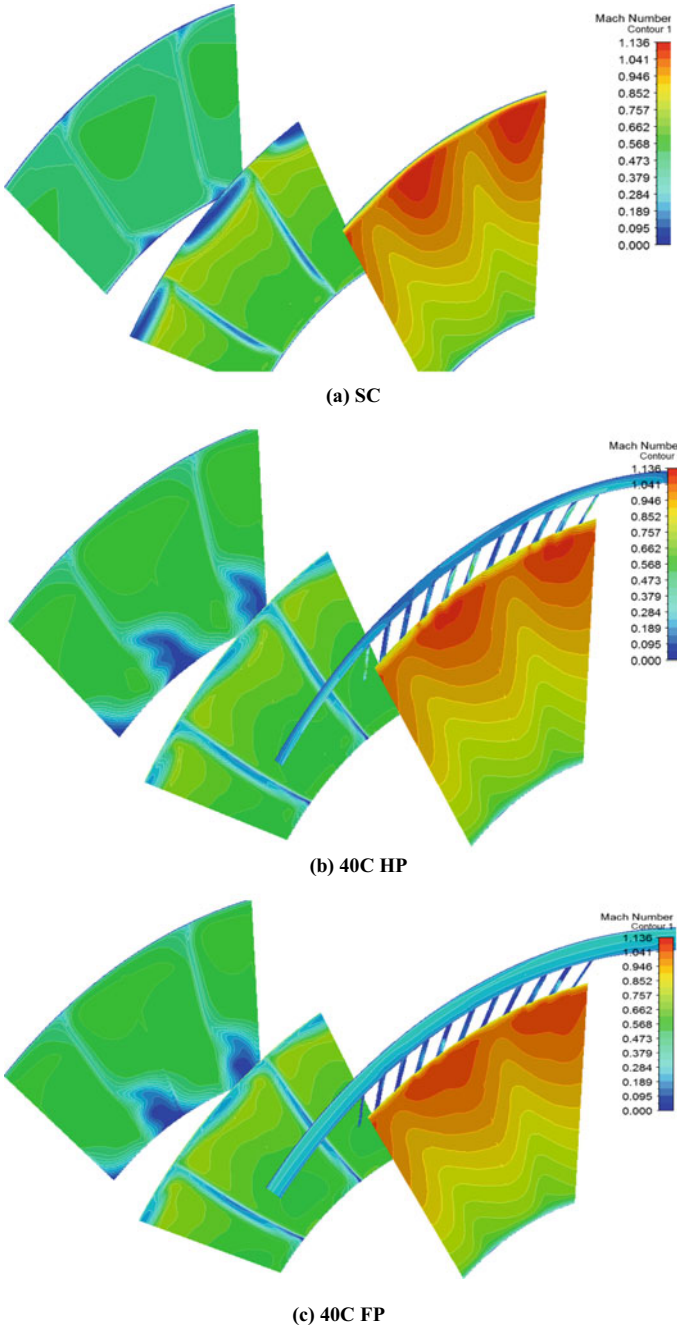
Fig. 25 Relative Mach number contours from hub to shroud at three reference locations and NS condition (100% RPM)

(a) SC   (b) 40C FP

(c) 40C HP
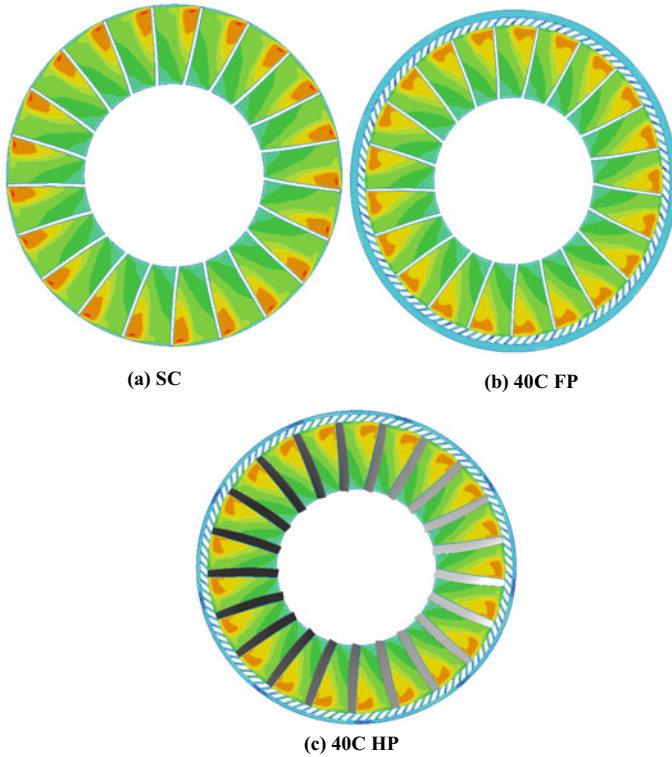
Fig. 26 Hub to shroud distribution of relative Mach number near rotor leading edge and NS condition (100% RPM)

10. High entropy region was generated with high total temperature near casing treatment due to flow recirculation and mixing.
11. Near the pressure side of blade flow recirculation by bleeding and injection was pre-dominant whereas near suction side depression and counter flow were observed.

References

1. Alone DB, Kumar SS, Thimmaiah MS, Mudipalli JR, Pradeep AM, Ramamurthy S, Iyengar VS (2014) Performance characterization of the effect of axial positioning of bend skewed casing

treatment retrofitted to a transonic axial flow compressor. In: Proceedings of ASME Turbo Expo 2014: Turbine technical conference and exposition. Düsseldorf, Germany

2. Suder KL, Celestina ML (1996) Experimental and computational investigation of the tip clearance flow in a transonic axial compressor rotor. ASME 118

3. Thompson DW, King PI, Rabe DC (1998) Experimental investigation of stepped tip gap effects on the performance of a transonic axial-flow compressor rotor. ASME 120

4. Beselt Ch, Eck M, Peitsch D (2014) Three-dimensional flow field in highly loaded compressor cascade. ASME 136

5. Haixin C, Xudong H, Song Fu (2006) CFD investigations on stall mechanisms and casing treatment of a transonic compressor. In: 42nd AIAA/ASME/SAE/ASEE joint propulsion conference and exhibit

6. Ross MH, Cameron JD, Morris SC, Haixin C, Ke Shi (2018) Axial compressor stall, circumferential groove casing treatment, and the tip-clearance momentum flux. J Propuls Power 34(1):146–152

7. Legras G, Castillon L, Trebinjac I, Gourdain N (2011) Flow Mechanisms induced by non-axisymmetric casing treatment in a transonic axial compressor. In: Proceedings of the 10th international symposium on experimental computational aerothermodynamics of internal flows. Brussels, Belgium

8. Shivayogi AK, Nagpurwala QH, Deshpande MD (2009) Numerical studies on the effect of slotted casing treatment on the performance of a transonic axial flow compressor. SASTECH 8(2)

9. Emmrich R, Honen H, Niehuis R (2007) Time resolved investigations of an axial compressor with casing treatment Part 1 experiment. In: ASME Turbo Expo 2007: power for land, sea and air, Montreal, Canada

10. Emmrich R, Kunte R, Honen H, Niehuis R (2007) Time resolved investigations of an axial compressor with casing treatment Part 2 simulation. In: ASME turbo expo 2007: power for land, sea and air, Montreal, Canada

11. Wang W, Wuli C, Zhang H (2015) Numerical Investigation on the effect of a plenum chamber with slot-type casing treatment on the performance of an axial transonic compressor. J Power Energy 229(4):393–405

12. Alone DB, Kumar SS, Thimmaiah MS, Mudipalli JR, Pradeep AM, Ramamurthy S, Iyengar VS (2014) on understanding the effect of plenum chamber of a bend skewed Casing treatment on the performance of a transonic axial flow Compressor. In: Proceedings of ASME Turbo Expo 2014: Turbine technical conference and exposition GT2014. Düsseldorf, Germany

Sensitivity Analysis of Weight Coefficients Used in Multiobjective Optimization in Genetic Algorithm Method for Axial Flow Compressor Design

NB Balsaraf and S. Kishore Kumar

Abstract The sensitivity of the fitness function comprising of weight coefficients assigned to performance variables in a genetic algorithm for meanline design of a transonic compressor is studied. The sum of the weight coefficients is unity. Six performance variables considered are the pressure ratio, efficiency, De-Haller numbers (for rotor and stator), and diffusion factors (for rotor and stator). Based on prior trials, the optimum weight coefficients for pressure ratio and efficiency were considered 0.3 each in the fitness function. Hence the sum of the weight coefficients for the two De-Haller Numbers and two Diffusion Factors considered is 0.4. The values of assigned weights have a significant impact on optimization outcome. Optimized design trials of weight coefficients with higher weightage to DFR resulted in higher efficiency with lower pressure ratio. Optimized design trials with higher weightages to DEHR and DEHS yielded into higher pressure ratio but lower efficiency. The data generated provides a guideline to choose combinations of weight coefficients for fitness functions for several performance requirements of a similar class of compressors for various applications.

Keywords Compressor design optimization · Genetic algorithm · Fitness function · Weighing functions · Meanline design

Nomenclature

Units

AR	Blade Aspect Ratio
3-D	Three-Dimensional
CFD	Computational Fluid Dynamics
DEHR	Rotor De-Haller Number

N. Balsaraf (✉) · S. Kishore Kumar
Gas Turbine Research Establishment, Bangalore, Karnataka, India
e-mail: nitinbalsaraf@gtre.drdo.co.in

DEHS   Stator De-Haller Number
DFR   Rotor Diffusion Factor
DFS   Stator Diffusion Factor
F   Fitness function
GA   Genetic Algorithm
H   Total enthalpy (J)
K   Flow blockage factor
N   Rotational speed rpm
P   Total Pressure (Pa)
PR   Total Pressure Ratio
T   Total temperature (K)
U   Blade velocity (m/s)
V   Absolute air velocity (m/s)
W˙   Mass flow rate (kg/s)
w   Weight coefficient

Symbols

α   Swirl
Δ   Property change (inlet to outlet)
η   Efficiency
γ   Ratio of specific heats
σ   Solidity
φ   Flow coefficient
ψ   Loading coefficient

Subscripts

1   Rotor inlet
2   Rotor exit
3   Stator inlet
4   Stator exit
θ   Circumferential direction
z   Axial direction

1 Introduction

Axial compressor design is an iterative process. The design is dependent on the designer's expertise and analysis tools. Multistage axial flow compressor design involves a choice of a large number of independent design variables which control design objectives like maximization of efficiency, maximization of total pressure ratio, maximization of mass flow rate, minimization of weight, maximization of durability as discussed in [1–7]. These design objectives have a conflicting requirement and achieving these design requirements largely depends upon choice and values of design variables. Optimization is very much essential to meet the required design objectives in a shorter time frame. The simplest approach to solve a multiobjective optimization problem is to combine all objectives into a single fitness function. Single fitness function method generally uses traditional methods like linear sum of weighing functions assigned to objective function. This approach consists of adding all the objective functions together using different weight coefficients for each one. The weight coefficients represent the relative importance of the objective function. It converts multiobjective optimization problem into a scalar optimization problem. The weight coefficients are generally selected in proportion to their importance.

In compressor design, the relative importance of the assigned weight coefficient to the objective function is subjected to design requirements. Detail study of the sensitivity of these weight coefficients on the aerodynamic performance of the transonic compressor is not available in the public domain. This study will provide the effect of the relative importance of weight coefficients assigned to objective functions on the aerodynamic performance of the compressor. The data generated will provide guidelines for the appropriate selection of values of weight coefficient for different design requirements.

2 Optimization

Genetic Algorithm (GA) and Artificial Neural Network (ANN) are the most popular methods to optimize turbomachinery designs which are multiobjective in nature. The genetic algorithm is a method for solving both constrained and unconstrained optimization problems. It is based on natural selection, the process that drives biological evolution as described in [8, 9].

Fitness function used in axial flow compressor design optimization is a multiobjective function with an assigned weight coefficient. Objective functions for compressor design optimization are pressure ratio, efficiency, and operating margin.

3   Fitness Function Formulation

The formulation of the optimization fitness function to evaluate the compressor performance is given below.

$$\text{Fitness function} = w_1 PR + w_2 \eta + w_3 DEHR + w_4 DEHS + w_5 DFR + w_6 DFS \quad (1)$$

PR is pressure ratio, η efficiency, DEHR Rotor De-Haller No., DEHS stator De-Haller No., DFR rotor diffusion ratio and DFS stator diffusion ratio. The definition of these design objects are explained in reference [10]. w_1, w_2, w_3, w_4, w_5 and w_6 are weight coefficients for the respective objective function. The summation of all the objective weight coefficients is one.

The fitness function is a combination of maximization of some of the functions (PR, η, DEHR and DEHS) and minimization of remaining functions (DFS and DFR). The objective weights for minimizing DFS and DFR are w'. As fitness function is to be maximized, the objective weights assigned to the objective function to be minimized are revised as below.

$$w_5 = (1 - w'_5) \quad (2)$$

$$w_6 = (1 - w'_6) \quad (3)$$

Three independent design variables namely stage loading coefficient, flow coefficient and swirl angle to rotor inlet are considered for performance optimization.

The lower and upper bounds for the stage loading coefficient (ψ) are 0.35 and 0.65 The lower and upper bounds for the flow coefficient (φ) are 0.35 and 0.65 The lower and upper bounds for rotor inlet swirl (alpha1) are 0 and 10 degrees. The choices of ranges of design variables are based on ref. [11]. Rotor profile pressure loss and shock loss calculations are based on test data and computational fluid dynamic analysis of similar types of compressors and available literature [12–14].

The initial population size is chosen as 100 generations. The selection function is based on the stochastic method. The elite count in reproduction is 2. The crossover fraction is 0.6. The mutation fraction is 0.06. For convergence of the code, the function tolerance is taken as 1e-06. Refs. [15–17] discusses population, stochastic method size, crossover and mutation fraction selection. Assessment and validation of these methods are discussed in detail in ref. [18].

4   Sensitivity Study of Weight Coefficients

Weight coefficients of the performance variables used in fitness function dictate the performance specifications. A sensitivity study of fitness function on existing design has been conducted. There are six performance variables. The two most

important performance variables out of the six are pressure ratio and efficiency. Weight coefficients of pressure ratio and efficiency considered are 0.3 each based on sensitivity study of the weight coefficient carried out for these variables as discussed in ref. [19]. Keeping weight coefficients of pressure ratio and efficiency constant weight coefficients of DEHR, DEHS, DFR and DFS are altered. Increase in weight coefficient on one of these functions is compensated by a decrease in the weightage of the other coefficients maintaining total weightage of all weight coefficients one.

4.1 Design Constraints

Based on interface components, the additional constraints imposed are maximum blade tip speed, maximum tip inlet diameter, axial length, exit hub and tip dimension. Based on the analysis of the existing design, mean solidity and aspect ratio of rotor and stator are modified and considered for the optimization to ensure minimal changes in overall dimensions of the compressor.

4.2 Design Trials

The details of design trials carried out for a combination of DEHR, DEHS, DFR, and DFS are plotted in Fig. 1.

5 Results and Discussion

Design trials of weight coefficients 0.4 of individual performance variables are carried out as shown in Table 1.

Results of optimized design trials of weight coefficient 0.4 are tabulated in Table 2.

Optimized design trials of DFS and DFR with 0.4 weighing function each resulted in maximum efficiency with a reduction in pressure ratio. Optimized DFS and DFR trial shows higher operating margin and efficiency at the cost of pressure ratio.

Optimized design trials of DEHS and DEHR with 0.4 weighing function each resulted into a higher pressure ratio with a slight reduction in efficiency.

Plots of fitness function with performance variables for optimized iterations of design trials of weight coefficient 0.4 of individual performance variables are shown in Fig. 2.

Design trials were carried out with 0.3 weight coefficient for one of the functions and varying weight coefficients of other variables to maintain the sum of weight coefficient to 0.4 for DEHR, DEHS, DFR and DFS. The design trials are carried out for weight coefficient combination as mentioned in Table 3.

Results of optimized design trials of weight coefficient 0.3 are tabulated in Table 4.
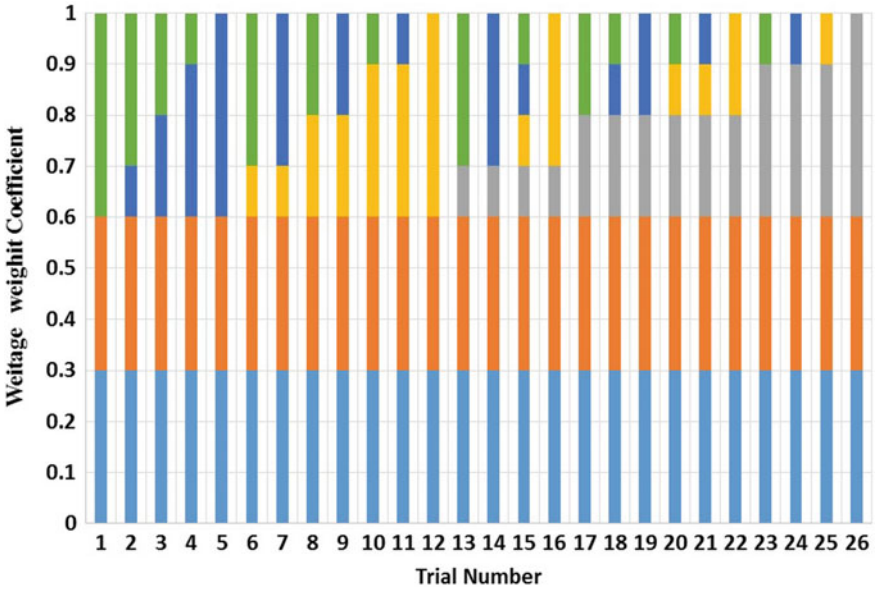
Fig. 1 Design trials carried out for combinations of weight coefficients

Table 1 Design trials of weight coefficient (0.4)

Sl. No.	PR	η	DEHR	DEHS	DFR	DFS
1	0.3	0.3	0	0	0	0.4
2	0.3	0.3	0	0	0.4	0
3	0.3	0.3	0	0.4	0	0
4	03	0.3	0.4	0	0	0

Table 2 Results of 0.4 weight coefficient trials

Sl. No.	Weighing function (0.4)	Aerodynamic performance					
		PR	$\eta(\%)$	DEHR	DEHS	DFR	DFS
1	DFS	1.54	88.5	0.662	0.762	0.504	0.487
2	DFR	1.55	88.5	0.660	0.758	0.508	0.492
3	DEHS	1.578	88.3	0.648	0.745	0.526	0.512
4	DEHR	1.584	88	0.644	0.738	0.533	0.52

Optimized design trial of weight coefficient combination of 0.3DEHS and 0.1DFR yielded into maximum pressure ratio. The optimized design trial of the weight coefficient combination of 0.3DFR and 0.1DFS resulted in maximum efficiency. The optimized design trials of the weight coefficient combination of 0.3DFS and 0.1DFR yielded into higher operating margin at the cost of pressure ratio and efficiency.
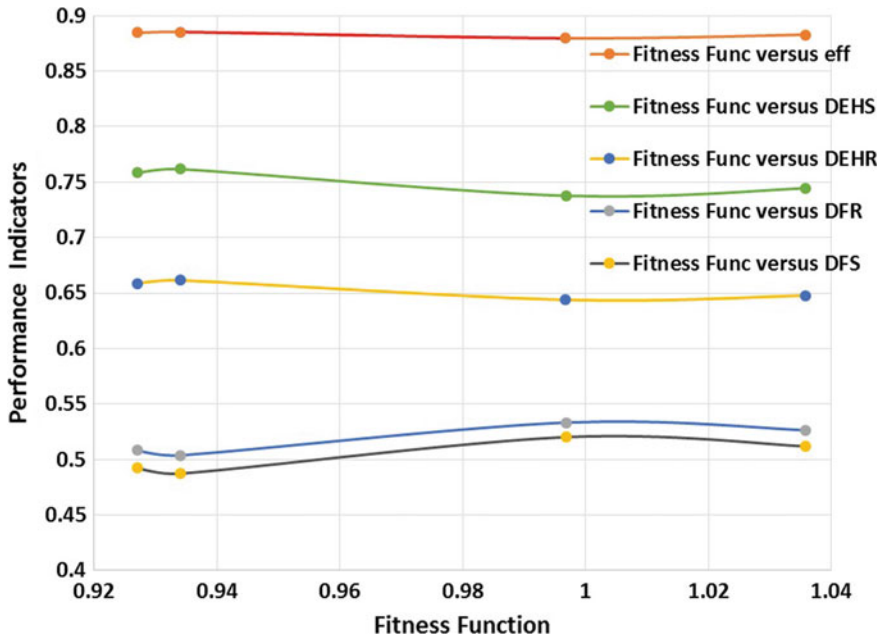
Fig. 2 Fitness function versus performance variables for 0.4 weight coefficient

Table 3 Design trials of weight coefficient (0.3)

Si. No.	PR	η	DEHR	DEHS	DFR	DFS
1	0.3	0.3	0	0	0.1	0.3
2	0.3	0.3	0	0	0.3	0.1
3	0.3	0.3	0	0.1	0	0.3
4	0.3	0.3	0	0.1	0.3	0
5	0.3	0.3	0	0.3	0	0.1
6	0.3	0.3	0	0.3	0.1	0
7	0.3	0.3	0.1	0	0	0.3
8	0.3	0.3	0.1	0	0.3	0
9	0.3	0.3	0.1	0.3	0	0
10	0.3	0.3	0.3	0	0	0.1
11	0.3	0.3	0.3	0	0.1	0
12	0.3	0.3	0.3	0.1	0	0

Table 4 Results of 0.3 weight coefficient trials

Sl. No.	Weight coefficient (0.3)/(0.1)	Aerodynamic performance					
		PR	$\eta(\%)$	DEHR	DEHS	DFR	DFS
1	DFS/DFR	1.50	88.1	0.688	0.783	0.474	0.455
2	DFR/DFS	1.56	88.5	0.655	0.754	0.514	0.499
3	DFS/DEHS	1.548	88.4	0.66	0.758	0.507	0.491
4	DFR/ DEHS	1.57	88.4	0.651	0.749	0.521	0.506
5	DEHS/ DFS	1.557	88.3	0.655	0.753	0.514	0.500
6	DEHS/ DFR	1.588	88	0.642	0.737	0.536	0.522
7	DFS/DEHR	1.549	88.4	0.659	0.758	0.508	0.492
8	DFR/DEHR	1.576	88.3	0.648	0.745	0.526	0.512
9	DEHS/DEHR	1.589	88.1	0.643	0.738	0.535	0.521
10	DEHR/ DFR	1.594	87.9	0.640	0.734	0.54	0.527
11	DEHR/DFS	1.574	87.7	0.644	0.736	0.533	0.521
12	DEHR/ DEHS	1.588	88	0.643	0.737	0.535	0.521

Plots of fitness function with performance variables for optimized iterations of design trials of weight coefficient 0.3 of individual performance variables are shown in Fig. 3.

Design trials are carried out with 0.2 weight coefficient for one or two of the functions and varying weight coefficients of other variables to maintain the sum of weight coefficient to 0.4 for DEHR, DEHS, DFR and DFS. The design trials were carried out for weight coefficient combination as shown in Table 5.

Results of optimized design trials of weight coefficients 0.2 are tabulated in Table 6.

Optimized design trial of weight coefficient combination of 0.2DEHR, 0.1DEHS and 0.1DFS yielded maximum pressure ratio with lesser operating margin. Optimized design trials of weight coefficient combination of 0.2DEHS and 0.2DFR yielded maximum efficiency with a higher operating margin at the cost of pressure ratio.

Plot of fitness function with performance variables for optimized iterations of design trials of weight coefficient 0.2 of individual performance variables is shown in Fig. 4.

Design trials are carried out with a weight coefficient combination of 0.1DEHR, 0.1DEHS, 0.1DFR and 0.1DFS as shown in Table 7.

The optimized solution of this trial resulted in DEHR as 0.643, DEHS as 0.739, DFR as 0.534, DFS as 0.520 with PR of 1.588 and efficiency of 88.15. This optimized design trial gave the highest pressure ratio with efficiency slightly lower than the maximum among all the trials.
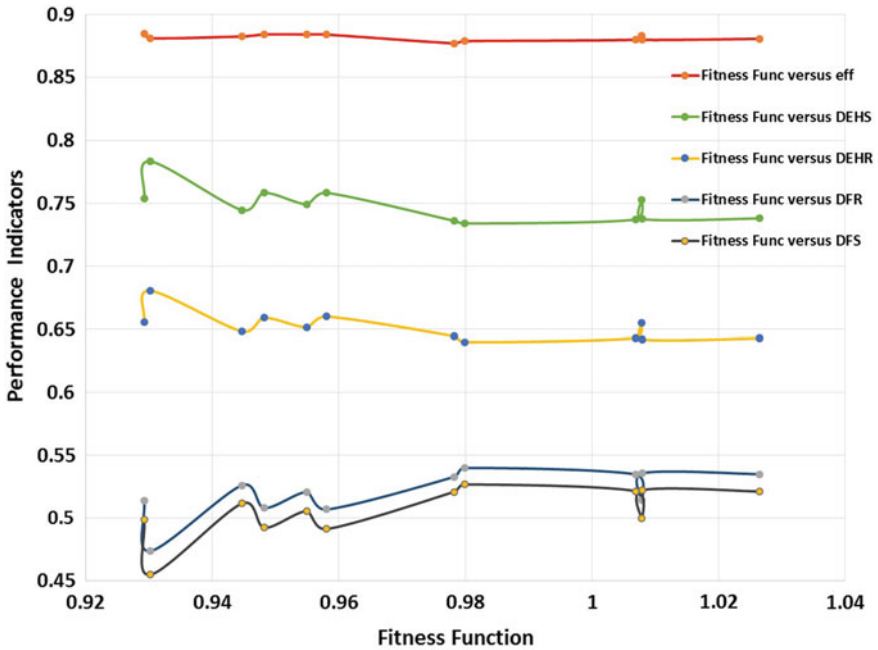
Fig. 3 Fitness function versus performance variables for 0.3 weight coefficient

Table 5 Design trials of weight coefficient (0.2)

Si. No.	PR	η	DEHR	DEHS	DFR	DFS
1	0.3	0.3	0	0	0.2	0.2
2	0.3	0.3	0	0.2	0	0.2
3	0.3	0.3	0	0.2	0.2	0
4	0.3	0.3	0.2	0	0	0.2
5	0.3	0.3	0.2	0	0.1	0.1
6	0.3	0.3	0.2	0	0.2	0
7	0.3	0.3	0.2	0.1	0	0.1
8	0.3	0.3	0.2	0.1	0.1	0
9	0.3	0.3	0.2	0.2	0	0

6 Conclusion

Figure 5 shows the results of optimum solution trial for all the optimized trials of weighing function 0.4, 0.3, 0.2 and 0.1.

Optimized design trials of weighing function with higher weightage to DFR resulted in higher efficiency with lesser pressure ratio. Optimized design trials with

Table 6 Results of design trials of weight coefficient 0.2

Si. No.	Weight coefficients (0.2)/(0.2)	Aerodynamic performance					
		PR	$\eta(\%)$	DEHR	DEHS	DFR	DFS
1	DFR/DFS	1.554	88.0	0.656	0.749	0.515	0.501
2	DEHS/ DFS	1.57	88.4	0.651	0.748	0.522	0.507
3	DEHS/ DFR	1.537	88.5	0.665	0.766	0.499	0.482
4	DEHR/DFR	1.572	88.2	0.648	0.745	0.525	0.511
5	DEHR/DFS	1.579	88.2	0.647	0.743	0.528	0.513
6	DEHR/DEHS	1.568	88,2	0.650	0.746	0.523	0.509
Si. No	Weighing function (0.2)/(0.1)/(0.1)	PR	$\eta(\%)$	DEHR	DEHS	DFR	DFS
7	DEHR/ DFR/DFS	1.576	88.3	0.648	0.745	0.526	0.512
8	DEHR/DEHS/DFS	1.587	87.7	0.642	0.733	0.537	0.525
9	DEHR/DEHS/DFR	1.578	88.3	0.647	0.741	0.528	0.515
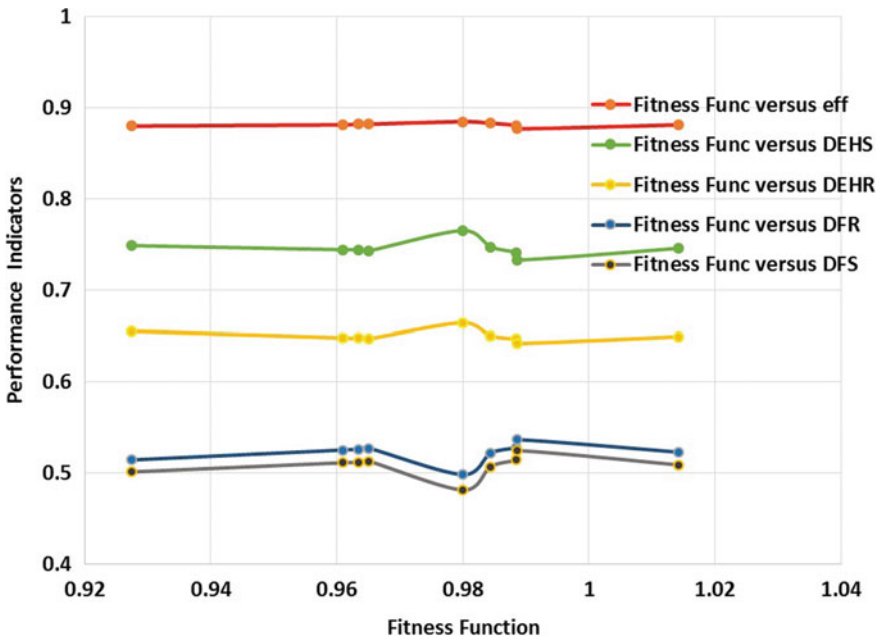
Fig. 4 Fitness function versus performance variables for 0.2 weight coefficient

Table 7 Design trials of weight coefficient (0.1)

Si. No.	PR	η	DEHR	DEHS	DFR	DFS
1	0.3	0.3	0.1	0.1	0.1	0.1
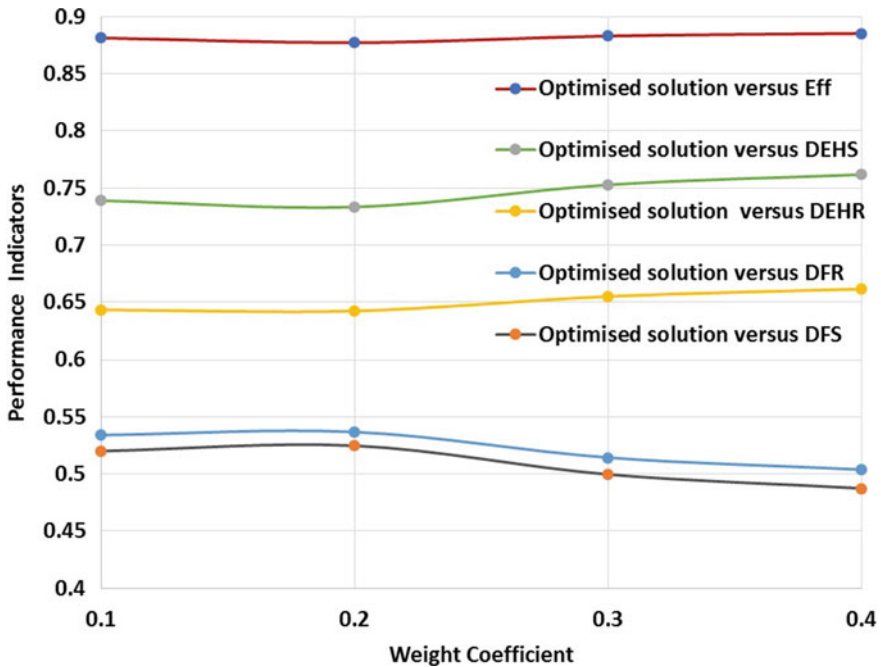
Fig. 5 Results of optimum solution trial for all the optimized trials

higher weightages to DEHR and DEHS yielded into higher pressure ratio but lower efficiency. Optimized design trials with 0.1 weight coefficients each (DEHR, DEHS, DFR and DFS) had a higher pressure ratio, efficiency but slightly higher diffusion ratios. This trial is considered for further design trials using through flow design. Diffusion ratio for this trial is not optimum but can be controlled using lean and sweep for optimum performance during subsequent phases of design.

The data generated provides a guideline to choose combinations of objective weights for different fitness functions for several performance requirements of similar class of compressors for various field applications.

References

1. Klaus S, Advanced compressor technology- key success factor for competitiveness in modern aero engines
2. Escuret JF, Nicoud D, Veysseyre Ph, Recent Advances in Compressor Aerodynamic Design and Analyses. RTO EN-1, 1998
3. Ernesto B (2010) Advances in aerodynamic design of gas turbines compressors (2010) Intechopen.com. Sciyo. ISBN 978-953-307-146-6
4. Tony D, Ivor D (2009) The design of highly loaded axial compressors. In: GT 2009-59291 proceedings of ASME Expo 2009: power for land, sea and air. Orlando, Florida, USA

5. Vad J, Kwedikha ARA, Horvath CS, Balczo M, Lohasz MM, Regert T (2007) Aerodynamic effects of forward blade skew in axial flow rotors of controlled vortex design. In: Proceeding of IMechE Part A: J. Power Energy 221

6. Gallimore SJ, Bolger JJ, Cumpsty NA, Taylor MJ, Wright PI, Place JM (2002) The Use of Sweep and Dihedral in Multistage Axial Flow Compressor Blading. In: Proceeding of ASME Turbo Expo 2002. Amsterdam, The Netherlands

7. Baljeet K, Balsaraf NB, Ajay P (2013) Study of existing multlistage axial flow compressor design for surge margin improvement. In: Proceeding of ASME 2013 Gas Turbine India conference

8. Massardo SA, Marini M (1990) Axial flow compressor design optimization: Part I- Pitchline analysis and multivariable objective function influence. Trans ASME J Eng. Power 112

9. Rao SS, Gupta RS (1990) Optimum design of axial flow gas Turbine stage part I: formulation and analysis of optimization problem. ASME J. Eng. Power 102

10. Balsaraf NB, Kishore Kumar S (2016) Design of transonic axial flow compressor using genetic algorithm method. In: Proceedings of the asian congress on gas turbines, ACGT2016, Indian Institute of Technology Bombay, Mumbai, India

11. Balsaraf NB, Kishore Kumar S (2018) Parametric study of transonic axial flow compressor stage using meanline design. Int J Mech Product Eng Res Develop (IJMPRD)

12. Members of staff of Lewis Research Center, Aerodynamic design of axial flow compressor (NASA SP-36). National Aeronautics and space administration, Washington, D.C. 20546

13. Cumpsty N (2004) Compressor Aerodynamics. Krieger Publishing Company

14. Biollo R, Benini E, State of art of transonic axial compressors. Chap 2, P25-43. Advances in Gas Turbine Technology. ISBN 978-953-307-146-9, Publisher Sciyo

15. Balsaraf NB, Kishore Kumar S (2017) Meanline design of multistage transonic axial flow compressor using genetic algorithm method. In: Proceedings of the 1st National Aerospace propulsion conference, NAPC-2017. IIT Kanpur, Kanpur, India

16. Carlos MF, Peter JF (1993) Genetic algorithms for multi-objective optimization: formulation, discussion and generalization. In: Proceedings of fifth international conference. San Mateo, CA

17. Goldberg DE (1989) Genetic Algorithms in search, optimization and machine learning. Addison-Wesley Publishing Company Inc

18. Kishore KS, Wake GC (1990) Optimization methods and assessment of genetic algorithm. MUNZ

19. Balsaraf NB, Kishore Kumar S (2018) Sensitivity of weighing functions in genetic algorithm for efficiency and pressure ratio optimization in transonic axial flow compressor. In: 8th symposium on applied aerothermodynamics and design of aerospace vehicle (SAROD 2018)

Aeroelastic Instability Evaluation of Transonic Compressor at Design and off-Design Conditions

Kirubakaran Purushothaman, N. R. Naveen Kumar, Sankar Kumar Jeyaraman, and Ajay Pratap

Abstract Aeroelastic flutter investigation of a three-stage transonic axial compressor rotor is discussed in this paper. Unsteady CFD analyses were used to evaluate the flutter instability of the test compressor. Investigation on the effect of inlet guide vane and blade stiffness on aeroelastic damping is the prime objective of this study. The blade was subjected to vibration in CFD domain at specified frequency and amplitude. The unsteady aerodynamic force and work done by the blade at each vibration cycle were evaluated using fluid structure interaction technique. Energy method and work per cycle approach were adapted for this flutter prediction. Based on the work per cycle value, aerodynamic damping ratio was evaluated. A computational framework has been developed to calculate work per cycle and thereby aerodynamic damping ratio. Based on the magnitude and sign of aerodynamic damping ratio, occurrence of flutter was evaluated at all operating conditions of the engine. The primary cause for blade flutter was identified as large flow separation and flow unsteadiness due to high incidence on blade suction surface. The flow unsteadiness resulted into aerodynamic load fluctuation which matched with blade natural frequency and further resulted in blade excitation. Flutter boundary was evaluated for both with and without inlet guide vane case. Significant improvement in flow pattern and flutter boundary was observed for the case with inlet guide vanes.

Keywords Aeroelastic flutter · Aerodynamic damping ratio · Fluid structure interaction · Energy method · Work per cycle · Flutter boundary

K. Purushothaman (✉) · N. R. Naveen Kumar · S. K. Jeyaraman · A. Pratap
DRDO-Gas Turbine Research Estabilishment, Bengaluru, India
e-mail: kirubakaran@gtre.drdo.in

N. R. Naveen Kumar
e-mail: nrnaveenkumr@gmail.com

S. K. Jeyaraman
e-mail: sankar@gtre.drdo.in

A. Pratap
e-mail: ajaypratap@gtre.drdo.in

Nomenclature

ADR   Aerodynamic Damping Ratio
C   Aerodynamic damping
C_{cr} Critical aerodynamic damping
EO   Engine Order
FSI   Fluid Structure Interaction
IBPA   Inter Blade Phase Angle
IGV   Inlet Guide Vane
KE   Average vibrational kinetic energy
M   Mach number
ND   Nodal Diameter
NLr   Corrected rotational speed
P_0 Total pressure
P   Static pressure
RMS   Root Mean Square
R1   First-stage rotor blade
STG   Stage
S1   First-stage stator Blade
T_0 Total temperature
W   Work done per cycle
a   Amplitude of vibration
c   Blade chord
f   Blade vibration frequency in Hz
k   Reduced frequency ($2\pi fc/V$)
kPa   Kilopascals
m   Mass of the blade
δ   Aerodynamic damping ratio
1F   First Flexural Mode

1   Introduction

Recent trend for military gas turbine jet engine is toward high thrust to weight ratio and wider operational envelope. Under these conditions, engines operate in a broad range of Mach number and altitude. Engine rotor components will be under high aerodynamic and structural loads at critical flight envelope points. This leads to aerodynamic instability and calls for higher stability margin of rotors. Aerodynamic flow induced vibration is a critical problem present in rotating components of gas turbine engines. Among a variety of phenomena that cause concern with regard to blade failures, perhaps the most serious is flutter [1]. Rotor blade vibration due to flutter and forced response are identified as the paramount structural mechanic issues in military gas turbines [2]. The unsteady aerodynamic forces generated on
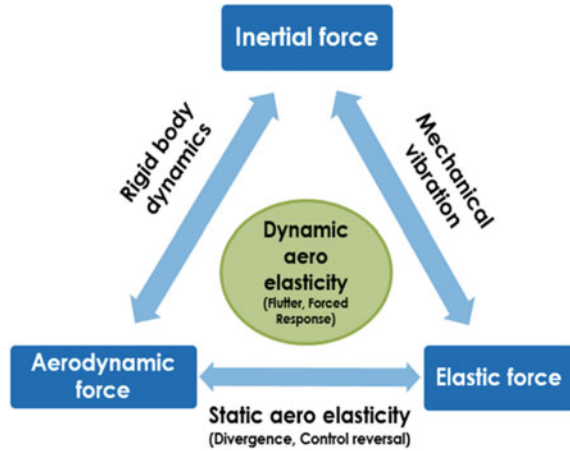
blades due to blade vibration are the primary cause for aeroelastic instability in
turbomachines. When frequency of fluctuating aerodynamic forces matches with the
blade natural frequency, it leads to flutter and increase in blade vibration amplitude.
Flutter is a dynamic aeroelasticity problem, where rotating blades are self-excited
due to interaction of inertial, structural, and aerodynamic forces [1]. This is shown
in Collar's triangle with interaction of three forces [3] as shown in Fig. 1.

Numerical flutter prediction methods help in predicting onset of flutter computa-
tionally and develop methods to alleviate flutter at blade design level. Numerous
prediction methods have been developed in recent years for evaluation of gas turbine
aeroelastic characteristics. Various studies have been carried out on flutter and forced
response of gas turbine blades. Sanders et al. carried out numerical and experimental
studies on stall flutter in a low aspect ratio transonic fan blisk [4]. Srivatsava et al.
did a flutter analysis on a transonic fan [5]. Chiang and Keilb developed an analy-
sis system for blade forced response [6]. Manwaring et al. performed blade forced
response study on a low aspect ratio transonic fan with inlet distortion [7]. Sayma
et al. developed an integrated nonlinear approach for prediction of turbomachinery
forced response characteristics [8]. Mehdi Vahdati et al. performed aeroelastic flut-
ter analysis on low aspect ratio fan rotor blade for several intake conditions and
geometry shapes including typical flight inlet duct shape [9]. Results showed flut-
ter boundary was significantly influenced by the intake configurations. Mark Wilson
et al. evaluated the influence of stagger variation in turbomachinery rotor components
[10].

In this paper, occurrence of flutter response in a three-stage transonic axial com-
pressor is investigated in detail. Large flow separation near the tip region of fan R1
blade has been identified as the reason for flutter occurrence at part speed condition.
Alleviation of flutter by adding an IGV and improving blade stiffness are discussed
in detail in this paper.

2 Objective

Evaluation of flutter occurrence and alleviation using inlet guide vanes in a transonic
axial compressor is the main objective of this study. Flutter boundaries are calculated
at design and off-design conditions for baseline compressor and compressor with
inlet guide vanes. In aircrafts, flutter on wings generally occurs at a particular flight
speed and factors causing its occurrence are fewer when compared with gas turbine
flutter problems. In gas turbine rotors, the influence of adjacent blades determines
the stability of rotor blades to a large extent. This is caused by the variation in shock
location and flow pattern due to adjacent blade vibration. Flutter in gas turbines
occurs at critical rotational speeds and at different inter-blade phase angles or nodal
diameters [1].

Flutter boundary for various inter blade phase angles are evaluated at different
rotational speeds of the compressor rotors. Influence of several aerodynamic and
structural parameters on flutter stability are calculated using which inputs are pro-
vided for future compressor designs [1]. Compressor blade flutter can be categorized
into different types based on the region it occurs in compressor map. Different flut-
ter zones on the compressor map of a transonic compressor are shown in Fig. 2.
Rotor stall flutter occurs at off-design speeds, especially at stall region. High flow
incidence results in flow separation in the suction side of rotor blades particularly
at off-design speeds. This further results in blade force fluctuation leading to stall
flutter. Choke flutter is usually associated with unsteady shock interaction between
blade passages. These flutter problems can be investigated using numerical Fluid
Structure Interaction (FSI) approach [1].

3 Test Case

A three-stage transonic axial flow low-pressure compressor with a design pressure
ratio of 3.3 and efficiency of 87% is considered for the study (Fig. 3). The first-stage
rotor blade (R1) is designed for 400 m/s tip speed and 1.4 tip relative Mach number.

Fig. 3 Three-stage
low-pressure compressor
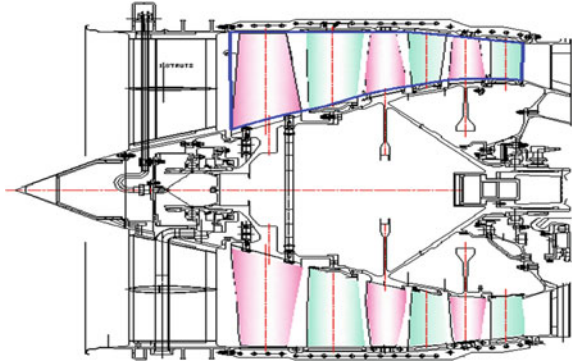
The R1 blades encountered flutter during operation at part speed condition and the same is investigated in this aeroelastic flutter study.

Flutter occurred in R1 blades at 75–85% design rotational speeds at first bending mode. Aspect ratio of R1 blade is 1.8 with a hub to tip ratio of 0.44 and tip solidity of 1.3. Compressor ambient inlet total pressure was the major parameter affecting the blade flutter stability during operation. Large blade vibration was observed at higher inlet pressure condition and blade response was increasing over time during test. Blade flutter was observed to be consistent with corrected operating speed than absolute speed and flutter was repeating at non-integral engine order. In this study, inlet guide vanes are incorporated to evaluate the effect of guide vanes in altering the flutter boundary.

4 CFD and Structural Models

4.1 CFD Model

Three-dimensional (3D) steady and unsteady simulation was carried out for three-stage axial compressor using RANS solver. H-block topology and O-grid around blade was modeled to capture the boundary layer flow. Grid was generated using hexahedral elements for all rotor and stator domains. Single sector periodic model was generated for rotor and stator domains and circumferential periodic interface condition was provided [1]. Based on the grid convergence studies, grid size was fixed around 250,000 elements for each rotor and stator blade domain. Near the tip clearance region of rotor blade domain, non-matching grid was used with general grid interface condition. Across rotor and stator domains, stage interface was provided for which circumferentially averaged flow parameters were transferred between the domains. In all the analyses, *kω-sst* turbulence model with max y+ less than 5 was chosen to resolve the boundary layer flow. The choice of turbulence model was fixed based on CFD validation studies.

Stationary frame total pressure and total temperature values were provided as boundary condition at compressor inlet region. The static pressure at compressor outlet was varied in steps to determine the compressor performance. To estimate surge point, simulations were carried out with incremental static pressure at compressor outlet. Exit static pressure was varied at an increment of 1 kPa near surge point. For convergence, mass and momentum RMS residuals were fixed at 1e–6 levels. Computational domain for three-stage transonic axial flow compressor is shown in Fig. 4.

Initially, steady-state analyses were carried out using the three-stage model and the same were provided as initial conditions for flutter analysis. Transient case was setup for flutter analysis, based on the blade natural frequency and number of vibration cycles. For flutter analysis, two-blade passage domain was modeled to simulate inter-blade phase angle as shown in Fig. 5.

Fig. 4 CFD model for three-stage low-pressure compressor
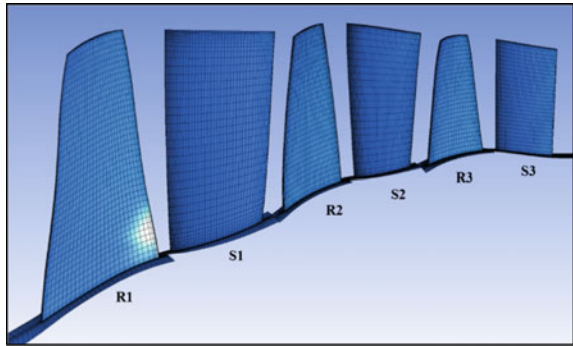
Fig. 5 Two-blade mesh domain for flutter analysis
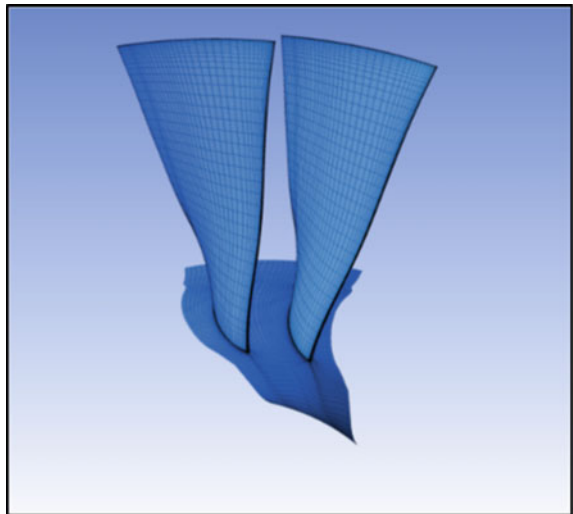
Fig. 6 Finite element model
of first-stage rotor blade
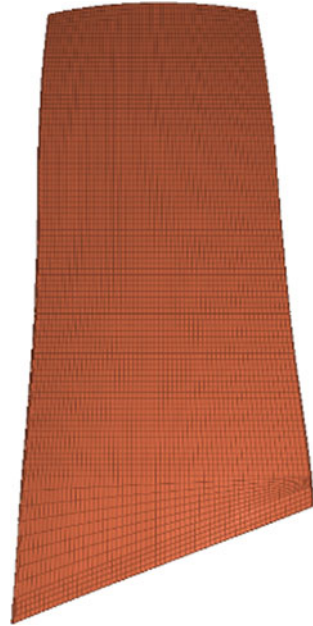
4.2 Rotor Blade Structural Model

Finite element mesh was generated in ANSYS workbench platform. Fine mesh
was generated as per the fluid structure interaction requirement to map blade sur-
face pressure and temperature data exactly from fluid domain to structural domain.
Around 40,000 hexahedral elements were generated for the R1 domain, as shown
in Fig. 6. Initially, static structural analysis was carried out followed by pre-stressed
modal analysis to extract blade static deflection and first bending mode shapes of the
blades. During evaluation of blade deflection and mode shape, aerodynamic loads
were mapped onto the structure from CFD domain to structural domain using FSI
approach.

5 Steady-State Performance

Initially, steady-state analysis was done for the three-stage compressor with and
without IGV for design and off design conditions. Simulations were performed at
standard International Standard Atmosphere Sea Level Static (ISASLS) condition.
Operating conditions of three-stage compressor are mentioned in Table 1.

Analyses were carried out for five rotational speeds ranging from 70 NLr to
100 NLr at different back pressure conditions as mentioned in Table 1. Compressor
map was generated for all back pressure conditions and performance was evaluated.

Table 1 Operating conditions for steady-state analysis

P01	101.325 kPa
T01	288.15 K
RPM	70, 80, 85, 90, 100 NLr
P02	80–310 kPa

Large flow separation was found near R1 tip region at lower speeds for normal case, whereas for the case with IGV, flow separation was reduced as shown in Figs. 7, 8 and 9. Large incidence mismatch was found at lower speeds near blade tip region which was identified as the cause for tip flow separation. Comparison of flow incidence angle on R1 blade at 90% span is mentioned in Table 2.

Without IGV

See Figs. 7 and 8
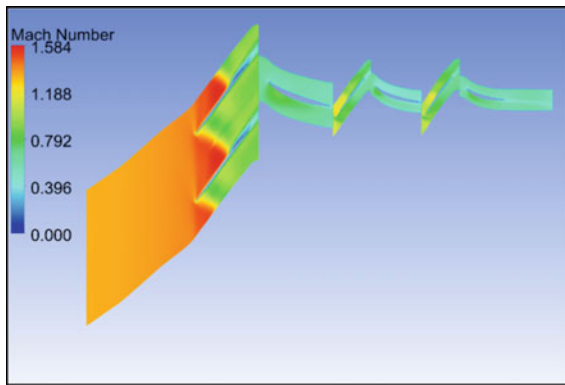
Fig. 7 Steady-state analysis at 100 NLr without IGV
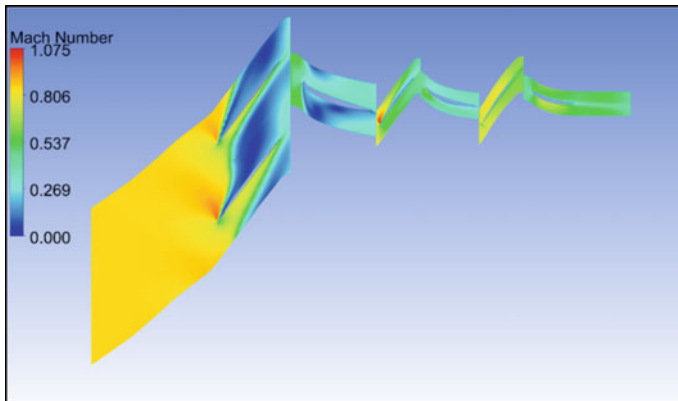
Fig. 8 Steady-state analysis at 70NLr without IGV
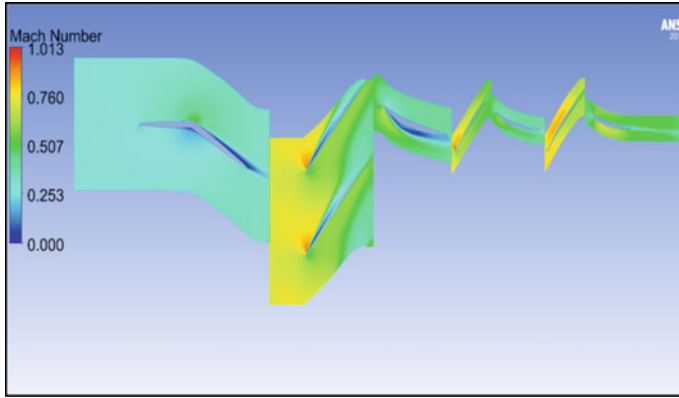
Fig. 9 Steady-state analysis at 70 NLr with IGV

Table 2 R1 incidence angle comparison with and without IGV

RPM (NLr)	Incidence angle Without IGV (deg)	Incidence angle With IGV (deg)	IGV angle setting (deg)
70	12.7	3	35
80	11.4	4.9	25
85	8.8	5.6	15
90	7.4	5.3	5
100	4.3	N.A	N.A

With IGV
See Figs. 9 and 10

Compressor characteristics generated for three-stage LP compressor with and without IGV at design and off design speeds are shown in Fig. 10.

6 Flutter Analysis for R1 Rotor Blade

Energy method and aerodynamic work per cycle approach were adapted for flutter prediction methodology [1]. Flow chart of the flutter prediction methodology is mentioned in Fig. 11.

The methodology adapted for this study is based on the earlier work carried out by the authors as mentioned in reference [1]. Initially modal analysis with FSI is done on blades models to obtain mode shapes and frequency values. Unsteady CFD analysis is carried out on rotor blades by using blade mode shape and frequency of that mode. R1 blade is subjected to first bending mode vibration in computational fluid domain. Due to blade vibration, blade incidence angle varies and this leads to
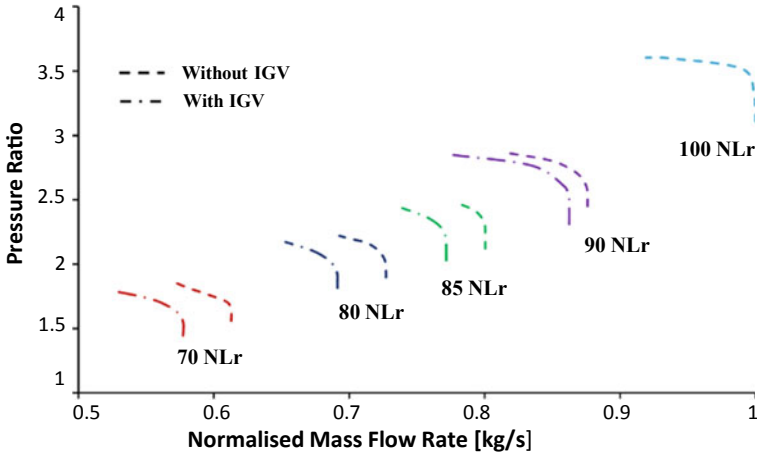
Fig. 10 Compressor map with and without IGV from steady-state analysis
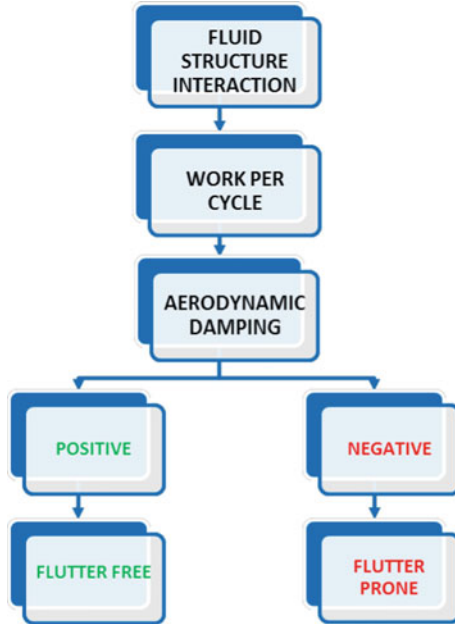
Fig. 11 Flow chart of flutter prediction methodology

unsteadiness in aerodynamic force on the blades. Further, work done is calculated using the unsteady aerodynamic load and blade displacement for each time step. This work done is integrated over time period of each blade vibration and work per cycle is calculated. Finally, work per cycle is normalized with average vibrational

kinetic energy of oscillating blades and aerodynamic damping ratio is calculated. Using aerodynamic damping ratio, rotor blades can be determined if flutter prone or flutter free. At positive damping ratio condition, energy transfer occurs from blade to fluid, whereas in negative damping ratio condition, energy gets transferred from flow to blade structure leading to blade excitation [1].

Nodal diameter signifies the blade vibration pattern with respect to adjacent blades in full assembly of blades. The blades vibrate with particular frequency and mode shape; however, this is associated with a phase difference between adjacent blades. For this purpose, two blade domains are modeled to evaluate flutter stability at various nodal diameters. Blade response pattern with amplitude at various nodal diameters of rotor blade are shown in Fig. 12.

During flexure mode, flutter usually occurs in first few nodal diameters [8]. Hence, analysis of R1 blade was carried out at lower nodal diameters, −6 ND to +6ND (Nodal Diameter). Based on steady-state results, blade surface pressure loads are extracted from fluid domain. This load is applied on R1 blade surface in the static structural model. Further, static structural and modal analyses are done with applied pressure and centrifugal force. Based on the structural analysis results, blade deflection and fundamental mode shape estimated.

Flutter analysis was done for 70–100% corrected speed, to evaluate work per cycle and aerodynamic damping using transient CFD analysis with blade vibration. Since flutter was prone to occur at first flexure mode for this test case, frequency and mode shapes were evaluated for that condition. First flexure mode shape of R1 blade is shown in Fig. 13. Fundamental frequency of R1 blade at various rotational speeds is shown in Table 3.
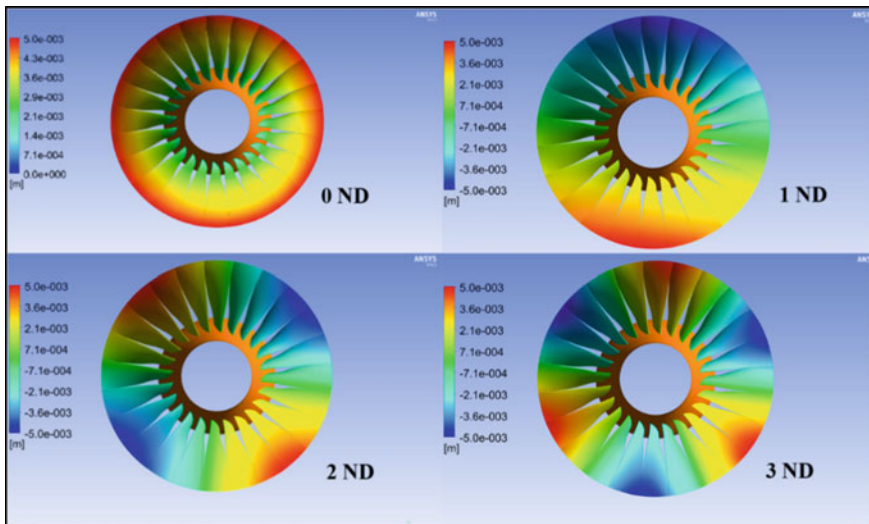
Fig. 12 Blade reponse pattern at different nodal diameter
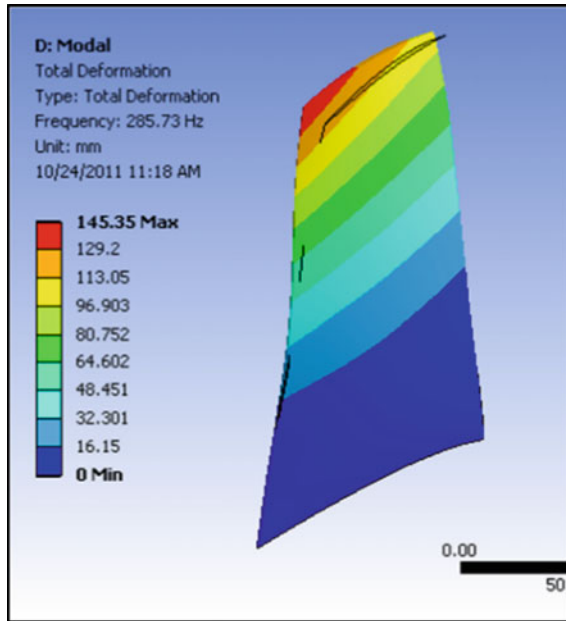
Fig. 13 First flexural mode shape of rotor blade

Table 3 Frequency variation of rotor blade for different operating speed

RPM (NLr) (%)	1F Frequency in Hz (f)
100	1
90	0.94
85	0.91
80	0.89
70	0.83

Flutter analysis is performed with blade vibration in first bending mode shape and frequency. Details of CFD case setup are shown in Table 4.

Three-stage compressor is modeled for this transient analysis and R1 blade is subjected to vibration. Two-sector mesh is modeled for R1 domain to provide inter-blade phase angle condition as shown in Fig. 14.

Fourier transformation condition was used for blade flutter analysis. Details of the work per cycle and aerodynamic damping ratio calculation are mentioned in following section.

Table 4 Vibration parameters for first bending mode

Number of R1 blades	24
Rotational speed	70–100% design RPM
Frequency	0.83f–1f
Mode	1st Flexural
Max blade deflection	3 mm
Nodal diameter	– 6 to +6
No of vibration cycles	10 cycles
Time steps for each cycle	32
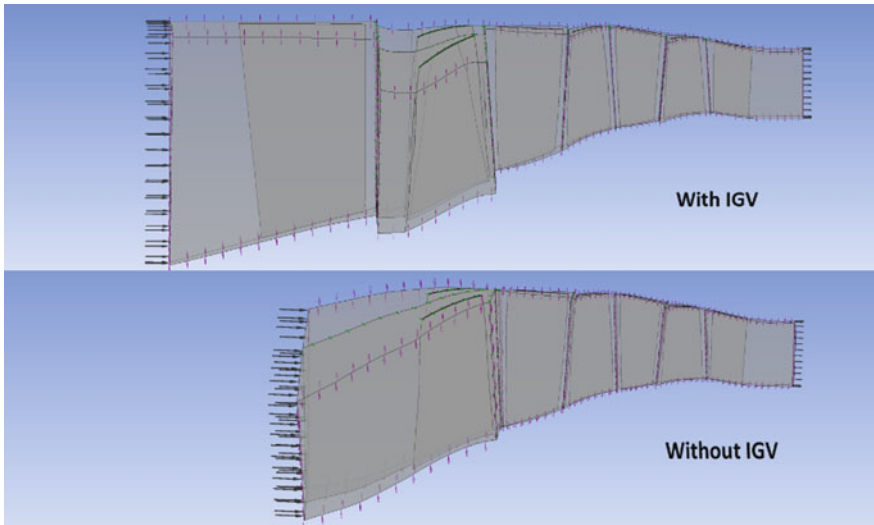
Fig. 14 Two-blade CFD case setup for flutter analysis with and without IGV

7 Work Per Cycle and Aerodynamic Damping Ratio

Work done is evaluated for blades from aerodynamic load and blade displacement at each incremental time step [1]. Work per cycle and aerodynamic damping ratio formulation is defined as.

$$W = (\text{Force} * \text{displacement})$$

$$W = \oint F \cdot ds$$

$$W = \oint \int (P * dA) \cdot ds \tag{1}$$

Work done by blade is integrated over one period of vibration and work per cycle is calculated. Generally, ten cycles of vibration are considered for analysis and work done at the end of tenth cycle is used for aerodynamic damping ratio calculation. Based on the sign of work per cycle, blades can be determined if stable or unstable.

$$\delta = \left(\frac{W}{8\pi \, KE}\right) \qquad (2)$$

δ C/C_{cr} ; $C_{cr} = 2m\omega$; $KE = m(a\omega)^2/4$
m   mass of blade;
ω angular velocity
a   amplitude;
KE   Kinetic Energy

Aerodynamic damping ratio calculation is shown in Eq. 2. Aerodynamic damping ratio calculated for various nodal diameters is shown in Fig. 15.

In this case, at 1ND and 2ND conditions, aerodynamic damping ratio of R1 blade is negative at 80% speed for without IGV case and the same is positive when IGV is added. Similar analysis was carried out at different operating speeds and back pressure conditions. Flutter analysis was carried out for 1ND case for all other points and aerodynamic damping value was calculated. The same has been plotted in the compressor map and flutter boundary was evaluated. Flutter bite plot on compressor map is shown in Fig. 16.

There is a phenomenal shift in the flutter boundary for the case with IGV. Originally flutter boundary was present in the operating zone of compressor map for normal inflow case and with IGV, the boundary was shifted above. Large flow separation present in normal inflow case was identified as the main cause for aeroelastic
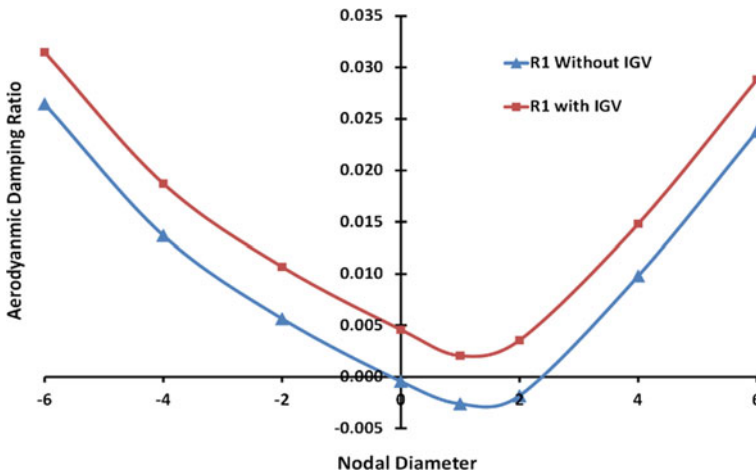
Fig. 15 80% RPM Aerodynamic damping ratio comparison of three-stage without and with IGV
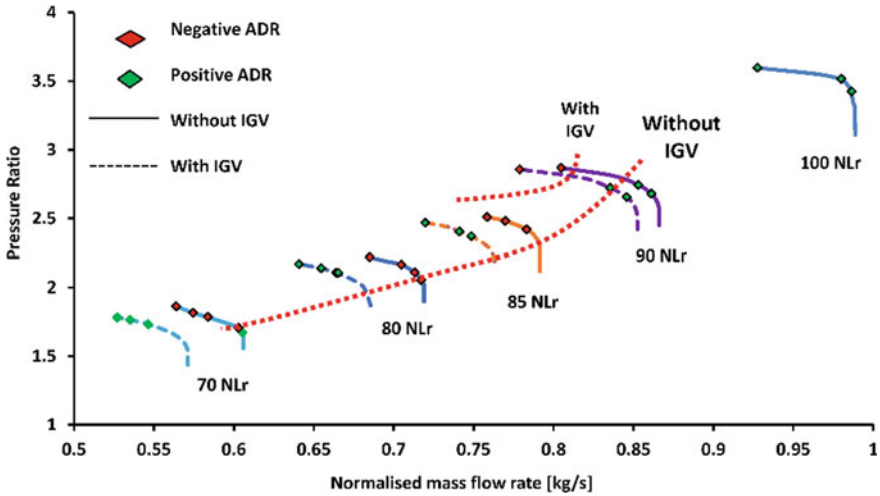
Fig. 16 Flutter bite plot with IGV and without IGV

instability. With IGV, flow separation was avoided by reducing the incidence angle in R1 blade and hence the flutter was alleviated by incorporating IGV. Details of incidence angle mismatch are mentioned in Table 2.

8 Comparison of Single-Stage and three-Stage Flutter Evaluation Without IGV

Similar analysis was carried out for R1 standalone blade case. S1 inlet flow properties were calculated and provided as boundary condition at standalone R1 exit. Steady-state and transient analyses were repeated for single-stage rotor domain case. Flow separation was not present in R1 blade passage as in three-stage case. Flow was attached for all backpressure conditions for varying rotational speeds. Aerodynamic damping ratio was positive in almost all cases and flutter boundary was above the operating range of compressor map. Test results were matching the results of three-stage analysis. Two-blade CFD mesh domain is shown in Fig. 17. Comparison of flow incidence angles is shown in Table 5.

Mach number contour for R1 standalone case and three-stage compressor case for 70 and 80% NLr case is shown in Figs. 18, 19, 20 and 21. Incidence angle at R1 inlet for standalone case is similar to that of three-stage case, but flow separation is less in standalone case rotor as the choke mass flow rate was high equivalent back pressure condition. Comparison of aerodynamic damping ratio at 80% rpm for three-stage and single-row blade for various nodal diameters is shown in Fig. 18. There is a clear shift in the aerodynamic damping for single-blade case and positive damping existing for all the nodal diameters.
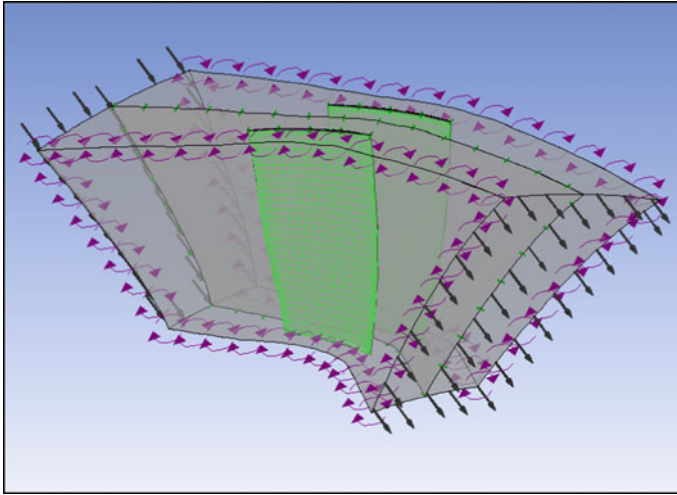
Fig. 17 Two-blade CFD case setup for flutter analysis

Table 5 Incidence angle for three-stage without IGV and R1 single-stage

RPM (%)	Incidence angle at R1 leading edge for three-stage case (deg)	Incidence angle at R1 leading edge for single-stage case (deg)
70	12.7	11.9
80	11.4	11
85	8.9	9.5
90	7.4	8.2
100	4.3	4.3
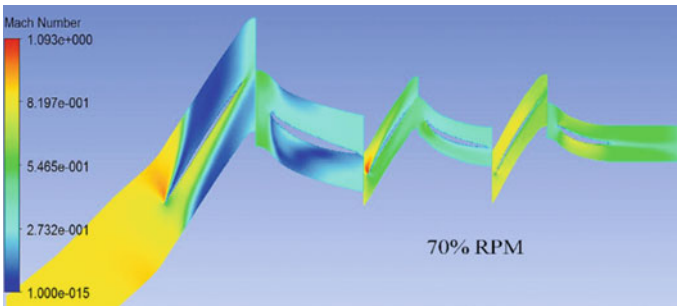
Fig. 18 Mach no. contour in three-stage compressor at 70% NLr
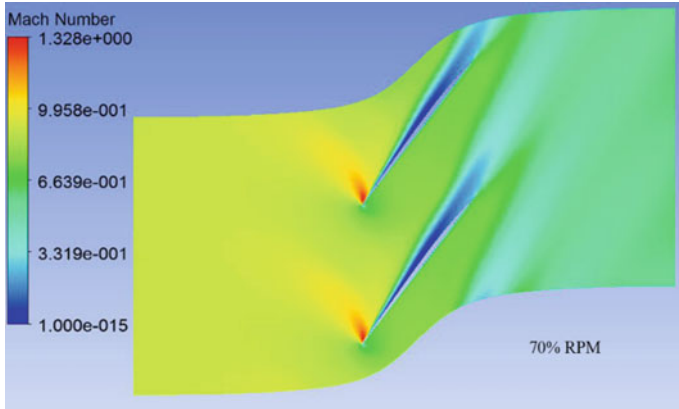
Fig. 19 Mach no. contours in standalone R1 case at 70% NLr
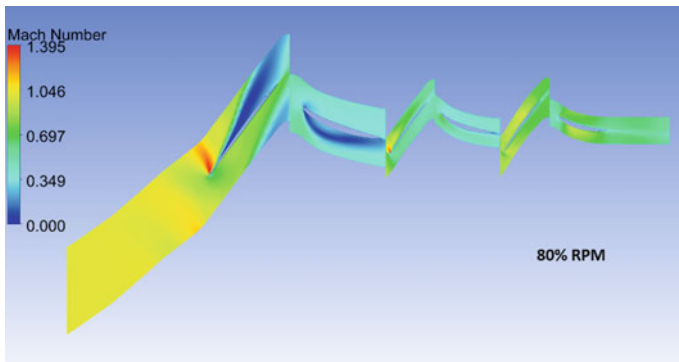
Fig. 20 Mach no. contour in three-stage compressor at 80% NLr
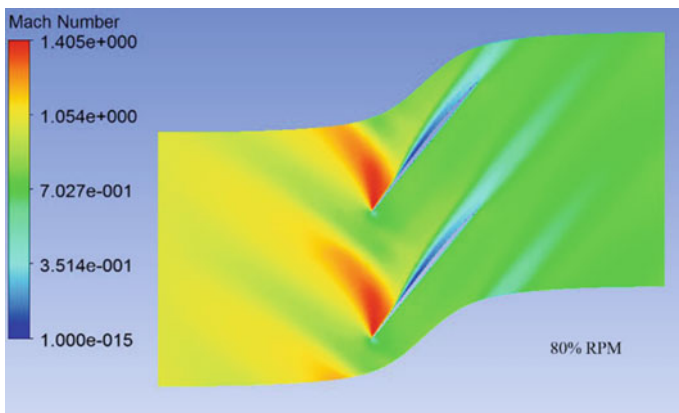
Fig. 21 Mach no. contour in standalone R1 case at 80% NLr
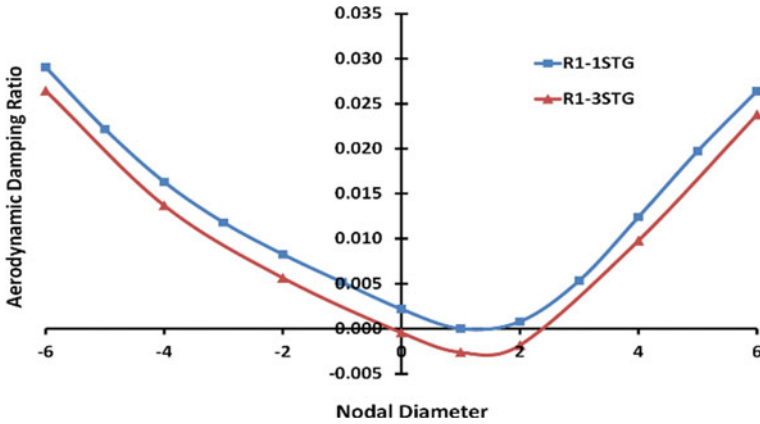
Fig. 22 80% RPM Aerodynamic damping ratio comparison single-stage and three-stage without IGV

Flutter bite plot for single-row blade case is shown in Fig. 23. Aerodynamic damping was positive for all cases and damping was negative only near surge points of 90 and 100% speeds. Flutter was not predicted at part speed conditions due to less flow separation. Choke mass flow rate for single-blade row case was high compared to that of three-stage case at part speed condition. At design speed, the choke mass flow rate was same for both cases. This was due to the fact that choke occurs in front-stage blades at 100% NLr and, at part speed conditions, choke occurs at rear-stage blades, whereas front-stage blades experience stall. Hence, in single blade row case, choke mass flow is higher for equivalent boundary conditions compared to multistage
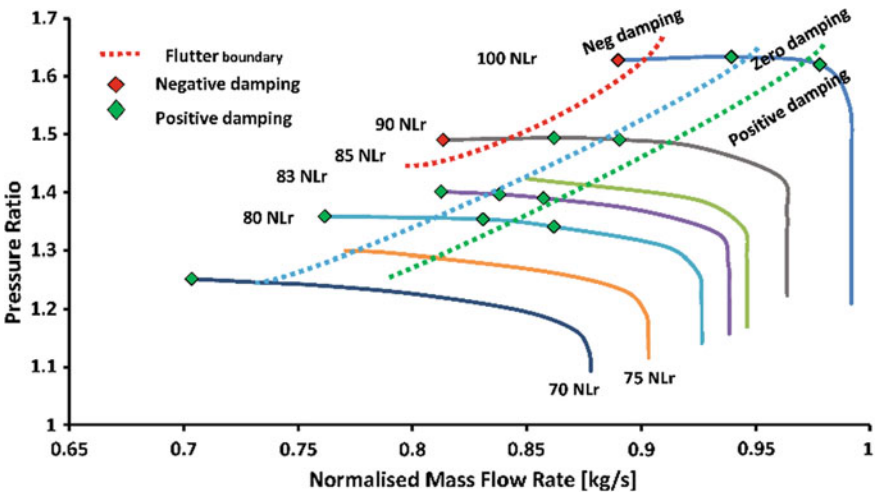
Fig. 23 Flutter bite map without IGV standalone case
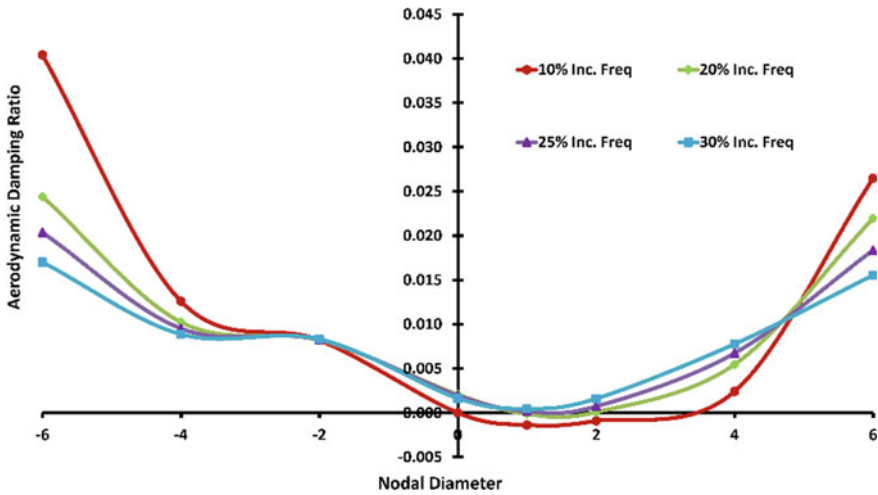
Fig. 24 Aerodynamic damping ratio vs nodal diameter with increased frequency

case. Flutter boundary evaluated for single-blade row case and multi-blade row case differs due to this reason.

9   Evaluation with Increased Frequency

In further study, flutter boundary was evaluated for single-blade case for varying blade stiffness. Blade natural frequency was increased by 10, 20, and 30% at design speed condition, and aerodynamic damping was evaluated. Comparison of aerodynamic damping for various blade frequency values is mentioned in Fig. 24.

Aerodynamic damping was increasing at lower nodal diameter region for increasing blade stiffness. Aerodynamic damping was positive for increased blade natural frequency. Further design trials were attempted to increase the blade stiffness to increase the flutter stability of the blades.

10   Validation of CFD Analysis Results

Validation of CFD analysis was performed for published test data on annular cascade blades. Schulz and Gallus [12] performed detailed experimental investigation to examine flow pattern inside an annular cascade of stator blades. This test case was used CFD validation purpose. Equivalent mesh density of rotor blade was used for analysis of annular compressor cascade case [1].
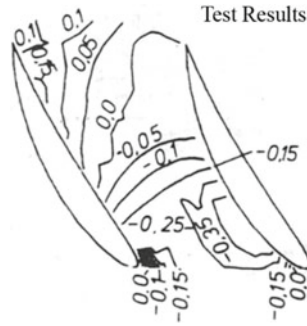
Fig. 25 Static pressure coefficient from experiment results

Experiments were done for Mach 0.3 inlet in a standalone stator configuration. Inlet swirl was generated using fixed guide vanes for the annular cascade blades. Wall static pressure measurement in stator passage, hub, and shroud surfaces was included in the experiment. CFD analysis was carried out for single-domain model representing annular cascade setup. In this simulation, total pressure loss was slightly over predicted and static pressure rise was less when compared with experimental results. Figs.25 and 26, shows comparison of normalized static pressure contour with experimental results at hub surface. The contour was similar to experimental results; however, the magnitude of static pressure coefficient was less by 0.1 in analysis [1].

Static pressure coefficient,

$$C_P = \frac{P - P_1}{P_{01} - P_1} \tag{3}$$

Where

P   Static pressure in blade to blade flow
P_1 Static pressure at inlet
P_{01} Total pressure at inlet

Further studies were done on blade structural part for validation. Experimental strain measurement from engine test was compared with FEM results of rotor blade at design operating condition. FSI analysis with aerodynamic force and centrifugal load were carried out at same operating condition as test and strain values were estimated. Strain gauge location and strain data comparison at same condition between test data and analysis are shown in Figs. 27 and 28.

Numerical prediction of strain value matched with test results with 3% error and this confirmed the operational blade shape of rotor blades.
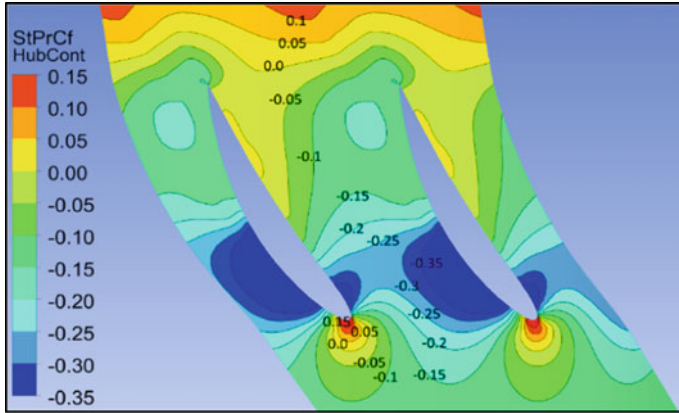
Fig. 26 Static pressure coefficient contour from numerical simulation results
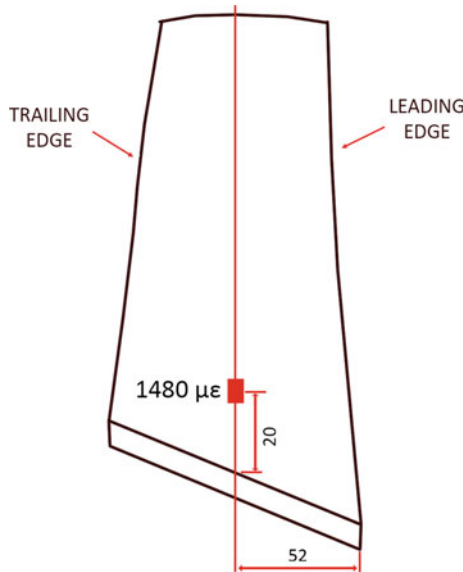
Fig. 27 Strain data on rotor blades suction side from static strain measurements

11 Conclusions

A computational framework was developed to evaluate flutter stability of rotor blades at design and off-design conditions. Energy method and work per cycle approach were used to estimate aerodynamic damping on blades. Negative aerodynamic damping indicated possibility of flutter occurrences. Initially, steady-state analysis was

Fig. 28 Strain value on
rotor blade suction side from
structural analysis
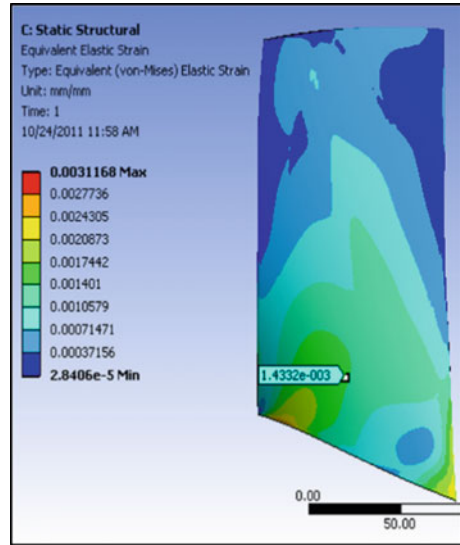
carried out for three-stage transonic axial flow compressors and flow pattern in blade
passage was studied for with and without inlet guide vane cases.

Flutter evaluation carried out for the first-stage rotor blade in three-stage com-
pressor proved that presence of inlet guide vanes alleviated flutter during off-design
conditions. Flow incidence angle mismatch and large pressure gradient was present
during off-design conditions near R1 blade tip region. This created large flow sepa-
ration leading to aerodynamic force fluctuation and self-excited vibration. This flow
separation and large unsteadiness in aerodynamic forces was avoided by IGV. Flutter
bite plot was generated for full compressor map at standard operating conditions.
A significant shift improvement in flutter boundary was observed for the case with
IGV.

Further investigation with blade stiffness proved that with increasing blade stiff-
ness, aerodynamic damping and flutter stability were increased. Later, analyses were
done for standalone rotor blade domains to compare the flutter stability results
obtained from three-stage case. Large mismatch in blade loading and choke mass
flow rate were observed in spite of providing equivalent boundary conditions as in
three-stage case. Flutter stability calculated from three-stage blade case matched the
test data closely.

References

1. Kirubakaran P, Sankar Kumar J, Ajay P, Kishore Prasad D (2017) Aeroelastic flutter investigation and stability enhancement of a transonic axial compressor rotor using casing treatment. In: ASME GTINDIA 2017–4767
2. Srinivasan AV (1997) Flutter and resonant vibration characteristics of engine blades. In: ASME-GT-533
3. AGARD Manual on Aeroelasticity in Axial-Flow Turbomachines, vol. 1, Unsteady Turbomachinery Aerodynamics
4. Sannders AJ, Hassan KK, Rabe DC (2004) Experimental and numerical study of stall flutter in a transonic low aspect ratio fan blisk. In: ASME
5. Srivastava R, Bakhle MA, Keith TG Jr (2002) Flutter analysis of a transonic fan. In: ASME Turbo Expo 2002, GT 2002–30319
6. Chiang HD, Keilb RE (1993) An analysis system for blade forced response. ASME J Turbomach 115(4):762–770
7. Manwaring SR, Rabe DC, Lorence CB, Wadia AR (1997) Inlet distortion generated forced response of a low aspect ratio transonic fan. ASME J Turbomach 119(4):665–676
8. Sayma AI, Vahdati M, Imergun M (2000) An integrated nonlinear approach for turbomachinery forced response prediction, Part I: formulation. J Fluids Struct 14:87–101
9. Vahdati M, Simpson G, Imregun M (2009) Mechanisms for wide chord fan blade flutter. In: ASME Turbo Expo 2009, GT 2009–60098
10. Wilson MJ, Imergum M, Sayma A (2007) The effect of stagger variability in gas turbine fan assemblies. ASME J Turbomach 129:404–411
11. Lumbomski JF (1980) Status of Nasa full-scale engine aeroelastic research. In: NASA Technical Report
12. Schulz HD, Gallus HE (1988) Experimental investigation of three dimensional flow in an annular compressor cascade. ASME J Turbomach 110:468–478

Combustion

Strategic Quality Management of Aero Gas Turbine Engines, Applying Functional Resonance Analysis Method

Johney Thomas, Antonio Davis, and Mathews P. Samuel

Abstract Failure analysis and defect investigation of aero gas turbine engines, which are complex and safety-critical systems, call for advanced tools and techniques in the customer perspective framework of Strategic Quality Management (SQM). Functional Resonance Analysis Method (FRAM) is such a tool for failure mode and root cause analyses, helpful in instituting suitable corrective and preventive actions. Repeated failure of the drive shaft of oil cooling system of a turboshaft aero-engine at the Shear neck resulted in many premature withdrawals affecting fleet serviceability. Defect investigations attributed the failure initially to the Nitrided surface of the drive shaft, then the Heat treatment process, and subsequently the machining method. SEM analysis of the fracture surface showed High-Cycle Fatigue (HCF) as the failure mode. Instrumented experimentation conducted subsequently revealed a "Backward Whirl" phenomenon, initiated from the unbalance of an adjacent component and manifested at a certain range of gas generator speed, as the root cause of the HCF and consequent failures. The FRAM methodology helped in completely obviating the failures by various remedial measures, like removal of the unbalance, micro-shot peening of the shear neck, and damping of backward whirl using bearing liner bushes and enhancing stiffness by increasing the shear neck diameter to shift the backward whirl beyond the operating range of the aero-engine. The case study also demonstrates the application of FRAM for defect investigation of aero gas turbine engines.

J. Thomas (✉)
Hindustan Aeronautics Limited, LCA-Tejas Division, Bengaluru, India
e-mail: johney.thomas@hal-india.co.in

J. Thomas · A. Davis
International Institute for Aerospace Engineering and Management, Jain (Deemed-to-Be University), Bengaluru, India
e-mail: antonio.davis@jainuniversity.ac.in

M. P. Samuel
Regional Centre for Military Airworthiness (Engines), CEMILAC, DRDO, Bengaluru, India
e-mail: drmatmail@gmail.com

Nomenclature

BW	Backward Whirl
FPI	Fluorescent Penetrant Inspection
FRAM	Functional Resonance Analysis Method
FW	Forward Whirl
HCF	High-Cycle Fatigue
LCF	Low-Cycle Fatigue
MPI	Magnetic Particle Inspection
NDT	Non-Destructive Testing
NG	Gas Generator Speed
OCS	Oil Cooling System
SEM	Scanning Electron Microscope
SQM	Strategic Quality Management

1 Introduction

Advanced aero gas turbine engines, with critical and highly stressed components,
operate at the limits of compressor pressure ratios, rotor speeds, operating temperatures, and service conditions. Failures occur in spite of the most accomplished prevention efforts in design, validation, manufacture, assembly, and testing. No human
endeavor or human-made system can be guaranteed to be absolutely free from hazard.
It is hence imperative to investigate the accidents, incidents, and defects of airborne
systems completely and systematically to establish the causes and evolve appropriate
remedial measures to prevent recurrence of the defects and failures. Defect Investigation is a part of this continual process of hazard identification and risk mitigation,
which is vital for ensuring flight safety.

Functional Resonance Analysis Method (FRAM), propounded by Prof. Erik Hollnagel (2011), is a powerful technique for understanding and resolving safety-related
issues in complex systems like aero-engines [1]. This paper is a narrative of the
application and applicability of FRAM as a defect investigation methodology for
analyzing safety events, and instituting suitable remedial measures, in an aero gas
turbine engine.

2　Functional Resonance Analysis Method

2.1　Looking Beyond the Obvious

"Ignorance of remote causes disposeth men to attribute all events to the causes immediate and instrumental; these are all the causes they perceive," wrote Hobbes (1651) in Leviathan [2]. "Perceive those things which cannot be seen", said Musashi (1645) in The Book of Five Rings [3]. The axiom that "what you look for is what you find" is especially true in defect investigations. "What you find is what you fix/learn" is a natural corollary [4, 5]. When things go wrong, we try to find the cause. The search for the cause is guided by how we think an event can happen. Establishing the real root cause of an event, an incident or an accident, may require looking beyond the obvious, and searching for factors remaining hidden and inconceivable [6].

2.2　Inductive and Deductive Models

There has been a number of system safety analysis techniques employed to perform hazard and risk analysis related to safety of an airborne system. These tools and techniques can be broadly categorized into inductive techniques and deductive techniques, as shown in "Fig. 1" [7, 8].

Inductive techniques are used to "Induce Forward" the consequences of an event using a forward-looking logic. An inductive model defines scenarios for an initiating event, which can have undesired consequences. Subsequent events are then identified which define possible progressions of the initiating event, and their manifestations

Fig. 1　Inductive and deductive techniques of system safety analysis

are conceived and linked to model scenarios. The consequence of each scenario is thus described in the inductive model.

Deductive techniques are utilized to "Deduce Backwards" the causes of an event using a backward-looking logic. A deductive model resolves the causes for an event, first into its immediate necessary and sufficient causal events, using appropriate logic. This stepwise resolution of events into immediate causal events proceeds until the basic primary cause or the root cause is identified through the deductive model.

2.3   Functional Resonance Analysis Method (FRAM), the Nonlinear (Systemic) Model

FRAM is a unique nonlinear (systemic) accident model, as compared to "Simple Linear" or "Composite Linear" cause–effect models [9]. FRAM is based on the presumption that accidents and incidents happen due to "Emergence" from a combination or "Resonance" of performance variability in the increasingly complex and incomprehensible sociotechnical systems [10]. The process variability is to be managed through learning, responding, monitoring, and anticipating (the "Four Abilities of Resilience Engineering"), and ultimately controlling [11, 12]. The resonance leads to mutual reinforcement of the adverse effects, leading to excessive variability of one or more of the downstream functions. The consequences may spread through the system by means of "tight couplings" rather than easily identifiable cause–effect links [13].

The FRAM diagram consists of hexagonal cells for activity/function/process, with each corner representing the "Six Aspects of FRAM Function" viz. input, time, pre-condition, control, resource, and output, as shown in "Fig. 2".

FRAM applies both forward-looking and backward-looking logics simultaneously, and hence is a unique inductive-cum-deductive model suitable for both prospective and retrospective analyses. A FRAM analysis consists of five steps [14]:

 (i)   Defining the purpose of the analysis.
 (ii) Identifying and describing the relevant system functions.
 (iii) Assessing and evaluating potential variability of functions.
 (iv) Identifying where functional resonance may emerge.
 (v)   Developing effective countermeasures.

2.4   Development of a New "FRAMED-IN-FRAM" Model

During the present research into the application of FRAM for strategic quality management of aero gas turbine engines [15], the authors have developed a simplified and flexible model based on Microsoft Excel for depicting the FRAM symbology diagram into a honeycomb-like arrangement of the hexagonal FRAM cells that depict
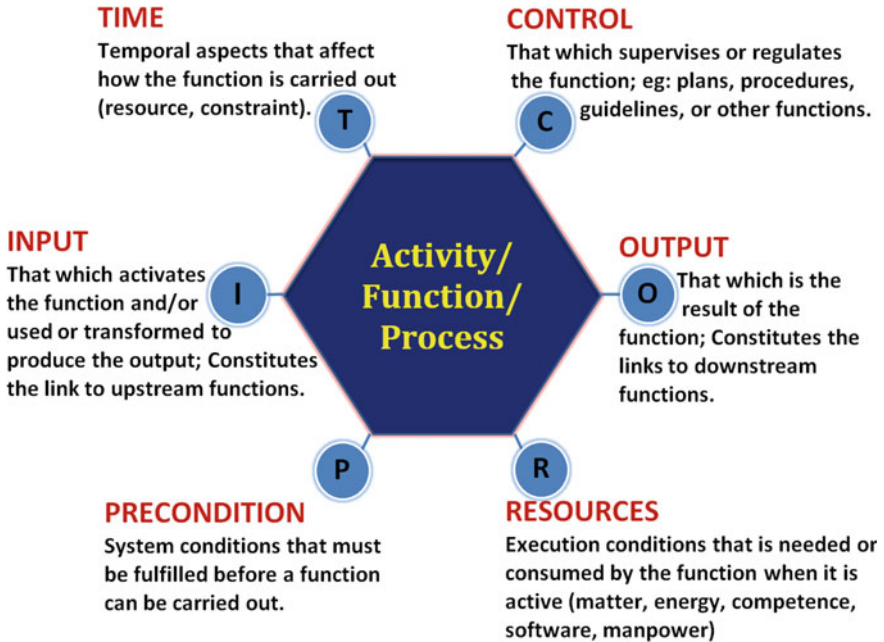
Fig. 2 The six aspects of a FRAM function

the function/process/activity. The interconnections between the various cells along the six aspects of the FRAM function are managed using the "Elbow Arrow Connectors" available in the Excel "Shape menu". The FRAM cells are numbered to indicate the sequence of evolution of the FRAM-based analysis and thinking, and colored to indicate the category of activity/function/process (viz. hazards to be resolved, actions to be implemented, and positives to be reinforced). This methodology is amenable for easy replication of the cells across the total domain, making further exploration and analysis unlimited and ever-expandable. The authors would like to call this new methodology as "FRAMED-IN-FRAM" model, "FRAMED" due to the neat, organized, and framed-like look of the diagram, and "-IN" because of the Indian connection. This new style of "FRAAMING" is used all along in this Technical Article.

3   The Curious Case of OCS Drive Shaft Failure

The case study presented here pertains to a turboshaft aero-engine having twin spool configuration, with aero-thermodynamically coupled Gas Generator (GG) and Power Turbine (PT) modules, and a gearbox to transmit power and motion. The aero-engine has got an Oil Cooling System (OCS) meant for cooling the scavenged oil from the
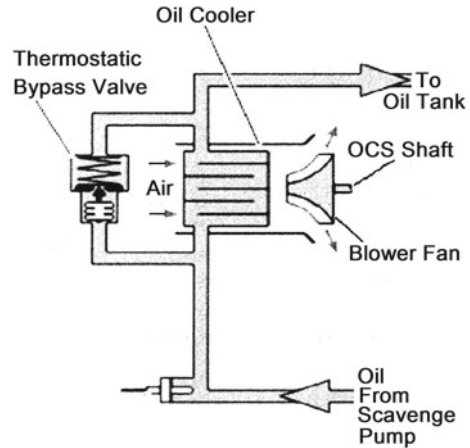
bearings and the gearbox before re-entering the oil tank. Heat transfer from the oil takes place in a heat exchanger through forced convection by means of air induced in by a blower fan fitted onto the end of a drive shaft, which is in fact the stem portion of the so-called OCS Gear fitted in the gearbox. A schematic diagram of the OCS is given in "Fig. 3".

The OCS drive shaft (called "OCS shaft" hereinafter) provides drive to the blower fan. OCS shaft has a "Shear neck" just before the blower fan location, which has been designed to act as a "Mechanical fuse" for breaking under over-resistant torque conditions. The purpose is to ensure protection of the aero-engine gearbox kinematic drivelines that provide necessary drive to all the critical auxiliary equipment assembled onto the gearbox like fuel pump and oil pump, obviating potential uncommanded engine shut down due to loss of fuel and oil feeding. The shear neck of the OCS shaft is of $\Phi 5.25$ mm, operates at a rated speed of 415 revolutions per second, and is designed for maximum breaking torque strength of 21.3–40.5 N m. In case of any restriction on free rotation of the blower fan assembly due to foreign objects or any other reason, the fuse is intended to break and thus protect the gear trains of the aero-engine gear box. A view of the OCS shaft arrangement is given in "Fig. 4".

4 Early Investigations and Remedial Actions

The OCS shaft was found ruptured at the shear neck in the port side engine of one of the helicopters at early hours of service exploitation. After a few days, the OCS shaft got ruptured in the starboard side engine of the same helicopter too. These in-service incidents on both the engines within a short span of time at early hours caused a lot of concern and apprehension by the manufacturers, customers, and the regulatory agencies. Prior to these incidents, there had been a similar case of OCS shaft rupture
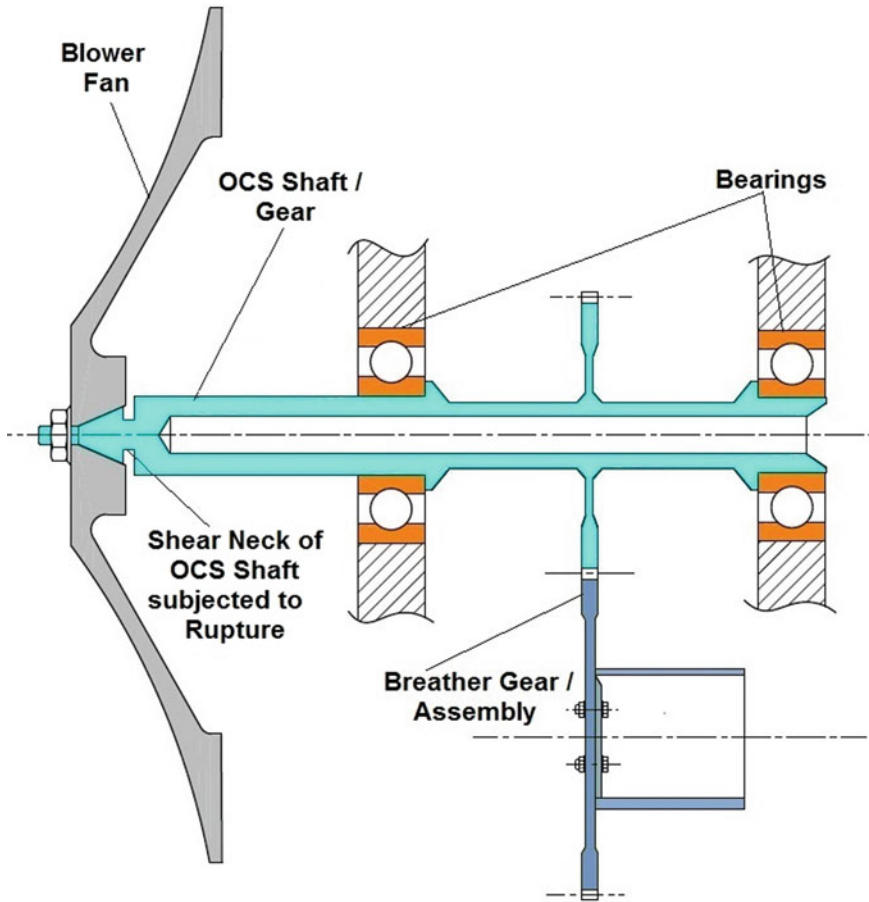
Fig. 4 Schematic view of OCS drive shaft arrangement

at shear neck on an aero-engine during its endurance test, which happened on ground in the testbed. Internal defect investigation carried out at that time zeroed in on three probable causes of the OCS shaft rupture. The following improvements were thus incorporated accordingly:

(i)   Manufacture of OCS shaft without nitriding at shear neck
(ii) Incorporation of improved magnetic particle Inspection.
(iii) Use of improved "Immobilizer tool" for blower fan assy.

4.1 Nitriding of OCS Shaft as the Root Cause

OCS shaft is the stem portion of the OCS Gear, as shown in "Fig. 4". Gears are case-hardened to get a hard and wear-resistant exterior of the involute profile surfaces which act in conjugate action to transmit power and motion, and at the same time to retain a soft and tough interior to take care of transmission loads to prevent gear tooth breakage. Case-hardening is done by processes like carburizing and hardening, nitriding, carbonitriding, etc., depending upon the type of component and its application. In case of the OCS gear having OCS shaft as its stem, nitriding process is carried out for case-hardening. As per the original design, nitriding was being done for the complete exterior surfaces of the OCS gear, including the shear neck of the shaft.

Hardness is associated with brittleness; and it was thought that the brittleness of the case-hardened surface of the OCS shaft shear neck could be the reason for its rupture. It was hence decided to manufacture the OCS gear without nitriding on the OCS shaft stem including the shear neck, thus changing over to a partially nitrided configuration of the OCS gear.

4.2 Improvement in Non-destructive Testing

Non-Destructive Testing (NDT) plays a vital role in detecting cracks and defects in a manufactured component. OCS gear, with the drive shaft as its stem, is crack-tested by Magnetic Particle Inspection (MPI). However, the original MPI process consisted of only circular magnetization by direct passage of current along the gear, which could detect only the longitudinal cracks. Since the cracks leading to OCS shaft ruptures were transverse cracks, the circular magnetization process was found to be inadequate to detect such cracks in the manufacturing stage, as shown in "Fig. 5".

Hence, longitudinal magnetization process using circular magnetic coils was additionally introduced as part of NDT, which could detect transverse and inclined cracks in addition to the longitudinal cracks.
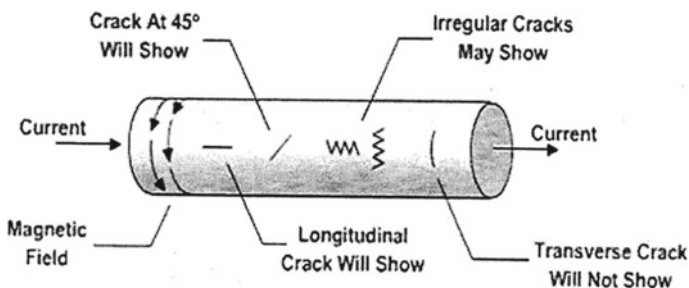
Fig. 5 Crack detection in circular magnetization

4.3   Use of Improved Assembly Tooling

There is a possibility of the OCS shaft getting twisted while the Blower fan is mechanically assembled onto the OCS shaft by torque-tightening. In order to take care of the possibility of crack generation due to the shear and bending stresses induced during the assembly, an "Immobilizer tool" was designed and fabricated. Introduction of this tool for assembly and disassembly of the blower fan prevented twisting of OCS shaft at the shear neck during assembly, thereby eliminating the probability of crack formation during assembly.

4.4   In Situ NDT Checks and Decision for Replacement

In situ examination was carried out at the shear neck of OCS shafts of all the aero-engines in service by the following three NDT methods, viz. (i) Eddy current inspection, (ii) Magnaflux inspection, and (iii) Fluorescent penetrant inspection (FPI).

Based on the large number of OCS shafts detected with crack at shear neck, all the aero-engines in service were replaced with OCS gears of partially nitrided configuration, to maintain shear neck without hardened layer having brittleness, which could lead to crack formation and consequent rupture. However, in spite of the aforementioned improvements including changeover to non-nitrided OCS shaft configuration, the shaft failures persisted, which prompted deep investigation into the other potential causes of OCS shaft rupture.

4.5   Metallurgical Failure Mode Analysis

Fractographic examination of the rupture surfaces of the broken OCS shafts was carried out as part of metallurgical failure mode analysis. The laboratory examination revealed two distinct surfaces in the shear neck rupture surfaces, as shown in "Fig. 6".

Firstly, there was a transverse crack in the radical plane, or at 90° to the shaft axis, having oxidized surface, black in color. Since such an oxidation could be reproduced only at high temperature (> 500° C) in the tests done in a metallurgical furnace, it was surmised that the crack was present before the heat treatment process of nitriding, and therefore the crack could have been generated during the manufacturing process.

Secondly, the inner surface was showing crack along a 45° plane, indicative of crack propagation under fatigue loading conditions, which eventually culminated in complete rupture.

The beach mark–fatigue striations on the fracture surfaces revealed by SEM at higher magnifications corroborated the theory of fatigue propagation of crack.
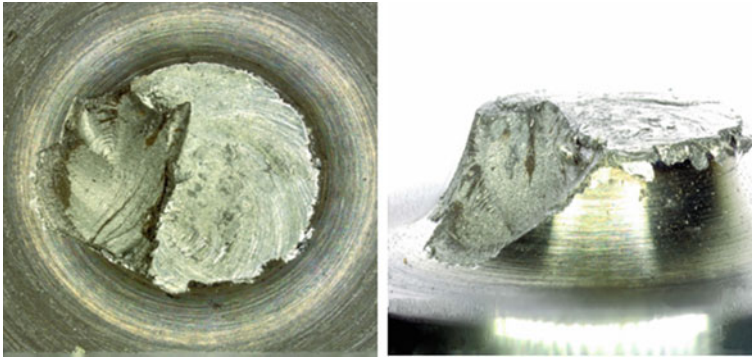
Fig. 6 Shear neck rupture surface features

4.6 Improvement in Machining Process

It was found that during machining of the narrow groove of the shear neck surface in OCS shaft after nitriding of the OCS gear, the shear neck area was subjected to excessive bending load (greater than 1000 MPa) because of high tool feed rate. In order to avoid the shear and bending stresses induced during the machining operation, the shear neck groove machining was separated out as the last machining operation on the component, and the machining programme was optimized with special tool geometry and tool trajectory, and also benign cutting speed, feed, and depth of cut, to get lower stresses at the shear neck during machining, to prevent the possibility of crack initiation, as shown in "Fig. 7".
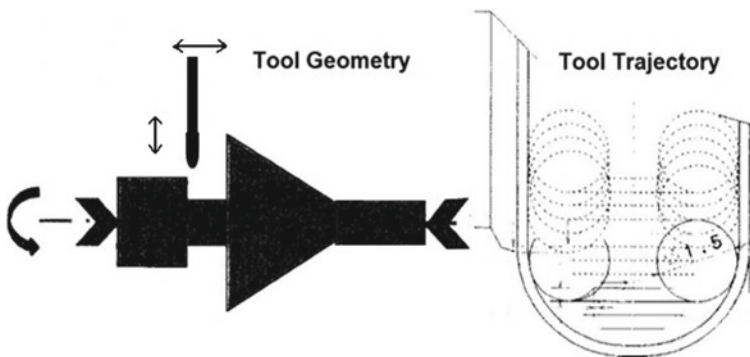
Fig. 7 Improved shear neck machining process

4.7 Additional Fluorescent Penetrant Inspection

Since the cracks generated during machining could not be detected by the conventional NDT processes, and since a comparison of the different NDT methods had shown that Fluorescent Penetrant Inspection (FPI) is more sensitive to detect transverse hair line cracks at the shear neck area, the FPI method was also introduced for crack detection of the manufactured component, in addition to the improved MPI process of longitudinal magnetization introduced earlier. Also, periodic in situ FPI check of shear neck also was introduced for early detection of cracks developed, if any.

4.8 Simulation Exercise

A simulation exercise was carried out in the aero-engine test bed to evaluate the effect of failure of the OCS due to OCS shaft shear neck rupture at the helicopter platform level [16]. It was found that after shutting down of the cooling air flow for the heat exchanger, the maximum oil temperature reached after 90 min of idling was only 125 °C. Thus, in the event of OCS failure, the engine is capable to be maintained at idle mode for up to 90 min, and to be subsequently brought back to flight mode (up to "TOP" rating) to perform safe landing of helicopter with both the engines. Hence, it was established that the loss of oil cooling function is not a safety-critical event [17, 18]. However, it continues to be a mission-critical event and a reliability issue, since the failed aero-engine is to be kept idle and the helicopter has to be brought back to the nearest landing point at the earliest.

5 FRAM Diagram of the Improvement Actions

In spite of the aforementioned investigations into the nature and causes of OCS shaft failure due to rupture at the shear neck section, and the remedial measures instituted based on the limited understanding provided by these investigations, the OCS shaft failures continued, this time even on the OCS shafts of partially nitrided configuration, having no nitriding at the shear neck section. This prompted the need for further deep dive into the depths of the problem, with the help of FRAM.

Even though the investigation so far had been of the nature of the linear cause–consequence–correlation models, we plotted a "FRAMED-IN-FRAM" diagram for the diagnostic findings and improvement actions instituted till then, which is shown in "Fig. 8".
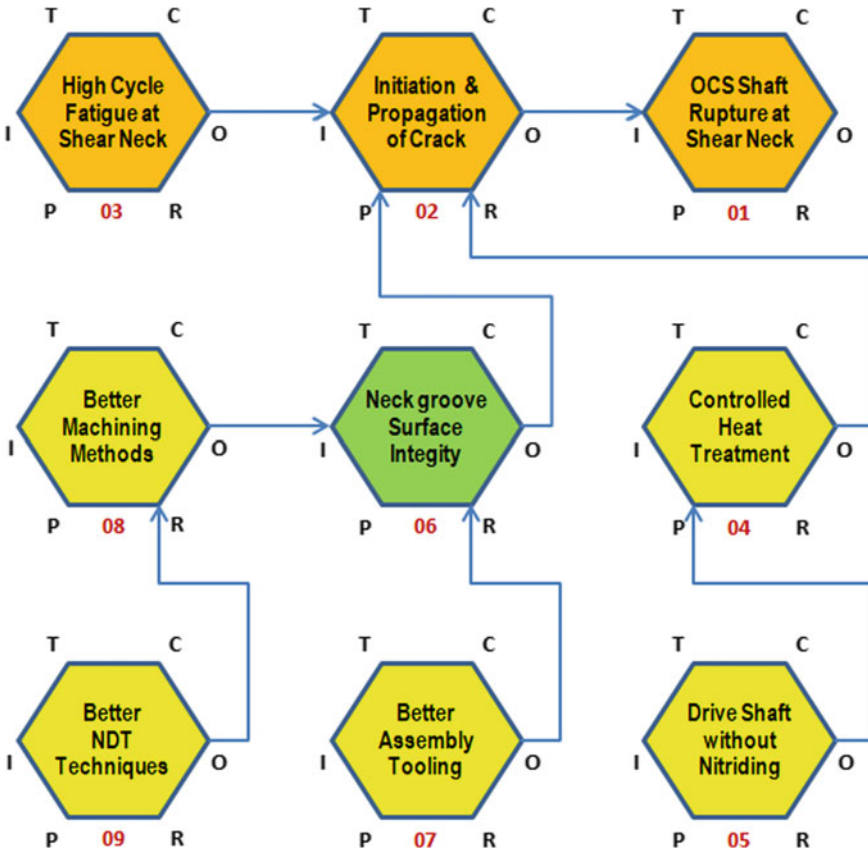
Fig. 8 "FRAMED-IN-FRAM" diagram—stage-1

6 In-Depth Studies on Vibratory Behavior

In spite of the aforedescribed improvement actions at various stages, the OCS shaft shear neck failure continued unabated, and manifested either as rupture during service exploitation of the aero-engine, or as cracks revealed in the shear neck during the in situ NDT examination by FPI method at periodic intervals, introduced as an action for risk mitigation. This necessitated further deep diving for exploring the unforeseen and unknown depths of the world of resonance vibration of aero-engine components and systems.

Aero-engines are susceptible to high-amplitude vibrations at resonance frequencies, predominantly due to out-of-balance conditions inherent in rotating components. The unbalances are brought to a minimum by static and dynamic balancing of engine discs, shafts, and rotors, both individually and as coupled units. However, rigid rotor balancing techniques at low speeds may not be sufficient for flexible

shafts and rotors, which can undergo lateral bending oscillations leading to flexural vibrations and bending modes at critical speeds [19].

The classical rotor dynamic theory describes the existence of lateral vibration of loaded shafts in the whirling speed range under out-of-balance conditions [20]. Vibration characteristics are determined by the mass and stiffness values of the rotor system, with damping (the ability to dissipate/attenuate the vibrational energy) playing an integral role in controlling the amplitude. The natural frequency of vibration is governed by the following equation [21]:

$$\text{Natural Frequency} = \sqrt{\frac{\text{Stiffness}}{Mass}}$$

The ratio of bearing stiffness to shaft stiffness has a significant impact on the mode shapes. Split resonance and backward whirl (BW), which cause lateral bending vibration of shaft, are influenced by its stiffness and damping. The literature on the subject has documented many instances of manifestation of BW mode, wherein the shaft/rotor whirls in the opposite direction as the spin direction, during lateral/flexural vibrations of loaded slender shafts under specific rotational conditions in presence of a gyroscopic effect [22, 23].

According to Millsaps et al., BW of the shaft/rotor is to be expected in cases where there is large asymmetry in bearing direct stiffness, like imperfections in the circularity of the bearing sleeves [24]. Also, a major cause of split resonance and BW is gyroscopic forces generated by overhung discs, as in the present case of blower fan fitted onto the OCS shaft. The magnitude of unbalances and the damping also had an influence on whether BW occurred. The gyroscopic affect occurs whenever the mode shape has an angular/conical motion component. Under the gyroscopic effect, increasing stiffness causes increasing natural frequency when the shaft speed increases for the forward whirl (FW), whereas the reverse effect of decreasing stiffness causing decreasing natural frequency happens for the BW, as can be seen in a Campbell diagram.

6.1 Engine Tests to Capture Vibratory Behavior

An instrumented engine test was carried out in the aero-engine testbed, as part of a detailed vibration analysis with an aim to experiment and understand the vibratory behavior of OCS shaft assembly, and to characterize the vibrations both in torsional mode, and in shaft/bending mode.

Dedicated instrumentation employed for detecting the frequency and amplitude level of the vibratory behavior of OCS shaft included: (i) An optical probe in front of the blower fan blade trailing edge and a proximeter (displacement sensor) in front of the OCS gear teeth, for torsional displacement characterization and (ii) a proximeter radially in front of the blower fan cover, for bending displacement characterization.

6.2 Backward Whirl Shaft Mode Signature

In the instrumented engine test, torsional mode vibration was undetectable, or was at very low amplitude, in the entire speed range. However, in the shaft mode, signature of split resonance with associated BW mode induced by the adjacent breather gear driving OCS gear was detected.

The test revealed that the first-order shaft/bending mode of OCS shaft was due to the gyroscopic effect, which consisted of two distinct modes:

(i) A FW shaft mode: The wave propagating in the same direction as the OCS shaft rotating direction (counterclockwise, looking from aero-engine rear side).

(ii) A BW shaft mode: The wave propagating in the opposite direction as the OCS shaft rotating direction (clockwise, seen from aero-engine rear).

The color map of the displacement level at the blower fan, measured at the outer periphery of the fan in the instrumented engine test, gave the signatures of the BW shaft mode of vibratory behavior of OCS shaft. The color map showed that both the modes were merged at null speed and then divided into two distinct modes when the rotating speed of the OCS shaft increased.

The Campbell diagram, or the theoretical frequency versus speed graph, based on the insights from the color map, is shown in "Fig. 9".

Both FW mode and BW mode signatures can be seen on the color map. The FW mode positioning is also confirmed. Normally, the FW shaft mode only is taken into account, because the BW shaft mode is usually not excited. However, in the case of OCS shaft, BW got manifested, and an unexpected response of excitation of
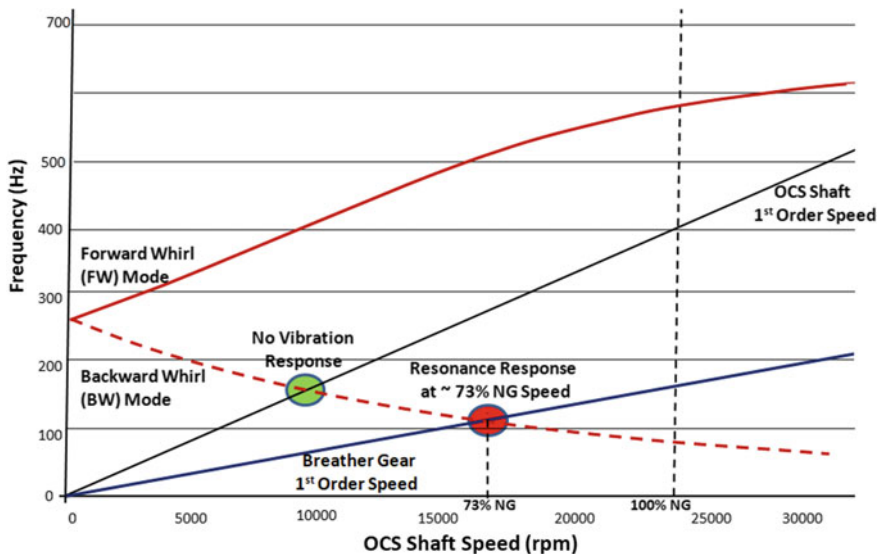
Fig. 9 Campbell diagram: high-amplitude resonance response due to backward whirl mode

"Resonance" was observed when crossing breather gear speed, which is around 73% of gas generator speed (NG).

Radial displacement of the blower fan to a very high level of transient value was measured just after starting, which subsequently decreased to a lower stabilized level.

The BW movement or "wave" can be understood as a "wobbling" in the direction opposite to the direction of rotation of the shaft, which, in the case of OCS shaft, induced a bending moment at the shear neck section.

6.3   Backward Mode Excitation/Aggravation Source

By experimentation, it was confirmed that the breather gear assembly, which is driving the OCS gear (the stem portion of which is the OCS shaft), was the source of initiation/excitation/aggravation of the BW shaft/bending mode in the OCS shaft coupled to the blower fan.

6.4   High-Amplitude Resonance Response

It can be seen from the Campbell diagram that the high-amplitude resonance response is happening at the intersection point of the BW mode line and the breather gear first-order speed line.

6.5   Pre-condition of Resonance Response

The Campbell diagram also shows that the high-amplitude resonance response due to BW mode happens at about 73% of the so-called NG speed, which is the rotational speed of gas generator which gives drive to the auxiliary gear trains, including the OCS gear and the breather gear (100% NG speed corresponds to about 24000 rpm).

6.6   Stress Analysis at the Shear Neck Section

The radial displacement of the blower fan due to excitation of the BW created a wobbling/wave effect on the OCS shaft, which caused alternating compressive and tensile stresses at the shear neck of the OCS shaft, the highest stress level being obtained when crossing the breather gear speed, which corresponds to about 73% of gas generator speed. The stress evolution in the shear neck section with reference to time is given in "Fig. 10".
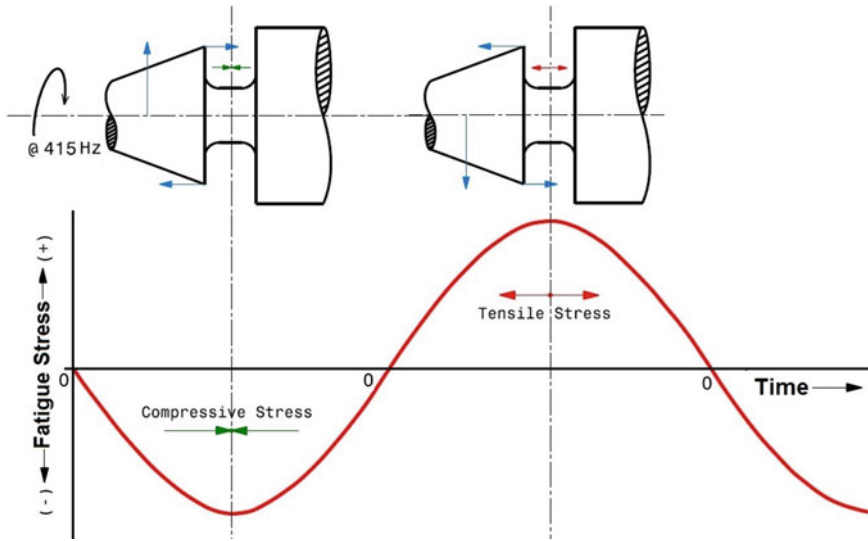
Fig. 10 Stress evolution at shear neck section

6.7 Confirmation of HCF Under Backward Whirl

Having understood the BW shaft mode phenomenon and its effect on initiation and propagation of crack at the shear neck of the OCS Shaft, additional experiments were conducted in the aero-engine test bed for confirmation of HCF due to BW mode phenomenon. The OCS shaft used was made as per the improved manufacturing process and was confirmed to be without any manufacturing crack by means of both MPI and FPI for transverse crack detection. Initially, a breather gear assembly of a low static unbalance of 0.66 cm g was coupled to the OCS gear, and the instrumented engine HCF test was conducted in thermally stabilized condition of the engine. The maximum resonance level was explored by periodical and regular NG scanning around 73% NG speed, which is the speed at which resonance vibration of OCS shaft was found to get manifested. Even after 10.2 million cycles performed at a high fan displacement (corresponding to about 8 cumulative test running hours), no cracks could be detected, demonstrating infinite life at this displacement level.

A second instrumented engine test also was conducted at the same engine test conditions at the same displacement level, but with a different breather gear assembly having a higher static unbalance of 2.37 cm-g (instead of 0.66 cm-g for the first test). The engine running was performed by always searching for the maximum displacement level by scanning the NG speed during the test. A new OCS shaft, verified to be crack-free, was used. Here, after 3.7 million cycles or 2.5 h of running (as against 10.2 million cycles in the first test), the frequency progressively decreased after increase in displacement level to 9.6 mm under resonance, indicating crack initiation and propagation in the shear neck section.
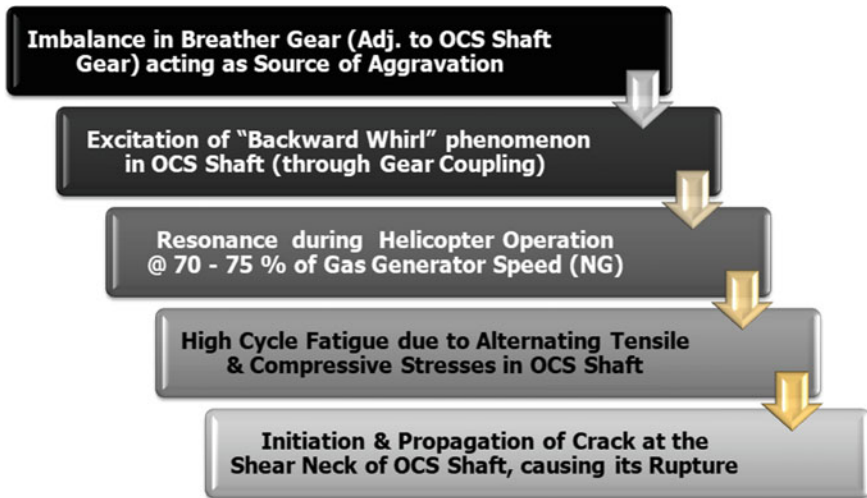
Fig. 11 Progression of events leading to rupture

In situ FPI carried out after removal of the blower fan confirmed generation of crack at the shear neck. Thus, the hypothesis was experimentally confirmed that the excitation caused by higher unbalance of the breather gear is the initiator and aggravator of the BW mode phenomenon of the OCS shaft, and that the resonance vibration occurring at ~ 73% of the NG speed leading to HCF caused the initiation and propagation of crack. The sequence of events leading to OCS shaft rupture is depicted in "Fig. 11".

6.8 *Metallographic Examination of Fracture Surfaces*

Examination of the fracture surfaces of the shear neck crack after crack opening in the laboratory revealed two distinct surfaces:

(i) Surface-1: Perpendicular to the shaft axis (90°), with an oxidized black color zone.
(ii) Surface-2: Inclined at 45°, starting from the edge of the 90° cracked surface, with fatigue failure features.

Surprisingly, the fracture features were of the same pattern as in the previous in-service OCS shaft rupture cases, previously attributed to manufacturing-related crack initiation and propagation.

It is now understood that the 90° crack surface corresponds to the HCF crack initiated and propagated due to high-amplitude resonance response under the BW shaft mode. The 90° direction is the same as the direction of fatigue stress induced

by the alternating tensile and compressive bending stresses under the wobbling/wave generated in the BW mode.

The oxidized layer of black color can be explained in terms of fretting corrosion effect due to successive tensile compressive cycles of both crack faces at high-frequency range of more than 400 Hz. Likewise, the 45° crack surface is related to fatigue crack propagation under torsional stress, which is consistent with the stress direction under torsion, probably a mix of HCF due to the vibrations and LCF due to aerodynamic torque. The absence of oxidation here can be explained by non-occurrence of high-cycle opening/compression phenomenon since the crack is kept open by aerodynamic torque under engine functioning during the latter phase.

Hence, the OCS shaft Shear neck rupture scenario can be explained in terms of the following three stages:

(i)   Crack initiation and propagation under the BW mode resonance.
(ii) Subsequent bending stress decrease due to resonance "deadening," and the corresponding torsion stress increase due to neck section reduction.
(iii) Finally, further crack propagation at 45° under torsion, eventually leading to the rupture.

6.9   Influencing Factors for Crack Occurrence

Three major influencing sources can be identified for the occurrence of crack and rupture as a result of the BW mode, as given in "Fig. 12":
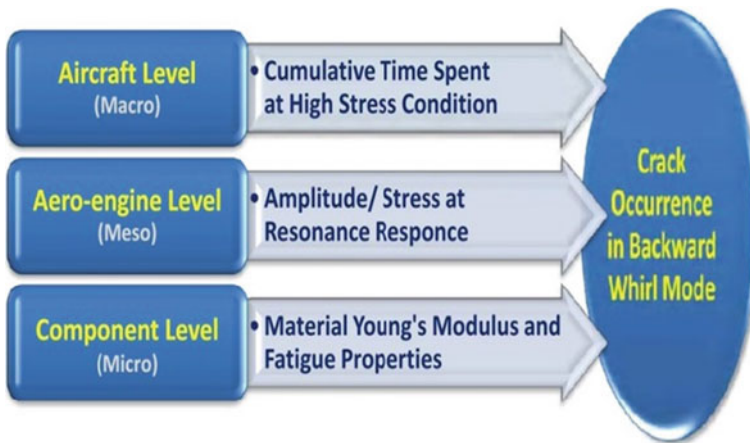
Fig. 12 Influencing sources of crack and rupture

(i) Fatigue properties of material (related to the OCS shaft): It consists of the OCS shaft batch, the manufacturing processes employed, the residual stresses induced, etc.

(ii) Amplitude/stress level during resonance (related to the aero-engine): This includes the breather gear characteristics like out-of-balance level, and the gearbox manufacturing and assembly aspects like tolerances, axial and radial clearances, etc.

(iii) Cumulative time spent at high stress level (related to both the aero-engine and the aircraft): This is the time when the NG resonance range and the NG usage range overlap each other.

As per the engine test experiments, the resonance can reach the highest level in the range of around 70–75% of NG speed. If both the aero-engines are kept in a different mode (stop/idle/flight), one engine will be below this range (zero power) and the other engine will be above the range. In-flight stabilization of this range is not usual. However, this NG range could be reached from the upper limit with both the engines running in the same mode (mostly idle mode). Hence, cumulative time spent at the high stress levels depends on the exact NG value at the resonance frequency and the actual NG values when both the engines are running at idle mode.

6.10 Resonance Positioning

The resonance response occurs when the resonance speed of the gas generator overlaps with the usage speed of the gas generator. In this respect, there could be three types of scatters, which collectively determine the occurrence of resonance:

(i) The resonance positioning scatter.
(ii) The NG range usage scatter and usage Rate.
(iii) The maximum stress-level scatter.

The resonance positioning depends upon several influencing parameters like:

(i) The OCS shaft neck dimension.
(ii) Young's Modulus of the material.
(iii) Fan weight and inertia.

The NG range usage scatter also depends upon many influencing factors which include:

(i) Mission type and pilot practice.
(ii) Aircraft production scatter.
(iii) Engine production scatter.

6.11 Defining Gas Generator Speed to Be Avoided

In view of the aforesaid, it became imperative to study the possibility to define the gas generator speed (NG) range to be avoided in service, since resonance was getting excited at a specific NG speed, lying within a narrow NG range due to the various scatters.

6.12 Avoiding Resonance Speed Range in Service

The range of gas generator speed at which the BW mode creates resonance vibration in the OCS shaft (found to be about 70–75% NG) had to be avoided to the maximum possible extent.

Also, long steady functioning, or dwelling, in that particular NG speed range had to be kept to the minimum (preferably not be more than 20 s) during the transient phase. This could be achieved by switching the two engines from idle to flight mode one after another, or by having both the engines at different modes, avoiding power demand sharing by both engines.

6.13 Balancing of Breather Gear Assembly

The unbalance of the adjacent breather gear assembly was identified as the potential source of excitation of the BW mode in the OCS shaft. This excitation can happen either directly through the gear interface or indirectly through the gearbox casing. High values of unbalance and large scatter thereof were evident, since the breather gear has the Air–mist separator cup assembled onto the concentrically machined gear, which could be a major source of unbalance, and hence the excitation.

Hence, it was decided to carry out dynamic balancing of the breather gear assembly to a stringent value of 0.4 cm g, to completely obviate the possibility of BW excitation under gyroscopic effect due to high unbalance levels.

6.14 Micro-Shot Peening of Shear Neck Section

Micro-shot peening is a strain hardening method used for improving fatigue strength of components subjected to alternating tensile and compressive stresses under cyclic loading conditions.
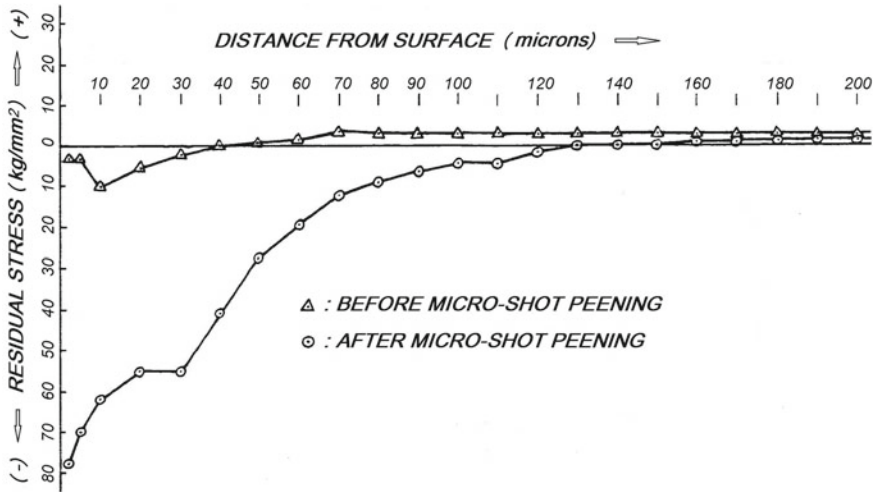
Fig. 13 Residual compressive stresses induced by micro-shot peening

During the operation, micro-shots are made to impinge at high pressure and velocity onto the surfaces to be strengthened, thereby inducing residual compressive stresses at the surface layers of the component, enabling it to withstand the alternating fatigue stresses.

The residual stress induced by micro-shot peening on the side flank surfaces of a broached dovetail slot w.r.t. the distance from the surface is illustrated in "Fig. 13" [25].

Since the shear neck of OCS shaft is subjected to HCF during the resonance vibration created by the excitation of BW mode, it was decided to introduce micro-slot peening at the shear neck to increase the fatigue strength to withstand the cyclic loading conditions and HCF prevailing at the time of resonance.

7 FRAM Diagram Based on Backward Whirl Mode Excitation, Resonance Vibration, High-Cycle Fatigue, and Improvement Actions

The discovery of resonance vibratory response of OCS shaft under BW mode phenomenon leading to HCF conditions at the shear neck, resulting in initiation and propagation of crack, culminating in the eventual OCS shaft rupture, opened up new possibilities toward prevention, protection, and mitigation of the resultant risks associated with the potential hazard of BW excitation, which were described in the earlier sections.
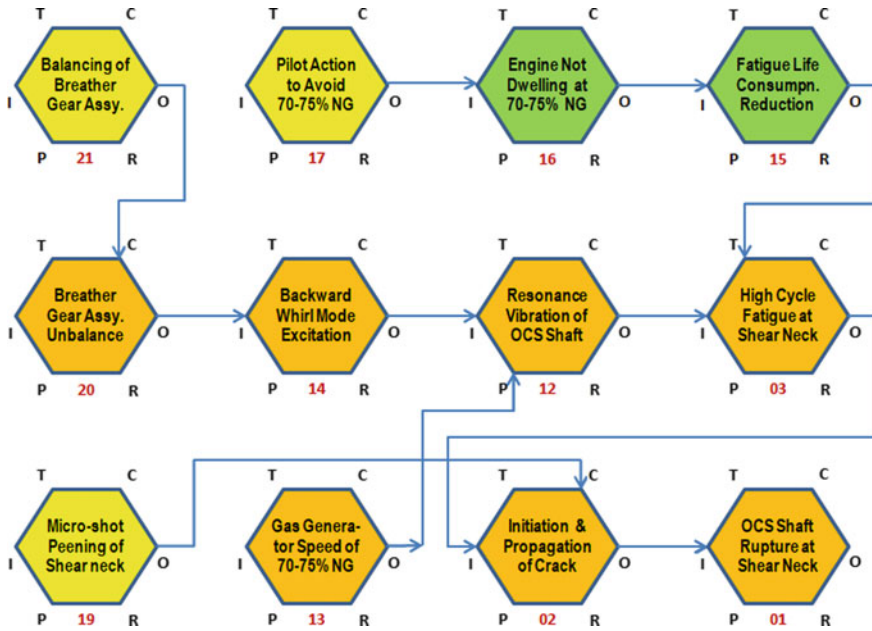
Fig. 14 "FRAMED-IN-FRAM" diagram—stage-2

The "FRAMED-IN-FRAM" diagram in accordance with the new findings on the eventual nonlinear systemic evolution of OCS shaft rupture problem is presented in "Fig. 14".

8 Shifting Backward Whirl Beyond Engine Operating Range, and Damping Its Excitation

The reliability of the aero-engine was seriously compromised by the high occurrence rate of crack/rupture at the shear neck of OCS shaft due to HCF generated by resonance response of the BW shaft mode of OCS shaft due to the breather gear first-order excitation. The resonance range was between 70 and 75% of gas generator speed (NG), as demonstrated through the dedicated instrumented engine test, and the HCF endurance test which enabled generation of the crack under the specific conditions.

Hence, based on the in-depth analysis with the help of FRAM, it was decided to improve the overall robustness of the OCS shaft toward the potential BW mode resonance (and also increasing the possible shear torque value), as a permanent solution to the problem.

8.1 Stiffness Enhancement OCS Shaft Shear Neck for Shifting of Backward Whirl Beyond Operating Range

It was decided to remove/offset the condition wherein BW crosses the breather gear first-order speed, so that the possibility of occurrence of resonance vibration is prevented totally. This would be possible by shifting the BW mode resonance vibration frequency outside/beyond the maximum possible gas generator speed (NG), by increasing the bending stiffness of the OCS shaft.

The bending stiffness increase of the OCS shaft was achieved by an increasing of the shear neck diameter by 2.45 mm (Φ5.25 mm to Φ7.7 mm), along with a decrease in the shear neck width by 0.7 mm.

The principle of shifting of BW/breather gear resonance beyond the operating range of the aero-engine gas generator through stiffness enhancement of the OCS shaft is depicted in the Campbell diagram shown in "Fig. 15". It can be seen from the Campbell diagram that the cross-over point of resonance occurrence has been shifted beyond 115% of gas generator speed, or beyond the aero-engine operating range, so that the BW can never be excited.
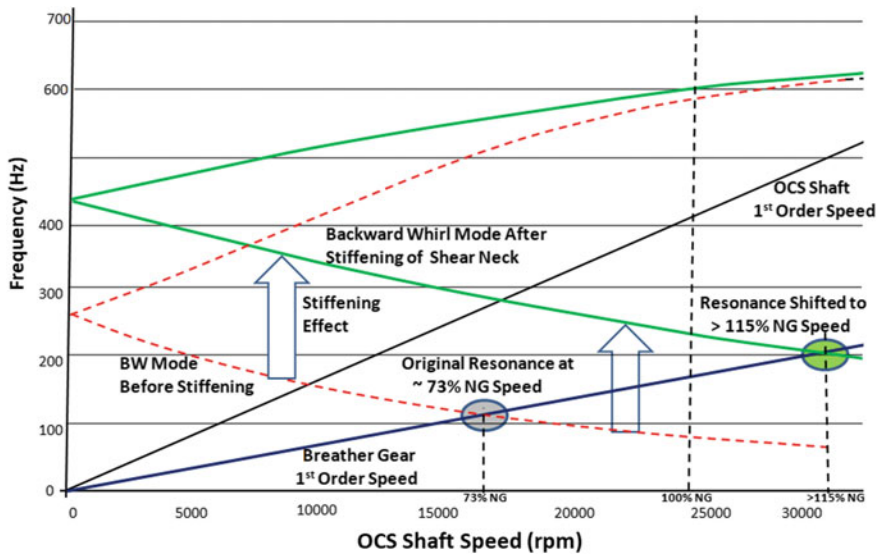
Fig. 15 Campbell diagram showing shift in resonance range with stiffened OCS shaft

8.2 *Additional Steel Ferrules to Increase Damping Effect Against Backward Whirl Excitation*

It was also decided to increase damping effect to take care of the situations when the BW mode is excited by even other possible sources (like gas generator or free turbine), by controlling the clearance of OCS shaft mounting bearings by providing steel ferrules in the bearing bores of the magnesium alloy casing of the gearbox wherein they are fitted.

Addition of steel ferrules in magnesium alloy casing helps keep radial clearance of bearings even/uniform during cold engine start and in a wide operating range, and provides the damping effect, especially for the cold start, so that BW mode excitation itself is completely obviated.

9 FRAM Diagram Based on Stiffening of OCS Shaft and Damping of Backward Whirl

This brings us to the third and final stage of FRAM analysis, the "FRAMED-IN-FRAM" diagram of which is illustrated in "Fig. 16".

10 The Final "FRAMED-IN-FRAM" Diagram

The "FRAMED-IN-FRAM" diagrams of the three distinct stages of FRAM analysis depicted earlier in this article have been merged together by "FRAAMING" the final combined "FRAMED-IN-FRAM" diagram for the whole case study, which is presented in "Fig. 17".

11 Conclusions

The usefulness and applicability of FRAM as a universal tool for strategic quality management in the field of aero gas turbine engines, especially for defect investigation and failure analysis, has been demonstrated by case study method in this technical article. It can be seen that FRAM is not only suitable for sociotechnical systems as envisaged by Hollnagel, but also for purely technical systems like aeroengines wherein resonance vibration is very often the root cause of many of the failures, and hence is a problem to be resolved. It can be seen that FRAM has got a universal applicability not only in the nonlinear systemic accident model, but also for the traditional simple/complex linear cause–effect models.
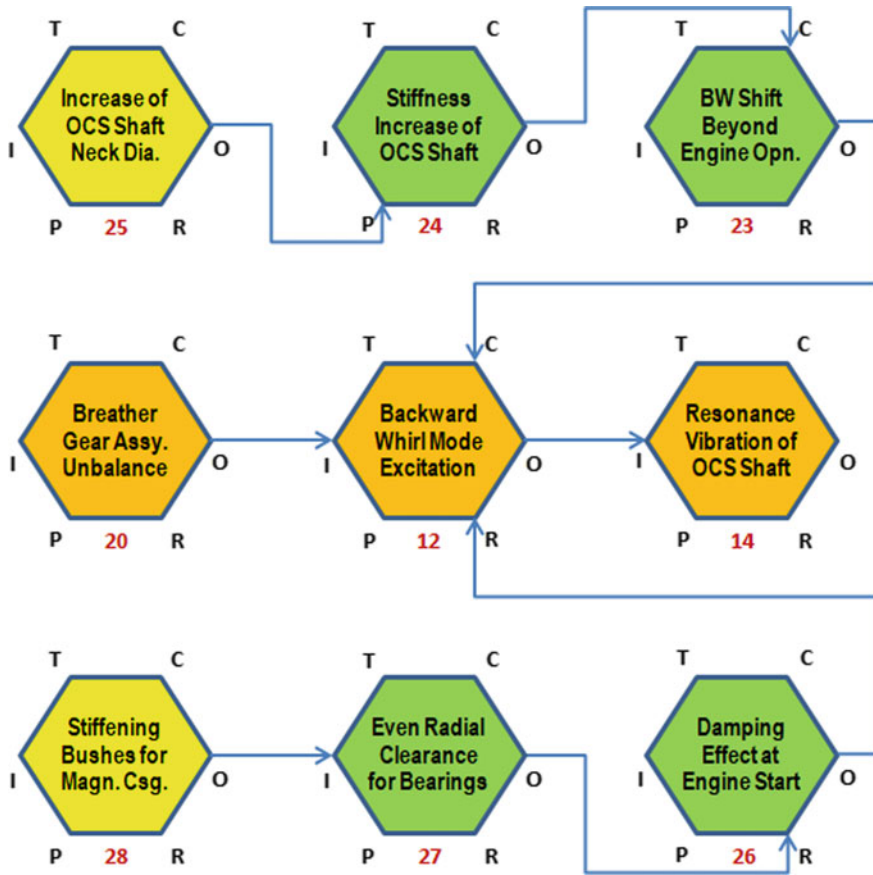
Fig. 16 "FRAMED-IN-FRAM" diagram—stage-3

"FRAMED-IN-FRAM" diagram, the Excel-based methodology devised by the authors for depicting the interrelationship of various functions/processes along the six FRAM aspects (viz. input, output, time, precondition, control, and resource) is very simple in its application and is extremely flexible for expanding the horizon of thinking and analysis, and also provides a neat and organized look to the otherwise clumsy FRAM diagram.
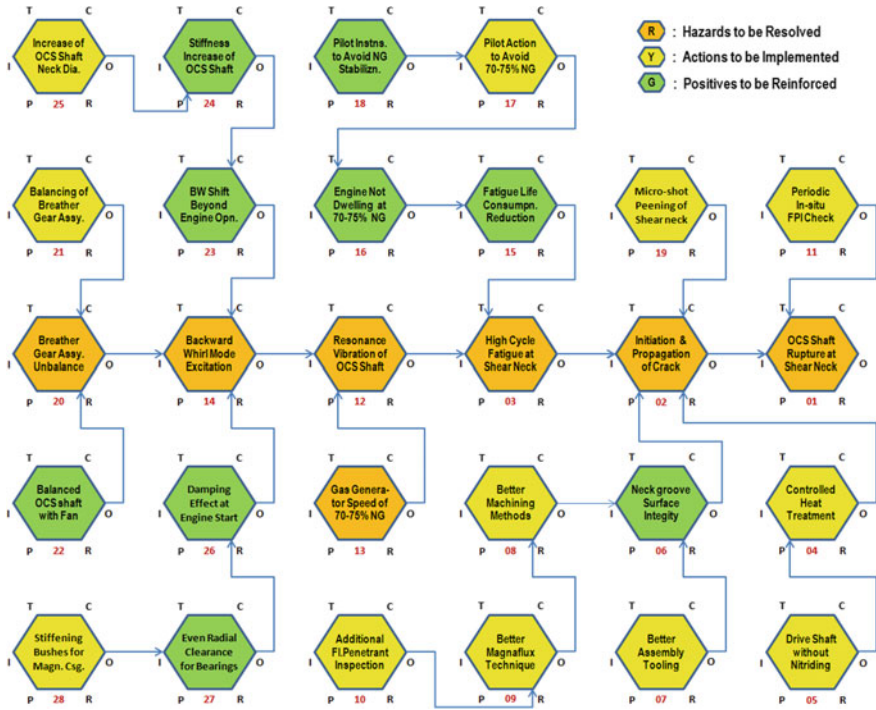
Fig. 17 Combined "FRAMED-IN-FRAM" diagram for the case study on OCS drive shaft

References

1. Hollnagel E (2011) Introduction to FRAM: the functional resonance analysis method. University of Southern Denmark
2. Hobbes T (1588–1679) "Leviathen". Ch. IX (1651)
3. Musashi, Miyamoto (1584–1645): "The Book of Five Rings". The Earth Book (1645)
4. Lundberg J, Rollenhagen C, Hollnagel E (2009) What-you-look-for-is-what-you-find—consequences of underlying accident models. In: Safety science. https://doi.org/10.1016/j.ssci.2009.01.0042009
5. Hollnagel E (2011) Understanding accidents, or how (Not) to learn from the past. University of Southern Denmark
6. Taleb NN (2010) The Black Swan: the impact of the highly improbable. Penguin Books. ISBN: 978-0-141-03459-1
7. Vesely B et al (2002) Fault Tree handbook with aerospace applications. In: NASA office of safety and mission assurance. NASA Headquarters, Washington

8. Hollnagel E (2015) Some Myths about industrial safety. In: Safety synthesis
9. Hollnagel E (2015) Safety-I and Safety-II: safety analysis and safety synthesis. In: Safety synthesis
10. Leonhardt J, Hollnagel E, Macchi L, Kirwan B (2009) A white paper on resilience engineering for ATM. In: European organisation for the safety of air navigation
11. Hollnagel E (2013) Resilience engineering—building a culture of resilience. In: Safetysynthesis
12. Hollnagel E (2014) The fundamentals of Resilient Organisational Performance. In: Safety synthesis
13. Hollnagel E (2010) On how (Not) to learn from accidents. Mines ParisTech, France
14. Hollnagel E (2015) Modelling transport systems with fram: flows or functions? In: Safety synthesis, information on FRAM. www.functionalresonance.com
15. Garvin DA (1988) Managing quality: the strategic and competitive edge. Harvard Business School, The Free Press. ISBN 0-02-911380-6
16. John SK et al (2018) Reliability improvement in aero engines during the infant mortality period of operations. J Failure Anal. Prevent
17. Churchwell J, Zhang KS, Saleh JH (2017) Epidemiology of helicopter accidents: trends, rates, and covariates. In: AHS international 73rd Annual forum, Fortworth, Texas, USA
18. Saravanamuttoo HIH, Rogers GFC, Cohen H (2006) Gas Turbine theory. In: Fifth edition—Pearson Education Ltd., ISBN: 81-7758-902-4
19. Nath A, Grant R (2011) The technology of balancing large flexible rotors. In: Technical seminar on vibration, balancing and condition monitoring, ABRO Balancing Inc., Texas, USA
20. Jeffcott HH (1919) The lateral vibration of loaded shafts in the neighbourhood of a whirling speed—the effect of want of balance. Lond, Edinburgh Dublin Philos Mag J Sci 37(219):304–314
21. Swanson E, Powell CD, Weissman S (2005) A practical review of rotating machinery critical speeds and modes. Sound Vib 10–17
22. Greenhill LM, Cornejo GA (1995) Critical speeds resulting from unbalance excitation of backward whirl modes. In: Proceedings, design engineering technical conferences, vol 3, Part B, ASME, pp 991–1000
23. Jahromi AF, Bhat RB, Xie W-F (2015) Forward and backward whirling of a rotor with gyroscopic effect. In: Sinha JK (ed), Vibration engineering and technology of machinery, mechanisms and machine science, vol 23, pp 879–887
24. Millsaps KT, Vejvoda CE (1996) Origin of split resonance and backward whirl in a simple rotor. In: Proceedings, international gas turbine and aeroengine congress and exhibition. Birmingham, UK, pp 1–6
25. Thomas J (1993) Design-related manufacturing aspects of MiG series aeroengine compressor components. In: Compendium of Technical Papers. vol I, Workshop on "MiG engine experience for Kaveri Project, pp 105–115

Measurements of Droplet Velocity Fields in Sprays from Liquid Jets Injected in High-Speed Crossflows Using PIV

Venkat S. Iyengar, K. Sathiyamoorthy, J. Srinivas, P. Pratheesh Kumar, and P. Manjunath

Abstract The present work reports the measurement of planar droplet velocity field of a plain liquid jet injected into a high-speed crossflowing airstream. PIV was employed to measure the instantaneous and average droplet velocity field in the far-field region of the spray. Water was injected from a 1-mm orifice and crossflow air velocities up to 110 m/s were investigated. The approach using PIV was validated using experimental PDPA data reported in literature. The increase of droplet velocity with axial distance was clearly observed. In the region considered for analysis, the droplet velocity showed a peak in the central region suggesting contributions primarily from surface breakup.

Keywords Jet in crossflow · PIV · Droplet velocity

1 Introduction

The behavior of liquid jets in subsonic crossflows is of significant interest in propulsion systems which include gas turbine combustors, aircraft afterburners and liquid fuelled ramjets. The fuel injection scheme and the characteristics of the ensuing spray are critical in the successful design of these systems due to the very limited residence time available for the various processes of atomization, vaporization, mixing, and

V. S. Iyengar (✉) · K. Sathiyamoorthy · J. Srinivas · P. Pratheesh Kumar · P. Manjunath
Propulsion Division, CSIR-National Aerospace Laboratories, Bangalore, India
e-mail: svenkat@nal.res.in

K. Sathiyamoorthy
e-mail: sathy_cim@nal.res.in

J. Srinivas
e-mail: srinivasj@nal.res.in

P. Pratheesh Kumar
e-mail: pratheesh@nal.res.in

P. Manjunath
e-mail: manjunathp@nal.res.in

combustion. To understand the spray characteristics better and rapidly realise optimal injector configurations, various parameters need to be reliably measured and possibly controlled, namely the penetration, droplet size and velocity distribution in the fuel spray which has motivated several investigators to understand the techniques and methods in injector design leading to the distribution of the right quantity of fuel at appropriate locations. The development of robust and reliable CFD models is required for efficient designs for reduction in development time and cost of these propulsion systems. A key challenge in the deployment of two-phase CFD models for these systems is in the proper specification of spray boundary conditions, typically in identifying the spatial locations from where the liquid phase can be injected in forms of droplets and the assignment of mass flux, drop size, distribution and velocity at these locations. This work aims to focus on one aspect of the issue by looking at 2D planar measurements of droplet velocity fields emanating from sprays injected in high speed subsonic crossflow environments for application in gas turbine and other propulsion systems.

Various studies have been reported on jets in subsonic crossflows focusing on different spray parameters and characteristics [1–5]. Inamura and Nagai [7] studied liquid water jets in subsonic crossflows from 0.2 to 0.3 Mach at momentum flux ratio's ranging from 6 to 12 using PDPA. They used a plain orifice injector of diameter 1 mm and made measurements at various axial locations. They found that the droplet velocity increases with an increase in air velocity and for an increase in momentum flux ratio, the minimum velocity decreases and the vertical location with minimum droplet velocity approaches the center from the bottom wall. While PIV is routinely used for analyzing velocity fields in gas-phase flows for different types of complex environments, its application to two-phase flows with the droplets themselves acting as seed particles is quite challenging due to the inhomogeneous distribution of the droplets and the variation in drop sizes giving rise to droplet clustering and intensity fluctuations. Careful experimentation and additional preprocessing is required to obtain good quality results. Elshamy et al. [8] studied the steady and dynamic behavior of liquid water jets in subsonic crossflows using a plain orifice nozzle at various momentum flux ratios and Mach numbers. They used both LDV and spray PIV for their measurements of droplet velocities. They reported good agreement for their spray PIV measurements with their LDV data and showed PIV to be a good tool to capture the aerostructure of spray generated by liquid jets in crossflows. Further, they observed that droplet velocity exhibited a minimum at the spray core and with increase in the momentum ratio the transverse location as well as the droplet velocity of the spray core increased, while the droplet velocity at the outer periphery decreased. Tambe [9] studied jets in subsonic crossflow at various conditions and showed that droplet axial velocities (Ud) exhibited a minimum below the spray core and increase with increasing transverse distance. Bellofiore et al. [10] studied kerosene jets injected in heated air with moderately low crossflow velocities of 25 m/s at low momentum flux ratios. They used a TSI PIV system to measure spray velocities in the vicinity of jets. Mashayek et al. [11] investigated liquid water jets from 0.5-mm injectors in low-speed crossflows (We = 55) for momentum flux ratios from 8 to 15 using PIV. It can be seen from some of the earlier studies that PIV

approach for spray droplet velocity measurements have compared quite well with the established LDV/PDPA approach. The PIV technique for spray droplet velocity measurements additionally offers a rapid means of obtaining spatially resolved velocity data which is quite important in minimizing tunnel run times for making detailed measurements. However, very few studies have explored the spray PIV technique for obtaining droplet velocity fields in high-speed crossflows and detailed studies in this regime are required as it is of great practical interest. This work aims to focus on one aspect of the issue by looking at 2D planar measurements of droplet velocity fields emanating from sprays injected in high-speed subsonic crossflow environments for application in gas turbine and other propulsion systems.

2 Experimental Methods

2.1 *Test Rig Details and Experimental Setup*

The measurements were carried out at the high-speed combustor test facility at NAL. A large 10-bar storage reservoir supplies air which feeds to an 8" air supply line in the facility. Downstream of the supply line is a rig which is designed and fabricated to investigate the study of liquid jets in subsonic and supersonic crossflows with provisions for optical measurements (Fig. 1). It consists of a transition section of

Fig. 1 Experimental setup used for the experiments
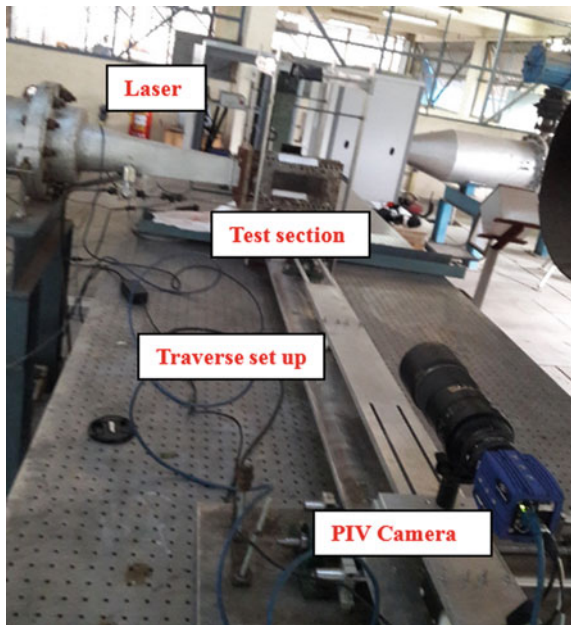
Fig. 2 Schematic of the test section and the measurement
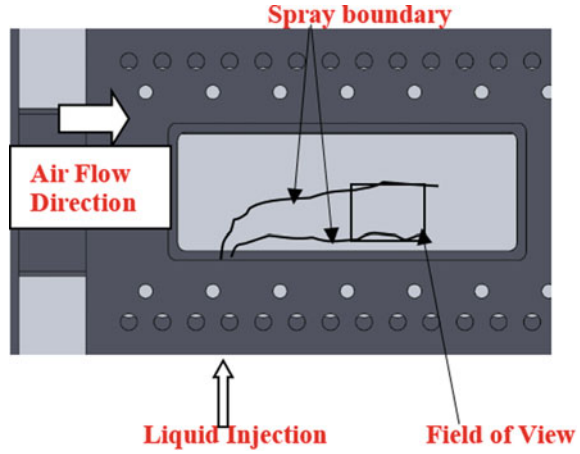
length 1200 mm which is preceded by a settling chamber. The transition section has exit dimensions to match the entry to the test section. The test section is about 365 mm long and has a rectangular cross section of 50 mm × 70 mm (Fig. 2). Three quartz windows about 15 mm thick are employed to provide optical access for diagnostic measurements. These windows are appropriately assembled for providing flush surfaces along the rectangular duct on both the sides and the top for optical access. The windows provide optical access for a length of 200 mm (about 180 mm downstream of the injector and 20 mm upstream of the injector) and a height of 70 mm covering the entire flow surface height. The top window is 30 mm wide and 200 mm long and allows the laser sheet to enter the test section The fuel injector is mounted at the bottom of the test section about 20 mm downstream of the test section entrance and is flush with the bottom wall of the test section. A K-type thermocouple is employed to measure the temperature and two pressure transducers are used to measure the total and static pressures to estimate the flow conditions. One pressure transducer (0–10 bar g with an accuracy of 0.2% FS) was placed far upstream in the rig in the settling chamber to measure the total pressure and the second pressure transducer (0–7 bar with an accuracy of 0.1% BFSL) was used to measure the static pressure just before in the entrance to the test section. A sturdy clamped support is provided to support the rig which extends into the optical table where the traverse arrangement is placed. A steady run time of 15 s for each test condition is ensured with an image recording time of 10 s at various desired air flow rates corresponding to different fuel flow rates for making experimental measurements.

2.2 PIV Setup for Droplet Velocity Measurements

For measurements of droplet velocities, a PIV setup was assembled using a dual-pulse Nd:YAG Laser, a PIV CCD Camera, a synchronizer, and a data acquisition

system. A 2-axis traverse system was fabricated and assembled in a optical table. Figure 1 shows the experimental setup for spray velocity measurement along with the traverse and other PIV components.

A Litron dual-pulse Nd: YAG laser is used as a light source. This laser can provide 15 pulse pairs per second at a maximum energy of 200 mJ for PIV measurements. A 2-axis traverse is assembled in the optical bench which has a lens and mirror arrangement to convert the circular beam from the laser to a sheet and guide the laser sheet into the test section from the top window. The beam is delivered through the top window as a 40-mm-wide and 1-mm-thick sheet using a slit. The optical axis of camera is normal to the laser sheet. Laser pulse pairs were generated at a laser repetition rate of 10 Hz and were synchronized and recorded by the camera such that the exposure from each pulse was recorded in a separate frame. Each image thus had two frames separated by the interframe time varying from 8 to 10 s. The CCD camera collected light over its entire array of 1200 by 1600 pixels that were each of 7 µm in size. The camera was operated with a 300-mm macro lens at an F number of 4.0. This was located about 1.45 m from the object plane. In order to filter out unwanted light from other ambient sources, a narrow bandpass filter (centered at 532 nm) was mounted in front of the lens. The image resolution obtained was 28.5 pixels/mm with this configuration.

2.3   Image Analysis and PostProcessing

After making background and dark image correction, the images are suitably preprocessed using PIVlab [6]. This involves the operation of applying a high-pass filter of 15 pixels and intensity capping on the images. To maximize valid particle displacements a minimum of 8–10 particle pairs per interrogation window is recommended. However, as the droplets from the spray constitute the seed particles, the number of particle pairs in each subregion varies according to the local extent of penetration in the flow. Thus due to this stochastic nature of the number of droplets in each interrogation region, some subregions are expected to have fewer particle pairs and produce spurious vectors. This effect was minimized by selecting suitable region of interest in the laser illuminated plane which has sufficient number of particles in both the frames. The PIVlab software used here employs cross-correlation to determine velocity information. Small subimages (interrogation areas) of an image pair are cross-correlated to derive the most probable particle displacement in the interrogation areas. The correlation matrix is computed in the frequency domain using fast Fourier transform. To start, a 64 by 64-pixel size is chosen for each subregion followed by one pass of 32 and 32 pixels with a 50% overlap. For detection of outliers, the data is validated for its reliability by using a standard deviation filter and choosing limits for acceptable velocities manually.

Table 1 Comparison of droplet axial velocities from PDPA data of Inamura and Nagai with current experiments at 80 mm from injector

S No	Height from the bottom wall (mm)	Droplet velocity in the flow direction (m/s)	
		Inamura and Nagai	Current spray PIV
1	13.5	60	62
2	16	65	59
3	19	66	63

3   Results and Discussion

3.1   Experiments with Water as Injectant from a 1-mm Orifice for Comparison with Benchmark PDPA Data

To confirm the approach used in the current spray PIV experiments, the benchmark experimental data of Inamura and Nagai (7) was considered and initial experiments were done using water with a 1-mm injector. One of the experimental test cases reported by them was replicated (Va = 110 m/s, Vl = 11.6 m/s with water injection from a 1-mm orifice) and the results were processed. The droplet axial velocity reported by them at a distance of 80 mm from the injector in the flow direction, for a few locations from the bottom wall, for the above condition is taken for comparison with our experiments. A reasonably good match (Table 1) was observed.

3.2   Experiments with Water from a 1.0-mm Plain Orifice for Various Conditions

The parameters Weber number and momentum flux ratio were used to characterize the sprays. The experiments conducted covered a Weber Number range from 100 to 300 and a momentum flux ratio range from 10 to 50. The coordinates x, y, and z denote streamwise, transverse and spanwise directions respectively. Water is injected perpendicularly into the high-speed subsonic crossflow at x/d = 0. The process of capturing distinct and adequate spray particles in two frames involved lot of trials for optimization of parameters in the image acquisition software DAVIS.

Typical results from two different crossflow velocities representing two different Weber numbers are discussed in the following paragraphs. The PIV analysis is done for a two-dimensional plane along the injector centerline (z = 0) bound by a region spanning 66–78 mm from the injector and 14–26 mm from the bottom wall.

Case A: Ua = 97 m/s, Ul = 11 m/s (We = 130, J = 12)
Figure 3 shows the raw image captured by the camera for the above flow conditions. As expected due to the stochastic nature of drop breakup and formation from the parent jet the droplets are not distributed evenly in the two frames and a small region

Fig. 3 Raw image at the injector centreplane 50 mm from the injector showing the region of interest for PIV analysis
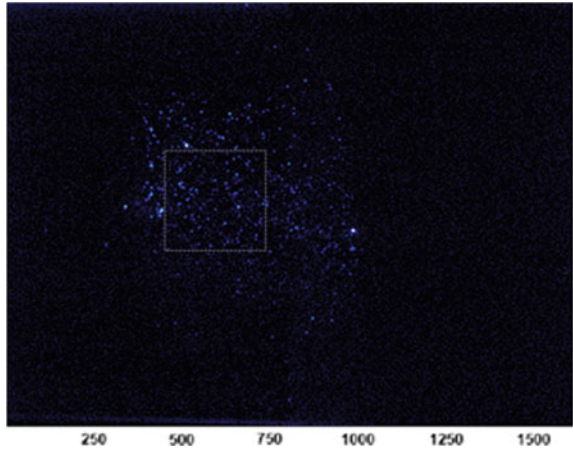
of interest is chosen around the spray core keeping in mind the presence of reasonable number of droplets in both the frames. The velocity vectors are clearly aligned along the flow direction as seen in Fig. 4. Figure 5 shows the droplet axial velocity contours in region of interest. The figures show the gradual acceleration of the drops with the droplet velocity almost reaching about 50% of the crossflow air velocity.

Case B: Ua = 106 m/s, Ul = 12 m/s (We = 160, J = 12)

Figure 6 shows the raw image captured by the camera for the above flow conditions. It is seen that the region of interest spans the outer boundary of the spray. Figure 7 shows the contour plot of droplet axial velocity in the same field of view. The gradual increase in droplet velocity with axial distance is clearly seen. The central region of the contour shows the presence of maximum droplet velocity. The velocity contours show a similar pattern as the earlier case with a nominal increase in the droplet

Fig. 4 Droplet velocity vectors in the region of interest
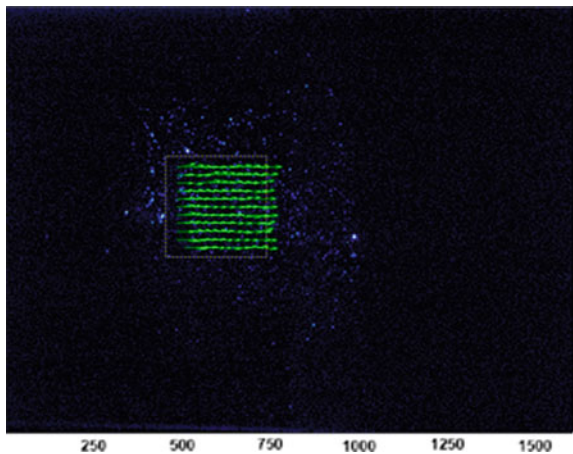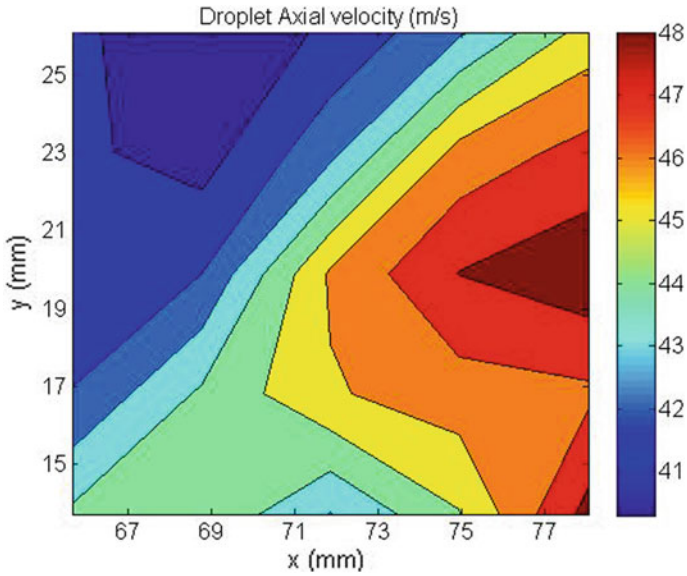
Fig. 5 Instantanous droplet axial velocity contours at the injector centreplane
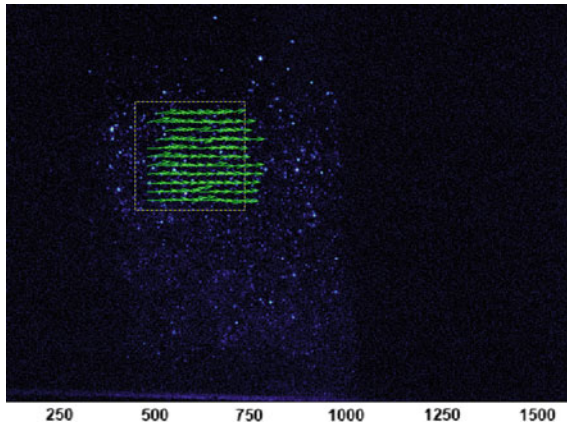
Fig. 6 Raw image at the injector centreplane 35 mm from the injector showing the region of interest for PIV analysis

velocity values corresponding to the higher crossflow velocity in this case. It is interesting to note that the droplets have only reached about 60% of the crossflow air velocity even at this far-field location.
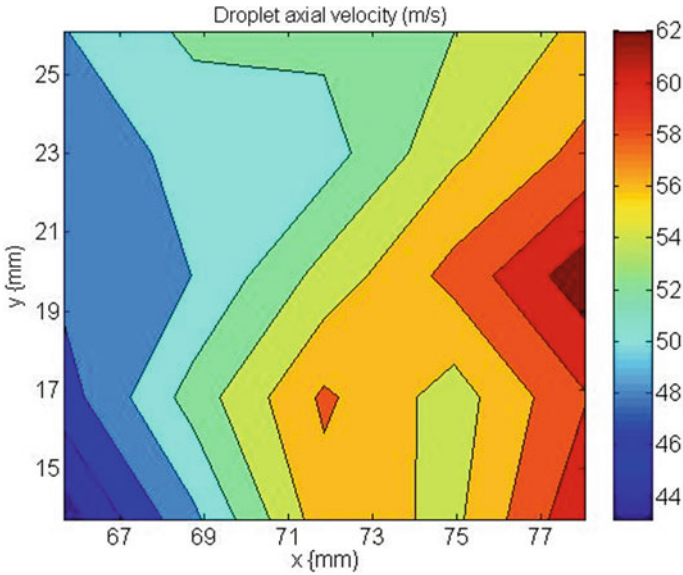
Fig. 7 Instantanous droplet axial velocity contours at the injector centreplane

4 Conclusions

PIV was successfully implemented to study the instantaneous and average droplet velocities of sprays generated by the breakup of liquid water jets in high-speed crossflow environments. The approach used in the experiments was compared and validated with benchmark data from published literature. The trends of increasing droplet velocities along the crossflowing airstream were captured. The peak of the droplet velocity is seen in the central region of the considered plane suggesting contributions from surface breakup. It was seen that the droplets velocities reached round 50–60% of the crossflow velocities at a distance of around x/d = 75. Reliable mapping of velocity field depends on the presence of sufficient number of drops in the field of interest.

References

1. Wu P, Kirkendall KA, Fuller RP, Nejad A (1997) Breakup process of liquid jets in subsonic crossflow. J Propuls Power 13(1):64–73
2. Wu P, Kirkendall KA, Fuller RP, Nejad A (1998) Spray Structures of liquid jets atomized in subsonic crossflow. J Propuls Power 14(2):173–182
3. Lin KC, Kennedy PJ, Jackson TA (2002) Penetratıon heights of liquid jets in high speed crossflows. In: 40th AIAA aerospace sciences meeting and exhibit reno. AIAA 2002–0873. Nevada, USA
4. Becker J, Hassa C (2002) Breakup and atomization of a Kerosene jet in crossflow at elevated pressure. Atomiz Sprays 12:49–61
5. Stenzler JN, Lee JG, Santavicca DM (2006) Penetration of liquid jets in a crossflow. Atom Sprays 16:887–906
6. Thielicke W, Stamhuis EJ (2014) PIVlab—towards user-friendly. Afford Accurate Digit Part Image Velocim J Open Res Softw 2(1):e30. https://doi.org/10.5334/jors.bl
7. Inamura T, Nagai N (1997) Spray Characterstics of a liquid jets traversing subsonic airstreams in crossflow. J Propuls Power 13(2):250–256
8. Elshamy O, Tambe SB, Cai J, Jeng SM (2002) PIV and LDV measurements for liquid jets in crossflows traversing subsonic airstreams in crossflow. In: 45th AIAA aerospace sciences meeting and exhibit reno. AIAA 2007–0873 NV
9. Tambe S (2004) Lıquıd jets in subsonic crossflow. MSc Thesis, University of Cincinatti
10. Bellifiore A, Cavaleire A, Ragucci R (2008) PIV Characterization of sprays generated by crossflow injection in high density airflow. ILASS08, 12–02
11. Mashayek A (2006) Experımental and numerical study of liquid jets in crossflow. MSc Thesis, University of Toronto

Turbines

Computational Investigations of Varying Solidity LP Turbine Cascade with Gurney Flap for Low Reynolds Numbers

G. S. Srivatsa and Gajanan Tatpatti

Abstract This paper reports computational investigation carried out on T106 LP turbine linear cascade to optimize the blade performance and reduce the blade count around the LP turbine rotor by decreasing blade solidity. T106 LP turbine blade of chord 196 mm and two different blade solidities of 1.25 and 1.176 were used. Passive flow control device—Gurney flap (GF) was attached to the trailing edge of the blade. The GFs of heights 1.33% Ch and 2% Ch were used in simulations. A two-equation eddy viscosity turbulence model, shear stress transport (SST) model was considered for all the computations along with gamma–theta (γ–θ) transition model. Computations were carried out for all the cases at four different Reynolds numbers. Lift coefficient, total pressure loss coefficient, overall integrated loss coefficient, and lift coefficient to overall integrated loss coefficient ratio were used as a measure of aerodynamic performance for the cascade. From the computations, it was found that on increasing the blade spacing by keeping the GF height constant, the performance of the turbine cascade decreases. But, the performance can be improved by increasing the flap height appropriately. For the cascade configuration with increased spacing, an optimal GF height was determined.

Keywords Gurney flap · LP turbine · Varying solidity

Nomenclature

C	Flow velocity
C_D	Drag coefficient
	$C_D = 2*(S/Ch)*\cos(\alpha_m)[(P_{01}-P_{02})/C_m^2]$

G. S. Srivatsa (✉) · G. Tatpatti (✉)
Department of Mechanical Engineering, R. V. College of Engineering, Bengaluru, Karnataka, India
e-mail: gramas1996@gmail.com

G. Tatpatti
e-mail: gajanan@rvce.edu.in

Ch   Chord (mm)
Ch_x Axial chord (mm)
C_L Lift coefficient
      $C_L = 2*(S/Ch)*\cos(\alpha_m)*[\tan(\alpha_1) + \tan(\alpha_2)] + C_D*\tan(\alpha_m)$
C_P Static pressure coefficient on blade surfaces
      $C_P = (P_{01}-P)/(P_{01}-P_1)$
H   Gurney flap height as a percentage of chord $H = h/Ch*100(\%)$
h   Gurney flap length (mm)
P   Pressure
Re   Reynolds number $(\rho.C.Ch/\mu)$
S   Cascade spacing (mm)
X   Non-dimensional axial distance (x/Ch_x)
x   Axial distance from leading edge (mm)
Y   Non-dimensional pitch wise distance (y/Ch_x)
y   Pitch-wise distance from leading edge (mm)

Greek Symbols

α Absolute flow angle
α_m $\alpha_m = \text{atan}[(\tan(\alpha_1) + \tan(\alpha_2))/2]$
ρ Density (kg/m^3)
μ Dynamic viscosity (Pa.s)
ψ Total pressure loss coefficient
      $\psi = [P_{01}-P_{02}]/(0.5*\rho*C_2^2)$
ψ_{int} Overall integrated loss coefficient
      $\psi_{int} = (\int \psi*C_{2x})/(\int C_{2x})$

Subscripts

0   Stagnation conditions
1, 2   Cascade inlet and outlet respectively
∞ Free stream conditions

1 Introduction

Gas turbines used in aero engine consist of a fan, low-pressure (LP) compressor (5–6 stages), high-pressure (HP) compressor (9–10 stages), combustion chamber, high-pressure (HP) turbine (2 stages), and low-pressure (LP) turbine (6–7 stages) [1]. Due

to the high power requirements of the fan, the LP turbine consists of several stages. Furthermore, the low rotational speed imposed by the fan leads to large diameters. As a result, the LP turbine is heavy, up to a third of the total engine weight, and expensive to manufacture [2].

The performance of LP turbines is dependent on Reynolds number (Re), incidence, and space–chord ratio. In these LP turbines, chord-based Re vary from as low as 25000 to as high as 500000. These LP Turbines are mainly designed to perform better at high Re, especially during takeoff and landing, but during high altitude cruise i.e. in thin air conditions and low velocities, the Re can fall as low as 25,000. Sharma [3] found that total pressure loss coefficient increases from around 0.03 to 0.10 with the decrease in Re. As the LP turbine blades have large flow deflection angles, the flow has a tendency to separate from the suction surface at low Re. The low momentum fluid flowing over the suction surface experiences an adverse pressure gradient thereby separating from the blade surface. The separation increases with the decreases in Re thereby increasing the width of the wakes downstream which in-turn results in increased total pressure losses. Hodson et al. [4] found that 60% of losses occur on suction surface. Hence, there is a need to control the laminar flow separation on LP turbine blade to decrease the total pressure loss coefficient at low Re as well as to meet the increasing demands of further higher altitude cruise.

Another concern for aero-engine operators is the total cost of engine ownership, which considers not only the capital cost but also the operating costs that are influenced by efficiency, weight, and reliability. Hence, it is necessary to reduce the weight of the turbine without decreasing the efficiency. Many developments are under way to reduce the total cost of the aero-engine. One of the ways to decrease the cost of the turbine is to decrease the number of blades in the LP turbine. As the number of blades reduces, the weight of the supporting structures like the casing and the hub also reduces. All these decrease the manufacturing cost of the turbine. Therefore, decreasing blade count of the LP turbine is also crucial.

Over the years, many flow separation control and lift enhancement devices have been invented. These flow control devices can be broadly classified into two main groups—passive and active flow control. Active flow controls adjust to the environment and provide better flow control but these require actuators which limit their usability because of their cost and space constraint. Passive flow control devices are generally geometric modification on the body for flow mixing, lift enhancement, or drag reduction.

Chishty et al. [5] used passive flow control device—dimples, on the blade in order to energize the flow to suppress boundary layer separation. The author also found the optimum size and position of the dimple for a particular blade configuration. Bons at el. [6] used an active flow control device, namely steady vortex generator jets and found that the total pressure loss coefficient was reduced by a factor of 2–3. Volino and Ibrahim [7] used pulsating vortex generator jets which showed increase in lift coefficient (C_L) by 20% and decrease in wake loss by 60% at low Re.

Guzel et al. [8] has studied the effects of passive flow control device—Gurney flap (GF) on the aerodynamic performance of VR-12. It was found that including GF

improved the lift characteristics of the airfoil. Dundi et al. [9] has carried out experimental studies on the performance of low-speed centrifugal fan with and without GF. The author observed improved performance for low Re but no significant improvement for higher Re. Chen et al. [10] conducted numerical investigation on decreasing space–chord ratio for low-pressure turbine using passive flow control devices. The author used flat, round, and smooth convex GFs as the passive flow devices.

Gajanan et al. [11] has investigated different sizes and shapes of GFs on T106 LP turbine linear cascade at low Re in order to reduce the total pressure losses due to laminar separation. They found out the optimal shape and height of the GF which can generate maximum lift and produce minimal total pressure losses for that specific space–chord ratio.

Previous studies were aimed at studying the effect of GF on the LP turbine cascade performance at various Re. In the current work, numerical flow analysis has been conducted on T106 LP Turbine linear cascade to study the performance at low Re for varying space–chord ratio and length of the GF. The GF was added to decrease the boundary layer separation and total pressure losses and, to increases the lift. Flow simulation has been carried out for space–chord ratio of 0.8 and 0.85 times chord and flap length of 1.33% chord and 2% chord. A comparison of performance parameters of different configuration has been plotted for a set of low Re and the optimal configuration is chosen.

2 Computational Methodology

2.1 Geometry

A high-lift LP turbine blade profile T106 was chosen to carry out the numerical analysis. Figure 1 shows the turbine blade profile. Cascade specifications are given in Table 1. The linear turbine cascade geometry was modeled in CATIA. The domain inlet was placed at more than 1.5 times chords upstream and the outlet was placed at more than 2.5 times chords downstream.

Figure 2 shows the mesh for the cascade geometry. The meshing was carried out in ANSYS ICEM CFD. A structured 2D mesh was created for the spatial discretization of the flow domain and the mesh was extruded span wise by one element thickness as CFX solver does not support 2D mesh. The minimum wall distance was chosen such that the y^+ value remains less than 0.01.

Figure 3 shows the different boundary conditions used for the simulations. Velocity BC was set at inlet and the magnitude of the inlet velocity was varied according to the required Re. Pressure BC (0 gauge pressure) was set at outlet.

No-slip boundary condition was imposed on blade surface. Periodic boundary condition was set between the upper and lower surfaces to simulate a linear cascade with infinite number of blades.
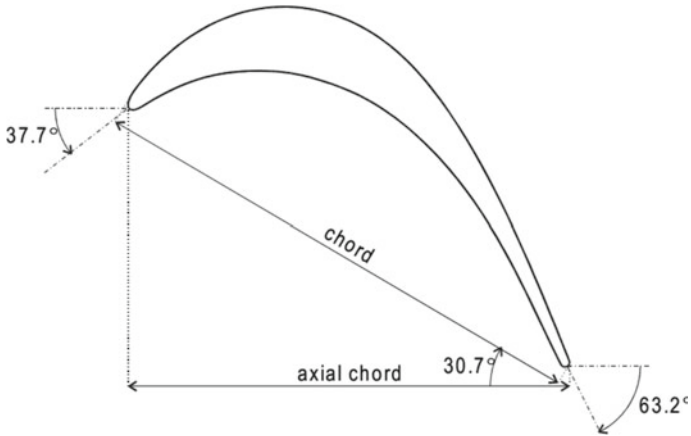
Fig. 1 T106 blade profile

Table 1 Cascade specifications

Geometry parameters	Value
Chord	196 mm
Axial chord	169 mm
Blade stagger	$30.7°$
Inlet blade angle	$37.7°$
Exit blade angle	$63.2°$
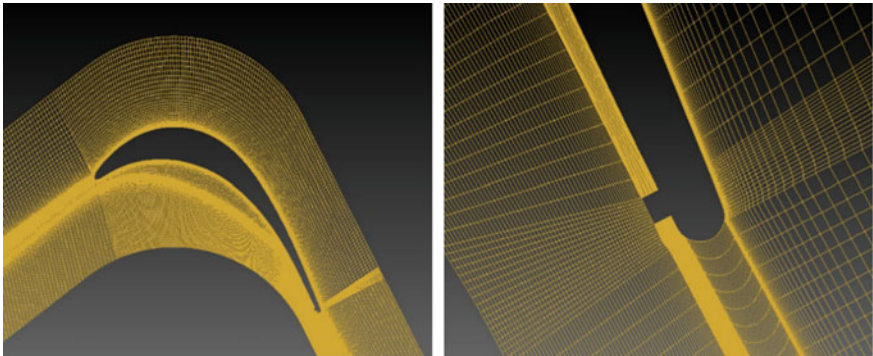
Fig. 2 Structured mesh

Fig. 3 Boundary conditions
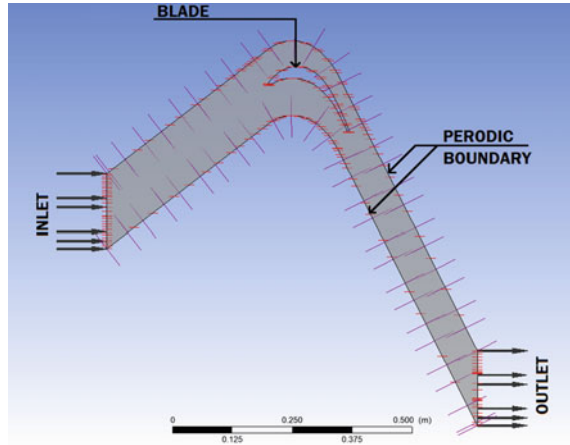
2.2 Computational Models

Steady-state analysis was carried out for the linear cascade model in ANSYS CFX, using Reynolds-averaged Navier–Stokes (RANS) solver. The partial differential equation of the solver is written as follows.

$$\frac{\partial Q}{\partial t} + \frac{\partial E}{\partial x} + \frac{\partial F}{\partial y} + \frac{\partial G}{\partial z} = \frac{\partial E_v}{\partial x} + \frac{\partial F_v}{\partial y} + \frac{\partial G_v}{\partial z}$$

Here, Q is the flow vector; E, F, and G are the inviscid flux vectors; and E_V, F_V, and G_V are the viscous flux vectors. SST k–ω turbulence model coupled with this gamma–theta transition model was used. This includes two equations; one for intermittency and one for the transition onset criteria in terms of momentum thickness Re. This model was used to predict the laminar to turbulent transition accurately. The turbulence intensity of the flow inlet flow was set to 1%.

3 Results and Discussion

Numerical analysis of turbine cascade models with varying space–chord ratio and height of GF was carried out for four different Re ranging between 25000 and 150000 for all the cases tabulated in Table 2. C_L, integrated total pressure loss coefficient (ψ_{int}), and ratio of lift coefficient to integrated total pressure loss coefficient (C_L/ψ_{int}) were chosen as performance parameters. Based on the analysis made from the simulation, the turbine cascade configuration with maximum space–chord ratio which would generate the C_L more than or equal to that of the baseline case and produce

Table 2 Blade cascade configuration

Blade configuration	Space–chord ratio	Blade solidity	GF height (H)
Case 1 (Baseline)	0.8	1.25	–
Case 2	0.8	1.25	1.33
Case 3	0.85	1.176	1.33
Case 4	0.85	1.176	2

less total pressure losses in comparison to that of baseline case has been selected as the most efficient.

Figure 4 shows the validation of simulation results for blade static pressure distribution at Re = 75,000 with the existing experimental values [11]. The simulation and experimental results were found to be in good agreement with each other except at few locations on suction side closed to the leading and trailing edge.
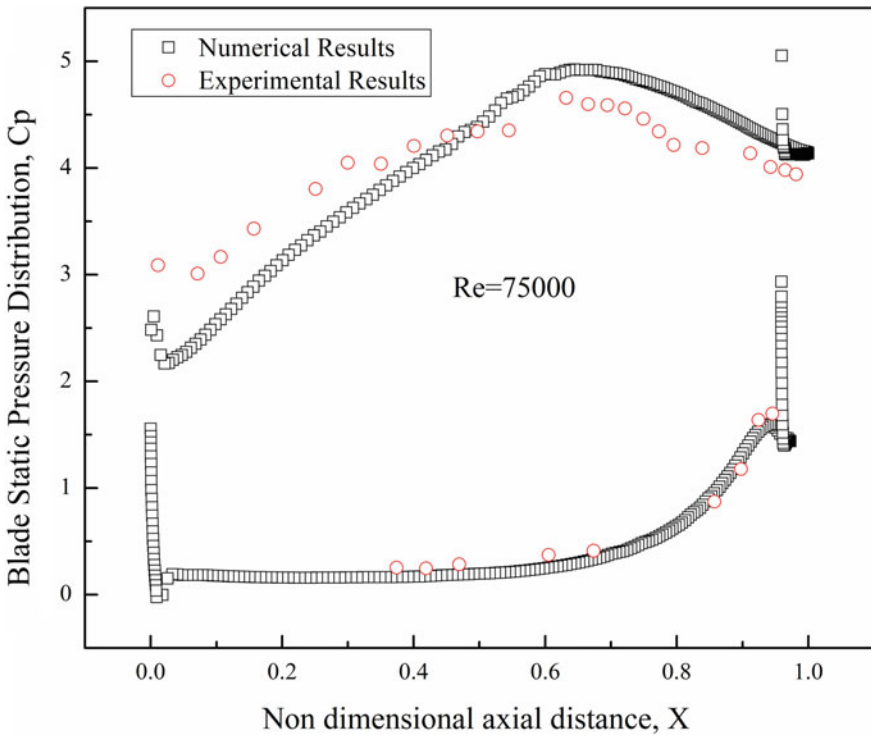
Fig. 4 Comparison of blade static pressure distribution obtained by numerical method and experimental results [11]

3.1 Effect of Varying Space–Chord Ratio and GF Height on the Turbine Cascade Performance

The addition of GF to the trailing edge of the blade will have an effect on performance parameters like C_L, drag coefficient (C_D), overall integrated loss coefficient(ψ_{int}), C_L/ψ_{int}, flow deflection angle of the blade. The effect of varying GF height and space–chord ratio is shown using blade static pressure distribution (C_P), velocity contours, C_L, ψ_{int}, C_L/ψ_{int} of the blade for four different Re cases.

Figure 5 shows the blade static pressure distribution for second, third and the fourth case at four different Re. A flat line of constant pressure at the end of the suction surface close to the trailing edge in the C_P distribution is an indication of flow separation. This implies that from the point of separation till the point of re-attachment the pressure remains constant.

Figure 5a shows the blade pressure distribution for the second case. It can be seen that static pressure distribution over the blade surface overlaps for all the Re without much difference. On the suction surface, there is no region of constant pressure distribution close to the trailing edge which means there is no flow separation. It also means the gurney flap was successful in eliminating separation at all Re for the given space–chord ratio.

Figure 5b shows the blade pressure distribution for the third case. It can be seen that except at Re = 150,000, there was a flow separation for all other Re. This was because of the increased spacing between blades resulting in increased flow separation. It was also observed that the flat region in the graph decreases with the increase in the Re of the flow.

Figure 5c shows the blade pressure distribution for the fourth case. It can be seen that the flat constant pressure region in the graph decreases as the height of the GF was increased to 2% of the chord for all the Re. The decrease in the flat constant pressure region is an indication of decreased flow separation.

From the velocity contours, it can be seen that the flow on the suction surface accelerates from leading edge till it reaches minimum pressure point and starts to decelerate further till the trailing edge. In the case of flow separation, the flow velocity goes to zero at the point of separation.

Figure 6 shows the velocity contours for the second case at four different Re.
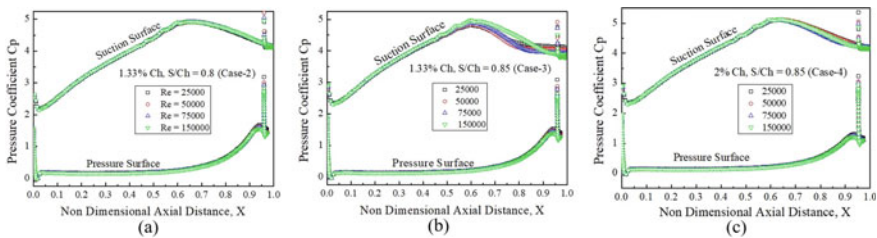
Fig. 5 Comparison of C_P distribution for all the three cases for different Re
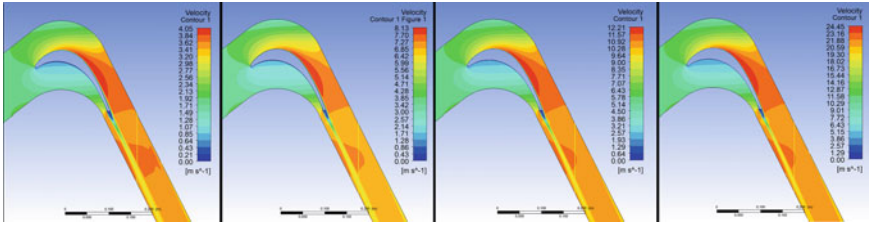
Fig. 6 Velocity contour for spacing of 0.8Ch and 1.33% Ch GF height for Re = 25, 50, 75, and 150 k

It was observed that there was no flow separation in any of the cases. This shows that gurney flap of 1.33% Ch is effective for space–chord ratio of 0.8 at low Re in eliminating separation.

Figure 7 shows the velocity contours, for the third case, at four different Re. It can be seen that for Re of 25,000, 50,000, and 75,000, there are large blue regions of flow separation and flow reversal on the suction surface close to the trailing edge. It can also be noticed that wake widths for these above-mentioned Re of case 3 were found to be broader in comparison to the wake widths of corresponding Re of case 2. Increase in the width of wakes leads to increase in total pressure losses. For Re of 150,000, the fluid has sufficient momentum to overcome the adverse pressure gradient in the forward direction on the suction surface close to the trailing edge. This shows that the GF of 1.33% Ch is not effective in eliminating flow separation when space–chord ratio was increased from 0.8 to 0.85.

Figure 8 shows the velocity contours at four different Re for the fourth case. It can be seen from velocity contours that the GF of 2% Ch was successful in almost eliminating flow separation for an increased space–chord ration of 0.85 at low Re.

Figure 9 compares the C_L for baseline case, cases 2, 3, and 4 at four different Re. It can be seen from the figure that the C_L is mostly independent of the Re and dependent on the height of GF flap and the blade spacing. For all the GF flap cases, it can be seen that C_L is always greater than that of the baseline case. With the addition of GF to the blade, the effective camber of the airfoil increases leading to increase in lift. As the spacing increases from case 2 to case 3, it was observed that the C_L as well as the flow deflection angle decreases. As the spacing increases, the fluid flow
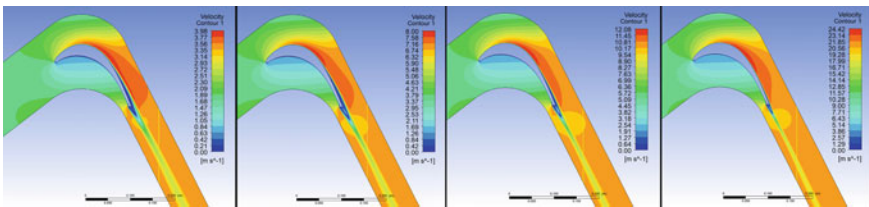
Fig. 7 Velocity contour for spacing of 0.85Ch and 1.33% Ch GF height for Re = 25, 50, 75, and 150 k
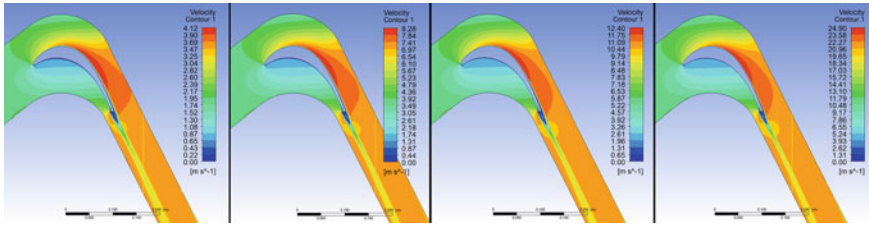
Fig. 8 Velocity contour for spacing of 0.85Ch and 2% Ch GF height for Re = 25, 50, 75, and 150 k
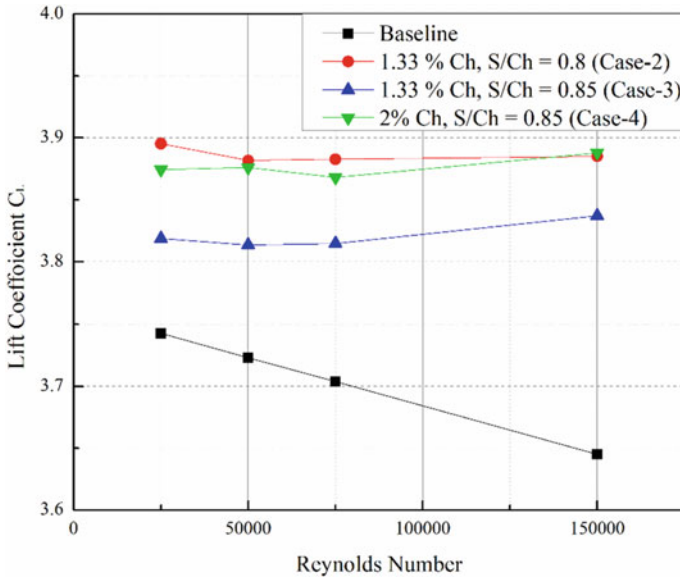
Fig. 9 The relationship between C_L and Re for different cases

gets more scattered from the actual flow path leading to decreased deflection angles and effective lift force. The C_L for the case 4 was found to be almost equal to that of the case 2. The effect of increased blade spacing is compensated by the increase in height of GF.

Figure 10a gives the relation between the ψint and Re for the baseline case, cases 2, 3, and 4. It can be seen that as the Re is decreased for the baseline case, ψint goes on increasing. The increase in ψint with decrease in Re can be related to increased flow separation and larger wake widths and wake heights at lower Re leading to larger total pressure losses. Similar trend of ψint variation was also witnessed even for GF cases. The decrease in the value of ψint is prominent from the Re 25,000–50,000 because of the high wakes produced at low Re, which decreases as the Re increases thereby decreasing ψint.
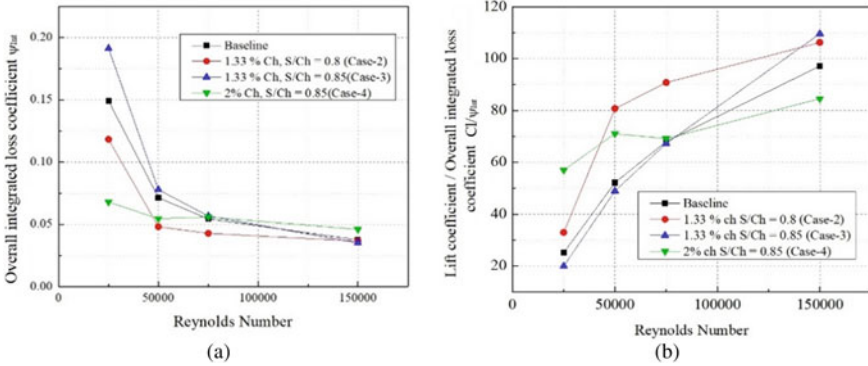
Fig. 10 **a** The relationship between overall integrated pressure loss coefficient and reynolds number for different cases **b** The relationship between lift coefficient/overall integrated pressure loss coefficient and reynolds number for different cases

It can be seen, from the figure, ψint for case 2 is less than that of case 1 for all the Re. This can be accounted for the fact that from case 1 to case 2, the separation of fluid flow that led to the formation of larger wake widths and wake heights downstream was eliminated. In case 3 as the blade spacing increases, flow separation becomes more pronounced as the fluid flow becomes more scattered in the flow passages and tend to lift off from the suction surface to the regions of lower pressures thereby increasing ψint. The amount of total pressure losses for case 3 were found to be larger in comparison to baseline case (case 1) at Re = 25,000 and Re = 50000, whereas at Re = 75,000 and Re = 150,000, the total pressure losses were found to be almost same. In order to decrease the total pressure losses for the spacing corresponding to case 3, a GF height was increased from 1.33% Ch to 2% Ch. This new GF configuration of case 4 with enhanced GF height was able to make the flow stick to the blade surface till the trailing edge and decrease the overall integrated loss coefficient as evident from the Fig. 10a.

The main purpose of using GF is to enhance the C_L generated by the blade and to decrease the overall integrated loss coefficient by eliminating separation. It would be more appropriate to understand the combined effect of lift enhancement and total pressure loss coefficient for different cases. To study the combined effect, Cl/ was plotted against Re for all the four cases as shown in Fig. 10b. We can see from the graph that the value of the C_L/ increases with the increase in Re. This is because for a particular case as Re increases the value of decreases, but C_L remains almost the same thereby increasing the value of CL/.The value of Cl/ for cases 2 and 4 were found to be higher than that of baseline case at all the Re, except at Re = 150,000 for case 4. Thus, there is a need to optimize the height of GF such that the ratio Cl/ for decreased solidity is always greater than that of the baseline case.

3.2 Optimum Height of the Gurney Flap

In order to find the optimal height of the GF for the increased space–chord ratio of 0.85, the new configuration should perform better than that of the baseline case at all Re. Considering cases 3 and 4 where only the length of the GF flap was varied and all other parameters were kept constant. It can be observed that as the length of the GF increases the separation at the lower Re decrease there by decreasing ψ, and increasing CL/ψint. At higher Re where the amount of separation is less (the losses induced by using a GF because of effective increase in trailing edge radius are more in comparison to losses due to amount of separation), the increase in GF heights leads to bigger wakes thereby decreasing CL/ψint. Assuming linear relationship between GF height and CL/ψint for each Re, the overall integrated pressure loss coefficient value was predicted for different GF height values. For space–chord ratio of 0.85, the GF height must be greater than 1.42% of chord in order to have a CL/ψint value higher than baseline case at low Re (Re < 150,000). For high Re (Re = 150,000), the flap length must be lesser than 1.67% of Chord. Therefore, the value of "H" must be between 1.42 and 1.67. In order to obtain the optimal performance at all Re, the flap length must be around 1.55% of chord corresponding to space–chord ratio of 0.85.

4 Conclusion

The following major conclusions can be drawn from the current work.

1. Lift coefficient, C_L with GF is always greater than that of baseline case.
2. The C_L is directly proportional to the flap height and inversely proportional to the blade spacing.
3. Overall loss coefficient (ψ_{int}) increases with the increase in blade spacing for the turbine cascade.
4. At low Re, increase in flap height leads to decrease in ψ_{int} and at high Re, increase in flap height leads to increase in ψ_{int}.
5. By attaching a GF of height 1.55% Ch, the solidity of the cascade can be decreased by 5.92% and still have better performance when compared to baseline case at all Re.
6. By employing a GF for the increased spacing of 0.85, one can have less number of blades around the rotor of an LP turbine and produce lift comparable to that of the baseline case with a spacing of 0.8. Less number of blades on the rotor mean decrease in weight of the LP turbine.

References

1. Curtis EM, Hodson HP, Banieghbal MR, Denton JD, Howell RJ (1996) development of blade profiles for low pressure Turbine applications. ASME 96-GT435
2. Stieger RD (2002) The effects of wakes on separating boundary layers in low pressure turbines. PhD thesis Cambridge University Engineering Department
3. Sharma O (1998) Impact of Reynolds number on LP Turbine performance. In: Minnowbrook II 1997 workshop on boundary layer transition in turbomachines, NASACP-1998–206958
4. Hodson HP, Banieghbal MR, Dailey GM (1993) Three-dimensional interactions in the rotor of an axial turbine. AIAA Paper 93–2255
5. Chisty MA, Hamdani H, Parvez K (2003) Effect of turbulence intensities and passive flow control on LP Turbine. In: Proceedings 2013 10th international Bhurban conference on applied sciences and technology (IBCAST). Islamabad
6. Bons JP, Sondergaard R, Rivir RB (2002) Control of low-pressure Turbine separation using vortex generator jets. J Propuls Power 18(4)
7. Ibrahim M, Kartuzova O, Volino RJ (2008) Experimental and computational investigations of separation and transition on a highly loaded low pressure Turbine airfoil: Part 1—Low free stream turbulence intensity. ASME Paper IMECE2008-68879
8. Guzel G, Sankar LN, Rhee M (2005) Computational investigation of the effects of Gurney flap on the aerodynamic performance of VR-12 airfoil. AIAA Paper, pp 2005–4960
9. Dundi TMK, Sitaram N, Suresh M (2012) Application of Gurney flaps on a centrifugal fan impeller, Paper No. O12008S. Int J Fluid Machin Syst 5(2):65–71
10. Chen PH, Qiao WY, Luo HL (2010) Investigation of low solidity LP Turbine cascade withflow control: Part 2–passive flow control using gurney flap, ASME Paper GT 2010–22330
11. Gajanan T, Viswanath K, Sitaram N (2017) Computational and experimental investigations of separation control of LP Turbine cascade blades using gurney flaps. In: Proceedings 6th Asian symposium on computational heat transfer and fluid flow

Unsteady Flow Analysis of a Highly Loaded High-Pressure Turbine of a Gas Turbine Engine

Vishal Tandon, S. N. Dileep Bushan Reddy, R. D. Bharathan, and S. V. Ramana Murthy

Abstract Advanced fighter aircraft requires a gas turbine engine with high thrust to weight ratio of the order 10 and low specific fuel consumption of the order 0.7 (kg/kg-hr) to meet the high maneuverability, long range, and low life cycle cost requirements. To meet high thrust to weight ratio and low specific fuel consumption, aero gas turbine engine demands high turbine entry temperature and high turbine efficiency. In order to reduce design cycle time typically, a turbo machinery design process is carried out with the assumption that the flow is steady. However, the fluid flow in turbo machinery is highly three-dimensional and inherently unsteady due to stator–rotor interactions through wakes, potential flow, and shock interactions. In this paper, an attempt is made to analyze the unsteady flow in a transonic High-Pressure (HP) turbine which is having high blade loading and low aspect ratio, and is designed for an advanced engine. The calculations are performed by using ANSYS-CFX, which is a commercial software. This software solves three-dimensional Navier–Stokes equations. Structured grids are used in this analysis and turbulence is modeled by using k–ω SST turbulence model. Sliding interface models are used for unsteady simulation studies to analyze the flow field of the turbine stage. Numerical study shows that total-to-total efficiency of the HP turbine stage decreases by 0.4% due to unsteadiness as compared to steady state.

Keywords Unsteady fluid flow · Stator and rotor interaction · Navier–Stokes equations · HP turbine · Total-to-total efficiency · Pressure loss coefficient · Mach number

V. Tandon (✉) · R. D. Bharathan · S. V. Ramana Murthy
Gas Turbine Research Establishment, Bangalore, Karnataka, India
e-mail: vishaltandon@gtre.drdo.in

R. D. Bharathan
e-mail: bharathan@gtre.drdo.in

S. V. Ramana Murthy
e-mail: ramanamurthy@gtre.drdo.in

S. N. D. B. Reddy
Visvesvaraya Technological University, Chikkaballapura, Karnataka, India
e-mail: dileepreddy412@gmail.com

Nomenclature

HP	High Pressure
M	Mach number
P	Total Pressure
SST	Shear Stress Transport
T	Total Temperature
Tu	Turbulence intensity
Yp	Pressure Loss Coefficient
k	Turbulence Kinetic Energy
ω	Turbulence Frequency
φ	Stagger angle
H/T	Hub to Tip ratio
H/C	Aspect ratio

1 Introduction

The HP turbines of advanced gas turbine engines are of single-stage arrangement in order to maintain low weight. Also by reducing the number of costly air-cooled airfoils the initial and maintenance costs can be minimized. Although using a single-stage results in a turbine which occupies lesser space and is having fewer part counts, it results in a higher turbine work loading and more expansion ratios for the single stage. These things results in decrease of the turbine efficiency, also the specific fuel consumption of the engine increases as a secondary effect of the decrease in turbine efficiency.

For turbine efficiency to be enhanced, it is required to understand the sources of various possible aerodynamic loss generation mechanisms in the turbine by under-standing in-depth the unsteady-flow conditions in which the turbine works. The fluid flow field in these advanced turbo-machineries is highly three-dimensional and unsteady because of periodically encountered flow disturbances which are created by the presence of blade rows in upward and downward directions. Unsteadiness has very profound penalties on the performance of the turbine, e.g., it impacts total-to-total efficiency, turbine blade loading, fatigue due to the change in magnitude of fluid forces, heat transfer, and fatigue issues due to heat. Generally, in turbo machines, unsteadiness is mainly due to potential field which is associated with row of blades, this can propagate both upward and downward. The strength of this potential field issue is a strong function of the Mach number and the axial gap between the blade rows, wakes from the blade rows in the upstream direction only gets convected down-stream this influences surface pressure, heat transfer, and boundary layer nature of the downstream blades. In low-aspect blades, the secondary flow and tip leakage flows results in streamwise vortices which gets convected downstream and influences flow properties of the downstream blade rows, shock system reflections, and interactions

with adjacent blades results in pressure fluctuations in turbines designed for transonic conditions, hot spots with nonuniform temperature in both radial and circumferential directions gets convected to downstream and this has major implications on both aerodynamic and heat transfer issues of the components in the downstream direction. Many researchers have studied turbine unsteady flows both numerically and experimentally [1–7].

Hilditch [8] has worked on unsteady flow analysis of single-stage turbine with the aim of obtaining the flow field in both stator and rotor. A two-dimensional (2D) unsteady-code "UNSFLOW" was used to study the flow physics. Valenti [9] has attempted to investigate the three-dimensional (3D) unsteady nature of rotor pressure field in HP turbine. It was noticed that the Mach number variation is highly sensitive to pressure ratio. The intensity and incidence of shocks strongly varies from hub to tip. Miller [10] has studied the different unsteady functions which cause due to the rotor and stator interactions. Wake, shock, potential field are the interactions involved. Davis [6] has made an attempt to study the unsteady interaction between transonic turbine stage and the downstream components. He observed along with stator–rotor interaction there exists an interaction among blade and the downstream transition duct, and the LPT vane. Sarkar [11] has studied the unsteady wake interaction on rotor blade for low-pressure turbine stage using 2D LES code. He observed that wakes from the upstream blade row interacts with separated boundary layer and makes it highly unsteady. Shyam [12] has attempted to study 3D unsteady simulation of a highly loaded transonic turbine stage and compared it with experimental results. He observed that the unsteadiness in tip gap is ruled by both inviscid and viscous effects due to the shock boundary layer interaction. Rose [13] has attempted to study the flows in axial flow turbine with an aim of designing high efficient turbines by controlling the unsteady-flow field. Govardhan [14] has attempted to decrease the secondary losses in an axial turbine stage using end wall contouring and leading edge fillets.

For estimating turbine performance, there are three approaches "Stage simulation," "Frozen rotor simulation," and "unsteady-flow simulation." In-stage simulation flow parameters are averaged in azimuthal direction at the boundary of stator and rotor on a mixing plane. In frozen rotor simulation, for one relative position of the rotor blade in relation with the stator, the entire simulation is carried out. Here, the various flow parameters are not averaged in azimuthal direction as is done in steady-state simulation rather an interpolation procedure is used to pass on the flow values to the next domain. In unsteady-flow simulation, the calculations are carried out like frozen rotor simulation for a particular time step but for the next time step the rotor is rotated relative to the stator using a transient sliding interface. Hence, in this simulation the correct physical position of rotor w.r.t. stator is used for each time step calculation throughout the simulation.

In this paper, an attempt is made to get an insight into the complex flows in an HP turbine stage designed for an advanced gas turbine engine by carrying out an unsteady simulation. The primary focus of the present study is to study the effects unsteadiness brings to the overall HP turbine performance.

Table 1 Non-dimensional parameters of HP turbine stage

Design parameter	Stator	Rotor
Total no. of airfoils	34	73
Mean s/c ratio	0.72	0.73
Mean φ angle (°)	51.5	23
H/C ratio	0.68	1.59
H/T ratio	0.84	0.84
Ratio of max. thickness to chord	0.20	0.25

2 Description of the Turbine Stage

The HP turbine in this study is a highly loaded, low aspect ratio, transonic turbine which is designed for an advanced gas turbine engine. The pressure ratio of HP turbine is 2.77, stage loading of turbine is 1.8, and flow coefficient is 0.55. Various parameters in non-dimensional form are presented in Table 1. For this simulation studies, it is assumed that vanes and blades are not cooled.

3 Computational Methodology

The analysis is carried out for the HP turbine stage by using the commercial 3D Navier–Stokes solver ANSYS CFX-14.5 [15] on an IBM DX 360 parallel computing system. For the simulation, ANSYS CFX version 14.5 is used. ANSYS CFX is a 3D, multi-block, and parallel fluid flow solver.

The Unsteady Reynolds-Averaged Navier–Stokes (URANS) equations are solved. The governing equations are discretized using finite volume method. The solution algorithm is based on an implicit scheme coupled with multi-grid acceleration techniques. k–ω SST turbulence model is selected to model the turbulence effects. It is a two-equation turbulence model and it is capable of correctly predicting the wall shear stresses in flows where adverse pressure gradient are present similar to the present study and also it is robust for complex flows.

4 Grid Generation

CFX-Turbo grid software has been used to generate the computational grid for this study [16]. Structured hexahedral grids are created using O, C, and H grids. The grids are multi-block.

Table 2 Grid sensitivity study

S. No	Grid size	Pressure ratio	Mass flow (kg/s)
1	50000	2.77	58.1
2	300000	2.77	61.0
3	500000	2.77	61.12

For stator grid, first an O grid is placed around the airfoil. Around the leading edge of stator and passage, a C grid is used and H grid has been used in the trailing edge of the stator. For rotor grid also, first an O grid is placed around the airfoil, whereas H grid is used in the rotor passage. The grids are joined periodically in a many-to-one fashion in pitch direction. No overlaps are used while attaching grids of non-moving stator and moving rotor grids. In unsteady simulation, transient sliding interface option has been used which moves the rotor grid to the next relative location w.r.t. the stator for each time step, which represents the true physical position of the rotor w.r.t. stator for every time step. Flow parameters are exchanged between the two grids by using a flux conservative algorithm. It is a second-order interpolation algorithm.

The grid sizes for the stator and rotor are fixed after the grid sensitivity analysis. The results of the grid sensitivity analysis are shown in Table 2 and the grid size of 0.3 million is fixed for both one stator and one rotor domains.

For stage simulations, one stator and one rotor blades are modeled, whereas for frozen and unsteady simulations, one stator and two rotor blades are modeled. In order to resolve boundary layer properly, enough nodes are kept close to the airfoil surfaces. For the finalized stator and rotor grids, y+ values are kept lower than 11. Grids skew angles are kept between 25 and 155°. Aspect ratio is maintained less than 100. Expansion ratio is kept less than 1.2. There is no abrupt change in mesh density.

3D computational grid of HP turbine stage is shown in Fig. 1.

5   Boundary Conditions

At the inlet of the stator uniform, total pressure and radially varying profile of total temperature is used as inlet boundary condition, whereas at exit of the rotor average, static pressure has been used as exit boundary condition by matching the HP turbine stage pressure ratio. Walls of the stator and rotor are considered as smooth and adiabatic. Also for the walls, no slip boundary condition is enforced. Since upstream of HP turbine combustor is there from which high turbulent flow comes out; hence, free stream turbulence intensity is assumed to be 8%. Ten percent of the inlet is taken as eddy length scale. Flow is considered as fully turbulent as Reynolds number is higher than 2×10^6. Appropriate periodic boundary condition is applied in blade to blade plane.

Fig. 1 HP turbine computational grid

6   Computational Time and Convergence

The simulations are carried out on IBM DX 360 parallel computing system using 8 parallel processors. For the convergence of the stage and frozen rotor simulations, the calculations were carried out until the maximum residuals drop below 10^{-4}. Difference between inlet and outlet mass flow values for the HP turbine stage is less than 0.02%. First simulations were ran using coarse grids and then the results of these simulation are given as interpolated guess for the stage and frozen rotor simulations which took approximately 7 h to converge.

Converged frozen rotor simulation results were given as initial guess for starting of the unsteady simulation. 20 time steps are selected for the rotor grid to cover one pitch of the stator so that various stator–rotor related flow phenomena's can be captured precisely and also keeping in mind the computation time involved in a unsteady simulation. For convergence in each time step which represent orientation of the rotor grid w.r.t. stator grid different from the last time step, a maximum of 20 inner loop iterations are used as converged results from frozen rotor simulation are supplied to the unsteady simulation.

For unsteady simulation, the calculation has taken around 2000 accumulated time steps for converging. Each time step took around 35 min of clock time. To decide if the unsteady simulation has converged or not, tangential force on the blades are observed. When periodic patterns were observed for the forces, the simulation was taken as converged as shown in Fig. 2. Stage pressure ratio is also observed for convergence and it also shows repeating pattern.
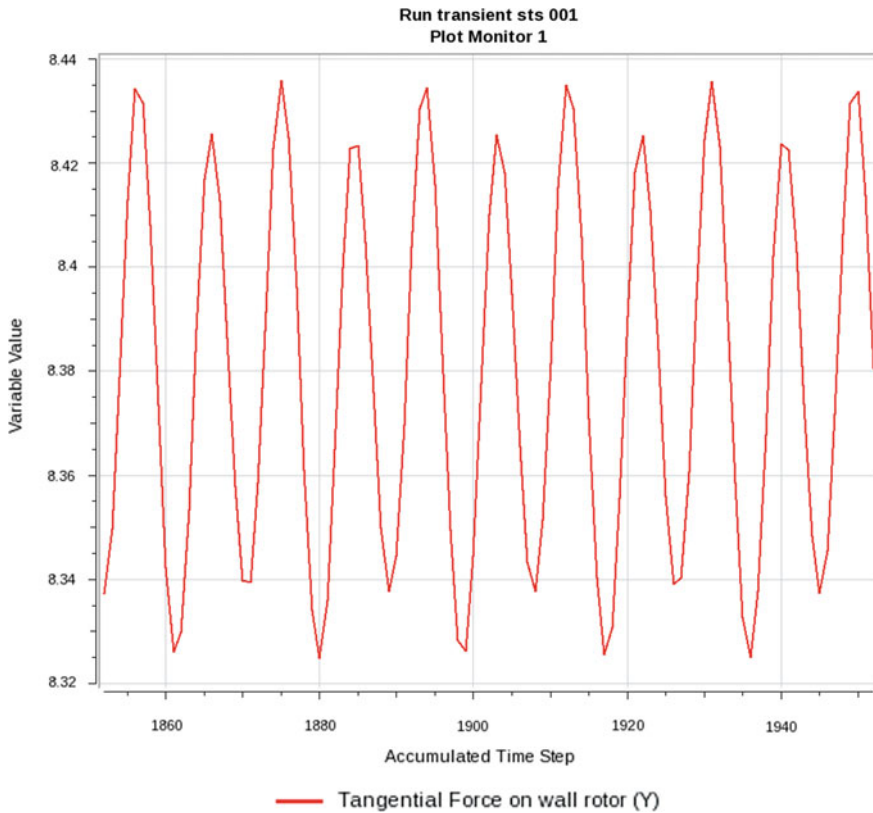
Fig. 2 Convergence criteria for unsteady simulation, tangential forces on the blades

7 Results and Discussions

Figure 3 shows the variation of the static pressure on the stator hub section for various time steps of the unsteady simulation after it is converged and static pressure variations from stage and frozen rotor simulation results are also shown in this figure. The trends in static pressure variation as predicted by unsteady, stage, and frozen rotor simulations are same all around the stator except trailing edge of the suction side.

Due to change in the relative position of the rotor w.r.t. the stator for different time steps, the shock pattern gets changed as the blockage offered by the rotor to the stator is a function of stator and rotor relative position.

Figure 4 shows how the outlet flow angle of the stator is varying in spanwise direction for different time steps. The unsteadiness is seen more toward the hub area of the stator as compared to tip area which seems to be less influenced by the downstream rotor blade blockage.

Figure 5 shows how the outlet relative Mach number of the rotor is varying in
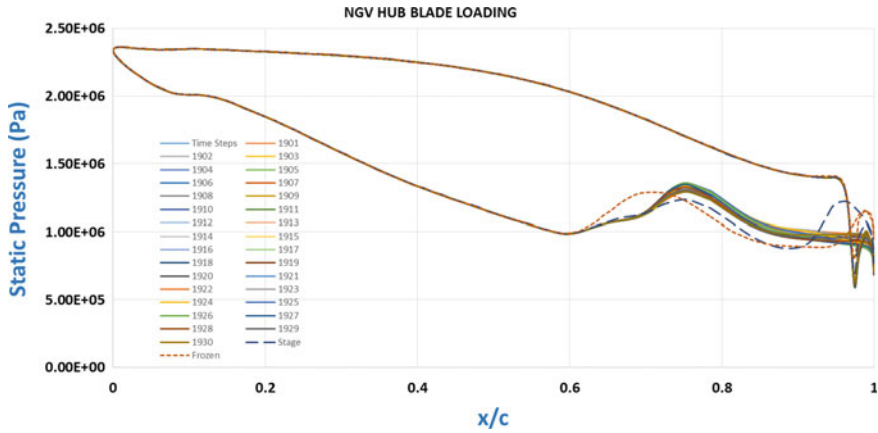
Fig. 3 Static pressure plot on hub section of stator
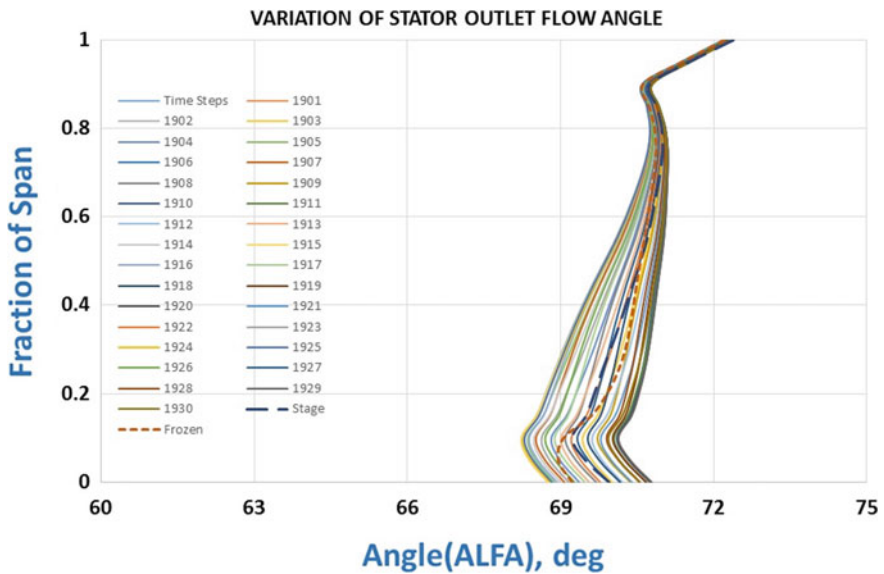
Fig. 4 Spanwise variation in stator outlet flow angle

spanwise direction for different time steps. In this figure, the outlet relative Mach number variation of the rotor as predicted by stage analysis is showing different trend than as predicted by frozen and unsteady analysis toward the tip area of the rotor blade.

Figure 6 shows how the outlet relative angle of the rotor is varying in spanwise direction for different time steps. In this graph, also the outlet relative flow angle
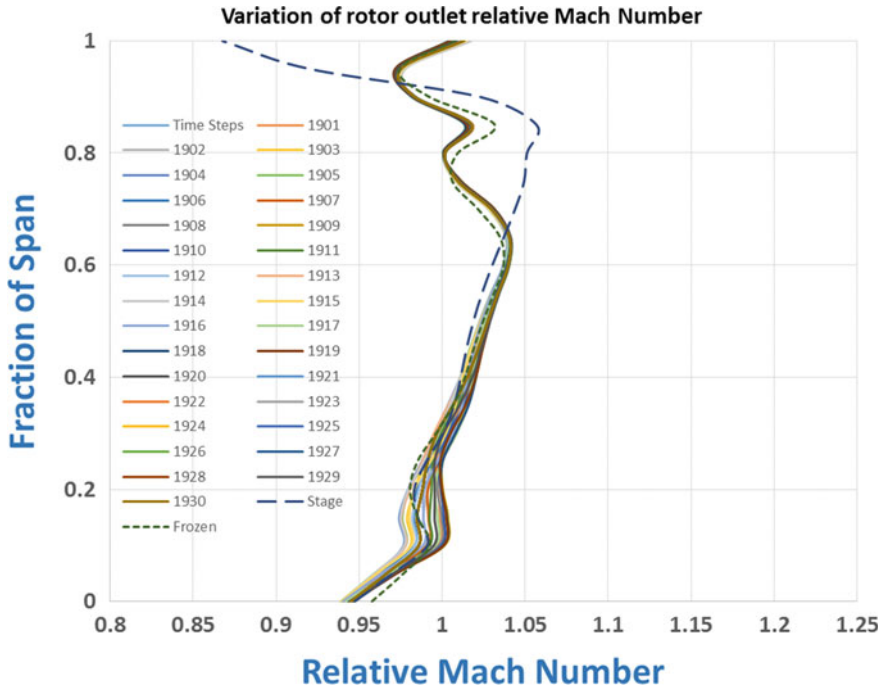
Fig. 5 Spanwise variation in rotor outlet relative Mach number

variation of the rotor as predicted by stage analysis is having different trend than as predicted by frozen and unsteady analysis in tip area of the rotor blade.

Figure 7 shows the variation of pressure loss coefficient in spanwise direction for the stator. It is seen from the figure that for some time steps, i.e., particular relative position of rotor w.r.t. stator the loss coefficient is lesser then even the one predicted by the steady-state stage analysis. In this figure, also the unsteadiness is more pronounced at hub section as compared to tip section.

Figure 8 shows the variation of pressure loss coefficient in spanwise direction for the rotor blade. The loss coefficient as predicted by stage analysis is having different trend than as predicted by frozen and unsteady analysis in tip area of the rotor blade, which shows steady state analysis is under predicting rotor loss coefficient in tip region. In this figure, also the unsteadiness is more pronounced at hub section as compared to tip section.

Figure 9 shows the static entropy contours at mean section for the HP turbine in blade-to-blade plane. Rotor blades are moving toward the downward direction. From these figures, we can see, in some cases the wakes shed from the stator blade are impinging on the leading edge of the rotor blade and in some cases the wakes are simply getting convected through the rotor blade passage without any interference with rotor blades. These figures show the intricate stator and rotor interaction in a typical turbine stage.
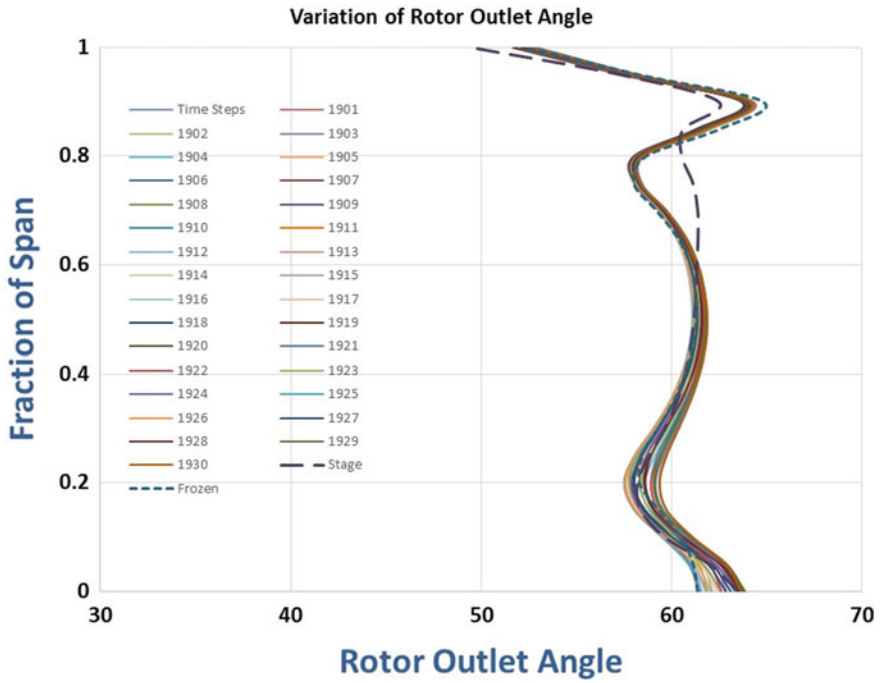
Fig. 6 Spanwise variation in rotor outlet relative flow angle
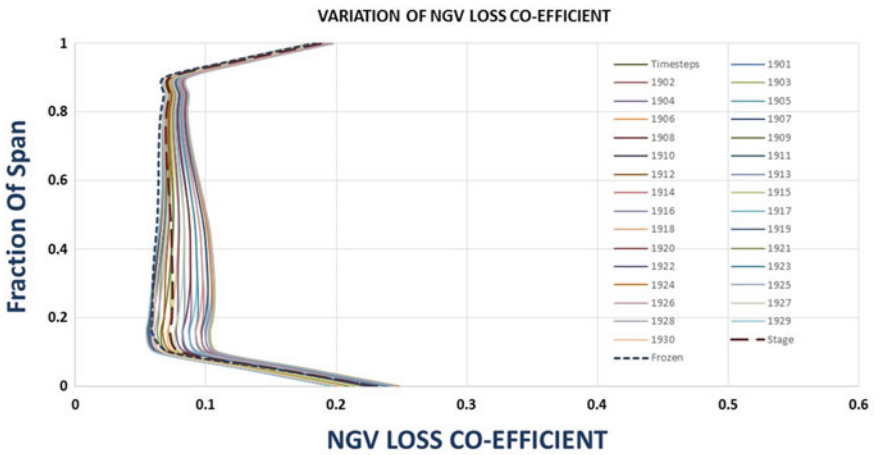
Fig. 7 Spanwise variation in stator pressure loss coefficient
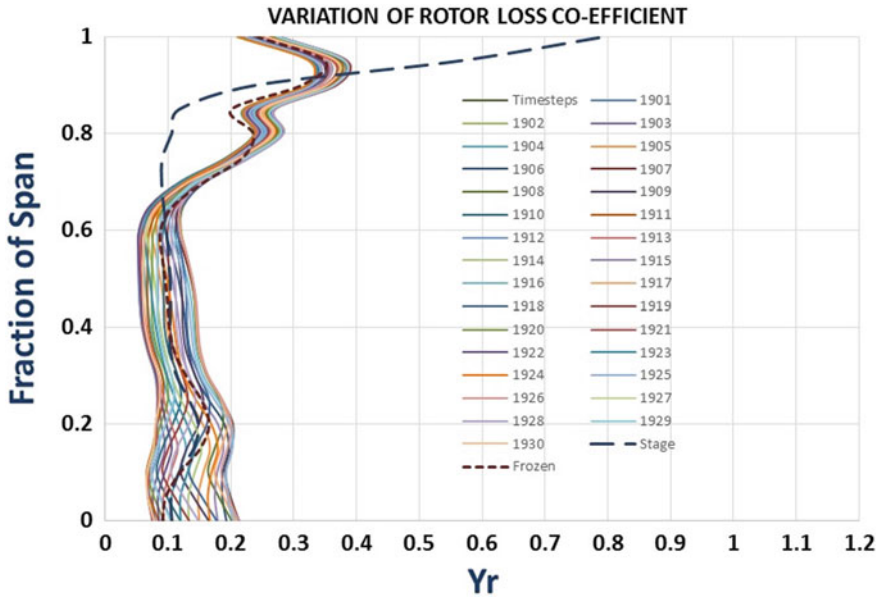
Fig. 8 Variation of rotor pressure loss coefficient
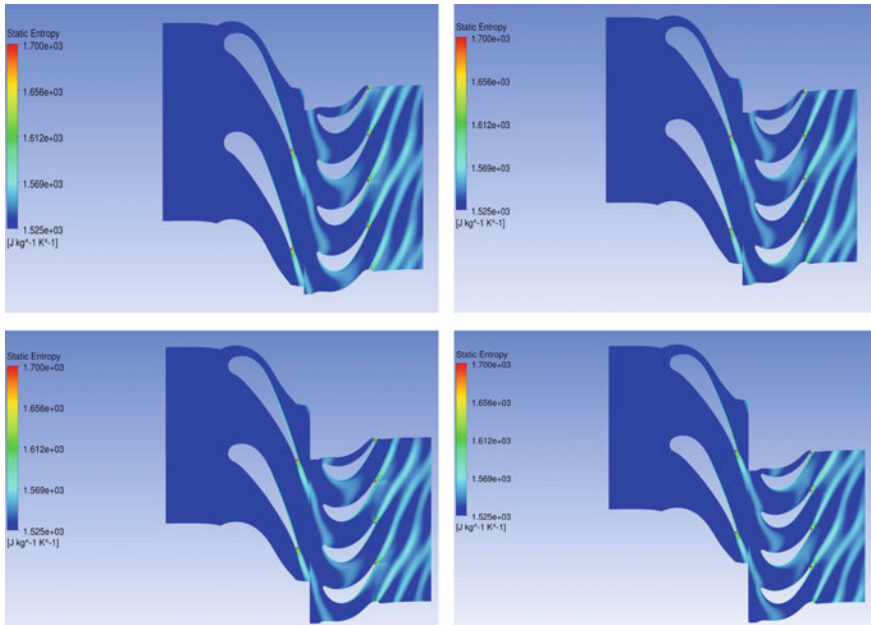
Fig. 9 Entropy variation in blade-to-blade plane
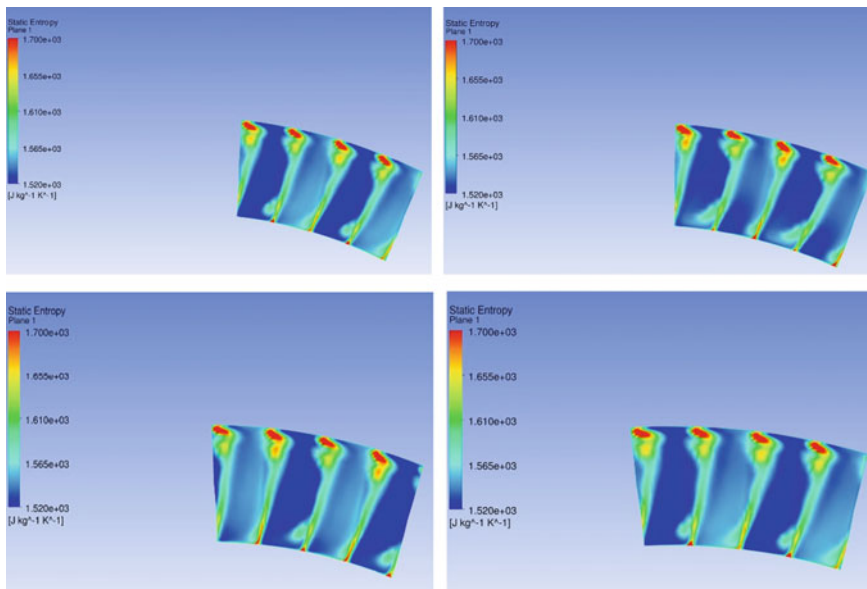
Fig. 10 Variation in static entropy in the rotor outlet plane in azimuthal direction

Figure 10 shows for the unsteady simulation the contour of static entropy in rotor blade outlet plane in azimuthal direction for different time steps. We can see from the figures for different time steps the behavior of hub secondary flows and tip vortex flows in azimuthal direction.

Figure 11 shows the total-to-total efficiency variation for the unsteady simulation for different time steps. The maximum efficiency observed is 88.8%; it occurs for the time step where the stator wake impacts on the rotor blade leading edge. The minimum efficiency is 87.3%; it occurs for the time steps where the stator wake gets convected through the passage of the rotor blade without interfering with the rotor blade.

8 Conclusions

Unsteady-flow simulation of a HP turbine stage is carried out using ANSYS-CFX, which is a commercial 3D Navier–Stokes solver software. The simulation has provided insight into the intricate stator and rotor interaction of the HP turbine which is a transonic turbine. The effects of unsteadiness are more pronounced toward the hub area of the stator and rotor, whereas the tip section is least affected. The total-to-total efficiency is lower by around 0.4% than as predicted by the steady-state stage analysis for time steps where the wake from the stator is getting convected through the rotor passage, whereas when the wake from stator is falling on the rotor blade leading

Efficiency Variation
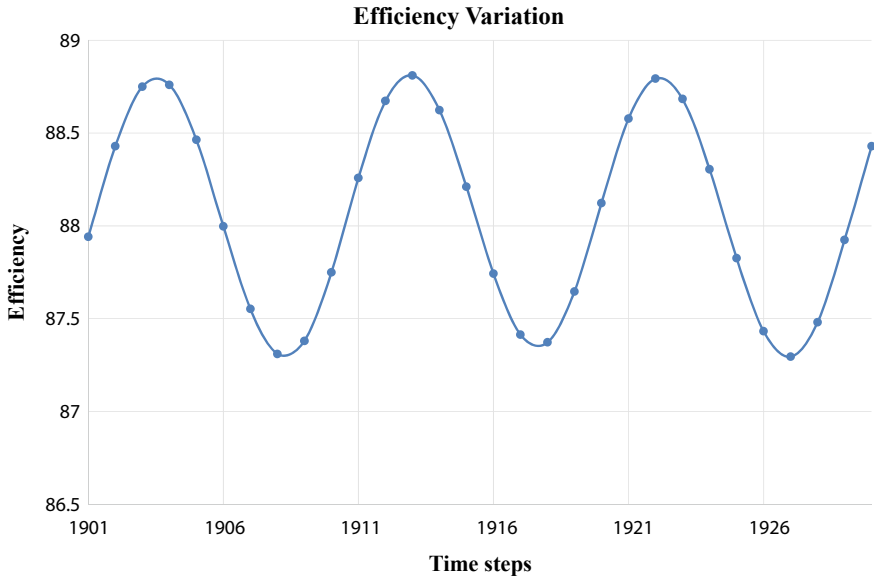
Fig. 11 Variation of total-to-total efficiency for different time steps

edge it improves efficiency, so it suggests that incoming wakes does not always leads to degradation of the efficiency.

References

1. Qi L, Zou Z, Unsteady flows in turbines, noise control, reduction and cancellation solutions in engineering
2. Payne SJ, Miller RJ, Ainsworth RW (2003) Unsteady loss in a high pressure turbine stage. Int J Heat Fluid Flow 698–708
3. Bohn D, Ren J, Sell M Unsteady 3D—Numerical investigation of the shroud cavities on the Stator and Rotor interaction in a 2-stage turbine. ISABE–2005–1155
4. Kasuga S, Yamamoto A, Miyachi T (2003) An experimental study on unsteady flow behavior in an axial flow turbine. In: IGTC2003—TS-056, Proceedings of international gas turbine congress
5. Pangiagua G etc Unsteady strong shock interactions in a transonic turbine: experimental and numerical analysis. ISABE-2007-1218
6. Davis RL etc (2002) Unsteady interaction between a transonic turbine stage and downstream components. GT-2002-30364, ASME TURBO EXPO
7. Sharma OP, Picket GF, Ni RH (1990) Assessment of unsteady flows in turbines. ASME Paper No. 90-GT-150

8. Hilditch MA, Smith GC, Singh UK (1998) Unsteady flow in a single stage turbine. International gas turbine and aero-engine congress exhibition
9. Valenti E etc (2002) Investigation of the 3D unsteady rotor pressure field in a HP turbine stage. GT-2002-30365, ASME TURBO EXPO
10. Miller RJ etc (2002) Wake, shock and potential field interactions in a 1.5 stage turbine. GT-2002-30435, ASME TURBO EXPO
11. Sarkar S (2009) Influence of wake structure on unsteady flow in a low pressure turbine blade passage. ASME J Turbomach, October
12. Shyam V (2010) 3-D Unsteady simulation of a modern high pressure turbine stage: analysis of heat transfer and flow. Engineering Doctoral Thesis, The Ohio State University
13. Rose MG (2010) Unsteady flow in axial turbines, Thesis, October
14. Govardhan M End wall contouring and leading edge fillets for reducing secondary losses in an axial turbine stage. MEE/14-15/332/GTREMGOV, GATET at GTRE
15. ANSYS CFX-12; ANSYS CFX release 14.5
16. CFX-Turbo grid, User documentation, version 14.5, ANSYS Inc

Numerical Investigation of Three-Dimensional Separation in Twisted Turbine Blade: The Influence of Endwall Boundary Layer State

Gaurav Saxena, Arun K. Saha, and Ritesh Gaur

Abstract The substantial adverse pressure gradient experienced by a turbulent boundary layer while approaching an endwall-mounted twisted turbine blade and caused the impending flow to separate three-dimensionally to form a dynamically active horseshoe vortex (HSV) system in the junction of the turbine blade with endwall. The large eddy simulations (LES) of the flow past a twisted turbine blade mounted on a curved endwall with periodic boundary condition in pitchwise direction is carried out for Re = 50000 to methodically investigate the HSV dynamics. The significant variations with Re in terms of mean flow quantities, heat transfer distribution, and coherent dynamics of turbulent HSV are shown in computed results. The HSV system consists of a multiple number of necklace-type vortices that are shed periodically at maximal frequencies. For high Re, we show that outburst of wall govern the instantaneous flow field, averaged vorticity affiliate with the growth of hairpin vortices that enclose around and dislocate the primary HSV. The time-mean endwall heat transfer is prevailed by two bands of high heat transfer which encircle the leading edge of the blade. The band of maximal heat transfer, occurs in the corner region of the juncture, while the secondary high heat transfer band (thin as compare to primary) develops upstream of primary band, in between primary and secondary bands a relatively low heat transfer region is identified.

Keywords Horseshoe vortex · Endwall boundary layer · LES · Junction flow

G. Saxena (✉) · A. K. Saha
Department of Mechanical Engineering, Indian Institute of Technology Kanpur, Kanpur 208016, India
e-mail: gsaxena@iitk.ac.in

A. K. Saha
e-mail: aksaha@iitk.ac.in

R. Gaur
Scientist E, Gas Turbine Research Establishment (GTRE), Bangalore, India
e-mail: riteshgaur@gtre.drdo.in

Nomenclature

SGS   Subgrid scale structures
HSV   Horseshoe vortex
SISM   Shear-Improved Smagorinsky Model
FVM   Finite Volume Method
MIM   Momentum Interpolation Method
FOU   First-Order Upwind
QUICK   Quadratic Upwind Interpolation Convective Kinematics
GSOR   Gauss–Seidel over-relaxation
CDS   Central Difference Scheme
Pr_{SGS} Turbulent Prandtl number

1   Introduction

Junction flows may experience from secondary flows such as horseshoe vortices and corner separations that can dramatically diminish the performance of aircraft. The substantial adverse pressure gradient is experienced by a turbulent boundary layer while approaching an endwall seated turbine blade and it goes through a three-dimensional separation forming a horseshoe vortex (HSV) system that muffles around the blade like a string. The existence of the turbine blade influences the mean flow distribution upstream of the juncture. In the juncture, the secondary flow system transports turbulence and mutate the mean flow, thus having a consequential effect on the distribution of turbulent stresses, the separation vortex plays an imperative role in this process. The junction flows in particular turbine blade hub-junctions are relevant to many engineering problems, i.e., lateral wings of the submarine, plate heat exchanger, and flow past surface-mounted cylinder (circular and rectangular). In the pioneering work, of Devenport and Simpson [1] investigated in detail the HSV structure at Re $= 1.15 \times 10^5$ is formed in the base of leading edge of a cylindrical wing explore the rich dynamics by analyzing their experimental measurement at the plane of symmetry. Their results showed that the HSV is distinguished by coherent low-frequency oscillations that generate the bimodal histogram of streamwise and spanwise velocity probability density functions (pdfs) close to the wall at the symmetry plane. Similar typical features in the turbulent stresses and complex interactions of vortical structures have also been measured around other configurations [2–5]. Simpson [6] revealed that many factors affect the evolution and dynamics of the HSV system, the presence of wall-mounted obstacle in the flow field created the adverse pressure gradient that determined by the geometrical features of the obstruction in the boundary flow. The evolution of complex HSV system is influenced by the flow Re along with boundary layer thickness that produces the high turbulent stresses at the leading edge of the wall-mounted obstacles [6, 7]. Baker [8] investigated the formation of turbulent HSV in front of a wall-mounted cylinder. Oil and

smoke flow visualization suggests that only four vortex system exist (i.e., for 4000 < UD/υ < 90000, 4 < D/δ^* < 30). He reported [8] that at the location of primary horse-shoe vortex pressure distribution pretence least possible magnitude. By measuring the near wall pressure, Baker [8] was first to determine the qualitative influence of the boundary layer on the average position of the primary HSV, observing that the HSV system moves closer to cylinder when D/δ^* increases. Dargahi [9] studied the flow around a vertical cylinder mounted in a rectangular channel. Hydrogen bubble flow visualization and hot film measurements were carried out for Reynolds number between 6.6×10^3 and 6.5×10^4 they showed the similar flow patterns that are observed in [8]. Instantaneous flow visualization techniques using a laser sheet and time resolved estimation of the wall-induced pressure, that are carried out by Agui and Andreopoulos [10] the results point out that the primary vortex consists of mul-tiple large-scale structures which have begun in the impending boundary layer and have drawn substantial additional vorticity, their measurements indicate that the rms pressure fluctuations increases as separation is approached and reach a maximum near attachment. Also reported [10], a highly intermittent quasi periodic flow. In the upstream of cylinder, a continuous eruption of near-wall fluid originating between the wall and the main horseshoe vortex, generating mushroom-like vortical structures that were lifted off the wall and interacted with the primary vortex. Many cases of vortex eruptions documented by Doligalski [7] produced by vortical structures near solid walls and formed the relation between secondary coherent vortices that are generating due to these bursting phenomenon with the ejection of counterclockwise rotating vorticity that engulfed the large structures. He reported [7] that at the sym-metry plane in a junction region formed by the obstacle and endwall, the vorticity spikes are noticed that accord to three-dimensional configuration of hairpin vortices that build on top of the primary HSV, these hairpin vortices create the instability among the vortex while generating the eruptions when the merging between the vor-tical structure begin. Similar observations for laminar junction flows has also been reported [11, 12] in that the emergence of the counterclockwise rotating vorticity spikes from the wall is observed that interact with HSV system, generating its dete-rioration and periodic restoration. The computational simulation in case of junction flow is quite challenging, to capture the correct flow physics in the HSV system the selection of accurate numerical scheme is essential at high Re. The experimental result of Devenport and Simpson [1] has been widely studied by using the com-putational method such as steady and unsteady Reynolds-averaged Navier–Stokes (RANS and URANS, respectively) turbulence models, including linear and nonlinear eddy viscosity models and second-moment closure models [13–15]. The following are the significant suggestions from the study of [13–16] are summarized as follows: The RANS and URANS have naturally failed to capture the unsteadiness of the HSV system as well as unable to predict the exact location and the shape of mean HSV even though the correct prediction of turbulence statistics in the proximity of junction is not well captured. The numerical simulation establish on second-moment closure models have been only able to interpret better result than eddy viscosity model. The size and the core location of the mean horseshoe structure can correctly approximate by second-moment closure models. The turbulence intensities near the endwall and

obstacle region are carefully resolved [13, 15, 16] but these more refined RANS models have failed to provide a very accurate prediction of the turbulent kinetic energy (C-shaped, double-peak structures), the spatial distribution of the vortical structures or to give any insights into the bimodal dynamics of turbulent fluctuations. Devenport and Simpson [1] also identify the limitations of standard RANS methods for this flow and is also discussed in the recent review by Simpson [6]. Large eddy simulation (LES) is the better option for simulating mutinous flows with reasonable computational resources. In LES, all the scales except the energy dissipating Kolmogorov scales are resolved. LES entirely resolves all the unsteady motion from substantial energy containing scales to the inertial range, it can be expected to be more accurate and reliable then RANS. LES is able to capture all the correct physics associated with the dynamics of HSV system. The several such studies have been reported in the literature [16–19]. For surface-mounted cube at Re = 40000, many LES computations have been performed their result reveal that calculated flow in the HSV region exhibit bimodal oscillations thus confirming the experimental findings [16–20]. The critical observation from LES simulations is that the stipulation of time-dependent, turbulent like inflow boundary condition is an essential for correctly predicting the location of HSV reported through experimentally, the steady inflow conditions when using with the LES simulations that are proficient in capturing the instability in the junction regions but the figured HSV is moderately upstream from its actual position [18, 19]. The instantaneous and time-averaged flow topology and the associated heat transfer in the leading edge endwall region of a symmetric airfoil are discussed by Praisner et al. [33, 34] the heat transfer is dominated by two bands of high heat transfer, which circumscribe the leading edge of the obstacle. The band of highest heat transfer occurs in the corner region of the juncture, reflecting a 350% increase over the impinging turbulent boundary layer. The secondary high heat transfer band develops upstream of the primary band, reflecting a 250% heat transfer increase and is characterized by high level of fluctuating heat load.

2   Numerical Methodology

1. **Governing equations and LES model**

In the present study, Newtonian, unsteady, incompressible Navier–Stokes equation along with energy equations in primitive variable form are employed to simulate the fluid flow and heat transfer through twisted turbine blade passage. The governing equations for LES are obtained by applying spatial filter (top-hat), to the Navier–Stokes and the energy equations to explicitly separate the large and subgrid scale structures (SGS), the equation in dimensionless form Saha and Acharya [21] are expressed as

$$\frac{\partial \bar{u}_i}{\partial x_i} = 0 \tag{1}$$

$$\frac{\partial \bar{u}_i}{\partial t} + \frac{\partial \bar{u}_i \bar{u}_j}{\partial x_j} = -\frac{\partial \bar{p}}{\partial x_i} + \frac{1}{\text{Re}} \frac{\partial^2 \bar{u}_i}{\partial x_j^2} + \frac{\partial \tau_{ij}}{\partial x_j} \tag{2}$$

$$\frac{\partial \bar{\theta}}{\partial t} + \frac{\partial \bar{u}_j \bar{\theta}}{\partial x_j} = \frac{1}{\text{Re Pr}} \frac{\partial^2 \bar{\theta}}{\partial x_j^2} + \frac{\partial q_j}{\partial x_j} \tag{3}$$

$$\tau_{ij} = \overline{u_i u_j} - \bar{u}_i \bar{u}_j = \overline{u_i' u_j'}$$

$$q_j = -\overline{u_j' \theta'} \tag{4}$$

where τ_{ij} and q_{ij} is the SGS stress tensor and subgrid scale energy flux. The governing equations are non-dimensionalized using length scale C, i.e., the axial chord of blade, velocity scale as u_{avg}, pressure by ρu_{avg}^2 and time with C / u_{avg}. The Reynolds number (Re) is hence defined as $\text{Re} = u_{\text{avg}} C / \nu$. Temperature is non-dimensionalized using a scale $\theta = (T - T_w) / (T_{m1}(t) - T_w)$, where T_w is the wall temperature and $T_{m1}(t)$ is the bulk temperature of the fluid evaluated at inlet of the computational domain. The SGS models as based on the gradient transport hypothesis correlating τ_{ij} to the large-scale strain rate tensor (Eq. 5), while the strain rate is $\bar{S}_{ij}$ shown in Eq. (6)

$$\tau_{ij} = -2\nu_T \bar{S}_{ij} + \frac{1}{3} \delta_{ij} \tau_{kk} \text{ and } \tau_{kk} = \overline{u_k' u_k'} \tag{5}$$

$$\bar{S}_{ij} = \frac{1}{2} \left\{ \frac{\partial \overline{u}_i}{\partial x_j} + \frac{\partial \overline{u}_j}{\partial x_i} \right\} \tag{6}$$

On substituting, Eqs. (4) and (5) in (2) the final form of the filtered Navier–Stokes equation can be written as

$$\frac{\partial \bar{u}_i}{\partial t} + \frac{\partial \bar{u}_i \bar{u}_j}{\partial x_j} = \frac{\partial \bar{p}}{\partial x_i} + \frac{\partial}{\partial x_j} \left[\left(\frac{1}{\text{Re}} + \nu_T \right) \frac{\partial \bar{u}_i}{\partial x_j} \right] + \frac{\partial}{\partial x_j} \left(\nu_T \frac{\partial \bar{u}_j}{\partial x_i} \right) \tag{7}$$

The subgrid scale energy flux, $q_j = -\overline{u_j' \theta'}$ in the Eq. (4) is given by Murata et al. [22] as shown in Eq. (8). Substitute Eq. (8) in (3), the final form of energy equation is given by Eq. (9)

$$q_j = \frac{\nu_T}{\text{Pr}_{\text{SGS}}} \frac{\partial \bar{\theta}}{\partial x_j} \tag{8}$$

$$\frac{\partial \bar{\theta}}{\partial t} + \frac{\partial \bar{u} \bar{\theta}}{\partial x_j} = \left(\frac{1}{\text{Re Pr}} + \frac{\nu_T}{\text{Pr}_{\text{SGS}}} \right) \frac{\partial^2 \bar{\theta}}{\partial x_j^2} \tag{9}$$

In Eq. (9) Pr_{SGS} is the turbulent Prandtl number for subgrid-scale components and in the present study its value is kept fixed to 0.5 as suggested in Moin et al. [23]. Smagorinsky [24] proposed model in which the eddy viscosity defined by equation

$\nu_T = (C_S\overline{\Delta})^2|\bar{S}|$, in which C_S is called the Smagorinsky constant whose value lies in the range 0.065–0.25 and $|\bar{S}| = (2S_{ij}S_{ij})^{1/2}$, where S_{ij} is the strain rate. There are certain drawbacks of Smagorinsky model (i) it is highly dissipative (ii) it cannot account for backscatter of energy from smaller to larger structure as the turbulent viscosity is always positive. So, the model is unable to capture the true transition to turbulence to overcome this problem Lévêque [25] modified the Smagorinsky model and defined eddy viscosity as $\nu_T = (C_S\overline{\Delta})^2(|\bar{S}| - |\langle\bar{S}\rangle|)$, where $|\langle\bar{S}\rangle|$ is the mean shear and whereas $|\bar{S}|$ is the instantaneous resolved rate of strain tensor while doing the ensemble averaging the mean shear rate is obtained which can be averaged spatially over the homogenous direction or an average in temporal direction. This proposed model is called as Shear Improved Smagorinsky model (SISM). In proposed model, the effect of mean gradient is removed venerating the energy budgets for both isotropic and shear turbulence Toschi et al. [26]. In the present study, the mean shear $\langle\bar{S}\rangle$ is obtained by temporal averaging of the velocity field at each computational node using the exponential averaging function. The eddy viscosity in (SISM) can exhibit important properties directly from the explanation of the model itself are discussed below:

i.   When the mean shear $|\langle\bar{S}\rangle|$ is zero the original Smagorinsky model is repossess. This property renders accumulative advantage for homogenous and isotropic turbulence where Smagorinsky model has already been established to function competently.

ii. In laminar flow regime $(|\bar{S}| = |\langle\bar{S}\rangle|)$ the predicted eddy viscosity faded without the stipulation of any special execution. This characteristic renders a distinctive supremacy over the primary Smagorinsky model which anticipate the eddy viscosity from becoming zero in a shear regnant region in a laminar flow.

iii. In SISM, the turbulent viscosity is defined as $\nu_T = (C_S\overline{\Delta})^2(|\bar{S}| - |\langle\bar{S}\rangle|)$, the third property emanate due to the subtraction of mean instantaneous resolved strain rate. This dampens the degree of the eddy viscosity near the boundaries.

2. **Numerical methods**

The present work uses finite volume methodology (FVM) on collocated grid as proposed by Eswaran and Prakash [27]. The detailed documentation of the method can be referred from Sharma and Eswaran [28]. To avoid pressure velocity decoupling, Momentum Interpolation Method (MIM) originally proposed by Rhie and Chow [29] has been used. Semi-implicit method is used for time advancement. Various upwinding schemes such as First-order Upwinding (FOU), Central Difference Scheme (CDS), and Quadratic Upwinding Interpolation Scheme (QUICK) are deployed for convective terms. Upwinding scheme, i.e., the FOU, stated above, makes the discretized sets of equations diagonally dominant thereby enhancing the convergence properties. However, FOU is extremely diffusive and is spatially a first-order scheme. CDS, which is second-order accurate in space, induces non-physical oscillations when applied for convective terms of the Navier–Stokes equations. The QUICK is also second-order accurate in space for non-uniform grids. The convection term in Eq. (2) hence can be hybridized as in Eq. (5) to take the advantage of

convergence property of FOU and second-order space accuracy of CDS.

$$CONV_{\text{flux}} = (1 - \gamma)[CONV_{\text{flux}}]_{\text{FOU}} + \gamma[CONV_{\text{flux}}]_{\text{CDS}} \tag{5}$$

where γ is the weight function have value between 0 and 1. Pure FOU is obtained for $\gamma = 0$, whereas $\gamma = 1$ results in pure CDS scheme. In present case, the value of γ is chosen as 0.98 so that it is as possible to 1 to attain higher order accuracy in space. The diffusion terms are discretized spatially using CDS and temporally using Crank–Nicolson scheme. To solve the Poisson pressure, GSOR method is applied. Code parallelization is achieved using commands from the MPI library. For LES implementation, SISM is used. The numerical method has been extensively evaluated various turbulent shear flows in complex geometrical configurations [5, 29].

3. Computational details

The present problem, deals with the study of flow and heat transfer of an HSV region at the leading edge of wall-mounted twisted turbine blade configuration. Figure 1 depicts the three-dimensional model of twisted turbine cascade, the geometrical details of the blade is depicted in Table 1. The computations are performed at Reynolds numbers of 50000. Instantaneous flow fields, time-mean quantities are presented. The objective of the study is to elucidate the detailed physics encountered in blade passage so the grid size used to perform simulations in x, y, and z directions is $465 \times 402 \times 182$. The grid density is kept high near the walls and blade surface in order to resolve the near wall viscous effects. The H-type grid configuration is executed on the computational domain in order to capture the correct physics a small
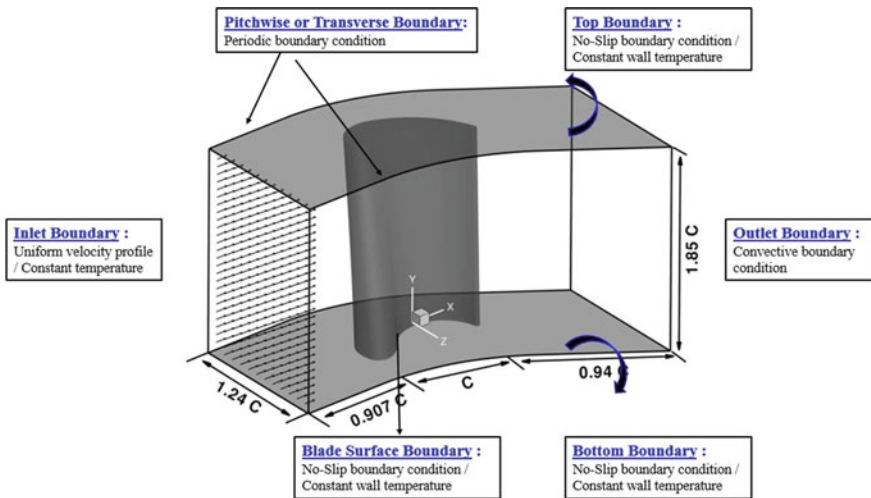
Fig. 1 Three-dimensional computational domain along with the geometrical parameters governing the flow physics

Table 1 Cascade geometry data

Axial chord length of the blade (C)	1.0
Pitch to chord ratio	1.21
Aspect ratio (Span/Axial chord)	1.85
Maximum thickness of the blade	0.41
Minimum thickness of the blade	0.29

boundary layer is formed along the blade surface by using the split block tool in ICEM CFD to ensure the fine numerical resolution. The grid simulations are carried out using non-dimensional physical time step of $\Delta t = 4 \times 10^{-4}$, respectively. The minimum and maximum grid spacing ranges for mesh in streamwise, spanwise, and pitchwise direction are given as $\Delta x = 0.0056 - 0.0070$, $\Delta y = 0.00077 - 0.0096$, and $\Delta z = 0.0034 - 0.0048$, respectively.

The boundary conditions (nondimensional form) used in the present numerical simulation are given below (Table 2):

4. **Scope and Organization of the paper**

The various generic junction flow configuration has been studied so far including wall-mounted wing (e.g., Devenport et al. [1]), cube (e.g., Martinuzzi et al. [3], Hussein et al. [4]), and circular cylinder (e.g., Baker [8], Dargahi [9], Agui et al. [10]) have increased considerably our understanding of the structure of the HSV system in front of the above-mentioned obstacles. In the junction flow, the three-dimensional flow field is obtainable from LES results a more meticulous picture of the flow can be procured by using the eddy-resolving numerical approach. In-depth exploration of the dynamics of eddies in the HSV system and of their interactions with the other dynamically, important coherent structures in the flow is thinkable.

Our major objective is to:

i. Provide a perceptible characterization of the changes in the structure and dynamics of the necklace vortices.
ii. Investigate the phenomenon, i.e., responsible of formation of legs of the string vortices and associated vortex surface interactions.

Table 2 Boundary conditions

Inlet	$\bar{u} = \bar{u}_{\text{avg}}, \bar{v} = 0, \bar{w} = 0, \bar{\theta} = 1$ and $\frac{\partial \bar{p}}{\partial n} = 0$
Outlet	Convective outflow boundary condition proposed by Orlanski [30] has been used. $\frac{\partial \overline{u_i}}{\partial t} + u_c \frac{\partial \overline{u_i}}{\partial n} = 0$ Here, u_c is the convective velocity at the outflow boundary plane. While the temperature $\left(\frac{\partial \bar{\theta}}{\partial n} = 0 \right)$ and pressure $\left(\frac{\partial \bar{p}}{\partial n} = 0 \right)$ gradient is implemented at outflow.
Top and bottom wall	$\bar{u}_i = 0, \bar{\theta}_w = 0$ and $\frac{\partial \bar{p}}{\partial n} = 0$
Transverse or pitchwise	Periodic boundary condition

iii. Provide an improved understanding of the physical mechanisms that give rise to elevated levels of endwall heat transfer in junction region.

3 Result and Discussion

The flow field near the endwall region of the blade passage is dominated by the boundary layer, strong pressure gradients, and crossflow in the pitchwise direction from the pressure side to the suction side. The resulting near-wall flow field is complex and consists of strong secondary flows and vortex roll-up. When the endwall boundary layer approaches the blade row, a vortex is formed near the junction of the blade leading edge and the endwall. This vortex is termed as the leading edge horseshoe vortex. The horseshoe vortex splits at the leading edge, and propagates downstream into the passage on both the pressure side and the suction side of the blade passage forming two legs of the early passage vortex flows. Corner vortices are also induced in the corner formed by the blade and the hub endwall. Figure 2 shown the various structures associated with twisted turbine blade passage.

The distribution of time-averaged streamline pattern colored with temperature and velocity vector colored with streamwise velocity for Re = 50000 is depicted in Figs. 3 and 4. The streamline pattern and vector field reveal some distinct feature of the time-averaged horseshoe vortex (HSV) as compared to other geometrical configuration [1–5]. The separation of the upstream boundary layer and the formation of a separation (stagnation line) on the bottom surface around the turbine blade are a consequence of the adverse pressure gradients induced by the wall-mounted turbine blade. The reorganization of the boundary layer vorticity downstream of the
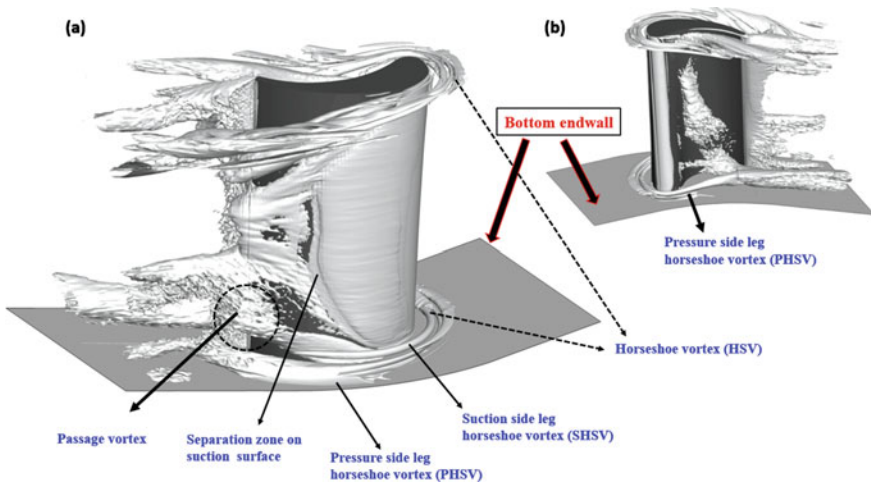
Fig. 2 Time-averaged iso-surface of Q-criteria (Structure associated with twisted blade)
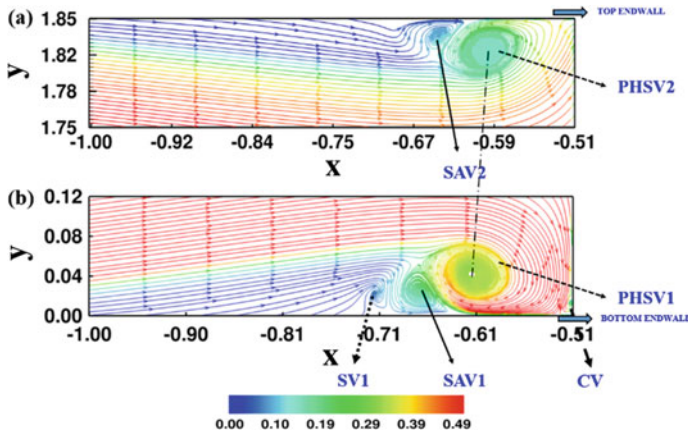
Fig. 3 Time-averaged streamline pattern colored with temperature at the blade endwall junction region **a** Top endwall, **b** Bottom endwall for Re = 50000
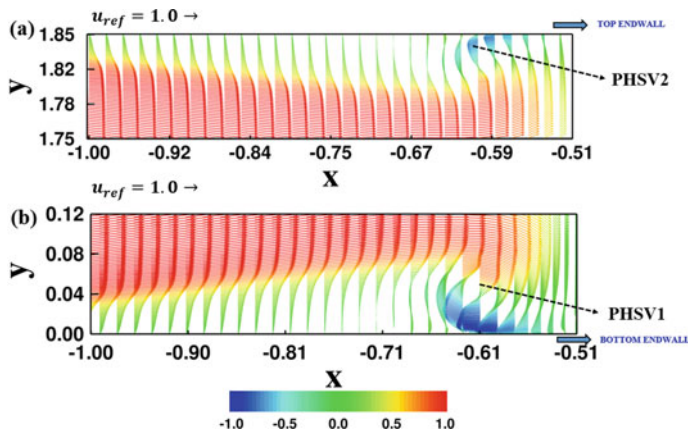
Fig. 4 Time-averaged secondary velocity vectors colored with streamline velocity at the blade endwall junction region **a** Top endwall, **b** Bottom endwall for Re = 50000

separation line results in the formation of a system of coherent necklace vortices. The blade–endwall junction region is occupied by an approximately elliptical in shape primary horseshoe vortex (PHSV) whose sense of rotation is in the clockwise direction (positive vorticity). It should be noted that for clarity grid points have been skipped while plotting the vectors. The relative strength of the secondary flow field can be ascertained through the reference vectors plotted at the top of each figure. From Fig. 3b, it is clearly observed that four types of vortices exist in the detached region that are generated through the different process region. This flow model can reasonably explain the flow field in the separated region on the x–y plane. Such a flow occurs at the leading edges of the turbomachinery blades. A substantial recirculation

behind the blade, namely PHSV1, a small secondary eddy trapped between PHSV1 and the blade called as corner vortex (CV), this is mainly formed by the separation of the boundary layer in the upstream face of the obstacle, i.e., blade leading edge (LE). The surface attached vortex (SAV1) also named as counter-rotating vortex and separation vortex (SV) which is also called as secondary vortex are also reported behind the PHSV1. The existence of four types of vortices reported by Ishii and Honami [35], i.e., corner vortex, horseshoe vortex, counter-vortex, and secondary vortex is confirmed in Fig. 3 for bottom endwall. The HSV with a large scale can be observed as the PHSV1 just head of the turbine blade. On the other hand, the separation vortices are formed by a roll-up of the wall shear layer. Basically, this is a manifestation of the impending reattachment and thinning of the shear layer as the boundary layer is swept laterally by the favorable pressure gradients created as a result of the flow around the leading edge of the blade. There are at least two vortices rotating in the clockwise direction and one smaller vortices rotating in the opposite direction. Meanwhile, for top endwall region, only two vortices are formed one is PHSV2 and another one is SAV2 both are rotating in opposite direction. The exact number of vortices was seen in Fig. 3 depending upon the flow speed and thickness of the blade, the number of vortices get reduced as the flow speed is increased. As compared with top and bottom endwall as shown in Fig. 3a, b, it is clearly observed from the time-averaged picture that the PHSV2 shift toward upstream of the blade, i.e., the core location is ($x = -0.60$, $y = 1.82$, $z = -0.178$), while for the PHSV1 the core location is ($x = -0.61$, $y = 0.042$, $z = 0.067$), and this shift of the PHSV shown by the dotted line. The size of the SAV2 is small as compared to SAV1 their respective core located at ($x = -0.649$, $y = 1.38$, $z = -0.180$) and ($x = -0.669$, $y = 0.023$, $z = 0.066$). The streamlined plot for Fig. 3 a, b suggests that the spatial variability regarding the position of the center of PHSV and SAV for the streamwise direction. The velocity vector profile is less full than for a standard two-dimensional flat plate boundary layer, indicating that the adverse pressure gradient is influencing the pattern due to the blockage of the blade. It is clearly observed from the Figs. 3 and 4 that strength of PHSV1 and SAV1 is higher as compared to PHSV2 and SAV2 this is because at the bottom endwall region the blade thickness is maximum as compare to top endwall region. At upstream of end wall, the location of saddle point at bottom surface is ($x = -0.74$, $y = 0.0069$, $z = 0.0097$), while for top surface is ($x = -0.71$, $y = 1.85$, $z = 0.136$), the vectors takes on the appearance of a two-dimensional boundary layer, through vortex stretching is present. Following the flow field from the saddle point toward the leading edge of the blade, the velocity vector indicates that flow in the boundary layer and outside of the boundary layer pitched downward rotated 180° and proved toward the saddle point, loss-free fluid outside the boundary layer stagnated at the end wall blade junction. This velocity vector field which is roughly elliptical structure, as shown in Fig. 4a,b, generates an excessive backflow by reversing fluid impinging on the end wall and leading edge of the blade. The backflow reaches maximum mean velocity and then decelerates giving the appearance of reseparation for bottom endwall between $x = -0.81$ and -0.51 in the vicinity of the line of low shear. In region $x = -0.65$, at the bottom endwall, the two inflection points exist this is because the surface attached vortices (SAV1) are
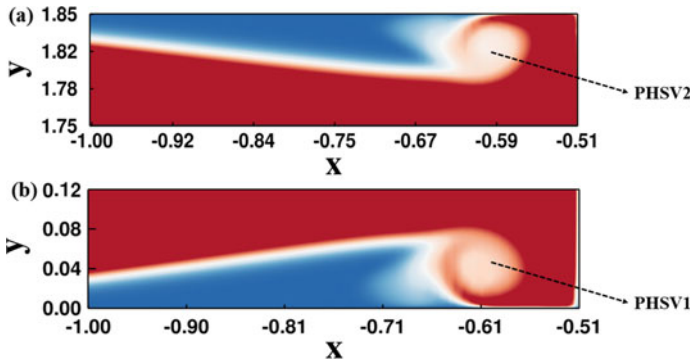
Fig. 5 Vorticity (Ω_z) at blade endwall junction **a** Top surface and **b** Bottom surface for Re $= 50000$

developed at the wall. However, the number of structures and their complexity varies with increasing Reynolds number [6]. The vorticity (Ω_z) contours in the x–y plane for both top and bottom endwall are calculated using central differencing scheme, it is evidenced from the Fig. 5a, b, the primary horseshoe vortex (light red color) shown by dotted arrow interact with endwall and generating opposite sign vorticity (blue color) via a local vortex induced pressure gradient effect [7] that manifest itself as a region both directly beneath the vortex and as growing tongue just trailing the vortex. Here, this negative and positive vorticities indicate the continuation of the horseshoe vortex system convecting downstream along the shear layer. This eruptive tongue in present case of high Reynolds number, i.e., increases in strength and penetration into the boundary layer and it occupies sizeable upstream distance. The primary HSV also undergo stretching. It is known that during stretching the circulation of a primary vortex will be conserved in the absence of flux or diffusion of vorticity across an endwall boundary that initially encompasses all the vortex vorticity. There are, two ways that viscosity could affect come into play. First, vorticity can diffuse across the boundary and, second, the vorticity comprising the vortex could cross-diffuse with the corresponding opposite sign vorticity that is generated at the surface and circulates the vortex.

The streamlines slightly above the bottom endwall in Fig. 6 show some distinct features of the endwall boundary layer flow. These features are identified by the separation lines in the Fig. 6. The streamlines along the blade leading edge bifurcate as they approach the saddle point. The saddle point is the location on the endwall where the 0° incidence line meets the separation line and corresponds to the lowest friction velocity. The incoming endwall boundary layer detaches along the separation line, and secondary vortical flows are formed in the regions immediately downstream and adjacent to the separation line. This is indicated by the high concentration of the streamlines adjacent to the separation line. The strong reverse flow in the vortex regions counter the boundary layer streamlines causing them to be concentrated more densely near the separation line. The leading edge horseshoe vortex immediately downstream of the saddle point is clearly evidenced in Fig. 6a, c. The region between
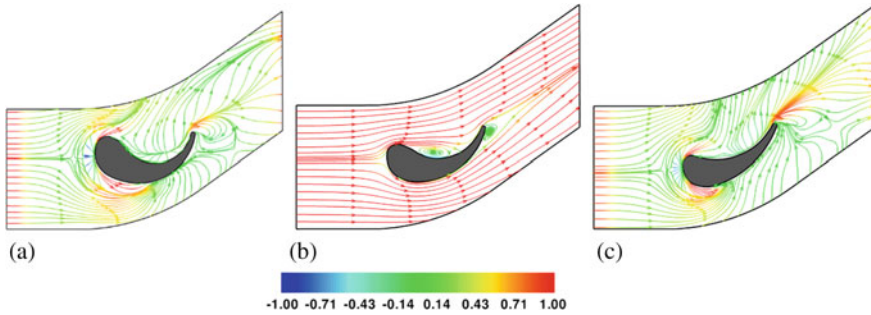
Fig. 6 Variation of time-averaged spanwise streamlines pattern colored with streamline velocity at **a** $y = 0.0$ **b** $y = 0.92$ and **c** $y = 1.85$ for twisted blade

the separation line and the blade suction side in Fig. 6a, c represents the suction side leg of the horse shoe vortex. The region along the separation line directed from the pressure side to the suction side represents the pressure side leg of the horseshoe vortex, and is driven by the passage pressure gradients. The suction side leg vortex and pressure side leg vortex meet together in the mid-passage region where the two separation lines in the passage merge. This location occurs close to the suction surface, and the merger of the two vortices forms a stronger vortex known as the passage vortex. The passage vortex then travels along the blade suction surface toward the passage exit. Downstream of the pressure side separation line, the endwall boundary layer region is very thin and skewed toward the suction side. This is evidenced by the streamline concentration being sparse in this region as they turn from the pressure side to the suction side. The strong vortical motions of the pressure side leg vortex entrain most of the fluid from the incoming boundary layer and a new boundary layer forms downstream. Comparing the streamlines in Fig. 6 a, c with those in the mid-span regions in Fig. 6b, it is clear that the turning of the streamlines inside the blade passage and around the leading edge is much greater near the endwall region which causes the cross flow here to be stronger. The uniform pressure distribution along the pressure surface span and very weak interaction of the boundary layers between the pressure surface and endwall are responsible for such flow behavior. However, the laminar boundary layer near the pressure surface leading edge may diffuse with a rise in surface pressure when the incoming flow is at high speed.

The spanwise vorticity pattern on the suction surface and pressure surface shown in Fig. 7 reveals some interesting features of the boundary layer behavior. The separation lines divide the flow on the suction surface into three regimes: (i) two-dimensional laminar boundary layer regime, (ii) turbulent boundary layer regime, and (iii) three dimensional flow regime.

(i) Two dimensional laminar regime: This regime extends from the leading edge to the lowest suction pressure on the suction surface and between the S2s separation lines near the two endwalls in Fig. 7. The laminar boundary layer
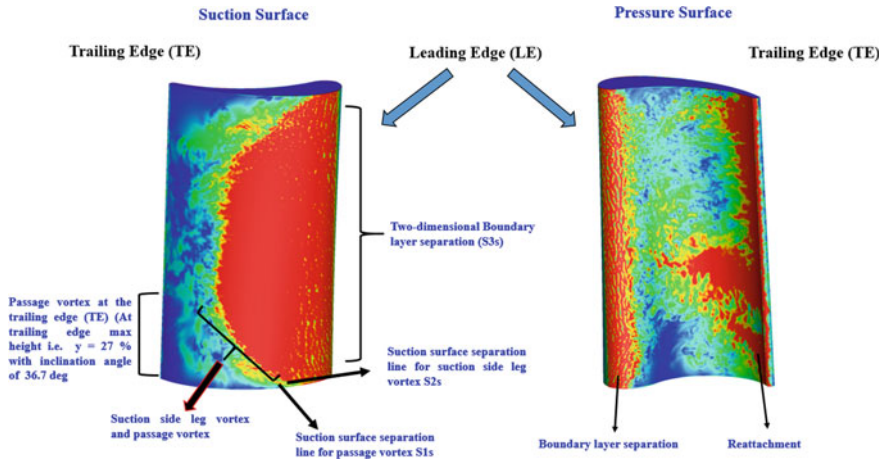
Fig. 7 Variation of instantaneous spanwise vorticity for both suction and pressure surface of twisted blade

starting at the leading edge undergoes a high acceleration on the suction surface. According to Hodson and Dominy, the over-acceleration in the boundary layer causes a two-dimensional separation bubble near the blend point of the circular leading edge and the suction surface. Following the re-attachment behind the separation bubble, the laminar boundary layer accelerates along the suction surface and continues to grow until the separation line S3s.

(ii) Turbulent regime: This regime is limited by the re-attachment line following the separation at S3s and trailing edge and between the S2s lines. The laminar boundary layer separates at the lowest suction pressure located at axial distance at S3s because of the adverse pressure gradient and forms another closed separation bubble. The boundary layer undergoes transition and becomes turbulent as the Reynolds number is increased; it is clearly evidenced in Fig. 7. The turbulent boundary layer grows along the suction surface and may separate again due to the adverse pressure gradient near the trailing edge to form the trailing edge wake.

(iii) Three-dimensional flow regime: This regime is indicated by the region between the separation line S2s and endwall. The regime begins at the location where the suction side leg of the leading edge horseshoe vortex and pressure side leg vortex from the adjacent blade meet on the suction surface. The pair then emerges as the passage vortex which then moves toward the span as it follows the suction surface toward the passage exit. The distinct appearance of the separation line S2s indicates that the suction side leg vortex maintains its existence in the axial development of the passage vortex. The locations of the separation bubbles and separation lines on the blade surface are strongly influenced by the inlet flow angle and Reynolds number of the incoming flow.

Figure 8a, b, is a time-averaged realization of Nusselt number distribution on the
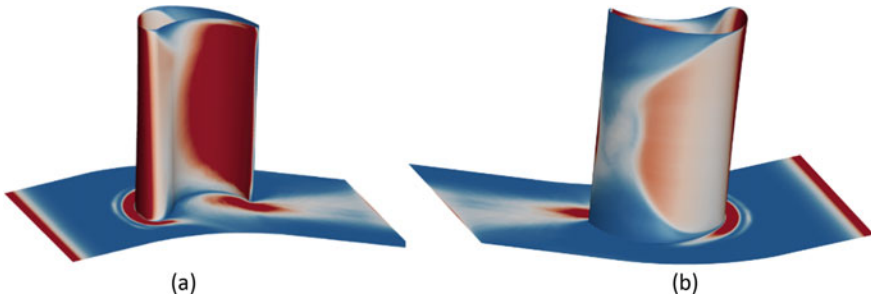
Fig. 8 Time-averaged Nusselt number contours for both **a** suction side **b** pressure side for Re = 50000

endwall. The impinging behavior of turbulent boundary layer immediately upstream of the endwall separation point ($x = -0.51$) just prior to the leading edge of the blade created the streak spacing behavior. The Fig. 8 reveals that the most spatially extensive or primary region of high heat transfer is a band (red color) located just upstream of the LE. The simulation result revealed that primary band of high heat transfer is caused by outer region boundary layer fluid that impinges on the LE of the blade and then flows down the face of the blade and hit on the endwall of Praisner et al. [33, 34]. The strength of this primary band around the blade LE depends upon the Reynolds number at low Re case (not shown), the region occupied by primary band is less as compare to the high Re. The primary band of high heat transfer was found to be temporary unstable demonstrating little change. From Nusselt number plot, another thin leg of high heat transfer region is observed which also wraps around the primary band and this second region is referred as secondary band. However, this secondary band or region of high heat transfer was found to be much more transient in its development and behavior. Figure 3 illustrates the time-averaged flow field data (streamlines colored by temperature) with the corresponding time-averaged heat transfer distribution. It is clearly evidenced from Fig. 3 that the PHSV1 is colored by moderate concentration of temperature and this PHSV1 is rest above a region of relative low heat transfer, the SAV1 separating the two bands of high heat transfer also a region of high heat transfer upstream of SAV1 is in fact spatially coincident with SV. The vortical structures of HSV system, i.e., PHSV1, SAV1, SV, and DV are labeled in Fig. 3. From streamline pattern, it is observed that incoming hot stream of fluid striking on the leading edge of the blade and then the streamlined fluid take U-turn and this reverse flow fluid strikes on endwall region, the HSV, and SV vortices rest on this reverse flow fluid, while this fluid is passing over the SAV1 after that it is merging with the flow. This reverse flow fluid it separate while passing over the SAV1 and then reattaches before SV. The flow reattachment at this location may be the reason for heat transfer on endwall. As expected, the strong recirculation regions formed by SAV1 results in poor heat transfer and are obvious from the contour of Nusselt number as shown in Fig. 8. In case of low Re, the large recirculation (not

shown), near the endwall degrade heat transfer by obstructing the fluid from the core region to replace the near endwall hot fluid.

4 Conclusion

We have carried out numerical simulations of the turbulent flow past the straight turbine blade configuration using LES approach based on (SISM) model. The alikeness between the time-averaged vorticity measurements at the junction region for different geometries (Devenport and Simpson [1], Paik et al. [31], Escauriaza and Sotiropoulos [32]) showed that present LES (SISM) model captures utmost analogous experimental and numerical trends with good characteristic and with significant accuracy. The HSV structures particularly for bottom and top endwall are of comparable sizes. Even at bottom wall the number of vortices formed are more because of more thickness of blade. The vortices are more organized and are shed in a nearly periodic manner. The structures near the wall breakdown as a consequence of complex nonlinear interactions due to flow inertia.

References

1. Devenport WJ, Simpson RL (1990) Time-dependent and time-averaged turbulence structure near the nose of a wing-body junction. J Fluid Mech 210:23
2. Chrisohoides A, Sotiropoulos F, Sturm TW (2003) Coherent structures in flat-bed abutment flow: computational fluid dynamics simulations and experiments. J Hydraul Eng 129:177
3. Martinuzzi R, Tropea C (1993) The flow around surface-mounted, prismatic obstables placed in a fully developed channel flow. J Fluids Eng 115:85
4. Hussein H, Martinuzzi RJ (1996) Energy balance for turbulent flow around a surface mounted cube placed in a channel. Phys Fluids 8:764
5. Paik J, Sotiropoulos F (2005) Coherent structure dynamics upstream of a long rectangular block at the side of a large aspect ratio channel. Phys Fluids 17:115104
6. Simpson RL (2001) Junction flows. Annu Rev Fluid Mech 33:415
7. Doligalski TL, Smith CR, Walker JDA (1994) Vortex interactions with walls. Annu Rev Fluid Mech 26:573
8. Baker CJ (1980) The turbulent horseshoe vortex. J Wind Eng Ind Aerodyn 6:9
9. Dargahi B (1989) The turbulent flow field around a circular cylinder. Exp Fluids 8:1
10. Agui JH, Andreopoulos J (1992) Experimental investigation of a three dimensional boundary layer flow in the vicinity of an upright wall mounted cylinder. J Fluids Eng 114:566
11. Seal CV, Smith CR, Rockwell D (1997) Dynamics of the vorticity distribution in endwall junctions. AIAA J 35:1041
12. Seal CV, Smith CR (1999) Visualization of a mechanism for three-dimensional interaction and near wall eruption. J Fluid Mech 394:193
13. Chen CH (1995) Assessment of a Reynolds stress closure model for appendage-hull junction flows. J Fluids Eng 117:557
14. Fu S, Rung T, Thiele F, Zhai Z (1997) In: Lesieur M, Launder BE, Binder G, Whitelaw JH (eds), Proceedings of the 11th symposium on turbulent shear flows, Grenoble, France, pp 6.7–6.12
15. Parneix S, Durbin PA, Behnia, M (1998) Computation of 3-D turbulent boundary layers using the V2F model. Flow Turbul Combust 60:19

16. Apsley D, Leschziner M (2001) Investigation of advanced turbulence models for the flow in a generic wing-body junction. Flow Turbul Combust 67:25
17. Rodi W (1997) Comparison of LES and RANS calculations of the flow around bluff bodies. J Wind Eng Ind Aerodyn 69:55
18. Krajnović SC, Davidson L (2002) Large-eddy simulation of the flow around a bluff body. AIAA J 40: 927
19. Rodi W, Ferziger J, Breuer M, Pourquié M (1997) Status of large-eddy simulation: results of a workshop. J Fluids Eng 119:248
20. Shah KB, Ferziger JH (1997) A fluid mechanicians view of wind engineering: large Eddy simulation of flow past a cubic obstacle. J Wind Eng Ind Aerodyn 67:211
21. Saha AK, Acharya S (2003) Parametric study of unsteady flow and heat transfer in a pin-fin heat exchanger. Int J Heat Mass Transf 46(20):3815
22. Murata A, Shibata R, Mochizuki, S (1991) Effect of cross-sectional aspect ratio on turbulent heat transfer in an orthogonally rotating rectangular smooth duct. Int J Heat Mass Transf 42:3803
23. Moin P, Squires K, Cabot W, Lee S (1991) A dynamic subgrid-scale model for compressible turbulence and scalar transport. Phys Fluids A 3(11):2746
24. Smagorinsky J (1963) General circulation experiments with the primitive equations: I. The basic equations. Mon Weather Rev 91(3):99
25. Lévêque E, Toschi F, Shao L, Bertoglio JP (2007) Shear-improved smagorinsky model for large-eddy simulation of wall-bounded turbulent flow. J Fluid Mech 570:491
26. Toschi F, Lévêque E, Ruiz-Chavarria G (2000) Shear effects in nonhomogeneous turbulence. Phys Rev Lett 85:1436
27. Eswaran V, Prakash S (1998) A finite volume method for Navier-Stokes equations. In: Third Asian CFD conference, Vol 1, Bangalore, India
28. Sharma A, Eswaran V (2003) A finite volume method. In: Muralidhar K, Sundararajan T (eds), Computational fluid flow and heat transfer. 2nd ed. Narosa Publishing House, New Delhi. Ch. 12, pp 445
29. Rhie CM, Chow WL (1983) Numerical study of turbulent flow past an airfoil with trailing edge separation. AIAA J 21:1525
30. Orlanski I (1976) A simple boundary condition for unbounded flows. J Comput Phys 21:251
31. Paik J, Escauriaza C, Sotiropoulos F (2007) On the bimodal dynamics of the turbulent horseshoe vortex system in a wing-body junction. Phys Fluids 19:045107
32. Escauriaza C, Sotiropoulos F (2011) Reynolds number effects on the coherent dynamics of the turbulent horseshoe vortex system. Flow Turbul Combust 86:231
33. Praisner TJ, Smith CR (2005) The dynamics of the horseshoe vortex and associated endwall heat transfer: Part I—Temporal behavior. In: ASME turbo expo. Proceedings of GT69088, vol 899
34. Praisner TJ, Smith CR (2006) The dynamics of the horseshoe vortex and associated endwall heat transfer—Part II: time-mean results. J Turbomach 128:755
35. Ishii J, Honami S (1986) A three-dimensional turbulent detached flow with a horseshoe vortex. J Eng Gas Turbines Power 108(1):125–130

Design and Analysis of Axial Turbine Using Three Different Vortex Laws

Sachin Verma, Anubhuti Sharma, Manish Kumar, M. Jaydip Pokiya, Prathapanayaka Rajeevalochanam, and S. N. Agnimitra Sunkara

Abstract In the present work, a single-stage axial turbine is designed using three design approaches for the same specifications. The three different designs were obtained using different classical vortex distributions, viz., *Free Vortex* (FVD), *Constant Nozzle Angle* (CNA), and *Constant Specific Mass Flow* (CSM). Kacker–Okapuu model is used for the estimation of pressure losses. To maintain consistency, the design is carried out for the same flow path and turbine stage parameters, viz., the stage loading, flow coefficient, and mean reaction. The hub-tip radius ratio is 0.72 for all the designs. The design point performance and flow analysis are carried using a commercial CFD solver. A comparative study of the performance obtained using the three different approaches is carried out. It is observed that for a turbine with a hub to tip ratio of around 0.7, the choice of vortex distribution does not yield any notable difference in efficiency output at design point.

Keywords Axial turbine design · Free vortex · Constant nozzle angle · Constant specific mass flow · CFD

Nomenclature

A	Annulus area
C	Absolute velocity
C_p	Specific heat at constant pressure
N	Turbine speed
P	Pressure
R	Gas constant
T	Temperature

S. Verma · A. Sharma · M. Kumar · M. J. Pokiya
Department of Aerospace Engineering, Punjab Engineering College, Chandigarh, India

P. Rajeevalochanam (✉) · S. N. A. Sunkara
CSIR- National Aerospace Laboratories, Bangalore, India
e-mail: prathap@nal.res.in

U	Blade speed
h	Blade height
o	Throat opening
r	Radius
c	Blade chord
c_x	Blade axial chord
t_{max}	Maximum thickness of an airfoil
s	Blade spacing
α	Flow angle
γ	Ratio of specific heats
ϕ	Flow Coefficient $= \frac{C_a}{U_m}$
ψ	Stage loading coefficient $= \frac{C_P \Delta T_0}{U_m^2}$
η_{tt}	Total- to- total efficiency $= \frac{\Delta T_0}{T_{01}\left[1-\left(\frac{1}{\pi}\right)^{\gamma-1/\gamma}\right]}$
ρ	Density
π	Expansion ratio $= P_{01}/P_{03}$

Subscripts

0	Stagnation quantity
1,2	NGV inlet and outlet planes, respectively
3	Rotor outlet Plane
a	Axial velocity component
m	Mean section
w	Whirl velocity component

1 Introduction

During initial stages of the design of an axial flow gas turbine, the flow is assumed to be two dimensional, i.e., the radial flow of fluid elements is ignored—which can be a reasonable assumption for short blades having a hub to tip ratio greater than 0.8 [1]. It is understood that the flow can have a small component of velocity in a radial direction due to the flaring of the annulus. In addition, the whirl velocity increases the pressure with radius to balance the inertia force causing the flow to have small radial motion; but it follows that the fluid elements are in radial equilibrium [2]. The performance of the turbine stage also depends on the spanwise distribution of work extraction.

In the present work, the design of a single-stage axial turbine is carried out using the three aforementioned vortex distribution, viz., free vortex (FVD), constant nozzle angle with free vortex for the rotor row (CNA) and constant specific mass flow (CSM).

The turbine designs are carried out for the same aero-thermodynamic parameters such as the stage loading and flow coefficients, mean reaction, and turbine speed. For the sake of consistency, blade parameters at the mean section, the dimensions of the meridional flow path, and axial chords at hub, mean and tip sections are maintained constant in all the designs.

1.1 Free Vortex Design (FVD)

For a free vortex stage, the stagnation enthalpy drop and the axial component of the velocity remain constant over the annulus. The result is that the whirl component of the velocity has to be inversely proportional to the radius, which is called the free vortex design. To obtain higher efficiency, the blade angles should closely match the gas angles at all radii. This results in a highly twisted blading. The variation of nozzle angle α_2 for FVD can be obtained from

$$C_w r = r C_a \tan \alpha = \text{constant} \tag{1}$$

1.2 Constant Nozzle Angle Design (CNA)

Constant nozzle angle vortex distribution is one approach used to satisfy the condition of radial equilibrium of fluid elements and it allows the manufacturing of simple untwisted stator blades.

The axial velocity variation for this type of distribution is

$$C_{a2} r^{\sin^2 \alpha_2} = \text{constant} \tag{2}$$

1.3 Constant Specific Mass Flow (CSM)

It is also possible to design a turbine with a condition of constant specific mass flow with zero radial velocity component. The equations relevant to this method, obtained and simplified from Ref. [3], are as follows:

$$\rho C \cos \alpha = K_1 = \text{constant} \tag{3}$$

$$\frac{T}{\rho^{\gamma - 1}} = K_2 = \text{constant} \tag{4}$$

$$C = C_m \exp \int_r^{r_m} \sin^2\alpha \, \frac{dr}{r} \tag{5}$$

$$\rho = \left[\rho_m^{\gamma+1} + \frac{\gamma+1}{\gamma} \frac{1}{R} \frac{K_1^2}{K_2^2} \int_r^{r_m} \tan^2\alpha \, \frac{dr}{r} \right]^{\frac{1}{\gamma+1}} \tag{6}$$

Equations (1)–(6) are used to calculate variations in the angle (α), velocity (C), and density (ρ), respectively, along the span. The flow quantity distributions are obtained for infinitesimal span Δr along the blade height.

1.4 Turbine Stage Configuration

The turbine under study in the present work is a single-stage axial turbine, expected to produce a power of 1350 kW at a pressure ratio of 2.33 with the desired efficiency of 91%. The turbine is a constant shroud diameter stage with a hub to tip radius ratio of 0.72. Rotor tip clearance is chosen to be 1% of the blade span. Other turbine stage parameters have been presented in Table 1. Three separate turbine stages are designed accordingly for FVD, CNA, and CSM to meet the required specifications.

2 Design Approach

The stage loading, flow coefficient, and reaction are chosen keeping in mind the target efficiency levels from standard charts (e.g., Smith's chart). Here, in this case, the initial target was 88%. If, during the meanline design, the performance is not met or the AN^2 parameter exceeds the limit, a different combination of the parameters is chosen and the process is repeated till a converged solution is obtained.

The turbine design for each vortex design approach starts with flowpath and meanline design based on deviation estimates by Ainley-Mathieson [4] and loss correlations by Kacker-Okapuu [5]. The final velocity triangles are obtained by accounting for estimated stator and rotor blade row pressure losses, incidence, and deviations for hub, mean, and tip sections. The velocity vector diagrams (representing Mach numbers) of the turbine mean section for all the three approaches CNA, CSM, and FVD are shown in Fig. 1a–c), respectively.

Table 1 Turbine stage parameters

ψ	1.37
ϕ	0.74
AN^2	$3.25e07$ m^2 rpm^2
Reaction	0.33

Fig. 1 Velocity triangles of
the turbine designed using
different vortex approaches
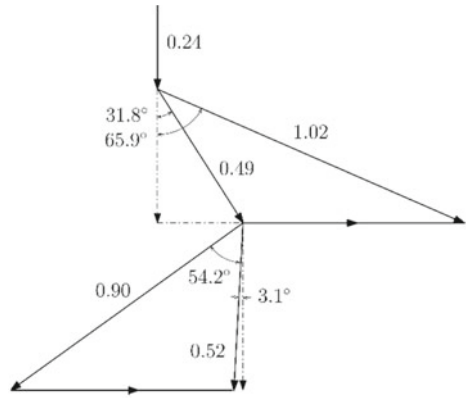
(a) CNA
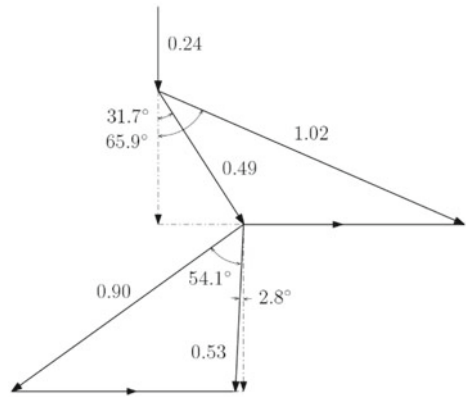
(b) CSM
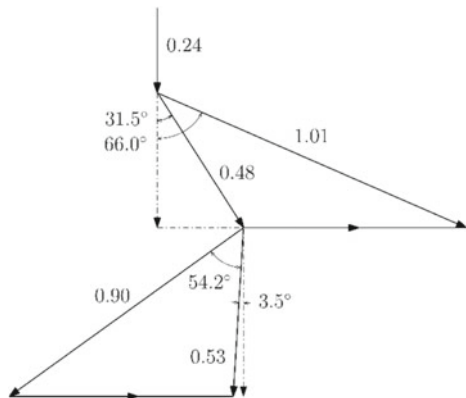
(c) FVD

Table 2 Mean blade section parameters

Parameter	NGV	Rotor
o/s	0.40	0.60
s/c	0.73	0.64
t_{max}/c	0.146	0.167
h/c_x	1.42	1.68

The stator and rotor blade count are chosen based on spacing-to-chord ratio; the point of least loss as shown in [4] and Zweifel coefficient as described in [6].

A survey of classical blade profile generation methods [7, 8] is carried out. The 2D airfoil sections are generated using Pritchard's method [7]. The 2D blade sections are then stacked to obtain the 3D blade geometry. The blade parameters for the mean section are listed in Table 2.

The designed blade profiles for FVD, CNA, and CSM have been compared in Fig. 2. The stator airfoil sections are stacked about their trailing edges and the rotor sections are stacked along the line joining the centers of gravity.

Fig. 2 Blade profile comparison
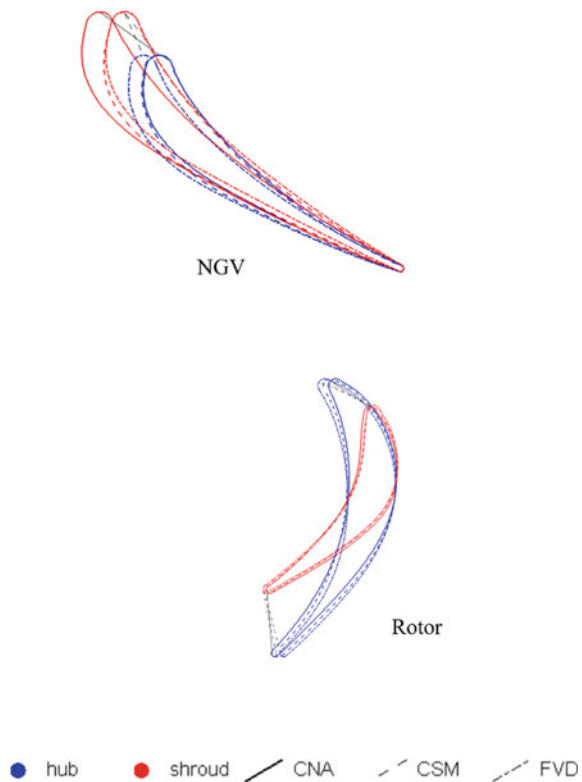
Fig. 3 Turbine stage geometry
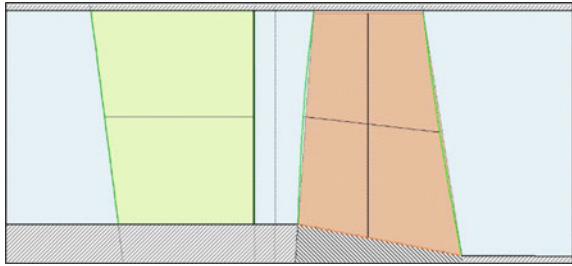
Airfoil and 3D blade generation are carried out in a commercial turbomachinery tool–AxCent™. Before finalizing the blade geometry, care has been taken to ensure that the blade passages of stator and rotor are wide enough to allow for machining. Also the thickness distributions, minimum trailing edge thickness are tailored to avoid any blade warpage or distortion during machining. From Fig. 2 it is observed that NGV blades have zero twist for CNA, moderate twist for CSM, and maximum twist for FVD design.

The turbine stage meridional flow path is shown in Fig. 3. After configuring the turbine geometry completely, 3D RANS CFD simulations are then carried out to obtain the performance parameters and to analyze the flow field characteristics of the designed turbine stages.

2.1 Computational Grid

The fluid domain required to carry out RANS CFD is generated using the Auto-grid5™ module of NUMECA. A multi-block structured grid approach is adopted to generate O4H meshes, as shown in Fig. 4. The H-type meshes are used for inlet, outlet, and passage blocks. O-H-type meshes used in the passage block primarily reduce the skewness and effectively capture the boundary layers around the blade surface.

The grid generation process involves the definition of the periodicity for stator and rotor rows, the rotor shroud gap definition, and the first cell width at the solid wall. The computational domain of the turbine stage has been shown in Fig. 5a. Through the grid quality report, it is observed that the spanwise expansion ratio is 1.34, average cell growth is around 1.2, and the minimum skewness achieved is 36°.

2.2 Numerical Setup

The boundary conditions and inputs given during the case setup are total pressure, total temperature, and flow direction at the inlet and average static pressure at the

Fig. 4 O4H grid topology
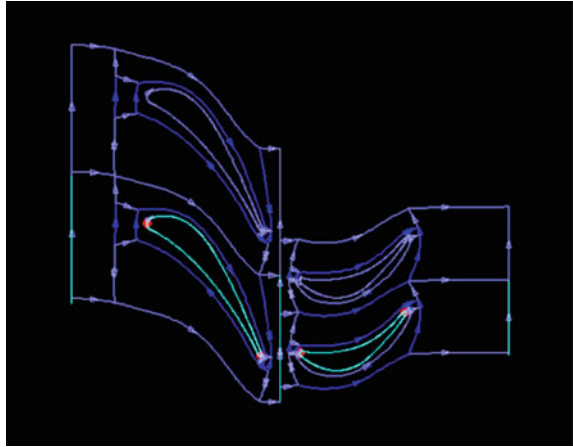
outlet. A no-slip, adiabatic wall boundary condition is imposed on blades and end walls. A single passage stage interface approach, i.e., a mixing plane that carries out circumferential averaging between the stator and rotor domains is considered. ANSYS-CFX generally uses a pressure-based solver which employs finite element based finite volume discretization [9]. The simulation is taken as converged when the mass flow imbalance between inlet and outlet vanishes and RMS of residuals reaches below 1e-6. At the inlet, a turbulence intensity of 8% is chosen for all the simulations [10].

Shear Stress Transport (SST) turbulence model [11] is chosen for the simulations owing to its ability to handle flow separations and adverse gradients which is typical of turbomachinery flows.

2.3 Grid Independence Study

In order to ensure that the solution is unaffected by the size of the grid, a grid independence study is carried. Four incremental grid sizes are considered as shown in Table 3. A grid size of 1.2 million was opted for all the simulations conducted in the study. The solution is taken as size independent if the difference in the predicted mass flow rate with respect to the next finer grid is insignificant. For the opted grid size, this difference is as low as 0.002%.

It can be observed that the y^+ distribution (Fig. 5b) indicates an overall value less than 5, this is within the prescribed limit of 11 for SST model with automatic wall function in ANSYS-CFX solver [9]. The detailed overall turbine design process using state-of-the-art design and analysis tools is clearly outlined and executed in the work carried out by Prathapanayaka et.al [12]. Further, reference [13] gives invaluable information about the design methods and the role of various flow analysis tools used in turbine design process.

Fig. 5 **a** Computational
domain **b** y+ contour
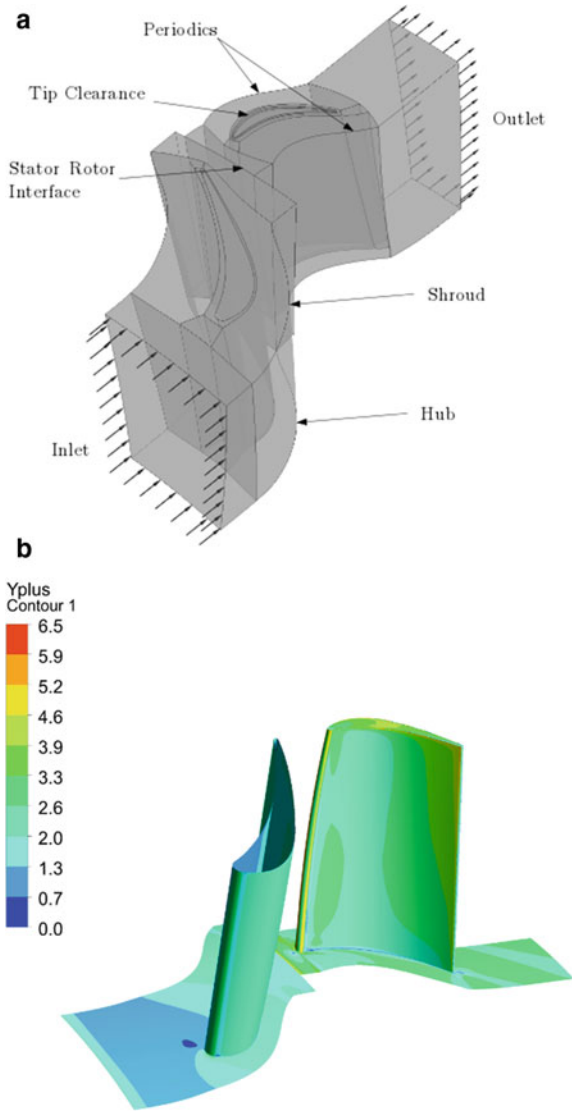
Table 3 Grid independence
study—FVD

Grid Size	Mass flow rate [kg/s]
0.3 million	5.683
0.6 million	5.6802
1.2 million	5.6812
2 million	5.6811

3 Results and Discussions

The design point performance of the turbine stages designed for the three different vortex distributions is approximated through CFD simulations. It is observed that the mass flow rate passing through all the three designs is the same as per the design requirement.

It can be observed from Table 4 that the power output of the turbine stages for all the designs match closely at the design point. Table 4 shows that CSM has a maximum efficiency of 91.1% compared to other designs which lie in close proximity. This need not be considered as a significant difference owing to the very high numerical sensitivity of the adiabatic efficiency on pressure ratio and inlet temperature. This suggests that, for different vortex distributions considered in this study, there need not be any significant improvement in efficiency for turbines of radius ratio around 0.72.

For a more comprehensive analysis, circumferentially mass averaged spanwise distributions across stator and rotor are plotted and studied. The efficiency distribution has been plotted in Fig. 6 which points out the lowest efficiencies near the shroud

Table 4 Performance parameters

Design	Mass flow rate [kg/s]	π	Efficiency [%]	Power [kW]
FVD	5.681	2.326	90.85	1358.8
CNA	5.681	2.324	90.9	1358.0
CSM	5.681	2.325	91.1	1360.8

Fig. 6 Spanwise efficiency distribution
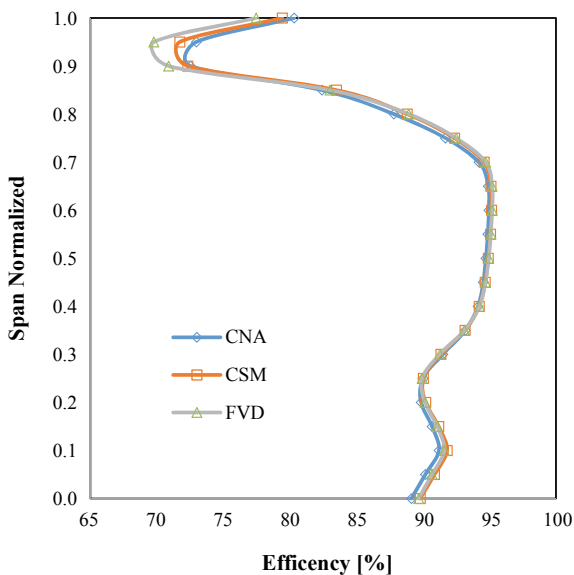
region, attributed to tip leakage losses. It is seen that, for all the designs, the trends are coherent with only minor differences. It can be found that FVD exhibits a relatively higher loss at the tip. Figure 7 is a plot of the spanwise distribution of temperature-based reaction. As compared to the design reaction of 33%, the CFD estimates the mean reaction to be slightly higher at around 35% for all the designs.

The variation of angles in Fig. 8 shows that for NGV, FVD shows the largest variation of exit blade angles whereas CNA shows minimum or no variation. The under-turning of the flow, which is apparent from the decrease of exit flow angle, near the hub and tip is due to the boundary layer and secondary flow interactions [14]. The dashed lines in Fig. 8 correspond to the exit flow angle from NGV estimated using the Ainley and Mathieson deviation model (1951) [4] used during the mean line design. It is to be noted that in spite of the constant nozzle exit blade angle design there are deviations in the NGV exit flow angle.

As observed from the normalized axial velocity plot (Fig. 9), CNA has the maximum variation in axial velocity across the span whereas FVD has the minimum variation as a consequence of respective vortex distributions. Referring to the criterion for FVD, a constant axial velocity is expected at the exit plane of NGV. However, due to compressible viscous effects and strong secondary flows near the endwalls, the flow behavior is different from that assumed during the preliminary design.

The averaged spanwise distribution of the flow angles for the rotor in the relative frame of reference at inlet and outlet is presented in Fig. 10a, b, respectively. At the exit of the rotor, overturning near the end walls and under-turning near the mid-span is observed. This is the main consequence of the secondary flow vortex structures in the passage as shown in Fig. 11. It can be observed that the hub passage vortex extends from hub to nearly 25% of the blade span. It can be said that the mid-span

Fig. 7 Spanwise degree of reaction
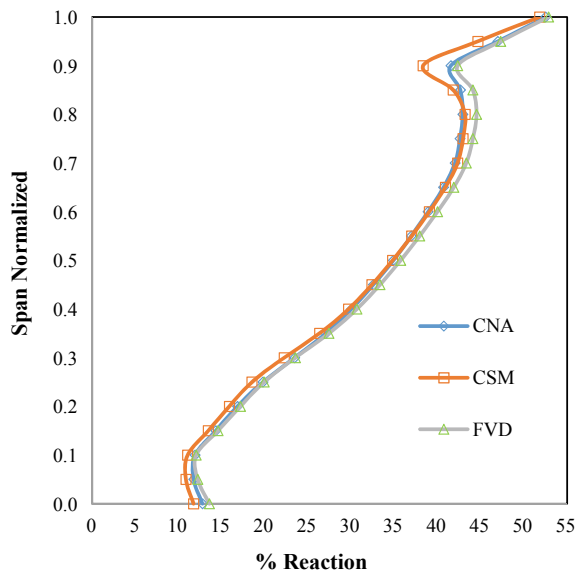
Fig. 8 NGV exit flow angle
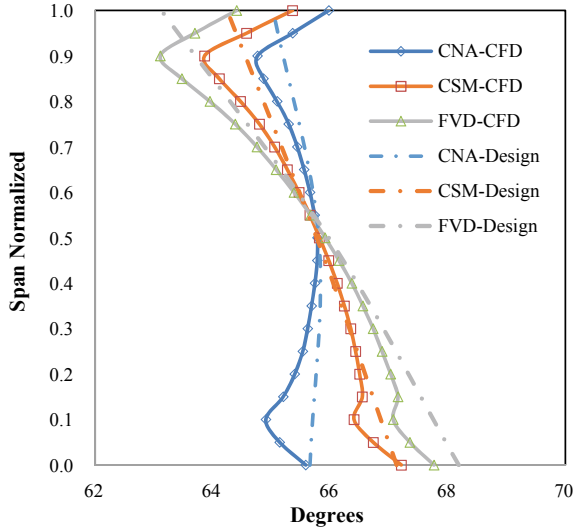
Fig. 9 Normalized axial velocity at NGV exit
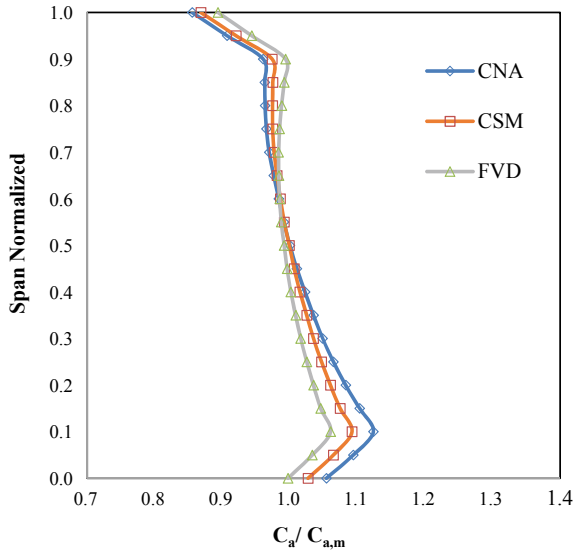
flow is affected, to some extent, being sandwiched between the hub passage vortex and the tip leakage vortex.

As the spanwise distribution of flow quantities in all the three approaches is the same as seen in Fig. 10a, b, it is reasonable to assume the same flow structure within the blade passages of CNA, FVD, and CSM designs.

The plot of the loss coefficient in Fig. 12, shows the variation of loss coefficient across the NGV. FVD has a slightly higher loss than CNA and CSM, which almost

Fig. 10 a Relative inlet flow angle for rotor **b** Relative exit flow angle for rotor
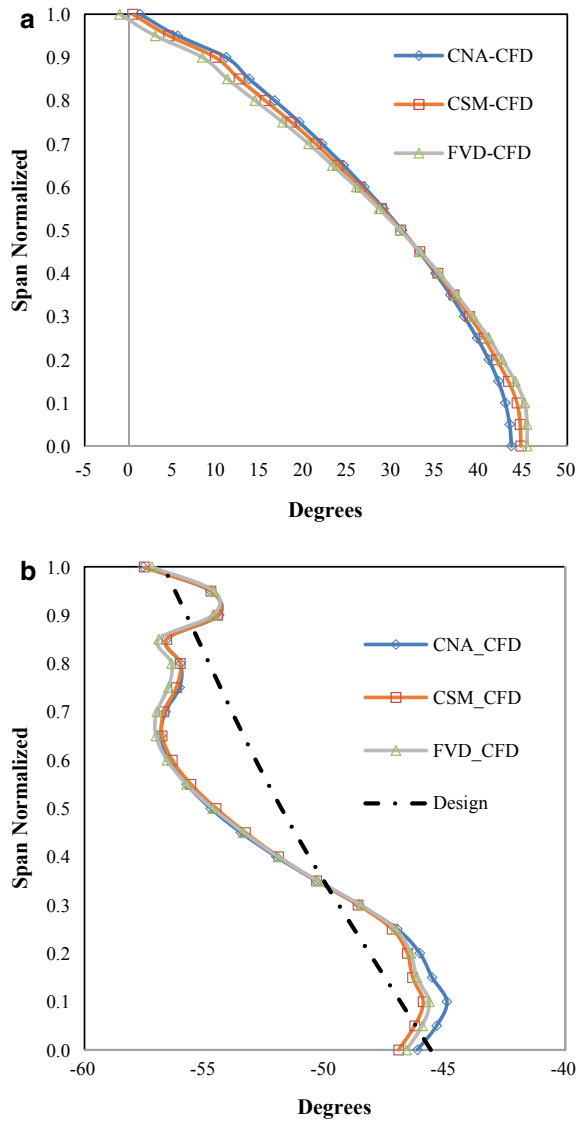
overlap each other and have an approximate value of 0.05 from 10% to 90% of the span.

The higher losses at the NGV hub and tip of the three turbines, which reach up to 20% and 15% respectively, are due to the formation of leading-edge horseshoe vortex and interaction of end wall boundary layers [14]. The mean section loss estimated by the K-O model [5] is 8% against the CFD prediction of about 5%.

Figure 13 illustrates the variation of loss coefficient for rotors of the three

Fig. 11 Vortex structures in rotor—CSM
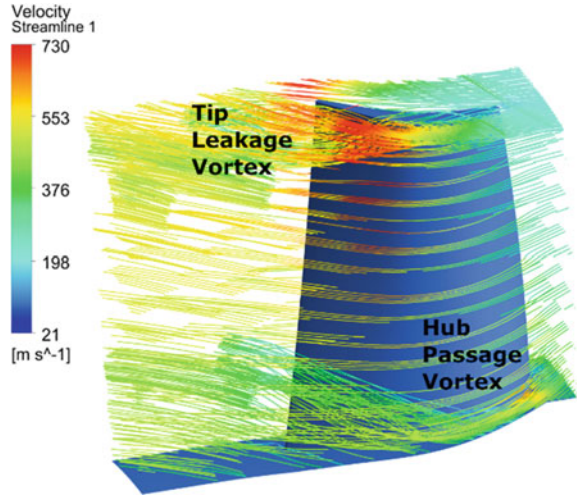
Fig. 12 NGV loss coefficient
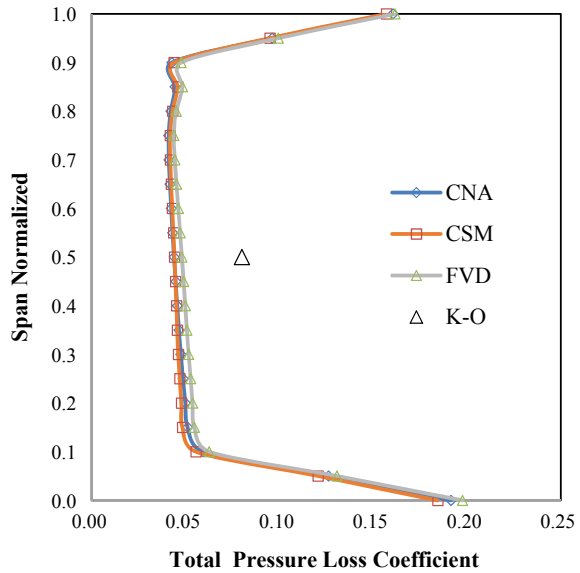
designs—which show a similar trend and closely overlap each other at various span-wise locations. It is evident from the figure that losses reach a maximum at 20 and 90% of the blade span. The increase in loss to about 25% near the hub (till 35%) is due to the presence of secondary flow vortex as shown in Fig. 11. The pressure loss estimate obtained from K-O model for the rotor mean section is about 17% against 9.4% obtained from CFD. This could be due to the limitation of either of the prediction methods. This can only be ascertained after detailed cascade row testing.

Fig. 13 Rotor loss coefficient
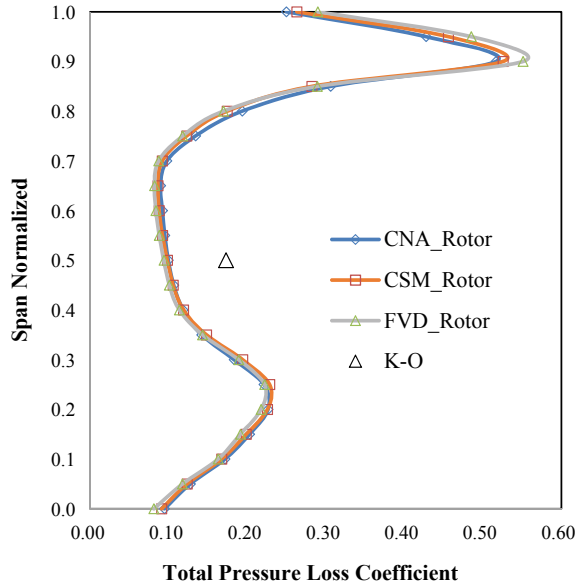
Figures 14 and 15 show the "Isentropic Mach Number" distributions over the blade surface at three different spanwise locations for NGV and Rotor, respectively. It can be noted the distribution trend for CNA has a slight variation compared to FVD and CSM which show closely matching plots. The hub and mean sections of NGV of CNA design is relatively more fore-loaded than those of CSM and FVD. The loading over the NGV at all the hub, mean, and tip sections for the CNA design is more gradual than the other two. FVD has the highest Mach number in all the three sections. This effect could be either due to the change in the exit Mach number distribution or due to slight differences in the blade profiles resulting from different stagger angles in respective designs.

From Fig. 15a–c it can be observed that there are considerable accelerations at the leading edge on both the suction and pressure sides. This could be due to the incidence effect or due to airfoil profile discontinuity at the leading-edge circle and the wedge–typical of Pritchard's airfoils. This can be addressed by using higher order Bezier curves.

As for the sake of completeness, the flow fields are shown in Fig. 16 for hub, mean, and tip sections in CSM configuration. It can be seen that there are no visible passage separations or shocks at the hub and mean sections, but the rotor passage at the tip section is choked. Similar trends are observed for CNA and FVD configurations as well.

Fig. 14 Isentropic Mach
number distribution for NGV
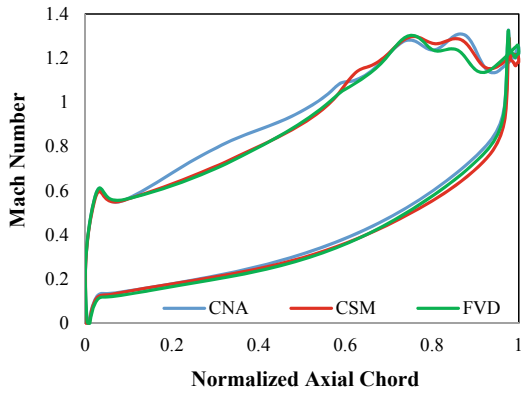
(a) 20% Span
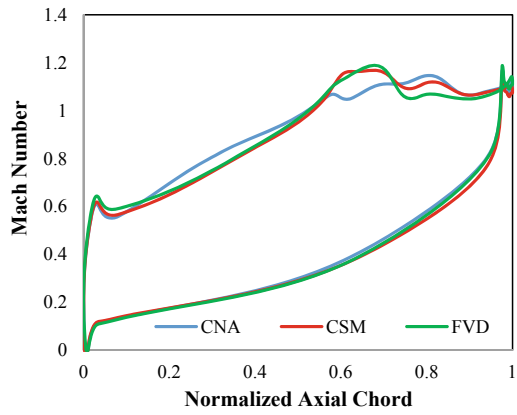
(b) 50% Span
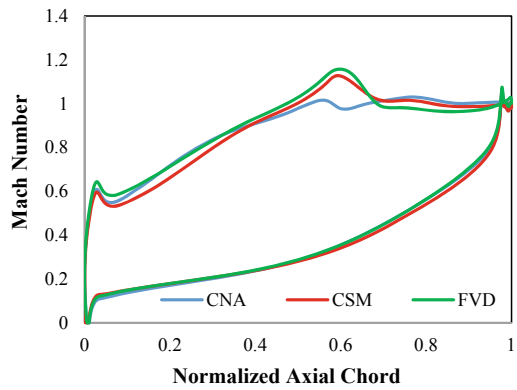
(c) 80% Span

Fig. 15 Isentropic Mach
number distribution for
Rotor
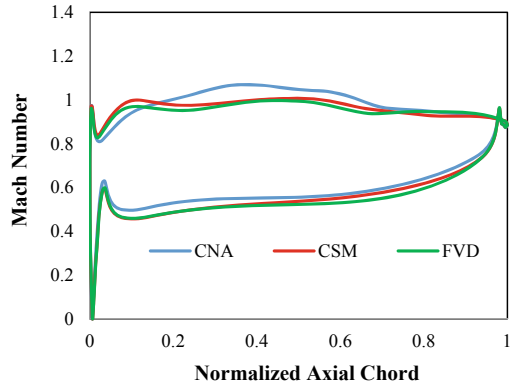
(a) 20% Span
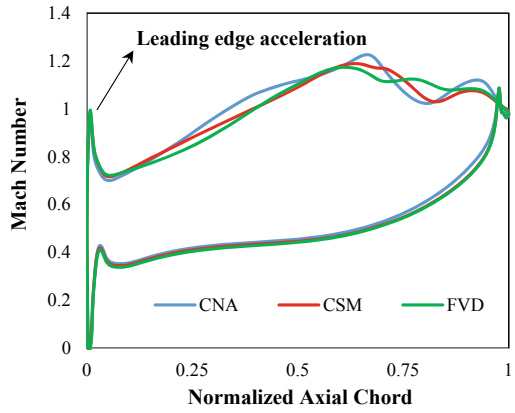
(b) 50% Span
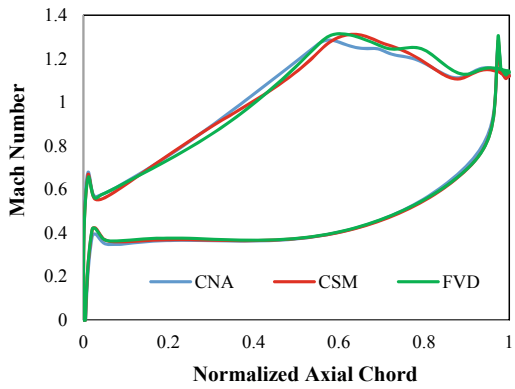
(c) 80% Span
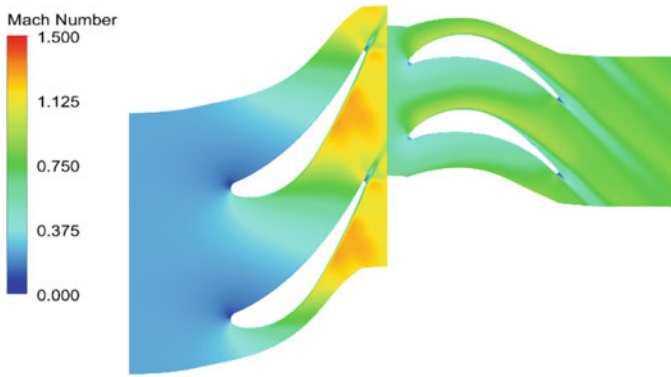
(a) Hub – 20 % Span
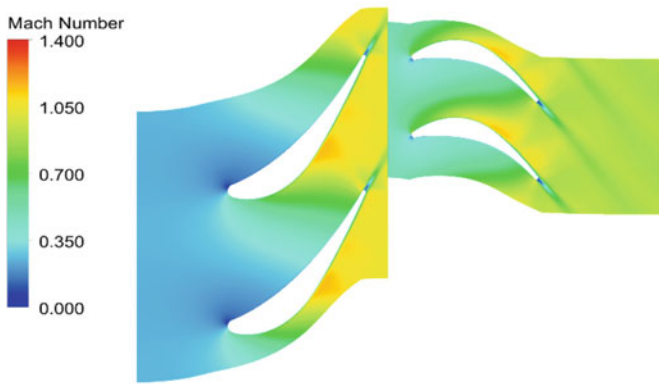
(b) Mean – 50% Span
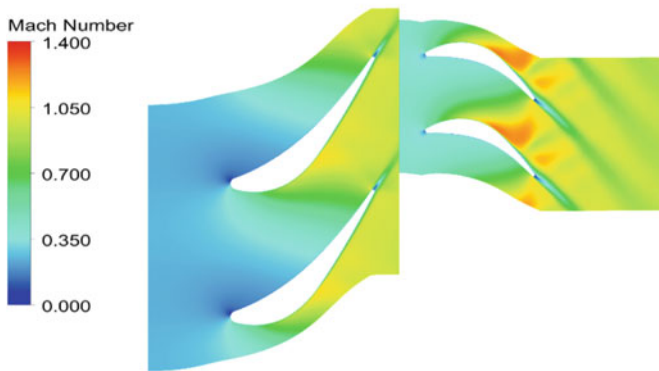
(c) Tip – 80% Span

Fig. 16 Relative Mach Number Contour—CSM

4 Conclusions

The aim of this paper was to design and compare performance parameters of three different single-stage axial flow turbines having the same aero-thermodynamic and flow path parameters but different vortex distributions, viz., Free Vortex, Constant Nozzle Angle, and Constant Specific Mass Flow. Designs are carried out for the same values of mean reaction, stage loading, and flow coefficients at mean section corresponding to all the three vortex distributions respectively. The overall performance and local flow effects are obtained using a 3D RANS CFD solver. The highlights of the study are as follows:

(1) As a consequence of vortex distribution, the NGV blades have no twist for CNA, moderate twist for CSM, and maximum twist for FVD design.
(2) Analyses predict CNA to have a maximum variation in axial velocity across the annulus, followed by CSM and FVD to have a minimum variation. This is in close agreement with the results obtained from the vortex laws.
(3) Spanwise variation of velocities, flow angles, degree of reaction, and loss coefficients show similar trends for all the designs but with different slopes.

The 3D CFD simulations predict CSM to give better overall turbine efficiency albeit by a small margin no greater than 0.2%. Thus, it can be inferred that for a blade with a hub to tip ratio of around 0.7, the vortex distributions considered in this study yield more or less the same efficiency output.

References

1. Saravanamuttoo HIH, Rogers GFC, Cohen H (1996) Gas turbine theory. 4th ed., Longman Group Limited, pp 169
2. Akeel SAMS, Najjar YSH (2013) Comparison of free- and forced vortex designs for computation of mass flux in an axial gas turbine stage. EEST Part A Energy Sci Res 31
3. Yahya SM (2002) Turbine compressor and fans, 4th edn. Tata McGraw-Hill Publishing Co., Ltd, pp 380–390
4. Ainley DG, Mathieson GCR (1951) A Method of performance estimation for axial flow turbines. British ARC, R & M 2974 (1951)
5. Kacker SC, Okapuu U (1981) A mean line prediction method for axial flow turbine efficiency. ASME Paper No. 81-GT-58
6. Zweifel O (1945) The spacing of turbomachine blading especially with large angular deflection. The Brown Boveri Review (December 1945), pp 436–444
7. Pritchard LJ (1985) An eleven parameter axial turbine airfoil geometry model. ASME paper 85-GT-219
8. Dunham J (1974) A parametric method of turbine blade profile design. ASME paper 74-GT-119
9. ANSYS CFX 14.0 Manual

10. Prathapanayaka R, Agnimitra Sunkara SN, Balamurugan M, Kishor Kumar (2015) CFD analysis of a highly loaded gas turbine stage. Proceedings of 17th AeSI annual CFD symposium, Bangalore
11. Menter FR, Kuntz M, Langtry R (2003) Ten years of experience with SST κ-ω turbulence model. Turbulence heat and mass transfer
12. Rajeevalochanam P, Agnimitra Sunkara SN, Mayandi B, Venkata Ganesh Banda B, Sesha Kumar Chappati V, Kumar K (2016) Design of highly loaded turbine stage for small gas turbine engine. In: Proceedings of ASME turbo expo GT2016-56178 (2016)
13. Moustapha H, Zelesky MF, Baines NC, Japikse D (2003) Axial and radial turbines. Concepts ETI Inc.
14. Sharma OP, Butler TL (1987) Predictions of endwall losses and secondary flows in axial flow turbine cascades. ASME J Turbomach

Investigation for the Improvement of Film Cooling Effectiveness of Effusion Cooling Holes

Batchu Suresh, Resham D. Khade, V. Kesavan, and D. Kishore Prasad

Abstract The operating gas temperatures of advanced military aero engines are continuously increasing to achieve a higher specific thrust. The gas temperature exposed by hot end components is beyond material allowable temperature limits. It is essential to cool these components to lower the metal temperatures to meet the designed life. Effusion cooling technique effectively brings down the hot components' metal temperature. The present study is focused on the numerical prediction of cooling effectiveness from effusion cooling holes. Conjugate heat transfer analysis is carried out using ANSYS Fluent ver.14.5 to estimate the film cooling effectiveness. The analysis is validated with experimental film cooling effectiveness data. K–ω SST turbulence model has given good agreement. To improve the film cooling effectiveness, further studies have been carried out by varying the geometrical parameters such as film hole inclination, porosity and thermal conductivity of the effusion plate. Three cases with different cooling configurations have been investigated.

Keywords Conjugate heat transfer (CHT) · Porosity · Effectiveness · Effusion plate

B. Suresh (✉) · V. Kesavan
Scientist 'G', GTRE, Bengaluru, Karnataka, India
e-mail: batchusuresh@gtre.drdo.in

V. Kesavan
e-mail: kesavanv@gtre.drdo.in

R. D. Khade
Apprentice Trainee, GTRE, Bengaluru, Karnataka, India
e-mail: reshamkhade@gmail.com

D. Kishore Prasad
Scientist 'H', GTRE, Bengaluru, Karnataka, India
e-mail: kishoreprasadd@gtre.drdo.in

Nomenclature

CHT   Conjugate Heat Transfer
d   Diameter of film hole
n   Number of film cooling holes
p   Transverse direction pitch
po   Porosity
s   Streamwise direction pitch
Tg   Main stream gas temperature
Tc   Coolant temperature
Tm   Metal temperature
Tw   Wall Temperature
X   Length of Plate
η   Film cooling effectiveness

1   Introduction

Effusion cooling is being extensively used in the cooling of gas turbine engine combustion liners. The combustion chamber of advanced aero engine needs to be cooled to attain design life with minimum coolant. Cerri et al. [1] have investigated for the reduction of combustion chamber wall temperature and increase film cooling effectiveness with different cooling methods. Krewinkle [2] has reviewed all work that has been carried out for effusion cooling and compared the benefits of effusion cooling with other methods of cooling like film cooling and transpiration cooling. He is of the opinion that the inclination of film hole and hole spacing/porosity are prime factors that effects the cooling effectiveness. Bruno et al. [3] have carried out the experimental analysis for two effusion cooled plates which are applicable for gas turbine combustor. They have compared film cooling effectiveness with simple cylindrical-shaped holes and elliptical-shaped holes with the same porosity. They have found that the elliptical-shaped holes have higher effectiveness for a higher blowing ratio. Hyung et al. [4] have studied different arrangements of holes like staggered, shifted and inline geometrical arrangement of impingement and effusion holes. They have concluded that staggered hole arrangement gives better interaction of coolant flow near wall and at mid-way region. Thus, staggered arrangement with impingement holes give greater enhancement of heat transfer. Yang et al. [5] have studied the influence of multi-hole arrangement of effusion film cooling holes using three different configurations with different transverse pitch to diameter (p/d) and stream wise pitch to diameter ratios (s/d). The arrangement with smaller p/d gives higher film cooling effectiveness and the effect of s/d ratio on effectiveness is less. Leger et al. [6] have studied the influence of multi-holed zone with different hole inclination and hole diameter on film cooling effectiveness and cooling mass flow consumption. They have concluded that if the inclination of hole is increased then

the film cooling effectiveness of plate is reduced as the coolant jet will mix with hot gases immediately. They proposed to reduce the coolant consumption by reducing the diameter of the holes downstream of the plate. Lefebvre et al. [7] highlighted that effusion cooling is the most practical and simplest approach of cooling technique for combustor. They found that penetration of coolant flow should be lower so that the mixing of coolant with hot gas reduces and higher film cooling effectiveness is obtained at the wall. Vishal et al. [8] have studied the film cooling effectiveness for a wide range of film hole diameters, hole inclination, stream wise pitch and transverse pitch. They have shown that 30° inclination hole is having higher effectiveness compared to 45°, 60° and 90°. At downstream of rows of holes, 90° angle is giving higher effectiveness due to the larger and thicker recirculation zone. They have introduced the concept of variable hole diameter so as to reduce cooling air consumption. Andrews et al. [9] have carried out on full coverage effusion cooling with inclined holes for angles of 30° and 90° and they concluded that an array of inclined cooling holes gives better performance than normal holes.

In this work, a study of effusion cooling on a flat plate applicable to the combustion liner of a military aircraft engines is carried out. Conjugate heat transfer analysis is carried out for a cooling configuration for which the experimental validation is available. CHT studies have been carried out for different cooling configurations to obtain a cooling configuration with lower metal temperature and cooling airflow requirement. The CHT analysis is validated with experimental results to identify the suitable turbulence model. K–ω SST turbulence model is matching well with the experimental results. The analysis for different configurations is carried out by varying hole inclination, porosity, conductivity of the plate.

2 Problem Definition

The aim of the present study is to analyse, validate and compare effusion film cooling effectiveness for different cooling configurations. CHT analysis is used as an analysis tool to estimate and compare the film cooling effectiveness. The analysis is carried out using ANSYS Fluent ver.14.5 and the cooling effectiveness is validated with the experimental data. A parametric study is carried out to study the effect of hole inclination angle, porosity and conductivity of the plate. Three cooling configurations with variable hole diameters and hole inclinations maintaining the same porosity have been analysed. Configuration with higher film cooling effectiveness and lower cooling air mass flow is selected.

3 Experimental Validation

The schematic layout of the experimental set up for measuring film cooling effectiveness is shown in Fig. 1. The plate consists of effusion holes from which the coolant is supplied through coolant plenum and hot mainstream air is supplied through the
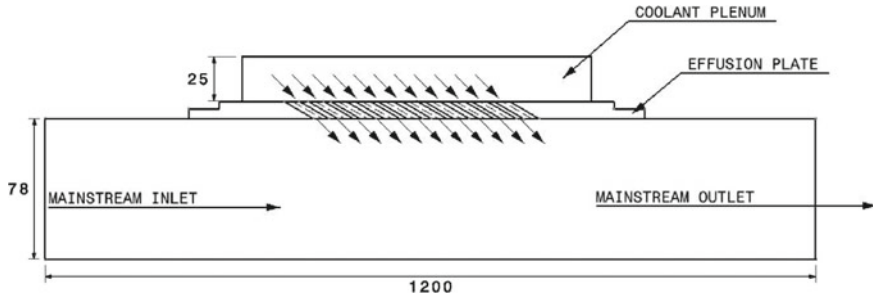
Fig. 1 Schematic layout experimental setup

mainstream test section as shown in Fig. 1. The geometrical details of the cooling holes are given in Fig. 2 in which 14 rows of effusion holes with a diameter of 2.4 mm, p/d of 7.25 and s/d of 3.625 and hole inclination of 30° is used. The plate material used is nylon-based material with low thermal conductivity of 0.3 W/m-K. Various tests have been carried out for estimating the film cooling effectiveness for different aerodynamic parameters such as pressure ratio and temperature ratio. Tests have been also conducted with different geometrical parameters like hole inclinations and porosity [10]. One of the experimental studies is taken for validation of CHT analysis. The boundary conditions which have been maintained during the experiments are shown in Table 1.
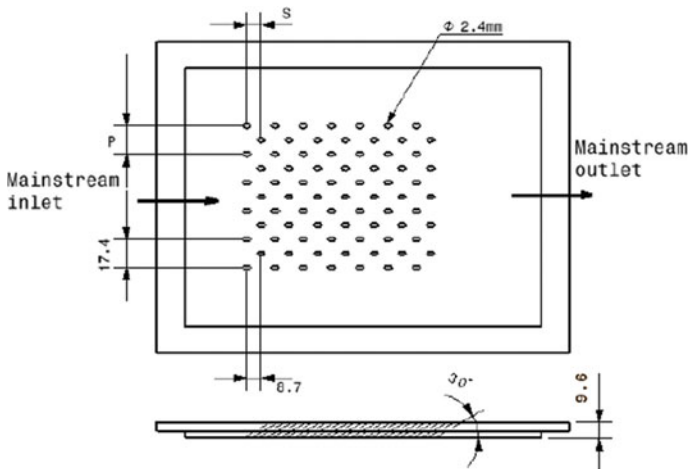
Fig. 2 Geometrical details of cooling holes

Table 1 Boundary conditions

Parameters		
Mainstream Pressure (gauge)	Inlet	199.5 Pa
	Outlet	0
Mainstream Temperature	Inlet	366 K
Coolant Pressure (gauge)	Inlet	3091.8 Pa
Coolant Temperature	Inlet	305 K

4 Numerical Method of Solution

Three-dimensional (3D) CHT analysis is carried out using a commercial computational fluid dynamics software ANSYS Fluent ver.14.5. 3D steady and compressible Navier–Stokes equations with K–ω SST turbulence model are solved. The equations are solved using second-order upwind scheme with least square cell-based gradient of implicit method. The convergence criteria for residuals are 1×10^{-6} for solving all turbulence and governing equations of fluid flow. The machine configuration of the IBM Parallel core cluster with Parallel processors and 90-GB RAM is used.

5 Computational Domain

The computational domain considered for the validation case is given in Fig. 3. The accuracy of the CHT solution depends on the grid which is modelled to reduce the errors and resolve the flow physics near the boundary layer. Thus, mesh generated for
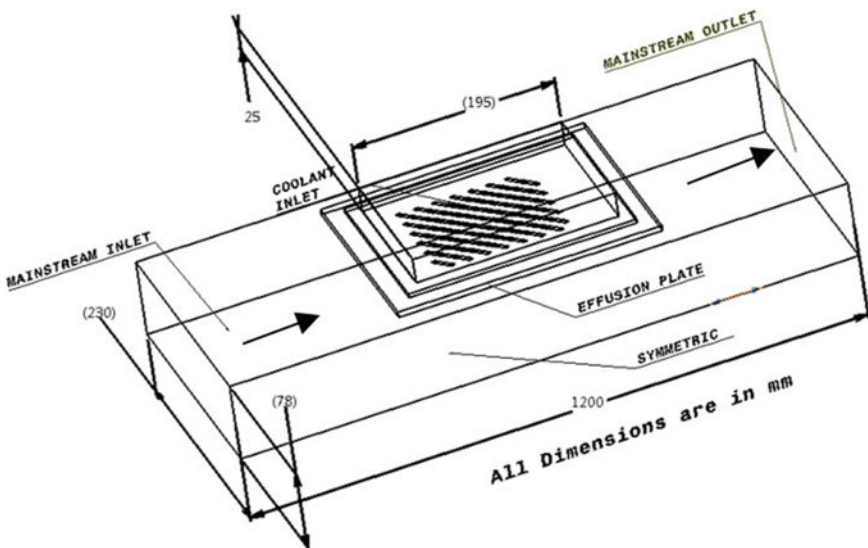
Fig. 3 Fluid domain for the validation case

fluid domain is coarse as compared to mesh generated near the holes of effusion plate where boundary layers are to be captured. ANSYS Workbench is used for meshing the geometrical cooling model and a fine mesh is employed near the cooling holes geometry near wall. The solid wall is also meshed to solve the equations for the analysis.

Figure 4 shows the zoomed portion of the meshed model near the cooling hole with inflation layers to capture the boundary layers near the walls.

Model is meshed with seven inflation layers and a fine mesh is generated near the surface of the effusion plate so as to maintain y^+ less than 1. The number of grids used for the model is 8.5 million and a grid independence check is also carried out to finalize the grid up to which the refining is required.

CHT analysis is carried with the boundary conditions given in Table 1. Inlet pressure and temperature are given for the coolant plenum and outlet pressure at the test section is used. 10% inlet turbulence intensity and operating pressure of 0.91997 bar are considered for analysis. Symmetric boundary conditions are applied for the side walls of the model. No slip boundary condition is used for the plate. The material properties used for the plate material are given in Table 2.

The analysis is carried out with realizable K–Ɛ with enhanced wall function and with K–ω SST turbulence models.

CHT analysis is carried out until the solution is converged. Film cooling effectiveness with CHT and experimental results are compared. Figure 5 shows the variation of area weighted average film cooling effectiveness along the axial length of the test section. The averaging of the film cooling effectiveness has been carried out in the

Fig. 4 Grids used near the wall surface
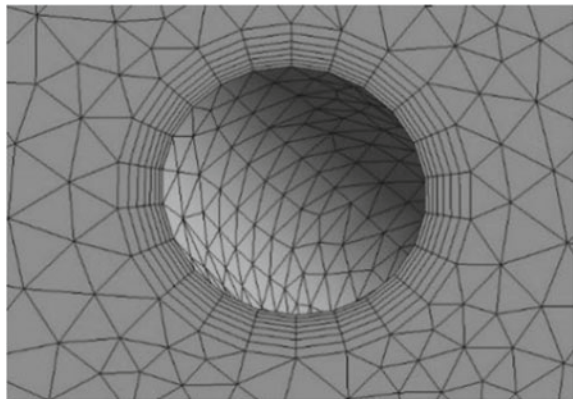
Table 2 Material properties of the effusion plate

Properties	Value
ρ (Density)	1020 kg/m^3
C_p (Specific heat constant)	1700 J/Kg-K
K (Thermal conductivity)	0.3 W/m-K
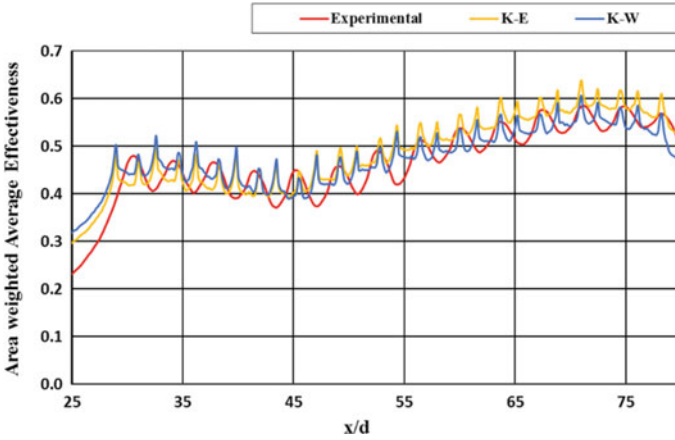
Fig. 5 Experimental effectiveness with realizable K–Ɛ and K–ω SST turbulence models

transverse direction of the plate. The film cooling effectiveness is defined as

$$\eta_{\text{overall}} = \frac{Tg - Tw}{Tg - Tc} \tag{1}$$

It is very clear from Fig. 5 that the K–ω SST model is predicting very close to the experimental values compared to realizable K–Ɛ turbulence model. So the further CHT analysis is carried out with K–ω SST turbulence model.

The average effectiveness of 0.6 is present at the end of the rows of holes. Figure 6 shows the effectiveness contours for experimental and CHT analysis. These contours depict film cooling effectiveness with CHT and experimental data. The distribution of effectiveness is very similar for both cases.

6 Results and Discussion

A parametric analysis is carried out to study the effect of film cooling effectiveness with hole inclination, porosity and plate thermal conductivity. The analysis is carried out for hole inclination of 22°, 30° and 78° maintaining the same geometrical parameters like diameter and hole spacing. The average film cooling effectiveness variation with axial distance is plotted as shown in Fig. 7. The film effectiveness for hole inclination of 22° is higher compared to the hole inclination of 30° and 78°. This increase in effectiveness with axial distance is due to the additive nature of the cooling holes. It is found that 22° inclination hole coolant film is adhering better to the surface. The effectiveness for 22° hole has increased steeply up to fourth row of holes after which the rate of rise is lowered. At the end of the tenth row, the film
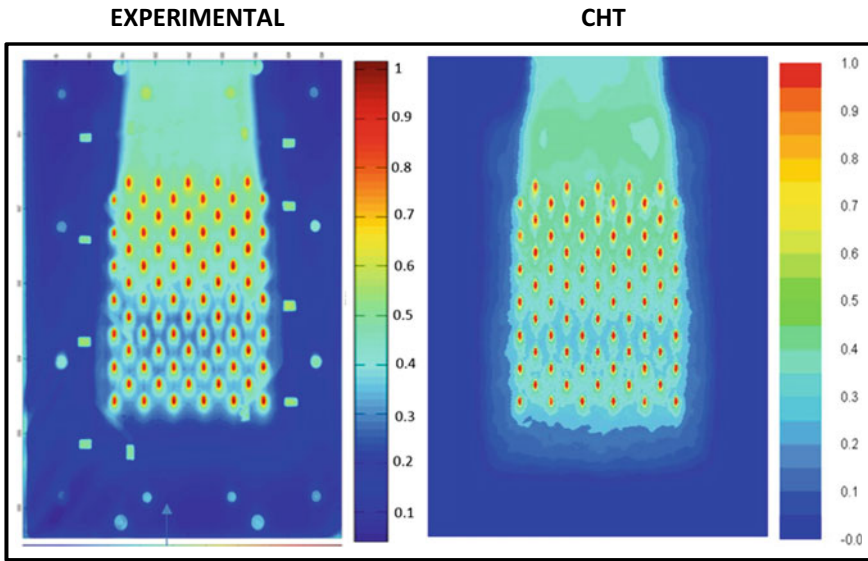
EXPERIMENTAL   **CHT**

Fig. 6 Effectiveness contour for experimental and CHT analysis
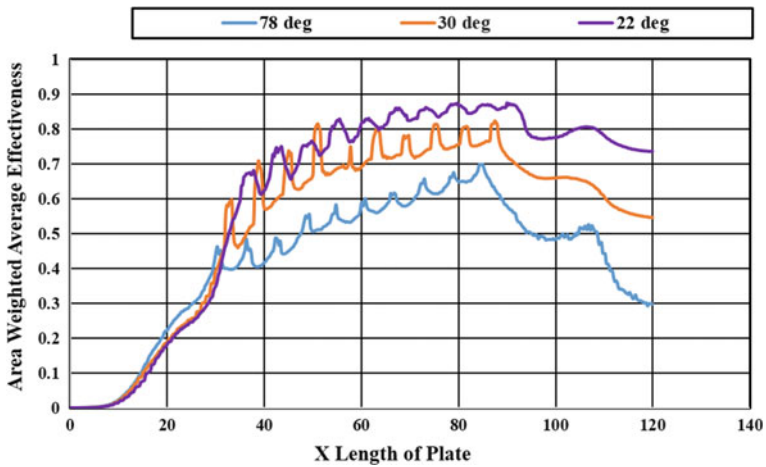
Fig. 7 Film effectiveness with different inclination

effectiveness has reached 0.7 for 78° hole and for 22° hole it has reached 0.88 so an increase of 20% film cooling effectiveness is achieved.

Table 3 shows the mass flows for different hole inclination. The mass flow is less for lower inclination. The mass flow rate for 22° is less as compared to 30°, 78° inclination. The length of the film hole is higher for 22° leading to higher pressure

Table 3 Mass flow rate for different inclination

	Hole inclination	Mass flow rate, g/s
1	78°	0.17
2	30°	0.15
3	22°	0.14

loss which results in lower mass flow for given pressure difference across the coolant plenum and mainstream.

Porosity is another important geometrical parameter that affects the film cooling effectiveness so the study is carried out with porosity of 1 and 1.6. Porosity, po is defined as

$$po = (n * 0.25 * \pi * d^2/(p * s)) \qquad (2)$$

The analysis is carried for two configurations with porosity of 1.6 (s/d of 8 and p/d of 6) and porosity of 1 (s/d of 11 and p/d of 7). Both configurations the hole diameter is 0.76 mm, inclination of 22° and conductivity of 0.3 W/m-K is used. The analysis is carried with the boundary condition specified in Table 1. Figure 8 gives the variation of film cooling effectiveness with axial distance for different porosity. So, the number of cooling holes present per unit area is more for porosity 1.6 compared to porosity 1. Hence, the effectiveness is higher for porosity 1.6 because of higher coolant mass flow passing through the coolant holes. The coolant air mass flow per unit area for porosity 1.6 is 0.5 g/s-mm^2 and porosity 1 is 0.3 g/s-mm^2. The effectiveness is increased by 21% with an increase in cooling air mass flow by 40%.

To study the effects of plate thermal conductivity on film cooling effectiveness CHT analysis is carried out with the boundary conditions which are similar to the
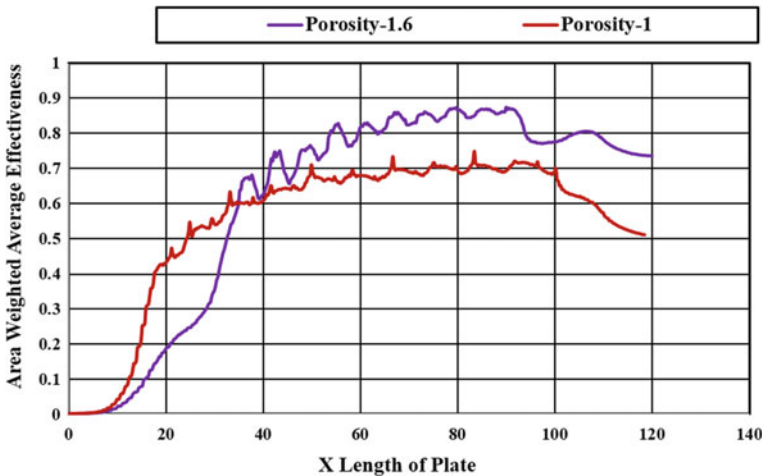
Fig. 8 Film cooling effectiveness with different porosity

Table 4 Boundary conditions for the typical condition

Parameter	Value
Mainstream pressure inlet	15.68 bar
Mainstream temperature inlet	2100 K
Coolant pressure inlet	17.43 bar
Coolant temperature inlet	790 K
Material density ρ	8980 kg/m^3
Specific heat	540 J/kg-K

operation conditions of an advanced gas turbine engine. The boundary conditions which are used for the analysis are shown in Table 4. The cooling configuration considered here is with porosity 1.6, hole inclination 30°, diameter of 0.76 mm and plate thickness of 1.5 mm. The analysis is carried out with nickel-based material having a thermal conductivity of 20 W/m-K and with nylon-based RPT material with a thermal conductivity of 0.3 W/m-K. Figure 9 shows the film cooling effectiveness variation with axial distance for different thermal conductivity. There is no improvement of the film cooling effectiveness with the conductivity but gives uniform effectiveness for the entire plate with thermal conductivity 20 W/m-K. The film cooling effectiveness is asymptotically increasing and becoming flat after 10 rows of holes. The effectiveness of 0.9 is obtained at the end of 10 rows.
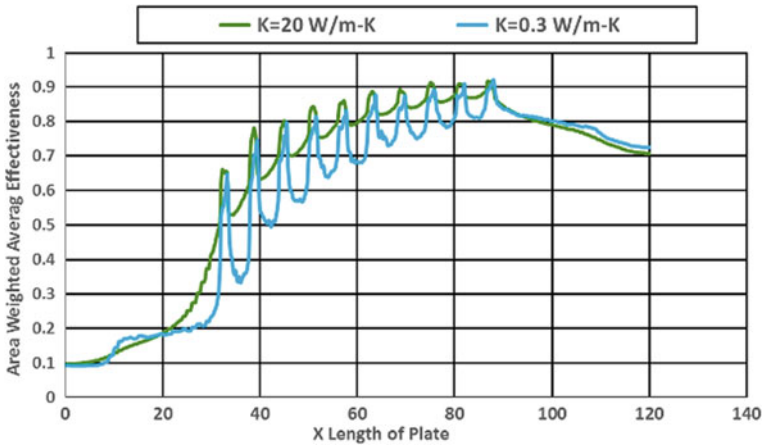
Fig. 9 Film cooling effectiveness for different thermal conductivity

7   Case Studies for Three Different Cooling Configurations

The analysis is carried out for three cases to study the film cooling effectiveness and cooling air consumption due to the combined effect of hole inclination, hole diameter and spacing of the cooling holes. This concept is known as variable diameter and inclination of the film holes.

In all the three cooling configurations, the porosity of 1.6 is maintained with wall a thickness of 1.5 mm. The three cases are analysed with 10 rows of film cooling holes using the boundary conditions given in Table 1. The geometrical parameters for the three cases are given in Table 5.

Case-I: Ten rows of holes with hole diameter of 0.76 mm and inclination 30° for all the holes.

Case-II: The first four rows of holes with hole diameter of 0.76 mm and inclination 30° and the remaining six rows of holes are with hole diameter of 0.76 and inclination is 90°.

Case-III: The first four rows of holes are with diameter of 0.76 mm and inclination 30° and the remaining six rows of holes with diameter of 0.5 mm and inclination is 90°.

Table 5 shows the geometric details of diameter and inclination of the cooling holes which have been considered.

Figure 10 shows the film cooling effectiveness for three cases which have been analysed. Figure 10 shows the variation of film cooling effectiveness with axial distance. The effectiveness is same for all the three cases up to four rows. The effectiveness is almost same for Case-I and Case-II because there is only change of orientation angle. The peak effectiveness is varying in axial position only due to the direct mixing of coolant with mainstream hot gases. The effectiveness for Case-III is also similar to other cases but covers up to the distance of 72 mm because the actual pitch of the last six rows of holes are smaller as compared to other cases. These geometrical parameters are considered to maintain same porosity.

Table 6 shows the comparison of mass flow rates for the three cases. The mass flow consumption is lowest for Case-III due to the lower diameter for last six rows. Case-III is better compared to Case-II and Case-I because the mass flow is less with nearly same effectiveness.

Figure 11 shows the film cooling effectiveness contours for the three cases. The flow spread is better for Case-I and Case-II due to the presence of film cooling holes up to 90 mm.

Table 5 Geometric details of three cooling different configurations

Case	Inclination	Diameter, mm	P/d	s/d
Case I	30°	0.76	6	8
Case II	30° and 90°	0.76	6	8
Case III	30° and 90°	0.76 and 0.5	6	8
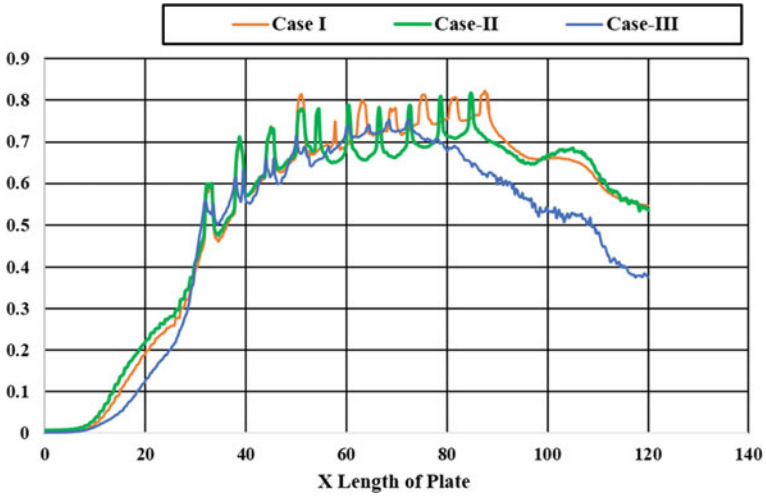
Fig. 10 Film cooling effectiveness for three cases

Table 6 Mass flow rate for three cases

Cases	Mass flow rate g/s
Case I	0.15
Case II	0.16
Case III	0.11
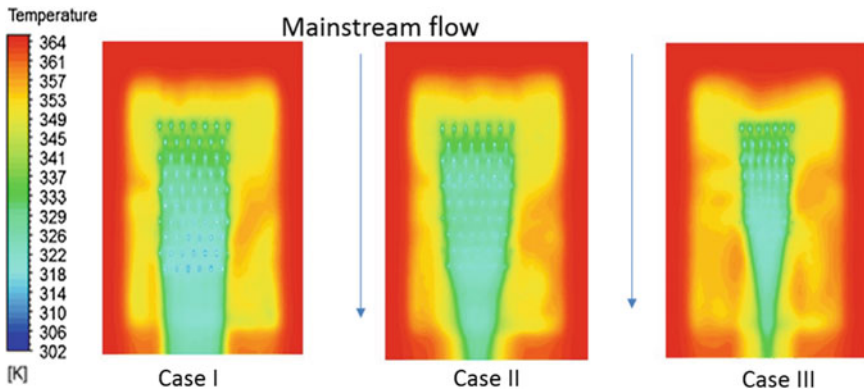
Fig. 11 Film cooling effectiveness contour for three cases

8 Conclusions

(1) CHT analysis of the effusion-cooled plate is carried out using ANSYS Fluent ver.14.5. The predicted film cooling effectiveness using K–ω SST turbulence model compares well with experimental results with 5–7% difference.

(2) The film hole inclination angle of 22° gives higher film cooling effectiveness by 20% compared to inclination angle of 78° and coolant mass flow required to cool the plate is also less by 18%.

(3) Effusion cooling configuration with porosity of 1.6 gives 21% higher film cooling effectiveness compared to porosity 1. The coolant mass flow rate per unit area consumption is higher by 40%.

(4) The film cooling effectiveness for the typical condition experienced in an aero engine condition shows that the variation of plate film cooling effectiveness with thermal conductivity 20 W/m-K is uniform, whereas with thermal conductivity of 0.3 W/m-K the cooling effectiveness varies from 0.8 to 0.9 at the end of 10 row film hole.

(5) Film cooling effectiveness for all the three cases is of the order of 0.7 and for case-III configuration the mass flow consumption is lowered by 27% compared to Case-I. Case-III is the best cooling configuration among three configurations analysed.

References

1. Cerri G, Giovannelli A, Battisti L, Fedrizzi R (2007) Advances in effusive cooling techniques of gas turbines. Appl Therm Eng 2:692–698
2. Krewinkel R (2013) A review of gas turbine effusion cooling studies. Int J Heat Mass Transf 66:706–722
3. Bruna F, Lorenzo T, Giuseppe C, Salvatore C (2009) Investigation of circular and shaped effusion cooling arrays for combustor liner application-Part-1 experimental analysis. In: GT2009-60037, ASME Turbo Expo 2009 power for land, sea and air
4. Hyung HC, Dong HR (2004) Effects of hole arrangements on local Heat/Mass Transfer for Impingement/Effusion Cooling with small Hole spacing. In: Proceedings of ASME Turbo EXPO, power for land, sea and air
5. Yang C, Zhang J (2012) Influence of multi-hole arrangement on cooling film development. Chin J Aeronaut 25:182–188
6. Leger B, Miron P, Emidio JM (2003) Geometric and aero-thermal influences on multiholed plate temperature: application on combustor wall. Int J Heat Mass Transf 46:1215–1222
7. Lefebvre AH, Ballal DR (2010) Heat transfer. In: Gas turbine combustion- alternative fuels and emissions, 3rd Ed. CRC Publications

8. Vishal V Shriram J, Bala VD, Subash K, Ratna KV, Shrikrishnan AR, Balajee R, Suresh B (2018) Studies of effusion cooling: impact of geometric parameters on cooling effectiveness and coolant consumption. J Aerospace Sci Technol 77:58–56

9. Andrews GE, Khalifa IM, Asere AA, Bazdidi-Tehrani F (1995) Full coverage effusion film cooling with inclined holes. In: Proceedings of ASME, 95-GT-274

10. Giridhara Babu Y, Felix J, Poornima N, Maria AS, Sanmuganantham M, Pradeep KA (2018) Effusion cooling studies on combustion liners. NAL-GTRE-GATET Technical Report PD-PR/2017/1025

After Burners and Nozzles

Experimental Studies on the Thermoacoustics of Afterburner Screech Combustion Instabilities in a Model Afterburner Test Rig

C. Rajashekar, Shambhoo , H. S. Raghukumar, G. Sriram, S. Chenthil Kumar, G. Udaya Sankara Athith, K. Vijayasankaran, Rajeshwari Natarajan, A. R. Jeyaseelan, K. Ashirvadam, and J. J. Isaac

Abstract Considerable efforts have been made by aero-engine manufacturers to understand, detect, attenuate, if not eliminate, high-frequency transverse screech combustion instabilities due to their destructive nature. Combustion dynamic stability problems arise in turbofan afterburners when fluctuations in the combustion energy release rates are coupled with the afterburner duct acoustics. Anti-screech liners have been used to attenuate the consequential pressure oscillations and mitigate the harmful effects of the transverse screech combustion instabilities. A versatile experimental test facility, using a single V-gutter flame holder as a driver to generate predetermined screech frequencies of interest of 1250 and 2000 Hz was used to conduct comprehensive experimental studies. Anti-screech liners of variable effectiveness with porosities of 3.5 and 10.0% were used for this investigation. The attenuation effectiveness of these liners was investigated under simulated test conditions specifically for the 2000-Hz screech frequency. For these comprehensive experimental investigations, a novel methodology to generate the predetermined screech frequency in a model afterburner test rig had been evolved. These anti-screech liners with variable effectiveness were not found to be effective in completely suppressing screech over the entire spectrum of operating conditions, probably because the complex modes present in the screech combustion instabilities, may have not been strictly transverse and the pressure amplitude may have been too large. Mitigation

C. Rajashekar (✉) · Shambhoo · H. S. Raghukumar · G. Sriram · S. C. Kumar · G. U. S. Athith · K. Vijayasankaran · R. Natarajan · A. R. Jeyaseelan
Propulsion Division, CSIR-National Aerospace Laboratories, Bengaluru, Karnataka, India
e-mail: rajashekarc@nal.res.in

Shambhoo
e-mail: shambhu_yadav@nal.res.in

K. Ashirvadam
Gas Turbine Research Establishment - DRDO, Bengaluru, Karnataka, India

J. J. Isaac
Former Head, Propulsion Division, CSIR-National Aerospace Laboratories, Bengaluru, Karnataka, India

187

efforts need to be attempted at the source of generation of the screech combustion instabilities.

Keywords Unsteady combustion · Screech · Afterburner · Rayleigh criterion · Combustion instabilities

Abbreviations

CAF	Compressed Air Facility
CSIR-NAL	Council of Scientific and Industrial Research, National Aerospace Laboratories
PXI	PCI eXtensions for Instrumentation
IEPE	Integrated Electronic Piezo-Electric
DAS	Data Acquisition System
FFT	Fast Fourier Transform
DAQ	Data AcQuisition

1 Introduction

Combustion instabilities are caused by coupling between acoustic waves and the unsteady heat release. It is considered to be one of the major problems faced in the development of afterburners [1, 2]. Although this problem has been increasingly studied for over the past five decades, no accepted theoretically based general rules have yet been established for designing stable afterburner systems; the complexity of the problem has prevented the achievement of a purely analytical solution [3]. Therefore, concerns on combustion instabilities are still present in every afterburner; the sooner the problem is detected during the development phase, the lower will be the additional expenses and shorter will be the time delays for successfully carrying out the development process. There is hardly any open literature available and currently employed empirical methods have limited use in design and usually fail when the results are extrapolated to predict screech and other combustion instabilities at different operating conditions and in different engines. Recipes for attenuation of afterburner combustion instabilities are closely guarded aero-gas turbine engine company secrets. A better understanding of the phenomena of combustion instabilities is needed along with development of cost-effective practical engineering methods for their passive control, without affecting the afterburner performance.

The unsteady coupling between the pressure oscillations and the combustion heat release could, under certain conditions, meet the Rayleigh criterion leading to combustion instability. Longitudinal modes with frequencies as low as 50–100 Hz have been identified and frequencies for radial and tangential modes could be as high as

5000 Hz. Screech is considered to be the excitation of a transverse resonant oscillation in the jet pipe [1, 3].

A complete understanding and control of these high-frequency screech combustion instabilities constitute the central problem in the development of high-performance afterburners. It was therefore necessary to study the underlying high-speed flow physics related to the crucial thermoacoustic coupling to acquire a predictive capability and to, hence, evolve a methodology for the attenuation of screech.

2 Experimental Test Facility

A test facility to carry out experimental studies on the thermoacoustics of afterburner combustion instabilities and their attenuation was established in the Propulsion Division, CSIR-NAL. The test facility consisted of an air feed line of 152.4 mm diameter with a maximum air delivery pressure of 1 MPa. The high-pressure air was supplied from the main reservoirs of the Compressed Air Facility (CAF) available at the Wind Tunnel Centre, CSIR-NAL. The air mass flow to the afterburner test model was controlled by a motorized valve airline and the test rig was designed to handle air mass flows of 1–2 kg/s as measured by an orifice plate. The test rig basically consisted of a main burner, settling chamber, transition ducts, and rectangular section afterburner ducts in which the section of the V-gutter flame holder could be fitted along with the fuel injection system. Figure 1a show a schematic and photograph of the test facility. The complete test rig was instrumented as per the instrumentation scheme shown in Fig. 1b. All raw data were acquired in a PC-based DAS using a LabVIEW program. The raw signals from the critical Kulite sensor and the FFT of the fundamental screech frequency derived from the Kulite sensor were displayed in the DAS during the experiments. The dimensions of the rectangular section afterburner which housed the V-gutter flame holder to generate selected screech combustion instability frequencies was carefully designed and was typically of around 1 m length.

Figure 2 show the afterburner test facility of 200 mm × 70 mm that was used to generate the screech frequency of 2000 Hz by a special technique. The afterburner fuel injector was located upstream of the V-gutter and the fuel was injected transversely through 0.5-mm holes of two rows of ten ports each. The rig had arrangements to simulate unvitiated air flow of the bypass flow (grazing flow) and bias flow. In the region of the V-gutter, the rectangular afterburner duct was provided with two complex Helmholtz resonator chambers, one on top and one below and these chambers had provision to attach variable effectiveness anti-screech liners of various porosities. The volume of the resonator could be varied by positioning the piston at different locations away from the liner. The anti-screech liner of variable effectiveness could be considered to be a parallel array of Helmholtz resonators embedded within it. Each Helmholtz resonator was considered to be centered around each port hole. The resonators were stacked together in a close array and shared a common volume defined by the backing distance of the piston head. Attenuation of screech could in principle,
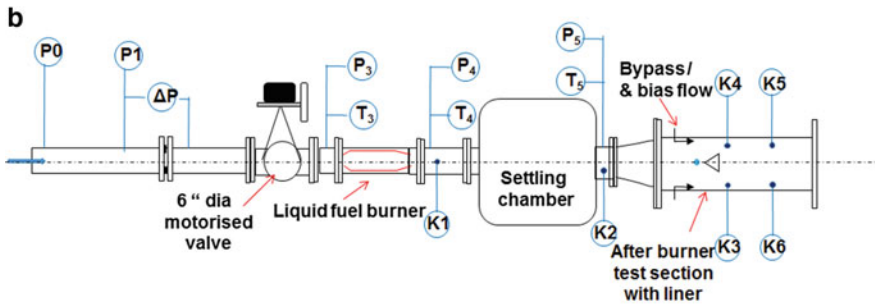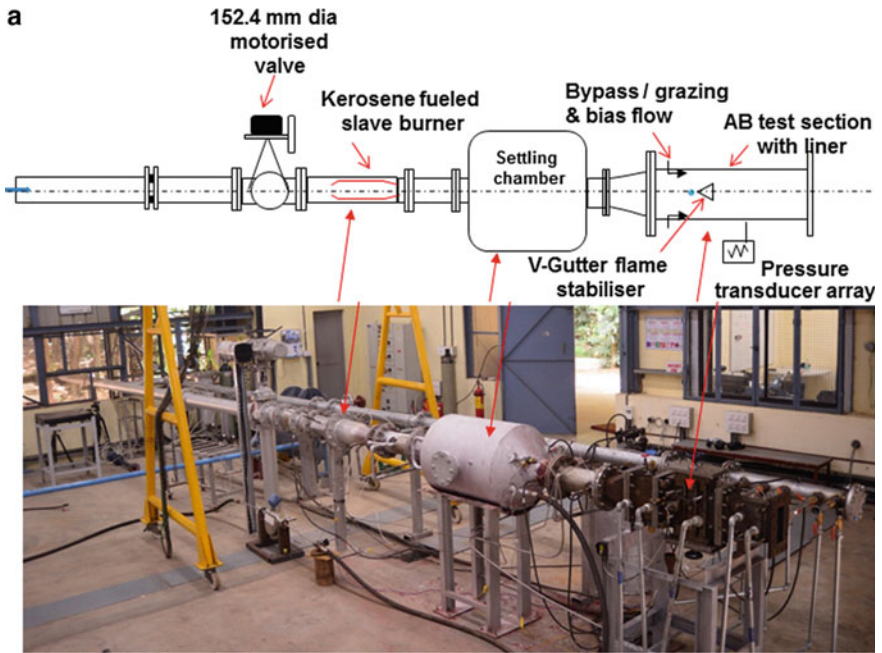
Fig. 1 **a** Schematic and photograph of the test facility, **b** Afterburner test facility instrumentation scheme
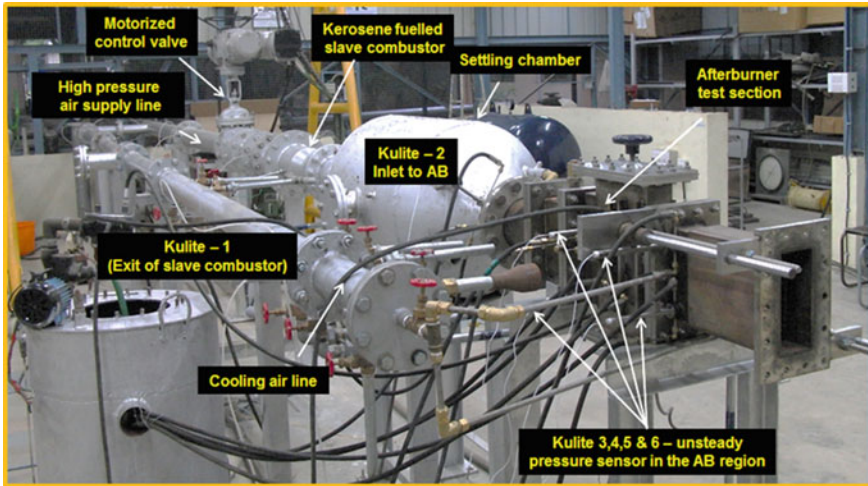
Fig. 2 Afterburner test facility for generating screech with frequency 2000 Hz

be obtained if the Helmholtz resonator frequency ($f = a/2\pi \sqrt{(A/(V\ l))}$), where (a = local sound velocity, A = total port area, V = total resonator volume, l = liner thickness) is matched to that of the screech by choosing the total port area (porosity × liner area) and varying the resonator volume by moving the piston, the Helmholtz resonator frequency could be changed as required. Helmholtz resonators are effective only if the dominant screech modes are essentially transverse and the pressure oscillations are not too high. Figure 3 show the schematic and sectional details of these arrangements and photographs of the typical liners used for the experiments. Screech liners with porosities of 3.5 and 10.0% with variable effectiveness were used during the investigation. The kerosene fuelled main burner (slave combustor) provided the hot air required to simulate vitiated air entry temperatures from 600 K to 1000 K at the afterburner inlet section. The exit of the slave combustor was connected to the settling chamber to ensure uniform pressure and temperature at entry to the afterburner section. Metered kerosene fuel was fed to the slave combustor and the afterburner using a nitrogen gas top loading method. The hot section of the test rig had proper cooling arrangements to avoid over heating of the critical afterburner section of the test rig.

3   Instrumentation and Data Acquisition System

The data acquisition and control system was configured to acquire static and dynamic pressures at different locations and to control the air flow rate in the rig. Two different DAQ modules carefully chosen (PXI-6259 and PXI-4472) were configured to acquire static and dynamic pressure data. PXI-6259 was intended to acquire static
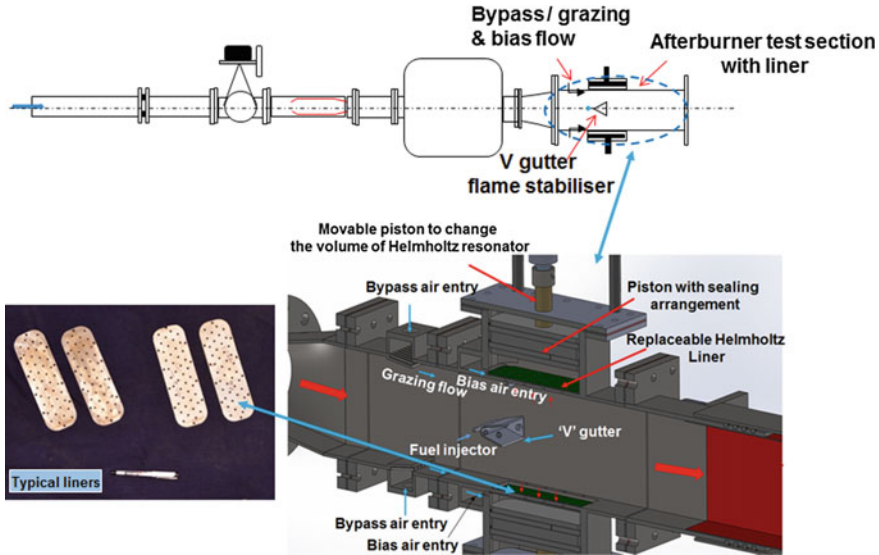
Fig. 3 Schematic of the test rig showing the afterburner section

pressures in the test rig and PXI-4472 was for acquiring unsteady pressure data from Kulite pressure sensors. The static pressures were measured with NI PXI 6259. The PXI 6259 was a multifunctional DAQ module and had 32 single-ended/16 differential analog input channels which could be configured to acquire the data at 1.25 MS/s with 16-bit resolution. NI PXI-4472 guaranteed high accuracy for frequency-domain measurements. The NI PXI-4472 simultaneously digitized the input signals over a bandwidth of DC to 0.4 fs. It had an IEPE enabled 8-input channels with 24-bit resolution, voltage range of -10 to $+10$ V and sampling rate (fs) of 102.4 kS/s/ch. Signals from the unsteady pressure sensors were directly fed to NI PXI-4472. Application software developed in Lab-View was used for acquisition and real-time monitoring of static pressures, and characteristics (FFT) of unsteady pressure oscillations.

4 Test Rig Operating Parameters

Tables 1 and 2 gives details of the test rig operating parameters and the details of the liners used for the experimental investigations.

Table 1 Test rig operating parameters

Sl no	Parameter	Operating range
1	Afterburner operating pressure	120–200 kPa
2	Afterburner inlet temperature	500–1000 K
3	Fuel injector (Transversely injected to the flow)	0.5 mm dia: 20 holes
4	Overall equivalence ratio (Slave combustor + afterburner)	0.5–1.1

Table 2 Screech frequency—2000 Hz, Liner details

S no	Liner thickness(mm)	Hole dia(mm)	Porosity(%)
1	1.5	3.2	3.5
2	1.2	4.8	10.0

5 Experimental Procedure

Initial experiments were carried out with an anti-screech liner of 0% porosity. A Nimonic sheet completely blocked the liner area and the piston in the Helmholtz resonator area was kept at zero position. The air flow to the AB test rig was controlled from a 152.4-mm-diameter motorized valve and the required air flow and pressure was set in the test rig for smooth ignition of the slave combustor. Once the slave combustor was ignited, the fuel flow and the line air pressure were controlled to get the required pre-set afterburner inlet pressure and temperature. The afterburner fuel flow was carefully injected and after the ignition of the afterburner and stable operating conditions attained, the AB fuel flow was further carefully increased slowly until screech was observed. The occurrence of screech was noted from the distinct high-frequency audible tone. Simultaneously, the FFT of the fundamental mode and the overtones were observed on the control room DAS monitor. The raw data and the derived data during the entire test run were acquired in the DAS.

Figure 4a, b show the typical FFT plot for 1250- and 2000-Hz screech frequencies. The maximum pressure excursions inside the afterburner duct were observed to be in the range of 30% for 1250 Hz and up to 12% for 2000 Hz. Detailed experiments for 2000 Hz have been carried out with two selected liner porosities as shown in Table 2. For these selected liner porosities, the Helmholtz resonator volume had also been varied to study the effect of the backing distance of the array of complex Helmholtz resonators. The effects of grazing and bias flow had also been checked out on the selected liners.
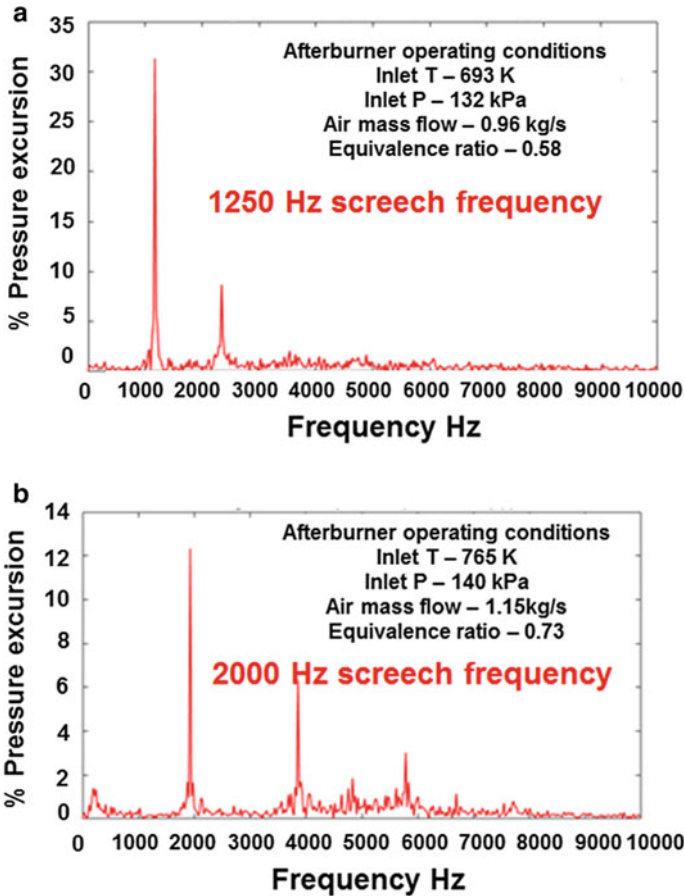
Fig. 4 a Typical screech characteristics frequency—1250 Hz, **b** Typical screech characteristics frequency—2000 Hz

6 Observations and Discussions

6.1 Lock-on Phenomena of Vortex Shedding Frequency

In an afterburner, depending on the flow conditions, the flow past the V-gutter bluff body flame holder starts shedding at a certain frequency "f2" which is characterised by the Strouhal number. This frequency of shedding is a variable parameter when screech conditions are not prevalent in the AB duct. But the duct fundamental transverse acoustic mode frequency "f1" is fixed for a given duct size and duct transverse mean temperature and cannot be essentially changed. This is what drives the shedding frequency from the V-gutter lip during the screech mode operation to get locked onto the duct frequency [4, 5]. Figure 5 shows the lock-on phenomena clearly indi-
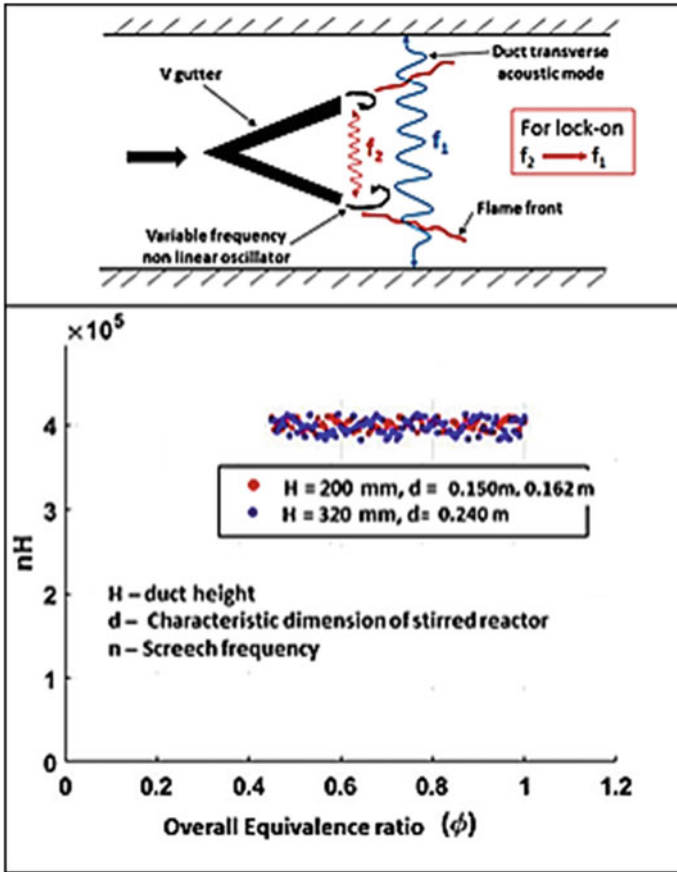
Fig. 5 Lock-on phenomena of screech frequencies

cating that the duct geometry had a dominant influence on the screech frequency and that the screech frequency was independent of the bluff body size beyond a threshold overall equivalence ratio and depended only on the duct height. The product of shedding frequency and the duct height was constant clearly indicating the lock-on phenomena of shedding frequency to the duct transverse mode frequency.

6.2 Effect of Afterburner Overall Equivalence Ratio Threshold on the Onset of Screech

Comprehensive experimental studies revealed that the sudden onset of screech happened when the fuel mass flow to afterburner crosses a certain threshold value. This sudden occurrence is a definite the characteristic signature of screech in a turbofan
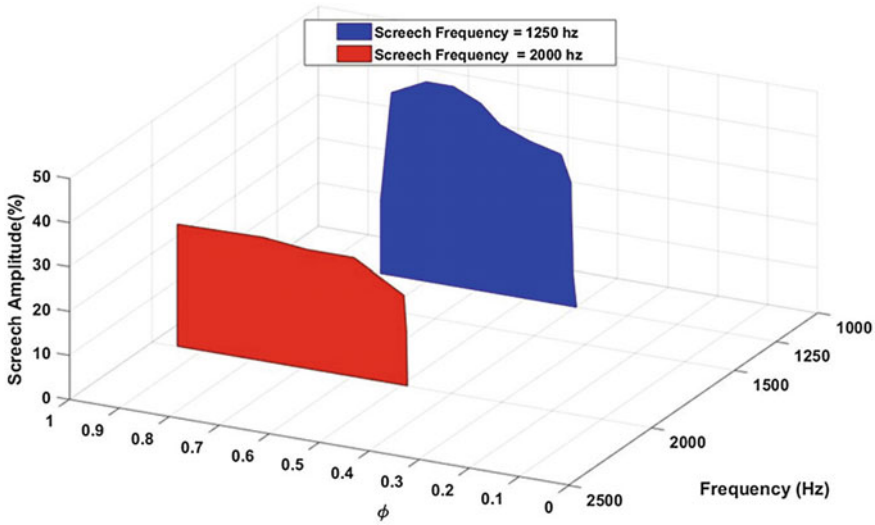
Fig. 6 Effect of overall equivalence ratio threshold on the onset of screech, while the inlet conditions to afterburner were held constant

engine. After establishing the desired inlet conditions of temperature and pressure in the afterburner duct, the fuel feed to the afterburner was gradually increased and screech was found to occur suddenly after exceeding a threshold value of fuel feed. A 3D plot (Fig. 6) shows clearly this feature. Screech would suddenly start at an overall equivalence ratio of 0.4 in the case of 1250 Hz and 0.5 in the case of 2000 Hz screech.

6.3 Effect of Afterburner Inlet Temperature on the Onset of Screech

Experiments were also carried out to study the effect of inlet temperature variation on the onset of screech in the afterburner duct for the two screech frequencies. The inlet temperatures to the afterburner were varied from 500 K to 1000 K. It was observed at both screech frequencies of 1250 and 2000 Hz, that the screech amplitude was high at low inlet temperatures of the order 500 K and gradually decreased and vanished at inlet temperatures close to 1000 K. Figure 7 shows the result of this study. This is a characteristic of turbofans; turbojets are known to be not plagued by screech. The relatively low temperatures in the bypass stream could lead to poor fuel vaporization and distribution, both of which could trigger screech.
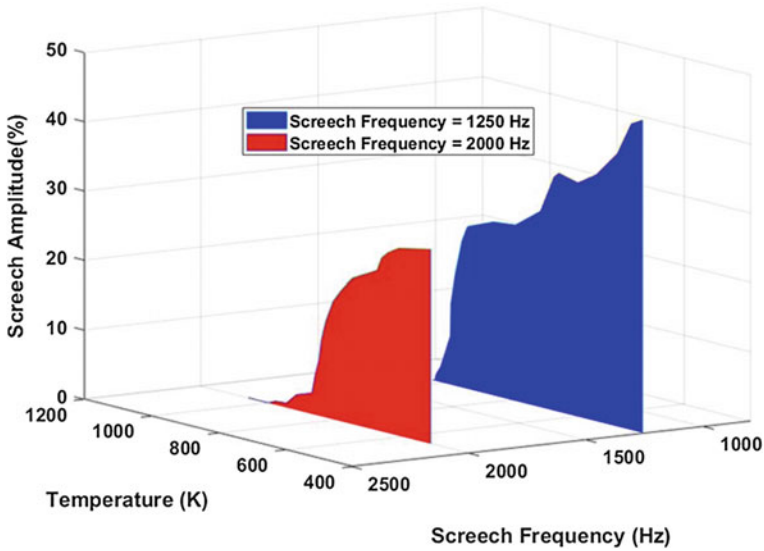
Fig. 7 Effect of AB inlet air temperature threshold on the onset of screech

7 Experiments on Liner Characterization for 2000-Hz Screech Frequency

Two variable effectiveness anti-screech liner porosities of 3.5 and 10% were tested for a screech frequency of 2000 Hz. Table 2 gives the details of the selected liners. Figure 8 shows a schematic of the test rig which had the facility to change the anti-screech liner Helmholtz frequency (liner aperture and backing volume by moving the piston) and also the arrangement to simulate bypass (grazing flow) and bias flow. Unvitiated air at the required pressure and temperature was allowed through the bias and bypass inlet at the V-gutter region during the experiments. A special heat exchanger arrangement was made to enable the unvitiated bias and bypass air to be injected at specified locations in the test rig to simulate the bias and grazing flow. Separate high-pressure air at regulated pressures was passed through a heat exchanger located inside the settling chamber to heat it to the required temperature; metered unvitiated bias and bypass air were simulated in the test rig at test conditions corresponding to a screech frequency of 2000 Hz. Metal-braded SS hoses were connected from the exit of the settling chamber to the specified entry locations on the test rig. The arrangement had the provision to simulate and choose only bias air entry or only bypass air entry or together both bias and bypass air entry into the afterburner section.
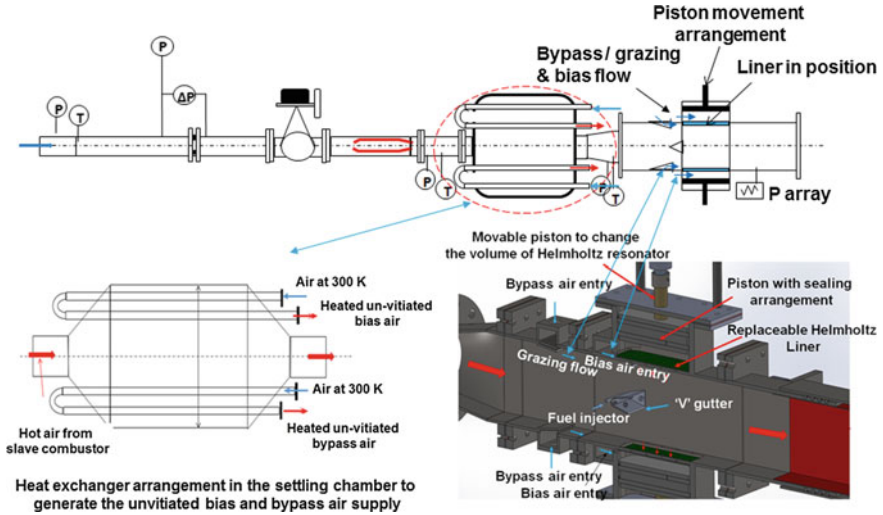
Fig. 8 Schematic showing the arrangement to simulate the unvitiated bias and bypass flow with Helmholtz resonator volume variation with piston movement arrangement together with liner porosity variation

7.1 Test Conditions

- Piston backing distance between 17 mm and 33 mm
- Afterburner pressure ~150 kPa abs
- Primary air mass flow ~0.8–1.3 kg/s
- Afterburner inlet temperature ~500 K and 700 K
- Bias air pressure ~200 kPa abs, (Pressure differential of 50 kPa maintained)
- Bias air temperature ~400–500 K
- Bypass (grazing) air pressure ~200 kPa (Pressure differential of 50 kPa maintained)
- Bypass (grazing) air temperature ~400–500 K
- Bias air mass flow ~8–9% of core flow
- Bypass air mass flow ~10% of core flow

Figure 9 show the amplitude of screech for the selected liners at piston backing distances of 17 mm and 33 mm. These backing distances correspond to a particular volume of the Helmholtz resonator. The piston backing distances were set by rotating the stud connected to the piston and its pitch for selected rounds of rotation to decide the backing distance. The effect of bias and bypass flow independently or together could not be clearly ascertained. At 17-mm piston backing distance and at higher afterburner inlet temperature of around 700 K, the liner with 3.5% porosity showed better attenuation characteristics than that of 10% porosity. Screech was found to occur at equivalence ratios of 0.8–1.0 for liner porosity of 3.5%, while for the liner porosity of 10.0% the screech was found to occur even at an equivalence ratio of 0.6.
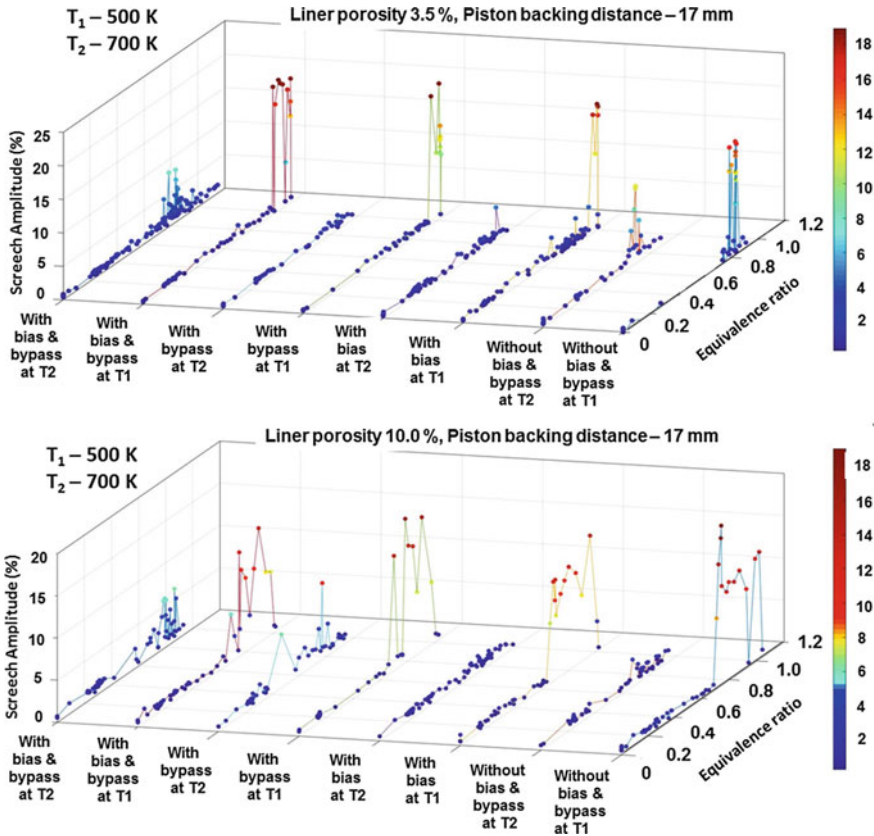
Fig. 9 Comparison of screech amplitudes for liner porosity of 3.5 and 10% and a piston backing distance of 17 mm (Screech frequency—2000 Hz)

At 33-mm backing distance, for both the liners of 3.5 and 10% porosity, screech was found to occur at all test conditions and the bias and bypass flow effects were not observed in significantly attenuating the screech amplitudes (Fig. 10).

8 Conclusions

A versatile test facility for carrying out an experimental investigation on the thermoacoustics of afterburner screech combustion instabilities and their attenuation has been established at CSIR-NAL. Extensive experimental investigations have been carried out resulting in a vast data and knowledge base in understanding screech combustion instability in a model afterburner. A novel method of producing controlled sustained screech has been developed and evaluated at two screech frequencies of 1250 and
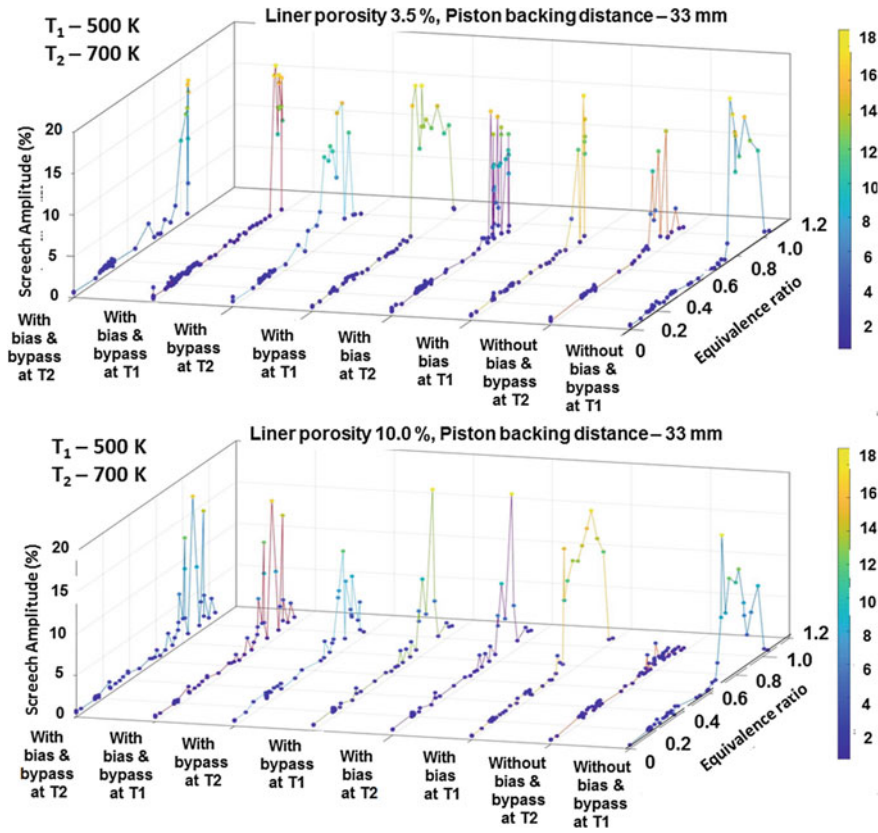
Fig. 10 Comparison of screech amplitudes for liner porosity of 3.5 and 10% and a piston backing distance of 33 mm (Screech frequency—2000 Hz)

2000 Hz. At lower inlet temperatures of around 450–500 K, it was observed that screech was found to occur spontaneously with significantly high amplitude and as the inlet temperatures were increased, screech was found to disappear. Sudden onset of screech was found to occur between overall equivalence ratios of 0.4–0.9 for both the screech frequencies of 1250 and 2000 Hz. Detailed experimental studies at simulated afterburner inlet conditions for characterizing the variable effectiveness screech liners of 3.5 and 10.0% were tested for their attenuation effectiveness at a screech frequency of 2000 Hz. The anti-screech liner with a porosity of 3.5% was found to give good attenuation at a piston backing distance of 17 mm, but failed to attenuate at lower afterburner inlet temperature test conditions. Overall, these anti-screech liners were found to be not effective over the entire spectrum of test conditions, probably due to the complex modes present in the screech combustion instabilities, which were not necessarily strictly transverse and that the pressure amplitudes were too large.

References

1. Sotheran A (1987) High performance turbofan afterburner systems. In: AIAA-87-1830 AIAA/SAE/ASEE 23rd joint propulsion conference, 29 June–2 July 1987
2. Ebrahimi H (2006) Overview of gas turbine augmentor design, operation, and combustion oscillation. In: AIAA-2006-4916 AIAA/SAE/ASEE, 42nd joint propulsion conference, 9–12, 2 July 2006
3. Culick FEC (1988) Combustion instabilities in liquid-fueled propulsion systems—An overview. In: AGARD 72B PEP meeting, Bath, England
4. Emerson B et al (2012). Frequency locking and vortex dynamics of an acoustically excited bluff body stabilized flame. In: AIAA-2002-0451 AIAA/SAE/ASEE, 50th AIAA aerospace sciences meeting including the new horizons forum and aerospace exposition, 9–12 Jan 2012
5. Hall MS, Griffin OM (1993) Vortex shedding and lock-on in a perturbed flow. J Fluids Eng 115(2):283–291 (9 pages)

Triggering of Flow Instabilities by Simulated Sub/Supercritical Rayleigh Heat Addition in an Aero-Gas Turbine Afterburner

P. Sreenath, Shambhoo , **H. S. Raghukumar, C. Rajashekar, A. Davis, and J. J. Isaac**

Abstract Military aircraft employ aero-gas turbines fitted with afterburners to meet the requirements of rapid increase in thrust for flight operations that involve combat maneuvers. The airflow rate through an aero-gas turbine remains unchanged even after an afterburner is invoked to ensure that there is no disruption in the turbomachinery operating characteristics. Triggering of flow instabilities leading, in turn, to combustor instabilities could occur due to the incorrect Rayleigh heat addition in the constant area afterburner. In normal operation, the propelling nozzle should be correctly opened up to pass the increased volumetric flow rate of the heated air due to heat addition in the afterburner. Any mismatch could result in violent flow instabilities including possible fan stall in a turbofan. The processes of triggering instabilities by sub/supercritical Rayleigh heat addition have been characterized. The gas dynamic equivalence of secondary mass addition to heat addition has been analyzed and experimentally validated in a model afterburner combustion test rig. Consequently, sudden sub/supercritical heat addition in an afterburner with its corresponding propelling nozzle closure has been studied and characterized for the equivalent mass addition in a separate model afterburner simulation test rig.

P. Sreenath · Shambhoo · H. S. Raghukumar · C. Rajashekar (✉) · J. J. Isaac
Propulsion Division, CSIR-National Aerospace Laboratories, Bengaluru, Karnataka, India
e-mail: rajashekarc@nal.res.in

Shambhoo
e-mail: shambhu_yadav@nal.res.in

A. Davis
Jain (To Be Deemed) University, Bengaluru, Karnataka, India

203

1 Introduction

Selection of the afterburner must be fast and reliable under all flight conditions with full thrust being achieved in a matter of seconds. Although the flow through the aero-engine remains unchanged when the afterburner is invoked in order to ensure that the turbomachinery characteristics remain unaffected, there will be a necessity for the variable area propelling nozzle to correctly open up to cater to the increased volumetric flow due to the heat addition [1].

For a pure turbojet application, the control of the afterburner is relatively simple as the choked flow through the turbine passages effectively prevents pressure transients within the jet pipe from influencing the aerodynamics upstream of the turbine. However, in a turbofan engine, there is a direct communication between the afterburner jet pipe and the fan through the bypass duct. The fan will immediately feel the mismatch between the afterburner combustion heat addition and the propelling nozzle area setting and the running line of the fan will rise or fall depending on the mismatch direction and resulting jet pipe pressure. On afterburner light up, there is inevitably a certain mismatch as the process of ignition is much faster than the follow-up nozzle area actuation time. This will thermally throttle the fan flow and cause its running line to tend toward unacceptable surge. So, in actual practice, to compensate for the likely initial mismatch and to prevent fan surge on afterburner light up, the propulsive nozzle is pre-opened to its minimum boost area setting before introducing and igniting the afterburner fuel. The fan running point would thereafter fall initially on selection of the afterburner ignition and this is would be immediately restored when the afterburner lights up. A similar effect can be realized if there is an afterburner flame blowout during flight [1, 2].

Clearly, the gas dynamics of Rayleigh heat addition in a constant area afterburner jet pipe duct, which terminates in a variable area propelling nozzle and which for practically all flight conditions operates with the nozzle throat choked has to be analyzed.

Rayleigh heat addition to the subsonic flow in the afterburner jet pipe will drive the flow Mach number toward the unity. At the nozzle throat, the Mach number will be unity and the mass flow parameter (MFP) will attain its maximum value. For a given mass flow, increase in stagnation temperature, decrease in area, and decrease in stagnation pressure will all tend to increase MFP. A significant increase in the stagnation temperature will tend to lead to an unacceptable increase in MFP beyond its permitted maximum value, and unless the nozzle area is increased to counter this, (which is done in practice) there will be a readjustment of the upstream flow with a consequent decrease in the corresponding inlet Mach number to accommodate the increased stagnation temperature. The readjustment through self-organization is brought about by a series of transient effects characterized by pressure waves propagating in both directions along the duct and when the flow reaches a steady condition, the flow would remain choked at the minimum area position [3]. The magnitude of this upstream influence depends on how strong is the aerodynamic coupling [4].

The question also arises whether such flow instabilities could, in turn, trigger combustion instabilities such as high-frequency transverse mode screech and longitudinal mode rumble/buzz. These are essentially caused by fluctuations in the energy release coupled with the acoustic modes, while meeting the Rayleigh criterion.

A study of gas dynamics will reveal that heat addition and mass addition in constant area compressible flows are equivalent. The effect of a fractional mass flow addition on flow properties is equivalent to twice that amount of fractional stagnation temperature increase [5].

Hence, this study of the gas dynamics of simulated sub/supercritical Rayleigh heat addition in a model aero-gas turbine afterburner has been carried out.

2 Rayleigh Heat Addition and Its Simulation by Equivalent Mass Addition

An afterburner is essentially a constant area jet pipe in which heat is released through combustion. This process could be gas dynamically simulated by considering it as an equivalent Rayleigh heat addition in a constant area duct. The Mach number increases on heat addition and the propelling nozzle would always operate with its throat choked. From Fig. 1 for Rayleigh heat addition between Sects. 1 and 2.

$$\left(\frac{T_{02}}{T_{01}}\right) = \left(\frac{M_2}{M_1}\right)^2 \left(\frac{2 + (k-1)M_2^2}{2 + (k-1)M_1^2}\right)\left(\frac{1 + kM_1^2}{1 + kM_2^2}\right)^2 \tag{1}$$

where T_0 is the stagnation temperature, M is the Mach number, and k is the ratio of specific heats. Critical Rayleigh heat addition is defined as the exact value of T_{02}/T_{01} for a given M_1, M_2. Now, the mass flow parameter (MFP) is
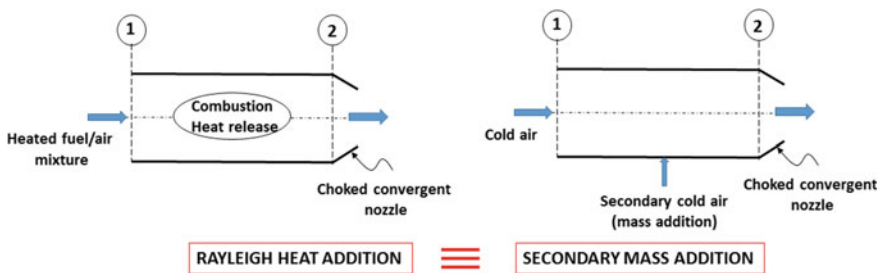
Fig. 1 Equivalence of Rayleigh heat (combustion) addition and mass addition in a constant area compressible flow

$$\text{MFP}(\text{P}_0) = \frac{\dot{m}\sqrt{T_0}}{AP_0} = \left(\frac{k}{R}\right)^{1/2}\left(\frac{M}{\left(1 + \frac{k-1}{2}M^2\right)^{\frac{k+1}{2(k-1)}}}\right) = F(k, M) \qquad (2a)$$

$$\text{MFP}(\text{P}) = \frac{\dot{m}\sqrt{T_0}}{AP} = \left(\frac{k}{R}\right)^{1/2}\left(M\sqrt{1 + \frac{k-1}{2}M^2}\right) \qquad (2b)$$

where $\dot{m}$ = gas flow rate, P_0 is the stagnation pressure, A is the flow area, R is the gas constant, which is virtually constant even with combustion, and P is the static pressure.

Now in Fig. 1, if the duct terminates in a fixed choked convergent nozzle, then M_2 is a constant whatever be the heat addition level. The upstream conditions will then change through a series of transient pressure waves and the Mach number will reduce to accommodate the heat addition (T_{02}/T_{01}) level increase, above the value which for a given M_1, leads to an M_2 consistent with the area ratio (A/A*) of the choked convergent nozzle. Any increase in T_{02}/T_{01} above this level will cause the upstream Mach number M_1 to reduce according to Eq. 1 and hence the inlet flow rate will also reduce according to Eq. 2a for a given T_{01}, P_{01}, and constant area A.

Heat addition through combustion in a model afterburner was carried out employing the test setup (Fig. 2a, b) which had a fixed convergent nozzle that was choked and hence M_2 was fixed for all the experiments. The heat was added in the model afterburner through combustion of kerosene/air mixture. The reduction in upstream air mass flow (consequent to a reduction in upstream Mach number M_1) was measured. This variation is shown in Fig. 3a. The stagnation temperature T_{02} at the end of the heat addition zone was estimated through the mass flow parameter (P) using the measured value of the kerosene/air mixture mass flow rate and the static pressure at station 2 which was just upstream of the convergent nozzle inlet.

This heat addition process could be simulated by considering the gas dynamics of the flow in a constant area duct (Fig. 1), where the same inlet Mach number M_1 and exit Mach number M_2 was maintained by bleeding in additional secondary air (at right angles to the flow to avoid any momentum errors).

By employing the mass flow parameter MFP (P) at stations 1 and 2 and equating the impulse function it may be shown that

$$\left(\frac{\dot{m}_2}{\dot{m}_1}\right)^2 = \left(\frac{M_2}{M_1}\right)^2\left(\frac{2 + (k-1)M_2^2}{2 + (k-1)M_1^2}\right)\left(\frac{1 + (1 - \Phi)kM_1^2}{1 + kM_2^2}\right)^2 \qquad (3)$$

where ϕ is a loss coefficient in the flow between stations 1, 2 and is based on the inlet dynamic pressure.

From Eq. 2 and Eq. 3 it is seen that

$$\left(\frac{T_{02}}{T_{01}}\right) = \left(\frac{\dot{m}_2}{\dot{m}_1}\right)^2\left(\frac{1 + kM_1^2}{1 + (1 - \Phi)kM_1^2}\right)^2 \qquad (4)$$
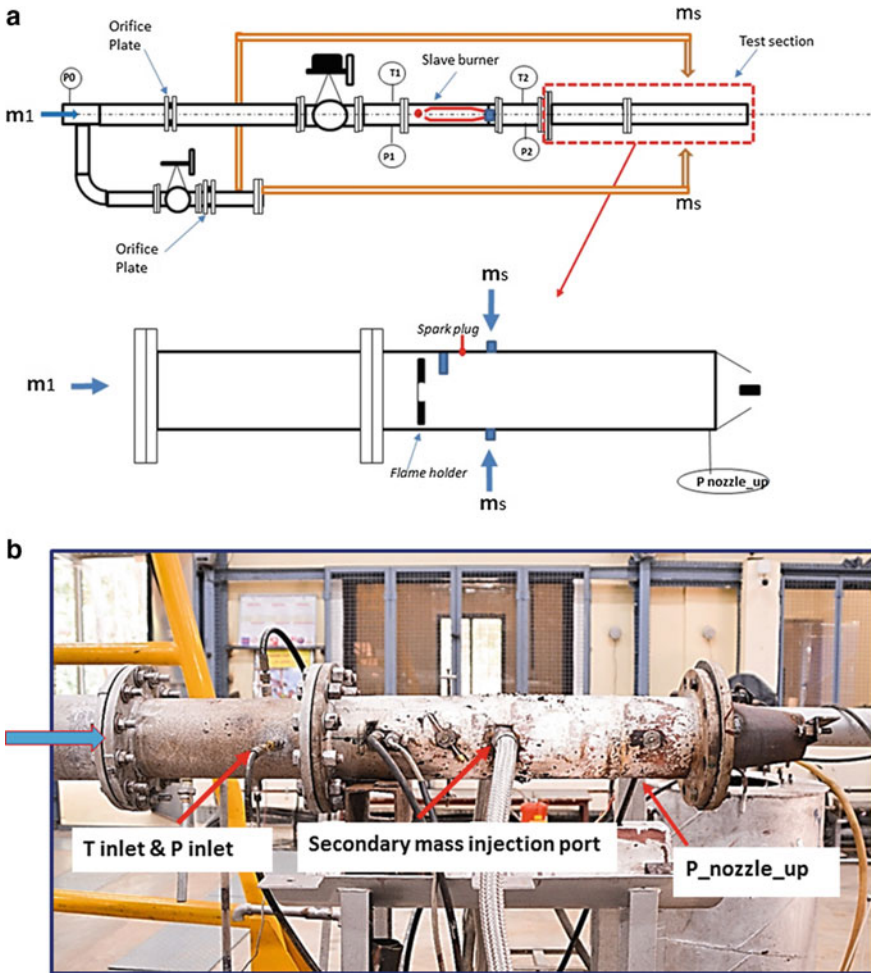
Fig. 2 **a** Schematic of the test setup—Rayleigh heat addition through combustion and its subsequent gas dynamic simulation by equivalent mass addition, **b** Photograph of the experimental test rig—Rayleigh heat addition through combustion and its subsequent gas dynamic simulation by equivalent mass addition

It may be seen that if there is ideal flow, $\phi = 0$

$$\left(\frac{T_{02}}{T_{01}}\right) = \left(\frac{\dot{m}_2}{\dot{m}_1}\right)^2 \tag{5}$$

giving an elegant relation showing that heat addition can have the same gas dynamic effects as mass addition. Further details of the analysis are available in Sreenath [6, 7].
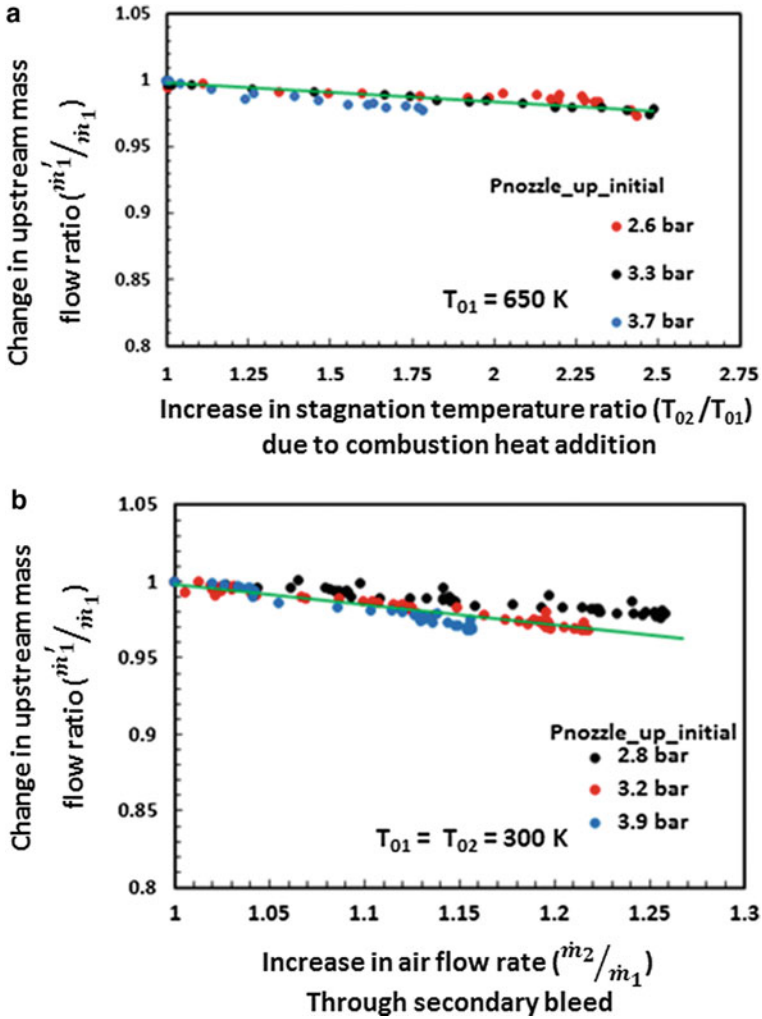
Fig. 3 **a** Variation of the change in upstream air mass flow rate due to Rayleigh heat addition through combustion and its equivalent gas dynamic simulation through mass addition

The test setup (Fig. 2a, b) was again employed. For a given choked nozzle inlet Mach number M_2, secondary air mass was bled in at right angle to the flow and the reduction in the upstream Mach member M_1 was ascertained by measuring the reduction is the upstream inlet air mass flow rate. This behavior is shown in Fig. 3b. Eliminating $\dot{m}_1/m_1$ which is the common change in upstream mass flow rate, a unique relation between the stagnation temperature ratio (T_{02}/T_{01}) and the mass addition ratio ($\dot{m}_2/m_1$) was captured (Fig. 4). The theoretical ideal variation is also shown against the actual variation. It is seen that there is a positive intercept in the latter case. From Eq. 4, it is seen that for a given inlet mass number M_1, the square
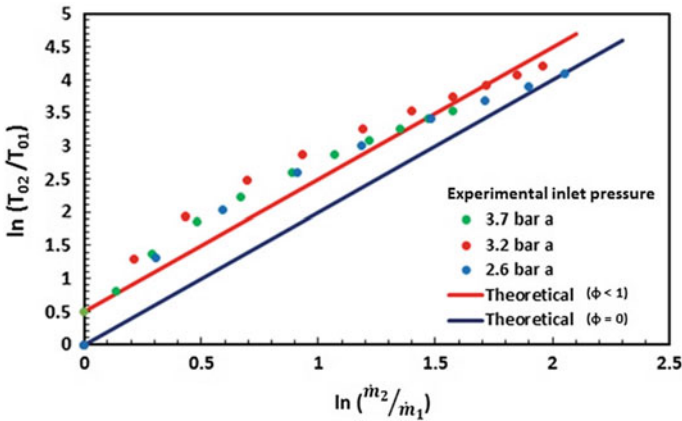
Fig. 4 Gas dynamic equivalence of Rayleigh heat addition and its simulation by mass addition

relationship is always obtained and since the factor

$$\left[\frac{1 + kM_1^2}{1 + (1 - \Phi)kM_1^2} \right] > 1 \qquad (6)$$

the intercept is always positive as $\phi > 0$. This clearly shows that Rayleigh heat addition can be gas dynamically simulated through an equivalent mass addition.

3   Flow Characteristics Due to Simulated Sub/Supercritical Rayleigh Heat Addition

With this confirmation that heat addition can gas dynamically be simulated by mass addition in constant area compressible flows, two operational conditions which are known to create significant pressure transients in the afterburner duct were considered for examination of the flow characteristics.

3.1   Supercritical Heat Addition

The flow in a turbojet afterburner was considered. This flow is characterized by two choked nozzles—one at the upstream turbine and one at the downstream propelling nozzle throat. The simulation setup shown in Fig. 5a, b was used. It had two choked nozzles, a pair of V gutter flame holder, a diffuser passage all simulating a typical turbojet afterburner. The primary inlet flow rate ($\dot{m}_p$) was set at 50 kg/min and the secondary bleed air flow rates ($\dot{m}_s$) were varied around 4.5 kg/min. At $\dot{m}_s = \dot{m}_{\text{critical}} =$
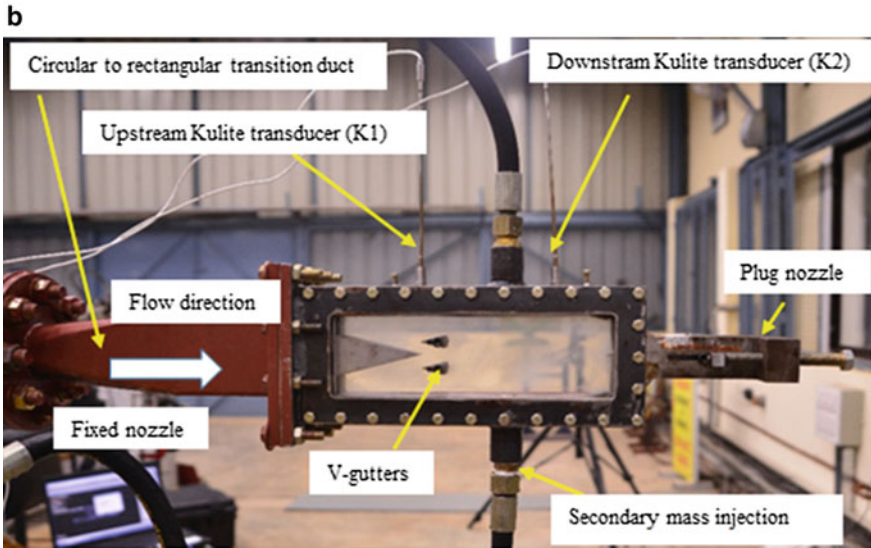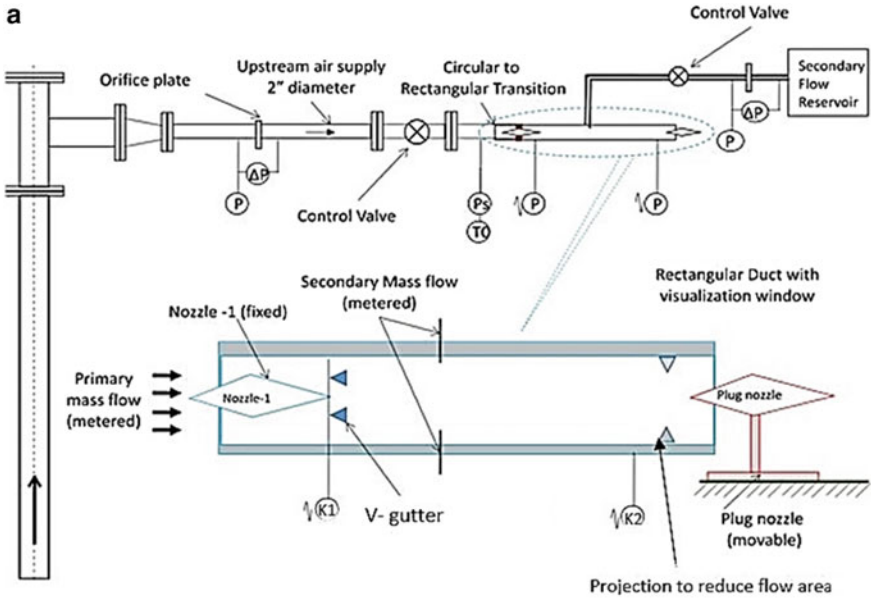
Fig. 5 a Schematic of the test setup for simulated Rayleigh heat addition through equivalent mass addition, **b** Photograph of the experimental test setup for simulated Rayleigh heat addition through equivalent mass addition

4.5 kg/min, both upstream and downstream throats were choked. The secondary bleed air was injected at right angles to the flow. It is seen that by gradually increasing $\dot{m}_s$ the upstream nozzle became unchoked while the downstream throat remained choked. (Fig. 6). This behavior can have serious implications. The pressure transients could trigger transverse or longitudinal combustion instabilities. The movement of the nozzle plug to increase the propelling nozzle area could have relieved the situation.

Moreover, in actual turbojet practice, increase of the jet pipe pressure would reduce the pressure drop across the turbine section together with the torque delivered to the compressor. The gas generator fuel control would now respond by increasing the fuel flow in order to maintain the high-pressure compressor spool speed and the air mass flow through the engine. Thus, the high-pressure compressor operating point would move along a constant speed line toward the stall boundary with its serious consequences [1, 2].

3.2 Subcritical Heat Addition

These are two situations which can be described by subcritical heat addition. If there is a sudden flame blow out, the heat release will fall with a consequent reduction in the volumetric flow rate. If the propelling nozzle area is not quickly closed to counteract this, the jet pipe pressure will fall and the pressure ratio across the turbine will increase leading to a change in the engine operational conditions. The flow downstream of the upstream nozzle will experience a shock train with its consequential flow losses with pressure transients which could also trigger combustion instabilities. A similar situation will arise if the propelling nozzle is prematurely opened before a planned afterburner light up which does not subsequently take place. Figure 7 shows a schlieren image sequence of this situation where the secondary bleed air is progressively reduced. The appearance of the shock train is seen.

3.3 Afterburer Duct Pressure Transients

Figure 8 shows typical afterburner duct pressure transients for supercritical Rayleigh heat addition as gas dynamically simulated by mass addition. The FFT is seen to have a dominant peak around 2000 Hz. Such pressure pulses are known to trigger and push the afterburner into unstable combustion modes. Hence, heat addition should be carefully modulated to avoid such pressure transients.
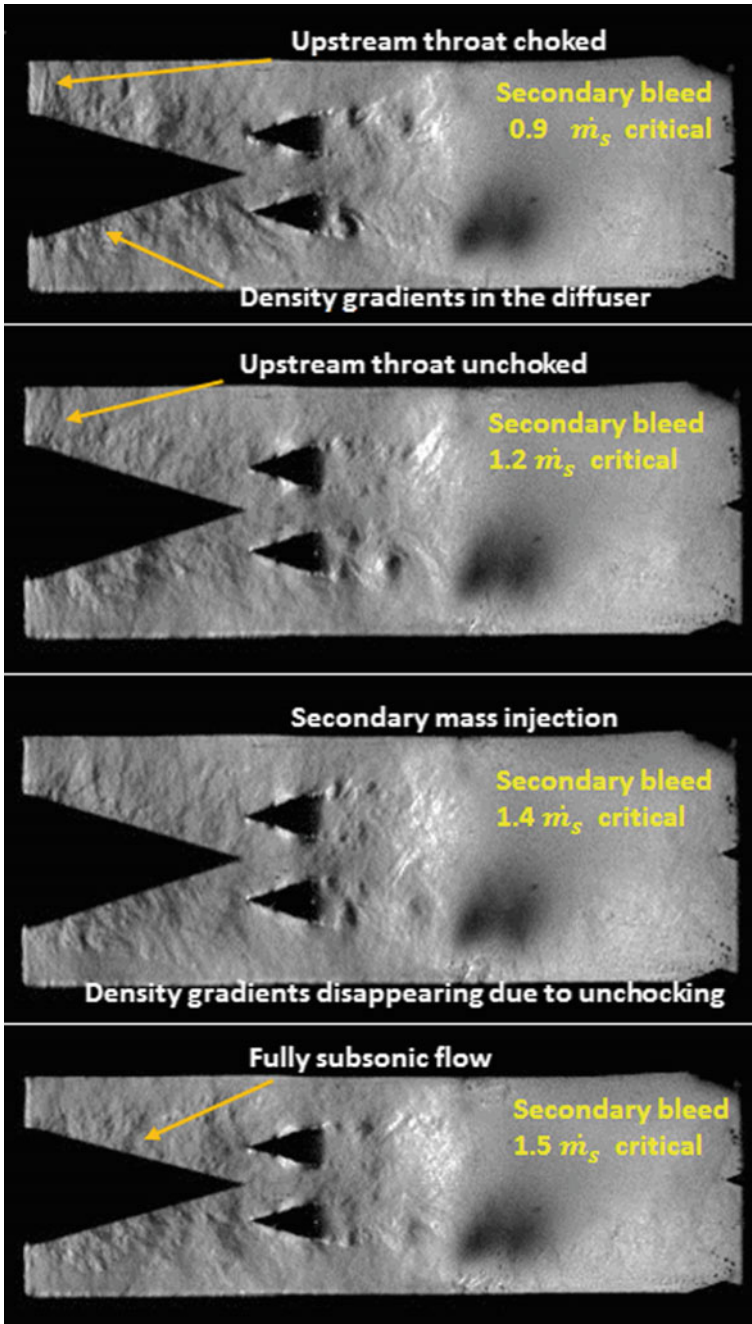
Fig. 6 Schlieren images of the sequential un-choking of the upstream choked nozzle due to the increase in simulated heat addition by equivalent secondary mass addition (supercritical Rayleigh heat addition with fixed downstream choked convergent nozzle)
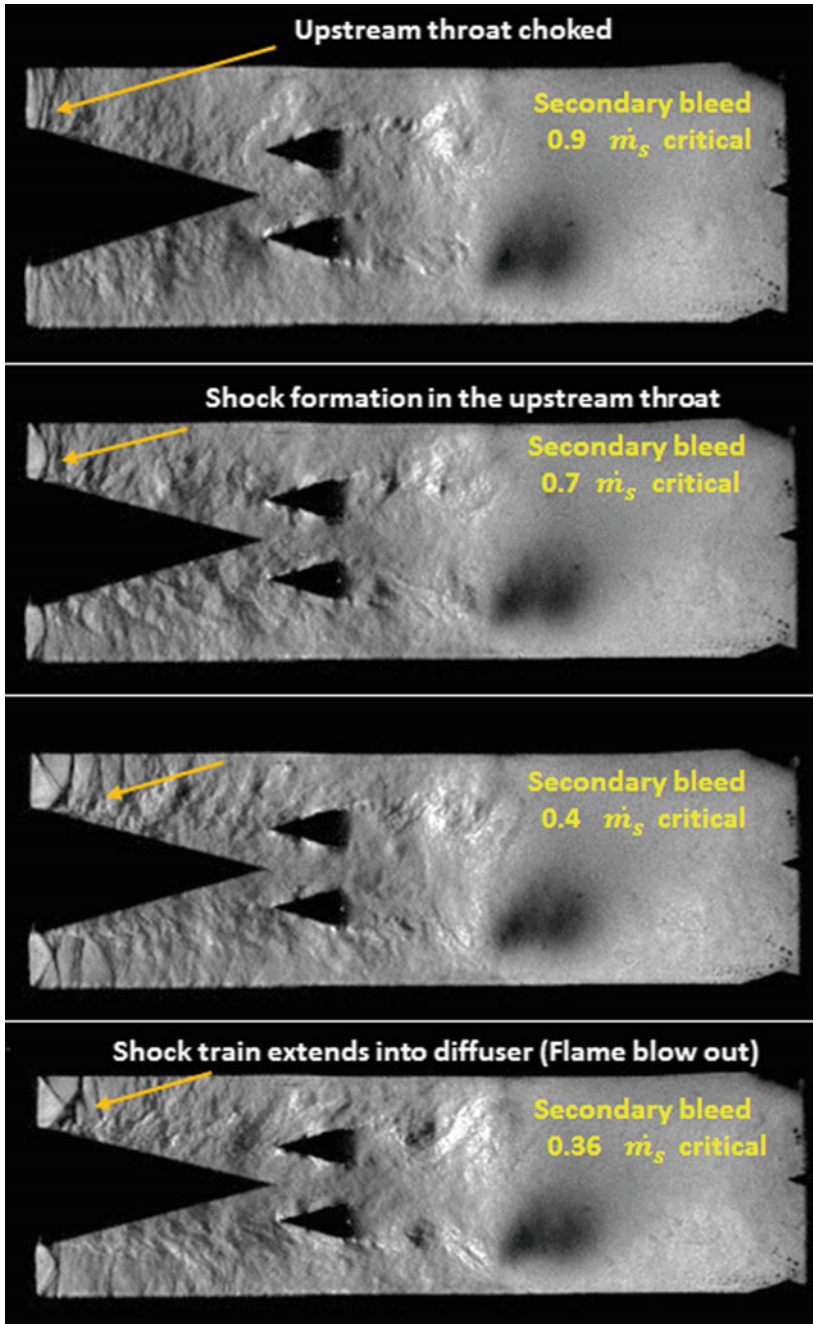
Fig. 7 Schlieren images of the sequential expansion outside the upstream choked nozzle due to a decrease in simulated heat addition by equivalent secondary mass addition (subcritical Rayleigh heat addition—flame blowout with fixed downstream choked convergent nozzle)
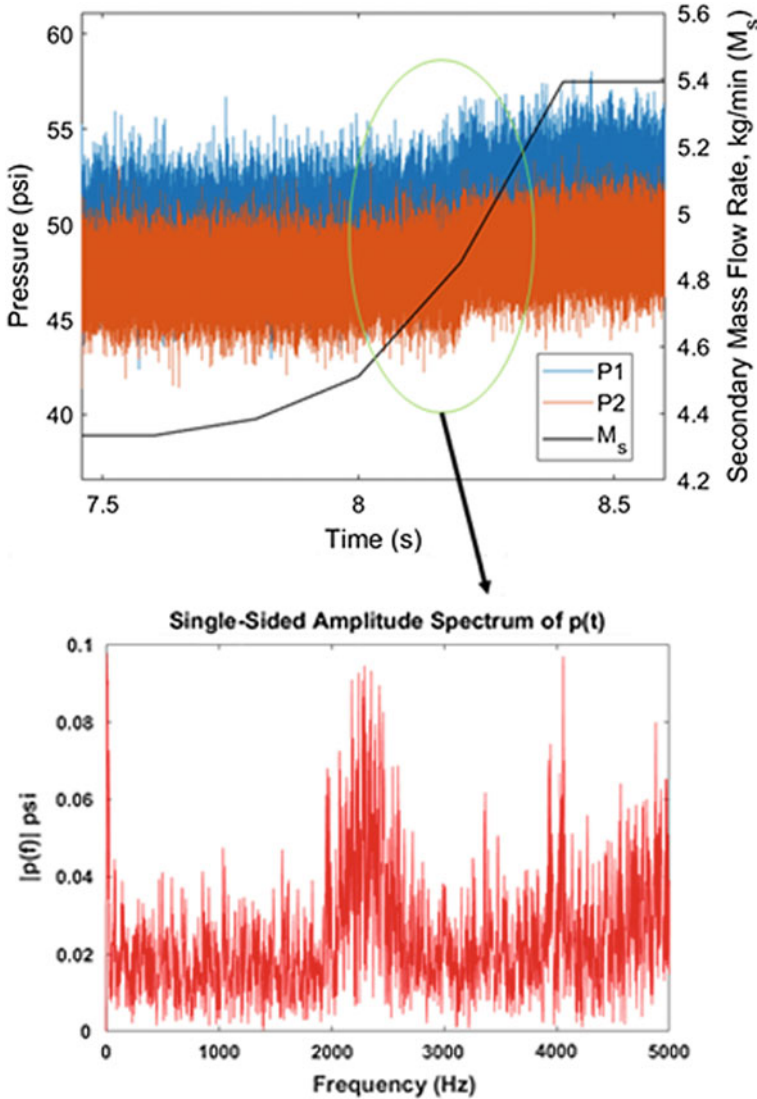
Fig. 8 Pressure transients in the afterburner duct due to simulated supercritical Rayleigh heat addition by equivalent secondary mass addition

4   Conclusions

The gas dynamic equivalence of Rayleigh heat addition with simulated mass addition in constant area compressible flows has been analyzed and validated in carefully conducted experiments. Both subcritical and supercritical heat addition simulations

have been carried out. The corresponding flow fields within the afterburner have been studied using high-speed schlieren flow visualization.

The advantage of gas dynamically simulating heat addition in an afterburner with equivalent mass addition is that any complex flow field could be studied easily without employing an actual afterburner with the difficult combustion heat release. The simulation procedures have been formulated and validated.

References

1. Sotheran A (1987) High performance turbofan afterburner systems, AIAA-87-1830
2. MacIsaac B, Langton R (2011) Gas turbine propulsion systems, Wiley
3. Shapiro AH (1953) The dynamics & thermodynamics of compressible fluid flow, vol 1. Ronald Press, NY
4. Greitzer EM (2006) Internal flow: concepts & applications, Cambridge University Press
5. Heiser WH et al (1995) Simulating heat addition via mass addition in constant area compressible flows. AIAA J 33(1):167–17
6. Sreenath P (2017) Studies on flow instabilities due to simulated supercritical Rayleigh heat addition in an afterburner, M. Tech thesis, Jain University, Bangalore, June
7. Sreenath P et al (2019) Supercritical heat addition in an afterburner. Project Document, PD-PR/2019/1011, CSIR-National Aerospace Laboratories

Gas Turbine Engine Health Monitoring, Performance and Starting

In-Depth Analysis of the Starting Process of Gas Turbine Engines

Chinni Jagadish Babu, Mathews P. Samuel, and Antonio Davis

Abstract In-flight flame out of a gas turbine engine is one of the worst nightmares of the aviators. Relight of the engine is the most benign action possible to restore the safe flight. In such circumstances, the starting process is a vital issue that needs careful study. The starting phase of the gas turbine engine is a highly complex and transient phenomenon. It involves the core aero-thermal portion of the engine and systems such as ignition system, fuel system, and control system and in some extreme cases of relighting assistance from starter also required. As far as the turbomachinery is concerned, the starting phase is an off-design condition, except for the starter and ignition system. From the flight safety point of view, the importance of reliable engine start, especially the in-flight relight of aircraft engine needs no explanation and assurance about midair restart capability need to be proven beyond doubt. The methodology demonstrated in this paper is a novel tool that can be used by maintenance engineers to identify the impending failures of the starting system. This paper highlights the outcome of the work carried out for a detailed analysis of the starting process via the starting trials of turboprop engines. Based on the detailed study of the starting process carried out during initial aircraft integration of the turboprop engine, the authors could identify the faults in the starting system of turboprop engine in the ground which has an effect on safe and reliable air starts. In-flight relights data and ground starts data have been analyzed as a part of this study to identify the novelties in the starting process so as to detect the faults.

Keywords Engine starting process · Start-up · Starting system · Fault detection · Fault detection parameter · Milestones · Novelty detection

C. Jagadish Babu (✉) · M. P. Samuel
RCMA (Eng), CEMILAC, C.V. Raman Nagar, Bangalore 560093, India
e-mail: jagadish.gtt@gmail.com

M. P. Samuel
e-mail: mathews@cemilac.drdo.in

A. Davis
IIAEM, Jain (Deemed-to-be-University), Jakkasandra, Kanakapura Taluk, Ramanagara District, Bangalore, India
e-mail: antonio9davis@gmail.com

Nomenclature

IGN	Ignition
RPM	Revolutions Per Minute
EGT/T	Exhaust Gas Temperature
EGR	Engine Ground Run
CFC	Cumulative Fuel Consumption
FCU	Fuel Control Unit
ISA	International Standard Atmosphere
SLS	Sea Level Static
NTS	Negative Torque Sensing
CAS	Calibrated Air Speed
EEC	Engine Electronic Control
SPD/N	Engine Speed
GPU	Ground Power Unit
MM	Manual Mode
$\sum_{ff}$	Cumulative Fuel flow
t	Time
dN/dt	Engine acceleration
dT/dt	Rate of change of EGT
G	Defect Group
W_f	Fuel Flow
T_S	Starter Torque
P_{ij}	jth Parameter at ith Milestone
M_i	ith Milestone
$\sum\sum D_{ij}$	Summation of faults at M_i and P_{ij}
k	Lower threshold limit
p	Upper threshold limit
P_1, T_1	Ambient Pressure and Temperature

1   Introduction

In a typical gas turbine engine, ground starting is initiated by pressing the start button by which the starter starts cranking the engine. This initiates the starting process by triggering a series of activities such as power supply to starter, fuel supply, ignition, and action of the control system. While the engine starts to crank, the compressor-turbine spool initiates rotation slowly enabling airflow through the engine. As cranking continues, at a stage where the working medium is in a conducive state to initiate combustion, ignition, and fuel injection are initiated. It is around 8–10% of engine speed. The fuel and air are, thus, inducted into the combustor chamber to form a combustible mixture, which is crucial for a successful light-off. (In this paper, we follow the convention of using the term "light-off" to indicate the condition of establishing

the flame in the combustion chamber and sustains the combustion process as used in Walsh and Fletcher [1]). A sharp rise in EGT is the indication of combustion/light-off and turbine power starts assisting starter-motor to accelerate the engine. The stable combustion of the fuel–air mixture is possible only with the continuous entry of the required amount of air into the combustion chamber under some excess pressure. By the term "'excess", we mean additional pressure for forcing air into the combustion chamber through the compressor. The starter assists in driving the engine up to 55–60% RPM. At or around 55% RPM, the ignition unit and the starter is disengaged. After starter cut-off surplus power to accelerate the engine depends on the amount of fuel addition and power developed by the turbine.

As we know, starting the engine, especially midair start is of utmost importance. The methodology illustrated in this paper helps the maintenance engineers to keep a track of the health of the engine in terms of a few events identified in the starting process. As indicated above, the starting process is a summation of the transient aerodynamics/ thermodynamics process coupled with nonlinear characteristics of the turbomachinery. As such starting process itself is considered as an off-design point for the turbomachinery. All these characteristics amplify the difficulties in analyzing the underlying process and hence attended by only a few researchers. However, considering its flight safety implications the authors have devised a methodology without compromising the utility and rigor for application by the maintenance engineers to foresee the sequential development of problems with the starting system.

Subsequent sections of this paper are arranged as follows: Sect. 2 defines the problem attempted along with the methodology and test details. Detailed discussion on engine start-up characteristics (the term "start-up" refers to the engine starting process as used in Hamid Asgari et al. [2]), key events in starting process, parameters for novelty detection, etc., are taken up in Sects. 3 and 4 are devoted to the distinguishing features of novelty. Baseline parameters for novelty detection are taken up in Sect. 5 and the details of fault detection and diagnosis on the basis of test results are presented in Sect. 6. Analysis of the in-flight relights are presented in Sect. 7 and finally the article is concluded in Sect. 8.

2 The Problem Addressed

In-flight restart (air start) is considered one of the most critical issues in flying and hence it forms an important test point in any developmental flight testing. However, intentionally switching off an engine in midair and testing its relight capability is an example of taking risks of a higher order, at least in the case of a single-engine aircraft. Even if the engine has a very good track record of operational reliability in terms of hours of exploitation, during midair start, the pilot invariably encounters a crucial situation that may pose certain challenges in managing it. Importantly, the piloting actions during air start and the readiness of subsystems that enable a successful relight. The topic of discussion of this paper pertains to the latter part, i.e., fault detection in starting system and methods to ensure the readiness of these systems

as and when required. Discovering the malfunction of any of the subsystem(s) at the point of relighting has no value as the engine has already flamed out in the air.

Naturally, this situation necessitates deeper exploration of the starting process and logically assessing the eventualities in a midair relight through a systematic study of the ground starting (which is the most benign form of testing and data generation). As it is well known, engineering systems give ample signals prior to the manifestation of a total failure. As engineers, it is our duty to listen to the system through careful data analysis and detect the forewarnings leading to failure of midair relight of the engine. So this study attempts to identify novelties in the starting system of gas turbine engines especially linked with mechanical systems supporting the starting process. Of course, the aerodynamics of midair relight is different from the ground conditions. However, the characteristics of mechanical systems, control logic, etc., can be very well established on the ground and can be extrapolated to the relight conditions with adequate levels of confidence. Once a novelty or systematic drift is observed in any of the critical parameters influencing the starting process through data analysis of ground start, it is an invaluable information for avoiding a probable in-flight relight failure. Therefore, a detailed study has been undertaken to understand the dynamics of the starting process and to detect the novelties that could manifest into a midair relight failure using ground test data of aero engines.

2.1 Methodology

Here we study a process that is transient, highly nonlinear, and seemingly difficult to handle by conventional modeling techniques. In this paper, we present a methodology of discretizing the starting characteristics maps (time vs. speed and temp) into 10 discrete points (say milestones for the sake of further discussion). Then experimental test data of a Turboprop engine is mapped to certain milestones keeping the time-stamp of milestones in starting processes such as fuel supply point, ignition on, light-off, etc., and the continuous track of data on spool speeds, fuel flow, and gas temperature till the starting cycle is completed. For a given make of the engine along with its starting system and the ambient conditions (say ambient pressure, temperature, and humidity) of a given operational base, we expect the measurable and computational parameters associated with a particular milestone should be repeatable with certain levels of accuracy, say within a given range of values if the basic behavior of the engine/starting system has not changed. We propose to evolve an appropriate threshold detecting methodology that detects any significant change in the basic behavior of the engine/starting system and tracking these changes through a set of parameters.

The parameters considered in this study are based on the milestones identified above. Each milestone has 3 direct measurements and 3 computed parameters [3]. The measured values include spool speeds, fuel flow, and gas temperature and the computed values include the rate of change of speed, rate of change of temperature, and cumulative fuel consumption. These 6 parameters at each of the 10 milestones

have been used to characterize the starting process and detect the novelties. Ideally, this set up of 10×6 parameter set on a range-based comparison can give rise to 60 direct comparisons. Once we establish a range of values of these 60 parameters based on certain initial successful starts carried out at a given location, by assuming the day-to-day ambient air temperature variations are negligible to cause a significant thermodynamics effect on the starting system, we check the new test (start) data if it falls in the earlier range or not. The departure of the new values forms the previously established range of corresponding values that indicate a change in the behavior of the system. Further details of the computational procedure and the logic used for fault detection have been presented in the subsequent sections. This simplistic methodology is devised keeping the easiness of implementation at an operational base with minimum computational facilities. Experiments were conducted both at ground conditions and midair conditions. The details of the experiments and the results are presented in the subsequent sections of this paper.

2.2   Test Setup and the Engine Used

The engine employed in this study is a single shaft turboprop engine, with an integral inlet, gearbox, two-stage centrifugal compressor, three-stage axial turbine, single annular combustion chamber, and turbine exhaust diffuser. The propeller control system is capable of operation in forward and reverse thrust. The rated power of the engine is 1100 shp at ISA, SLS conditions, with SFC of 0.547 lb/shp-hr. It is a constant speed engine with a propeller running at 2000 rpm. Engine has an Electronic Engine Control (EEC) unit with hydro-mechanical/Manual Mode (MM) back up. Engine is started by the electrical starter motor, which drives the engine main shaft through a reduction gearbox. The propeller is directly mounted on propeller shaft, which is driven by a reduction gearbox. During starting propeller is on "Start Locks", to avoid excessive load on the starter motor. Bleed port is closed during starting. The test setup of the engine integrated into a developmental aircraft with propeller is schematically shown in Fig. 1. In this study, we use ground test data of an aircraft propeller integrated test setup configuration in order to get a maximum similarity to the flight configuration.

2.3   Test Points

The tests plan for exploring the starting system has been planned in synchronization with the developmental flight trial/test requirements of the aircraft so that huge savings in time and money can be achieved without compromising the technical intend and the scientific rigor of the study. Simultaneous testing for multiple objectives is the current norm in the aeronautical industry and other cost-intensive development programs. The hardware tests are planned in a comprehensive manner and the data
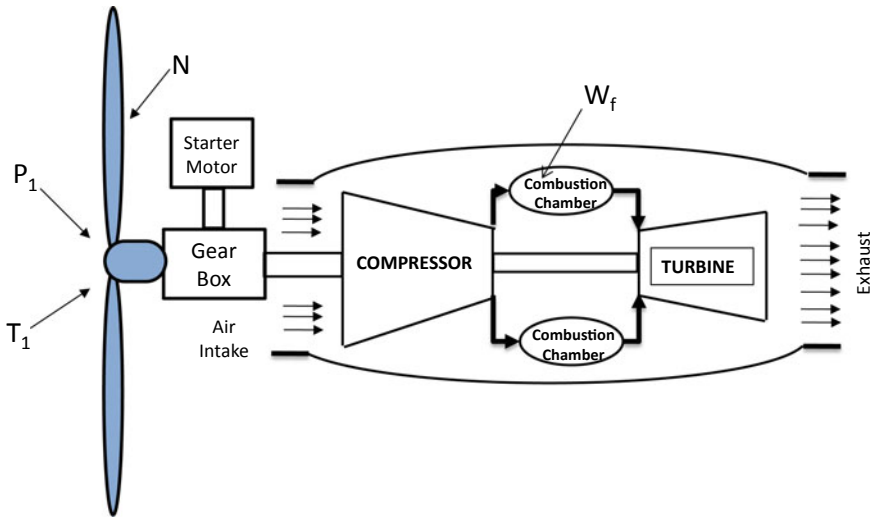
Fig. 1 Turboprop engine integrated to developmental aircraft with a propeller

shared among various subsystem groups to enable analysis and study according to their specialization and focus of study. For the purpose of this study aimed at starting system evaluation, data generated in four sets of experiments in the developmental flight tests were used. Three sets of experiments were ground tests done under different conditions and the fourth set of test were flight tests. For the engine start, we have two modes of start, viz., EEC and Manual mode. EEC start is an automatic mode of start, where the process is initiated by pressing the start button keeping in power lever in Flight Idle or Ground Idle positions. All other actions required are automatically accomplished by an engine control system such as ignition ON, fuel injection, ignition off, starter cut-off, etc., including the fuel enrichment. In manual mode start, EEC is disabled, so the pilot needs to do all the action including the fuel enrichment. The following table (Table 1) summarizes the Engine Ground Run (EGR) both in EEC and Manual Modes. In this study, we selected the test (EGR) data of engine starts to develop our methodology and validate it.

Further, multiple test points (8 test points) have been planned as shown in Table 2 to prove the relight capability over the complete flight envelope. The in-flight start tests points were chosen after due process of analysis and study keeping the flight safety implications. Benign test points are prioritized in the beginning so as to minimize

Table 1 EGR test points

Sl No	Test conditions	Tests done
1	ISA SLS conditions	Cumulative of 300 starts
2	At 1000 ft above sea level including three consecutive starts	
3	At hot weather conditions including three consecutive starts	

Table 2 In-flight relight test points

Test sequence	Altitude (ft)	CAS (kt)	Mode
1	15000	120	EEC mode
2	10000	130	EEC mode
3	10000	120	Manual mode
4	10000	110	EEC mode
5	10000	92	EEC mode
6	19000	92	EEC mode
7	10000	100	Manual mode
8	5500	150	EEC mode
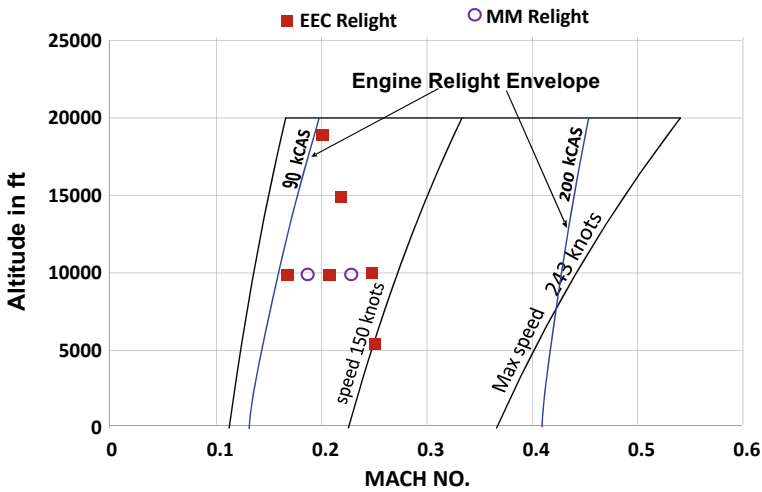
Fig. 2 In-flight relight test points marked over engine relight envelope

the uncertainty and sequentially increase the severity of the test. Thus engine starting envelope has been explored moving forwarded from benign test points to difficult test points within the envelope. In EEC Mode operation, Engine Electronic Control is fully functional. The engine can work under full power, i.e., EGT 650 Dec C or 2889 ft-lb torque (whichever occurs first). Manual Mode is a degraded mode where EGT is limited to 560 °C only. The details of in-flight relight test points are marked in the starting envelope in Fig. 2.

3 Engine Start-up Characteristics

By definition, the starting phase is said to be completed, when the engine is brought to a stage where the power produced by the turbine is just sufficient to run the compressor and driving the accessories continually [1]. Continuous acceleration of the engine
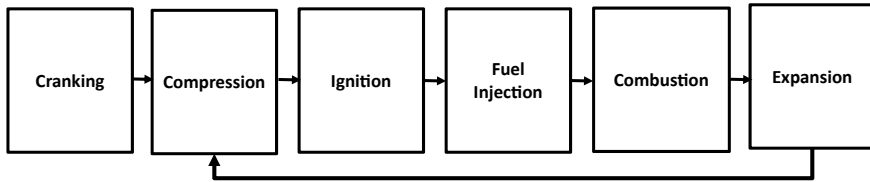
Fig. 3 Sequence of starting process in ground

rotor during the starting phase is possible only when both the starter and turbine power exceeds the power required for rotating the compressor and overcoming the various types of forces of resistance in the engine. This surplus/excess power accelerates the engine to a self-sustaining idle speed and the time required for attaining the idle state depends on the surplus power. The sequence of the starting process in ground is as given in Fig. 3. Once the turbine develops adequate power to sustain the compression process, the engine attains the self-sustaining speed.

Sometimes unintentional engine shutdowns due to flameout may happen in the air due to exhaustion flame in the combustion chamber. Flameout may be due to the malfunctioning of various engine systems or operating/flying conditions. Engine control systems are built with auto-relight capability by detecting flame out situation in the air. If auto-relight is unsuccessful, windmill relight has to be initiated in turboprop engines.

Another possibility of the requirement of midair relight arises in the case of aircraft employed for training the pilots. To train the new pilots, intentional shutdowns are made. In such cases, aircraft would have sufficient forward speed and altitude as described in respective engine manuals. After the intentional shutdown of engine, the pilot keeps the propeller blades in the feathering position to keep the propeller drag minimum. In order to start the engine in air, propeller wind-milling forces are used to increase the engine RPM instead of the starter. To accomplish the same, the propeller is driven out of the feather position by oil pressure from the un-feathering pump. As the propeller moves out of the feathering position, the propeller starts rotating due to the forward speed of aircraft and at 8–10% RPM, fuel and ignition are introduced and the sequence of operation/events is the same as ground starts. The sequence of starting process in the air in case of turboprop engines is as given in Fig. 4.
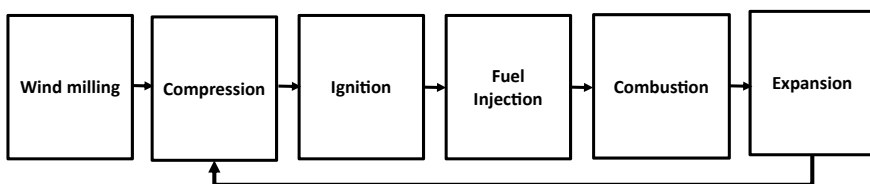
Fig. 4 Sequence of starting process in the air in case of turboprop engines

In a typical turboprop engine, the following systems come into action during both ground starts and air starts and are being put into action during the course of this study also.

(i)   Starter Motor (Generally in ground start only).
(ii)   NTS System (During shutdown before air start).
(iii) Un-feathering System (Air start only).
(iv)   Ignition and fuel system (Common to both ground and air starts).
(v)   Control System: speed logic, starting fuel scheduling logic, fuel enrichment logic, EGT limiting logic (for both ground and air start).
(vi)   Various sensors: pressure, temperature, speed, differential pressure sensor, etc.,

3.1 Start-up Profiles of a Turboprop Engine

Comparative analysis of gas turbine engine starting has been clearly illustrated by Beyene [4]. Walsh and Fletcher [1] described a sequence of steps in the starting of gas turbine engines. Steps are dry cranking, ignition on, light-off, acceleration to idle. Engine Assistance-Resistance power is an unbalance power after considering the power required for compressor, propeller (in case of turboprop engine), and power off-take of various accessories, frictional resistances, and power produced by the turbine. It can be observed from Fig. 5 that the engine assistance-resistance is negative up to 10% of engine speed and turns to positive once the turbine comes to operation. Engine light-off happens around 10% of engine speed after the introduction of fuel and ignition. Starter continues to assist up to approximately 40% of engine speed above which the engine goes into self-sustaining mode.

A typical start-up cycle for the turboprop engine as obtained from one of the test results is shown in Fig. 6 for reference and further discussion.

For the in-depth analysis of the starting process, various milestones have been identified based on the judgment of the underlying technical process. The 10 milestones starter engagement, ignition on, fuel injection, light-off, self-sustaining RPM,

Fig. 5 Typical engine assistance-resistance for a single spool engine
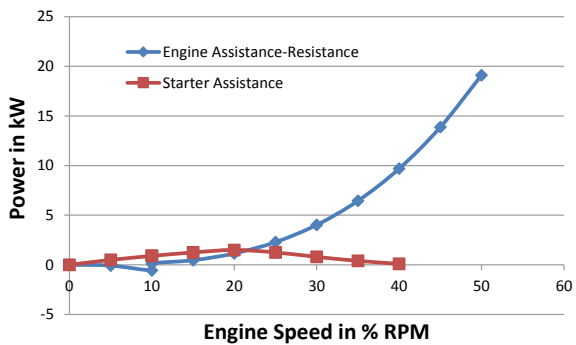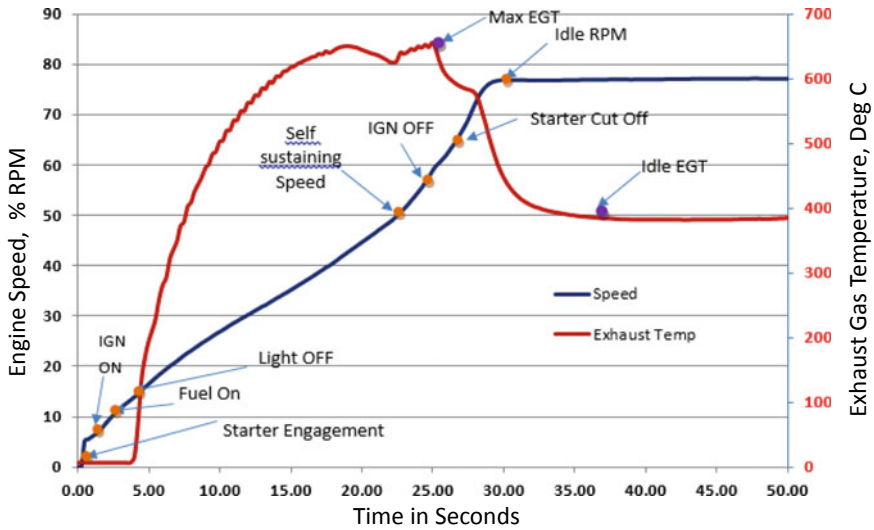
Fig. 6 Turboprop engine starting profile

ignition off, starter cut-off, Max EGT, Idle EGT, Idle RPM are illustrated in Fig. 6. These milestones are discrete events to be monitored on a sequential basis in each of the experiments.

For each milestone events, we recorded (i) the time to reach the milestone, (ii) the RPM at which the milestone is realized, and (iii) the exhaust gas temperature at the time of realization of the milestone event and calculated derivatives of speed, exhaust gas temperature, and cumulative fuel flow as indicated in Table 3. The successful starts provide the baseline for the time, speed, and temperature corresponding to each

Table 3 Milestones and parameters considered in the starting process

Milestone	Point of attaining the milestone	Measured parameters	Calculated parameters
M1	Starter engagement	Time, RPM, EGT	dN/dt, dT/dt, $\sum_{ff}$
M2	Ignition ON	Time, RPM, EGT	dN/dt, dT/dt, $\sum_{ff}$
M3	Fuel injection	Time, RPM, EGT	dN/dt, dT/dt, $\sum_{ff}$
M4	Light-off	Time, RPM, EGT	dN/dt, dT/dt, $\sum_{ff}$
M5	Self-sustaining speed	Time, RPM, EGT	dN/dt, dT/dt, $\sum_{ff}$
M6	Ignition OFF	Time, RPM, EGT	dN/dt, dT/dt, $\sum_{ff}$
M7	Max EGT	Time, RPM, EGT	dN/dt, dT/dt, $\sum_{ff}$
M8	Starter Cut-off	Time, RPM, EGT	dN/dt, dT/dt, $\sum_{ff}$
M9	Idle RPM	Time, RPM,EGT	dN/dt, dT/dt, $\sum_{ff}$
M10	Idle EGT	Time, RPM, EGT	dN/dt, dT/dt, $\sum_{ff}$

of these milestone points and deviation if any form the baseline data with supporting corroboratory evidence used to generate a novelty that can lead to the early detection of a potential failure unfolding at a future time. Range-based statistical parameters of the time, speed, temperature, etc., corresponding to each of these milestone points tabulated in Table 3 serves as the basis for novelty detection.

3.2 Parameters for a Reliable Engine Start-up

Following factors ensure reliable start-up:

(a) Battery Power/Voltage: Battery voltage is the indication of power available for the proper functioning of all the electrical systems like starter motor, igniters, etc. Time taken to reach idle rpm is directly proportional to battery power. If engine start is attempted with low battery power/voltage, the engine will have sluggish acceleration and will take more time to reach Idle rpm or Hung Start may occur. Time, rpm, $\sum_{ff}$, dN/dt will get affected at different milestones. If the igniters do not get sufficient power due to low battery or due to faulty igniters, light-off gets affected. Time, rpm, EGT, dT/dt gets affected at milestone-4.

(b) Capability of starter motor: Maximum drying cranking rpm in a given condition is the indication of starter motor capability. A faulty starter motor will affect engine acceleration and engine will take more time to reach Idle rpm or Hung Start may occur. Time, rpm, $\sum_{ff}$, dN/dt will get affected at different milestones.

(c) Fuel Control Unit (FCU): Starting fuel scheduling is done by FCU during engine starting. Engine acceleration depends on the amount of fuel addition in the combustion chamber. Faulty FCU may affect time, rpm, EGT, dN/dt, dT/dt, $\sum_{ff}$ different milestones.

3.3 Categorization of Starting Faults

Start-up faults are broadly classified four groups and milestones are mapped to these fault groups as illustrated in Fig. 7:

Group 1   Battery Faults, Starter Motor Faults, Engine Rub (rubbing of rotating parts with stationary parts), Engine drag (slow rpm buildup due to higher loading such as higher propeller blade angle etc.,)

Group 2   Ignition Faults (low-intensity ignition, improper fuel–air mixture resulting in light-off problems)

Group 3   Fuel system and control system faults (low and high fuel flow, improper fuel scheduling, etc.,)

Group 4   Degraded Engine (compressor fouling, low component efficiencies)
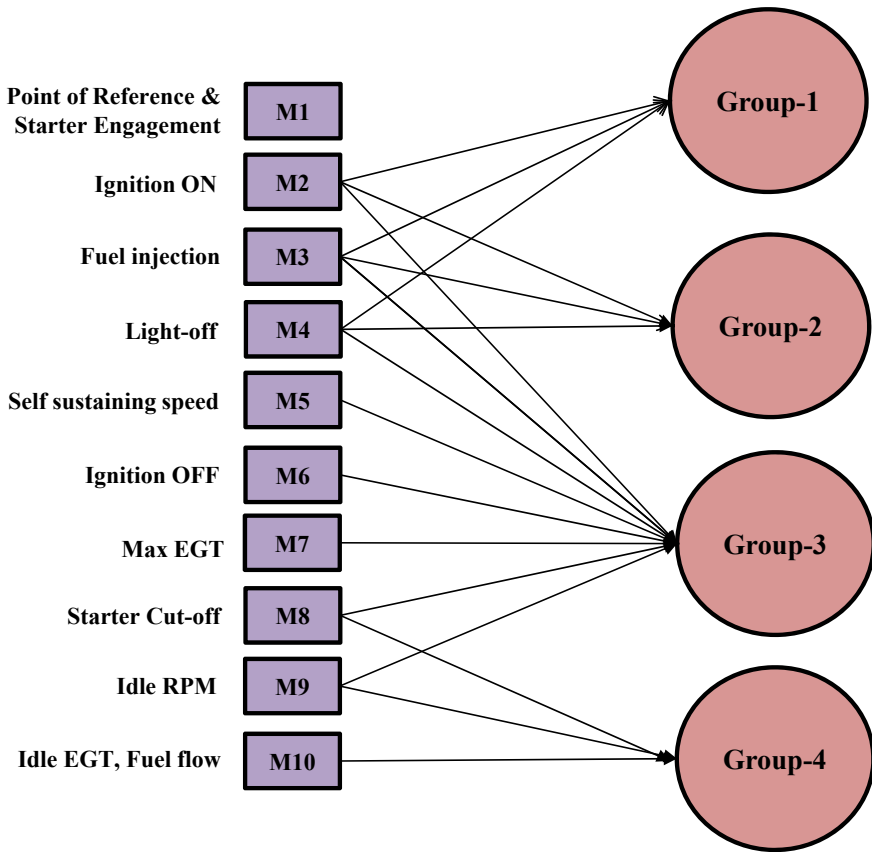
Fig. 7 Mapping of milestones to fault groups

Faults related to starting are detected using the novelties observed in the features of the time, RPM, and temperature measurements obtained at each of the 10 identified milestones in the starting cycle. The processing of classification and mapping of novelties into a certain group of faults and diagnosing the starting system health conditions can be done either using heuristic methods or by using Artificial Intelligence techniques such as expert systems, neural networks, etc., [2]. The scope of this paper is limited to developing a methodology for fault detection of the starting system of a gas turbine engine and the interested readers are referred to following papers for further discussions on the diagnosis.

Fault detection and diagnosis in the turbine engine using hidden Markov models was attempted by Menon [5]. A computational method for modeling of the start-up transient behavior is provided by Meher-Homji et al. [6]. Extending the operational envelope of a turbofan engine simulation into the sub-idle region was attempted by Chapman et al. [7]. Further discussions on the modeling and diagnostic aspects are beyond the scope of this paper and shall be taken up elsewhere.

4 Distinguishing Features of Novelty

The starting process is conceptualized in this paper as 10 discrete sub-events (Refer Table 3 and Fig. 6) unfolding as a function of time, RPM attained, and the engine EGT. For a given engine and test conditions, we expect these characteristics should be repeatable with certain levels of accuracy, say within a given range of values. For the time being, we do not address the issue of quantification of this range and refinement of the range for improving the fault detection accuracy. At the outset, we intend to propose a methodology and demonstrate its feasibility and optimization shall be taken up subsequently.

Discrete events, i.e., 10 milestones identified in the start-up characteristics from the time signals of Engine Speed, Exhaust Gas Temperature have been extracted for different P_1, T_1 conditions, hot/cold starts and recorded separately for identifying the novelty as shown in Fig. 8. The engine data are recorded in the digital recorder at a sampling rate of 4 samples for a second.

In the proposed theoretical framework, we have 10 milestones (M_1–M_{10}) and each milestone has 6 parameters (P_{ij}, $i = 1$–10 and $j = 1$–6) to monitor and each of these parameters can take two positions, i.e., either within the range or outside the established range. Hence these indicators either within range or out of range shall map the health of the starting system. For example, if all the parameters are within the range, we need not have any doubt about the health of the starting system. Similarly, if any of the parameters are out of range, we should naturally doubt the health of the starting system. Thus the values of each of these parameters have some information about the health of the starting system. Starting fault detection methodology is given in Fig. 9.

The fault detection criterion is as follows:

$$D_{ij} = 0 \ \text{if} P_{ij} \min < P_{ij} < P_{ij} \max$$
$$= 1 \ \text{Otherwise}$$

where

P_{ij} is the observed value of the jth parameter at ith milestone;

Fig. 8 Recording of start-up characteristics
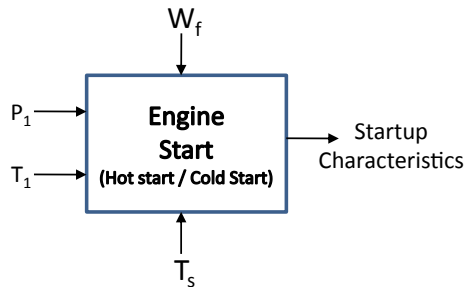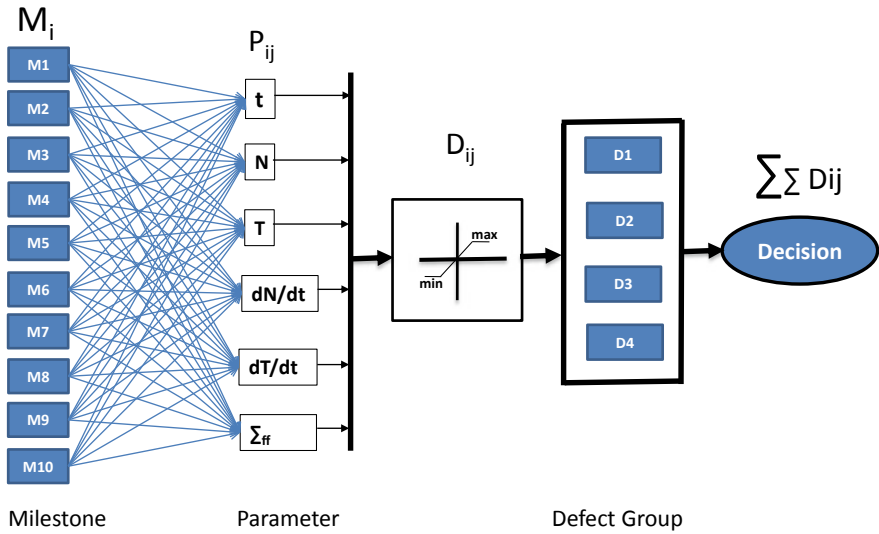
Fig. 9 Fault detection methodology

P_{ij}min and P_{ij}max are the minimum and maximum values of the established ranges of the jth parameter at ith milestone.

The assessment of a given situation is based on the values of $\sum\sum D_{ij}$, where $i = 1$–10, $j = 1$–6.

Starting system good:

$$0 \leq \sum_{i=1}^{10} \Sigma_{j=1}^{6} D_{ij} < k \tag{1}$$

Starting system to be reviewed and closely monitored:

$$k \leq \sum_{i=1}^{10} \Sigma_{j=1}^{6} D_{ij} < p \tag{2}$$

Starting system to be repaired:

$$\sum_{i=1}^{10} \Sigma_{j=1}^{6} D_{ij} \geq p \tag{3}$$

Engine start-up data corresponding to engine starts in which all the starting systems functioned normally are referred to as "good starts" and where some of the starting systems were faulty are referred to as "faulty starts". Around 150 engine good starts and 20 faulty starts are analyzed during this work and remaining data used for validation.

The lists of features extracted and used for fault detection are as tabulated in Table 3.

4.1 Engine Acceleration (dN/dt) Characteristics

Engine acceleration is a function of surplus power. An acceleration curve gives an in-depth understanding of starting characteristics, which will help for fault detection and diagnosis of gas turbine engines. Values of dN/dt at each milestone has been extracted as a distinguishing feature of novelty.

4.2 Rate of Change of Exhaust Gas Temperature (dT/dt) Characteristics

Rate of change of exhaust gas temperate indicates the stability of combustion in the combustion chamber which is very important for a reliable start-up. Values of dT/dt at each milestone has been extracted as a distinguishing feature of novelty.

4.3 Cumulative Fuel Consumption ($\sum_{ff}$)

The surplus power to accelerate a given engine depends on starter and turbine. During the engine start-up, after light-off, the amount of fuel added to the engine decides the rate of acceleration and the total time to reach Idle rpm. At any instantaneous point of time on starting characteristics, $\sum_{ff}$ indicates the total fuel consumed for the engine to reach that state. A parameter of Cumulative Fuel Consumption (CFC) helps in understanding and identifying the starting problems. $\sum_{ff}$ can be drawn with respect to time and engine speed. Values of $\sum_{ff}$ at each milestone have been extracted as a distinguishing feature of novelty.

5 Good Starts: Creation of Baseline

5.1 Discrete Events

During the integration of engine to a developmental aircraft, many engine ground runs have been carried out to ensure proper engine integration and start-up characteristics thus recorded data has been used for creating the base line. A sample of minimum P_{ij} (min) and maximum P_{ij} (max) values of features extracted for all the milestones are as given in Table 4:

Table 4 P_{ij} (min) and P_{ij} (max) values

Milestone	Time (s)		% RPM		EGT in Deg C	
	Min	Max	Min	Max	Min	Max
1.	0	0	0	0	25	44
2.	0.25	1.25	5.81	8.81	25	44
3.	0.75	1.75	8.56	9.93	25	44
4.	3.5	4.75	14.4	15.5	91	147
5.	22.5	25.75	54.75	55.56	647.5	686
6.	23	26.25	56.62	57.63	650.5	686
7.	23.25	26.5	57.68	58.94	653	687
8.	23.5	27.25	60	60.81	633	671
9.	28.5	33.25	75.12	78.2	418	500
10.	34.25	38.25	75.18	78.2	374.5	445
	dN/dt		dT/dt		$\sum_{ff}$	
1.	0	0	0	0	0	0
2.	3.25	32.25	0	0	0	0
3.	2.5	3.5	0	0	0.0045	0.00878
4.	2	2.75	168	272	0.06333	0.8819
5.	3.5	4	−14	28	0.56229	0.68574
6.	4	4.75	−14	24	0.58524	0.71038
7.	4.25	5.25	−14	14	0.59545	0.71975
8.	2.5	4.5	−78	−32	0.62041	0.74829
9.	0	0.5	−40	−24	0.86354	1.03378
10.	0	0.25	−4	0	1.08854	1.25711

6 Fault Detection and Diagnosis

Faults detected using the novelty feature referred above are discussed below through various case studies demonstrating the proposed framework. It can be observed that in practical data sets, due to various problems some data points are not fully captured, leaving no clue on the performance of the system. However, in this paper, we demonstrate that even partial data in the proposed framework has a lot of information to convey. Since the proposed framework is based on discrete events, inadvertent loss of data at a few measurement points does not jeopardize the utility of the conclusions drawn. Through various case studies presented in this section, we demonstrate the robustness of the proposed framework in different practical scenarios.

In this section, we present two case studies (Case 1 and Case 2) to illustrate the working of the proposed framework and in Case-3 we illustrate the effect of changes in the basic setup giving rise to false alarms if adequate care is not taken in

segregating data and reassigning the values of range for the parameters and detection criteria thresholds.

6.1 Demonstration—Case 1

A typical case of start-up characteristics recorded during the engine ground run is as given in Fig. 10. The following conditions that are assumed invariant as far as the proposed framework is concerned and efforts have been taken to experimentally control the variations or at least group homogenous set of conditions for analysis are Ambient Temp. = 30 °C, Relative Humidity = 65%, Ambient Pressure = 91 kPa, Electrical Supply = GPU, Mode of Start = EEC Start.

The fault detection methodology discussed above has been implemented. The fault detection criteria $D_{ij} = 0$ if P_{ij} within the limits and $D_{ji} = 1$ if P_{ij} is out of limit has been recorded in Table 5. One practical exception, in this case, is that milestone 3 and milestone 6 are not recorded. During the above EGR, fuel flow values could not get recorded by the data acquisition system and ignition was ON continuous. However other 8 milestones are captured correctly.

Figures 11 and 12 illustrates total faults detected at different parameters and milestones, respectively. It can be observed from Fig. 12 that faults initiated at milestone 4 (light-off) and increased cumulatively till the milestone 10. $\sum\sum D_{ij}$ is 16 and has crossed and upper threshold limit ($p = 10$) and hence the starting system of the engine needs repair. Please note that for given test conditions, we had arrived at $p = 10$ and $k = 5$ based on several starting trials. The framework proposed could detect the fault and indicated the need for immediate maintenance action.

On further observation of data (time, dN/dt at different milestones) and engineering investigations, it revealed that there is a delay in "light-off" and subsequently
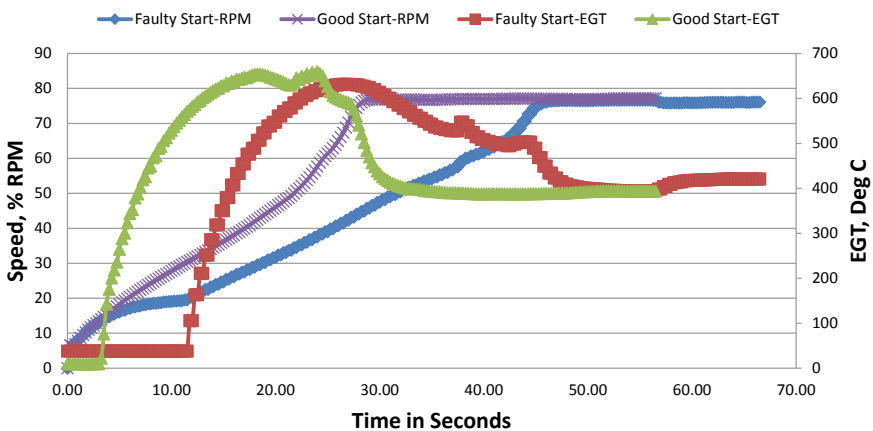
Fig. 10 Start-up characteristic curves of a good start and faulty start-demonstration Case 1

Table 5 Results of fault detection-Case 1

Milestone	Time	RPM	EGT	dN/dt	dT/dt	$\sum_{ff}$	$j = 6$ $\sum D_{ij}$ $j = 1$
1	0	0	0	0	0	–	0
2	0	0	0	0	0	–	0
3	Not registered						
4	1	1	0	0	0	–	2
5	1	1	1	0	1	–	4
6	Not occurred						
7	1	1	1	1	0	–	4
8	1	0	1	0	0	–	2
9	1	0	0	1	1	–	3
10	1	0	0	0	0	–	1
$i = 10$ $\sum D_{ij}$ $i = 1$	6	3	3	2	2	–	16
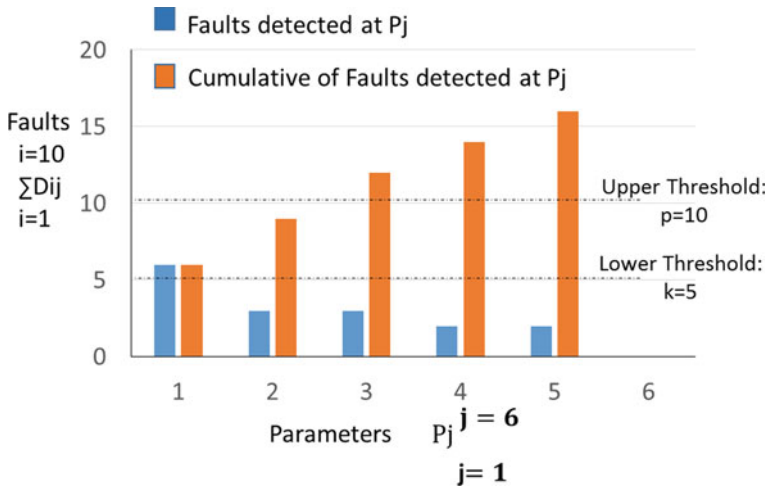
Fig. 11 Faults detected at Pj-Case 1

delay in reaching the idle rpm due to improper fuel scheduling. Delayed light-off may be due to faulty igniter or improper fuel–air mixture. Detailed examination revealed that the igniters are not faulty and the delay in light-off is due to starting fuel scheduling. Subsequent technical investigations have shown that the Fuel Control Unit (FCU) has been tuned/adjusted to solve the problem.
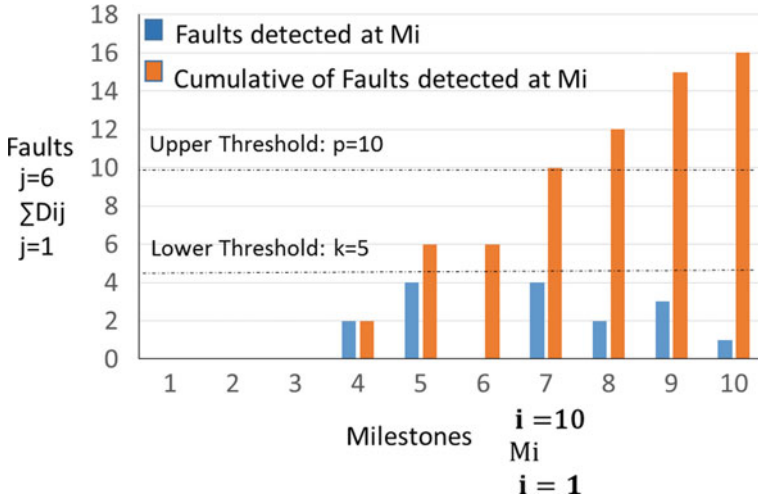
Fig. 12 Faults detected at Mi-Case 1

6.2 Demonstration—Case 2

A typical case of start-up characteristics recorded during the engine ground run is as given in Fig. 13. The following conditions that are assumed invariant as far as the proposed framework is concerned and efforts have been taken to experimentally control the variations or at least group homogenous set of conditions for analysis are Ambient Temp. = 29 °C, Relative Humidity = 66%, Ambient Pressure = 91 kPa, Electrical Supply = GPU, Mode of Start = EEC Start.
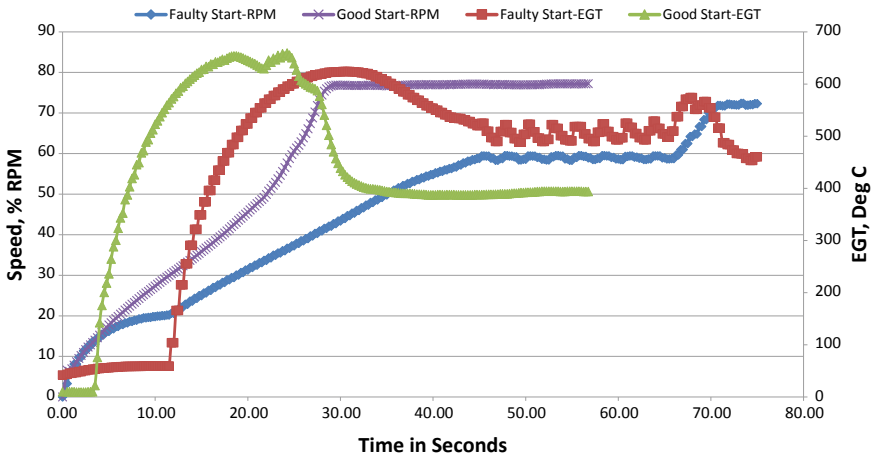
Fig. 13 Start-up characteristic curves of good start and faulty start-demonstration Case 2

The fault detection criterion has been recorded in Table 6. As in the previous case, here also during EGR, fuel flow values could not get recorded by the data acquisition system.

Figures 14 and 15 illustrate total faults detected at different parameters and milestones, respectively. It can be observed from Fig. 15 that faults initiated at milestone 4 (light-off) and increased cumulatively till milestone 8. During starting, the engine

Table 6 Results of Fault detection

Milestone	Time	RPM	EGT	dN/dt	dT/dt	$\sum_{ff}$	$j = 6$ $\sum D_{ij}$ $j = 1$
1	0	0	0	0	0	–	0
2	0	0	0	0	0	–	0
3	Not registered						
4	1	1	0	0	0	–	2
5	1	1	1	0	1	–	4
6	1	0	1	1	1	–	4
7	1	1	1	1	1	–	5
8	1	0	1	1	1	–	4
9	Engine could not reach this milestone						
10	Engine could not reach this milestone						
$i = 10$ $\sum D_{ij}$ $i = 1$	5	3	4	3	4	–	19
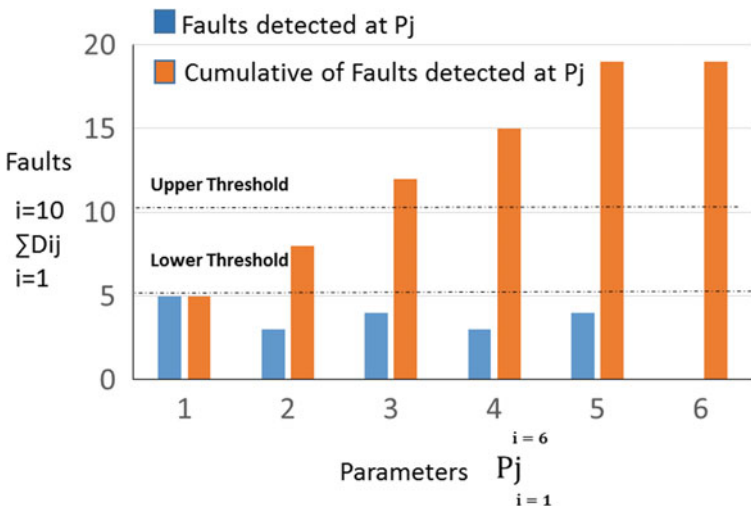
Fig. 14 Faults detected at Pj-Case 2
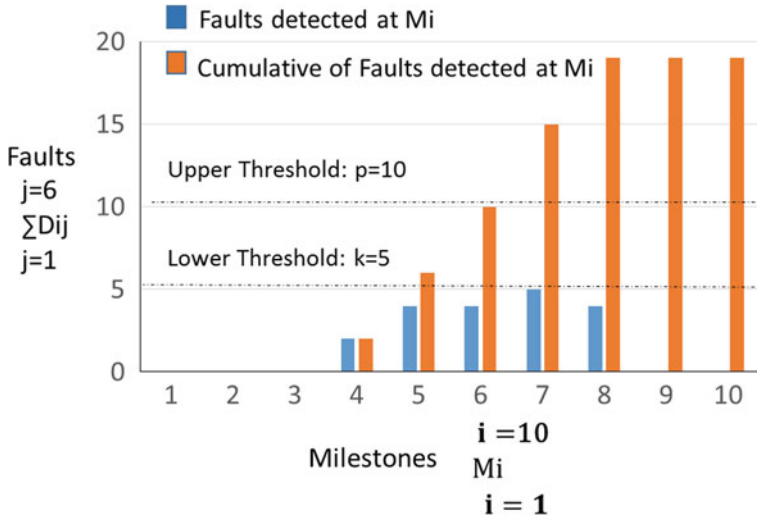
Fig. 15 Faults detected at Mi-Case 2

could not reach milestone 9 and milestone 10. $\sum\sum D_{ij}$ is 19 and has crossed the upper threshold limit ($p = 10$) and hence the starting system of the engine needs repair. The framework proposed could detect the fault and indicated the need for immediate maintenance action.

On further observation of data (time, dN/dt at different milestones) and engineering investigations, it revealed that there is a delay in "light-off" and engine rpm is getting stagnant at 60% rpm, indicating a hung start due to low fuel scheduling. Subsequent technical investigations have revealed that Fuel Control Unit (FCU) is faulty.

6.3 Demonstration—Case 3

This case study illustrates the effect of change in one of the conditions of start for a good starting system. This Case study 3 amplifies the requirement of strict control on the experimental variable. If it is overlooked, the decision criteria for the defect detection will fail and a false alarm will be raised. It is imperative that the value of range (P_{ij} min to P_{ij} max) and values of threshold for $\sum\sum D_{ij}$, i.e., value of k and p are to be derived for a given set of conditions and as and where these conditions changes, the range for the parameters and thresholds for the design criteria need to be reestablished based on trial starts.

As part of the developmental activity, the engine has been started with internal battery (aircraft-mounted battery, which supplies power to all the engine systems during to starting). The following conditions that are assumed invariant as far as

Table 7 Results of fault detection

Milestone	Time	RPM	EGT	dN/dt	dT/dt	$\sum_{ff}$	$\sum_{j=1}^{j=6} D_{ij}$
1	0	0	0	0	0	0	0
2	1	0	0	1	0	0	2
3	1	0	0	1	0	0	2
4	1	1	0	1	0	1	4
5	1	1	0	1	0	1	4
6	1	1	0	1	0	1	4
7	1	0	1	0	0	1	3
8	1	0	1	0	0	1	3
9	1	0	0	0	0	1	2
10	1	0	0	0	0	1	2
$\sum_{i=1}^{i=10} D_{ij}$	9	3	2	5	0	7	26

the proposed framework is concerned and efforts have been taken to experimentally control the variations or at least group homogenous set of conditions for analysis are Ambient Temp. = 29 °C, Relative Humidity = 64%, Ambient Pressure = 91 kPa, Electrical Supply = Battery, Mode of Start = EEC Start. Table 7 shows the results of the hypothetical case if someone uses the parameter ranges established for GPU Start in Battery Start mode. We can notice that False alarm is generated even when the starting system is healthy.

From the above table, it is observed total faults detected $\sum\sum D_{ij} = 26$. $\sum\sum D_{ij}$ has crossed upper threshold limit ($k = 10$) and detection recommends for immediate repair, which is a false alarm.

Further investigation has been carried out to find differences in GPU start and Internal Start. Figure 16 illustrates the acceleration curves at GPU Start and Battery Start. Time taken to reach idle rpm in GPU start is around 30 s, whereas in Battery start engine has taken around 58 s to reach to idle rpm. In GPU start, power source is significantly high and not depleting with rpm. Whereas in battery start, battery power was continually depleting over-usage. It is observed that the acceleration curves for GPU start are above the Battery start indicating higher engine acceleration (higher surplus power) in GPU start. To handle such variations in the starting conditions, we need to have separate trials at both conditions and parameters range (P_{ij} min and P_{ij} max) for $i = 1–10$ and $j = 1–6$ have to be established separately. Also, the detection thresholds p and k for $\sum\sum D_{ij}$ needs to be established and used according to the prevailing test conditions.

So we explicitly make it clear that care must be exercised when adopting this framework at different places and conditions such as high altitude versus sea level, high ambient temperature versus low ambient temperature, GPU Start versus Battery
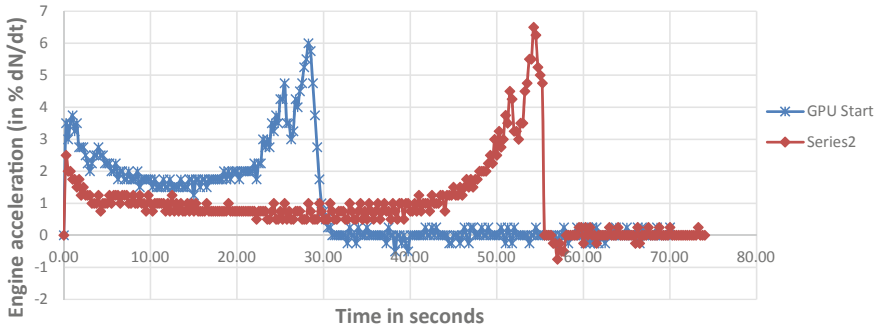
Fig. 16 Turboprop engine acceleration curve: effect of GPU start versus battery start

Start, etc. In such circumstances values of the range for the parameters and thresholds of $\sum\sum D_{ij}$ need to be re-evaluated. Otherwise false alarms as illustrated in Case study 3 would be triggered.

7 In-Flight Air Starts

When the fault detection parameter $\sum\sum D_{ij}$ is within the lower threshold k, the starting system found to be good and the health of the starting system is beyond any doubt. A good engine start-up in ground indicates that all the starting systems of the engine are functioning in normal conditions. This gives fare confidence to pilot to take-up intentional in-flight restarts in case of training or during developmental flight trials or in the event of flame out of engine in midair during the routine sortie. Table 8 illustrates 6 cases of in-flight restarts (at different altitudes and calibrated airspeed) and corresponding ground starts. It is observed that the fault detection parameter $\sum\sum D_{ij}$ was lower than the lower threshold limit (actual value 0) during the ground start, which has demonstrated the successful in-flight restart.

Table 8 In-flight air starts

Flight test	Altitude and CAS	Fault detection $\sum\sum D_{ij}$—Ground starts	In-Flight restart
1	13000 ft and 127 CAS	0	Successful
2	9989 ft and 128 CAS	0	Successful
3	10140 ft and 128 CAS	0	Successful
4	10100 ft and 109 CAS	0	Successful
5	9960 ft and 92.5 CAS	0	Successful
6	18890 ft and 93.5 CAS	0	Successful

8 Conclusion

This paper analyzes the starting characteristics of the turboprop engine in-depth and conceptualized a discrete sub-event modeling of engine starting for fault detection and diagnosis. A simple framework to monitor the parameters at different events within the range or outside the established range has been evolved. The approach has been applied to the test data collected during engine ground runs. The proposed novel tool will be an invaluable asset for maintenance engineers to identify the impending failures of the starting system. The present work demonstrates the features extracted on engine starting characteristics and establishes different starting system defects. It also demonstrates the possibility of false alarms if there are deviations to the test conditions and robustness of the framework in the event of loss of data at certain milestones. Fault detection threshold limits and usage of the same for decision-making in terms of maintenance action can be established using this approach. Using the fault detection criteria $\sum\sum D_{ij}$ and framework evolved in this work, it is demonstrated that good start-up in ground enhances the confidence and eventually leads to a successful flight start.

References

1. Walsh PP, Fletcher P (2004) Gas turbine performance, 2nd edn.
2. H Asgari et al (2014) Modeling and simulation of the start-up operation of a heavy-duty gas turbine using NARX models. In: Proceedings of ASME Turbo Expo 2014, Düsseldorf, Germany, 16–20 June 2014
3. Jagadish Babu C, Samuel MP, Davis A (2016) Framework for development of comprehensive diagnostic tool for fault detection and diagnosis of gas turbine engines. J Soc Aerosp Qual Reliab (SAQR) 6(1) (Special Issue):35–47, Feb
4. Beyene A, Fredlund T (1998) Comparative analysis of gas turbine engine starting, international gas turbine & aero engine congress & exhibition, The American Society of Mechanical Engineers, 98-GT-419, Sweden, 2–5 June 1998
5. Menon S, Nwadiogbu EO (2003) Fault Detection and diagnosis in turbines using hidden markov models. In: International joint power generation conference, 2003, ASME Turbo Expo 2003, Vol 1
6. Meher-Homji CB, Bargava R, Condition monitoring and diagnostic aspects of gas turbine transient response. Am Soc Mech Eng 92-GT-100
7. Chapman JW, Hamley AJ, Guo T-H, Litt JS (2016) Extending the operational envelope of a turbofan engine simulation into the sub-idle region. In: AIAA science and technology forum and exposition, AIAA-2016-1043, San Diego, CA, Jan 2016

Performance Trends of a Generic Small Gas Turbine Engine

Balaji Sankar and Tahzeeb Hassan Danish

Abstract Small gas turbine engines are increasingly used in cruise missile applications. In the design stage of these engines, aero-thermodynamic models are used to evaluate the expected performance of the engine for a given set of component characteristics. The throttle characteristics and altitude-Mach number characteristics of the engine are iteratively analyzed using this model. This paper describes the use of such a model to show the expected performance of a set of design choices at different altitudes and Mach numbers. These small engines are operated at maximum possible Turbine Inlet Temperatures (TIT) for maximum thrust. Theoretical relations that give the slope of the operating line for constant turbine inlet temperature operation is derived. Using these expressions, the reduction of stability at high altitude and low Mach number is shown.

Keywords Small gas turbine engine · Thermodynamic modeling

1 Introduction

Small turbo jet gas turbines are used as expendable engines for cruise missile applications. They are compact, reliable and require very little maintenance as exemplified by the Teledyne CAE J 402 engine. When designing these types of engines, the designer has to repeatedly assess the operating envelope and the performance of the designed engine. This has to be done so that the engine suits the end application, which will have a desired operating envelope, and meets thrust and SFC requirements. The designer will typically choose a compressor, turbine, and combustor geometry, which are typically derived from similar earlier engines. Aero-thermodynamic models are useful to assess the performance of the engine for the chosen compressor, combustor, and turbine characteristics. This work describes the use of such an aero-thermodynamic model to assess the performance of small gas turbines theoretically in the design stage.

B. Sankar (✉) · T. H. Danish
CSIR-NAL, Bangalore, India
e-mail: balajis_dd.thdanish@nal.res.in

A brief description of the Harpoon missile engine is given in the next section. The modeling is done for engine specifications similar to that of this engine. Analytically, it is shown that the turbine pressure ratio does not change during off-design operation for this engine. Also for maximum speed, expendable engines such as this are at maximum turbine inlet temperatures constantly. The variation of slope of operating line with altitude and Mach number for this constant high TIT is discussed. The off-design analysis results for throttle variation at International Standard Atmosphere—Sea Level Static (ISA SLS) are presented. The trend of Specific Fuel Consumption (SFC) and thrust variation with altitude and Mach number is discussed next using the performance simulation model, Harpoon missile engine description.

2 Harpoon Missile Engine Description

The Harpoon missile is one of the most used cruise missiles employing a turbojet engine. The specifications for the engine of Harpoon missile were drawn up after extensive survey by the US government in the 1960s and the main requirement was to have long storage life and low cost of acquisition. The maintenance needs were to be reduced by bringing down the parts count of the engine. The engine also had tight diameter and length restrictions imposed by the size of the Harpoon missile. The engine had to have 99% reliability of starting after 5 years of storage and accelerate to full thrust in 5 s. The performance characteristics of J402-CA-400 engine (shown in Fig. 1) made by Teledyne (in 1972) satisfying these tight requirements are described in detail in Leyes and Fleming [1]. Teledyne decreased the cost and parts count by using investment casting for a number of parts including the airfoils and brazing together subassemblies. The lubrications system was also simplified. The front ball bearing had closed sump arrangement and rear roller bearing was grease packed. All subassemblies were run directly on the main shaft at engine RPM to reduce gearing. The fuel scheduling was done by a full authority analog engine control system for reliability. The engine has a 2 stage compression system (transonic axial + centrifugal). 20% of the main flow through the compressor passed through the NGV for cooling before entering the slinger type combustor. This not only decreased the

Fig. 1 Teledyne CAE J402 engine, from Leyes and Fleming [1]
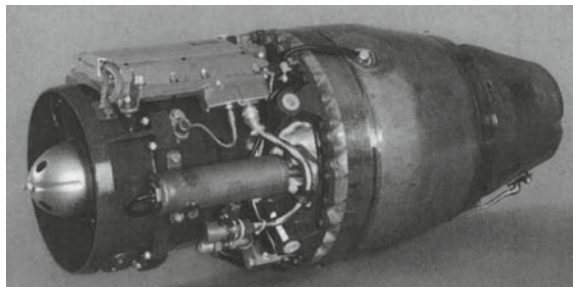
heat loads on the NGV blades but also acted as pre-heater for the combustor inlet air. The engine delivers 2.93 kN thrust and weighs only 46 kgf and hence has a T/W of 6.6. The diameter of the engine was 31.7 cm and length was 74.1 cm. Since this is a missile application, the operating life is only 1 h with one time starting capability provided by a pyro-charge.

3   Engine Simulation Models

Pilidis [2] has presented the procedure to carry out digital simulations of gas turbines. Methodology to include the effect of clearances and heat soakage effects on the gas turbine performance is given. Since these effects are difficult to test individually, the results were not validated. Ismail and Bhinder [3] have presented the equations to model a turbojet performance and have given the variation of thrust and SFC with Mach number without any experimental results. As the ambient inlet temperature increased from ISA SLS by 35 °C, the power output from the engine dropped by 20%. Vivek Sanghi has given a detailed survey of the simulation techniques and their advancement over the years in Sanghi et al. [4]. NATO [5] has prepared an extensive summary of the models for engine simulation used by designers and maintainers of the gas turbines. The limits of the performance of the engine and the flight envelope of the aircraft in terms of altitude and Mach number are described in this document.

4   Analytical Thermodynamıc Model

A simplified analytical thermodynamic model is used to show the variation of turbine pressure ratio at off-design conditions and the change of slope of the operating line with altitude and Mach number. The major assumptions made to simplify the analytical model are given in the next section.

Assumptions: The major assumptions in the off-design analysis carried out here is

- Turbine entrance nozzle guide vanes and the exhaust nozzle choked to maintain constant turbine pressure ratio.
- Turbine cooling, power take-off and air take-off are not considered to maintain constant mass flow through the engine.
- Variation of γ and C_p with temperature at a particular station and fuel to air ratio are not considered to simplify the analytical expressions.

5 Π_t Change During off-Design Operation

The variation of the turbine pressure ratio over the RPM range when the engine is
tested at the ground test bed is studied in this section. The mass flow rate of air as a
function of total pressure and temperature is given by

$$\dot{m} = \frac{MAP}{\sqrt{T}} \sqrt{\frac{\gamma}{R} \left(1 + \frac{\gamma - 1}{2} M^2\right)^{-\left(\frac{\gamma+1}{2(\gamma-1)}\right)}}$$

In the above expression, M = Mach number, A = Cross section area of flow, P =
total pressure upstream, and T = upstream total temperature. The station numbers
used in this work are shown in Fig. 2. Since both the turbine and nozzles are choked
($M = 1$), mass flow through them is same and gas properties (γ, R) are assumed
constant, the area ratio can be written as

$$\frac{A_4}{A_8} = \frac{P_8 \sqrt{T_4}}{P_4 \sqrt{T_8}} = \frac{\pi_t \pi_{\text{td}}}{\sqrt{\tau_t \tau_{\text{td}}}}$$

Simple gas turbines such as this have smooth transition duct between the turbine
exit and the nozzle exit plane. The pressure drop (π_{td}) in this duct can be assumed
to be constant at different flow rates and without afterburner, the temperature ratio
is unity ($\tau_{\text{td}} = 1$). The choked areas of the turbine and the nozzle are also constant.
Substituting for turbine pressure ratio we get

$$f(\tau_t, \eta_t) = \frac{\left(1 - \left(\frac{1-\tau_t}{\eta_t}\right)\right)^{\frac{\gamma}{\gamma-1}}}{\sqrt{\tau_t}} = \text{constant}$$

Thus if the turbine efficiency does not vary much during the off-design operation
from flight idle to full speed, the turbine pressure ratio remains constant in off-design
conditions also.

Fig. 2 Station numbering
for the small gas
turbine(SAE convention)
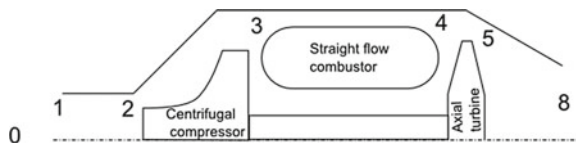
6 Operating Line Slope with Altitude and Mach Number

The operating line is essentially the variation of the compressor pressure ratio with corrected mass flow rate through the compressor. Since the turbine entry is choked, it can be used to calculate the mass flow rate through the compressor

$$\dot{m}_4 = \dot{m}_2 = \Gamma \frac{A_4 P_4}{\sqrt{T_4}}$$

where

$$\Gamma = \sqrt{\frac{\gamma}{R}} \left(\frac{\gamma + 1}{2} \right)^{-\left(\frac{\gamma+1}{2(\gamma-1)} \right)}$$

The corrected mass flow rate at the compressor inlet is given by

$$\dot{m}_c = \dot{m}_2 \frac{\sqrt{\frac{T_2}{288.15}}}{\left(\frac{P_2}{101325} \right)}$$

Substituting mass flow rate at compressor inlet using mass flow rate at turbine inlet in the expression for corrected flow rate,

$$\dot{m}_c = 5969 * \Gamma A_4 \left(\frac{P_4}{P_2} \right) \sqrt{\frac{T_2}{T_4}}$$

$$\dot{m}_c = 5969 * \Gamma A_4 \frac{(\pi_b \pi_c)}{\sqrt{\tau_b \tau_c}}$$

In the above expression, π_b and τ_b are the burner pressure and temperature ratio. π_c and τ_c are compressor pressure and temperature ratio. To change the operating point along the operating line, the turbine inlet temperature is typically controlled by the user by means of the Power Lever Angle (PLA). The ratio turbine inlet temperature to the compressor inlet temperature is given by τ_λ and ram temperature rise is given by τ_r. Writing the above equation in terms of controlled temperature ratio τ_λ, we get

$$\dot{m}_c = 5969 * \Gamma A_4 \frac{(\pi_b \pi_c)}{\sqrt{\frac{\tau_\lambda}{\tau_r}}}$$

If burner pressure loss is assumed constant, then the operating line can be expressed as

$$\pi_c = \left(\frac{\sqrt{\frac{\tau_\lambda}{\tau_r}}}{5969 * \Gamma A_4 \pi_b} \right) \dot{m}_c$$

From the above equation, it appears that the slope of the operating line depends only on the controlled temperature ratio and ram temperature ratio. This dependency can also be removed if the energy balance between the compressor and turbine is used. This energy balance can be written as

$$\tau_r \tau_c - \tau_r = \eta_{\text{mech}} (\tau_\lambda - \tau_\lambda \tau_t)$$

$$\tau_c = 1 + \eta_{\text{mech}} \left(\frac{\tau_\lambda}{\tau_r} \right) (1 - \tau_t)$$

$$\left(\frac{\tau_\lambda}{\tau_r} \right) = \frac{1}{\eta_{\text{mech}}} \left(\frac{\tau_c - 1}{1 - \tau_t} \right)$$

Substituting this in the expression for the operating line,

$$\pi_c = \left(\frac{\sqrt{\frac{1}{\eta_{\text{mech}}} \left(\frac{\tau_c - 1}{1 - \tau_t} \right)}}{5969 * \Gamma A_4 \pi_b} \right) \dot{m}_c$$

In the above expression, the compressor temperature ratio still depends on the compressor pressure ratio through the compressor efficiency ($\tau_c = f(\pi_c, \eta_c)$). For constant transition duct pressure loss and turbine efficiency, it has been shown earlier that the turbine temperature ratio and pressure ratio are constant ($\tau_t = $ constant). Hence, the slope of the operating line is constant for a given turbine inlet area (A_4) and burner pressure drop (π_b). It does not change with ambient conditions or Mach number of flight.

6.1 Reason for Increasing Stability Margin at High Mach Numbers for Expendable Engines

In expendable small gas turbines, the turbine inlet temperature is maintained constant at the max safe limit at all operational altitudes to get maximum thrust. At constant Turbine Inlet Temperature (TIT), the operating line shifts to the left toward surge with increase in altitude and shifts right away from surge with increase in Mach number.

Fig. 3 Compressor
operating line shifting to the
right with increase in mach
number at constant turbine
inlet temperature
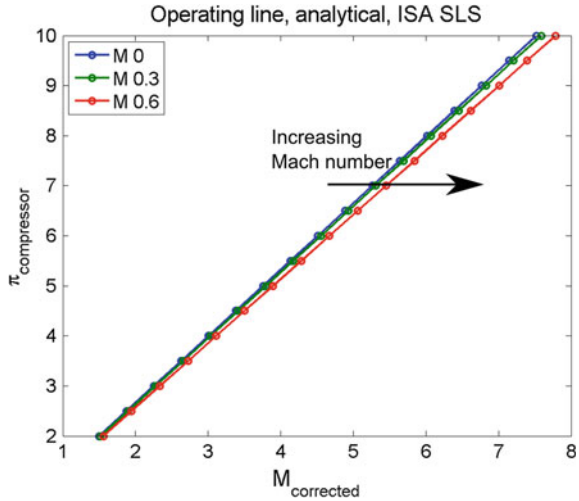
This is because, at constant TIT, the mass flow through the engine increases as
Mach number increases. If τ_λ was kept constant, the TIT would have increased with
increase in ram air temperature as the density at choke point would have reduced. But
since TIT is kept constant and not τ_λ, the density does not decrease in relation with
increase in ram air temperature. So the mass flow increases, and the surge margin
increases for a given pressure ratio. This trend is shown in Fig. 3. For similar reason,
increase in altitude decreases the mass flow through the engine as the fixed TIT does
not allow the density at the turbine inlet to increase. Hence mass flow through the
engine decreases and operating line moves toward the surge as shown in Fig. 4. So
surge margin decreases with increase in altitude.

Fig. 4 Compressor
operating line shifting to the
left with increase in altitude
at constant turbine inlet
temperature
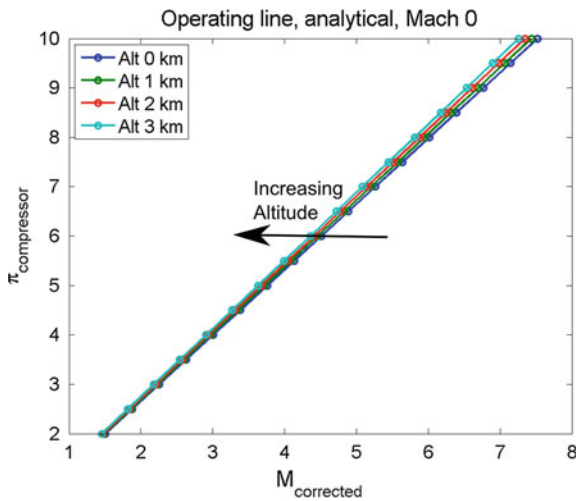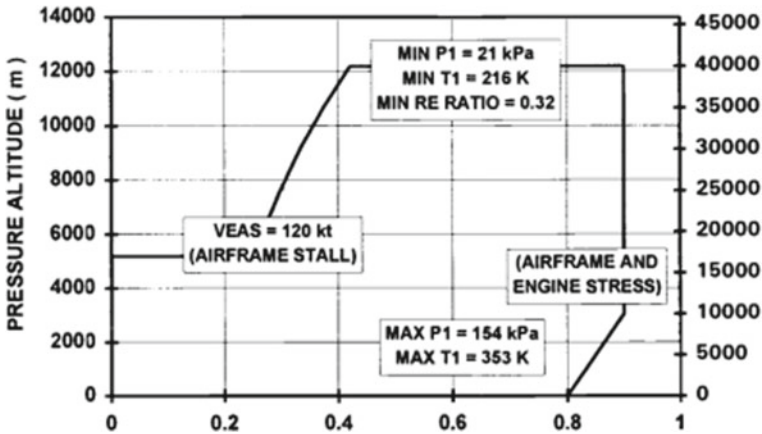
Fig. 5 Operational envelope for a subsonic air-breathing missile, from Walsh [6]

For these two reasons, the upper left corner of the flight envelope, where the engine encounters high altitude, low Mach number, is susceptible to surge of the gas turbine. This region of operation is avoided as shown in Fig. 5.

7 Design Point Specifications

The small gas turbine (turbojet) engine without afterburner has been thermodynamically analyzed theoretically for its design point performance. Figure 2 shows the configuration and stations of the engine. The engine comprises a centrifugal compressor, straight flow combustor, axial turbine, and convergent fixed area nozzle. For simplicity of analysis, turbine nozzle guide vanes and nozzle are assumed to be choked, power off-take and turbine cooling are not considered, fuel-air ratio is assumed very small, and specific heat capacity and specific heat ratio of the air at a particular station is assumed constant. The design point parameters of the engine are given in Table 1. The thrust and SFC of the engine at design point are 3.1 kN and 0.116 kg/N-h.

Table 1 Design point parameters of the turbojet engine

Parameter	Value
Compressor pressure ratio	6
Compressor efficiency	0.79
Turbine efficiency	0.9
Design Mass flow rate, kg/s	5
Burner efficiency	0.97
Design fuel flow rate, kg/s	0.101
Turbine inlet temperature, K	1220
Burner pressure ratio	0.94
Nozzle pressure ratio	0.98
Discharge coefficient of nozzle	0.98
Thrust coefficient of nozzle	0.98
Leakage flow, kg/s	0.01
Inlet pressure recovery	0.95
Compressor exit pressure drop	0.98
Mechanical efficiency	0.99

8   Off-Design Performance Analysis

Off-design performance analysis mainly consists of two parts. First is the throttle characteristics, which the response of the engine to variation in N1 RPM at a fixed ISA SLS condition. Second is the variation of performance at various altitudes and Mach number combinations. In altitude-Mach characteristics, typically, the analysis is carried out to find the maximum possible thrust at each altitude and Mach number. This determines the maximum possible acceleration of the vehicle from this condition. Both throttle analysis and altitude-Mach characteristics require component characteristics maps. The normalized compressor characteristics, turbine, and nozzle characteristics map used in this work are shown in Figs. 6 and 7. The methodology of off-design simulation is given in detail in Walsh and Fletcher [6], Cohen et al. [7], Cumpsty [8], and Mattingly [9]. The authors have used similar off-design modeling programs using Matlab for the performance analysis of legacy aircraft engines as reported in and is not repeated here.
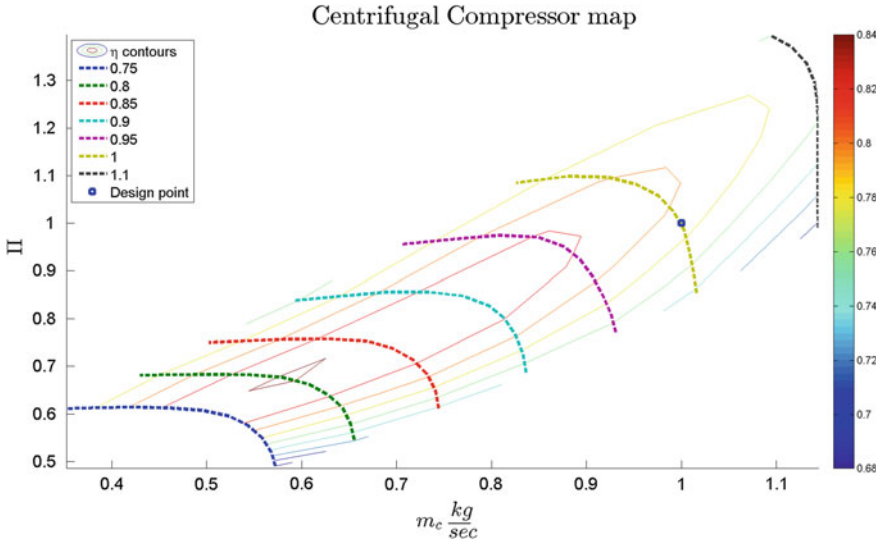
Fig. 6 Compressor characteristics map showing with normalized mass flow rate and pressure ratio
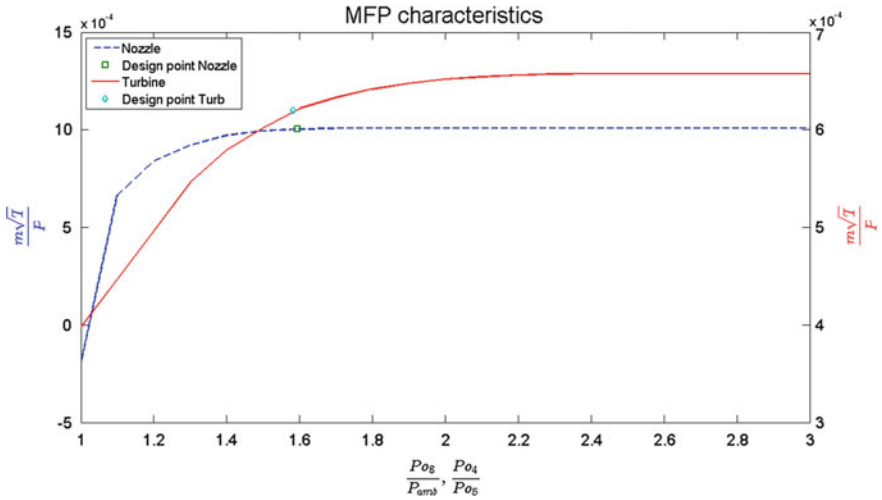
Fig. 7 Convergent nozzle characteristics map showing mass flow function dependence on pressure ratio

8.1 Results of Throttle Characteristics Simulation at ISA SLS

The performance of the engine in terms of thrust and fuel consumption at ISA SLS for various RPM is shown in Figs. 8 and 9. The values are normalized using design point values. From Fig. 8 we can infer that the nozzle chokes above 90% RPM and the engine generates pressure thrust, which increases the total thrust of the engine.

Fuel to air ratio variation and turbine corrected RPM ($N1T_c$) variation are shown in Fig. 10. The turbine corrected RPM (shown in green) increases and is maximum at 85% $N1_c$ due to the variation of burner exit temperature (TIT) with RPM. The variation of TIT (shown in Fig. 11) is almost parabolic with respect to RPM and a corresponding parabolic trend is seen in $N1T_c$. The trend of variation of fuel to air ratio also follows the trend of variation in TIT. Pressure variation, which is similar to the temperature variation, is shown in Fig. 12.

The operating line of the engine on the compressor map is shown in Fig. 13. We can see that the operating line becomes steeper as the RPM increase. As expected for a single spool engine, the surge margin of the compressor is high at low RPM and low at high RPM. The engine is more susceptible to surge at as the RPM increases above design RPM.

Fig. 8 Thrust variation at ISA SLS for various RPM
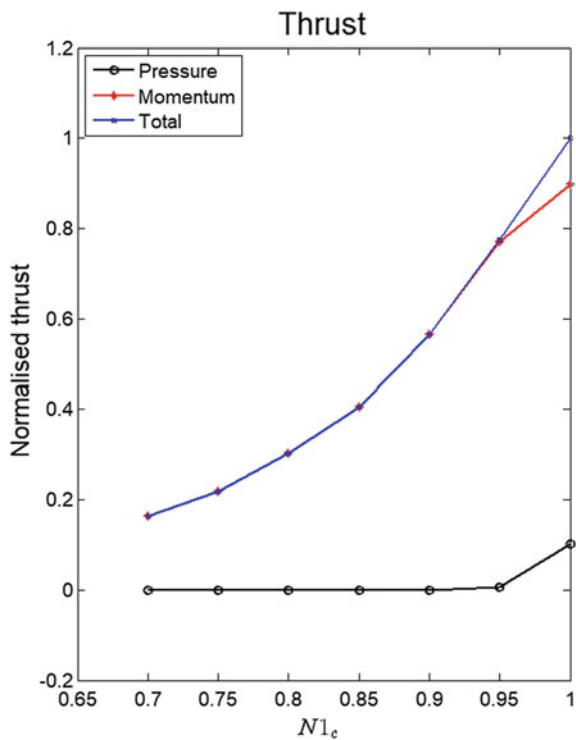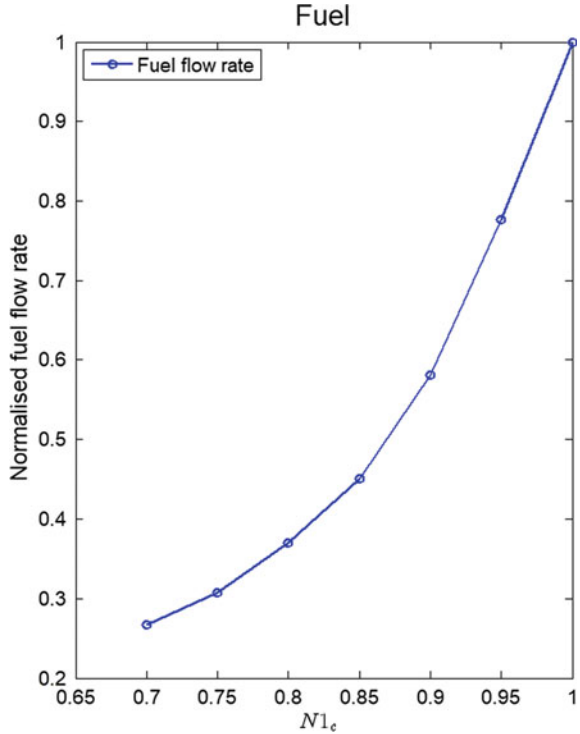
The operating point of the engine on the turbine and nozzle Mass Flow Parameter (MFP) curves is shown in Fig. 14. Design point of the engine lies in the region where both the turbine and nozzle are choked and MFP is constant. As the RPM reduces, the pressure ratio across both the components drops and the mass flow parameter reduces. This forces the engine to ingest lower mass flow at lower RPM.

8.2 Results of Altitude-Mach Characteristics off-Design Simulation

Typical variation of peak thrust with Mach number at different altitudes for a turbojet engine is shown in Fig. 15. It can be seen that at sea level, initially thrust drops due to inlet air momentum increase. It again rises beyond Mach 0.5 due to ram pressure rise. Similar trend in thrust can be seen in the contour plot as shown in Fig. 16.

The change in N1c RPM is shown in Fig. 17. At high altitudes and low Mach number, inlet temperature is low and velocity of sound is hence low. Thus N1c is high at top left corner of the envelope. Since compressors have a limitation on maximum N1c due to shock losses, the gas turbine may not operate satisfactorily in this region.
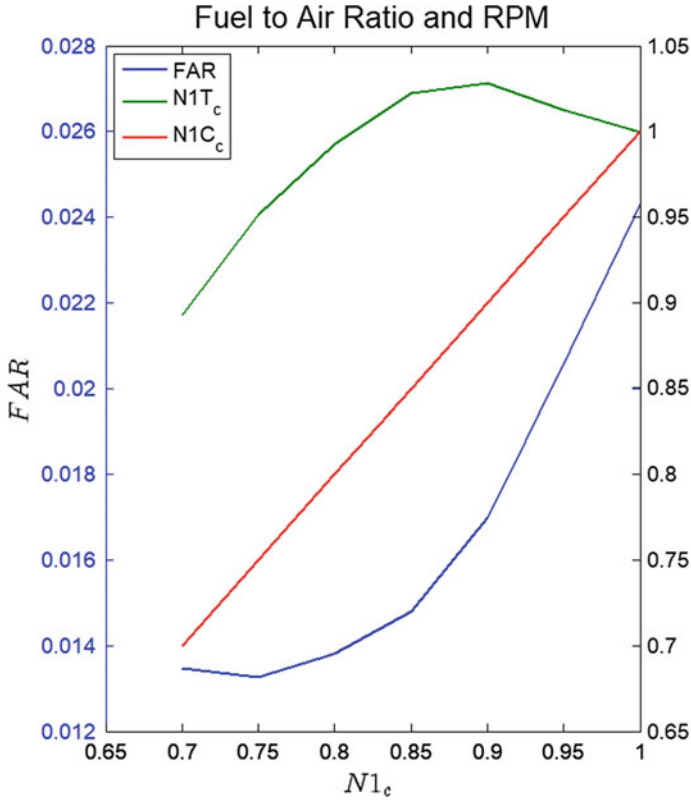
Fig. 10 Fuel to air ratio and turbine corrected RPM variation at different stations at various RPM

When this high RPM region of operation is removed from thrust characteristics, the resulting contour plot is shown in (Fig. 17) Fig. 18.

When the RPM is held constant at 100%, the TIT drops below design value at the lower right corner of the envelope (Fig. 19). This is because, at low altitude and high Mach numbers, the mass flow rate into the engine increases. To keep MFP constant, the TIT has to be reduced. For the same reason, TIT increases at low Mach number high altitude conditions. Since there are material limitations on the TIT values for uncooled turbines, the engine cannot be operated in these high TIT regimes. When this high TIT region of operation is removed from thrust characteristics, the resulting contour plot is shown in Fig. 20.

Fig. 11 Temperature variation at different stations at various RPM (Normalized using ISA SLS temperature)
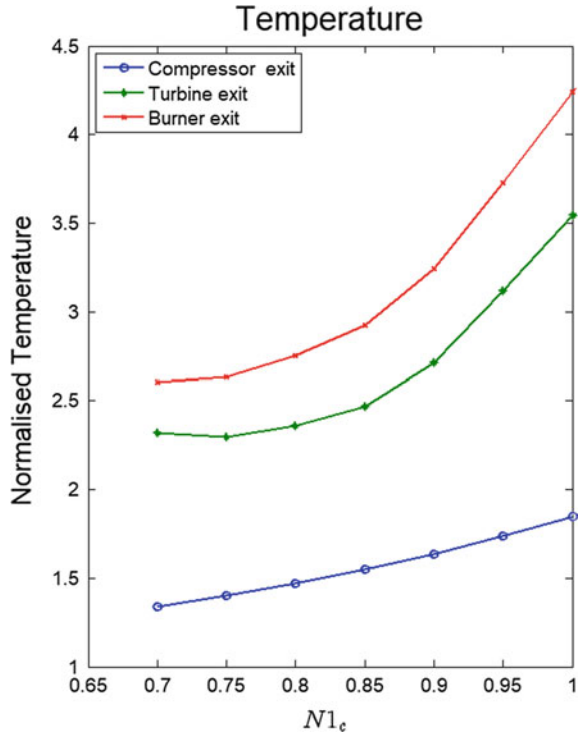
8.3 SFC Variation with Altitude and Mach Number

Typical variation of SFC with Mach number at different altitudes for a turbojet engine is shown in Fig. 21. It can be seen that at all altitudes, SFC increases with Mach number. At higher altitudes, SFC of the engine reduces for the same Mach number. Similar trend can be seen in the SFC contour plot shown in Fig. 22.

9 Conclusions

The performance analysis of a generic turbojet engine was carried out using an aero-thermodynamic model in this work. Design point and off-design analysis (throttle and altitude-Mach characteristics) were carried out. Performance trends obtained in altitude-Mach characteristics were similar to published trends in literature. The reason for not operating in high altitude and low Mach number combination was shown from both high N1c and high TIT points of view. Also it was shown analytically
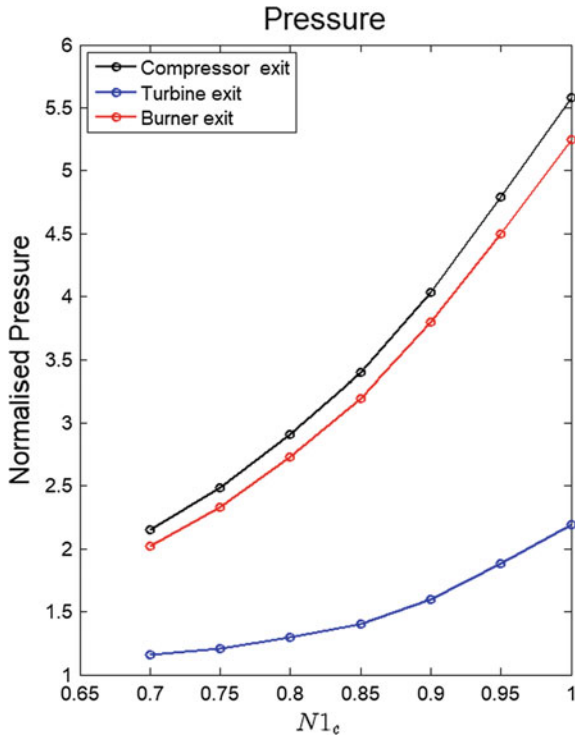
Fig. 12 Pressure variation at different stations at various RPM
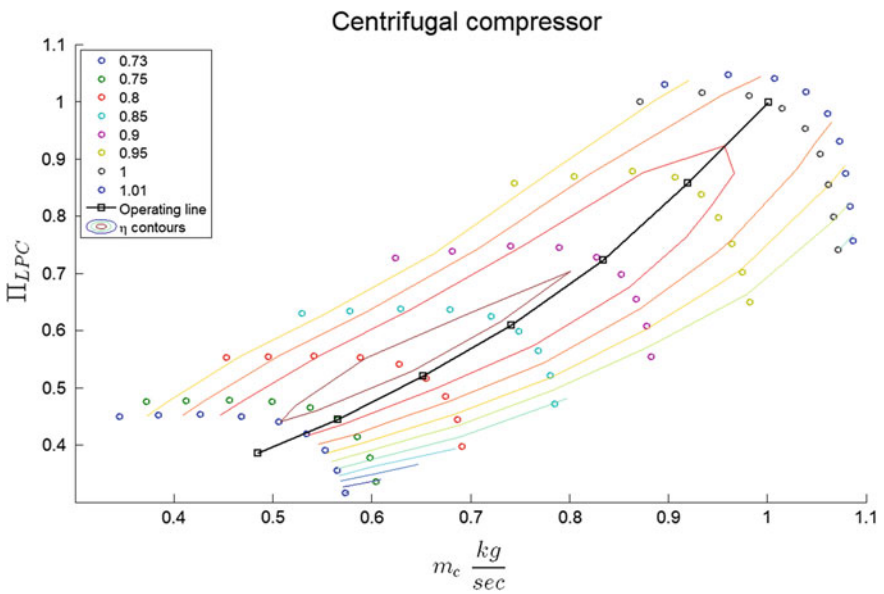
Fig. 13 Normalized compressor map with operating line during throttle input variation
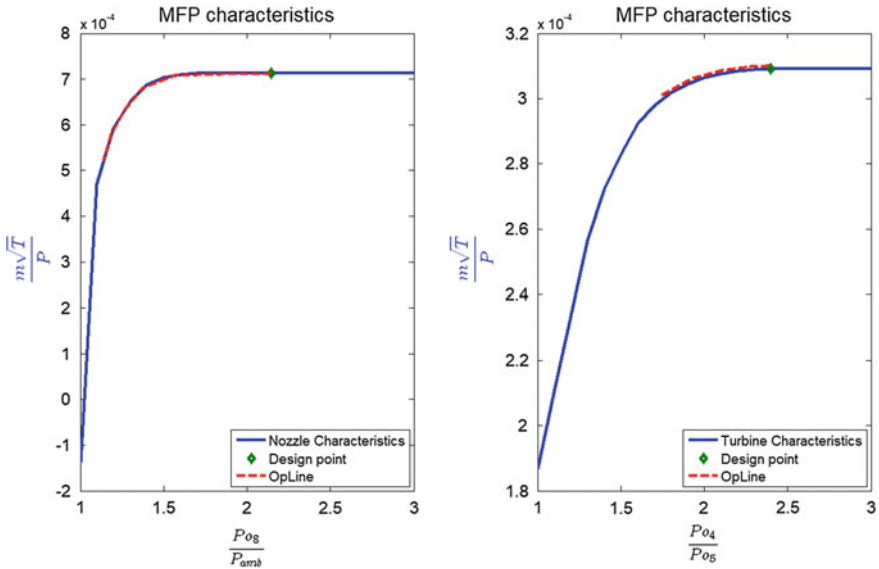
Fig. 14 Turbine and nozzle mass flow parameter curves with operating line during throttle input variation

Fig. 15 Variation of thrust at 100% RPM with Mach number at different altitudes, from Mattingly [9]
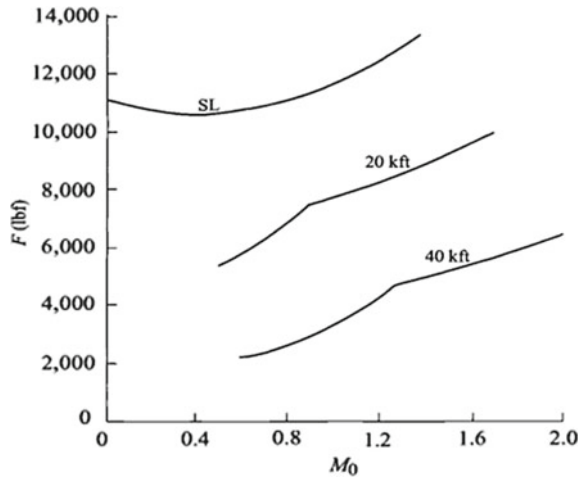
that the slope of the operating line increases at high altitude and low Mach number for constant TIT operation. This increasing operating line slope decreases the surge margin available.
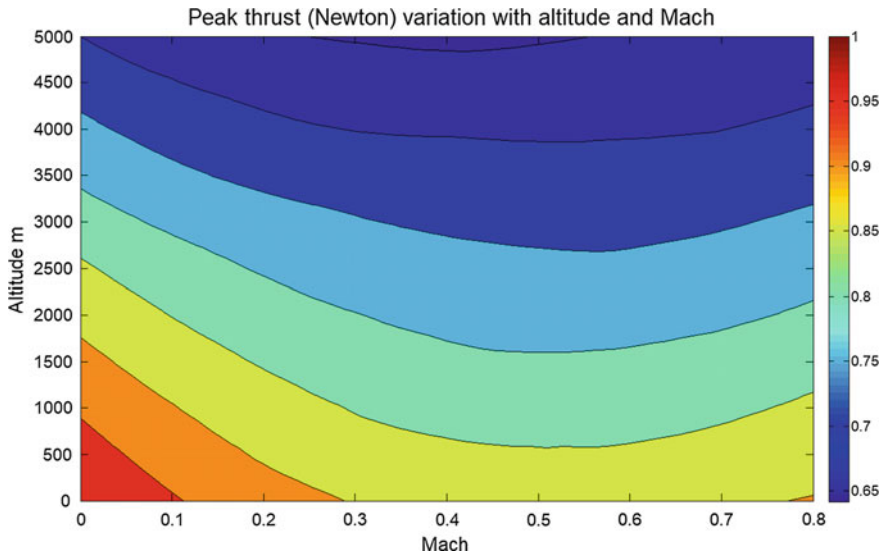
Fig. 16 Variation of peak thrust with altitude and Mach number at constant 100% physical engine RPM
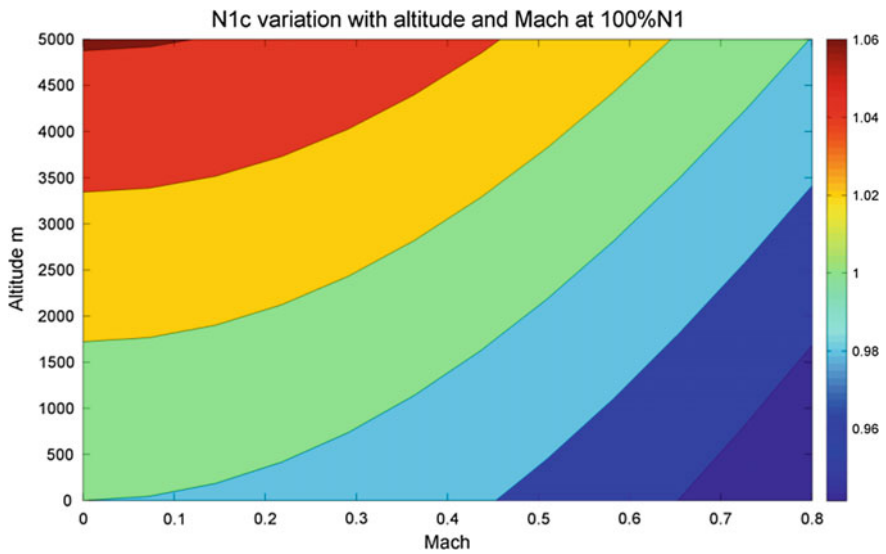
Fig. 17 Variation of corrected engine RPM with altitude and Mach number at constant 100% physical engine RPM
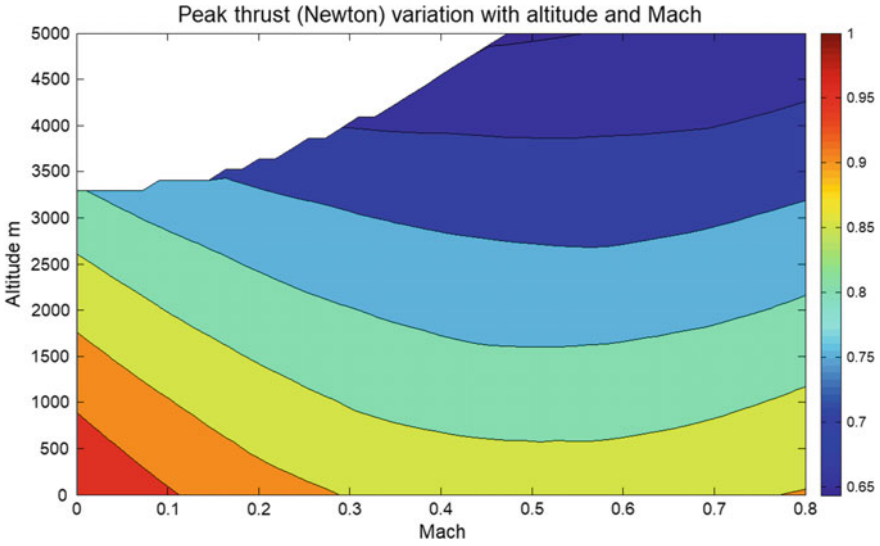
Fig. 18 Variation of thrust at 100% RPM with altitude and Mach number at constant 100% physical engine RPM. N1c has been limited to 1.04
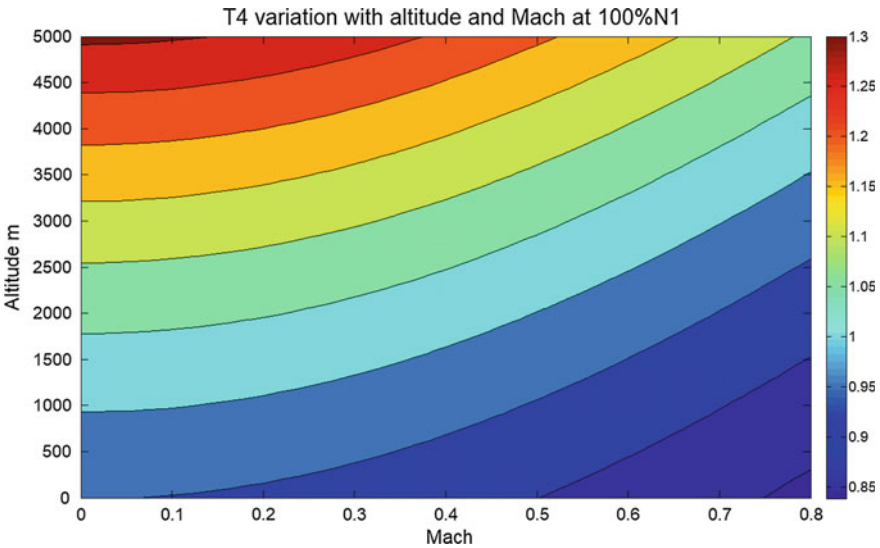
Fig. 19 Variation of combustor exit temperature with altitude and Mach number at constant 100% physical engine RPM
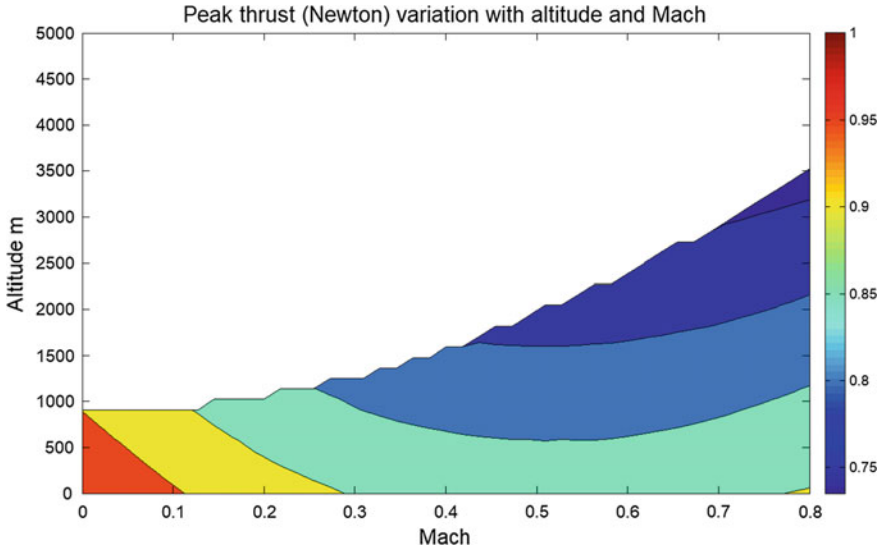
Fig. 20 Variation of thrust at 100% RPM with altitude and Mach number at constant 100% physical engine RPM. TIT has been limited to 1220 K

Fig. 21 Variation of SFC at 100% RPM with Mach number at different altitudes., from Mattingly [9]
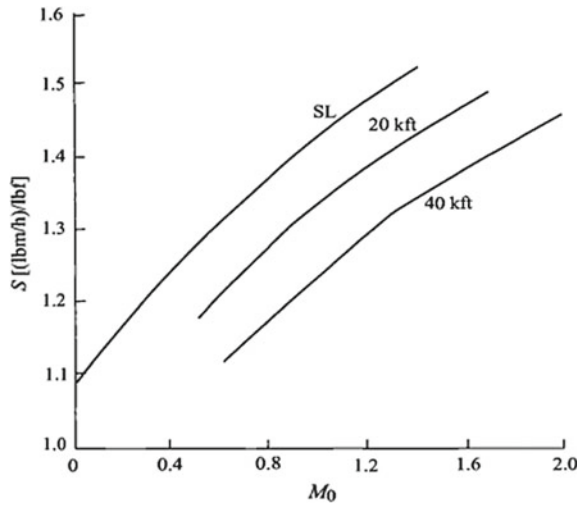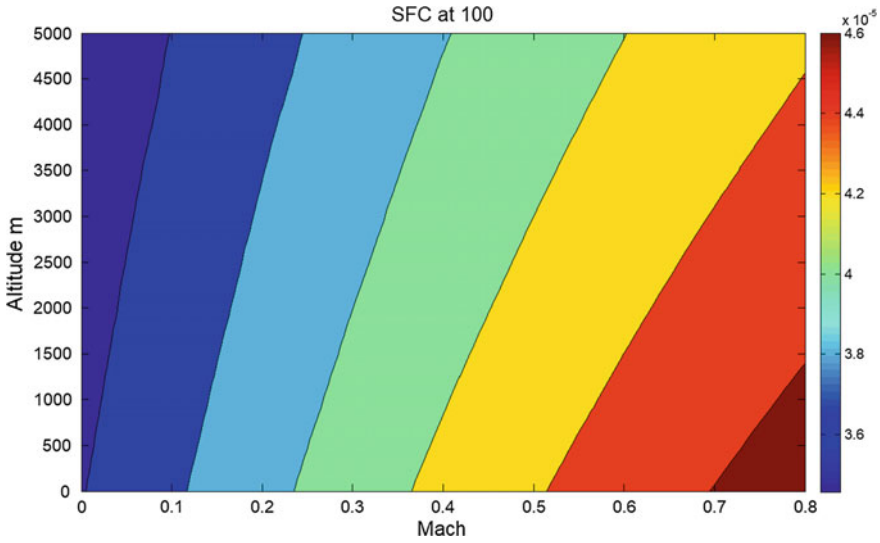
Fig. 22 Variation of SFC at 100% RPM with altitude and Mach number

References

1. Leyes RA, Fleming WA (1999) The History of North American Small Gas Turbine Aircraft Engines. AIAA
2. Pilidis P (1983) Digital simulation of gas turbine performance, Doctoral dissertation. University of Glasgow
3. Ismail IH, Bhinder FS (1990) Simulation of aircraft gas turbine engines. In: ASME 1990 international gas turbine and aeroengine congress and exposition. American Society of Mechanical Engineers, pp V002T02A033–V002T02A033
4. Sanghi V, Lakshmanan BK, Sundararajan V (2000) Survey of advancements in jet-engine thermodynamic simulation. J Propul Power 16(5):797–807
5. NATO (2002) Performance prediction and simulation of gas turbine engine operation, RTO TR-044/AVT-018
6. Walsh PP, and Fletcher P (2004) Gas turbine performance, 2nd edn. Blackwell science, Oxford
7. Cohen H, Rogers GFC, Saravanamuttoo HIH (1996) Gas turbine theory, 4th edn. Longman House, Essex
8. Cumpsty N (2003) Jet propulsion. United Kingdom at the University Press, Cambridge, Cambridge University Press
9. Mattingly, JD (2006) Elements of propulsion: gas turbines and rockets. AIAA Education series, Blacksburg, Virginia

Rotor Blade Vibration Measurement on Aero Gas Turbine Engines

T. Devi Priya, Sunil Kumar, Devendra Pratap, S. Shylaja, T. N. Satish, and A. N. Vishwanatha Rao

Abstract Rotor blade vibration in turbomachinery has been a major cause of failure due to HCF, often resulting in catastrophic damage. The primary aeromechanical design concerns are blade flutter and forced vibration that need to be quantified. The severity of blade vibratory response is almost impossible to predict using theoretical tools as it depends on the strength of excitation. Hence in order to evaluate the HCF characteristics of rotating blades, aero industry depends on measurements for actual vibratory response during engine tests. Various methods are used for measurement of rotor blade vibration. Conventionally strain gauges are extensively used for characterizing vibratory signatures of rotating blades. However, the strain gauges have their own limitations posed by operating temperatures and high-end technology is required to transmit signal from rotating components. Hence only a few blades in a rotor can be instrumented resulting in limited data capture. This paper presents a non-contact type of measurement technique using blade tip timing to capture vibratory signatures of all the blades of the rotor stage. This method is used to characterize monitor rotor blade vibrations of Low-Pressure Compressor and Low-Pressure Turbine of a developmental gas turbine engine. It has provided valuable data with respect to incipient damages, preventing catastrophic failure.

Keywords HCF · Blade resonance · Flutter

1 Introduction

Since the advent of gas turbines, and their applications in various industrial sectors, blade failures have proven to be a major cause of breakdown, often resulting in catastrophic damage [1]. The most common types of vibration problems that concern the designers are resonant vibration occurring at an integral order and flutter, an aeroelastic instability occurring generally as a non-integral order vibration, having

T. Devi Priya (✉) · Sunil Kumar · Devendra Pratap · S. Shylaja · T. N. Satish ·
A. N. Vishwanatha Rao
Gas Turbine Research Establishment (GTRE), Ministry of Defence, Bangalore, Karnataka, India
e-mail: devipriya@gtre.drdo.in

the potential to escalate, into larger stresses thereby may lead to structural failure of the blades.

Measurement of blade stresses by conventional method involves instrumenting selected set of blades with strain gauge. High-speed slip ring or telemetry unit housed inside the engine is required for data transfer from rotating strain gages to stationary data acquisition systems. As robust case mounted sensors are used by NSMS system, it can perform long term health monitoring tests with minimal probe maintenance as against the conventional strain gauges which have a high mortality rate. The more innovative, Non-intrusive Stress Measurement System using blade tip timing method uses time-of-arrival to characterize and monitor the blade vibratory response of all blades. The present study elaborates the usage of NSMS system for monitoring LP Turbine and Fan blade vibration in a developmental aero engine program.

2   Blade Tip Timing Technique

BTT is a non-intrusive technique for characterizing vibrations of bladed systems in rotating turbomachinery [2–5]. Figure 1 shows the schematic of BTT technique. The system consists of tip timing sensors, signal conditioners, PXI based data acquisition, and monitoring system to acquire the response of every single blade on a rotor stage.

The case mounted sensors sense every blade pass to give an analog signal. The sensor outputs are suitably conditioned and processed to generate TTL pulse for each blade pass using BVSI unit. The generated TTL pulse is then timed accurately using high speed (80 MHz) counter/timer hardware. This data is then used in conjunction with a 1/rev sensor mounted on the shaft of the engine to compute blade time-of-arrival information for each blade which is a measure of blade tip deflection.
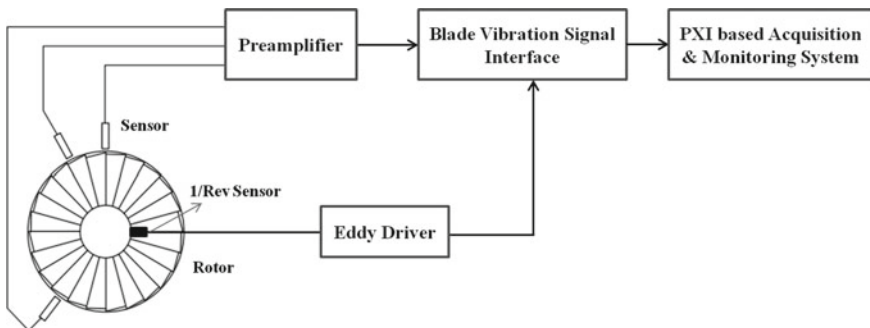
Fig. 1 Schematic of BTT technique

3   Computation of Blade Tip Deflection Using TOA

The calculated time-of-arrival defines the actual position of a blade. In case of a uniformly spaced rotor with vibrations, a difference between the calculated and measured TOA is reported as a blade lag, either positive or negative. However, a uniformly spaced rotor with no vibrations will always have the same TOA, assuming the static deformation to be constant [6, 7], Fig. 2.

The TOA of each blade is converted to deflections using the following equation

$$\text{Blade Tip Deflection} = \text{Vt} = 2\pi r\left(\frac{\Delta t}{T}\right)$$

where
Rotational Velocity (V)—revolutions per minute
Radius to blade tip (r)—inches
Δt = calculated TOA—measured TOA
T—time for one revolution of all the blades

From the blade tip deflections, stress levels can be calculated using stress to deflection ratios obtained from FE models.
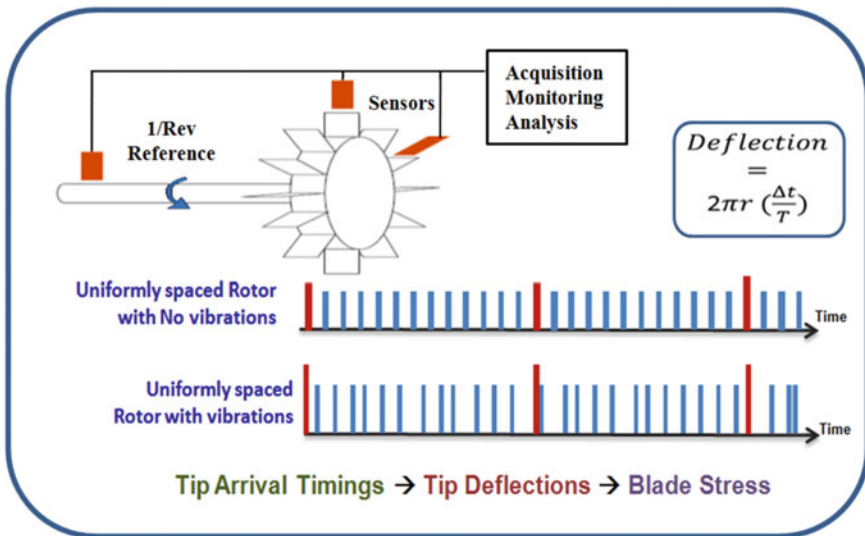
Fig. 2 Computation of blade tip deflection

4   Instrumentation

NSMS instrumentation consists of a set of case mounted sensors that determine the time-of-arrival of a blade tip at a particular case location. This characterizes the entire rotor stage, including the disk. Various types of sensors such as passive eddy current sensors, optical sensors, capacitive sensors, and magnetic sensors can be used to produce a signal for each blade pass [8–10]. The tip timing method utilizes these signals to measure the arrival times of the rotating blades with respect to the non-vibrating reference signal, to compute the blade vibrations for every revolution. However in this method, knowledge about the existing vibration modes is a prerequisite.

Sensors selection and placement on the rotor circumference is critical in configuring the NSMS system for blade vibration during resonance. This location is decided based upon the blade modes of interest and expected engine order crossovers in the operating regime [4]. Figure 3 shows the angular positions of the sensors as implemented on Fan, Bearing housing (1/rev), and LPT. Measurements are made on the blade trailing edge based on the max deflection pattern obtained from finite element analysis and site availability on the blade tip. Figure 4a shows photograph of a once
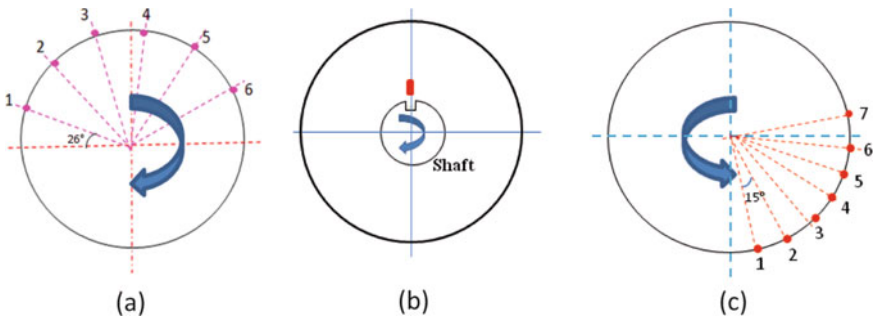
Fig. 3 a Circumferential sensor location on Fan casing **b** 1/Rev sensor in bearing housing **c** Circumferential sensor location on Turbine casing
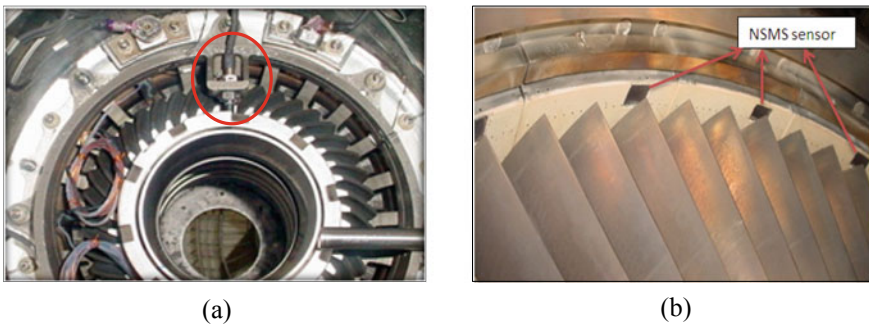
Fig. 4 a 1/Rev sensor installed on engine **b** NSMS sensor installed on the Turbine casing
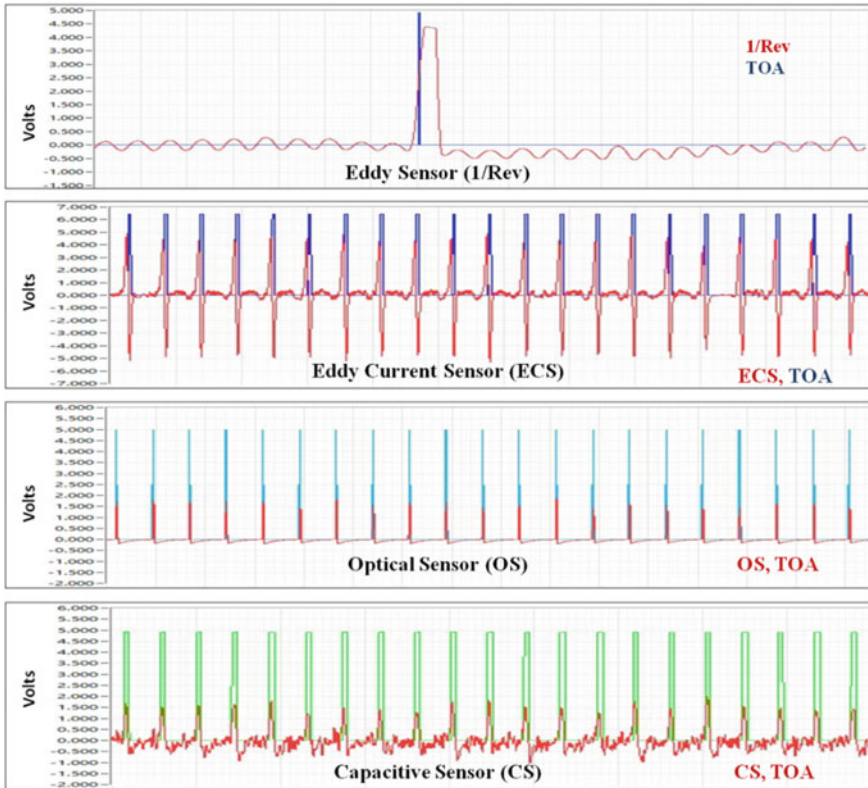
Fig. 5 Sensor output and its TOA from various types of sensors

per revolution (reference) sensor mounted in the bearing housing. Figure 4b shows photograph of NSMS sensors installed on the turbine casing facing the tip trailing edge of the blade. The sensor output and TOA pulse captured for one revolution for various types of sensors are given in Fig. 5.

5 Tip Timing Data Analysis

During engine testing rotor blades usually undergo two kinds of blade vibration— Forced vibration and Flutter. Forced vibrations are due to the stationary disturbances that could be upstream and downstream vanes or inlet flow distortion. Synchronous resonances are assembly modes that are excited at integer multiples of the rotational speed. This multiple is referred to as the Engine Order (EO) of excitation. At a given speed, the phase of the response remains fixed relative to a stationary (and arbitrary)

datum. Asynchronous vibration mainly occurs because of aerodynamic instabilities and hence both the resonant frequency and the phase of the response can be arbitrary. NSMS system has different algorithms to process synchronous and asynchronous vibration. It uses SDOF curve fit for analyzing synchronous vibration and spectral analysis for asynchronous vibration. SDOF curve is used to extract resonance characteristic parameters—amplitude, frequency, phase, and q-factor [4, 9].

6 Engine Test Results and Case Studies

6a Case Study-1: Low-Pressure Turbine Blade Failure Avoidance during Engine Testing

In the case of synchronous vibrations, the blade frequency of vibration is an integer multiple of the rotational frequency of the assembly. The blade tips have nominally the same displacement every time they pass the probes if the assembly is running at a constant speed. Hence, the displacement data are essentially repeated at each revolution and the analysis of the data becomes a lot more difficult.

The synchronous analysis method, therefore, needs an RPM sweep across the expected critical speed where the displacement data will vary for each revolution. When the computed TOA data for every revolution is plotted against engine RPM, this data forms the resonance Frequency Response Function (FRF). The vibratory response parameters—resonance frequency, response amplitude, resonance factor, and phase are then computed, through an SDOF curve fit approach. The process characterizes the resonant response of each blade in the disk. The critical resonance crossovers in the operating regime are predicted using FEM and analytical Campbell diagram generated is shown in Fig. 6.

Damage in rotor blades, including cracks, tend to shift the blade's resonant frequencies. Blade resonances have thus envisioned as damage indicators [11–13]. In this case study, the low-pressure turbine stage of a developmental aero engine is instrumented with high-temperature eddy current and optical sensors. The sensors are placed circumferentially on the turbine casing as shown in Fig. 4c to capture third and fourth engine order (3EO and 4EO) resonances for the first blade bending mode (1F). During engine tests blade vibratory amplitude and resonance frequency of all the blades are monitored. Post-test analysis is carried out to extract vibratory response parameters. The SDOF curve fit for LPT blade-12 in healthy condition during 3EO resonance crossover from all the sensors is shown in Fig. 7a. During a particular Engine test, it was observed that blade-12 had a drop in its 3EO resonance frequency. Suspecting a propagating crack in the particular blade, the engine operator was cautioned to abort the engine test. Post synchronous analysis (SDOF) indicated four percent drop in 3EO frequency accompanied by reduction in resonant amplitude, as shown in Fig. 7b. The 3EO frequency scatter of all LPT blades for the normal and the aborted engine tests is shown in Fig. 8. The test Campbell diagram of the suspected blade-12 is plotted in Fig. 9. Later the engine was removed for detailed
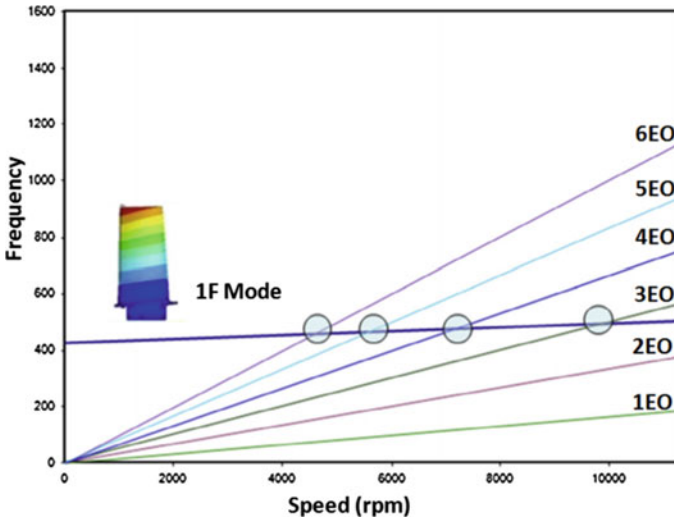
Fig. 6 Analytical Campbell diagram

inspection. The suspected blade was subjected to Fluorescent Penetrant Inspection. FPI confirmed a major crack in the suspected blade. Thus a major catastrophic engine failure was averted.

6b   Case Study-2: Flutter Detection in Fan Blades

In the case of asynchronous vibrations, blades vibrate at frequencies that are not multiples of Engine order [9, 13–15]. The traveling wave analysis is used for non-synchronous responses, such as flutter, where the blades vibrate at same frequency and constant phase difference. The best way to analyze flutter data is to process it as a coherent vibration where each blade is treated as a sampling of this waveform. Nodal Diameter (ND) pattern of the response can be determined by comparing the measured phase of the cross-spectrum between two sensors and comparing it to the circumferential angle between sensors. As blade vibrations are measured in the stationary frame of reference, true blade frequency in the rotating frame is then computed using the following equation

$$f_{observed} = f_{true} \pm ND\ f_{shaft}$$

where ND is the number of nodal diameters in the vibration pattern.

In this case study, Fan first stage rotor of a developmental aero engine is instrumented with eddy current, capacitive and optical sensors. The sensors are placed circumferentially on the fan casing (Fig. 4a) to capture both integral and non-integral engine order resonances in the operating regime. During one of Engine test, high asynchronous vibratory response was observed at 86 % dwell. Since the response amplitude was exceeding the limits, warning was provided to abort the test. Detailed
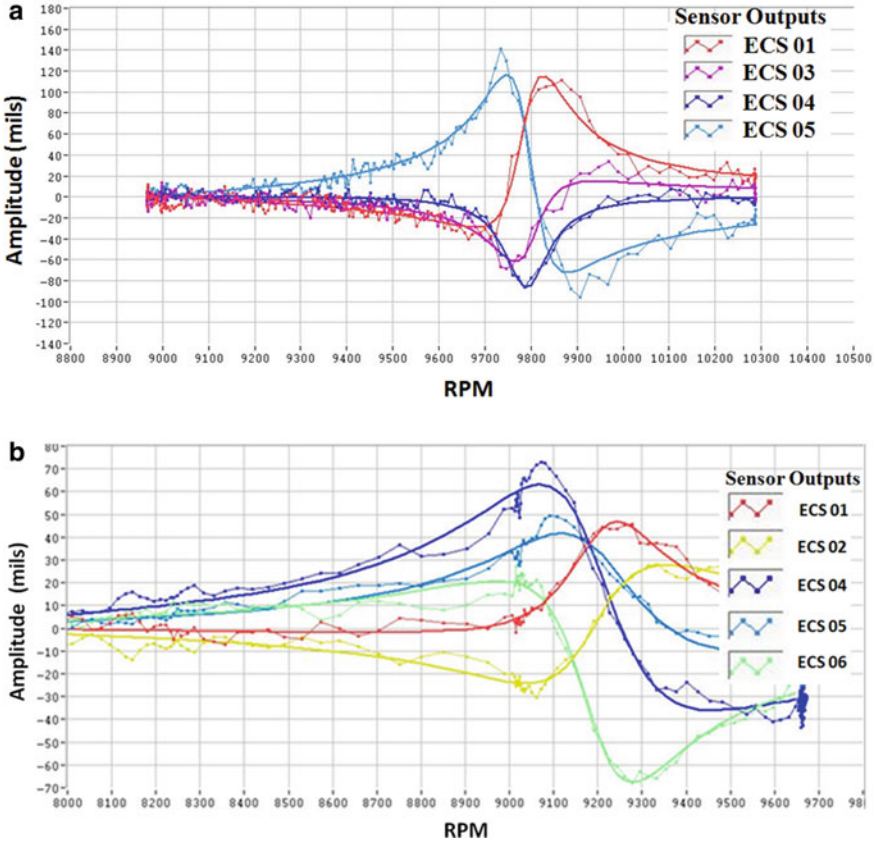
Fig. 7 **a** 3EO SDOF curve fit for blade-12 in healthy condition **b** 3EO SDOF curve fit of blade-12 indicating 4 % drop in frequency
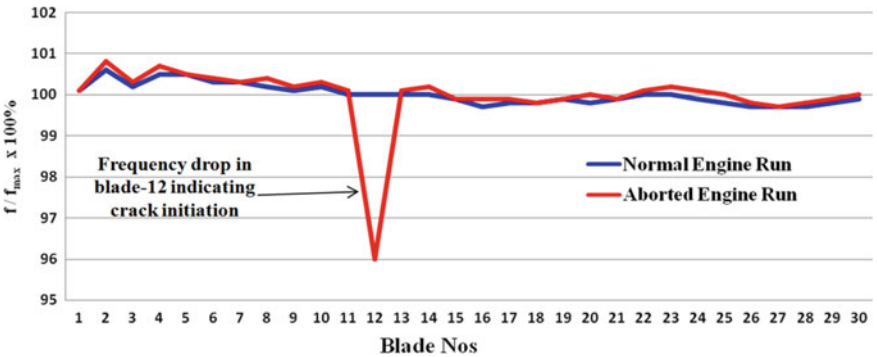
Fig. 8 3EO frequency scatter of LPT blades during normal and aborted engine runs
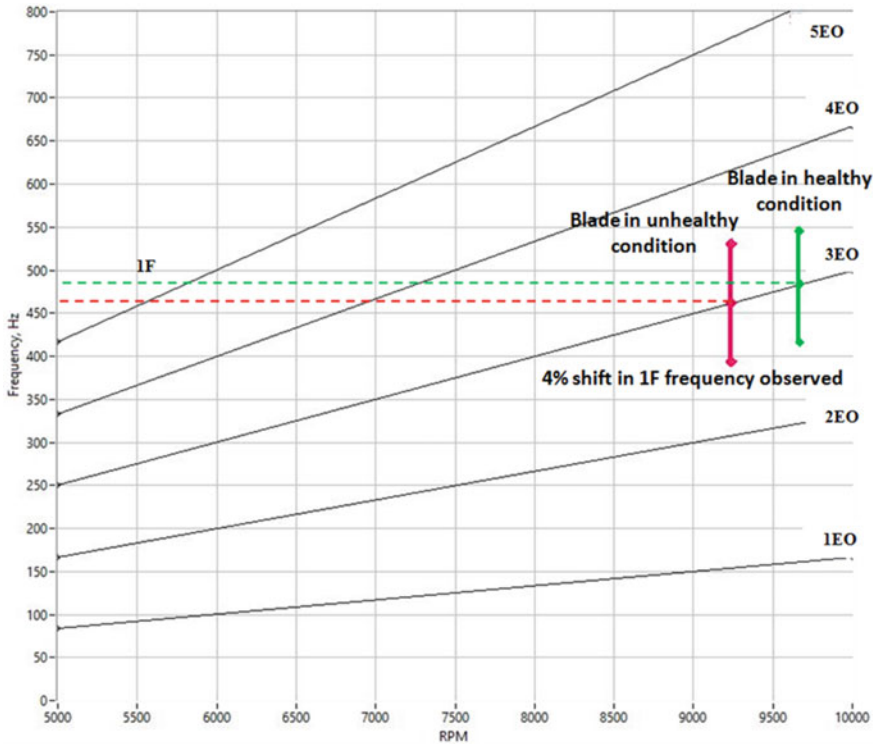
Fig. 9 Test Campbell diagram of blade-12

offline analysis was carried out to investigate the cause of high amplitudes. Test Campbell diagram (Fig. 10) indicated that blades vibrated at 1.8EO, dominant with 2ND. The investigation revealed that flutter was the cause for high blade vibration.

7 Conclusion

The ability of NSMS system for monitoring synchronous and asynchronous vibration of rotating blades has been demonstrated with two case studies. It has provided valuable data with respect to incipient damages, preventing catastrophic failures.
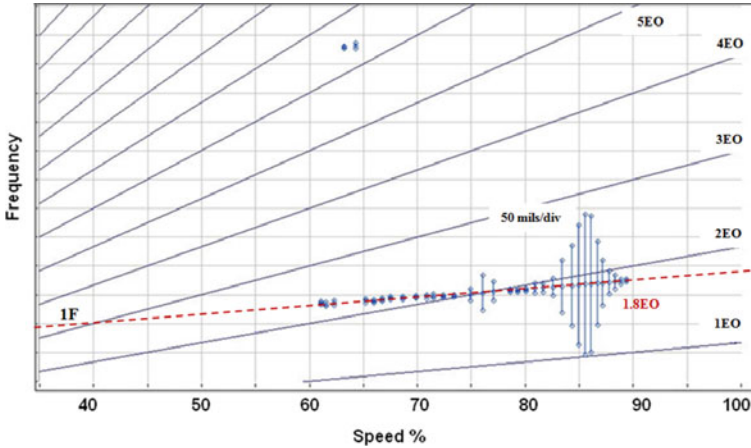
Fig. 10 Test Campbell diagram during Fan1R flutter

References

1. Meher-Homji CB, Gabriles G, Gas turbine blade failures - causes, avoidance and trouble shooting. In: Proceedings of the 27th turbomachinery symposium
2. Heath S, Imregun M (1998) A survey of blade tip-timing measurement techniques for turbomachinery vibration. J Eng Gas Turbines Power 120(10):784–791
3. Zielinski M, Ziller G (2005) Noncontact blade vibration measurement system for aero engine application. In: 17th international symposium on air breathing engines, Paper No. ISABE-2005-1220, Munich, Germany, September 2005
4. Zielinski M, Ziller G (2000) Noncontact vibration measurements on compressor rotor blades. Meas Sci Technol 11:847–856
5. Von Flotow A, Mercadal M (2002) Turbine rotor health management with blade tip sensors: from laboratory tool to fielded system. Proc Int Instrumen Symp 48:277–286
6. Computation of blade tip deflection. www.hoodtech.com
7. Computation of blade tip deflection. www.agilis.com
8. Von Flotow A, Drumm MJ (2004) Blade tip monitoring with through the case eddy current sensors. Sens Mag 21:6–10
9. Imregun M, A review of analysis techniques for blade tip-timing measurements. In: Proceedings of the ASME 1997, international gas turbine and aero engine congress and exhibition
10. Capacitive sensors used for tip-timing. www.rotadata.com
11. Mercadal M, Von Flotow A, Tappert P (2001) Damage identification by NSMS blade resonance tracking in mistuned rotors. IEEE Aerosp Conf Proc 7:3263–3277
12. Siddhartha SG, Shylaja S, Kumar S, Murthy R (2013) Pre-emptive rotor blade damage identification by blade tip-timing method. In: Proceedings of the ASME 2013 gas turbine india conference, GTINDIA2013, Bangalore, India, December 2013

13. Zielinski M, Ziller G, Noncontact crack detection on compressor rotor blades to prevent further damage after HCF-Failure
14. Srinivasan AV (1997) Flutter and resonant vibration characteristics of engine blades. J Eng Gas Turbines Power
15. Srinivasan M, Jeyaraman S, Jain R, Chandramohan S, AnandaRao Seshadri S (2013), Flutter and forced vibration characteristics of a turbo fan bladed disk rotor. In: Proceedings of the ASME 2013, gas turbine india conference, GTINDIA2013, Bangalore, India, December 2013

Challenges in Engine Health Monitoring Instrumentation During Developmental Testing of Gas Turbine Engines

A. N. Vishwanatha Rao, T. N. Satish, Anagha S. Nambiar, Soumemndu Jana, V. P. S. Naidu, G. Uma, and M. Umapathy

Abstract Developmental testing of gas turbine propulsion systems involves iterative experimental studies right from First Engine to Test (FETT) till production release. During initial design validation tests, engines require dedicated instrumentation for carrying out online monitoring with a capability to detect and isolate impending failures which may lead to structural damage. Instrumentation may be optimized further over the developmental lifecycle to determine the general engine health and life consumption of critical parts. Instrumentation generally focuses on monitoring of structural and aerodynamic behavior of engine subsystems. It is challenging to arrive at optimum instrumentation and methodologies of measurement with respect to engine performance and structural health monitoring. Structural health monitoring of rotating engine components poses challenges in acquiring high bandwidth data through either contact or non-contact sensing techniques and further data processing. Special instrumentation systems used for measuring various parameters from rotating parts as a part of health monitoring include slip rings, rotating telemetry, and non-intrusive strain measurement systems. Instrumentation of other engine parameters includes temperature, pressure, rotational speed, casing vibration, control actuator positions, flow rate, clearance between stationary and rotating parts and lubrication oil quality. Gas turbine engines are a complex assembly of rotating and stationary parts which operate at extreme temperatures which limits the operational capability of sensors. It is a challenging task to error budget complete measurement chains and arrive at uncertainties. Various aspects discussed in this paper are complex and inter disciplinary in nature. This paper provides a bird's eye view of the challenges associated with measurement systems during developmental stage of a gas turbine engine.

A. N. Vishwanatha Rao (✉) · T. N. Satish · A. S. Nambiar
Gas Turbine Research Establishment (GTRE), Ministry of Defence, Bangalore, Karnataka, India
e-mail: vishwanatha@gtre.drdo.in

S. Jana · V. P. S. Naidu
CSIR-NAL, Bangalore, Kartnataka, India

G. Uma · M. Umapathy
National Institute of Technology, Tiruchirapally, Tamil Nadu, India

1 Introduction

Propulsion system of an aircraft is not only the flight-critical system but also one of the complex systems encompassing various disciplines of science and technology. Apart from the fact that it is the primary source of propulsive power for the vehicle, it also provides the power for various other functions such as complete requirements of the vehicle in terms of electrical, hydraulic, and pneumatic power for various safety-critical subsystems of the vehicle. Health of the propulsion system is of paramount importance and is handled by a combination of onboard and ground-based engine health and usage monitoring systems. Topics covered in this paper are wide in scope. Authors of this paper have tried to bring out a profile of the challenges involved in identifying the requirements of health monitoring systems, sensor selection for performance and health evaluation, associated uncertainty issues, and sensor data fusion aspects during developmental testing an aero engine. Briefly the paper enumerates the instrumentation challenges encountered during performance evaluation of engines during normally aspirated and high-altitude tests.

2 Aero Engine Health Monitoring Architecture

The Engine Health Monitoring (EHM) functions in an aircraft operational context are distributed between several onboard engine mounted systems as shown in Fig. 1 [1, 2].

2.1 Engine Performance Monitoring

Modern engines are equipped with Full Authority Digital Engine Control (FADEC) systems. FADEC systems ensure optimum operability of the engine without violating safety limits within the flight envelope. Thrust of the engine is maintained at acceptable levels based on the throttle command throughout the engine life. Engine control schedules are designed to ensure thrust requirements are met even when engine wears out during normal operational service by allowing upward creep in rotational speed limits and exhaust gas temperature. When the operating parameters approach the limit, Built-In Test (BIT) codes are issued by FADEC so that engines are withdrawn for scheduled maintenance. In addition, significant and abrupt deterioration of the engine performance is handled by FADEC through onboard detection & revisionary algorithms and cockpit warnings leading to pilot action [3].
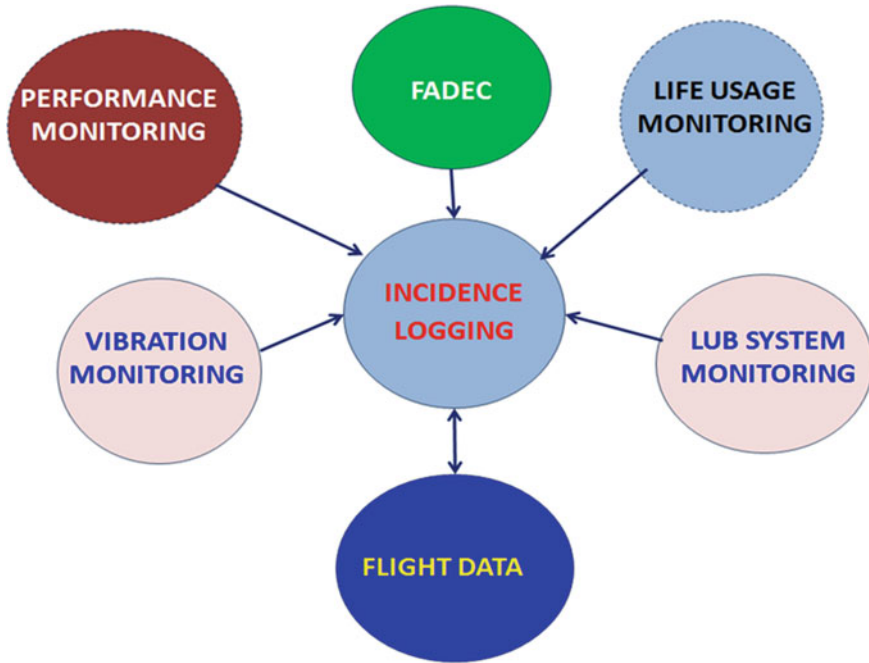
Fig. 1 Onboard systems to accomplish the engine health monitoring functions

2.2 Engine Vibration Monitoring

Structural vibration is an important health parameter throughout the operating life of an engine. Vibration signal is processed to get Root Mean Square (RMS) levels for quick onboard actions. Further, broadband signal is analyzed for frequencies tracked to rotational speeds of the shafts to identify the forced responses from telltale vibratory signatures of structural elements. Limits are specified for the broadband RMS vibration levels and the tracked-to-spool-speeds vibration levels to be within certain values for engine steady state and transient conditions [4, 5].

2.3 Life Usage Monitoring

It has been reported that engine accounts for a significant number of failures during air crash investigations. Out of this, almost 50 % of engine failures are attributable to Fatigue failures. Therefore, life usage monitoring based on engine exploitation considerations like the type of missions carried out, severity levels, and durations under operating conditions becomes essential for planning major maintenance actions. The Low Cycle Fatigue (LCF) life consumption of rotating parts are monitored using life

counters developed based on engine speed, stresses, temperature parameters at critical locations. High Cycle Fatigue (HCF) life tracking models are built using dynamic analysis and strain measurements. The thermal creep life consumption models are also developed from creep test data of materials used for hot end parts. Exhaust gas temperature measured using a set of sensors is used to predict the Turbine Entry Temperature (TET) and thereby assessing the creep life [4].

2.4 *Rotor Support and Lubrication System Monitoring*

Lubrication system of the aero gas turbine engine is another fundamental subsystem that has a strong bearing on the overall health of the bearings, gears, pumps, and other oil wetted parts of the engine—failure of lubrication systems leads to engine catastrophe. Hence, health of the lubrication system needs to be monitored continuously, both onboard and on-ground. Typical parameters used for lubrication system monitoring are oil pressure, oil level in tank, low oil pressure warning switch, differential pressure across filter, oil temperature (with high/low warning), oil quality, and oil debris content [2, 4].

3 Performance Monitoring of Developmental Engine

3.1 *Engine Operability Evaluation*

Aero engine health monitoring systems in an operational context are, as discussed in previous paragraphs, outcome of developmental tests of engines right from FETT to full Qualification Tests (QT) and flight tests. Engine health monitoring requirements during developmental phase throw up its own challenges since baseline performance and structural integrity of engine get established throughout the development cycle. Development phase has the luxury of utilizing abundant instrumentation both for performance and health monitoring and to troubleshoot various problems encountered. Development phase provide an opportunity to define a framework for defining the engine health monitoring framework tailored for the end use, associated algorithms along with validation tests and analysis tools required for operational phase. The development approach traditionally follows (a) understanding the complete design information, (b) development of simulation models, (c) subsystem level tests, (d) elaborate engine tests at normally aspirated ground test cells, (e) simulated altitude tests, (f) accelerated mission tests, (g) flight tests in a flying test bed, and (h) flight tests on target platform. During these developmental tests engine health monitoring algorithms initially defined evolve progressively and get firmed up with limiting numbers, usage aspects, and maintenance schedules. Traditionally limits are defined to be conservative to start with so as not to miss a potential hazardous fault from being

detected. As and when more engines get tested, more and more data gets accumulated which provide a better statistical database for fine-tuning of limits [4].

3.2 Gas Dynamic Stability Monitoring

During development of compressor and fan modules of an aero engine, initially its operating lines are estimated based on Computational Fluid Dynamics (CFD) studies. Subsequently, component level tests provide a better estimate of surge margin available. Further, fan and compressor modules are evaluated during engine-level tests, progressively increasing level of severity right from FETT stage till qualification tests stage. Engine level tests by introducing intake distortion and throttle transient are conducted to demonstrate the operability of the engines. Engine performance at steady state and transient conditions is essential to arrive at fan and compressor operating lines and control schedules [6]. Engine test data obtained from several tests needs to be processed to arrive at steady-state performance data [7, 8].

During component level tests, fan/compressor tests are conducted by spinning rotor at various speeds to vary the mass flow and throttle the exit plane till occurrence of stall signatures to increase the pressure ratio. Generally operating line estimates are obtained at steady-state mass flow and pressure ratio conditions. However engine operability requirements call for transients by the way of engine power settings to meet flight necessities. Transient migration of fan and compressor operating line cannot be taken up at the component level tests owing to the limitations of the test rig. It is the industry practice to arrive at the transient working line at engine level through dedicated engine-level tests. For compressor stages, the optimization study is required at the core engine level where variable geometry of the compressor stages is suitably staggered to get acceptable surge margin while providing required pressure ratio as depicted in Fig. 2.

During the exploration of engines for transient capability, especially during FETT, where the exact operating line is not yet established, there is a likelihood of engine surging. Since the exit plane of the compressor would be interfaced with combustor module at the engine level, surge of the engine invariably leads to exposure of many engine parts to hot gas. Surge at the engine level may lead to damage of engine. Hence there is a need to closely monitor engine operating line excursion online by suitable sensors and measurement systems during developmental tests. Dedicated instrumentation for online measurement of mass flow, pressure ratio through flow path pressure/temperature probes, and high bandwidth pressure sensors with a bandwidth of 2000 Hz to capture stall signatures at fan/compressor delivery are essential [9, 10]. In order to meet this requirement, systems with engine mass flow measurement having at least 5 Hz bandwidth and fan/compressor pressure ratio measurement with a bandwidth of 5 Hz are developed. Online compressor and fan operating maps as shown in Fig. 3 are provided during engine tests. This system aids monitoring of operating line migration during engine inlet distortion tests, throttle transient slam/chop tests, and after-burner tests.
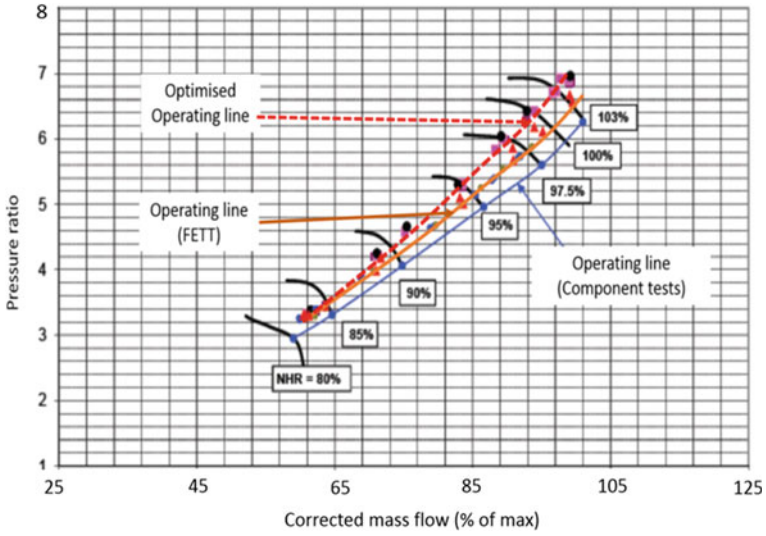
Fig. 2 Core engine compressor operating line optimization
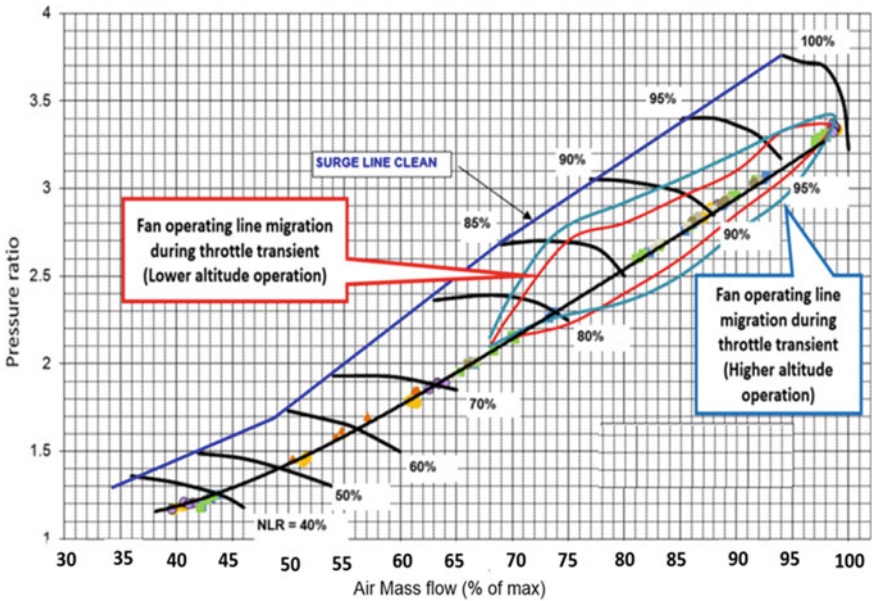
Fig. 3 Online monitoring of fan operating excursion during throttle transient tests

Fan and compressor surge margin varies with the inlet temperature variations within the flight envelope and hence there is a need to slow down the transients to conserve the surge margin at altitude conditions [9]. Transient working line excursions are handled by control algorithms which decide suitable fuel flow schedules. A fast acceleration requires aggressive fuel increase which moves the operating line of the compressor close to engine surge and similarly a fast deceleration moves the fan operating line close to surge line. There are guidelines [9] which specify the limits on the transient timings as a function of the flight point. During altitude testing of the developmental engines, fan and compressor operating line need to be closely monitored during transient tests wherein the control schedules are optimized for the transient timings as well as loss of surge margin.

3.3 Measurements for Transient Operating Line Monitoring

Engine gas path stagnation temperature and stagnation pressure at inlet and exit panes of fan and compressor are required for monitoring of engine operating line. Special flow path multi-point probes with suitable keils which give recovery factors better than 99 % (for pressure) and 96 % (for temperature) are developed and installed on the engine as shown in Fig. 4a, b [11]. Closed bead K type thermocouple wires of 1 mm diameter, in mineral insulated Inconel 718 tubes are placed within the keils to sense the temperature, whereas 1 mm diameter hypodermic Inconel 718 tubes are placed within the keils to sense the stagnation pressure in the pressure probes. During engine operation, temperature and pressure would always have a radial and circumferential distribution. It is essential to get an annulus average of the temperature and pressure for computation of engine mass flow and pressure ratio. An algorithm to find out

(a) (b)
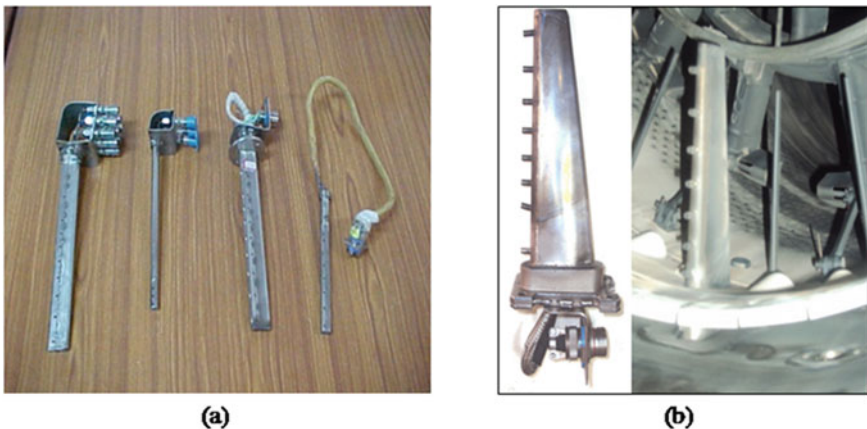
Fig. 4 Gas path measurement probes (**a**) Stagnation Pressure sensing probes (**b**) Exhaust gas temperature probes installed in the flow path on an engine [11]

the median of all the measurements made in a specific plane of measurement by recursive elimination method has been adopted.

It must be noted that temperature measurement would always have a lag compared to pressure measurement. Computation of corrected speed and mass flow requires temperature as one of the parameters. Since a throttle transient test calls for increasing the power setting of the engine from idle to maximum setting in less than five seconds, temperature measurement would lag the pressure measurement. Therefore there is a need to provide a lead compensator for the temperature measurement. Gas path pressure parameters sensed by engine probes are interfaced with the pressure scanners located close to the engine. Pressure measurement is accomplished with Commercial off the Shelf (COTS) pressure scanners which use Micro Electro Mechanical Systems (MEMS) technology-based pressure sensors with thermal compensation [12].

Rotational speed of the fan and compressor is measured by magnetic pulse probes [10]. These probes are variable reluctance sensing devices where a toothed wheel rotates underneath the probe as shown in Fig. 5. The frequency output from the probe is related to the speed of rotation of the toothed wheel which has a direct relationship with the rotor speed. Generally, the magnetic probe is mounted on the engine gearbox for measuring the High-Pressure Compressor (HPC) spool speed. For Low-Pressure Compressor/fan (LPC) spool speed measurement, the probe is mounted on the bearing housing and senses the serrations on the LP spool.
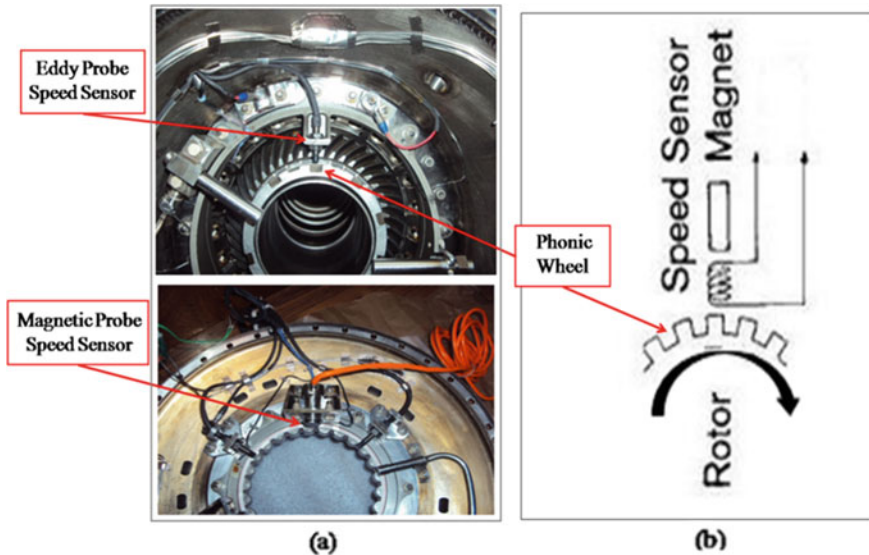
Fig. 5 Speed measurement on gas turbine engine (**a**) Installation of magnetic pulse probe and eddy current 1/rev probes (Courtesy: GTRE engine assembly documents) (**b**) Working principle of speed sensing [10]
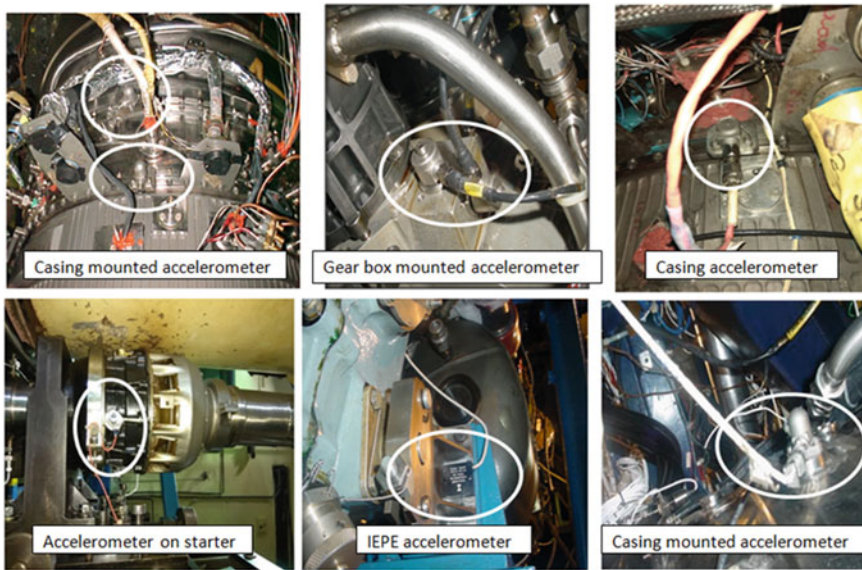
Fig. 6 Vibration transducer installation on aero engine components (Courtesy: GTRE engine assembly documents)

4   Health Monitoring of Developmental Engine

4.1   Structural Vibration

Piezoelectric accelerometers are universally used for measuring structural vibration (Fig. 6) of the engine. They are extremely robust and can also withstand reasonably high temperatures. While the bandwidth requirements for casing vibrations are typically of the order of 2 kHz, gearbox vibrations require a bandwidth of the order of 20 kHz. Charge amplifiers are required for conditioning the output of the accelerometers and the signal is further integrated to obtain vibration velocity (Fig. 7). MEMS-based accelerometers with integrated electronics for conditioning could be considered for low-temperature regions [10, 13, 14].

4.2   Rotor Blade Tip Running Clearance Monitoring

The clearance between the rotor blades and the casing in the fan, compressor, and the turbine stages is an important parameter that decides the efficiency of the component and the overall engine (Fig. 8). For engines used for fighter aircraft applications, the design clearance has to ensure that the components can withstand quick transients
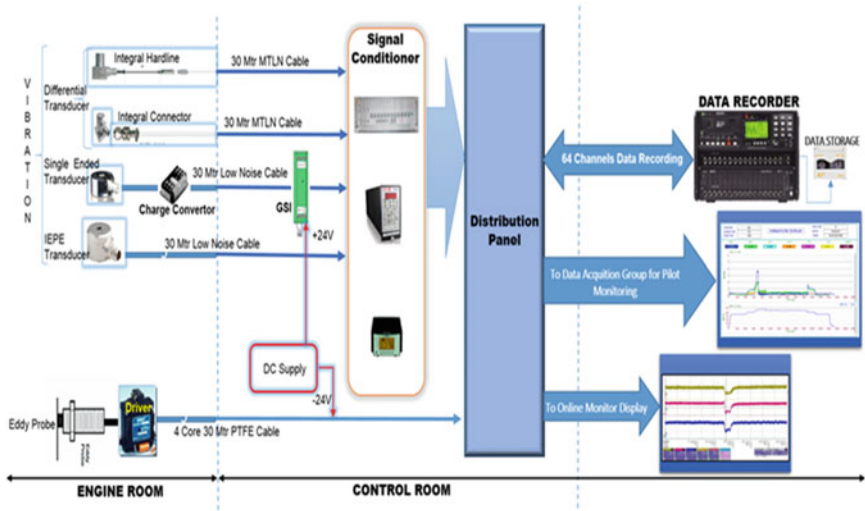
Fig. 7 Block diagram of vibration measurement system
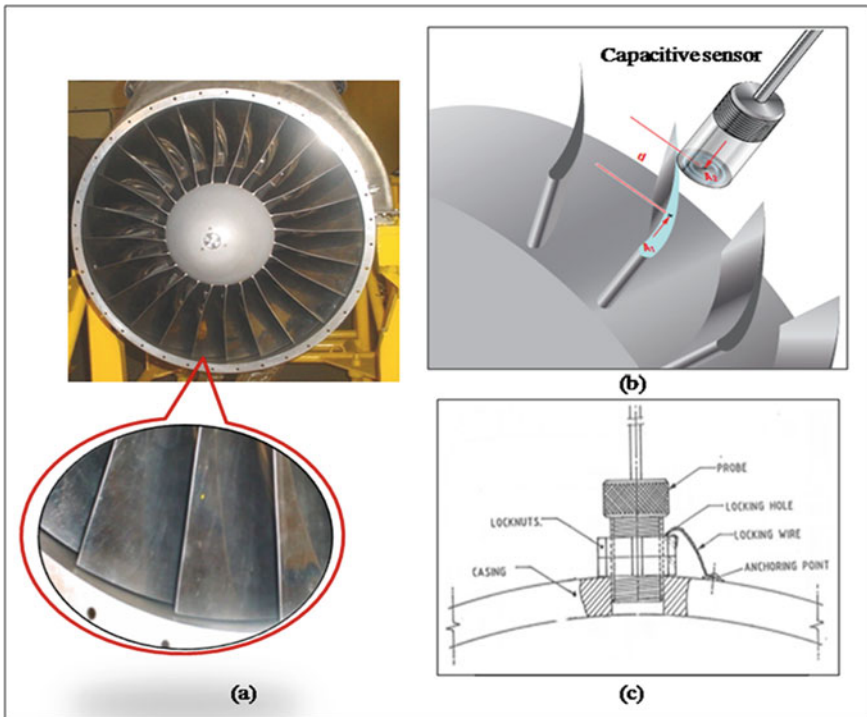
Fig. 8 Tip clearance measurement (**a**) Clearance between rotor tip and casing (**b**) Measurement concept (Courtesy: AOIP, www.aoip.com) (**c**) Sensor installation

and also aircraft maneuvers [15]. Non-contact sensing techniques are used to measure clearance. Most of engine houses use capacitive sensors located on the engine case for clearance measurement. The combined aero, thermal, and mechanical loads on the blades and casing results in the narrowing of clearance during engine test. If this parameter is not measured online during developmental tests, there is a chance that rotor blades could rub with the casing. For a FETT, the clearances are intentionally kept high in order to ensure safety and to capture the extent of possible growths and reduction of clearance, but this is at the cost of efficiency. Arriving at the exact clearance through measurement is a very complex and challenging process. During design, growths and expected running clearances are estimated through analytical tools. Simultaneously, aero, thermal, and mechanical loads act on rotating components like blades, disc, and static components like engine case. This results in differential growths. In case of a bypass engine, core and bypass cases grow relatively during engine operation. All these factors result in relative shift in the sensor position from its initial position. This apart, blade tip experiences untwist due to aerodynamic load resulting in shift in reference point which would have been used as a calibration point in cold state of engine, as per the engine mount positions. Probable sources of uncertainties are attributed to engine component deformations under aero-thermal loading, variation in dimensional parameters such as manufacturing tolerances, inspection/acceptance band, assembly errors, and finally measurement system errors. These errors have considerable effect on the tip clearance values. All sources of uncertainties need to be evaluated using analytical and experimental studies to cumulatively arrive at appropriate correction factors. Figure 9a shows the typical fan rotor arrangements, 9b shows the concept of axial shift, 9c shows the sensor response variation for shifted positions, and 9d shows the actual clearance arrived after applying the correction factor.

Uncertainty in measurements can be arrived at by estimation of bias and precision errors associated with each measurement factor and using typical statistical analysis to arrive at confidence levels above 95 %. The challenge here is to basically identify the factors involved and resolving them appropriately.

4.3 Rotor Blade Vibration

Traditionally blade vibration is measured using strain gages during development phase of the engine. Strain gage is the sensor element used for measurement of strains experienced by structures. Types of strain gages are mechanical, electrical, and optical strain gage. Strain sensitive material of electrical foil type strain gages is constantan, iso-elastic alloy, or karma alloy. Advantages of foil type resistance strain gages are that they are extremely small in size, insignificant in mass, easy to attach to the member being analyzed, highly sensitive to strain and capable of indicating both static and dynamic strains. Strain is sensed as change in the resistance of the element through a Wheatstone bridge-based signal condition circuit. Thermal compensation of the measurement is achieved through calibration coefficients. Strain
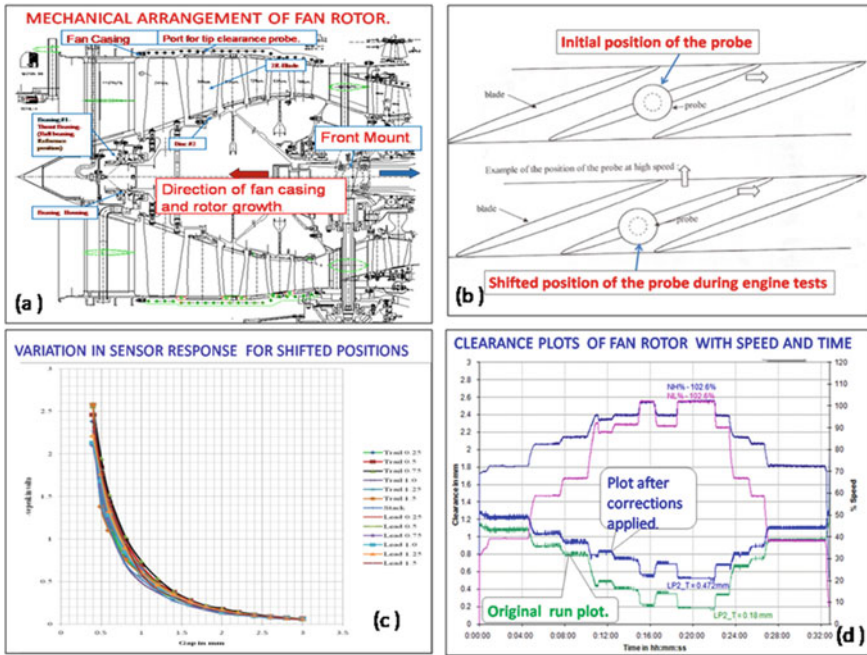
Fig. 9 Tip clearance measurement (**a**) Typical mechanical arrangement of fan rotor (**b**) Axial shift concept (**c**) Sensor response variation for shifted positions (**d**) Plot of actual clearance after applying correction factor [15]

from the rotating components is measured by routing the signals through slip ring arrangement (Fig. 10).

Disadvantages of instrumenting rotating parts are (a) high mortality rate (b) complex installation procedure involving modifications to engine rotor shaft to include slip ring assembly, and (c) limitation on the number of gages that can be used. Since the strain measurement is carried out on rotating fan blades, a high-speed slip ring is used for transferring the strain data from rotating blades to stationary data acquisition systems. Modifications are required on the engine components to provide a passage for the lead wires from the blade mounted strain gages to the slip ring unit mounted at the forward end of the engine. Holes have to be made on the fan rotor blades and disc to provide the passage for the lead wires. Hence, utmost care has to be taken to ensure the proper integrity of the lead wires as their failure can result not only in data loss but also may cause Internal Object Damage (IOD), that can be detrimental to engine.

However, the availability of non-contact blade vibration measurement systems (Fig. 11) [16] has opened up the possibility of monitoring the blade vibrations during the entire life of an engine, so that these can be used for both diagnostic and prognostic purposes. A number of casing mounted sensors, in each stage of the rotor (fan, compressor, or turbine) are used for obtaining the blade tip timing information,
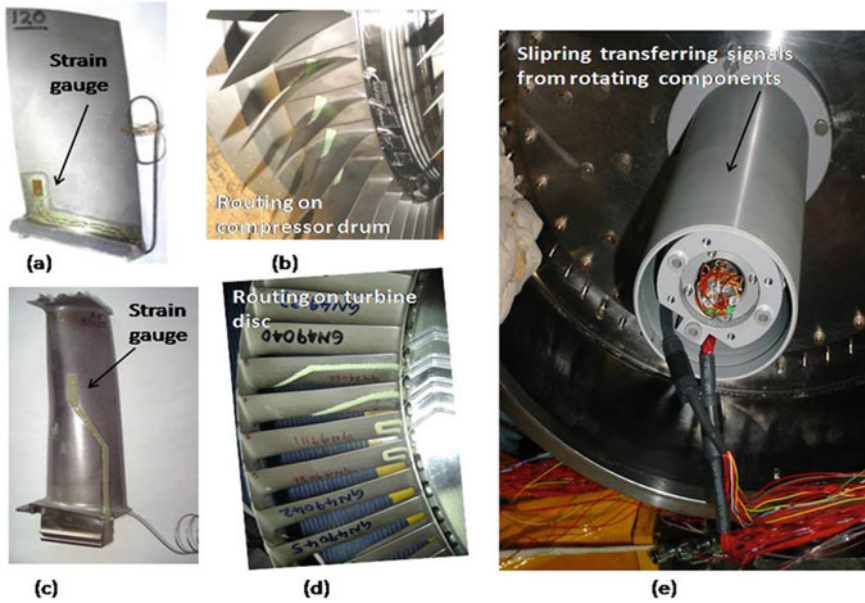
Fig. 10 Measurement of strain on rotating components (**a**) Strain gage installation on fan blade (**b**) Leads routing through compressor drum (**c**) Strain gage installation on turbine blade (**d**) Leads routing through turbine disc (**e**) Strain signal measurement through slip ring

which, coupled with the 1/rev reference signal, can be used to calculate the extent of blade vibration in terms of amplitude, frequency, and the modes. The system can monitor the health of each and every blade and can detect impending failures by measuring the shift in the resonance frequency and the blade lean. Capacitive, eddy, and optical sensors could be used for this application. Recently, microwave sensors have also been tried for sensing the blade tip timing. In addition, all these sensors have the potential to measure the tip clearance as well, thus serving two purposes.

Non-intrusive Strain Measurement System (NSMS) relies on a few proximity sensing probes mounted on the casing to measure rotor blade vibration [17]. The probes capture the Time of Arrival (TOA) of each blade relative to a non-vibrating reference, a 1/rev probe mounted on the rotor shaft. The TOA at the probe locations varies depending on frequency and amplitude of vibrations. The difference between the TOA of a vibrating blade and its computed TOA had it not been vibrating, provides the instantaneous blade amplitude.

The present case shows measurements made on fan blades of developmental aero engine by rotating instrumentation with strain gages and non-contact strain measurement system. During the test, fan blades encountered flutter in the first flexural mode (1F). Figure 12 shows the strain gage data indicating the magnitude of second engine order resonance of a small amplitude just before the blades latched on to the 1F flutter vibration mode. Figure 13 is the blade vibration due to flutter captured by the NSMS Campbell diagram indicating fan flutter.
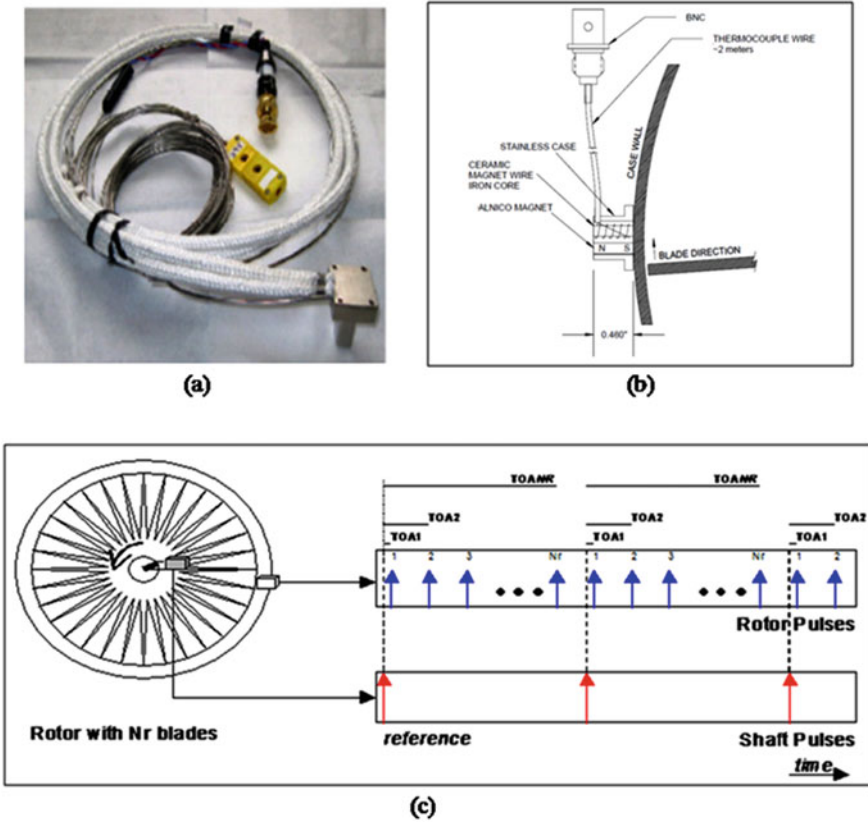
Fig. 11 Non-intrusive stress measurement system (**a**) Sensor (**b**) Sensor installation (**c**) Measurement concept (Courtesy: The Hood Technology Corporation, www.hoodtech.com) [16]
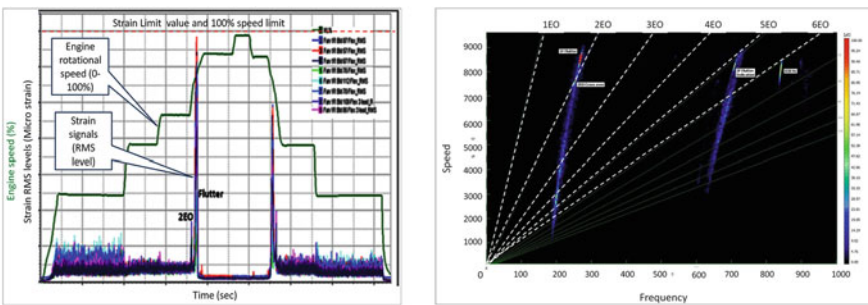
Fig. 12 (**a**) Trend plot of strain data (**b**) Campbell diagram of strain data
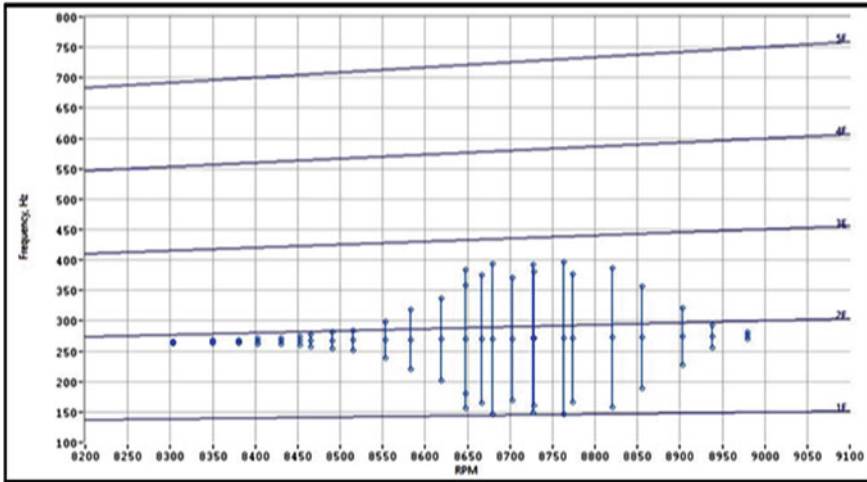
Fig. 13 Campbell diagram of 2 EO cross over and flutter as captured by NSMS

5 Sensor Suite Selection and Optimization for Engine Health Estimation

Traditional approach in terms of usage of sensors had been (a) To use a comprehensive suite of sensors during the development phases of the aero engine for ground testing (including testing in simulated altitude test facility), (b) To use a reduced set of sensors for flight trials, concentrating more on the engine-airframe interaction requirements, and finally (c) To use minimal set of sensors for the operational phase, primarily to detect abrupt degradation in the health of the engine requiring pilot action [18]. For an engine under design and development the sensors required for monitoring is large and may count more than a thousand. Broad requirements and gas turbine specific installation requirements are brought out in Table 1. Gradually as the algorithms are evolved, the numbers of sensors are reduced and finally an engine under service may have less than 20 sensors as depicted in Fig. 14.

During developmental tests on aero gas turbine engine, instrumentation is provided at subsystem level right from intake to exhaust planes of the engine. Table 1 enumerates the broad measurement requirements along with the environmental challenge in selection of sensors [3, 4, 11].

5.1 Challenges in Incrementing Engines for EHM and Mitigations

Table 2 lists the sensing parameters in EHM application, the associated challenges

Table 1 Gas turbine engine health monitoring sensor requirements

Module	Sensed variable	Sensor requirements	Sensor environment
Inlet	Static pressure	0–500 Hz bandwidth, 0.1 % accuracy, casing mounted installation	15–105 kPa, −60 to + 55°C
Inlet	Dynamic pressure	100 kPa differential, 10 kHz, 0.5 %	15–105 kPa, −60 to + 55°C
Compressor	Static pressure	35 kPa dynamic range, 0.2 % accuracy, 5–100 kHz bandwidth, case mounted	15–1800 kPa, −60 to 500/700°C
Compressor	Static pressure	35 kPa dynamic range; 0.5 % resolution; 20–100 kHz bandwidth (depending upon the flow phenomena measured)	15–1800 kPa, −60 to 500/700°C
Compressor	Clearance	2.5 mm range; accuracy 25 μm; 50 kHz bandwidth; case mounted	15–1800 kPa, −60 to 500/700°C
Compressor	Arrival time	Capacitance, eddy current or microwave probes; accuracy <25 μm; 50 kHz bandwidth; case mounted	15–1800 kPa, −60 to 500/700°C
Combustor	Static pressure	10 kPa dynamic range; 5% accuracy; 1 kHz bandwidth	300–4000 kPa, 700–1700°C
Combustor	Emissions (CO, CO_2, NO_x)	5% accuracy; <5 Hz bandwidth; Installation in HPT	300–4000 kPa, 700°C–1700°C
Combustor	Temperature	5°C accuracy; <1 Hz bandwidth; installation on HPT stator vanes	300–4000 kPa, 700–1700°C
Turbine	Clearance	2.5 mm range; accuracy 25 μm; 50 kHz bandwidth; case mounted	300–4000 kPa, 700–1700°C
Turbine	Surface temp turbine stator blade	Min resolution 5°C steady state; 1 Hz bandwidth	300–4000 kPa, 700–1700°C
Turbine	Static pressure	Equivalent to compressor flow control; steady flow control may be based on operating point	300–4000 kPa, 700–1700°C
Nozzle	Dynamic pressure	35 kPa dynamic range, 40–800 kPa static; 20–10 kHz	40–800 kPa, −60 to 700°C
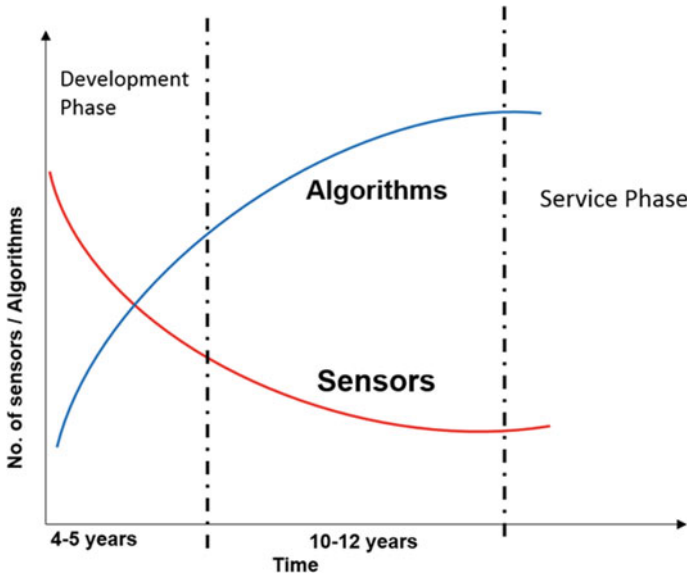
Fig. 14 Sensors on an aero gas turbine engine

in their instrumentation and mitigations arrived at based on several case studies and adherence to industry practices [11].

5.2 Data Interpretation and Decision Making

A high-end data acquisition and monitoring system hold the key for an efficient data capture and interpretation leading to right decision making. During a regular engine operation, engine and component performances are monitored through steady-state parameters measured across different stations of the engine. However in order to study the component life, creep and engine performance during transient operation it is required to measure fast-rising transients of all involved parameters using a high bandwidth system. Engine and component performance parameters are bench-marked with theoretical predictions using dedicated software tools for Finite Element Model (FEM), CFD, and Computational Heat Transfer (CHT) analysis. However there is always a deviation from theoretical predictions. Normally such deviations are attributed to component manufacture deviations, change in operating conditions, etc. Decision making is the art of interpreting huge amount of data coming from various sensors. This generally comes with experience after accumulating and cross-verifying with events and failures that were encountered [19]. Any failure analysis is a challenge as there is a need to analyze data from heterogeneous sensors which are acquired at different sampling rates from different sensing systems [19].

Table 2 Sensing parameters, instrumentation challenges, and mitigations

Parameter	Instrumentation challenges	Mitigations
Gas path temperature and pressure measurement	• Sensor probe protruding into the gas path. It could result in engine damage if it fails • Disturbs flow conditions • Engine performance gets affected	• Sensor rigidity ensured by design and validated by structural integrity tests • CFD done to compute blockage factor and suitable correction factors are established
Engine rotational speed	• Measuring with an accuracy of 0.01 % • Eliminating the uncertainty of 1/rev reference signal	• Multi serration phonic wheel for speed sensing. • Accurate machining of serrations
Pressure pulsation	• Temperature limitation prevents flush mounting of sensors • Extended tubing results in lower bandwidth systems but of acceptable levels	• Semi-infinite line tubes are used to increase bandwidth of measurement [18]
Structural vibration	• Difficult to route the sensors from internal structures like bearing housing	• Special cables like Mineral Insulated (MI) cables and PTFE are designed and installed
Blade vibration (a) Rotating instrumentation	• Routing of slip ring leads • High mortality of slip ring lead wires	• Special instrumentation process for slip ring
Blade vibration (b) Non-intrusive Stress Measurement System (NSMS)	• Measuring the accuracy of time periods (<80 µs)	• FPGA based COTS systems to measure time period with <2 % error
Fuel flow	• A single sensor has to address high flow at lower altitudes and low flow at higher altitudes	• Usage of extended range flow meters
Rotor to stator running clearance	• Axial and radial expansion of rotor blades and casing due to thermal and centrifugal loads	• Obtain correction factors experimentally and validate it through studies

Entire data needs to be synchronized with a common time stamp as per Inter Range Instrumentation Group (IRIG-B) [20]. During an engine-level fault leading to a failure there will be close correlation between several measurements which must be analyzed together to reconstruct the events leading to the failure. One such comprehensive study has been presented in [21]. Here, sensor data fusion techniques were adopted for efficient data interpretation and decision making.

During the initial developmental phases, guidelines from MIL standards, AGARD reports, handbooks, and previous works reported by reputed engine houses are considered as standard guidelines toward making decisions. However each engine house develops their own analysis tools, algorithms which drive toward making right decisions. Normally such tools are proprietary in nature as they are built over years based on experience. The following figure, Fig. 15 enumerates methodologies adopted for
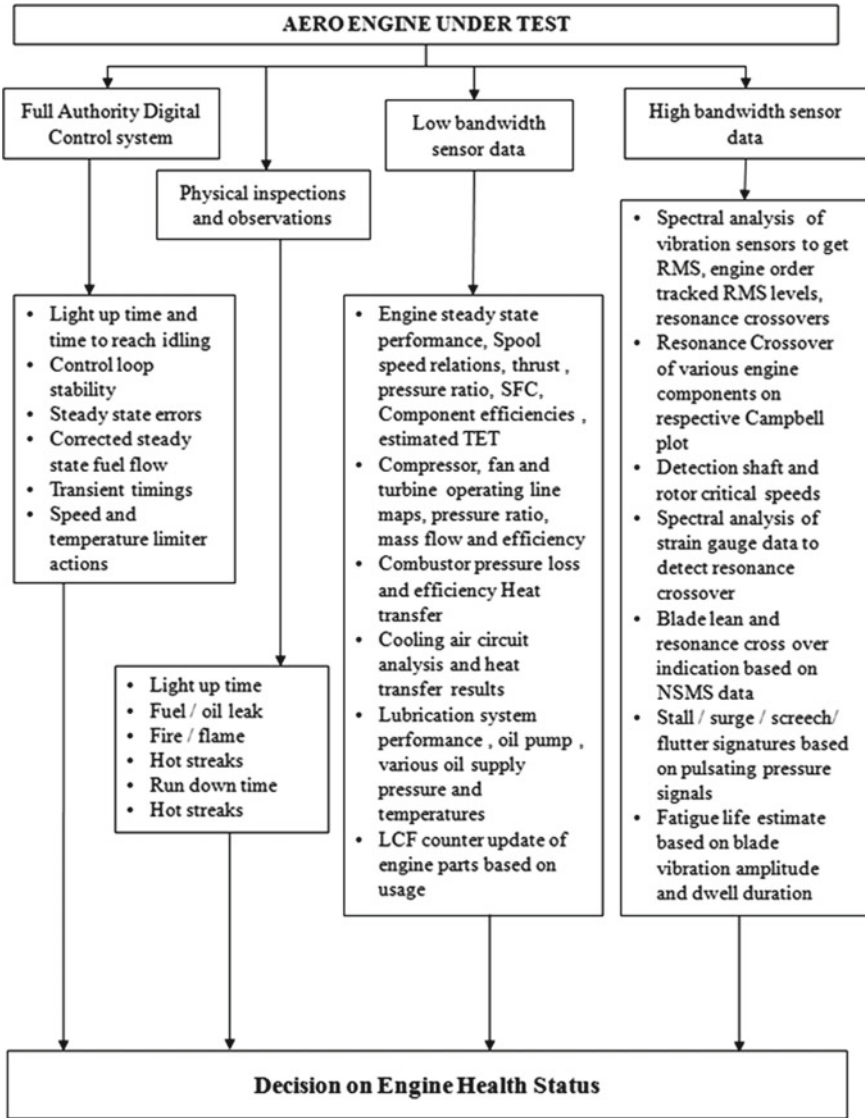
Fig. 15 Engine test analysis framework for engine health monitoring

standardizing the health monitoring data.

5.3 Incident Logging

An elaborate incident monitoring mechanism is built into the overall propulsion system health monitoring. The FADEC system, the EHMS, Engine Vibration Monitoring system, and the Lubrication System Monitoring system together detect and monitor various incidents of the engine triggered by engine structural or aerodynamic aspects, subsystems, and external causes. Sudden deterioration in the engine health condition is detected and suitable cockpit warnings are generated for pilot response. All incidents are stored in a database along with relevant engine sensor data for about 30–45 s prior to and post the incident.

6 Conclusion and Way Ahead

Recognizing the benefits of diagnosis and prognosis, the aero engine industry is looking at ways and means of providing on-condition maintenance support to aero engines. Current sensing technologies which aids not only in detecting abrupt changes in the performance of the engine, but also to track the gradual degradation of the engine due to wear and tear, are to provide better health and usage monitoring capabilities. However, current sensing technologies are limited to mostly ground tests.

Rugged and miniature versions of these sensing technologies are essential for adoption and usage on production/in-service engines so as to accurately predict the maintenance schedules without compromising the reliability and safety of the flight. Current onboard EHM systems mostly provide warnings which require pilot action to react to the situation. Incase these reactions need to be acted upon by onboard FADEC, there is a challenging need to arrive at an optimized sensor suite, fault detection, isolation, and reconfiguration algorithms. The algorithms thus developed would have to address the steady state and transient performance of the engine.

References

1. Horl F, Richter K (1995) Monitoring the EJ200 engine. In: Proceedings of the 18th symposium 'aircraft integrated monitoring systems', Stuttgart, Germany, 19–21 September 1995
2. Zoller T (2001) Advanced engine monitoring and diagnosis systems: actual system for the EJ200 engine of the EuroFighter 2000 aircraft and future trends. In: RTO AVT symposium on 'ageing mechanisms and control: part B—Monitoring and management of gas turbine fleets for extended life and reduced costs', Manchester, UK, 8–11 October 2001
3. More intelligent gas turbine engines. RTO Technical Report, TR-AVT-128, 2009

4. Recommended practices for monitoring gas turbine engine life consumption. RTO Technical Report RTO-TR-28 (2000), RTO Technical Report RTO-TR-28, 2000
5. Turner IY, Bajwa A (1999) A survey of aircraft engine health monitoring systems. In: Proceedings, AIAA, AIAA-99-2528
6. Viassolo DE, Adibhatla S, Brunell BJ, Down JH, Gibson NS, Kumar A, Mathews HK, Holcomb, LD (2007) Advanced estimation for aircraft engines. In: Proceedings of the 2007 American control conference, New York City, USA, 11–13 July 2007
7. Simon D (2008) A comparison of filtering approaches for aircraft engine health estimation. Aerosp Sci Technol 12:276–284
8. Simon DL, Litt JS (2011) A data filter for identifying steady-state operating points in engine flight data for condition monitoring applications. J Eng Gas Turbines Power 133:071603-1
9. MIL-E-5007D/E: Military specifications engines, aircrafts, turbojets and turbo fans, general specifications for, 1983
10. Ernest OD, Measurement systems Application and design. 4th ed., McGraw-Hill Publishing Company, ISBN 0-07-017338-9
11. Recommended practices for measurement of gas path pressures and temperatures for performance assessment of aircraft turbine engines and components. AGARD AR-245, 1990
12. Electronic pressure scanning modules Data Sheet No. G 480. www.scanivalve.com, ZOC 33
13. Craig M, Harvey TJ, Wod RJK, Masuda K, Kawabata M, Powrie HEG (2009) Advanced condition monitoring of tapered roller bearings, part I. Technol Int 42:1846–1856
14. Abdul-Aziz A, Woike MR, Oza N, Matthews B, Baaklini GY (2010) Propulsion health monitoring of a turbine engine disk using spin test data. NASA/TM – 2010-216743
15. Satish TN, Murthy R, Singh AK (2014) Analysis of uncertainties in measurement of rotor blade tip clearance in gas turbine engine under dynamic condition. Proc IMechE Part G: J Aerosp Eng 228(5):652–670
16. Overview of blade vibration monitoring capabilities, 2011. www.hoodtech.com
17. David HD, Stephan H (2018) A novel method for the design of proximity sensor configuration for rotor blade tip timing. J Vib Acoust 140(6):061003, Paper no. VIB-17-1510, March. https://doi.org/10.1115/1.4039931
18. Simon DL, Garg S (2009) A systematic approach to sensor selection for aircraft engine health estimation. In: Proceedings, ISABE, ISABE 2009-1125
19. Patnaik BVA, Rao ANV (2017) Key elements of engine health monitoring systems. AIS-2017-26. J AeroSp Sci Technol 69:168–173, February. ISSN 0972-950x
20. Overview of IRIG-B Time Code Standard 200-04. Technical Note TN-102, 2017. www.cyber-sciences.com
21. Dilip K, Sanjay B, Suresh TN (2013) Gas turbine blade damper: a design optimization study to mitigate high resonance blade vibration. In: ASME 2013 gas turbine india conference, paper no. GTINDIA2013-3748, pp V001T05A018-V001T05A024. https://doi.org/10.1115/gtindia2013-3748

A Practical Approach to Enhance the Flight Endurance of a Fixed-Wing UAV

Rajesh Mahadevappa, T. Virupaksha, and L.N. Raghavendra

Abstract This paper presents a summary of research toward extending the flight duration of fixed-wing unmanned aerial vehicles at ADE. A historical context to extended flight is provided and particular attention is paid to research in establishing the best operating profile for the Reciprocating Piston engine to meet the extended endurance target. With the limitation of the fuel capacity in the UAV, it is imperative to identify and operate the UAV at the lowest fuel consumption regime without compromising the mission objectives. Usage of variable pitch propeller along with operation of mixture control of the engine has resulted in the extension of endurance of up to 12 h. Autonomous flying presents a unique set of challenges whereby the flight computer of the aircraft must command and control the engine to be operated at the best operating regime. The basic mechanisms of variable pitch propeller operation are examined. During the present work, automation tables were evolved to aid the flight control computer.

Keywords UAV · Endurance · Variable pitch propellers

Nomenclature

c	Specific fuel consumption
C_t	Coefficient of Thrust
C_L	Coefficient of Lift
C_D	Coefficient of Drag
E	Endurance
m	Mass flow of air
T	Thrust
η	Propeller Efficiency
W_o	Gross Weight of Aircraft

R. Mahadevappa (✉) · T. Virupaksha · L.N. Raghavendra
Aeronautical Development Establishment, Bangalore, India
e-mail: rajeshm@ade.drdo.in

W1   Empty weight of Aircraft
L/D Lift to Drag Ratio
V   Forward Velocity
V_o Air Entry velocity
V_j Exit Velocity
VPP Variable Pitch Propeller
W   UAV weight
FPP Fixed Pitch Propeller
GCS Ground Control Station
HST High Speed Taxi

1   Introduction

Unmanned Aerial Vehicles (UAVs) play a vital role in surveillance and reconnaissance operations. The operations are typically dull, dirty, and dangerous in nature. The aircrafts need to be in the air and on target for longer durations to meet the mission objectives.

Historically, attempts have been made to arrive at the best possible operations of small aircrafts to achieve fuel efficiency and thereby stay in air for longer duration, as discussed in Carson et al. Ref. [1]. Carrying additional fuel tanks, using glide potential of the aircraft, operating at high L/D ratio, operating the aircraft engine at best specific fuel consumption, all have been looked at.

Rustom-I, a short-range UAV, is under development at ADE. This UAV is a conversion of twin-seater LongEz aircraft for unmanned applications. The Rustom Flight Control Computer (RFCC) replaces the pilot inside aircraft. The command and control of the aircraft is carried out through a Ground Control Station (GCS).

Lycoming O-320 B3B engine is the powerplant for this UAV. It is a 160 hp, naturally aspirated, carburetor engine using AVGAS 100 LL as fuel.

Fuel tank capacity is 200 Ltrs. The average fuel consumption, during cruise at an altitude of 8000 ft was 23 liter/h. Simple mathematics show, this aircraft cannot achieve 10 h of endurance target in its present configuration. Most efficient use of the available fuel can result in an improved endurance figure.

Description of parameters and their effect on endurance are explained below.

1.1   Endurance

By definition, endurance is the amount of time that an airplane can stay in the air on one load of fuel. Equation (1) is the general equation for the endurance E of an airplane. If detailed variations of C_t, L/D, and W are known throughout the flight, Eq. (1) can be numerically integrated to obtain an exact result for the endurance.

For preliminary performance analysis, Eq. (1) is usually simplified. Assuming flight at constant C_t and L/D the equation becomes

$$E = \int_{W_1}^{W_0} \frac{1}{C}\frac{1}{D} \text{In} \frac{\mathrm{d}Wf}{W} \tag{1}$$

Since the specific fuel consumption for propeller-drive airplanes is given in terms of power rather than thrust, the relation between c and C_t is

$$C_t = cV / \eta$$

Thus,

$$\text{Endurance} \quad E = \frac{1}{C_t}\frac{1}{D} \text{ In } \frac{W_0}{W_1} \tag{2}$$

Thus from Eq. (2), for achieving maximum endurance of the airplane the following conditions are to be met.

1. Cruise at maximum C_L/C_D.
2. Select a propeller with the highest propeller efficiency.
3. Operate the UAV at the lowest possible SFC.
4. Carry maximum amount of fuel onboard.

1.2 Lift-to-Drag Ratio

Traditionally, maximum Lift-Drag (L/D) ratio has been accepted as a primary figure of merit for a given airplane.

The L/D ratio enters the aircraft endurance calculations in an obvious way as explained in Eq. (2). Neglecting the variations in propeller efficiency (considering the constant-speed propellers to be integrated on this aircraft), it can be shown that the speed which maximizes range, is that corresponding to the best L/D for a propeller-driven aircraft. However, the speeds corresponding to maximum L/D ratio, does not seem to be practical for the reasons explained by Carson (1982) Ref. [1].

1.3 Propeller Efficiency

Propeller Efficiency is defined as the ratio of useful power converted as thrust to available power. The thrust produced is given by the Eq. (3)

$$T = m\left(V_j - V_o\right) \tag{3}$$

Thus, propeller efficiency is $\eta = 2 / 1 + \left(V_j / V_o\right)$ However, the airplanes operate at different forward speeds. Thus to operate an aircraft at the highest propeller efficiency with a fixed pitch propeller is next to impossible.

1.4 Specific Fuel Consumption

The specific fuel consumption is a technical figure of merit for an engine which reflects how efficiently the engine is burning fuel and converting it to power. For an internal combustion reciprocating engine, the specific fuel consumption c is defined as weight of fuel burned per unit power per unit time. The specific fuel consumption is insensitive to changes in altitude and forward velocity as seen in Chap. 3 of Anderson (2010). Ref. [2].

1.5 Variable Pitch Propeller

Propellers are classified as Fixed Pitch Propellers (FPP) and Variable Pitch Propellers (VPP). The propeller blade angle cannot be changed in FPP. The loss in performance of engines having fixed pitch propellers led to the development of VPP viz., (a) adjustable pitch propeller (b) controllable pitch propeller, and (c) constant speed propeller.

Fixed Pitch Propeller (FPP) is one-piece made of either wood or metal and is used in low-powered aircrafts. The drawback is that the engine output cannot be readily changed to meet the various conditions under which aircraft is flown. During the take-off and climb extra power is needed and propeller of low pitch is desirable. While cruising propeller of high pitch and lower engine output are most effective. When the UAV is in air, the engine has to be throttled back to prevent over speeding with a corresponding loss of power and speed.

In case of Adjustable Pitch Propeller, the angle at which blades are set can be changed while the UAV is on the ground.

Controllable Pitch Propeller, the blades may be rotated while UAV is in flight mode by hydraulic mechanism. It can be two, three, or multi-position system. The angle of blade setting varies with the engine power.

Constant Speed Propellers are equipped with system controller that automatically alters the pitch by hydraulic or electrical mechanism. Centrifugal governor regulates aircraft engine speed by continually varying pitch of propeller to match propeller torque (engine load) to engine developed torque as changes occur in flight conditions Ref. [4].

1.6　Lean Mixture Control

Lycoming O-320 is a carburetor fed engine with a provision for mixture control to compensate for the change in density of air at high altitudes. The mixture control lever, when operated regulates the amount of fuel delivered at the venturi of the carburetor for a particular throttle opening. Pilot controls this lean mixture lever, corresponding to the altitude of flying, while monitoring the exhaust gas temperatures and engine rpm as the reference parameters.

1.7　Propeller Selection

Lycoming O-320 has been used in aircrafts with various propellers including fixed pitch, variable pitch, constant speed propellers. A constant speed variable pitch propeller, manufactured by MT propellers was selected considering the engine horsepower, gear ratio, ground clearance, UAV operating speeds, and weight of the propeller.

2　Engine Control Logic for Uavs

All the three engine controls viz., throttle, propeller rpm, and mixture control were to be operated by the pilots in the sequence established during the ground tests and taxi runs. Also the lookup tables were prepared for automating the propeller rpm and mixture controls for specific forward speeds of the aircraft and cruise altitude. A sample profile for an UAV mission and the engine controls is described below in Fig. 1

3　Theoretical Estimation

A higher endurance demanded to carry full fuel, which increased the AUW of the aircraft, which in turn demands higher thrust. Thrust can be increased by using a bigger propeller or high-efficiency propeller. A constant-speed propeller manufactured by MT Propellers, Germany was found suitable for this application. Studies were carried out to estimate the performance of Lycoming O-320 engine (160 Hp) with Fixed Pitch Propeller (FPP) and with Variable Pitch Propeller (VPP). A mission analysis was also carried out using the following conditions of UAV to predict performance improvements of UAV (Fig. 2).

Maximum Take-Off Weight (MTOW)　650 kg, 730 kg, and 780 kg
Altitude ft. AMSL　　　　　　　　SL to 14000 ft.
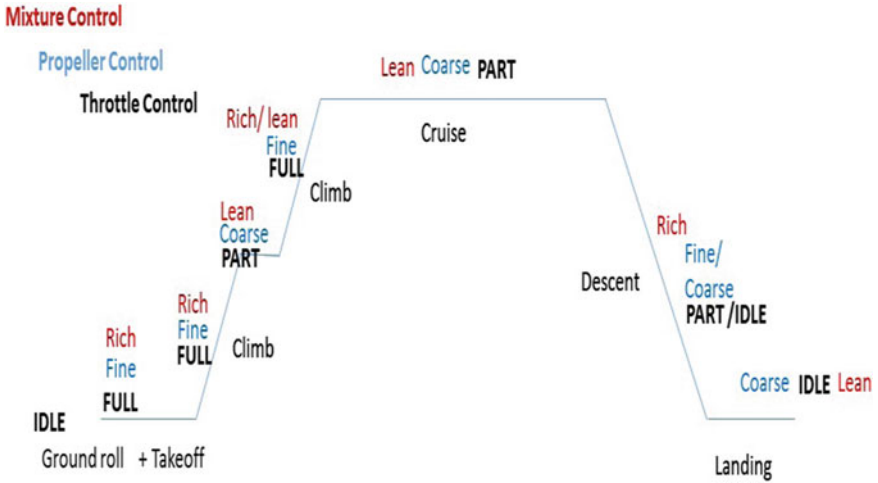
Fig. 1 Engine controls required during the UAV mission
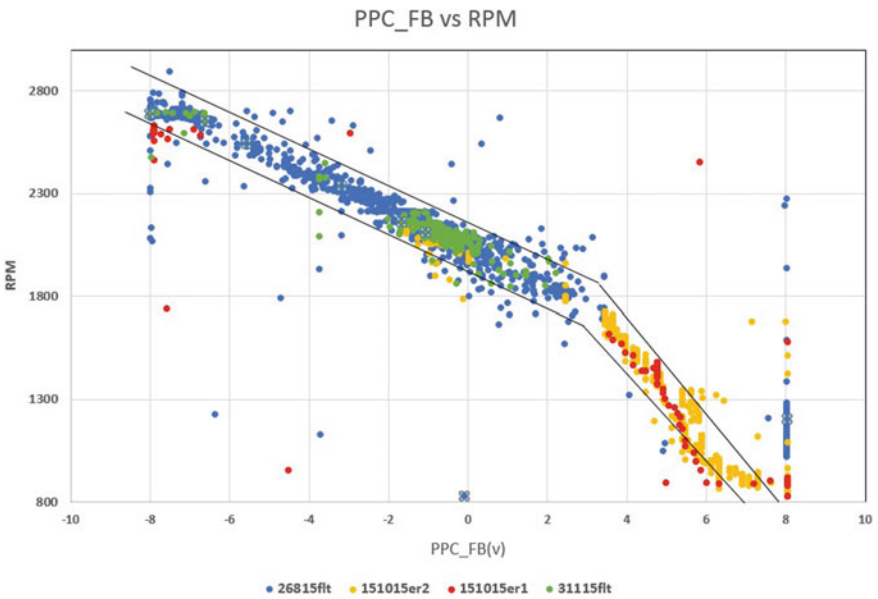
Fig. 2 Governor position Vs. Engine rpm during ground test and Taxi trial results

Aircraft speed, Knots	60–120
Fuel weight, kg	150–123
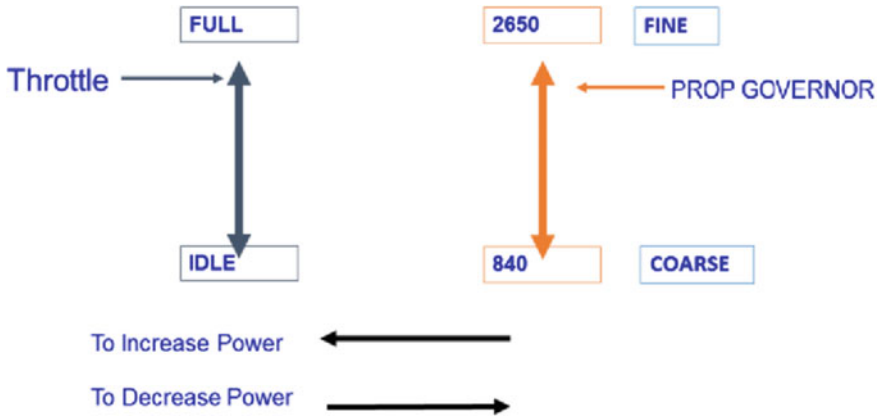
Fig. 3 Sequence of throttle and rpm control operation

The theoretical analysis shows an improvement in Take-off Ground Roll (TGR) distance and rate of climb of Lycoming O320 engine with VPP than that of Lycoming O-320 engine with FPP.

The analysis result shows that the take-off ground roll distance at sea level for 160 HP engine with Fixed Pitch Propeller (FPP) is 500 m with max AUW of 780 kg. The same engine with Variable Pitch Propeller (VPP) has shown 325 m take-off ground roll distance. The TGR distance has reduced to 175 m for a UAV with VPP. Engine with VPP can provide 35 % increase in take-off ground roll distance.

Rate of Climb (ROC) for 160 HP engine power with FPP at aircraft speed of 100 knots with AUW of 780 kg is 3.8 m/s. In case of same engine with VPP and 780 kg AUW at aircraft speed of 100 knots, the ROC has increased to 4.9 m/s. An increase of 28 % in ROC is observed for the engine with VPP with AUW of 780 kg at speed of 100 Knots.

4 Evaluation of Engine and Propeller on Test Bed

In order to evaluate performance of VPP prior to integration on to the Rustom-1, the VPP system was mounted on test bed engine and carried out performance run for rpm and full static thrust. It is observed that engine was able to attain max speed of 2600 rpm and was able to generate static thrust of 191 kg against 133 kg thrust of two blade fixed pitch propeller as shown in Table 1. Two actuators were used operation of throttle and governor lever.

First step was to establish the throttle vs engine rpm on the test bed. The throttle actuator was commanded in steps after the engine warm-up. The full travel of the actuator was calibrated for the idle and maximum engine rpms. Table 2 was arrived after multiple engine runs on test bed.

Table 1 Performance of VPP on test bed engine

Propeller	Engine rpm	Thrust Kgf
FPP	2200	133
VPP	2600	191

Table 2 Throttle versus RPM on test bed

Throttle (%)	RPM	Thrust (Kgf)	Fuel consumption (Ltr/h)
0	840	40	7.4
10	1140	49	8.9
20	1360	90	21.6
30	1880	131	27.9
40	2210	157	35.2
50	2410	175	40.5
60	2500	179	44.7
70	2560	180	46.2
80	2590	182	48.9
90	2610	190	50.4
100	2650	191	52

Next is to evaluate the governor position. The governor actuator was controlled through analog voltage electrical command—10 V to 10 V. Considering the governor travel required and the actuator linear travel available, the governor operation was restricted to—8 V to +8 V. The throttle command and governor actuator were commanded together and in sequence to arrive at the governor position for a selected engine rpm. The governor command vs engine rpm is established as given in Table 3.

All naturally aspirated, carbureted aero engines are equipped with a mixture control lever, to be exercised by the pilot as per the altitude of UAV operation. As the density of air decreases at altitudes, the fuel needs to be metered before its entry into the carburetor (Fig. 4).

The levers in a Marvel Scheibbler make carburetor used in the Lycoming O-320 engine is shown in the Annexure-1, Fig. 5. The mixture control lever was adjusted during flight tests at different altitudes and a lookup table was derived which is shown in Table 4.

The sequence of operation is explained below in Fig. 3. To increase power the propeller rpm control is put to fine position first and the throttle is increased to full rpm position next. Similarly to decrease power the throttle is reduced first and propeller rpm control is operated next.

Table 3 Governor RPM settings based on ground tests and taxi trials

Governor actuator voltage	Engine RPM
8	850
7	1000
6	1100
5	1200
4	1300
3	1400
2	1500
1	1600
0	1725
− 1	1925
− 2	2050
− 3	2200
− 4	2300
− 5	2400
− 6	2500
− 7	2575
− 8	2650

5 Flight Tests

Having successfully integrated VPP system to Rustom-1 UAV, it was subjected to LST and HST to check the functional behavior of the VPP system. Subsequent to number of taxi operation the first flight of Rustom-1 with VPP was flown at Kolar Flight Test Range. The critical parameters of VPP engine were observed and analyzed. The parameters are, engine rpm, throttle, fuel flow rate, aircraft speed, altitude, PPC_POS_FB, RPM_DEMAND & RPM_COMMAND. All engine parameters were within limits.

The governor restricted the max rpm to around 2695. AUTO mode of governor operation was exercised during flight. The series of flight trials of VPP led to the decision to conduct 10 h endurance flight of Rustom-1 UAV for an AUW of 757 kg. Fuel filled 193 liters.

The objective was to fly the UAV at 8000 ft altitude and 75 knots for a duration of 10 h. The engine rpm was maintained at around 1500–1600 during the cruise phase at 8000 ft altitude (Table 5).
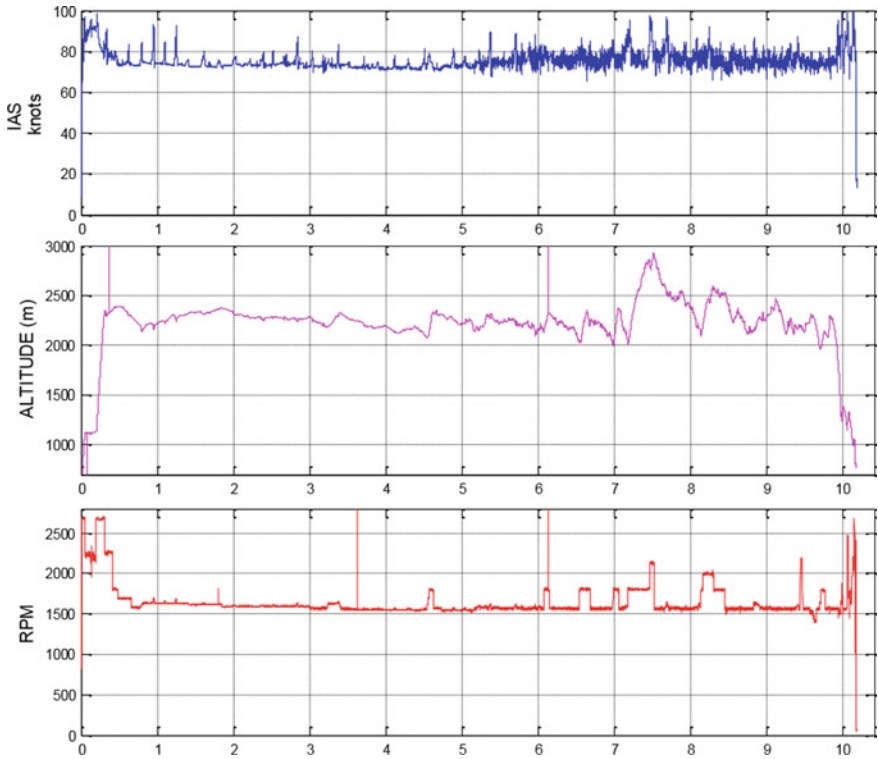
Fig. 4 Plot. 1: Rustom-1 mission profile (X-axis- No. of Hours)

6 Results and Discussion

Plot-1 shows the mission profile of the Rustom-1 UAV. An aircraft speed of 73–80 knots was maintained during the cruise operation. The engine rpm was maintained at around 1500–1700 rpm.

Plot-2 shows the cruise of Rustom-1 for 10 h. The engine rpm was maintained by controlling the propeller governor. The Lean mixture control was also operated at 25 %. All engine parameters were within control and no abnormal parameters were noticed. An optimum fuel consumption of 15 l/h was achieved using VPP for maintaining average aircraft speed of 73–80 knots.

Table 6 shows the comparison of Rustom-1 UAV with fixed pitch and variable pitch propellers
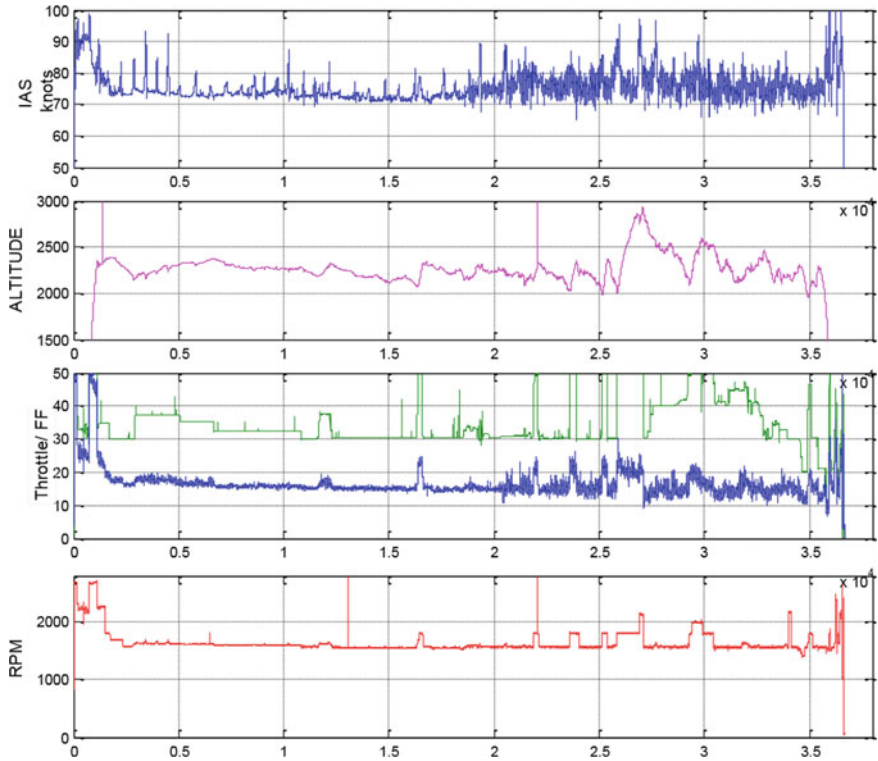
Fig. 5 Plot. 2: Rustom-1 Cruise data

Table 4 Lean mixture control lever setting w.r.t altitude

Altitude (Ft)	<6000	6000–8000		8000–10000		10000–20000	
% Throttle	0–100	<50	50–100	<50	50–100	<50	50–100
LMCU setting (%)	100	50	80	37.5	80	25	50

7 Conclusion

A research was initiated to enhance the endurance of Rustom-1 UAV. Higher endurance demanded to carry more fuel, thus increasing the AUW of the aircraft which needed higher thrust from the engine propeller combination. All historical methodologies like carrying additional fuel tanks, selecting an engine with a better SFC were considered. A feasible solution comprising of a variable pitch propeller and mixture control was found encouraging.

Table 5 Phases of operation of 10 h endurance flight

Phase of flight	Operational conditions	Average Fuel consumption rate	Time (min)
Engine run on Ground	Engine IDLE, MAX Throttle at ~ 12 % 1200 Engine RPM	9 lt/hr	23
Climb to 8000 ft altitude	100 % throttle 100 % LMCU VPP AUTO mode	51.5 lt/h during climb 27 lt/h during cruise @ 1400 m	18
Cruise @ 8000 ft	30–37 % throttle 12.5% LMCU Engine RPM 1600 IAS 71–73 knots	16 lt/h	282
Cruise @ 8000 ft	30–50% throttle 8–15% LMCU Engine RPM 1800~ 1900 IAS 73–80 knots	15 lt/h	300
Descent and Landing	20 ~ 30% throttle LMCU 100% VPP to AUTO mode	18 lt/h	10

Table 6 Comparion of flights with FPP and VPP propellers

	R1–42 (with FPP)	R1–55 (with VPP)
AUW	630 kg	757 kg
Fuel Carried	36 kg	140 kg
ROC to 8000 ft	650 ft/min	680 ft/min
Cruise Altitude	8000 ft	8000 ft
Duration of cruise	40 min	~10 h
IAS	80–90 knots	73–80 knots
Engine RPM during cruise	1900–2000	1600–1700
Fuel consumption during Cruise	18 ltr/h	15 ltr/h
Throttle % during cruise	40–50%	35–40%

The ground tests and taxi trials conducted with the VPP has resulted in sufficient data to automate the engine controls for the UAV flight profile.

In conclusion, Rustom-1 UAV, in its newly configured propulsion system has successfully met the endurance requirement of 10 + hours. Lookup tables generated during this work has been extensively used by the pilots in programmed mode flying. The methodology evolved for the selection of best operating points of the aircraft engine, will be utilized for planning the UAV missions in future.

governor, actuators, fabrication of support brackets, and cowling modifications. Sincere thanks to Director ADE, DRDO for permitting the publication of this work.

References

1. Carson: Fuel Efficiency in Airplanes. Proceedings, ISABE, ISABE 2009–1267, pp 1–10
2. Anderson JD (1991) Aircraft performance and design. Tata McGraw Hill Education Private Limited. Section 5.14, p 302
3. Vijayanand P, Rajesh M: Rustom-1 Installed thrust data with constant speed propeller, Report No. ADE/RADT/REP/01/2015
4. Lycoming Flyer: Operations Manual

Measurement Techniques

Development of Time-Efficient Multi-hole Pressure Probe Calibration Facility

Ajey Singh, Akchhay Kumar, Gaurav Tayal, and Chetan Mistry

Abstract Multi-hole pressure probes have a wide range of applications in terms of measurements in special applications like turbomachines flow field, wind tunnel experimentation applications, etc. The primary measurement variables of interest are static pressure, dynamic pressure, three velocity components, flow direction, etc., which we can measure using a multi-hole pressure probes with higher accuracy. The applications of such probes in measurement fields demands for higher accuracy of calibration, especially in terms of flow angularity and precision. The manual calibration of the multi-hole probe is a difficult and time-consuming task in an acceptable range of pitch, and yaw angles. The present paper discusses the low-speed multi-hole pressure probe calibration facility developed at IIT Kharagpur using a two-axis angular traverse mechanism. Special algorithms using LabVIEW were developed for automatic traverse both for yaw and pitch direction and also for pressure data acquisition using pressure scanner, to achieve precious measurement with short time spend with angular precision in terms of $0.5°$. This facility is capable of calibrating multi-hole pressure probes for different Reynolds numbers and angular ranges. The paper also discusses the initial calibration of the tunnel using total pressure probe rakes. A four-hole probe was calibrated using non-nulling calibration technique using the aforementioned test facility. It was calibrated for yaw and pitch angle range of $\pm30°$ and $\pm70°$, respectively. In this study, we are discussing three calibration methods, namely, the conventional method, the two-zone method and three-zone method to understand their behavior in terms of calibration coefficients, operable angular range, and uncertainty. The range for the pitch angle of the conventional method was observed to be $\pm35°$. However, an extended range for pitch angle up to $\pm60°$ for two-zone method and three-zone method was observed. The uncertainty analyses of the results have been performed to study the sensitivity of the probes at prescribed angular ranges.

A. Singh (✉) · A. Kumar · G. Tayal · C. Mistry
Indian Institute of Technology Kharagpur, Kharagpur, West Bengal, India
e-mail: singhajey6689@gmail.com

Nomenclature

C_i	Normalized pressure coefficients for the probe hole number i
C_{Po}	Total pressure coefficient
C_{Ps}	Static pressure coefficient
C_α	Pitch coefficient
C_β	Yaw Coefficient
P_1, P_2, P_3, and P_4	Pressure measured by probe holes 1–4
Q	Normalization factor of the conventional method
Q_{2Z}	Normalization factor of the two-zone method
Q_{3Z}	Normalization factor of the three-zone method
u	Velocity Component along the x-axis
v	Velocity Component along the y-axis
$\vec{V}$	Velocity vector
w	Velocity Component along Z-axis
α	Pitch Angle
β	Yaw Angle
$\left\vert \delta C_j / C_j \right\vert$	Error of calibration coefficients normalized with the full-scale range

1 Introduction

Turbomachines form an integral part in many applications such as aviation, power generation, marine gas turbines, air handling units for HVAC systems, turbochargers to name a few. The overall performance of a Gas Turbine engine is decidedly a direct implication of performance of constituting turbomachines. High-performance and high-efficiency turbomachinery design are essential for modern Gas turbine engines and other various applications. This requires a sound understanding of the physics of three-dimensional and unsteady flow inside a turbomachinery passage. Hence, we need to devise either a numerical or an experimental study to evaluate the characteristics of the flow. With the advancement in computational facilities, one can predict the flow field numerically using CFD. However, it has its own limitations in the context of time consumption and reliability [5]. On the other hand, a well-designed experimental study is well timed and reliable. The field of study of the flow characteristics of turbomachines has been developed significantly in terms of flow measurement instrumentation. There are advanced flow measurement techniques such as laser-Doppler velocimetry (LDV), hot-wire anemometry (HWA) and particle image velocimetry (PIV), but it is still challenging to employ these techniques in turbomachinery passages due to intricate geometrical complexities. LDV and PIV offer a high spatial resolution [11] over conventional techniques but require direct optical exposure to desired test field. HWA has an excellent frequency response [10] but it is extremely delicate for flow fields encountered inside turbomachines. The

higher cost of these advanced instrumentations is one other limitation dissuading extensive application. The multi-hole pressure probes are one of the extensively used measurement instrument. These probes may be a viable choice in terms of robustness, simplicity, and relatively cheaper in cost for the flow measurement of turbomachines.

The use of multi-hole probes for measurement of three-dimensional flow dates back to 50s [17] due to their reliability and ease of construction. Multi-hole pressure probes are a combination of Pitot-tubes incorporating multiple pressure orifices arranged at a particular angular position relative to each other. One of the salient features of multi-hole pressure probes is that they can simultaneously measure the velocity, static pressure, and dynamic pressure along with flow direction [16]. This saves the experimentation time and effort in experimental data reduction. The difference in pressure sensed by two symmetrically arranged orifices is reduced as the direction of incoming flow. The angular orientation of the probe is adjusted until the pressure difference in the two symmetrically located orifices becomes zero. Then the central orifice points against the flow incidence angle. This is called nulling method for flow measurement and involves minimum effort in terms of data reduction. However, this method requires angular traverse arrangement and can be used only for steady flow measurements. Instead, the probe can be pre-calibrated in a known velocity field by changing the orientation of probe to different angles and recording the pressure differences in symmetrically located holes as a function of angular position. The difference in pressures is normalized by suitable factors in order to make it independent of the calibration Reynolds number. The normalized coefficients are plotted as a function of incidence angle and pressures. When used for measurement, the coefficients are determined from the pressure reading in orifices and the calibration curves are anti-interpolated to give flow incidence and pressure. This is called the non-nulling method and it is the most preferred method for multi-hole probes. Once calibrated, the probes can be directly inserted into the test area for measurement of flow velocity and pressure. The pre-calibrated multi-hole probes can also be used for measuring unsteady flows with high response pressure transducer.

The non-nulling probe calibration technique requires a multi-axis precise angular probe traverse system, which is used to orient the probe in the known velocity field at different angular positions. Both effectiveness and reliability of calibration process depend largely upon the functionality of angular traverse system. A variety of probe traverse systems have been proposed by different researchers in the domain for easy and efficient positioning of the probe. The basic requirement of any traverse system is its ability to position accurately the probe inside the flow field at various angles. Town and Camci [15] have described the initial design and improvisation of a two-axis probe traverse system suited for open jet probe calibration. The authors proposed a better design over the original in order to achieve the same angular range with least departure of probe head from the core flow domain. Georgiou and Milidonis [6] designed a similar probe traverse system for calibration of a miniature five-hole probe in an open jet. Zhang et al. [18] have described a two-axis probe traverse system and its integration with Data acquisition system using LabVIEW platform.

Multi-hole pressure probes come under intrusive flow measurement devices, so it is important to keep their physical dimensions as small as possible without compromising the strength. Additionally, the geometrical shape of the probe head plays an important role in the sensitivity of measurement [3, 13]. It is desirable to use a small geometry probe capable of measuring three-dimensional flows with highest possible angular range. Five-hole and seven-hole probes can measure the three-dimensionality of flow with high accuracy but possess the drawback of larger velocity gradient and blockage due to their increased head size. Sitaram and Suresh [14] provide a comparative study of the suitability of different probe types for three-dimensional flow measurements. Four-hole probes seem to be a better choice for measuring three-dimensional flows with least blockage effects due to relatively small head diameter.

The angular range of the multi-hole probe is an important parameter, which depends on the properties of the normalization factor. The conventional normalization factors in use often lead to singularities or non-monotonic behavior of Coefficient curves in higher angular ranges, which limit the operational range of the probe. Ostowari and Wentz [9] suggested a calibration method for increasing the angular range of the five-hole probe. They managed to achieve an operative range of $\pm 85°$. However, the method of calibration required nulling mode of operation. For the non-nulling method, the operative ranges of a multi-hole probe can be increased by appropriate selection of normalization factor. In general zonal calibration methods Sitaram and Govardhan [12] are used for obtaining a higher angular range. Zonal methods incorporate the idea of different definitions of the angular coefficient in different operational zones of the probe. This minimizes the possibilities of singular points and ensures monotonic behavior of calibration coefficients. Babu et al. [4] managed to obtain a working range of $\pm 80°$ for a seven-hole probe using this method. Similar zonal methods are also proposed by Argüelles Díaz et al. [1] for Cobra probe where authors managed to obtain an operational range of $\pm 105°$.

In the present study, authors are discussing a successfully developed two-axis angular traverse mechanism for calibrating different kinds of probes. The in-house wind tunnel dedicated to performing calibration studies has been examined for uniform flow stream characteristics in the area of interest with the help of a total pressure rake. This paper also presents the development of an in-house fabricated four-hole probe and its calibration study by three different calibration methods, namely, conventional, two-zone, and three-zone methods. The two-zone or extended calibration technique prescribed by Argüelles Díaz et al. [2] for three holes has been implemented for this probe. The thee-zone method implemented by Munivenkatareddy and Sitaram [8] for a four-hole probe with a hemispherical probe head is applied to this probe. The paper also presents an uncertainty analysis of four-hole probes based on these calibration methods.

2   Calibration Tunnel

The low-speed calibration tunnel facility of Propulsion Laboratory at Indian Institute of Technology, Kharagpur was developed for calibration of probes (see Fig. 1a). It is operated by a centrifugal fan, which is powered by a variable frequency-controlled electric motor. The fan imparts a non-uniform highly turbulent flow of air, which is passed through a series of sieves and honeycombs before entering into the settling chamber. The air enters the square test section via a high contraction passage of 7.5:1 and finally exits through the diffuser. The tunnel can maintain a stable test section velocity from 10 to 50 m/s with precise velocity increments facilitating a wide range of speed variations. The test section has two static pressure ports along with a dedicated Pitot-static probe accommodation. The advantage of using a closed square test section instead of an open jet calibration setup decreases the possibility of external aerodynamic interferences. In addition, open jet streams possess the possibility of flow entrainment, which becomes a major concern away from the center of the jet. The entrained flow region is non-uniform and its slightest effect on the calibration may increase the uncertainties of measurement. The diffuser after the test section of the tunnel is for the kinetic energy recovery of the flow, which in turn reduces the power consumption of motor and improves the overall efficiency. This leads to a reduction of the overall operating cost of calibration.
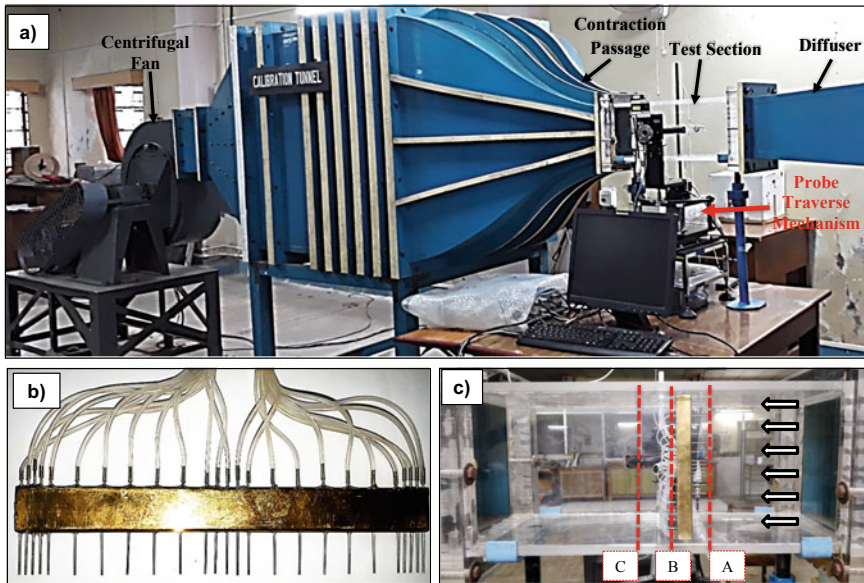
Fig. 1 *Calibration tunnel*: **a** a photo of calibration tunnel, **b** a photo of the Pitot-tube rake, and **c** a photo of tunnel test section with mounted Pitot-tube rake

2.1   Test Section Flow Field

The velocity field inside the test section has been measured using a specially designed Pitot-tube rake at desired calibration speeds (see Fig. 1b, c). A non-uniform vertically symmetric grid as shown in Fig. 2 has been implemented for capturing the flow field inside the test section. The rake used for the measurement has 25 probes distributed unevenly from top to bottom as per area of interest. The rake constitutes of fine grid near the walls up to 5.5% of test section height to facilitate the study of the influence of boundary layer and wall effects. Relatively coarse grid points up to 43.5% of section height follow fine grids. The central portion contains a region of fine grid points, which are 12.5% of section height for capturing velocity field in the core region. The vertical rake traversed across the test section width using a linear traverse in equal increments of 2.5% of test section width. We found total pressure distribution in the test section core to be satisfactorily uniform (see Fig. 2). The distortion near side wall region is due to the presence of the probe insertion slot. The extent of distortion is limited to the vicinity of the tunnel wall away from the calibration domain. Additionally, the probe insertion slot was sealed adequately during calibration, which further minimizes the effect of slot opening. The test section velocity field was appropriate for calibration with least concern for external fluidic disturbances, which is a major concern in an open jet calibration. Due to unavailability of turbulence measuring instruments like hot-wire anemometry, turbulence intensity was not measured and is not included in this paper.

Fig. 2 Grid of measurement points and color map of the total pressure, obtained for the tunnel test section perpendicular to the flow
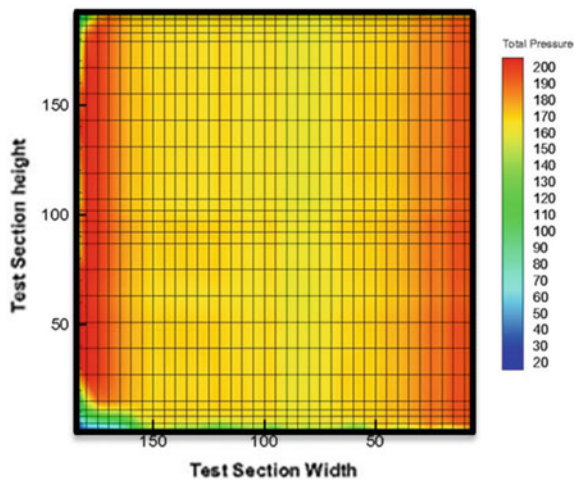
3 Calibration Mechanism

The calibration mechanism was designed with a view to achieving maximum flexibility in terms of usage and least possible sophistication for easy operation. The mechanism consists of dedicated two axes automatic traverse integrated with motion control and onboard data acquisition system (DAS). The probe positioning and orientation were achieved with the help of two independently controlled stepper motors (model 57SH76-1A), $M1$ and $M2$ controlling pitch and yaw, respectively, (see Fig. 3). The stepper motor $M2$ is connected to the rotary plate P via a rotary incremental encoder $E1$. The encoder generates signals, which are processed to provide an accurate estimate of angle turned by the plate. Similarly, motor $M1$ is connected to a rotary chuck with another encoder, which provides a measure of angle turned by the chuck. In addition to the motors, there are provisions for precise manual control of height and horizontal position of the mechanism for proper alignment of probes relative to test section height. The probes can be mounted on the chuck of calibration
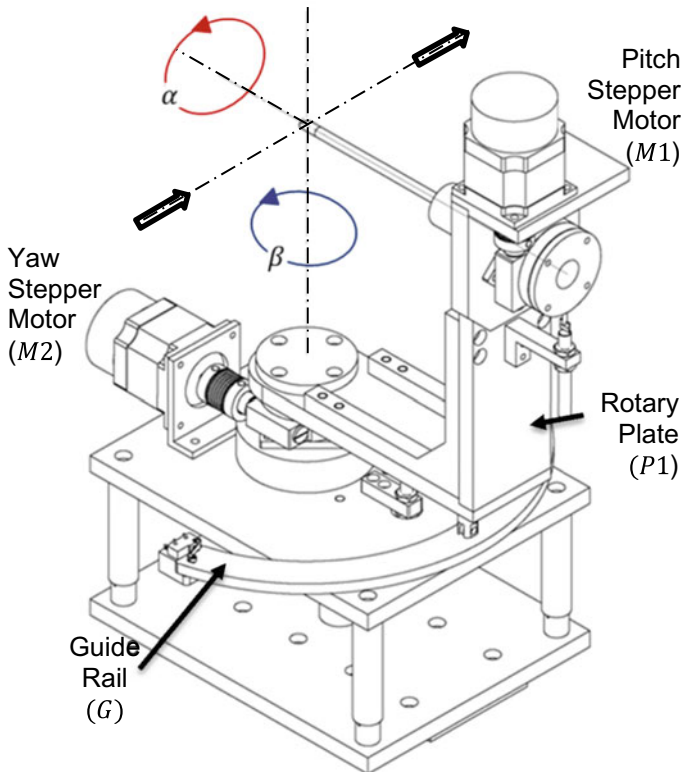

Fig. 3 Two-axis angular probe traverse rig (α and β denoting pitch angle motion and yaw angle motion, respectively)

mechanism, which facilitates the insertion of probes at the core of test section. Dedicated drivers independently control both the stepper motors. The motors are capable of providing high precision motion control of probes of the order of ~50° for both yaw and pitch. The calibration has to be performed in a closed test section rather than in an open jet, so mechanism operates in a close proximity to test section walls. The pitch motion has no restrictions and probes can rotate freely from 0° to ±90° as per the requirement. However, at extreme yaw angle positions, the plate $P1$ may bump into the tunnel walls. To avoid any such instance two limit switches have been provided on either side of the guide rail G to stop the yaw motion if mechanism reaches a certain extreme position. The mechanism has an angular traverse range of ±90° and ±45° for pitch angle (α) and yaw angle (β), respectively, and a resolution of 0.5° for both angles.

The motion control module consists of a controller and the two motor drivers. The motor drivers respond to control signals from the motion controller, which receives instructions through the host PC as per requirement. The motion controller and onboard data acquisition system (DAS) have been programmed using user-friendly LabVIEW platform and are integrated for synchronous data acquisition. The 16-channel pressure scanner from Scanivalve (model DSA3217®) was used for data acquisition and it can be triggered remotely by the data acquisition system. The data acquisition system has been designed specially to provide flexibility in terms of varying sampling rate and settling time before pressure data acquisition. The motion controller, data acquisition hardware, and pressure scanner were connected to the host PC through a LAN interface. Proximity Switches are located for both the axis at home position, i.e., position of 0° angle and are used to position the probe at home at the beginning or during the calibration process.

A user-friendly and interactive Probe Traverse Control Interface is developed using LabVIEW software (see Fig. 4). The functions of this interface are to check the hardware, to communicate between the pressure scanner and the computer, and to
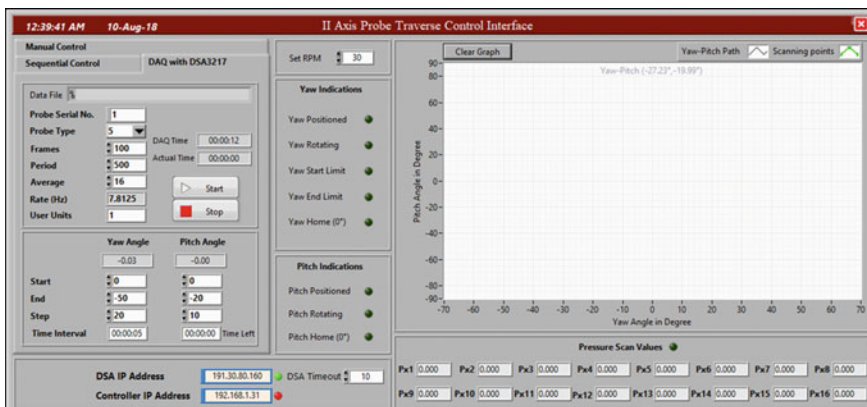

Fig. 4 Front panel of the two-axis angular traverse control interface

communicate between the motion controller and the computer. This custom designed interface fulfills the requirements of positioning home, reading the probe positions and limits, changing RPM of stepper motors, moving the probe to desired angular positions, and acquiring data from pressure scanner DSA3217. Suitable indicators are placed on the interface to display the ongoing and completed operations such as positioning, rotating, home, etc. A graph is also placed on the screen to display the actual angle of yaw and pitch motion of the probe during experimentation. The mechanism with the aid of the software interface can be operated in three different modes as per the requirements of users: Manual Control, Sequential Control, and DAQ with DSA3217. Firstly, in Manual Control mode, it is possible to position the probe at home, rotate the probe to the desired position and stop the probe if required in the middle of an operation. Secondly, in Sequential Control mode, the probe can be positioned sequentially to a number of yaw and pitch angle positions specified by the range and step-size of the motion. Thirdly, in DAQ with the DSA3217 mode, the interface communicates with the pressure scanner DSA3217 to set the input parameters of data acquisition such as Frames and Period for acquiring the data as per the desired rate (see Fig. 5). For the given ranges and step-sizes of yaw and pitch angles, the probe is positioned to all specified positions within the range in a sequential manner, and the measured data can be acquired and saved in a data file. The algorithm, as shown in Fig. 5, has been adopted for the process of calibration, but the authors do not rule out the possibility of alternative approaches. It can be observed that a yaw increment is done after the completion of the full pitch traverse and the process continues until complete yaw range is traversed. This has been proposed to avoid continuous incremental motion of stepper motor $M2$ (which feeds the yaw motion) as it carries a higher load in comparison to pitch control stepper motor $M1$.

4 Development and Calibration of Four-Hole Probe

The use of a multi-hole pressure probe is to measure the three-dimensional flow field with primary measurement variables of interest as static pressure, dynamic pressure, three velocity components, flow direction, etc. In this study, we are presenting the calibration results of a four-hole probe. Figure 6a depicts the assigned hole number of this probe and Fig. 6b signs convention relative to the physical domain with respect to probe head. As shown in the figure, the flow angles relative to the probe tip, the flow is said to have a positive pitch, α when it is incoming from the lower side toward the tip of the probe. When viewed from downstream of the probe perpendicular to stem the flow has a positive yaw (β) when it comes from left to right. The directions of the velocity vector $\vec{V}$, its components u, v and w as shown in figure are positive.

The four-hole probe consists of a brass probe head brazed upon a hollow stainless steel tube of 350 mm length. The probe head maximum diameter was kept at 7 mm in order to accommodate the four holes as shown in Fig. 6c. The probe head has a cylindrical shape with a slanted sectional cut at an angle of 45°. The beveled face
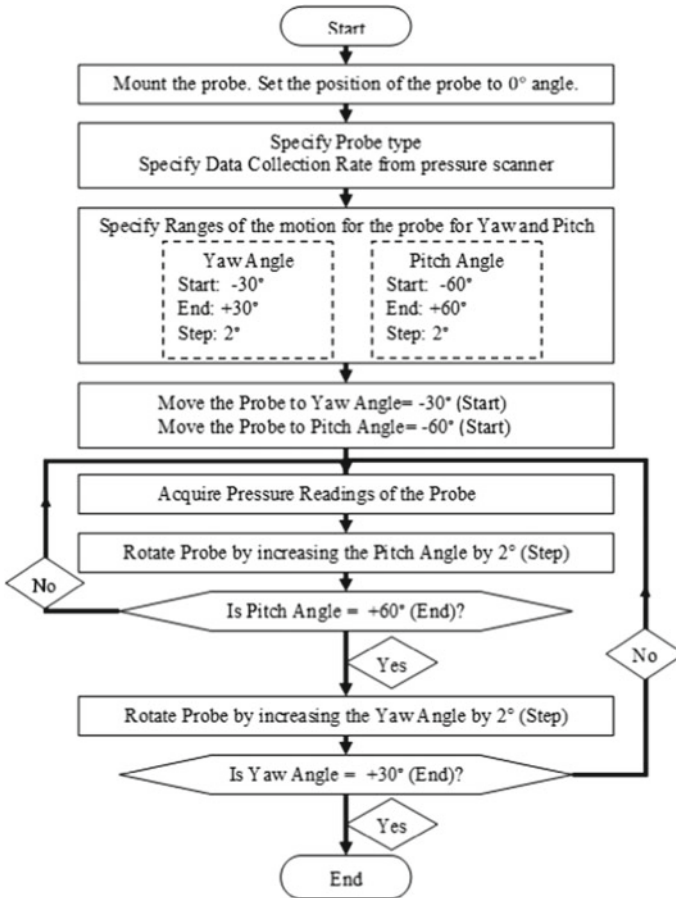
Fig. 5 Flow diagram for data acquisition of pressure readings of probes by incrementing sequentially the yaw angle and pitch angle by their step-sizes and within their given ranges

increases the desirable yaw angle sensitivity. The yaw angle sensitive hole on a cylindrical surface is located slightly displaced from the line of pitch angle sensitive holes to avoid influence on pith angle on yaw measurement.

The calibration of the four-hole probe was performed in the dedicated probe calibration tunnel facility developed at IIT Kharagpur. The calibration tunnel details have been described already in the previous section. A non-nulling method was adopted for the calibration, which involves orientation of probe at different angles in a known velocity field and calculation of direction coefficients for each position. The velocity field was determined using a Pitot-static tube stationed in the test section parallel to the flow direction. Additionally, static pressure taps present at the top and bottom of the test section were used to obtain static pressure in the test section. The calibration was performed for two different calibration speeds of 25 and 35 m/s
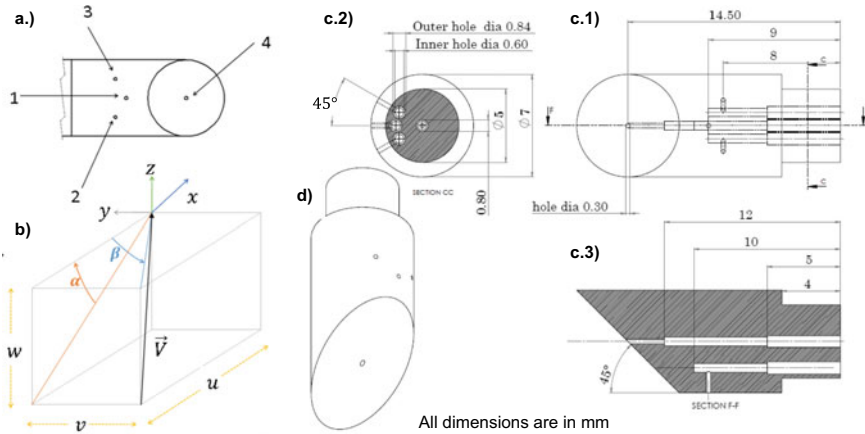
Fig. 6 *Four-hole probe*: Figure showing, **a** assigned hole numbers, **b** positive pitch and yaw angles, velocity vector and positive velocity components, (c.1, c.2, and c.3) orthogonal view, and **d** isometric view of the head geometry with dimensions

resulting in Reynolds number of 1.1×10^4 and 1.5×10^4. The probe positioning mechanism described previously was used for orienting the probes inside the test section. The data acquisition was done at a moderate sampling rate of 10 Hz. Prior to this study, an experiment was performed to study the effect of the data-sampling rate. However, no noticeable differences in the calibration coefficients were observed within the sampling rate interval of 5–20 Hz. The data reduction was performed using an in-house developed MATLAB program. One of the primary objectives was to explore the application of different calibration methods on the overall operational range and measurement uncertainty of the probe. In order to do so, the calibration was performed for a pitch angle range of $\pm 70°$ and a yaw angle range of $\pm 30°$ with a step-size of 3° for both. The alignment of the probe in the flow direction was ensured by comparing the pressure readings of hole-2 and hole-3 (see Fig. 6). The flow alignment and 0° pitch position was ensured by having same pressure readings through hole-2 and hole-3 and was done through number of iterations to ensure the perfect alignment of probe with airflow.

Analysis of pressure readings for each hole was performed. The pressure readings are converted to non-dimensional coefficients, which are defined as $C_i = (P_i - P_s)/(P_0 - P_s)$. Here i is the hole number and $i = 1, 2, 3$ and 4 corresponding to center, left, right, and bottom holes, respectively, and P_0 and P_S are total pressure and static pressure, respectively. The iso-lines of these coefficients are plotted with respect to pitch angle and yaw angle, as shown in Fig. 7. The coefficients became maximum for the free-stream flow, which indicates that the flow aligned with the hole-axis of the probe.

The responses of all four holes were observed as expected. The responses of hole-1 and hole-4 are maximum for pitch angle, $\alpha = 0°$ and its decreases as it moves away from $\alpha = 0°$ in both positive and negative directions. Whereas the responses
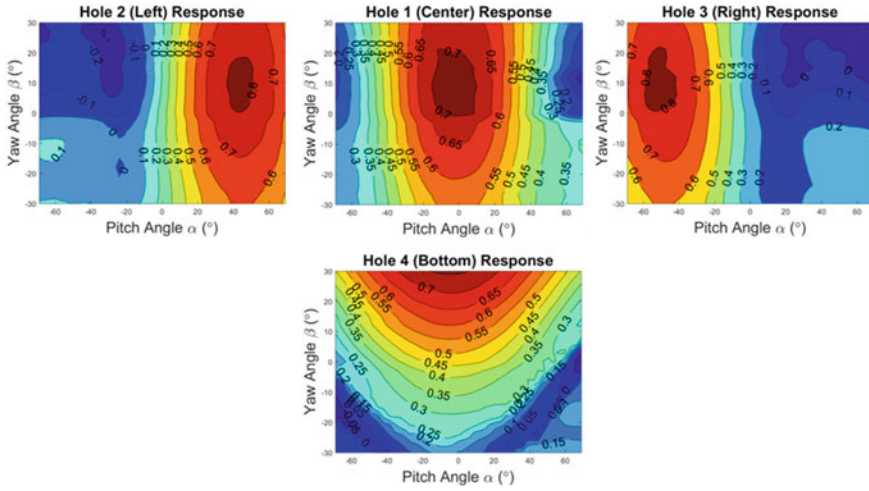
Fig. 7 Iso-lines showing non-dimensional pressure coefficients for the four-hole probe with respect to the pitch angle, α (°) and yaw angle, β (°)

of hole-2 and hole-3 are maximum when the flow is aligned to hole-axis, which is occurring within $\alpha = +40°$ to $+50°$ and $= -40°$ to $-50°$, respectively.

Hole-4 response for the yaw angle is increasing from negative yaw to positive. This is evident from the fact that as the yaw angle increases, the hole-axis will be gradually aligning to the flow, hence increasing the response. However, the responses of hole-1, hole-2, and hole-3 are not maximum for yaw angle, $\beta = 0°$. It is occuring around for a shift of $\beta = 10°$. It is observed for probes with symmetric probe head geometries where all holes are arranged in a regular geometric pattern; the response for holes may show a symmetric behavior around the zero pitch angle and zero yaw angle [6]. In our case, the four-hole probe has asymmetric probe head geometry as hole-4 is placed at an inclined plane of angle 45° to other three holes plane or pitch angle plane. This may have been forming the streamline of the flow such that the maximum responses are occurring for the yaw angle around 10°. This also has been observed for the four-hole probe by Munivenkatareddy and Sitaram [8]. However, their probe head geometry was hemispherical, but still asymmetric in shape as ours. An aerodynamic study of these kinds of probe need to be undertaken to evaluate the effects of asymmetricity of the probe head shape on flow field characteristics. The results here are analyzed using three different calibration approaches, namely, conventional, two-zone, and three-zone method as suggested in past literatures.

4.1 Conventional Calibration Method

For the conventional calibration method, the normalized calibration coefficients are defined by using a normalization factor Q as follows,

$$Q = P_1 - P_{avg} \tag{1}$$

where $P_{avg} = (P_2 + P_3 + P_4)/3$. The calibration coefficients, normalized with respect to Q, are expressed as

$$C_\alpha = \frac{P_2 - P_3}{Q} \tag{2}$$

$$C_\beta = \frac{P_1 - P_4}{Q} \tag{3}$$

$$C_{Po} = \frac{P_0 - P_1}{Q} \tag{4}$$

$$C_{Ps} = \frac{P_0 - P_S}{Q} \tag{5}$$

here C_α and C_β represent angular coefficients, namely, pitch angle coefficients and yaw angle coefficients, respectively. C_{Po} and C_{Ps} are the total pressure coefficient and static pressure coefficient, respectively. The iso-lines of pitch angle, with respect to the calibration coefficient C_α and C_β, as shown in Fig. 8 shows that C_α is primarily a function of pitch angle and C_β is of yaw angle. However, C_β is influenced by pitch angle beyond the angle range $\alpha = \pm 25°$. The iso-lines for C_{Po} and C_{Ps} shown in figure displays uniform variations with respect to C_α and C_β.

The uncertainty analysis was performed by the method proposed by Kline and McClintock [7] and employed by Argüelles Díaz et al. [2]. An estimate of percentage errors in coefficients by assuming error in pressure reading unity is shown in Fig. 9

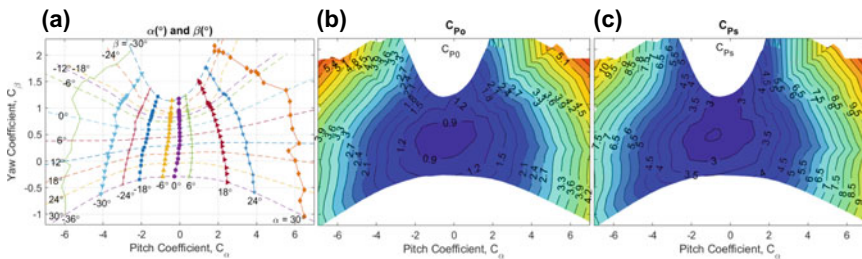**Fig. 8** Iso-lines of the four-hole probe of conventional method with respect to calibration coefficients C_α and C_β for **a** pitch angle, α (°) and yaw angle, β (°), **b** total pressure coefficients C_{Po}, and **c** static pressure coefficients C_{Ps}
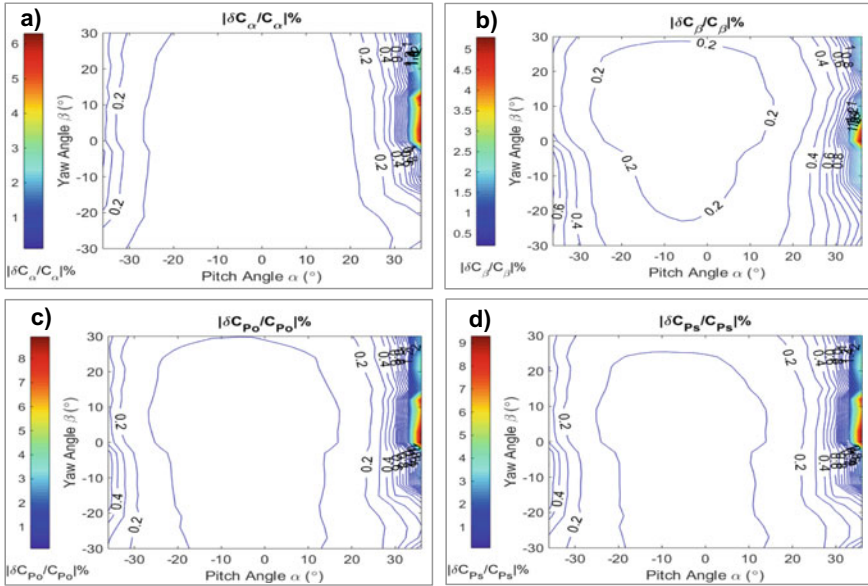
Fig. 9 Figure of the Percentage Errors with respect to pitch angle $\alpha(°)$ and yaw angle $\beta(°)$ of conventional method for: **a** C_α, **b** δC_β, **c** δC_{Po}, and **d** δC_{Ps}

with respect to pitch angle $(\alpha°)$ and yaw angle $(\beta°)$. The distribution of percentage error for pitch angle coefficient is satisfactory in an effective operating range of probe. The error distribution is symmetric about the pitch angle, which means that both positive and negative pitch measurements have the same order of accuracy. The maximum percentage error being 0.2% depicts the suitability of results in operating range. The asymmetric flow field in the yaw plane causes the error in pitch coefficient to increase in the higher yaw angle domain. As the yaw angle increases, the response of hole-1 decreases (Fig. 7) which results in a decrease in the value of normalization factor Q. Additionally it can be observed from Fig. 9a that pitch angle coefficient is nearly independent of the yaw angle, particularly in the positive yaw angle domain. Together these two factors result in increased percentage error in pitch coefficient. The distribution of error in the yaw angle coefficient is shown in Fig. 9b. It can be seen that as the yaw angle increases the estimated error decreases. Since yaw angle coefficient has a relatively more dependence on pitch angle (see Fig. 9b), the distribution of error was not symmetric about zero pitch position. The estimated error in the yaw angle coefficient was greater than that in pitch angle coefficient in the operational range of ±35°. The distribution of static pressure and total pressure percentage errors are almost similar with acceptable values in the prescribed operational range in conventional methods.

The limitation with conventional calibration method is the smaller angular range for measurement. The occurrences of singular points can be due to the normalization factor Q becoming zero. In this case, this was happening around the pitch angle,

$\alpha = \pm 40°$. Thus, the applicable range for this case was restricted to $\alpha = +35°$ to $-35°$.

The range of angles for these probes can easily be enhanced to a wider range as shown by Munivenkatareddy and Sitaram [8] and Argüelles Díaz et al. [2] by simply modifying the normalization factor. This can be done by dividing the complete angular range into a number of zones. This way we can eliminate the possibilities of occurring singular points.

Argüelles Díaz et al. [2] discussed the two-zone method for three-hole probes. This can be used readily for this particular configuration of the four-hole probe. The advantage of this particular configuration is the three holes of the probe, other than hole-4, are on the same plane, and shows similar behavior to that of a three-hole probe.

4.2 Two-Zone Calibration Method

The complete angular range of the calibration points can be divided into a number of zones. We can define a different normalization factor for each zone, thus eliminating singular points. However, this is important to consider that during application of probe in experimentation, the pressure reading data may not be distinguishable to deduce back the information required. Therefore, we should consider the zone range, which is clearly disguisable during calibration as well as during the application of the probe in experimentation.

One may identify two zones of negative and positive angles for the pitch angle range for which hole-2 pressure readings, P_2 and hole-3 pressure readings, P_3 have distinct values. For this probe geometry, it is easy to understand that when pitch angle $\alpha = 0°$, these two holes display equal pressure readings. For this position of the probe, hole-2 and hole-3 are located symmetrically opposite on the cylindrical surface. Hence, these will exhibit equal pressure readings. As the probe rotates away from $\alpha = 0°$ either in the direction of positive or negative angles, one of the either holes will be aligned relatively more to the flow stream than the other and having a higher value. Thus, the angular range can be divided into two distinct zones on the positive and negatives side from $\alpha = 0°$ Argüelles Díaz et al. [2].

The normalization factor Q_{2Z} for Two-Zone the method is defined as follow

$$Q_{2Z} = \begin{cases} P_1 + P_2 - 2P_3 \text{ for } \alpha > 0° \text{ or } P_2 > P_3 \\ P_1 + P_3 - 2P_2 \text{ for } \alpha < 0° \text{ or } P_2 < P_3 \end{cases} \qquad (6)$$

The angular calibration coefficients with respect to pitch angle and yaw angle are as shown in Fig. 10. Using the two-zone method, the pitch angle range has been extended to a range of $\pm 60°$. C_α and C_β are varying between 0.8 to -0.8 and -0.2 to 1.4. It is showing uniform behavior with respect to 'α' and 'β'. The C_{Po} and C_{ps} iso-lines are uniform for this extended range as well. However, dual points are

Fig. 10 Iso-lines of the four-hole probe of two-zone method for Zone-1 and Zone-2 with respect to calibration coefficients C_α and C_β of, (a.1) and (a.2) pitch angle, α (°) and yaw angle, β (°), (b.1) and (b.2) total pressure coefficients C_{Po}, and (c.1) and (c.2) static pressure coefficients C_{Ps}
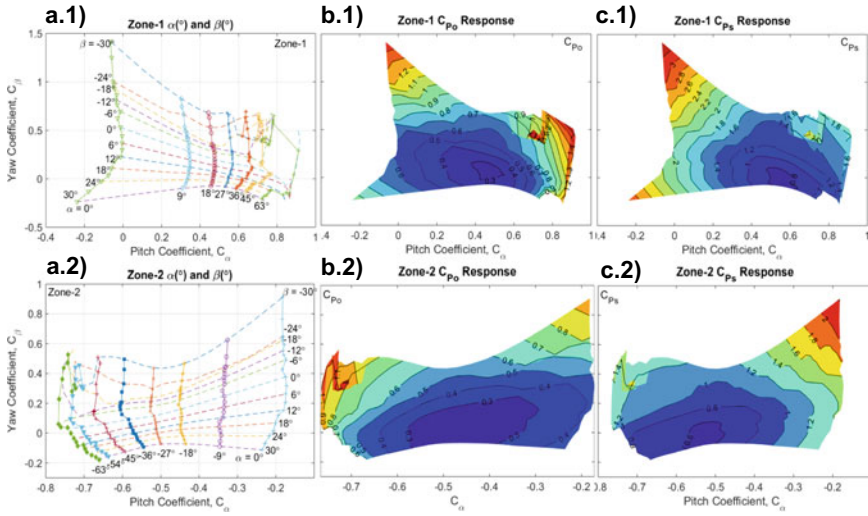
occurring for the pitch angle beyond $\pm 60°$ and the yaw angle less than $-20°$, limiting the range of operation of the probe.

The definition of normalization factor for the two-zone method is different in the two halves of pitch range (Eq. (6)). This ensures a positive non-zero value of normalization factor and a monotonous behavior of coefficients with angular position. The uncertainty in the values of angular and pressure coefficients is shown in Fig. 11 as relative percentage error. It is observed that estimated error is quite low in the extremities of the extended operational range but increases around the center regime. This result may be attributed to the behavior of normalization factor in the central regime of pitch range (around 0° pitch value). When the probe is at 0° pitch, the pressures in holes 2 and 3 are almost equal and the value of the normalization factor becomes very less in this region. The difference between the behavior of pitch angle and yaw angle error distribution can be observed as shown in Fig. 11a. The pitch lines are almost constant and unidirectional in the negative yaw angle region with slightly decreasing values as one move from 0° yaw to positive yaw domain. In other words, the value of the pitch coefficient is least affected by the yaw angle in the negative yaw domain and decreases as yaw becomes more and more positive. This aerodynamic behavior is reflected in the error distribution of pitch angle coefficient, which is less in the positive yaw domain and increases gradually as yaw angle decreases. It is observed from Fig. 11b that error distribution in yaw angle is greater than that in pitch angle for decreasing values of yaw angle. As the yaw angle decreases the value of yaw coefficient increases, which evidently leads to an increase in yaw coefficient error. The two-zone normalization factor increases as one moves away from the central regime in either direction with decreasing percentage error in the
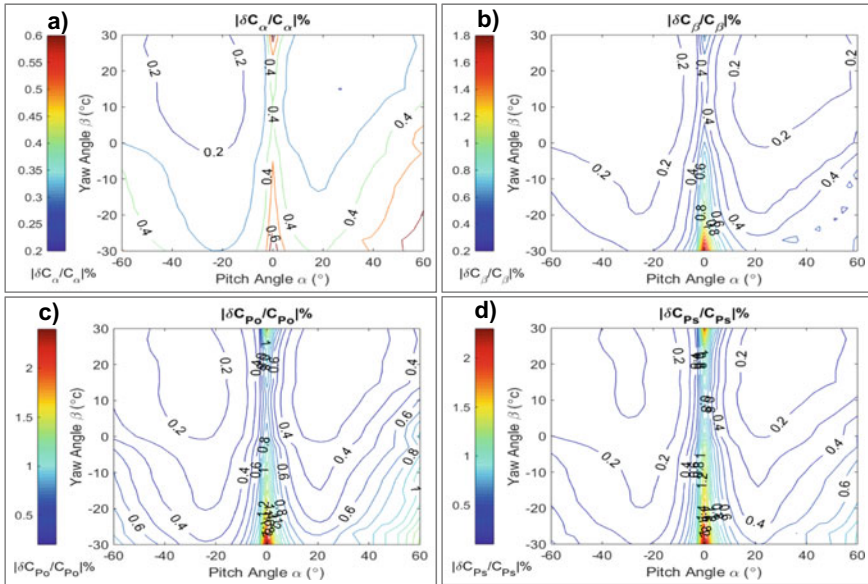
Fig. 11 Figure of the Percentage Errors with respect to pitch angle $\alpha(°)$ and yaw angle $\beta(°)$ of two-zone method for: **a** δC_α, **b** δC_β, **c** δC_{Po}, and **d** δC_{Ps}

calibration coefficient. The error distribution of P_0 and P_s (see Fig. 11c, d) shows similar behavior to that of the yaw angle and pitch angle, but these have relatively higher magnitudes.

4.3   Three-Zone Calibration Method

The three holes of pitch angle plane on the cylindrical surface of the four-hole probe present the case of dividing the whole range of operations into three zones [8]. As the pitch angle of the flow changes within the range of calibration, it will be the case that pressure reading of one of either three holes will be maximum. This hole will be relatively more aligned to the flow stream than the other two. The normalization factor Q_{3Z} are defined in three zones as follows

$$Q_{3Z} = \begin{cases} P_1 - (P_2 + P_3)/2 \text{ for } P_1 > P_2, P_3 \cdots \text{Zone} - 1 \\ (P_1 + P_2)/2 - P_3 \text{ for } P_2 > P_1, P_3 \cdots \text{Zone} - 2 \\ (P_1 + P_3)/2 - P_2 \text{ for } P_3 > P_1, P_2 \cdots \text{Zone} - 3 \end{cases} \qquad (7)$$

From the pressure readings, we may identify the regions of pitch angle, where conditions of Eq. (7) are meeting. The three zones may be identified as Zone-Fig. 11 from $\alpha = -21°$ to $+18°$, Zone-2 when $\alpha \leq -24°$, and Zone-3 when $\alpha \geq +21°$(see

Fig. 12 *Three-zone method*:
zone division of the
calibration points of the
four-hole probe

Fig. 12.). Iso-lines for pitch angle α, yaw angle β, total pressure coefficients C_{Po}, and static pressure coefficients C_{Ps} with respect to angular coefficients C_α and C_β are shown in Fig. 13 for all three zones. It is evident that for Zone-1, the coefficients $C_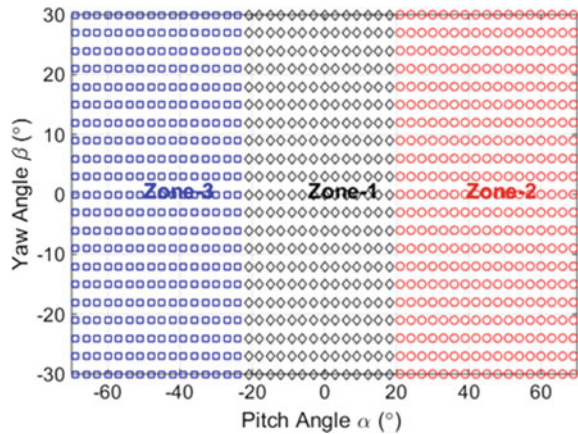\alpha$ and C_β are primarily a function of α and β, respectively. Coefficients C_{Po} and C_{Ps} are also varying uniformly with C_α and C_β. The response for Zone-2 and Zone-3 for all the parameters are nearly a mirror image to each other, except dual points occurring on the region of yaw angle, β below $-20°$ and pitch angle beyond $\pm60°$. This behavior of response is also been observed for two-zone method.

The error distribution for the three-zone method has the similar characteristics as seen for both the conventional method and the two-zone method (see Fig. 14). The characteristics of the normalization factor in the three-zone method are similar to the conventional method for the central zone (Zone-1). This explains the similarity in error distribution for both pitch and yaw coefficient. The boundary of Zone-1 has a very low value of normalization factor for all three zones. The distribution of error for angular coefficients is quite low in Zone-1 and increases toward its boundaries. The errors start decreasing as one move toward the extremities of terminal zones (Zone-2 and Zone-3). Thus, an estimate of the error in coefficients is satisfactorily low for three-zone calibration technique in the majority of angular range.

The use of different normalization factors in different angular regimes increase the operational range of probe. The distribution of error for the two-zone and three-zone method, however, seek caution for their suitability. The two-zone method has a higher estimated error near the zero pitch location, which reduces gradually as one move toward high pitch angle regions (see Fig. 11.). However, around a pitch angle of $\pm40°$ the percentage error increase to unacceptable limits. Thus, the increased angular range due to two different normalization factors in two domains has a narrow range of acceptable uncertainty. The three-zone method (see Fig. 14), on the other hand, has acceptable error distribution in the central region ($\pm15°$ pitch angle) and extremities (pitch angle $40° - 60°$). A region of higher uncertainty lies in the core
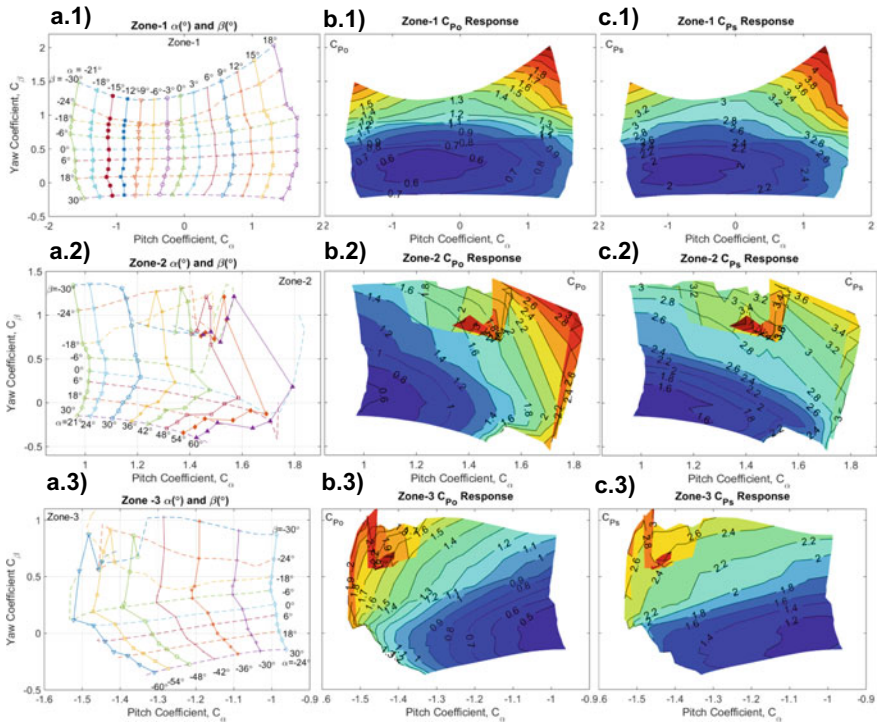
Fig. 13 Iso-lines of the four-hole probe of three-zone method of Zone-1, Zone-2 and Zone-3 with respect to calibration coefficients C_α and C_β for pitch angle $\alpha(°)$ and Yaw angle $\beta(°)$ (a.1, a.2 and a.3), total pressure coefficients C_{Po} (b.1, b.2, and b.3), and static pressure coefficients C_{Ps} (c.1, c.2 and c.3)

of effective operating range $[\pm(20° - 40°)]$. Thus three-zone calibration technique is suited for flows with high angularity.

The increased angular range due to the two-zone and the three-zone methods comes at the price of regions of higher uncertainty in the operating range. The choice of the calibration approach depends largely on the flow field to be measured. The conventional method although has a narrower angular range but the distribution of error in the operating range is quite satisfactory and increases as one moves away from the operating zone. The conventional method is suited for measurement of flows with very less angularity. The two and three zone methods facilitate increased angular range but regions of increased error lie well within the domain of operation. A higher error distribution near zero pitch location may restrict the suitability of the two-zone method for measurement of flows with very low angularity. The three-zone method is suitable for measuring flows with high angularity since it has acceptable error distribution in the extremities.
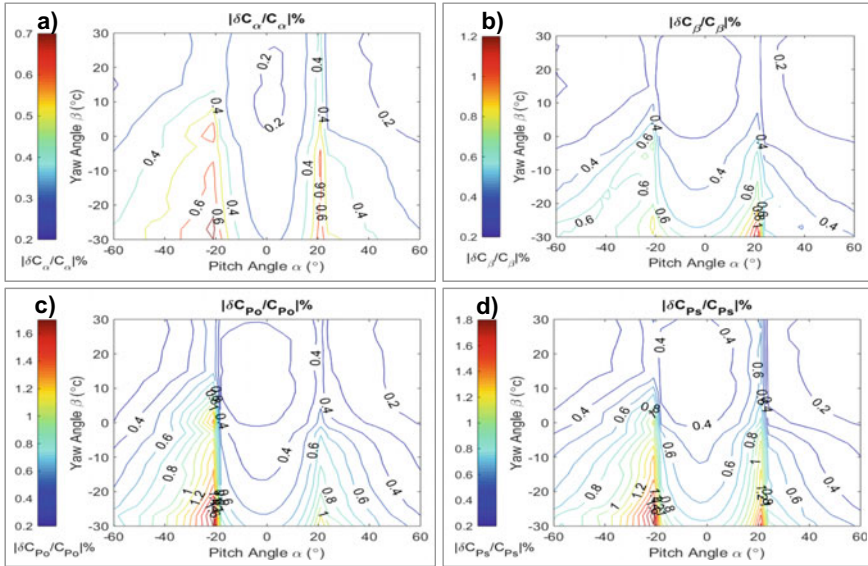
Fig. 14 Figure of the Percentage Errors with respect to pitch angle $\alpha(°)$ and yaw angle $\beta(°)$ of three-zone method for: **a** δC_α, **b** δC_β, **c** δC_{Po}, and **d** δC_{Ps}

5 Conclusions

In the present study, the two-axis angular traverse mechanism for calibrating different kinds of probes by easy, automated, and time-efficient means has been successfully developed. A four-hole probe was fabricated and its calibration study using three methods, namely, the conventional method, the two-zone method, and three-zone method has been carried out.

The following important conclusions are drawn from this study:

- The developed calibration facility permits accurate, reliable, time-efficient, and a convenient way of calibrating probes with minimal human involvement.
- The advantage of using a closed test section flow over open jet is the elimination of external aerodynamic interferences and possibility of flow entrainment.
- This facility can operate within the speed range of $10 - 50$ m/s of the test section airflow and can allow an extended range of angular motion (pitch $\pm90°$ and yaw $\pm45°$).
- The conventional method of calibration has the limitation of having a small angular range of pitch angle $\alpha = \pm35°$ and yaw angle $\beta = \pm30°$. However, within this range, this method gives accurate and reliable results with respect to all calibration coefficients and angles. The conventional method although has a small angular range, the distribution of error in the operating range is satisfactory. It increases as one moves away from the operating zone.

- The selection of normalization factor Q acts differently for different zones of angular range, which hints to incorporate the zone-based method to be used for enhancement of the angular range.
- Two-zone method and three-zone method, both have an extended range of pitch angle, $\alpha = \pm 60°$
- The two- and three-zone methods facilitate increased angular range. However, the regions of increased error for $\beta < -20°$ restricts its usage to values greater than this angle.
- The four-hole probe has restricted response to a certain region of angular range due to its asymmetric head geometry. The occurrences of dual points beyond pitch angle, $\alpha = \pm 60°$ and yaw angle, $\beta < -20°$ restrict the usage of this probe in these ranges.
- The three-zone method has acceptable error distribution in the extended angular range and is suitable for measuring flows with high angularity.

Annex A: Uncertainty Analysis of Calibration Methods of the Four-Hole Probe

We consider a function R and its uncertainty δR represented in form of $R \pm \delta R$. If several independent variables X_i are used in the evaluation of R, the uncertainty of the function δR is given by the root-square method.

$$\delta R = \left\{ \sum \left(\frac{\partial R}{\partial X_i} \delta X_i \right)^2 \right\}^{1/2} \tag{8}$$

In our calibration procedure, one of the independent variables is pressure readings of the probe. For different holes of the probe measuring pressure using a multi-channel pressure scanner, we can safely assume that

$$\delta P_1 = \delta P_2 = \delta P_3 = \delta P_4 = \delta P \tag{9}$$

and for total and static pressure readings as well,

$$\delta P_0 = \delta P_S = \delta P \tag{10}$$

Uncertainty Associated with Calibration Coefficients

We can write a general expression for all the calibration coefficients used in our analysis in the form,

$$C_j = (P_x - P_y)/Q \tag{11}$$

The uncertainty of coefficient C_j by the root-square method in the form of its variables

$$\delta C_j = \left(\left(\frac{\partial C_j}{\partial P_x} \right)^2 * \delta P_x^2 + \left(\frac{\partial C_j}{\partial P_y} \right)^2 * \delta P_y^2 + \left(\frac{\partial C_j}{\partial Q} \right)^2 * \delta Q^2 \right)^{1/2}$$

or

$$\delta C_j = \left(\frac{1}{Q^2} \left(2\delta P^2 + C_j^2 \delta Q^2 \right) \right)^{1/2} \tag{12}$$

Conventional Method

For the conventional method, the uncertainty of normalization factor Q as shown in Eq. (1),

$$\delta Q = \left(\left(\frac{\partial Q}{\partial P_1} \right)^2 \delta P_1^2 + \left(\frac{\partial Q}{\partial P_2} \right)^2 \delta P_2^2 + \left(\frac{\partial Q}{\partial P_3} \right)^2 \delta P_3^2 + \left(\frac{\partial Q}{\partial P_4} \right)^2 \delta P_4^2 \right)^{1/2}$$

Or

$$\delta Q = \left((4/3) * \delta P^2 \right)^{1/2} \tag{13}$$

Hence, the uncertainty of the calibration coefficient,

$$\delta C_j = \left(\frac{1}{Q^2} * \left(2 + \frac{4}{3} C_j^2 \right) \delta P^2 \right)^{1/2} \tag{14}$$

Two-zone method

The uncertainty of Q_{2Z} as given in Eq. (6),

$$\delta Q_{2Z} = 6\delta P^2 \tag{15}$$

Hence, the uncertainty of the calibration coefficient,

$$\delta C_j = \left(\frac{1}{Q_{2Z}^2} * \left(2 + 6C_j^2\right)\delta P^2 \right)^{1/2} \tag{16}$$

Three-zone method

The uncertainty of Q_{3Z} as given in Eq. (7),

$$\delta Q_{3Z} = (3/2) * \delta P^2 \tag{17}$$

Hence, the uncertainty of the calibration coefficient,

$$\delta C_j = \left(\frac{1}{Q_{3Z}^2} * \left(2 + \frac{3}{2}C_j^2\right)\delta P^2 \right)^{1/2} \tag{18}$$

References

1. Argüelles Díaz KM, Fernández Oro JM, Blanco Marigorta E (2008) Extended angular range of a three-hole cobra pressure probe for incompressible flow. J Fluids Eng 130(10):1–6
2. Argüelles Díaz KM, Fernández Oro JM, Blanco Marigorta E (2009) Cylindrical three-hole pressure probe calibration for large angular range. Flow Meas Instrum 20(2):57–68
3. Argüelles Díaz KM, Fernández Oro JM, Blanco Marigorta E, Barrio Perotti R (2010) Head geometry effects on pneumatic three-hole pressure probes for wide angular range. Flow Meas Instrum 21(3):330–339
4. Babu CV, Govardhan M, Sitaram N (1998) A method of calibration of a seven-hole pressure probe for measuring highly three-dimensional flows. Meas Sci Technol 9(3):468–476
5. Denton JD (2010) Some limitations of turbomachinery CFD. ASME Turbo Expo 2010 Power Land, Sea, Air, pp 735–45
6. Georgiou DP, Milidonis KF (2014) Fabrication and calibration of a sub-miniature 5-hole probe with embedded pressure sensors for use in extremely confined and complex flow areas in turbomachinery research facilities. Flow Meas Instrum 39:54–63
7. Kline S, McClintock FA (1953) Describing uncertainties in single sample experiment Kline. Mech Eng 3–8
8. Munivenkatareddy S, Sitaram N (2016) Extended calibration technique of a four-hole probe for three-dimensional flow measurements. Int J Rotating Mach 2016:1–12
9. Ostowari C, Wentz WH (1983) Modified calibration technique of a five-hole probe for high flow angles. Exp Fluids 1(3):166
10. Ramond A, Millan D (2001) Measurements and treatment of LDA signals, comparison with hot-wire signals. Exp Fluids 28(1):58–63

11. Saga T, Hu H, Kobayashi T, Murata S, Okamoto K, Nishio S (2000) A comparative study of the PIV and LDV measurements on a self-induced sloshing flow. J Vis 3(2):145–156
12. Sitaram N, Govardhan M (2002) Large angle calibration of five hole probes. J-Aeronaut Soc India 54(3):265–272
13. Sitaram N, Srikanth K (2014) Effect of chamfer angle on the calibration curves of five hole probes. Int J Rotating Mach 2014:1–11
14. Sitaram N, Suresh M (2017) Comparison of single hole, two hole and four hole probes for three-dimensional flow measurements. In: International Conference on Theoretical and Applied Computational and Experimental Mechanic, pp 1–10
15. Town J, Camci C (2011) Sub-miniature five-hole probe calibration using a time efficient pitch and yaw mechanism and accuracy improvements. In: Proceedings of the ASME Turbo Expo 2011, pp 1–11
16. Treaster AL, Yocum AM (1978) The calibration and application of five-hole probes. Pennsylvania State University Applied Research Laboratory, pp 1–57
17. Winternitz FAL (1956) Probe measurements in three-dimensional flow: a comparative survey of different types of instrument. Aircr Eng Aerosp Technol 28(8):273–278
18. Zhang XH, Gong WQ, Liu CC (2015) Study on multihole pressure probe system based on LabVIEW. Exp Tech 39(3):42–54

An Experimental Investigation of the Performance of an Acoustic Pump Employing Dynamic Passive Valves

B. Akash, Sonu Thomas, and T. M. Muruganandam

Abstract An experimental study is conducted to investigate the performance of a non-uniform area resonator-based acoustic pump for air. Higher peak pressure amplitudes can be obtained by employing a non-uniform resonator. The pressure obtained has an oscillatory nature about the ambient pressure, with the frequency of operation equal to 933 Hz. The extraction of useful energy from the resonator is achieved by no-moving-part valves. In the present study, four different configurations of no-moving-part valves have been used for rectification. A series combination of three 15 mm length flow individual diode elements showed expected results with the diode having smaller diameter exhibiting better rectification. However, single diodes with length of 45 mm exhibited rectification in the opposite direction. The performance of the acoustic pump is evaluated based on its tank filling characteristics for a given driving power and a particular valve configuration. Maximum tank pressures of the order of 1000 Pa are obtained at maximum flow rates of the order of 10 slpm for the available range of driving powers.

Keywords Acoustic compressor · Non-uniform area resonator · Dynamic passive valves

1 Introduction

Pumping of fluids is one of the most common processes encountered in a wide variety of engineering applications. Several technologies for pumping have been developed since times immemorial. However, most of these make use of a large number of components which are either in continuous or intermittent motion. Friction and inertia of such components lead to loss of useful energy. A valveless pump, while not avoiding the use of valves altogether, eliminates some of this friction by getting rid of valves with moving parts [1].

B. Akash (✉) · S. Thomas · T. M. Muruganandam
Indian Institute of Technology Madras, Chennai, Tamil Nadu, India
e-mail: byjuakash@gmail.com

Some of the biggest developments in valveless pumping technology have been associated with the area of micro-pumping. In Micro Electro Mechanical Systems (MEMS) micro-pumps, there is an urgent need to do away with ordinary valves as they often cannot be easily miniaturized and even if successfully miniaturized, they prove to be an encumbrance on the rest of the micro-hardware. Three key valveless pumping technologies have been developed over the years, namely, valveless reciprocating pump, valveless impedance pump, and valveless standing wave pump. The first technology is closely related to ordinary positive displacement pumps in that an oscillating chamber volume is used to pump fluid [2]. Flow rectification is achieved using diffuser/nozzle elements. In valveless impedance pumps, two tubes of different impedances are connected together [3]. One of the tubes is pinched periodically leading to the generation of traveling waves which get reflected at the impedance mismatch boundary and thereby produce net flow.

Compared to the above two techniques, the valveless standing wave pump is relatively a new addition to valveless pumping technology. The use of standing waves to obtain pumping action has been around for some time. However, it was only recently that this concept was applied for the first time to valveless pumping by replacing mechanical valves used in previous embodiments with nozzle/diffuser elements such as those used conventionally with valveless reciprocating pumps [4]. Nozzle/diffuser elements, placed at the pressure node and antinode locations of standing waves generated in a chamber rectify the flow, lead to a net flow into and out of the chamber.

A major limitation associated with standing wave pumps which use constant cross-sectional ducts is the generation of shocks as the energy input to the standing wave is increased. Shock formation leads to the dissipation of energy and limits the compression ratio that can be attained in standing wave pumps. A major breakthrough in overcoming this came with the development of Resonant Macrosonic Synthesis (RMS) technology wherein shaped resonators instead of uniform area cross-sectional resonators are used [5]. It was found that such resonators could sustain shockless standing waves of higher amplitude than that is possible with constant cross-sectional resonators for the same energy input. However, the original inventors of RMS always used mechanical valves in their embodiments.

A study of the development of standing wave valveless pumping and RMS technology reveals that the former mostly concentrated on the flow problem associated with valveless rectification and attempted to improve their devices solely by improving the rectification efficiency associated with the so-called "leaky" valves while on the other hand the latter group of researchers were mainly concerned with the acoustic side of the problem and almost invariably used ordinary mechano-fluidic valves to rectify the flow from their resonators. These two separate streams of studies were finally merged to develop the non-uniform resonator-based acoustic blower employing fluidic diodes and the non-uniform resonator-based valveless standing wave suction pump [6, 7]. The fluidic diode used was nozzle/diffuser element. But unlike in standing wave pumps discussed earlier, both the inflow and outflow diodes were placed at the pressure antinode of the resonator. Also, instead of a single diode element, multiple diode elements were connected in series to obtain flow rectification.

The oldest fluidic diode is attributed to Nikola Tesla [8]. Since then, a plethora of designs for fluidic diodes have been conceptualized and investigated experimentally as well as numerically. Fluidic diodes exploit "minor loss" associated with either sudden change in flow direction or sudden change in channel geometry to set up a directional pressure drop and thereby rectify flow [9]. The physics of fluidic diodes operating in periodic flow conditions is not well understood. The time-dependent nature of the problem renders computational investigation quite difficult [10]. Experimentally, although a lot of ground has been covered, all the parameters governing the working of these devices have not yet been brought to light. Even in the case of experimentally investigated parameters, an underlying physical explanation linking all the observed phenomena remains to be uncovered. The aim of the present study is to widen the range of experimental knowledge of the behavior of fluidic diodes subjected to high amplitude oscillating pressure input. The invention of an optimum diode configuration could in turn lead to further development in acoustic standing wave pump technology and make concepts such as the multistaging of these pumps viable.

Fig. 1 Schematic of the experimental setup
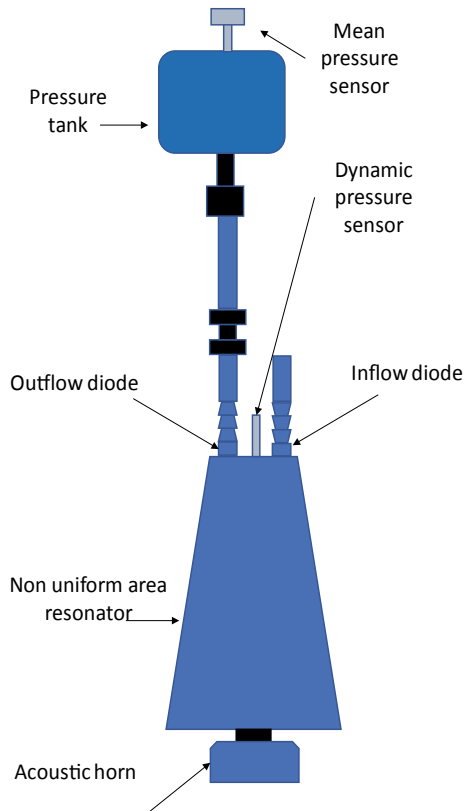
2 Experimental SetUp

2.1 Standing Wave Pump Arrangement

The standing wave pump arrangement consists of the following: non-uniform area resonator, acoustic driving unit, a pair of dynamic passive valves (one for inflow and the other for outflow) with each valve consisting of nozzle/diffuser elements arranged in different configurations (Fig. 1). The resonator used has linear area variation given by

$$A(x) = ax + b \tag{1}$$

where $a = 22.5$ mm, $b = 1000$ mm^2 and $0 \leq \times \leq 200$ mm.

The driver unit is threaded to a flange at the large end of the resonator. The dynamic passive valves are threaded to a flange at the smaller end of the resonator.

2.2 Fluidic Diode Configurations

In the present study, four different pairs of fluidic diode configurations were used. Three fluidic diode elements as shown in Fig. 2a were glued together to obtain series combination of diodes. Single diodes as shown in Fig. 2b constituted the next two pairs of diodes. Hereafter, the diodes in Fig. 2a will be referred to as series diodes and those in Fig. 2b will be referred to as single cone diodes. All the diodes were constructed out of stainless steel. The joints between the diodes and the uniform tube sections were sealed using epoxy resin to prevent air leakage.

2.3 Measurement Technique

A tank filling-based flow measurement technique is used to determine the outflow. A steel tank of volume 220 ml is connected to the outflow diode at the small end of the resonator. This tank is fitted with a mean pressure sensor. The volume flow rate at any instant is directly related to the instantaneous rate of change of mean pressure inside the tank using the ideal gas equation as follows:

$$\dot{V} = \frac{1}{\rho} \dot{P}_T \left(\frac{V_T}{RT} \right) \tag{2}$$

where $\dot{V}$ = Flow rate (in slpm), $\dot{P}_T$ = Rate of change of tank pressure, V_T = Volume of tank, ρ = Density of air flow, R = Specific gas constant, and T = Temperature

Fig. 2 **a** Series combination of 4 mm (top) and 6 mm (bottom) diodes in outflow (left) and inflow (right) configurations. **b** Single cone type fluidic diodes of 4 mm (top) and 6 mm (bottom) in outflow (left) and inflow (right) configurations
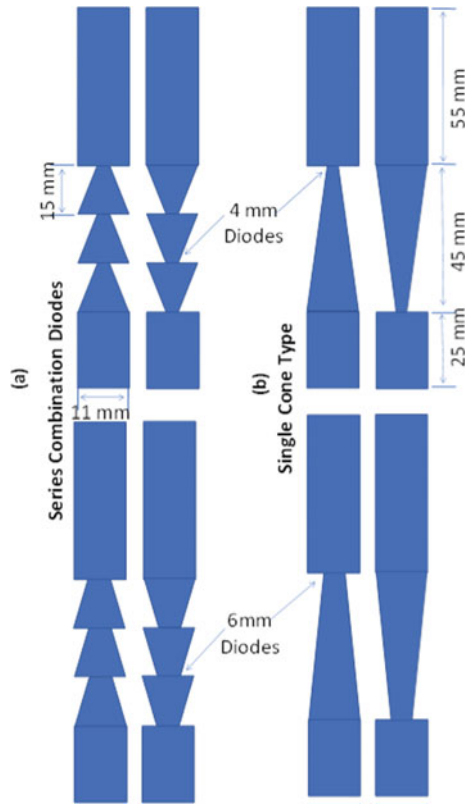
of air in the tank. The small change (~1.5%) in temperature due to adiabatic compression/expansion of the gas has been neglected. The driver is switched on with sinusoidal input at resonant frequency. After a brief period of transience, resonance is set up in the non-uniform area duct. Once this happens, the inflow diode and outflow diode rectify the acoustic oscillation at the small end of the resonator. The inflow diode permits flow into the resonator while outflow diode permits flow out of the resonator. The tank which is connected to the outflow diode thus gets filled.

2.4 Instrumentation

The acoustic horn driver unit used in the experiment was Capital 2165/150 W speaker. It was driven by a power amplifier (AHUJA SSA-350) and this was used to set the amplitude of the input to the horn driver. A function generator (Tektronix AFG 30220B) was used to feed sinusoidal input to the driver unit at resonance frequency. Dynamic pressure transducer (PCB model 113B27) was used to measure dynamic

pressure at the small end of the resonator. Omega PX143, solid-state piezo-resistive pressure sensor was used to monitor the pressure change in the tank due to the rectifying action of the outflow diode. Data was recorded at 25 kS/s. Omega PX143 series transducer used in tank pressure measurement has a resolution of ± 13 Pa. The driving amplitude in terms of voltage was measured using a Yokogawa digital multimeter (Model 73201). The error in voltage is 0.01 V.

3　Results and Discussions

The pumping fluid used in the experiment was air under standard atmospheric conditions ($T = 300$ K and $\rho = 1.2256$ kg/m^3). The fundamental harmonic frequency of the non-uniform resonator coupled with the diodes was found by monitoring the FFT of the pressure trace at the small end of the resonator. This frequency was found to be 933 Hz. The frequency varied very little (1–2 Hz) for different fluidic diode arrangements at the small end of the resonator. Once this frequency was found, the loudspeaker driver was excited at this frequency using a sinusoidal input from the function generator. Since the amplifier takes some time to build up power, a dummy driver was used. Whenever the acoustic pump was not excited, power was switched to this dummy driver. Thus, power could be instantaneously transferred to the acoustic pump driver whenever required by flipping a two-way switch between the two drivers. The sensors would be set to read mode and then this switch would be quickly flipped thereby delivering power to the acoustic pump driver. The rectifying action of the diodes caused the tank pressure to change and this spike in the tank mean pressure was monitored. The experiment was repeated for two different voltage levels applied to the driver viz. 15 and 25 V for each of the four different diode configurations. The pressure oscillation at the small end of the resonator acts as an input to the two dynamic passive valves. This is shown in Fig. 3 for the two voltages used.

3.1　Tank Pressure Data

The sound waves that enter the collecting tank along with the rectified flow through the outflow diode the pressure inside the tank is partly oscillatory in nature. However, what matters is only the change in mean pressure due to rectified flow entering or leaving the tank. Thus, the pressure data from the tank sensor is smoothed to eliminate local fluctuations superimposed on the tank mean pressure. A moving average scheme is used for this purpose and is illustrated in Fig. 4a, b. The time evolution of the small end acoustic pressure shown in Fig. 4c indicates that there will be a brief delay before the standing wave in the resonator reaching steady state. Thus, a portion of the initial tank filling data is transient in nature.

　　The tank filling data for 15 V, plotted in Fig. 5a reveals that the series connection of diodes, both 4 and 6 mm, behaved as expected. The 4 mm series arrangement
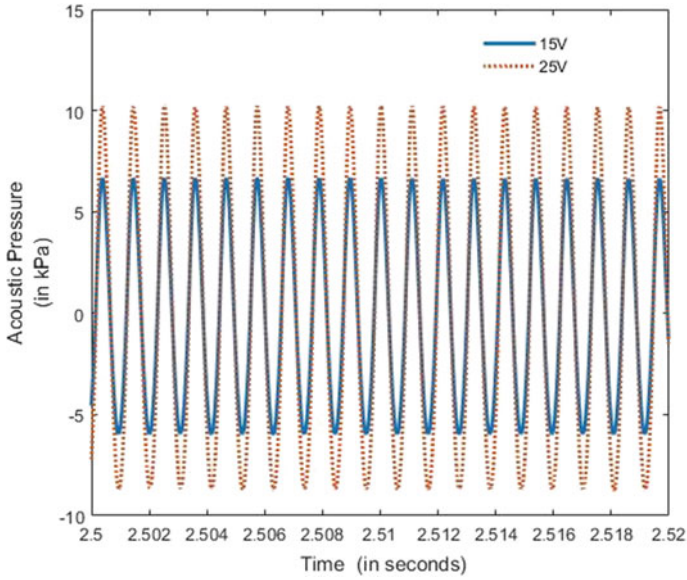
Fig. 3 Comparison of acoustic pressure amplitude at the small end of the resonator for two different driving voltages
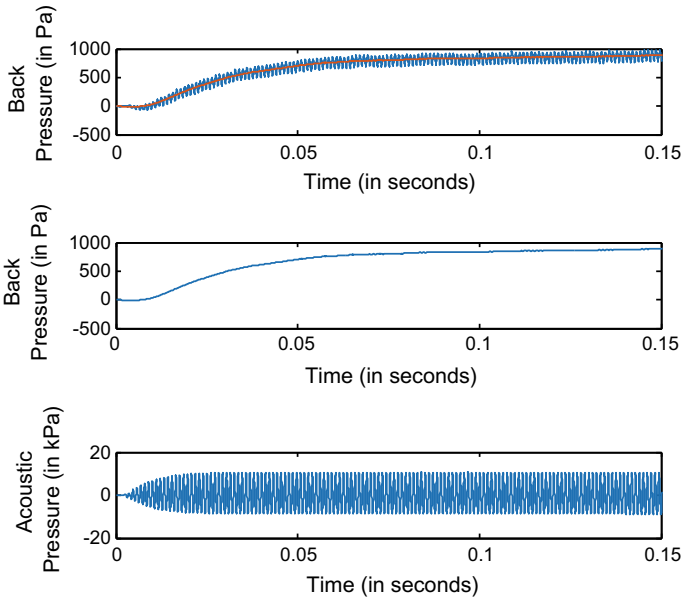

Fig. 4 **a** Raw tank mean pressure data. **b** Tank pressure data after smoothing. **c** Acoustic pressure amplitude at resonator small end indicating initial transient behavior
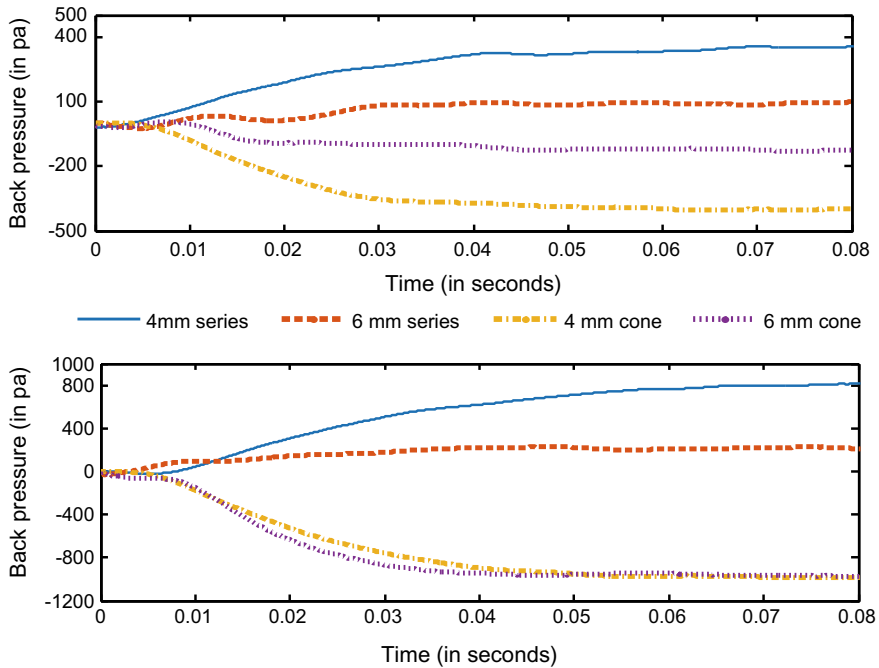
Fig. 5 Increase/decrease of back pressure with time for voltage input of **a** 5 V and **b** 25 V

clearly has superior rectification efficiency as indicated by the higher back pressures achieved. But the behavior of both single cone diodes is unexpected. It is conjectured that there would be forward flow in the nozzle direction as was seen in the case of series-connected diodes and therefore the nozzle configuration was used as the outflow diode and the diffuser configuration as the inflow diode. However, when used in this fashion, the pump acted in suction mode and the mean pressure in the tank went below the ambient. Even at this mode, the 4 mm diode exhibited better rectification at 15 V. However, at 25 V, the difference in performance between the two diodes seems to have reduced as shown in Fig. 5b. In fact, for a short period of time, the 6 mm cone diode appears to be performing better than its 4 mm counterpart. Also, it is worth noting that the suction performance obtained using the cone diodes appears to be better than the pumping performance obtained using the series-connected diodes with regard to the suction pressures obtained. The maximum tank back pressure (positive for pumping mode and negative for suction mode) increases with increase in driving amplitude.
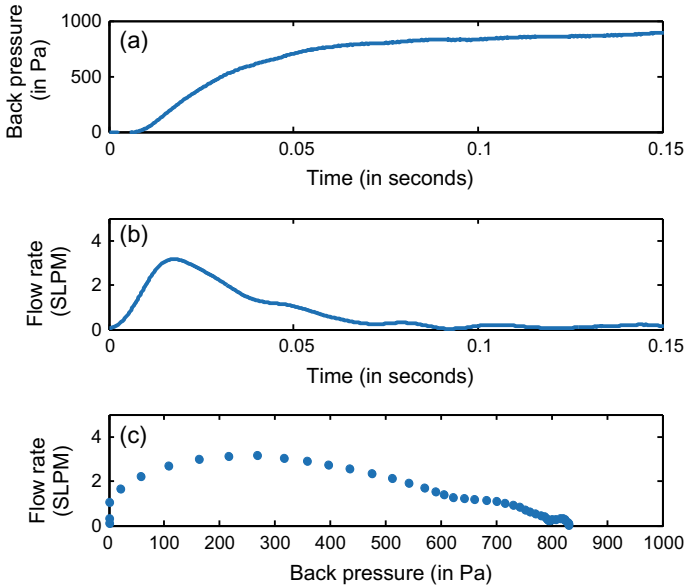
Fig. 6 **a** Smoothed tank pressure data. **b** Instantaneous flow rate calculated as a function of time. **c** Flow rate plotted against back pressure (pump characteristics)

3.2 Calculation of Instantaneous Flow Rate

Instantaneous flow rate is calculated using Eq. (2). $\dot{P}_T$ is computed by numerically differentiating the smoothed tank pressure data points with respect to time. The resulting flow rate into the tank as a function of time is given in Fig. 6b. The rising part of the curve is again due to transience. It can be noted that the sharp change in flow rate with time is an accurate indicator of the point at which the resonance in the pump attains steady state. Data to the left of this peak is not a part of the steady-state characteristics of the acoustic pump. Hence, this part is omitted in Fig. 7.

3.3 Pump Characteristics

The non-dimensional back pressure versus flow rate characteristics of the pump at steady state is plotted in Fig. 7. Analogous to dc voltage and dc current are obtained after rectification of ac voltage and ac current in electronic diodes; two quantities are defined for the fluidic diodes viz dc pressure and dc flow rate. The obtained back pressure and flow rate have been non-dimensionalized using these two fictitious quantities. The acoustic pressure amplitude at the small end of the resonator is considered as input to the fluidic diodes. Now, dc pressure and dc flow rate are related to the acoustic pressure amplitude P_{peak} and the acoustic velocity amplitude

Fig. 7 Non-dimensional
acoustic pump characteristics
corresponding to voltage
input of **a** 15 V and **b** 25 V
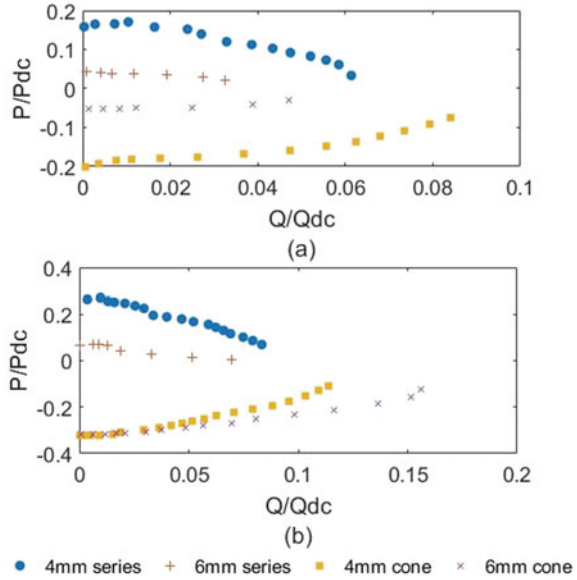
U_{peak} at the resonator small end, respectively, through the following relations:

$$P_{\text{dc}} = \frac{P_{\text{peak}}}{\pi} \tag{3}$$

$$Q_{\text{dc}} = U_{\text{dc}} \times \frac{\pi}{4} \times d^2 = \frac{U_{\text{peak}}}{\pi} \times \frac{\pi}{4} \times d^2 \tag{4}$$

Equation (3) is analogous to the relationship between dc voltage output and ac voltage input for a half wave rectifier circuit in electronics. The d in Eq. (4) is the tube diameter of the diodes, i.e,. 11 mm. U_{peak} is obtained from P_{peak} by assuming the following relation from linear acoustics to be valid:

$$U_{\text{peak}} = \frac{P_{\text{peak}}}{\rho \times c} \tag{5}$$

where ρ is the mass density of the acoustic medium and c is the speed of sound in the medium. It must be noted that Eq. (3) is valid only for sinusoidally varying input. Also, P_{dc} and Q_{dc} may not be the theoretical maximum possible values of pump pressure and flow rate, respectively. However, until the physics of the flow phenomenon occurring inside the diodes is elucidated, these two ad hoc quantities will be useful for comparing pump performances in non-dimensional form. The back pressure versus flow rate characteristics of the pump at steady state are plotted in Fig. 7. Note that the flow for the cone diodes are opposite in direction to that for the

series diodes. Hence, the flow rate values should actually be negative. However, for reasons of clarity only the magnitude of flow rate is plotted.

Note that the flow for the cone diodes is opposite in direction to that for the series diodes. Hence, the flow rate values should actually be negative. However, for reasons of clarity only the magnitude of non-dimensional flow rate is plotted. At 15 V input, these characteristics clearly reveal the superior performance of the pump with 4 mm diodes for both the series combination and single cone diode. The situation may not be entirely symmetric when the inflow and outflow diodes are switched and the single cone diodes are operated in pumping mode.

At 25 V, the relative performance of the 4 mm and 6 mm series combination remains unchanged whereas the 6 mm cone diode surpasses the 4 mm single cone in suction performance. Although the performance becomes nearly identical at full load conditions, the 6 mm single cone has a higher zero-load flow rate as well as better suction performance at intermediate back pressures. Again, at 25 V, the performance difference between the series diodes and the single cone diodes is easily noticeable. The zero-load flow rate for both single cone diodes is higher than that obtained using series combination of diodes at 25 V. However, it must be kept in mind that the comparison is not straightforward since the series diodes are pumping while the single cone diodes are in suction mode.

4 Conclusions

The behavior of a non-uniform resonator coupled with four different fluidic diode configurations was experimentally investigated. The increase of back pressure with increase in driving amplitude for a given flow rate has been reconfirmed. The superior performance of 4 mm series diodes in comparison with 6 mm series diode config-uration has been verified. It was found that, contrary to expectation, single cone diode elements with 45 mm length exhibited forward flow in the diffuser direction as opposed to the nozzle direction. The same dependence of pumping characteristics on diode diameter was not observed with single cone element. At increased driving amplitude, the 6 mm single cone diode element outperformed the 4 mm single cone diode element with respect to tank suction characteristics. This might be indicative of a different rectifying mechanism for the single cone element as opposed to that of series diode configurations. The suction characteristics of the single cone elements were found to be better than the pumping characteristics of the series diode config-urations although it has not been verified if the same can be said about the pumping characteristics of the single cone diode configuration.

References

1. Valve-Less VT (2015) Rectification pumps. Encycl Microfluid Nanofluidics, 3399–3415. https://doi.org/10.1007/978-1-4614-5491-5_1656
2. Olsson A, Stemme G, Stemme E (2006) The first valve-less diffuser gas pump. In: Proceeding of IEEE-MEMS'97, pp 108–113. https://doi.org/10.1109/memsys.1997.581780
3. Manopoulos CG, Mathioulakis DS, Tsangaris SG (2006) One-dimensional model of valveless pumping in a closed loop and a numerical solution. Phys Fluids 18. https://doi.org/10.1063/1.2165780
4. Nabavi M (2009) Steady and unsteady flow analysis in microdiffusers and micropumps: a critical review. Microfluid Nanofluidics 7:599–619. https://doi.org/10.1007/s10404-009-0474-x
5. Lucas TS (1999) RMS energy conversion
6. Thomas SK, Muruganandam TM (2015) Acoustic blower using fluidic diodes and a nonuniform resonator. Int J Flow Control 7:55–66. https://doi.org/10.1260/1756-8250.7.1-2.55
7. Thomas SK, Muruganandam TM (2017) Nonuniform resonator based valve-less standing wave suction pump for gases. Sens Actuators Phys 261:40–48. https://doi.org/10.1016/j.sna.2017.05.004
8. Nguyen N-T, Huang X, Chuan TK (2002) MEMS-micropumps: a review. J Fluids Eng 124:384. https://doi.org/10.1115/1.1459075
9. Boluriaan S, Morris P (2003) Acoustic streaming: from Rayleigh to today. Int J Aeroacoustics 2:255–292. https://doi.org/10.1260/147547203322986142
10. Morris PJ, Boluriaan S, Shieh CM (2004) Numerical simulation of minor losses due to a sudden contraction and expansion in high amplitude acoustic resonators. Acta Acust United Acust 90:393–409

Alternate Schlieren Techniques in High-Speed Flow Visualization

S. Vaisakh and T. M. Muruganandam

Abstract This article discusses about schlieren methods which can draw hidden details in high-speed flow visualization. Mainly, two schlieren techniques are used, namely, inclined schlieren and focusing schlieren. These two techniques have been applied to visualize normal-shock–boundary-layer interaction in ducts. The paper explained the possibility to measure normal shock oscillation in spanwise/transverse direction. Identification of shock location across the duct span is also illustrated, using focusing schlieren. Further, the possibilities and limitations of focusing schlieren in high-speed flow visualization have been discussed.

Keywords Supersonic flow · Shock waves · Schlieren methods

1 Introduction

Schlieren imaging is one of the primitive and yet a powerful tool in high-speed flow visualization. Even though different types of schlieren methods and arrangements exist, conventional Z-type schlieren is the most commonly used one. The line of sight integration of schlieren image limits its applicability in extracting three-dimensional data. Focusing schlieren [1, 2] can limit this problem to a certain extent by using the knowledge of optical system point spread function and focusing on a narrow region in the optical axis. Hence, it gains more attention in recent years [3–5], even if it was introduced 60 years ago. The advent of digital image processing helps focusing schlieren to extract more information about the flow field. Inclined schlieren [6] is another variant, which basically looks at the flow field/problem in a different angle to extract hidden details. This paper discusses some of the advantages and challenges of these schlieren variants (inclined schlieren and focusing schlieren) in supersonic flow

S. Vaisakh (✉) · T. M. Muruganandam
Department of Aerospace Engineering, Indian Institute of Technology Madras, Chennai 600036, India
e-mail: vaisakh0123@gmail.com

T. M. Muruganandam
e-mail: murgi@ae.iitm.ac.in

visualization. Different schlieren visualizations of shock-wave/boundary-layer inter-
action and shock–shock interaction, obtained from different experimental setups, are
presented in this paper.

2 Experımental Facılıty

Results from two separate experimental setups are presented in this paper. Figure 1
shows the details of those two setups. The first setup (termed as 'setup I') is designed
to study normal shock-wave–boundary-layer interaction in a duct. The field of view
for the first setup is marked in Fig. 1a. This field consists of a normal shock interacting
with the boundary layer in a rectangular duct. The duct top wall has a divergence
of 4° to stabilize the normal shock. The Mach number ahead of the normal shock is
1.5. This Mach number is strong enough to cause a large adverse pressure gradient
across the normal shock, and the wall boundary layer is not capable of overcoming
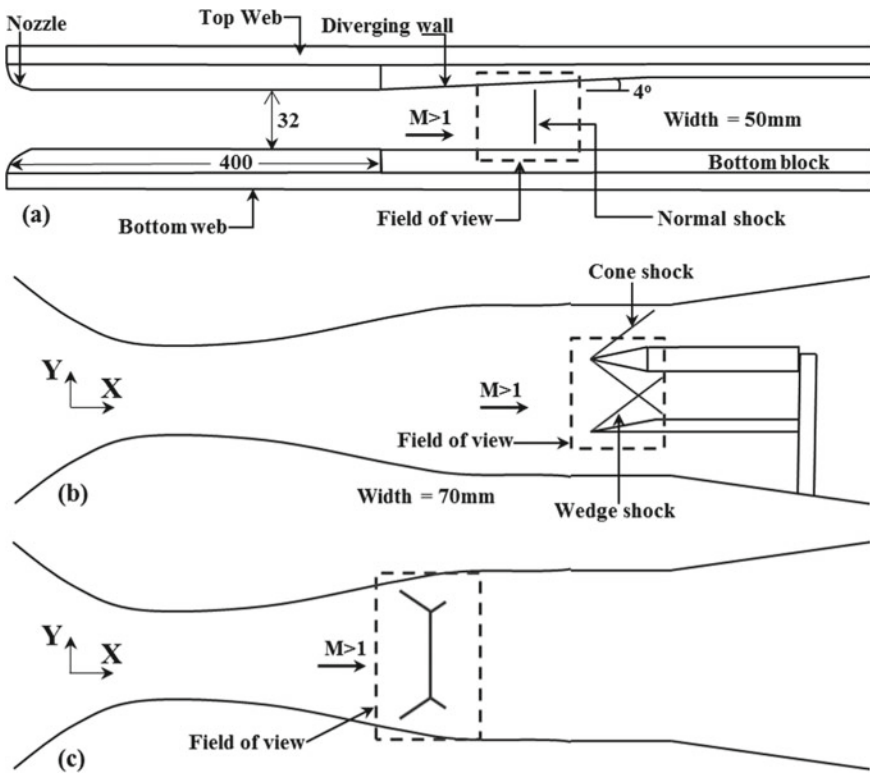this adverse pressure gradient without separation. Hence, boundary layer separation

Fig. 1 Details of experimental setups

occurs and leads to bifurcation of the normal shock. A 'lambda foot' shock pattern is formed at the shock-wave/boundary-layer interaction region. So the flow is three dimensional in the duct. The settling chamber pressure is kept constant to 1.65 bar, during flow visualization.

The second setup is a C-D nozzle with a small diverging diffuser and is used in two styles (Fig. 1b, c). The field of views for the second setup in two styles are marked in Fig. 1b, c. In the first style (Fig. 1b), termed as 'setup II'), the visualization field consists of a cone (cone half angle = 22°) and wedge (wedge angle = 15°). Spanwise-width and diameter of wedge and cone are 30 mm and 9 mm, respectively. The Mach number ahead of the cone/wedge apex is 1.8. The Mach number and cone-wedge angles were chosen in such a way that, the resulting cone-wedge shock interaction led a Mach reflection. This led to a three-dimensional shock structure. In the second style (Fig. 1c), termed as 'setup III'), the setup has a C-D nozzle followed by a diverging diffuser only. Figure 1c shows the second setup without cone and wedge, instead a normal shock stands in the C-D nozzle. The Mach number ahead of the normal shock is 1.6. The normal shock interacts with the nozzle boundary layer and causes flow separation. This normal shock-wave/boundary-layer interaction is the region of interest in this case.

3   Inclined Schlieren

In conventional schlieren imaging, the parallel beams from first mirror/lens pass perpendicular to the test section is termed here as 'normal' schlieren. If the conventional schlieren is arranged at an angle, i.e., the parallel beams from the first mirror/lens pass at an angle through the test section, then it is termed as 'inclined' schlieren. This section is intended to show the ability of 'inclined' schlieren in extracting hidden details, which 'normal' schlieren can't. Figure 2 shows the 'normal' schlieren image of a normal shock-wave/boundary-layer interaction taken with the experimental setup shown in Fig. 1c. The normal shock-wave/boundary-layer interaction in the duct can lead to separation of boundary layer, bifurcation of the normal shock and 'lambda foot' formation at the interaction region, along with a secondary shock wave [7, 8]. These features can be captured with 'normal' schlieren and are indicated in Fig. 2. It is important to note that the bifurcation of shock happens across the duct cross section. So the 'normal' schlieren cannot give information about the spanwise shock bifurcation. The 'inclined' schlieren image of a normal shock is shown in Fig. 3. This 'inclined' schlieren image of a normal shock-wave/boundary-layer interaction is taken with the experimental setup shown in Fig. 1a. With inclined schlieren, the left and right edges of the normal shock parallel to left and right side walls are imaged. From the knowledge of this projected distance between shock edges and schlieren inclination angle (θ, see Fig. 4), it is possible to obtain the 'spanwise-length' of the 'normal part' of the normal shock [6].

The 'normal' schlieren images in Fig. 2 are taken with vertical knife edge, but the 'inclined' schlieren image in Fig. 3 is taken with horizontal knife edge. Figure 4
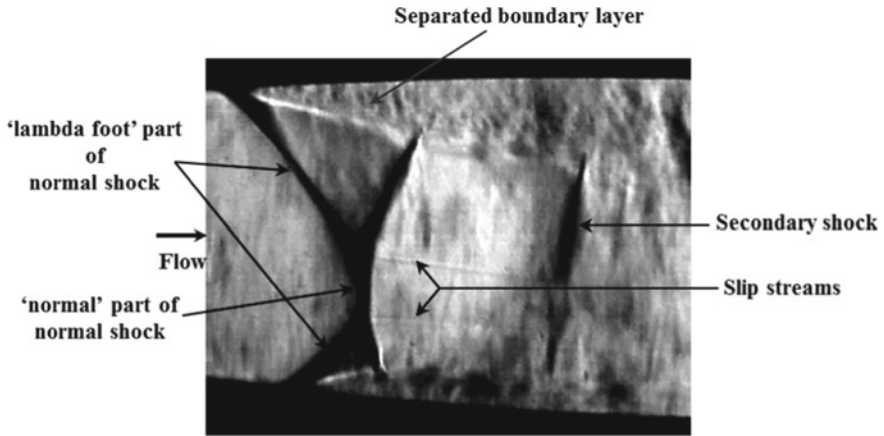
Fig. 2 'Normal' Schlieren image (from setup III) of normal shock-wave/boundary-layer interaction
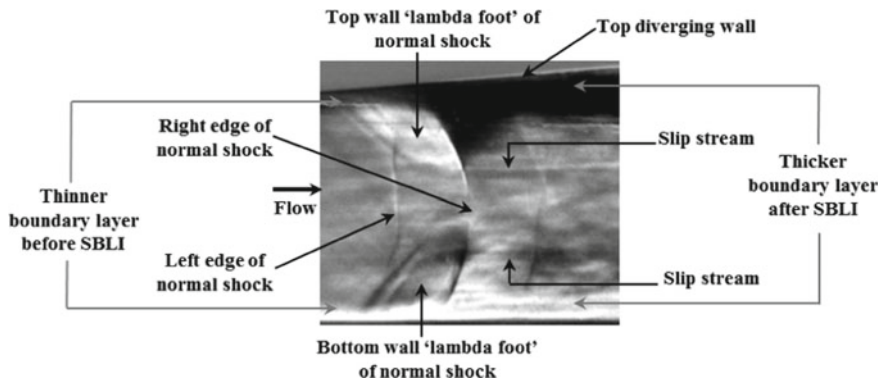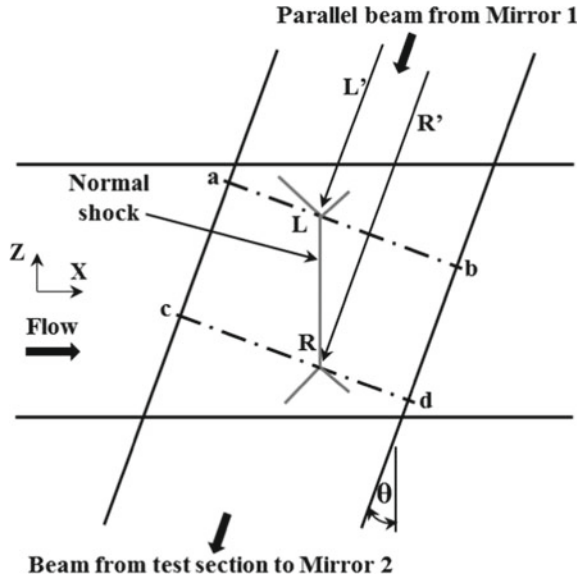

Fig. 3 Inclined Schlieren image of normal shock-wave/boundary-layer interaction with horizontal knife edge (from setup I)

shows a schematic of the 'inclined' schlieren beam path across spanwise-length of normal shock (i.e., top view of the bifurcated normal shock in the test section). 'L' and 'R' represent the left and right edges of the normal shock. In the field of view of 'inclined' Schlieren, the left and right edges of the normal shock falls on the plane a-b and c-d, respectively. In the vicinity of 'L', the light rays will refract towards 'b', due to positive density gradient across 'L' in plane a-b. Similar ray refraction happens at right edge also. The normal shock has a curvature and hence the left and right edges get picked up in this horizontal knife edge schlieren (Fig. 3).

The shock-wave/boundary-layer interaction causes shock oscillation in axial direction around a mean location (for a fixed stagnation pressure) [9]. The shock in a duct can also oscillate in the spanwise direction [6] and hence in transverse direction also.

Using 'inclined' schlieren, the 'spanwise-width' variation can be calculated [6]. In order to capture the spanwise shock oscillation, a combined ('normal' and 'inclined') schlieren arrangement is required. This arrangement consists of simultaneous use of 'normal' and 'inclined' schlieren imaging. The focal planes for both 'normal' and 'inclined' schlieren have to be calibrated against the laboratory coordinates. The 'normal' schlieren gives the axial shock location. The 'inclined' schlieren gives the 'spanwise-width' of the normal part of normal shock. To get spanwise oscillation, the locations of left edge (L) and right edge (R) in the laboratory coordinates need to be known. Since the axial location of the normal shock is known from 'normal' schlieren, the L and R should locate in the rays L' and R' passing through these points, respectively (see Fig. 4). The angle of the rays L' and R' are same as that of the tilt angle of 'inclined' schlieren. The ray passing through both shock edges (triple points) is T'. The point where L' meets T' is the location of L for a given instant of time. Similarly, the point where R' meets T' is the location of R for a given instant of time.

So far, the discussions were concentrated on left and right edges of the normal shock. A bifurcated normal shock in a duct has two more edges, namely, top and bottom edges, which are not visible in 'inclined' schlieren with vertical knife edge. Figure 3 shows 'inclined' schlieren image of normal shock-wave/boundary-layer interaction with horizontal knife edge. The top and bottom edges of the normal shock are not getting picked up like vertical knife edge case. The reason can be the low density gradient in the vertical direction at this tilt angle. A sharp top and bottom edges may appear if the tilt angle θ increases more than 70°. 'Inclined' schlieren tilt is limited by field of view blocking from edges of test section. The amount of tilt possible depends on span of the test section. As span increases, the possible

tilt without interference of test section edges decreases. However, the top wall and bottom wall 'lambda feet' along the duct span is imaged in Fig. 3. In top wall 'lambda feet', the region upstream of the leading edge of right shock 'lambda foot' appears as bright, and the region downstream of it appears as dark. This is because across the leading edge the density gradient is positive in upward direction, and across the trailing edge the density gradient is positive in downward direction. In bottom wall 'lambda feet', the intensity jump is opposite to the top wall. This is similar to the appearance of top wall boundary layer and bottom wall boundary layer as dark and bright regions, respectively.

4   Focusing Schlieren

Figure 5 shows focusing schlieren system aligned to a small supersonic wind tunnel in the Gas dynamics lab of IIT Madras. The light source, lenses, source and cut-off grids, and camera are mounted on a straight aluminum beam, which again mounted on a large traverse. So the entire focusing schlieren system can be moved in the spanwise direction. In focusing schlieren images, the schlieren effect is limited to a small region adjacent to camera focal plane. This helps to isolate high-speed flow phenomena like shock waves, expansion fans, and undesirable wall effects which cannot be removed using background subtraction.

The focusing schlieren can be used to reveal three-dimensional shock structures in a supersonic flow. Figure 6 shows a three-dimensional shock structure resulting from the Mach reflection of a cone-wedge shock interaction. Figure 6a shows the flow field
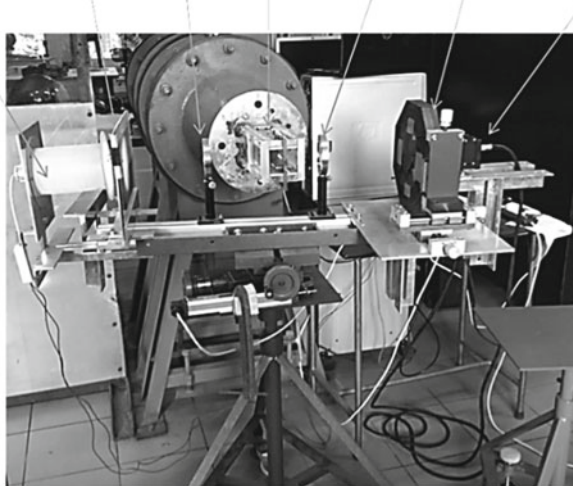

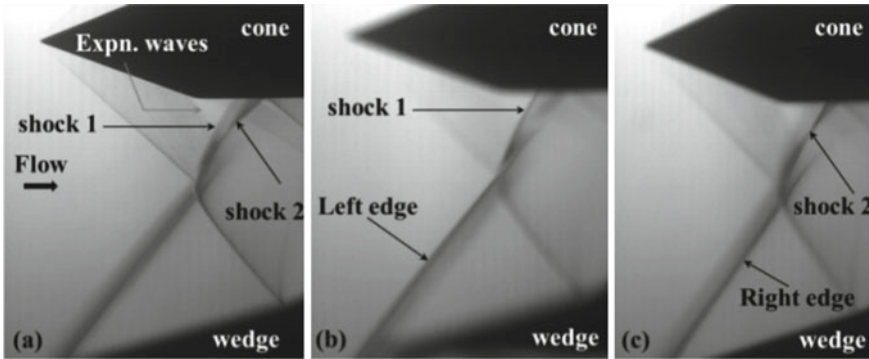**Fig. 5** Focusing schlieren system

Fig. 6 'Normal' focusing Schlieren images from spanwise scan (from setup II)

with the 'normal' focusing schlieren focal plane aligned at the cone center plane. The shock reflection toward the cone has two shock edges, marked as shock 1 and 2. In conventional schlieren, it is difficult to identify the position of these shocks, i.e., whether shock 1 or 2 is located left/right to the cone center plane. It is possible to solve this ambiguity by imaging the flow field with focal plane away from the cone center plane in the spanwise direction. Figures 6b, c show the schlieren images acquired with focal planes left and right (to the flow) to cone center plane, respectively. Shock 1 is sharp in Fig. 6b, while shock 2 gets blurred. Conversely, shock 2 is sharp in Fig. 6c, while shock 1 gets blurred. This reveals that shock 1 and 2 are located at the left and right sides of the cone center plane, respectively. Moreover, the left and right edges of the incident oblique shock from the wedge are sharp in Fig. 6b, c, respectively. This is due to a small tilt in the model alignment. In Fig. 6a, both edges of this incident oblique shock are in blurred form, as the schlieren focal plane is at the cone center plane. Figure 7 shows 'inclined' focusing schlieren images of a bifurcated normal shock in a duct flow. The schlieren focal plane is scanned from right side wall to left side wall. In this scanning process, first the right edge of the shock appeared as sharp (Fig. 7a) and then gets blurred out (Fig. 7c). Both left and right edges of shock become visible (but not sharp) at mid-way of scan (Fig. 7b),
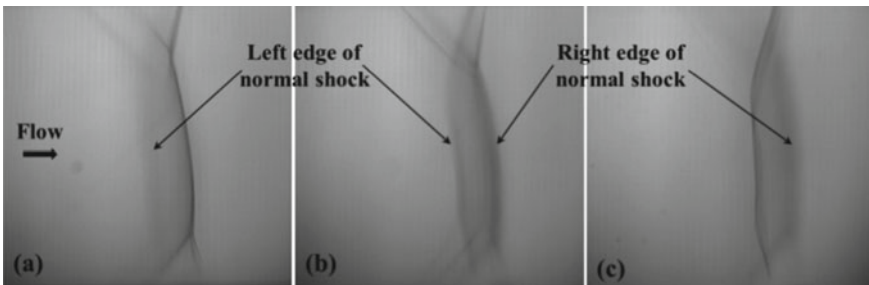

Fig. 7 'Inclined' focusing Schlieren images from spanwise scan (from setup I)

and toward the end of scan the left edge of the shock becomes sharp (Fig. 7c). A full spanwise scan with 'inclined' focusing schlieren can give the distance between these shock edges, and hence measure the spanwise-width of the 'normal' part of a bifurcated normal shock.

5   Summary

Using 'inclined' schlieren, the spanwise-width of a bifurcated normal shock can be calculated. This implies that simply by looking at the flow problem at a different angle can help in its diagnostics. A combination of 'normal' and 'inclined' schlieren can help to estimate the spanwise oscillation of the bifurcated normal shock in a duct. In order to visualize the top and bottom edges of the bifurcated normal shock, this study suggests to go for a tilt in which θ is more than 70°. Focusing schlieren can avoid disturbances from the wall side windows. Again, 'inclined' focusing schlieren along with spanwise scan can reveal three-dimensional shock structures and quantitative measurements in a supersonic flow.

References

1. Kantrowitz A, Trimpi RL (1950) A sharp focusing schlieren system. J Aeronaut Sci 311–314
2. Dixon-Lewis G, Isles GL (1962) Sharp focusing schlieren systems for studies of flat flames. J Sci Instrum 39:148–151
3. Hargather MJ, Lawson MJ, Settles GS, Weinstein LM, Gogineni S (2009) Focusing-schlieren PIV measurements of a supersonic turbulent boundary layer. In 47th AIAA Aerospace Sciences Meeting, AIAA, pp 2009–2069
4. Kouchi T, Goyne CP, Rockwell RD (2015) Focusing schlieren visualization in a dual mode scramjet. Exp Fluids 56:211
5. Vaisakh S, Muruganandam TM (2017) Schlieren tomography to visualise three dimensional supersonic flows. In: Proceedings of the 31st international symposium on shock waves
6. Vaisakh S, Muruganandam TM (2018) Schlieren measurement of 'normal-spanwise length' of a bifurcated normal shock wave in a rectangular duct. Exp Thermal Fluid Sci 96:43–47
7. Papamoschou D, Zill A (2009) Supersonic flow separation in planar nozzles. Shock Waves 19:171–183
8. Bruce PJK, Burton DMF, Titchener NA, Babinsky H (2011) Corner effect and separation in transonic channel flows. J Fluid Mech 679:247–262
9. Matsuo K, Kim HD (1993) Normal shock oscillations in supersonic diffusers. Shock Waves 3:25–33

Development of a Retro-Reflective Screen-Based Large-Field High-Speed Shadowgraph Flow Visualization Technique and Its Application to a Hydrogen-Fueled Valveless Pulsejet Engine

C. Rajashekar, Shambhoo [ID], H. S. Raghukumar, Rajeshwari Natarajan, A. R. Jeyaseelan, and J. J. Isaac

Abstract Large field flow visualization of the unsteady combusting flow inside a hydrogen-fueled valveless pulsejet engine has been successfully demonstrated by using a retro-reflective screen based high-speed shadowgraph technique. A rectangular cross-sectional valveless pulsejet engine with optical access has been designed, fabricated, and successfully used for demonstrating the effective use of a retro-reflective shadowgraph technique for large and spatially wide flow fields of interest. The aspect ratio of the engine considered for the study was 13.5 and the technique helped to understand the acoustically coupled combusting flow structures from the intake to the tailpipe of the pulsejet engine. A Photron FASTCAM SA4 camera was used in this study. High-speed shadowgraph videos were captured with a frame rate of 13500 frames per second with a resolution of 1024×272 pixels.

Keywords Shadowgraph · Flow visualization · Pulsejet engine · Unsteady combustion · Valveless pulsejet

1 Introduction

Over the years, several flow visualization techniques have been developed and are being used in getting more insight in understanding the complex flow field structures in fluid dynamic devices of scientific interest. Flow visualization studies help in understanding the flow phenomena, to evolve and verify flow models, help make theoretical predictions, and also validate computed solutions. These flow visualization techniques are particularly useful to study complex flow phenomena such as

C. Rajashekar (✉) · Shambhoo · H. S. Raghukumar · R. Natarajan · A. R. Jeyaseelan · J. J. Isaac
Propulsion Division, CSIR-National Aerospace Laboratories, Bengaluru, Karnataka, India
e-mail: rajashekarc@nal.res.in

Shambhoo
e-mail: shambhu_yadav@nal.res.in

unsteady combustion in propulsion systems. Schlieren and shadowgraph are simple, but very effective, non-intrusive flow visualization techniques that have been extensively used by the scientific community [1, 2].

The general well-established methods of flow visualization by shadowgraph and Schlieren techniques capture the flow patterns which have strong density gradients and hence variations in the refractive indices. The common "Z" method is to have a pair of collimating mirrors of the same focal length and a light source which is placed at the focal length of the first mirror which converts the divergent beam from the light source into a parallel beam passing through the test section and this beam is then reflected back by the second mirror to the camera to capture the density gradient (Schlieren) or gradient of the density gradient (Shadowgraph) characterizing the flow field depending on whether a knife-edge is used or not (Fig. 1). In this setup, capturing of the optical field of the flow pattern by Schlieren and Shadowgraph methods is normally limited by the diameter of the collimating mirrors. In situations, where the size of the flow field under study is spatially wide with high aspect ratio, the diameter of the collimating mirror will be a limitation, as it will have an unnecessary vertical optical coverage; it becomes very costly to make such large diameter mirrors; it also becomes impractical to make such mirrors. Specific examples of spatially wide, high aspect ratio flow fields relate to studies of unsteady combusting flow phenomena characteristic of screech and buzz combustion instabilities in gas turbine afterburners and conventional subsonic combustion ramjets and their variants, such as pulsejets. A unique twin-beam shadowgraph technique [3] was developed at CSIR-NAL (which helped to capture the spatially wide flow fields, Copyright applied for). But this technique still could not help to visualize the complete specially wide flow structures inside the pulsejet engine. In such situations, the present method of using a retro-reflective screen becomes very handy and effective.
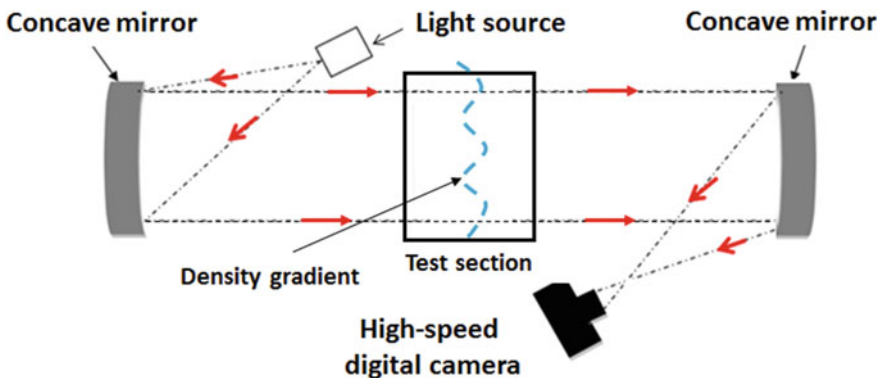

Fig. 1 Schematic of the conventional "Z" shadowgraph arrangement using collimating mirrors

2 Retro-Reflective Screen-Based Flow Visualization SetUp

This method of flow visualization employed a variation of the "Edgerton" method of shadowgraphs using a retro-reflective screen which allowed large-field flow visualization. In this method, the retro-reflective screen used was a 3 M Scotchlite 7610 type which was gray in color and had an adhesive material on its backside for fixing it onto a surface. Figure 2 shows the schematic arrangement of the setup. It consisted of a 1000 W Xenon arc lamp (Newport Corporation, USA) which was a high-intensity light source and a convex lens system for focusing the light beam, a high-speed camera, and a retro-reflective screen. The concentrated light beam from the light source was, diverted using a 45°, 6 mm diameter coated rod mirror which was fixed on the camera lens, and made to pass through the flow field of interest and fall on the retro-reflective screen. Refractive index changes in the flow field due to the fluid dynamic phenomena created a shadow on the screen by bending the light path which was captured by the camera. The distance of the screen from the flow field was varied to get the best shadowgraph image. The sensitivity of the optical system was found to be maximum if the ratio of d_1/d_2 distances was in the range of 0.3–0.7 [4].
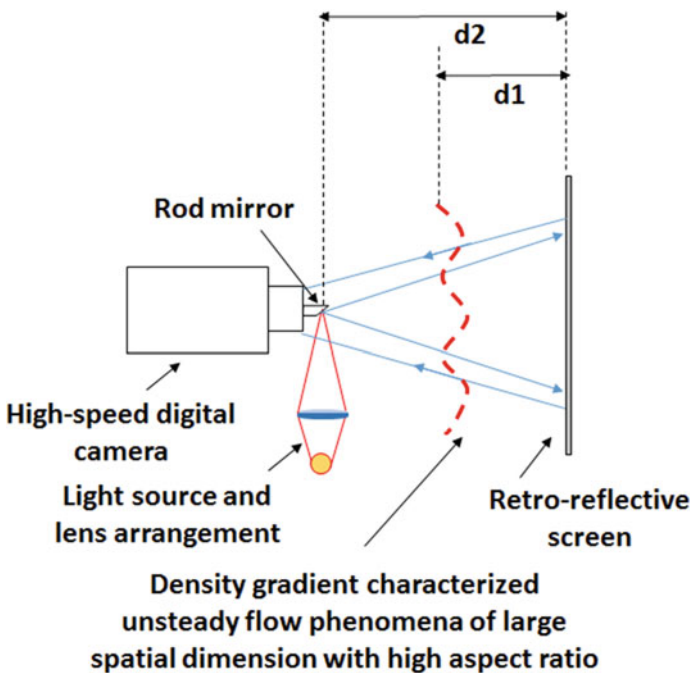
Fig. 2 Schematic of the flow visualization technique using a retro-reflective screen [4]

3   Valveless Pulsejet Engine

A valveless pulsejet engine is a propulsion system with no moving parts. Its main parts are inlet, combustion chamber, and tail pipe. The unsteady flows and the combustion processes that occur within are highly coupled. Figure 3 shows a schematic of the engine and the sequential processes that occur inside such an engine.

Fig. 3 Schematic of a typical valveless pulsejet engine and the sequential processes during its operation [5]

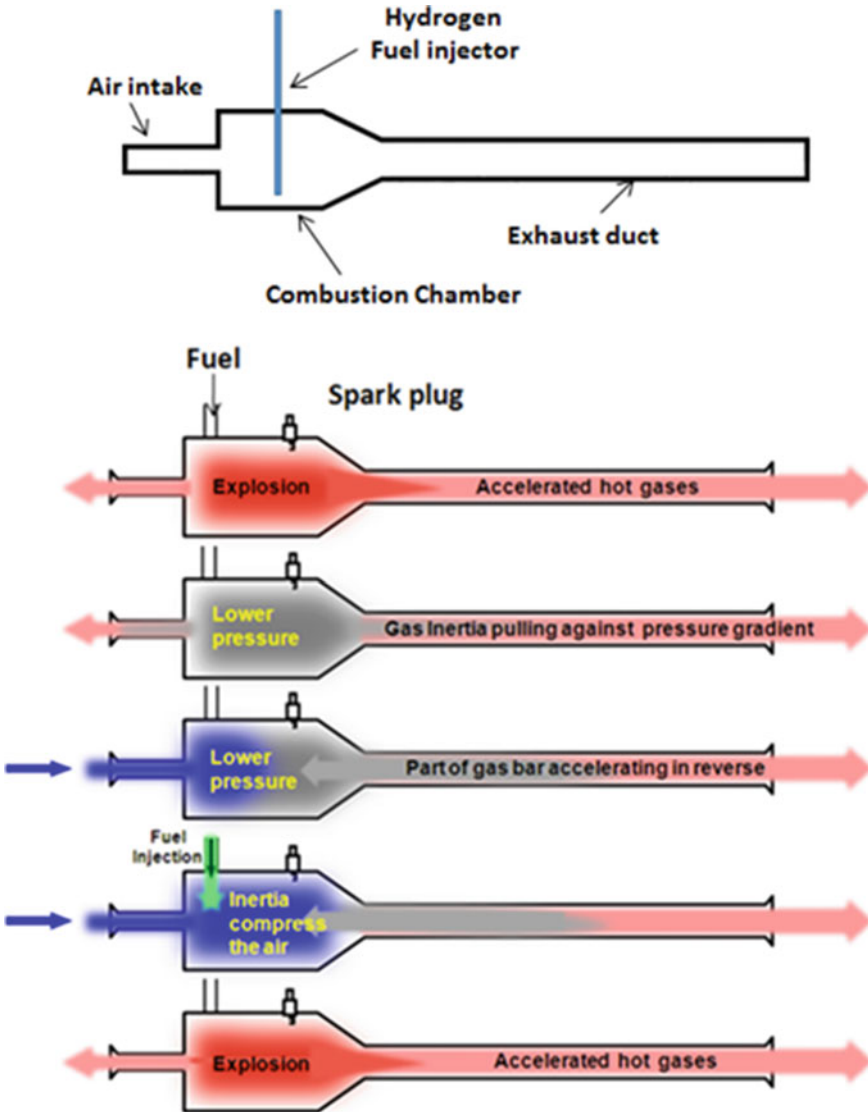The burnt products from the combustion chamber are thrown out from the inlet and the resonant tail pipe. The hot gases from the tail pipe are sucked back which in turn ignites the fresh charge and the pulsations continue. A partial vacuum, due to the "Kadenacy effect," produced in the combustion chamber due to the rapid exhausting of the combustion products allows the fresh air to be inducted into the combustion chamber through the valveless intake which then mixes with the gaseous fuel and gets ignited for the next uniform cycle of stabilized wave interactions.

4   Experimental Setup and Procedure

An optically accessible rectangular cross-sectional valveless pulsejet engine with arrangements for fixing quartz glass view windows at critical zones for flow visualization studies was designed and successfully operated with hydrogen fuel. The dimension of the engine is shown in Fig. 4.

The combustion chamber and the tail pipe windows were fitted with a 3 mm thick quartz glass plate. The tail pipe was divided into two sections to fix smaller width quartz glasses. Fuel was injected by a 6 mm diameter tube with 1.0 mm × 6 (3 × 2) choked ports. A NRV and mass flow device was used in the fuel feed line. The unsteady pressure signal was measured by a KULITE pressure transducer. NI DAS was used for data acquisition. Figure 5 shows the schematic of the experimental test setup.

The engine was started by igniting the fuel and push in a puff of compressed air to aid the mixing of the fuel and help generate turbulence for initiating the pulsating combustion. External flame torch was used for igniting the hydrogen fuel.

Figure 6 shows a typical test result of the pulsejet engine under investigation for the flow visualization studies. The dominant frequency was found to be around 170 Hz. The fuel flow rate of hydrogen gaseous fuel was around 23.2 g/min.

5   Flow Visualization Studies

Figure 7 shows the arrangement of the high-intensity light source and the high-speed camera arrangement. The inset shows the rod mirror mounted on the camera lens. Proper care was taken for the alignment of the light source and the high-speed camera.

Figure 8 shows the pulsejet mounted on the test stand for flow visualization studies. The shadow cast on the retro-reflective screen can also be seen. A Photron FASTCAM SA4 camera was used for capturing the high-speed shadowgraph video. A Nikon lens 28–105 mm was used on the high-speed camera. High-speed shadowgraph videos were captured at a frame rate of 13500 frames per second at a resolution of 1024 × 272 pixels.

As mentioned earlier, the pulsejet was operated using an external flame torch to ignite the hydrogen fuel and a jet of compressed air was used to initiate the pulsations
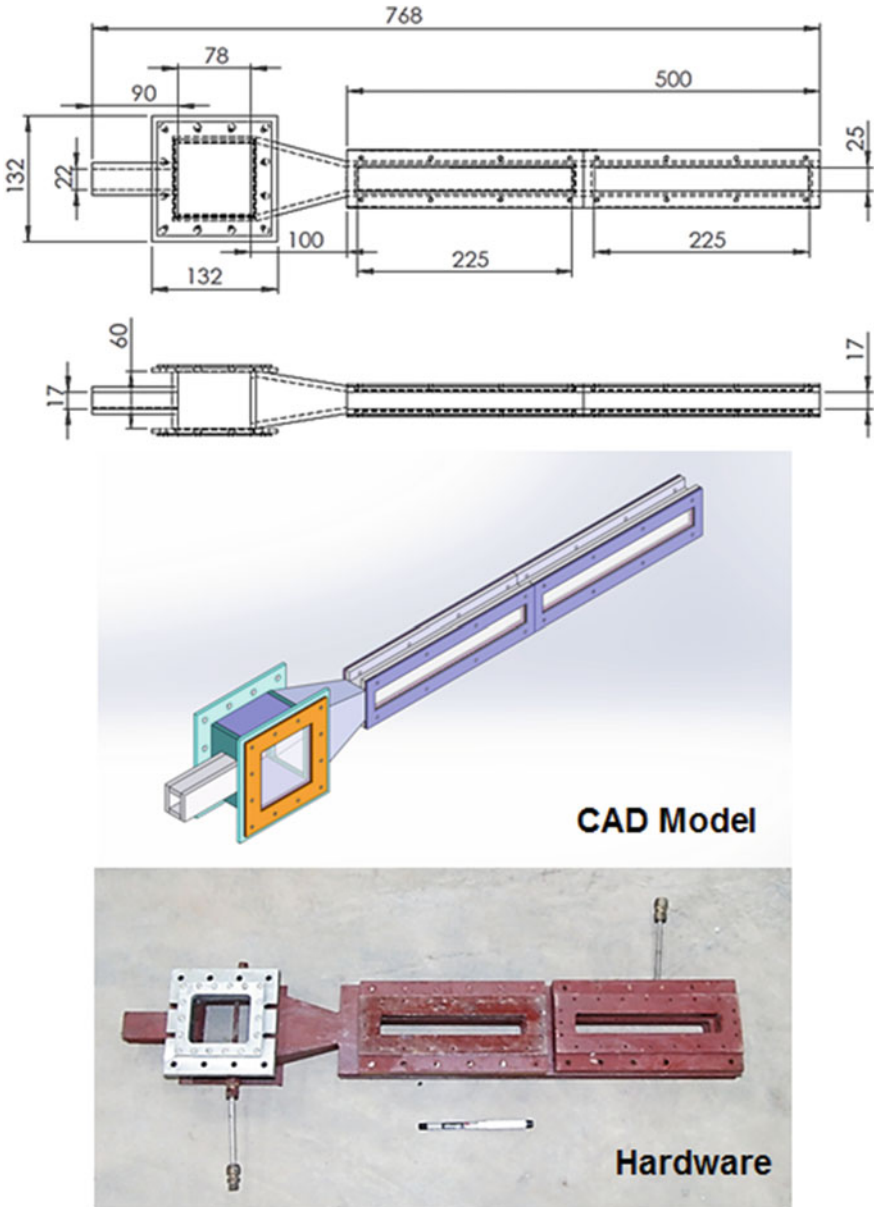
Fig. 4 Dimensional details of the rectangular cross-sectional optically accessible valveless pulsejet engine and the hardware
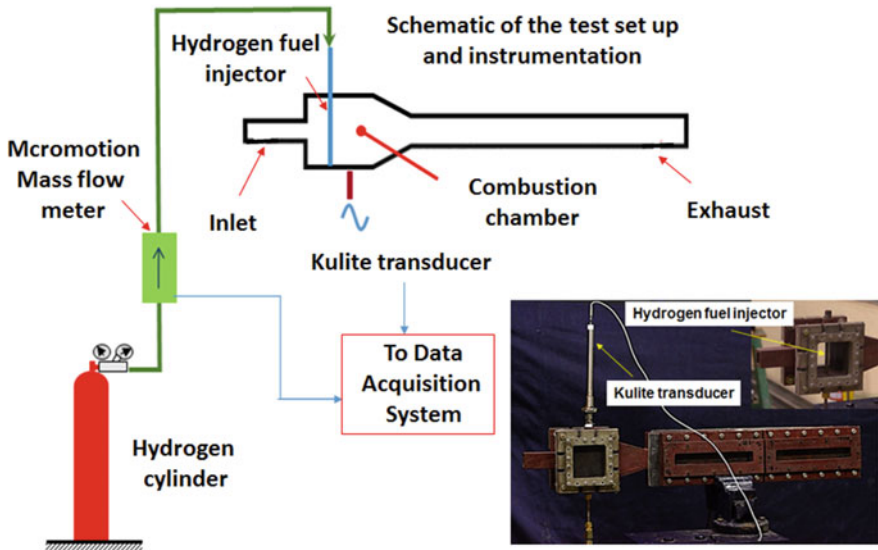
Fig. 5 Schematic of the hydrogen-fueled valveless pulsejet engine test setup and a photograph of the engine mounted on the test stand
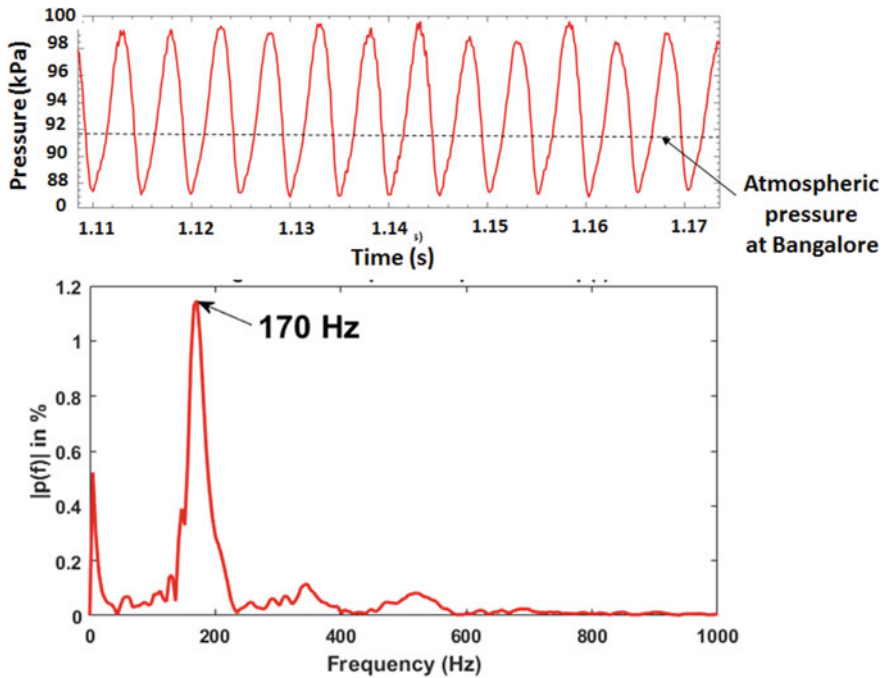
Fig. 6 Unsteady combustion chamber wall pressure variation and the corresponding FFT
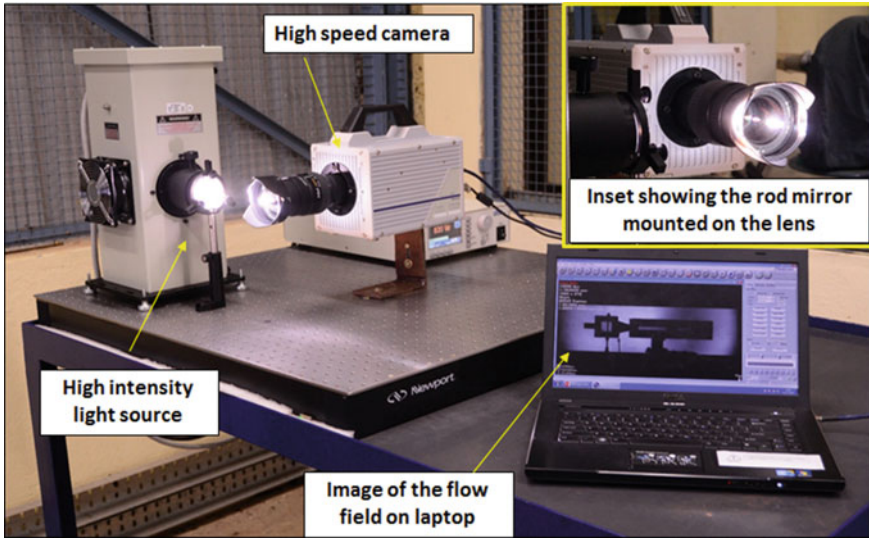
Fig. 7 Photograph of the high-intensity light source and the camera arrangement for high-speed shadowgraph flow visualization studies
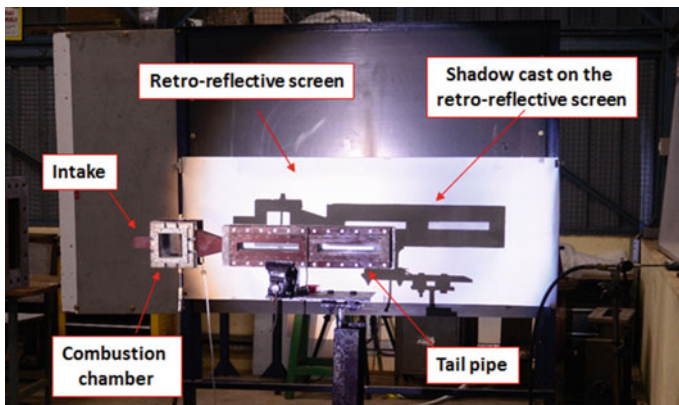
Fig. 8 Photograph of an optically accessible valveless pulsejet engine and its shadow on the retro-reflective screen

in the engine. Figure 9 shows the sequence of high-speed shadowgraph images of events that occurred inside and ahead of the pulsejet engine before the self-sustained pulsations were initiated.

Frame 1 of Fig. 9 shows the shadowgraph image of the hydrogen flame emanating from the inlet and an external air jet gun that was held in front for injecting the air. Frames 2, 3, and 4 show the images when the air jet was being injected through the inlet to create the necessary turbulence for proper mixing in the combustion chamber
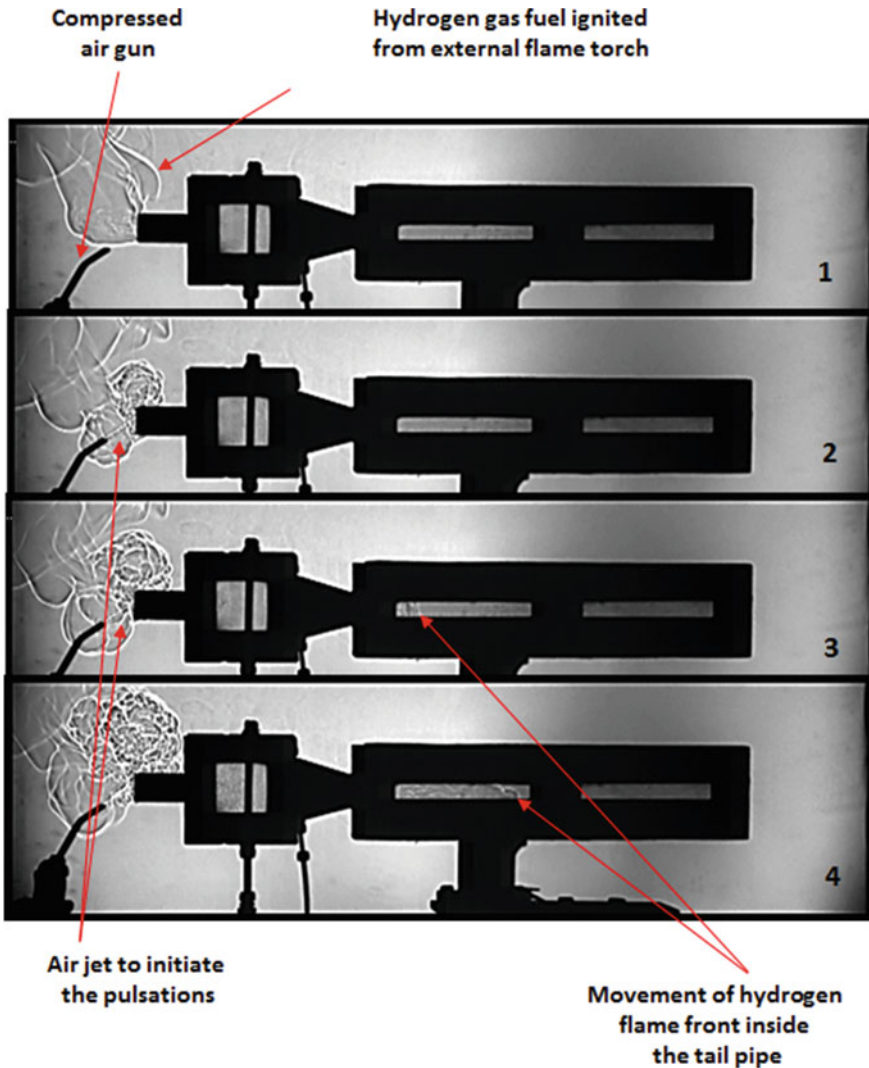
Fig. 9 High-speed shadowgraph images of initiation of self-sustained pulsations in the hydrogen-fueled valveless pulsejet engine

to trigger the onset of the self-sustained pulsations. The movement of the flame front in the tail pipe toward the exhaust can be clearly seen in frames 3 and 4.

Figure 10 shows the critical images of the sequence of events in the pulsejet engine leading to the onset of stable self-sustained pulsations. Frame 1 shows that the air jet that was initially used for mixing has been stopped and the mixed burnt gases being pushed out at the exhaust. Frame 2 shows the hot gases just being ejected both at the inlet and at exhaust simultaneously and indicates the presence of positive
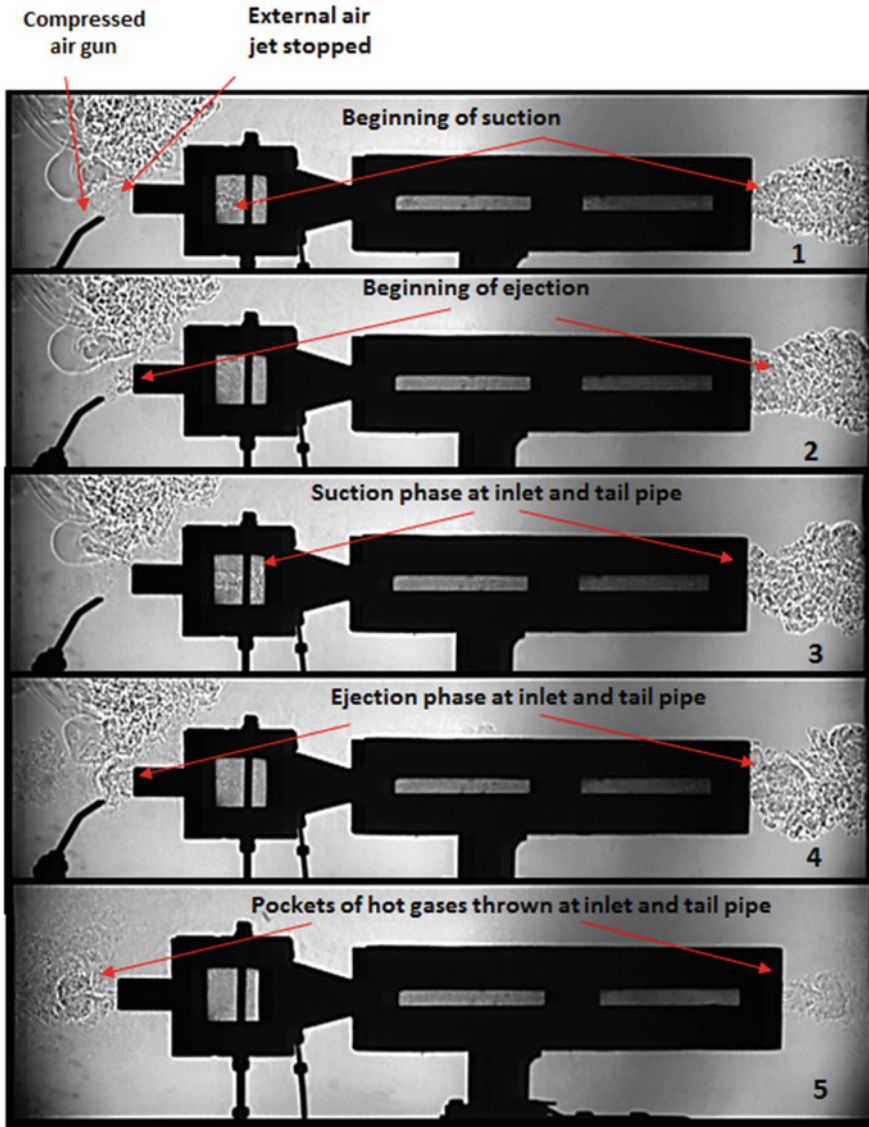
Fig. 10 High-speed shadowgraph images showing the critical stages of onset of self-sustained pulsations in the valveless pulsejet engine

pressure inside the engine. The next frame 3 clearly shows that a negative pressure had set in due to the "Kadenacy" effect and the hot gases were being sucked in from both the inlet and the exhaust. Frames 4 and 5 show the reversal of the process of increase in pressure and the pockets of hot gases being thrown out, thus setting in the self-sustained pulsations.

The back and front movement of the hot gases inside the engine happened due to the increase of pressure inside the engine and ejection of the burnt gases both from the inlet and the exhaust. Once these gases were thrown out, the next cycle set in sucking the fresh air from the inlet and the burnt hot gases from the tail pipe which helped to ignite the fresh air fuel mixture. These motions kept happening until the heat addition was in phase with the pressure rise inside the duct. Once the Rayleigh criteria were met, the self-sustained pulsations continued and the repeated stable pulsations occurred signifying resonant combustion.

Pressure oscillations in the pulsejet are sustained satisfying the Rayleigh criteria. The dimensions and even the shape of these parts play a crucial role for an optimal design of a pulsejet engine. The effective length of the exhaust pipe determines the natural frequency of oscillations, but the fuel and oxidizer(air) input rates also influence the sustained combustion behavior.

Figure 11 shows the time-lapsed frames extracted from the high-speed video clearly showing the flow structures at the inlet, combustion chamber, tail pipe, and the exit region of the tail pipe. The frequency based on the time interval between each pulsation gave a pulsating frequency of 167 Hz which was close to the experimental FFT value of 170 Hz as measured by a Kulite transducer. Frames 2–6 clearly show the ejection of hot gases from the inlet and the exhaust tail pipe, whereas frame 6 indicated the end of the ejection phase and partial beginning of the suction phase. Frames 7–13 show that the negative pressure inside the engine helped in drawing in of fresh air/fuel mixture from the inlet and sucking of some of hot gases from the exhaust for ignition. Some of the flow structures inside the tail pipe of the engine were not clearly visible probably because the narrow tail pipe part of the pulsejet engine had a recess step of 3 mm which was required for assembly of the quartz glass window.

6   Conclusions

A rectangular cross-sectional valveless pulsejet engine with optical access has been designed, fabricated, and successfully operated. The critical zones of the pulse-jet operation were effectively captured by high-speed shadowgraphs using a retro-reflective screen thus demonstrating the effective use of the retro-reflective shadow-graph technique for large and spatially wide flow fields of interest. The shortcoming of using conventional collimating mirrors in which the diameter becomes a serious hurdle both in terms of practical usage and the huge cost involved in making them in studying such large flow fields has been overcome by using this cost-effective, high-speed retro-reflective screen method.
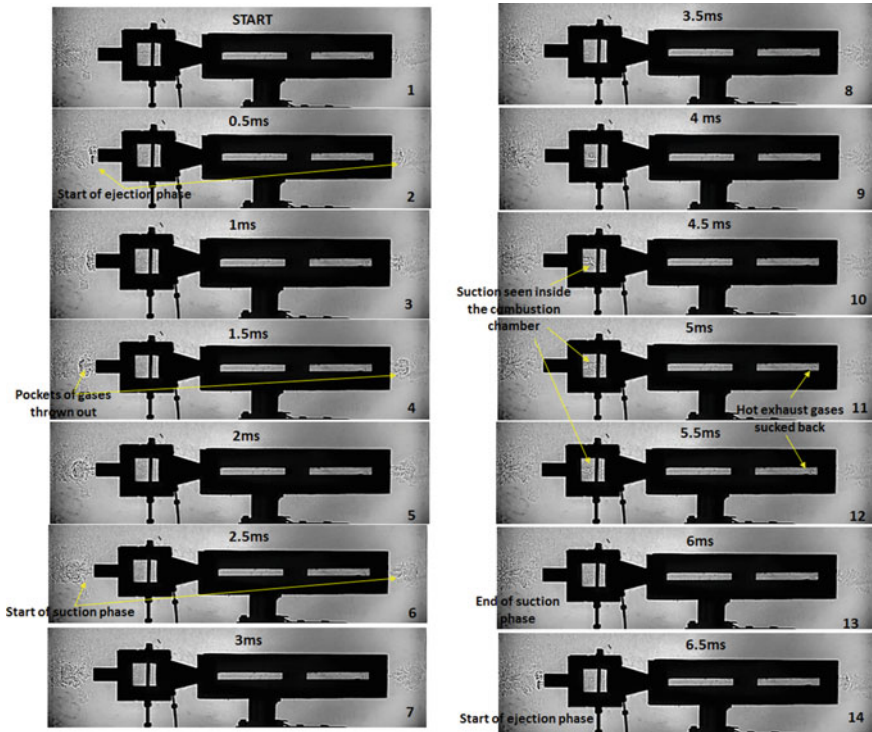
Fig. 11 Time-lapsed high-speed shadowgraph images showing the structure of the large and spatially wide flow field of a valveless pulsejet engine captured by the retro-reflective screen flow visualization method

The complex flow structures related to unsteady resonant combustion and the influence of the pulsejet internal configuration were clearly captured by this flow visualization technique. Since there is no established design methodology of the pulsejet engine, at present this study has helped in understanding the complex flow structure inside such engines, and this information will help model the related complex unsteady combusting flow and hence evolve a design methodology.

References

1. Settles GS (2001) Schlieren and shadowgraph techniques. Springer, Berlin, Heidelberg
2. Wolfgang Merzkirch (1987) Flow visualisation. Academic Press Inc.
3. Rajashekar C, Janaki Rami Reddy M, Raghukumar HS, Isaac JJ (2012) High speed shadowgraph visualization of the unsteady flow phenomena in a valveless pulsejet engine. In: 15th international symposium on flow visualization. Minsk, Belarus
4. Michael JH, Settles GH (2009) Retroreflective shadowgraph technique for large scale flow visualization. Appl Opt 48(22), 4449–4457
5. https://en.wikipedia.org/wiki/Valveless_pulsejet, Accessed May 2018

High-Speed Shadowgraph Flow Visualization Studies on the Mechanism of the Onset of Screech and Its Attenuation in a Model Afterburner Test Rig

C. Rajashekar, Shambhoo , **H. S. Raghukumar, G. Sriram,**
S. Chenthil Kumar, G. Udaya Sankara Athith, K. Vijayasankaran,
K. Ashirvadam, and J. J. Isaac

Abstract Screech combustion instabilities continue to be one of the most detrimental and, in fact, fatal issues for the development of a high-performance afterburner. It is essential to study the underlying flow-physics related to the crucial thermo-acoustic coupling to acquire a predictive capability and to evolve a methodology for the attenuation of screech. A versatile test facility using a single V-gutter flame holder was used to generate the predetermined screech frequency of 2000 Hz in a controlled and sustained manner. The test facility had the capability to run the afterburner model under simulated inlet conditions of pressure and temperatures. The critical zone of flame stabilization near the V-gutter flame holder had complete optical access with quartz glass windows to study the vortex shedding phenomena during the afterburner operation. The critical operating parameters of the test rig were measured using a high-speed NI-based data acquisition system. Flow visualization studies using a high-speed shadowgraph technique was effectively used to understand the onset of screech. A FASTCAM SA-4 Photron high-speed camera was used in this experimental investigation. It was found that the cause for the onset of screech was the vortex shedding frequency from the flame holder locking on to the duct transverse acoustic resonant mode frequency.

Keywords High-speed shadowgraph · Unsteady combustion · Screech · Afterburner · Rayleigh criterion · Combustion instabilities

C. Rajashekar (✉) · Shambhoo · H. S. Raghukumar · G. Sriram · S. Chenthil Kumar · G. U. S. Athith · K. Vijayasankaran · J. J. Isaac
Propulsion Division, CSIR-National Aerospace Laboratories, Bengaluru, Karnataka, India
e-mail: rajashekarc@nal.res.in

Shambhoo
e-mail: shambhu_yadav@nal.res.in

K. Ashirvadam
Gas Turbine Research Establishment - DRDO, Bengaluru, Karnataka, India

1   Introduction

High frequency, transverse mode, screech combustion instability in an aero-gas tur-
bine afterburner is characterized by its high, audible frequency and by the fact that its
sustaining mechanism is not affected by fluctuations in the fuel or air flow rates. The
occurrence of screech can have disastrous consequences and hence its mitigation is
one of the serious challenges in the development of high-performance afterburners
[1–3]. Flames possess intrinsic instabilities associated with the combustion process.
These could become unstable when subjected to pressure oscillations. The unsteady
coupling between the pressure oscillations and the combustion heat release could,
under certain conditions, meet the Rayleigh criterion, leading to combustion insta-
bility. Specifically, screech refers to an acoustic instability of resonant combustion,
with the frequency and phase of the wave oscillations corresponding to those for the
transverse acoustic resonance of the afterburner duct.

A complete understanding and control of these high-frequency screech com-
bustion instabilities constitute the central challenge in the development of high-
performance afterburners. Longitudinal modes with frequencies as low as 50–100 Hz
have been identified and frequencies for radial and tangential modes could be as high
as 5000 Hz. Hence, it was necessary to study the underlying high-speed flow-physics
related to the crucial thermo-acoustic coupling to acquire a predictive capability and
to evolve a methodology for the attenuation of screech.

2   Experimental Test Facility

The test facility consisted of an air feed line of 152.4 mm diameter with a maximum
air delivery pressure of 1 MPa. The critical components of the test facility consisted
of the kerosene-fueled slave combustor, the settling chamber, and the transition ducts
followed by the rectangular section afterburner duct where the V-gutter flame holder
was fitted with the fuel injection system. The primary air supply line was connected
to the main reservoirs of the Compressed Air Facility (CAF) available at the Wind
Tunnel Centre, CSIR-NAL. The air mass flow to the afterburner test rig model was
controlled by a motorized valve airline and it was designed to handle air mass flows of
1–2 kg/s, measured by an orifice plate. Figure 1a shows a schematic and photograph
of the test facility and Fig. 1b shows the instrumentation scheme. A PC-based DAS
was used to acquire the raw data using the LabVIEW program.

Figure 2 shows a 200 mm × 70 mm rectangular cross section afterburner which
was carefully designed to generate the screech frequency of 2000 Hz by a special
technique. The afterburner fuel injector was located upstream of the V-gutter and
the fuel was injected transversely through 0.5 mm holes of two rows of ten ports
each. In the region of the V-gutter, the rectangular afterburner duct was provided
with two complex Helmholtz resonator chambers, one on top and one below and
these chambers had provision to attach variable effectiveness anti-screech liners of
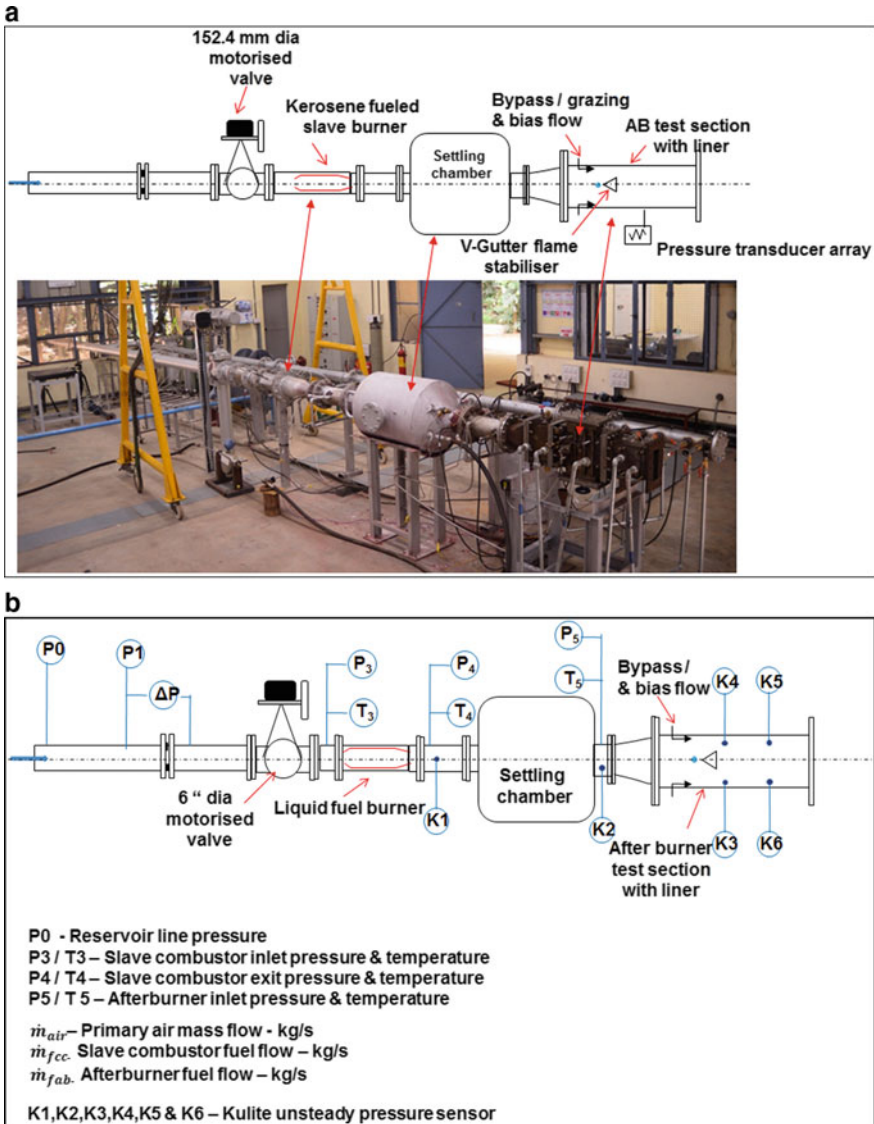
Fig. 1 **a** Schematic and photograph of the test facility. **b** Afterburner test facility instrumentation scheme

various porosities. For the present flow visualization studies, blank liners without any holes were used to isolate the effect of anti-screech liners. The kerosene-fueled main burner (slave combustor) provided the hot air required to simulate vitiated air entry temperatures from 600 to 1000 K at the afterburner inlet section. The exit of the slave combustor was connected to the settling chamber to ensure uniform pressure
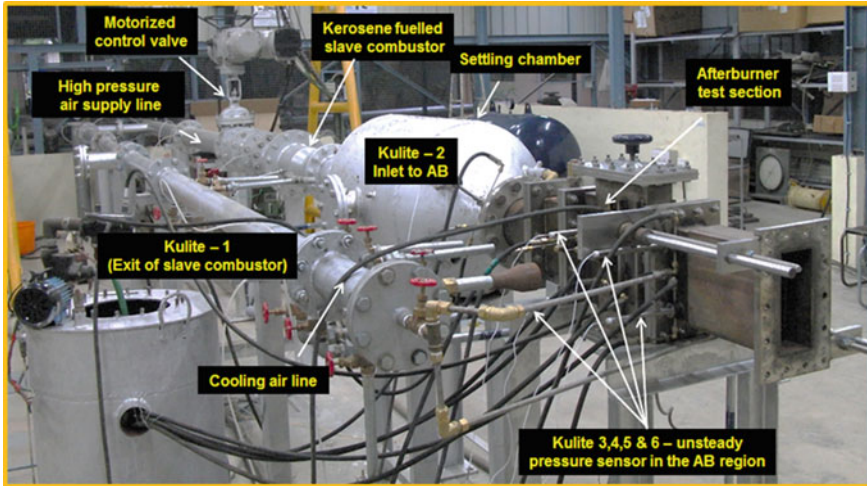
Fig. 2 Afterburner test facility for generating screech with a frequency 2000 Hz

and temperature at the entry to afterburner section. Metered kerosene fuel was fed to the slave combustor and the afterburner using a nitrogen gas top-loading method. The hot section of the test rig had proper cooling arrangements to avoid over heating of the critical afterburner section of the test rig.

3 Afterburner Test Rig with Optical Access Arrangement for Flow Visualization Studies

The critical section of the afterburner test facility was appropriately modified with optical access to carefully study the physics behind the triggering of the screech mechanism. The afterburner section of the test facility had a quartz glass window arrangement to capture both direct flame photos and also to carry out the high-speed shadowgraph flow visualization experimental studies. Conventional Z-type arrangements with collimating mirrors of 300 mm diameter and focal length of ~2.8 m were used for the shadowgraph studies. A PHOTRON FASTCAM SA 4 camera was used to capture the unsteady flow structure in the V-gutter region; camera speeds up to 13500 frames per sec were used. Figure 3 shows a schematic of the complete test setup and the conventional Z-type mirror arrangement for flow visualization studies.
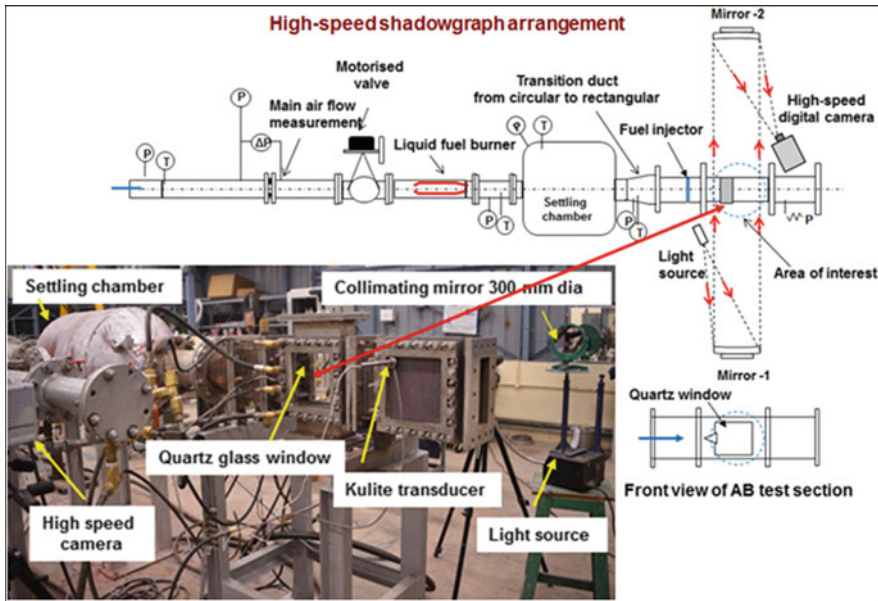
Fig. 3 Afterburner test facility with optical access arrangement for flow visualization studies

4 Flow Visualization Studies on the Afterburner Screech Mechanism

For the flow visualization studies, initial experiments were carried out with the anti-screech liner of 0% porosity and metal side plates were used to cover the V-gutter zones of the afterburner. Experiments were conducted to generate a controlled and sustained screech frequency of 2000 Hz by a special technique at selected after-burner inlet temperatures of around 500–1000 K. The air flow to the AB test rig was controlled from a 152.4 mm diameter motorized valve and the required air flow and pressure was regulated in the test rig for smooth ignition of the slave combustor. Once the slave combustor was ignited, the fuel flow and the line air pressure were controlled to get the required preset afterburner inlet pressure and temperature. The afterburner fuel flow was carefully regulated and after the ignition of the afterburner and stable operating conditions attained, the sudden afterburner fuel flow was care-fully further increased until screech was observed. The occurrence of screech was noted from the distinct high-frequency audible tone. Simultaneously, the FFT of the fundamental mode and the overtones were observed in the control room DAS moni-tor. The raw data and the derived data during the entire test run were acquired in the DAS. Figure 4 shows the typical characteristics for a screech frequency of 2000 Hz. The maximum pressure excursions inside the afterburner duct were observed to be in the range of around 12%.
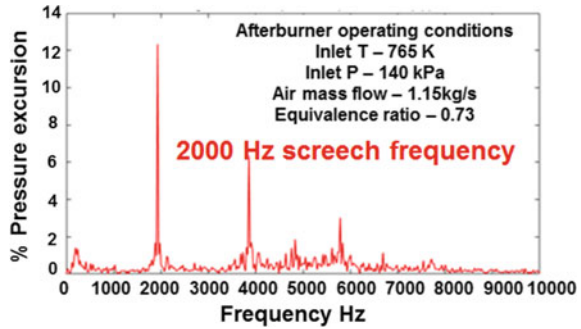
For flow visualization studies, the metal side plates in the V-gutter zone were replaced with quartz glass plates to enable complete optical access. The experiments were carefully conducted to capture high-speed shadowgraph videos during stable afterburner combustion and during the onset of screech. Direct flame photographs using a Nikon D 800 camera were captured during smooth combustion and while screech combustion instability was triggered. Direct photographs (extracted from a video) of the region downstream of the V-gutter flame holder base show the mixing/combustion zones without screech and with screech (Fig. 5a, b). The flame coverage with screech was seen to be broader than that without screech. This is consistent with the general observation that there is an increase in the combustion efficiency with screech. Simultaneously, high-speed photography was also carried out to capture the combustion instability phenomena.
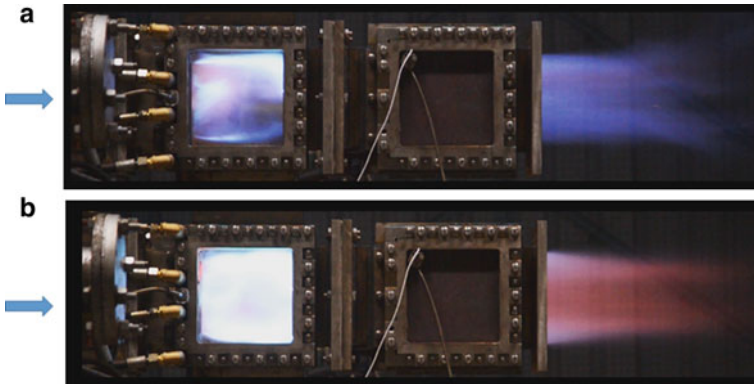

Fig. 5 a Typical afterburner flame photograph during smooth combustion. **b** Typical afterburner flame photograph during screeching combustion

5 Observations and Discussions

It is well known from theory that the unsteady coupling between the pressure oscillations and the combustion heat release could, under certain conditions, meet the Rayleigh criterion leading to combustion instability. It has also been well understood that for screech to occur, the vortex shedding frequency from the V-gutter flame holder lip has to lock-on to the duct fundamental transverse mode acoustic resonant frequency [4, 5]. For a given approach temperature, the fixed fundamental duct frequency which cannot be substantially changed (for a given duct size and mean temperature across the duct) forcibly drives the variable shedding frequency of the V-gutter to shed at the duct mode frequency once it gets locked on by the onset of screech.

In an afterburner, depending on the flow conditions, the flow past the V-gutter bluff body starts shedding at a certain frequency "f2" which is characterized by the Strouhal number. This frequency of shedding is a variable parameter when screech conditions are not prevalent in the AB duct. But the duct fundamental transverse acoustic mode frequency "f1" is fixed for a given approach temperature and cannot be substantially changed. This is what drives the shedding frequency from the V-gutter lip during screech mode operation to get locked on to the duct frequency. Figure 6 shows the lock-on phenomena clearly indicating that duct geometry had a dominant influence on the screech frequency and that the screech frequency was independent of the bluff body size beyond a threshold size and overall equivalence ratio and depends only on the duct height. The product of shedding frequency and the duct height is a constant clearly indicating the lock-on phenomena of the shedding frequency to the duct resonant acoustic mode frequency.

The flow visualization studies have clearly revealed that the major instability-driving mechanism has been identified to be vortex shedding from the flame holder lip coupled with the associated oscillatory flame area variation, fuel atomization, vaporization, and mixing. The high Reynolds number flow past a V-gutter array was dominated by the presence of vortices characterized by the Kelvin–Helmholtz instability (KH), which is a convective flow instability related to the shear layer separating from the V-gutter lip. It was observed that during stable afterburner operation, the flow field in which the mixing layer forms substantially axially downstream of the flameholder lip and within this mixing layer, discrete vortical structures, characteristic of the Kelvin–Helmholtz (KH) instability were seen to symmetrically entrain reactants from the upper side of the mixing layer and combustion products in the recirculation zone, from the lower side of the mixing layer (Fig. 7a).

With the onset of screech, the relatively stable Kelvin–Helmholtz instability transitioned into the unstable Benard–Von Karman instability (Fig. 7b). The unstable flow field was distinctly different. Large vortical structures dominated the unstable flow field. These vortical structures were seen to form periodically and shed downstream to complete a cycle, corresponding to the characteristics of a Benard–Von Karman instability.

Fig. 6 Lock-on phenomena
of screech frequencies
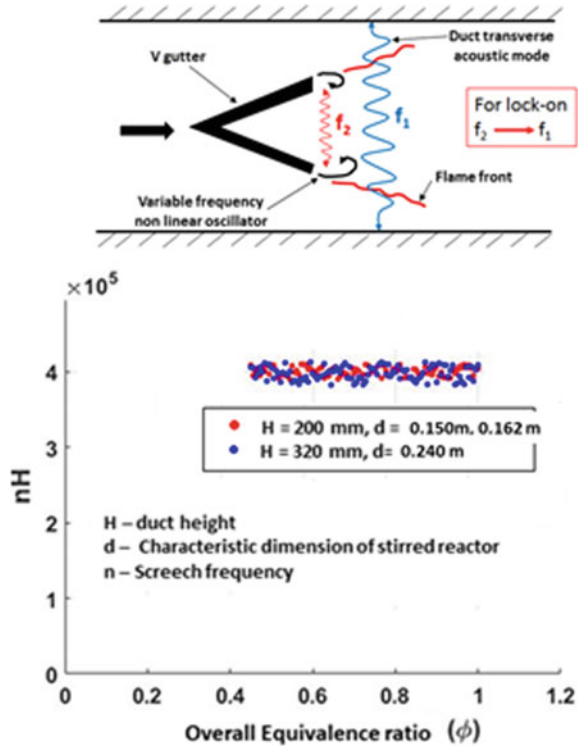
The structured vortex evolution, extracted from the high-speed video shadowg-raphy, is shown in Fig. 7c. The vortex evolution has been tracked for a single cycle and the vortex shedding frequency, within the limits of experimental accuracy, and is seen to be close 1930–2000 Hz, the measured screech frequency. This is distinctly different from an expected Strouhal frequency. It is seen that the vortex shedding frequency had "locked-on" to the duct resonant acoustic transverse mode frequency.

6　Conclusions

A versatile test facility with optical access arrangement for carrying out high-speed shadowgraph flow visualization studies on the physics of the thermo-acoustics of afterburner combustion instability was setup and comprehensive experimental inves-tigations had been carried out in this test rig using a single V-gutter flame holder as the driver to generate the required screech frequency with a special technique. Con-clusive evidence has been established to show that vortex shedding was the cause of the screech combustion instability in an afterburner. The shedding frequency from
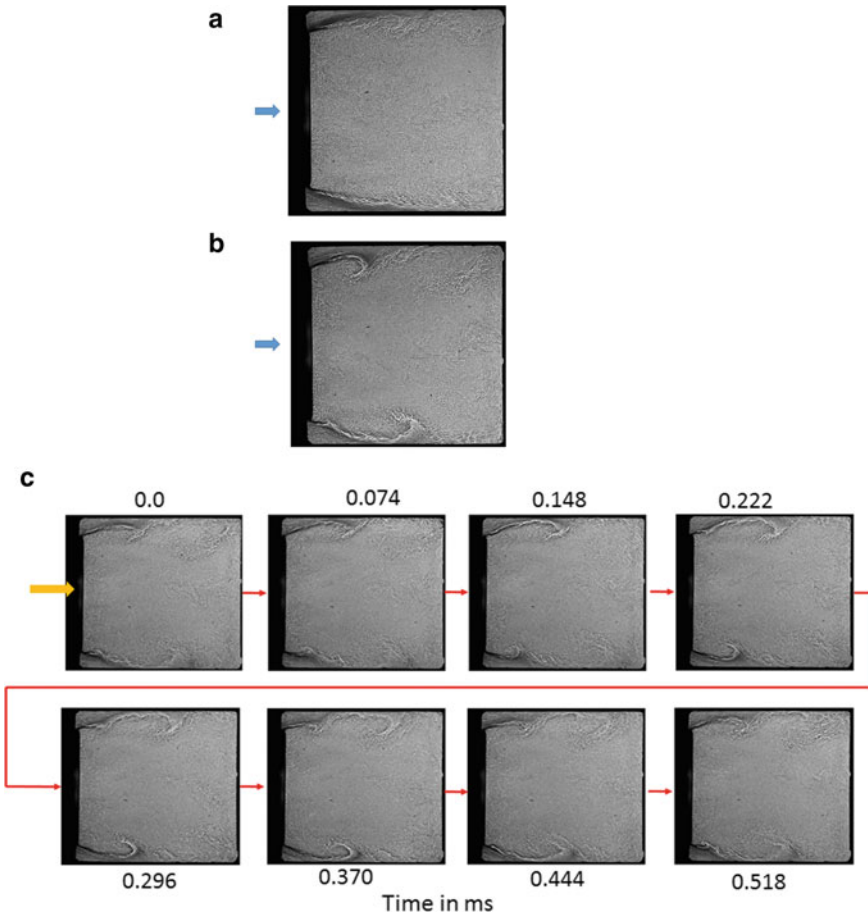
Fig. 7 a Kelvin–Helmholtz instability, which is a convective flow instability related to shear layers separating from the V-gutter lip (stable combustion without screech). **b** Benard–Von Karman instability, which is related to an asymmetric vortex shedding in the flame holder wake. (Combustion with screech). **c** Time-resolved vortex shedding images for one cycle of screech

the tip of the V-gutter flame stabilizer was found to lock on to the duct resonant acoustic frequency during screech combustion instability.

References

1. Sotheran A (1987) High performance turbofan afterburner systems. In: 23rd joint propulsion conference on AIAA-87-1830 AIAA/SAE/ASEE
2. Ebrahimi H (2006) Overview of gas turbine augmentor design, operation, and combustion oscillation. In: 42nd joint propulsion conference on AIAA-2006-4916 AIAA/SAE/ASEE
3. Culick FEC (1988) Combustion instabilities in liquid-fueled propulsion systems—An overview. In: AGARD 72B PEP meeting, Bath, England
4. Emerson B et al (2012) Frequency locking and vortex dynamics of an acoustically excited bluff body stabilized flame. In: 50th AIAA aerospace sciences meeting including the new horizons forum and aerospace exposition on AIAA-2002-0451 AIAA/SAE/ASEE
5. Hall MS, Griffin OM (1993) Vortex shedding and lock-on in a perturbed flow. J Fluids Eng 115(2):283–291 (9 pages)

Space Propulsion

Near-Field Effectiveness of the Sub-Boundary Layer Vortex Generators Deployed in a Supersonic Intake

G. Humrutha, K. P. Sinhamahapatra, and M. Kaushik

Abstract In aircraft engines operating at high Mach numbers, it is exigent to reduce the magnitude of flow speed from supersonic to subsonic before entering the burner, to accomplish a proficient ignition. It is accomplished by a progression of oblique shocks as well as a normal shock wave in supersonic intakes. However, the advantage of shock enabled compression in intakes does not come independent but with colossal losses due to shock-boundary layer interactions, which includes intake unstart and an abrupt thickening/separation of the boundary layer. Controlling these interactions by boundary layer control using micro-vortex generators (MVGs) has gained prominence. In the present study, an attempt is made to control the interactions at the shock impact point in a Mach 2.2 mixed compression intake. Two types of MVGs; a conventional configuration and an innovative ramped-vane configuration were experimentally investigated by varying the MVG heights as 600, 400, and 200 µm. Also, the near-field effects of MVGs are quantified in terms of static pressure variation in the internal flow. It is found that the innovative MVGs of height 200 µm leads to favorable pressure drop in both the upstream and downstream region, due to enhanced flow mixing near the boundary layer.

Keywords Shock wave · Boundary layer · Micro-Vortex generators · Near-field effects · Supersonic intake

List of Abbreviations

SBLI   Shock–Boundary Layer Interaction
MVG   Micro-Vortex Generator
C Side length of the MVG
H Height of the MVG

G. Humrutha · K. P. Sinhamahapatra · M. Kaushik (✉)
Department of Aerospace Engineering, Indian Institute of Technology Kharagpur, Kharagpur 721302, India
e-mail: mkaushik@aero.iitkgp.ac.in

L	Length of the intake model
P	Wall static pressure
S	Spanwise pitch distance between MVGs
W	Base width of the MVG
n	Number of MVGs in a single row
x	Distance from the model leading edge in the x-direction
α	Half angle of the MVG
β	Oblique shock angle
δ	Boundary layer thickness
γ	Specific heat ratio
θ	Flow deflection angle
A_c	Intake capture area
A_t	Intake throat area
M_0	Freestream Mach number
P_0	Stagnation pressure in settling chamber
P_{ts}	Static pressure in the test section
R_c	Contraction ratio
R_{Limit}	Limiting contraction ratio
T_0	Total temperature in settling chamber
A^*	Sonic contraction ratio

1 Introduction

Shock waves in a supersonic flow interact with the viscous boundary layer and lead to increased boundary layer thickness and quite often to separation [14]. Also, Shock–Boundary Layer Interactions (SBLIs) lead to drastic consequences in internal flows such as a supersonic intake, where shock waves are intentionally generated to reduce the flow Mach before entering the burner. Thus, the control of SBLIs is of utmost necessity. An effective method to control the SBLIs is by controlling the boundary layer control. The boundary layer control alters the characteristics of the near wall flow field ahead of an SBLI to prevent or reduce the shock-induced separations in the supersonic intake [13]. This approach is adapted to minimize viscous drag and delay or prevent the emergence of unsteady flow, such as shock-induced buffet. The Sub-Boundary Layer Vortex Generators (SBVGs), also referred to as micro-vortex generators are used in re-energizing the boundary layer with minimal parasitic drag. They have been proven to be surprisingly effective in reducing shock-induced separation [2, 10–12]. The vortices produced by the MVGs transport high-momentum fluid toward the wall, thus creating a fuller velocity profile that is less prone to separation. Ramp type MVGs are known to be effective in reducing the shock-induced separation [1, 3, 4]. However, the counter-rotating vane-type MVGs were found to be more efficient as they eliminated the shock-induced separation [5].

The present study aims to extend the insights on near-field characteristics of two different MVG configurations and to quantify the static pressure variation due to the MVGs in the internal flow field of a supersonic intake. A new type of MVG configuration which utilizes the advantages of both the ramp and vane-type MVGs is tested and compared with the characteristics of the conventional MVG configuration.

2 Experimental Methodology

Cold flow experiments were performed in a supersonic Mach 2.2 blow-down wind tunnel facility, with compressed air as the working fluid. The settling chamber total pressure P_0, as the controlling parameter in the present investigation, is maintained constant at ~340 kPa during each run. Experiments are conducted at the settling chamber total temperature of $T_0 = 303 \pm 3$ K, which is the same as the ambient temperature. From the isentropic relation, the test section Mach number (M_0) is calibrated to be 2.2, using the measured test section static pressure (P_{ts}) and the settling chamber total pressure (P_0). The calculated flow Reynolds number per unit length is 4.6×10^7. Piezo-resistive pressure transducers (GE DRUCK PMP-4110) are used to measure the static pressure distributions (P) from the wall-mounted pressure ports of the model. The accuracy in measuring the pressure is $\pm 0.1\%$ FS with a frequency response of 3.5 kHz.

A generic two-dimensional mixed compression intake model with dual compression ramps is experimentally investigated. Here a series of oblique shock waves are generated both externally and internally to compress the incoming flow with minimum total pressure losses. From the findings of Kaushik [8], the condition for maximum pressure recovery in a system of (n − 1) oblique shocks in two dimensions is given by Eq. (1). For a free stream of $M_0 = 2.2$ and the specific heats ratio of $\gamma = 1.4$, the Mach numbers at each zone can be found from for the oblique shock equations. The photographic view of the designed intake is shown in Fig. 1.

$$M_0 \sin \beta_1 = M_1 \sin \beta_2 = M_2 \sin \beta_3 \qquad (1)$$

The contraction ratio as given in Eq. (2), plays a vital role in determining the characteristics of the internal flow. The Kantrowitz condition defines a limit to the contraction ratio (R_{Limit}), in the sense that any smaller value implying a greater degree of compression would result in the intake becoming unstart [9]. Equation (3) defines the Kantrowitz condition for limiting contraction ratio in terms of free stream

Fig. 1 Uncontrolled intake model

Fig. 2 Comparison of
limiting contraction ratio
with sonic area ratio
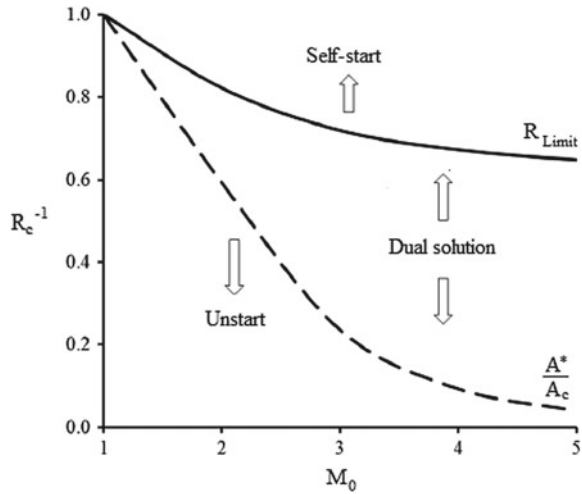
Mach number. Figure 2 shows the free stream Mach number versus contraction ratio
(A_t/A_c) plot, which depicts ideal start–unstart regime for a particular free stream
Mach number. It shows both self-starting R_{Limit}, which is obtained through quasi-
one-dimensional theory by Kantrowitz [9] and the maximum R_c, calculated from
isentropic area ratio at which intake-start condition is possible. In the present study,
the model is tested at five different R_c, to study the near-field effect of MVGs at
the intake-start and unstart conditions. As we can see from Fig. 2, the intakes with
contraction ratio of 1.14 and 1.16 fall in the self-start region, whereas, the other tested
contraction ratios of 1.19, 1.22, and 1.25 falls in the dual solution zone.

$$R_c = \frac{A_c}{A_t} \tag{2}$$

$$R_{\text{Limit}} = \left(\frac{A_t}{A_c}\right) = \left[\frac{\gamma - 1}{\gamma + 1} + \frac{2}{(\gamma + 1)M_0^2}\right]^{\frac{1}{2}} \left[\frac{2\gamma}{\gamma + 1} - \frac{\gamma - 1}{(\gamma + 1)M_0^2}\right]^{\frac{-1}{\gamma - 1}} \tag{3}$$

Single row of MVGs having two different configurations was experimentally
tested. Firstly, the conventional MVGs with optimum dimensions (as shown in
Table 1) are deployed in the intake core [1]. In addition, a new configuration which
combines the benefits of both ramp type and vane-type MVGs is examined (Fig. 3a,
b). The MVGs are placed at $x/L = 0.6$ in intake core before the impact of cowl

Table 1 Dimensions of the
micro-vortex generator

Half angle	α	24° (H)
Side length	C	7.2
Spanwise pitch	S	7.5
Base width	W	6.0
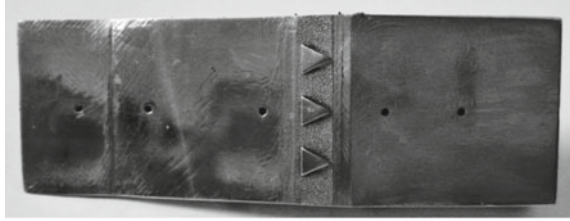
(a) Intake with H = 600 μm conventional MVGs
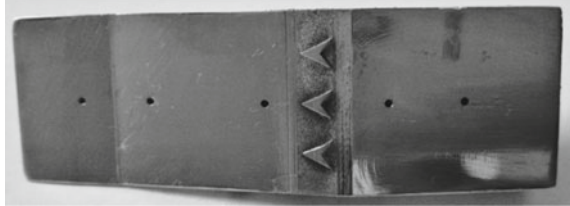
(b) Intake with H = 600 μm innovative MVGs

generated shock. The tested height of the MVGs were $H = 600, 400$, and 200 μm. The maximum internal flow blockage offered by the MVGs is 4.7% ($H = 600$ μm).

3 Results and Discussions

The near-field efficacy of the MVGs is quantified by plotting and comparing the variation of non-dimensional static pressure at specified locations over both the uncontrolled and MVGs controlled intakes. The measured wall static pressure (P) is made non-dimensional with the settling chamber stagnation pressure (P_0). For each intake contraction ratio, the static pressures are measured along the centerline of the intake core, at five different axial locations of 0.13, 0.27, 0.48, 0.7, and 0.83L, as shown in Fig. 4. To investigate and compare the influence of the conventional and innovative MVGs in near-field locations, which is the objective of the present study, the 3rd and 4th ports are specifically constructed at $x/\underline{L} = 0.48$ and $x/L = 0.7$, upstream and downstream locations of the MVGs, respectively.

The percentage variation in static pressure at the near upstream and near downstream locations of 0.48L and 0.7L, respectively, are calculated. These results are tabulated (Tables 2 and 3 of Annex A) to study the upstream and downstream influences of the conventional and innovative MVGs in controlling the intake, at all the tested contraction ratios. For the purpose of easy understanding, the bar charts showing the variation in static pressure which compares the MVG controlled and uncontrolled intakes are discussed here (Figs. 5, 6, 7, 8, 9, and 10).

With the exception of $R_c = 1.14$ and 1.16, the uncontrolled intake is unstart at all other contraction ratios, as observed in Fig. 2 and as shown in Humrutha et al.

Fig. 4 Static pressure ports located at the intake core controlled using innovative MVGs
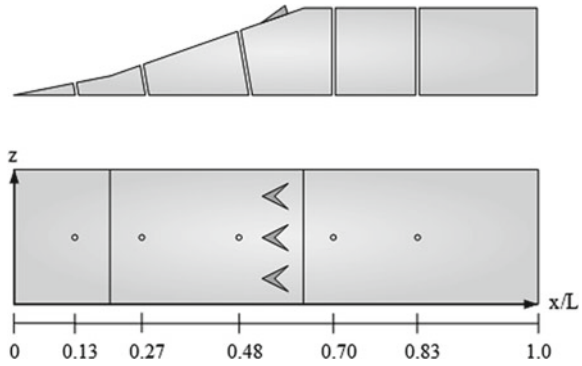
Fig. 5 Upstream influence of the MVGs of height 600 μm
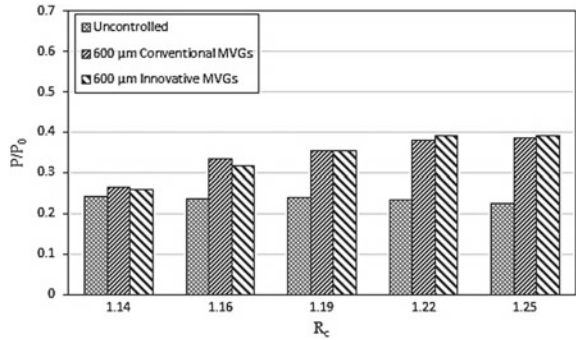
Fig. 6 Upstream influence of the MVGs of height 400 μm
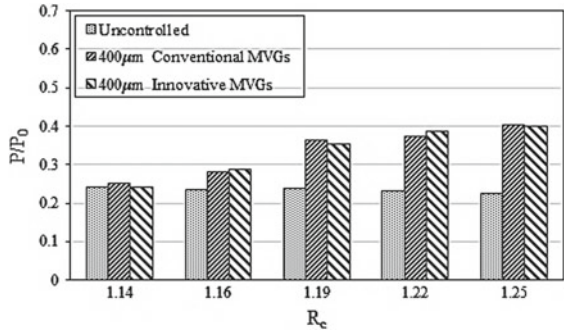
[6]. It can be noted from Figs. 5 and 6 that, in the intakes controlled by $H = 600$ and 400 μm MVGs (both conventional and innovative configurations), the amount of static pressure increase in the near upstream location is directly proportional to the contraction ratio and thus the internal flow blockage. Here both the conventional and innovative micro-devices of height 600 μm create a certain amount of blockage (4.7%) in the flow entering the intake. The amount of blockage produced by the MVGs has been discussed in Humrutha et al. [7]. This internal flow blockage offered

Fig. 7 Upstream influence of the MVGs of height 200 μm
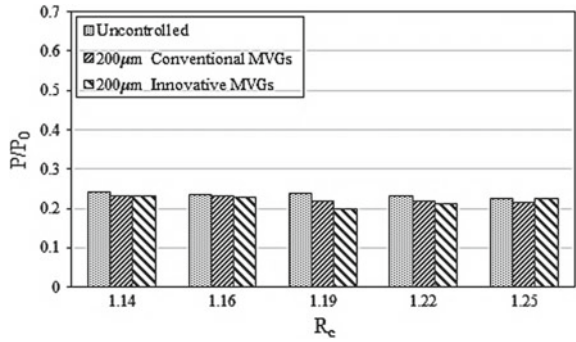
Fig. 8 Downstream influence of the MVGs of height 600 μm
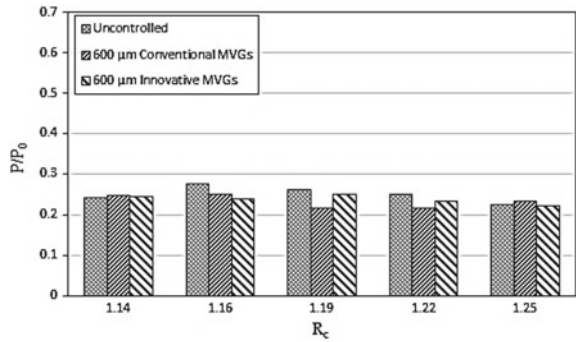
Fig. 9 Downstream influence of the MVGs of height 400 μm
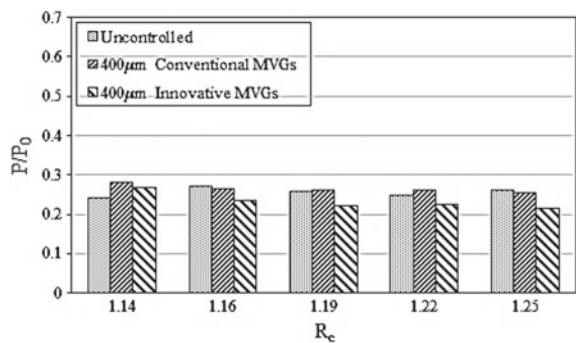
by the MVGs leads to a mismatch in the amount of air flow through the intake capture area and the amount of flow through the intake throat. Thus, in order to satisfy the law of conservation of masses (the amount of air flow has to be the same at the intake lip and throat), the cowl shock is pushed forward. This increases the cowl shock angle, consequently, increasing the static pressure behind it. From Fig. 5, it can be seen that the conventional MVGs of height 600 μm produce an unfavorable increase in static pressure up to 72% in the intake operating at the contraction ratio of 1.25. This

Fig. 10 Downstream
influence of the MVGs of
height 200 μm
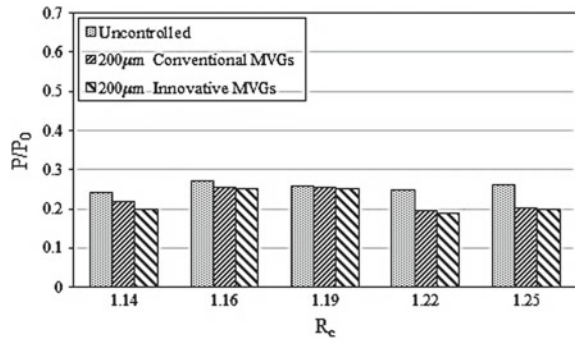
increase in static pressure is, however, less compared to the 76% increase produced
by their innovative counterpart. Further, at the self-start contraction ratios of 1.14
and 1.16, it can be seen that the pressure rise due to innovative MVGs is almost 6%
lesser than the pressure rise due to the conventional configuration. However, when
the contraction ratio increases, the pressure rise due to innovative MVGs is large
compared to their conventional counterpart.

Similar observations can be made in case of the intake controlled by $H = 400$ μm
MVGs, which creates an internal flow blockage of 1.4%. Figure 6 shows the upstream
influence of the $H = 400$ μm MVGs in terms of non-dimensional pressure. Here, an
80% increase in static pressure is observed in the intake controlled by conventional
MVGs of height 400 μm, operating at $R_c = 1.25$, which is borderline higher than the
78% increase produced by the innovative MVGs. Similar to the previous case, the
pressure rise due to innovative MVGs increases as the contraction ratio increases,
larger than the conventional MVGs. However, this observation does not hold true for
the innovative MVGs of height 200 μm.

Figure 7 shows that, at all the tested contraction ratios, the $H = 200$ μm conven-
tional MVGs produce desirable upstream influence by reducing the static pressure up
to 8.4% compared to the uncontrolled intake (at the contraction ratio of 1.19). Even
at the self-start contraction ratio of 1.14, a 4.4% decrease in pressure is observed at
$x/L = 0.48$. Hence, we can infer that the MVGs of height 200 μm is most effective
in re-energizing the momentum upstream of the control technique with a desirable
outcome of decreased static pressure at both the intake-start and unstart conditions. In
addition, at all the tested contraction ratios, the innovative MVGs of height 200 μm
produce desirable upstream influence by reducing the static pressure up to 17% com-
pared to the uncontrolled intake (at the contraction ratio of 1.19). Further, except at
the contraction ratio of 1.14 and 1.25, the pressure drop at the upstream location of
the innovative MVGs is almost double than the pressure drop due to the conventional
MVGs (as shown in Table 2, Annex A). Hence, this verifies the superiority of the
innovative MVGs of height 200 μm in re-energizing the momentum of the boundary
layer upstream of the control technique at both the intake-start and unstart conditions.

The static pressure variation at the near downstream location of 0.7L is presented
in Table 3, Annex A, and Figs. 8, 9, and 10. The pressure downstream of both the

conventional and innovative MVGs of height 600 µm decreases at all the tested contraction ratios, except when $R_c = 1.14$, where a subtle increase is measured. A maximum reduction of 15.4% is recorded in the intake controlled with innovative MVGs at $R_c = 1.25$ (Fig. 10).

However, the $H = 400$ µm conventional MVGs increase the static pressure downstream of them at all contraction ratios except at $R_c = 1.16$ and 1.25, where a subtle decrease in pressure is recorded to be 2.7 and 2.5%, respectively. Similarly, the 400 µm innovative MVGs decrease the static pressure downstream of them at all contraction ratios except at $R_c = 1.14$, where approximately a 10% increase in pressure is recorded. Further, it can be seen in Fig. 9 that the intake controlled with innovative MVGs of height 400 µm outperforms their conventional counterpart by generating a profound decrease in pressure at the near downstream location of up to 18% (Table 3, Annex A).

In comparison to the uncontrolled intake, the wall static pressure downstream of the $H = 200$ µm conventional MVGs decrease to a great extent of up to 23.6% at $R_c = 1.25$. This is almost equal to the 24% decrease produced by the innovative MVGs. In the case of conventional MVGs, even at the self-start R_c of 1.14, a profound pressure decrease of approximately 10% is observed. However, at the same contraction ratio, the intake controlled by the innovative MVGs is subjected to a comparatively increased pressure drop of 18%, which 8% is more than their conventional counterpart. At $R_c = 1.19$, both the conventional and innovative MVGs of height 200 µm are least effective in decreasing the static pressure, compared to all other tested contraction ratios. However, the influence of innovative MVGs is felt more than the conventional MVGs.

From this investigation, it can be observed that the conventional and innovative MVGs of height 200 µm have both profound upstream and downstream influences at all the tested contraction ratios. However, the enhanced performance of the $H = 200$ µm innovative MVGs may be due to the formation of smaller and stronger counter-rotating vortices closer to the wall, which consequently enhances the mixing of high-momentum inviscid flow with the low momentum viscous flow inside the boundary layer.

4   Conclusions

In the present study, the near-field effects of the conventional and innovative MVGs of varying heights, such as 600, 400, and 200 µm, are quantified in terms of static pressure variation in the internal flow of Mach 2.2 intake. It can be observed that the intake controlled with 200 µm innovative MVGs shows superior performance at both design contraction ratio as well as off-design conditions. These MVGs produce a desirable upstream influence by reducing the static pressure up to 17% compared to the uncontrolled intake. In addition, the wall static pressure downstream of the 200 µm innovative MVGs decreases to a great extent of up to 24% at $R_c = 1.25$. Even at the self-start R_c of 1.14, a substantial decrease in pressure decrease of about

18% is observed, which is 8% more than the conventional MVGs. Hence, the better performance of innovative MVGs of height 200 μm is profound for both upstream and downstream locations.

Furthermore, the $H = 200$ μm innovative MVGs show that the smallest MVG height incurs the largest pressure drop. This superior near-field influence may be due to the formation of smaller and stronger counter-rotating vortices closer to the wall, which consequently enhances the mixing of high-momentum inviscid flow with the low momentum viscous flow inside the boundary layer.

In addition, the innovative MVGs of height 600 and 400 μm have considerable downstream influence. However, the large increase in static pressure at the upstream location due to these MVGs is highly undesirable.

Annexure A: Percentage Variation in Static Pressure with Respect to Uncontrolled Intake

See Tables 2 and 3.

Table 2 Percentage variation in static pressure upstream of the MVGs

R_c	Conventional MVGs			Innovative MVGs		
	600 μm	400 μm	200 μm	600 μm	400 μm	200 μm
1.14	10.116	3.427	−4.418	5.822	−0.124	−4.418
1.16	40.551	18.644	−2.415	34.407	22.373	−3.093
1.19	48.326	51.799	−8.368	48.368	47.406	−16.904
1.22	61.638	61.681	−5.388	66.897	66.552	−8.836
1.25	72.155	80.143	−4.373	76.082	77.912	0.134

Table 3 Percentage variation in static pressure downstream of the MVGs

R_c	Conventional MVGs			Innovative MVGs		
	600 μm	400 μm	200 μm	600 μm	400 μm	200 μm
1.14	1.768	16.036	−10.115	0.164	10.238	−18.257
1.16	−7.332	−2.690	−6.522	−11.570	−13.817	−7.885
1.19	−15.657	0.971	−0.894	−2.720	−13.287	−2.758
1.22	−13.803	4.829	−21.690	−6.278	−9.899	−23.662
1.25	−11.534	−2.512	−23.639	−15.379	−17.929	−24.058

References

1. Anderson BH, Tinapple J, Surber L (2006) Optimal control of shock wave turbulent boundary layer interactions using micro-array actuation. In: Proceedings, 3rd AIAA flow control conference, San Francisco, California
2. Ashill PR, Fulker JL, Hackett KC (2005) A review of recent developments in flow control. Aeronaut J 205–232
3. Babinsky H (2008) Understanding micro-ramp control of supersonic shock wave boundary layer interactions. Technical Report 0074, Air Force Research Laboratory, United States Air Force
4. Blinde PL, Humble RA, van Oudheusden BW, Scarano F (2009) Effects of micro-ramps on a shock wave/turbulent boundary layer interaction. Shock Waves 19:507–520
5. Holden H, Babinsky H (2007) Effect of micro vortex generators on separated normal shock/boundary layer interactions. J Aircr 44(1):170174
6. Humrutha G, Kaushik M, Sinhamahapatra KP (2017a) Micro-vortex generator controlled shock- boundary layer interactions in supersonic intake. In: Proceedings, 31st international symposium on shock waves, Nagoya, Japan
7. Humrutha G, Kaushik M, Sinhamahapatra KP (2017b) Shock-boundary layer interaction control using innovative micro-vortex generators in supersonic intake. In: Proceedings, 47th AIAA fluid dynamics conference, Colorado, USA
8. Kaushik M (2019) Theoretical and experimental aerodynamics (1st edn). Springer Nature. Singapore (ISBN: 978-981-13-1677-7)
9. Kantrowitz A, Donaldson C (1945) Preliminary Investigation of supersonic diffusers. Technical Report L5D20. National Advisory Committee for Aeronautics
10. Lin JC (2002) Review of research on low-profile vortex generators to control boundary-layer separation. Prog Aerosp Sci 38:389–420
11. Seddon J (1970) Boundary-layer interaction effects in intakes with particular reference to those designed for dual subsonic and supersonic performance. Technical Report 3565. Aeronautical Research Council
12. Titchener N, Babinsky H (2015) A review of the use of vortex generators for mitigating shock-induced separation. Shock Waves 25(5):473–494
13. Valdivia A, Yuceil KB, Wagner JL, Clemens NT, Dolling DS (2014) Control of supersonic inlet-isolator unstart using active and passive vortex generators. AIAA J 52(6):1207–1218
14. Zheltovodov AA (1996) Shock waves/turbulent boundary-layer interactions-fundamental studies and applications. In: Proceeding, 27th AIAA fluid dynamics conference, New Orleans, Louisiana, Los Angeles, USA

Experimental Investigation of Cavity Flows with Rear Corner and Face Modifications

T. V. Krishna, P. Kumar, S. L. N. Desikan, and S. Das

Abstract Experiments were performed to study the effect of cavity rear wall modification at different L/D ratios of an open cavity. All the experiments were carried out at Mach 2.0 and corresponding Reynold's number of 5.5×10^5 based on cavity depth. Unsteady pressures were measured at several locations to obtain the fluctuating flow field behavior and the pressure spectrum. Results indicate that cavity rear geometry modification has its influence toward the instabilities and subsequent flow oscillations inside the cavity at all L/D's.

Keywords Cavity flameholder · Supersonic flows · Scramjet combustion

Nomenclature

D	Depth of Cavity (mm)
k	Ratio between convective and free stream velocities
L	Length of the cavity floor (mm)
m	Rossiter mode number
S	Body oriented coordinate (mm)
X	Distance along cavity floor
OASPL	Overall Sound Pressure Level (dB)
SPL	Sound pressure level (dB/Hz)
α	Empirical Constant
P_∞	Freestream Pressure (Pa)

T. V. Krishna · P. Kumar · S. Das (✉)
BIT Mesra, Ranchi, Jharkhand, India
e-mail: sudipdas@bitmesra.ac.in

T. V. Krishna
e-mail: sri.vamsi1432@gmail.com

S. L. N. Desikan
VSSC, ISRO, Thiruvananthapuram, Kerala, India
e-mail: sln_desikan@vssc.gov.in

P_{rms} Root Mean Square Pressure (Pa)
Q_∞ Free stream dynamic pressure (Pa)

1   Introduction

Flow over the rectangular cavities has been studied extensively over the past few decades due to its complexity and practical interest. Flow regimes over the cavities could be from subsonic to hypersonic speeds. Few applications of cavities are aircraft bomb bays, weapon bays, scramjet combustor, etc. Based on the cavity length to depth ratio (L/D), cavities are classified into open (L/D < 10) and closed (L/D > 10) cavities. Open cavity flows will take place in the majority of aerospace applications and these flows are complex in nature. Krishnamurthy [1], Heller et al. [2] and Rossiter [3] have observed that the flow inside the rectangular open cavities are highly unstable. The behavior of flow inside an open cavity is unsteady, due to self-sustained oscillations occurring inside the cavity. These oscillations could be estimated based on cavity L/D, M, Re, etc., using empirical relation given by Rossiter and further modified by Heller et al. [2].

Cavity assisted flame holding is one of the techniques available for flame holding and ignition in scramjet combustors. For stable combustion and flame holding inside the Scramjet combustor, cavity plays a vital role. For stabilizing flow field inside cavity, researchers have used the concept of rear wall ramping. Gruber et al. [4] reported that with an increment of ramp angle, flow inside the cavity gets stabilized. Shallow ramp angles lead to increment in the residence time and increases the drag of the cavity. Ali and Job [5] as well as Vikramaditya and Kurian [6] suggested that shallow ramp angle can be effectively used for suppression of oscillations and entrainment. The lower L/D ratio cavities are more stable with a lower ramp angle than the higher L/D ratio cavity. Micka and Driscoll [7], Webb and Samimy [8] used cavity-based flame holders for their studies. Malhotra and Vaidyanathan [9] have conducted studies on rear wall offset and noticed higher offset ratios giving more stabilized flows. Other methods of suppression of oscillations are through using external devices such as vortex generators by Perng and Dolling [10], spanwise cylinder, and spoilers by Dudley and Ukeiley [11].

Majority of researchers obtained reduction in the broadband and narrow band tonal peaks by using modifications to rear wall. Although the rear wall ramp cavities improve the entrainment rate, stability and provide higher combustion efficiency, it has certain drawbacks with regards to cavity residence time, cavity drag, and total pressure loss. The present study attempts to investigate the advantage of ramping, retaining the characteristics of rectangular cavity shape. Also the responses of all these shapes at different L/D ratios were also attempted.

2 Experimental Details

2.1 Wind Tunnel Facility

The current studies were conducted using the supersonic blowdown wind tunnel (Fig. 1a) available at Aerodynamics laboratory of the Department of Space Engineering and Rocketry at Birla Institute of Technology, Mesra, Ranchi, India. This facility uses compressed dry air from an external reservoir. The wind tunnel has a provision to change nozzle blocks within the range of Mach number 1.8–2.5. Present experiments were conducted at Mach number 2.0 with test section size of 50 mm × 100 mm. The wind tunnel is operated through computer-controlled pressure regulating valve and gate valves. The stable run time of wind tunnel is 10–15 s. Test conditions were maintained so as to have a Reynolds number of the order of 5.5 × 10^5 based on the cavity depth.
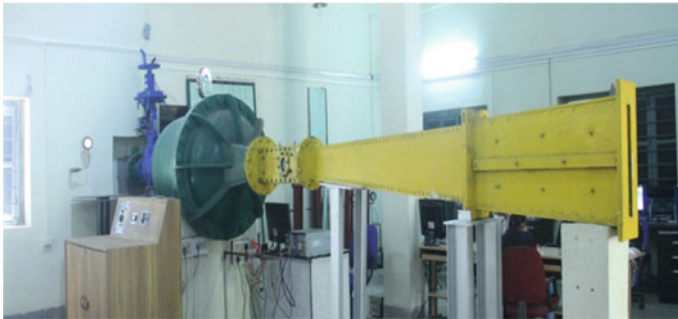
(a) Wind Tunnel
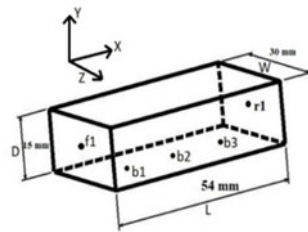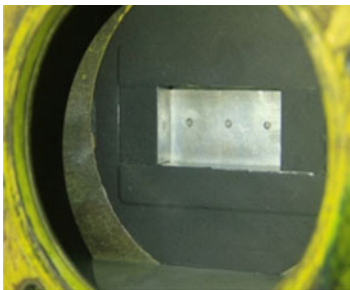
(b) Cavity geometry and the sensors

Fig. 1 Wind tunnel setup and sensors mounting inside the cavity
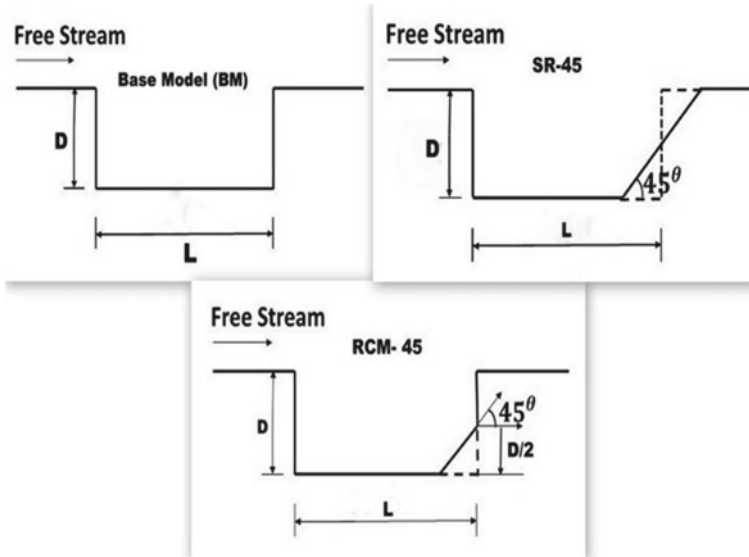
Fig. 2 Cavity configurations

2.2 Model

A wall-mounted cavity model was used in the current study (Fig. 1b). The cavity model was made of different small aluminum blocks for simple handling, and to change different geometry modifications. In this study, depth of cavity (D) and width (W) were fixed to 15 mm and 30 mm, respectively. For altering the L/D ratio, length of the cavity model was changed accordingly to obtain L/D of 2.0, 3.6, and 4.3. In this study, geometric modifications were made to the rear wall of the cavity. Figure 2 shows the modifications made to the rear wall to study the effect of Single Ramp modification (SR-45) and Rear Corner Modification (RCM-45).

2.3 Visualization

Oil flow visualization was performed using a proper mixture of Titanium Dioxide, Oleic acid, and lubricating oil. A black color acrylic sheet of thickness 0.1 mm was pasted over the cavity surface for better visualization. The mixture was sprayed evenly over the cavity surfaces before the test run. After obtaining the oil flow streak lines from the test run, images were taken with the help of DSLR camera (Canon EOS-7D).

2.4 Unsteady Pressure Measurements

Unsteady pressure measurements were made using Kulite-XTL-140 M-15D (on the cavity floor) and XCL-100-25A (on the front and rear walls) pressure transducers. The signals from the transducers were obtained simultaneously using NI-PXIe-6366 and signal conditioner (NI-1520). The unsteady data were sampled either at 40 kHz or 100 kHz for 1 s depending on L/D ratios. Data were analyzed using MATALB and FFT was performed by dividing unsteady pressure data into the block size of 4096 with the frequency resolution of either 9 Hz or 24 Hz based on the L/D ratio.

3 Results

3.1 L/D = 3.6

Figure 3 shows the surface flow pattern inside the regular base cavity and modifications to rear wall at L/D of 3.6. Figure 3a shows surface oil flow pattern inside cavity base model at Mach 2.0. From Fig. 3a, it has been observed that the flow impinges on the rear face of the cavity and it moves toward the floor. The flow separation is the region formed at rear face corner. Near to the front face large counter-rotating vortices are formed on the cavity floor. Both the side walls show that near to the front face there is a flow separation from counter-rotating vortices on the cavity floor. From Fig. 3b, it is observed that the floor flow pattern changes due to the ramping of the rear wall and is expected to alter the steady pressure characteristics. For change in geometry on the rear wall near to the corner (RCM-45), shown in Fig. 3c, the change was observed on the floor near to the rear corner. The other characteristics of Base model were retained. The front face and the floor near to front face exhibit similar behavior. The oil flow pattern for SR-45 model major variation compared to RCM-45 model which may be due to retaining of flow characteristics of rectangular cavity by the RCM.

Figure 4 shows the pressure spectra for Base model at different locations inside the cavity. It is seen that the narrowband and broadband frequencies inside the cavity at different locations are captured well. The discrete peaks shown in Fig. 4 represent the various modes inside the cavity. At all locations inside cavity, similar narrow band tones are observed. All the narrow band tones inside the cavity were well matched with Rossiter modes, which are represented by dashed lines and marked as m = 1, 2, 3, and 4 indicating the mode values. Rossiter modes were calculated using empirical relation with the values of k = 0.6 and α = 0.2. The highest amplitude spectra was observed for rear wall and amplitude of the sound pressure level increases from front wall to the rear wall. Figure 5 shows the pressure spectra obtained for Base model, RCM-45 and SR-45 for L/D of 3.6 on front wall, floor, and rear wall. It is observed from Fig. 5 that a narrowband tonal peak vanishes for SR-45 configuration, whereas for RCM-45 configuration, the reduction of narrow tonal peaks is marginal.

Fig. 3 Oil flow visualization
for regular cavity with L/D
= 3.6
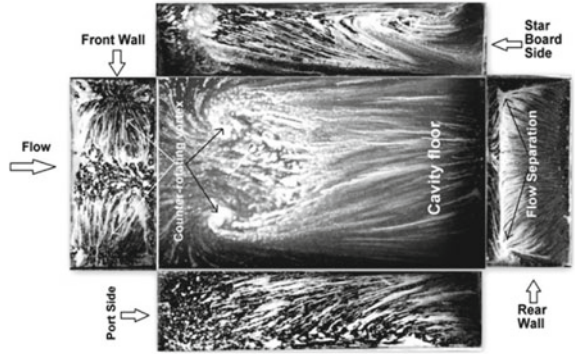
(a) BM
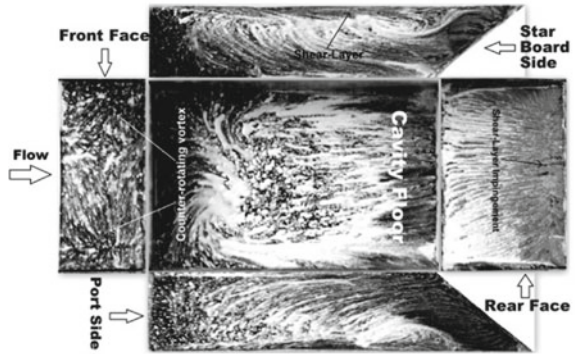
(b) RCM-45
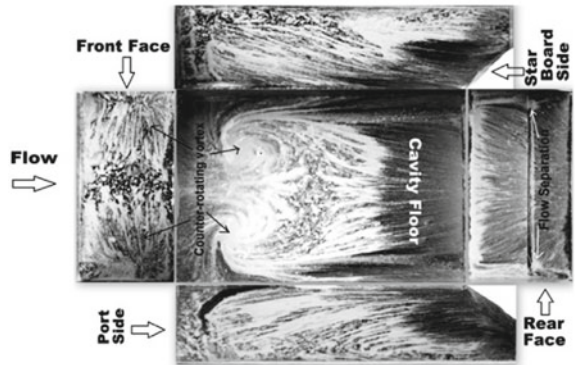
(c) SR-45

Fig. 4 Pressure spectra at different locations inside regular cavity for L/D ratio of 3.6
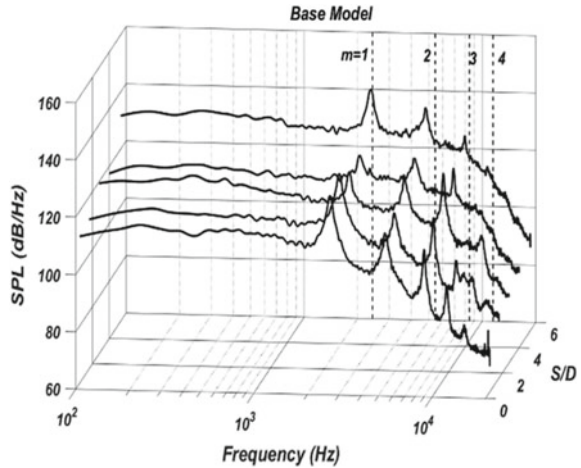
Pressure fluctuations along the cavity length are shown in Fig. 6. It shows for Base model that the fluctuations are large at rear wall of the cavity compared to front wall. The fluctuations rapidly increase at the rear wall. The cavity modification shows the reduction in the pressure fluctuations and the highest reduction is observed for SR-45. The rms pressure for RCM-45 has maximum reduction at the floor location near to the front wall. The reduction in rms pressure becomes maximum for SR-45 from S/D = 2.8 onward. The reduction in the pressure fluctuations at rear wall location is 33% for RCM-45 configuration and 69% for SR-45 configuration compared to the Base model.

3.2   L/D = 2

Figure 7 shows the unsteady pressure spectra inside regular base cavity for L/D of 2.0. The oscillations inside the cavity are quite evident from the tonal peaks observed in Fig. 7. However, if the frequencies are compared with the one obtained from relation considering L/D = 2.0, there it is seen that few additional peaks are also among other Rossiter peaks. This could be due to dominance of transverse oscillation for such L/D ratios. Similar to L/D = 3.6, all the surfaces of the cavity (L/D = 2.0) exhibit frequencies of periodic nature. The broadband level for L/D = 2.0 is less compared to cavity with L/D = 3.6. The rms pressure obtained for cavity L/D = 2.0 for all configurations tested are presented in Fig. 8. A low value throughout and marginal changes in the values for different configurations are observed, which could be due to the influence of L/D only. However, there seems to be a drop in the rms pressure from base to RCM-45 to SR-45 cavity models. The trend of drop in rms values is similar to the L/D = 3.6 trend.

Fig. 5 Pressure spectra at
different locations inside
cavity for L/D ratio of 3.6
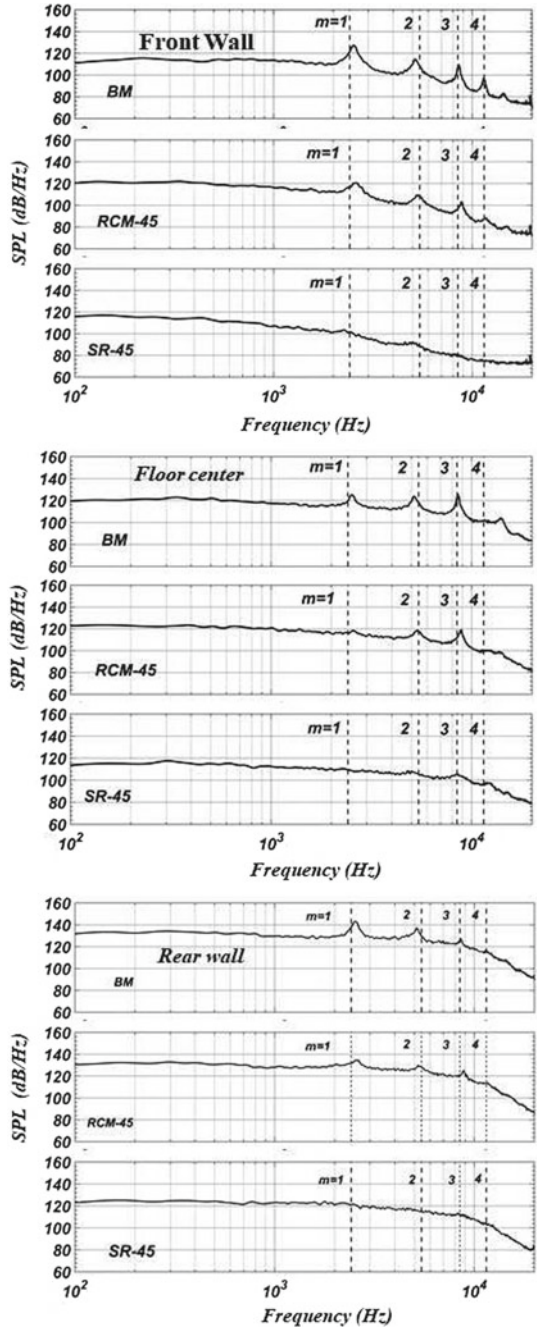
Fig. 6 P_{rms}/Q for different cavity configuration at L/D of 3.6
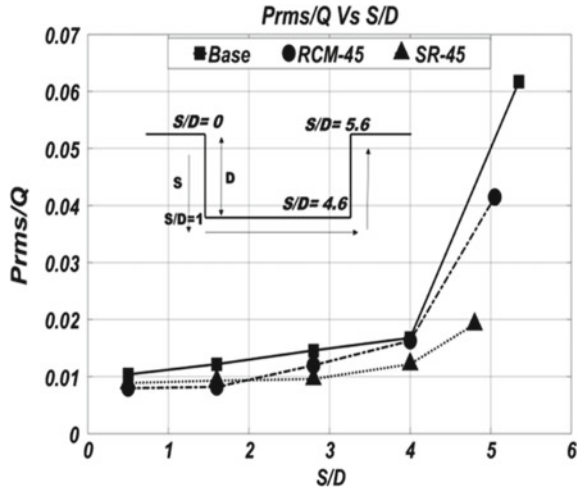
Fig. 7 Unsteady pressure spectra at different locations inside regular cavity for L/D ratio of 2.0
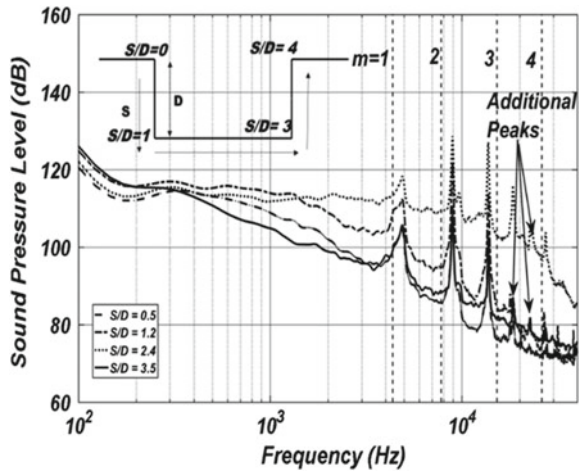
3.3 L/D = 4.3

Pressure spectra obtained at various locations inside the cavity with L/D of 4.3 is shown in Fig. 9. From the figure it is observed that all the frequencies are well matched with Rossiter modes, throughout the cavity length. A similar type of flow has been noticed for L/D of 3.6 as well. Broadband and narrowband tonal frequency amplitudes increase from the front wall to rear wall. The first mode is dominant among the other modes.

The rms pressure along the cavity length for the Base model and rear wall modifications to the base cavity with L/D of 4.3 are shown in Fig. 10. The rms pressure fluctuations increase from the front wall to rear wall for all the configurations. The

Fig. 8 P$_{rms}$/Q for different cavity configuration at L/D of 2.0
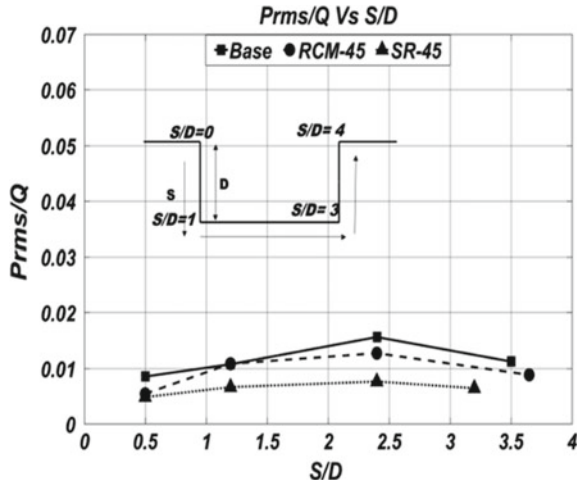
Fig. 9 Unsteady pressure spectra at different locations inside regular cavity for L/D ratio of 4.3
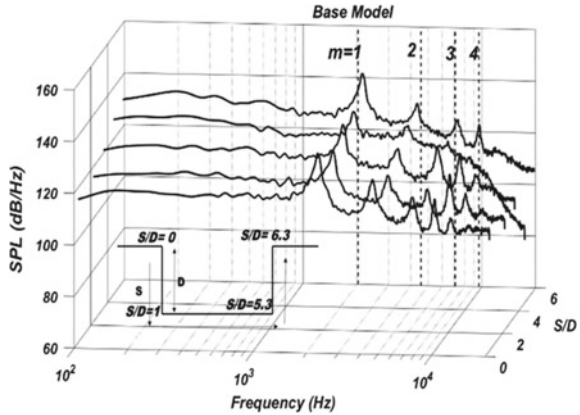
trend of reduction in rms pressure with different configurations remains similar with different L/D.

3.4 Effect of L/D Ratios

OASPL values on the front wall, for different L/D ratios of 2.0, 3.6, and 4.3 are shown in Fig. 11. On the front wall with increasing the L/D ratio, the OASPL increases. The RCM-45 configuration has shown the noticeable improvement for all the L/D ratios. For SR-45 configuration, the highest improvement has been observed at L/D of 4.3 and other L/D ratios significant reduction is noticed.

Figure 12 shows the OASPL values on the floor for L/D ratios of 2.0, 3.6, and

Fig. 10 P_{rms}/Q for different cavity configuration at L/D of 4.3
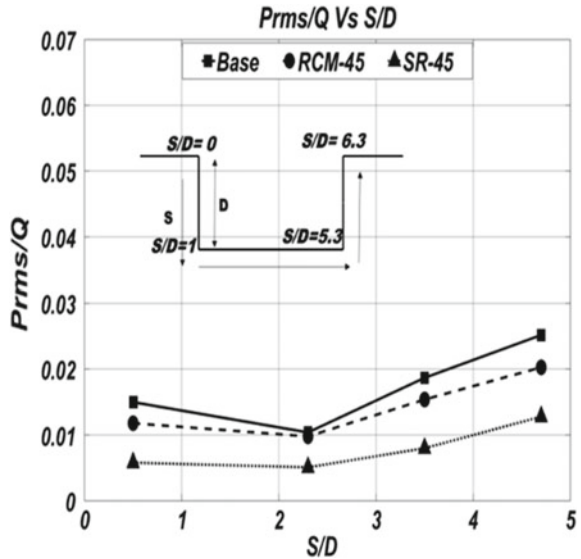
Fig. 11 OASPL on the front wall for L/D ratios of L/D of 4.3
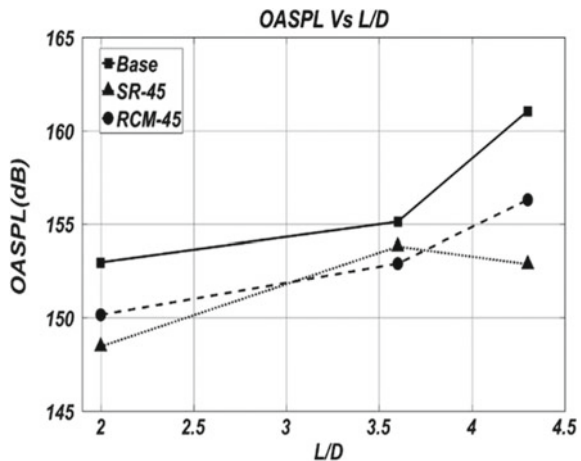
4.3. From Fig. 12, it is observed that for RCM-45 configuration, improvement in the OASPL is noticed at L/D ratio of 4.3. For the L/D ratios 2 and 3.6, RCM-45 configuration is ineffective. For SR-45 configuration, the improvement in OASPL is observed for all the L/D ratios and highest improvement is observed at L/D of 4.3. For RCM-45 model, it is observed that the rear corner has an influence on flow behavior inside the cavity. But it retains the rectangularity of the cavity flow. This resulted in a small reduction in both pressure fluctuations and OASPL. The RCM model is more effective at higher L/D ratios than the lower L/D ratio.

Fig. 12 OASPL on the floor
for L/D ratios of 2.0, 3.6, and
4.3
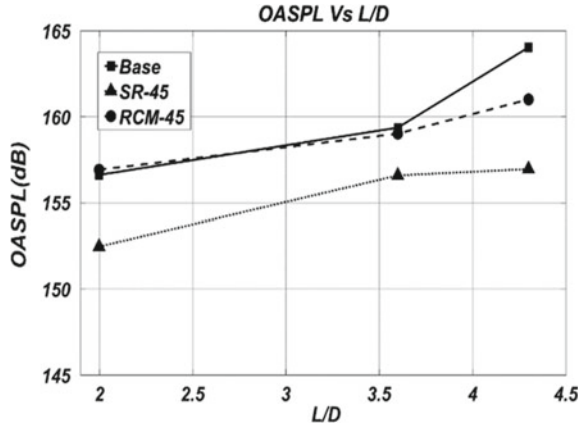
4   Conclusions

Open cavity flow field studies have been performed at Mach number of 2.0 for cavity
L/D ratios of 2.0, 3.6, and 4.3. Geometric modifications were given to the rear wall
by adopting a single ramping (SR-45) and Rear Corner Modification (RCM-45). The
influence of these geometric changes to the cavity for different L/D ratios has been
obtained. The flow has been visualized by oil flow visualization and quantitative
details were obtained using unsteady pressure measurements which were performed
at various locations inside the cavity symmetrical plane. Results indicate that SR-
45 configuration does well toward reduction in pressure fluctuation and tonal peaks
compared to RCM-45 configuration. This observation was true for all the L/D's
tested. However, the RCM model retains the rectangularity of the cavity, and induces
a marginal change to all the tonal peaks, rms pressures, and OASPL. This leads to a
conclusion that the rear corner plays a bit of a role in inducing the instabilities and
the consequent acoustic wave movements inside the cavity.

References

1. Krishnamurty K (1956) Sound radiation from surface cut outs in high speed flow. PhD thesis,
   California Institute of Technology
2. Heller HH, Holmes DG, Covert EE (1971) Flow-induced pressure oscillations in shallow
   cavities. J Sound Vib 18(4):545–553
3. Rossiter JE (1964) Wind tunnel experiments on the flow over rectangular cavities at subsonic
   and transonic speeds. Technical Report 3438, Aeronautical Research Council Reports and
   Memoranda
4. Gruber MR, Baurle RA, Mathur T, Hsu KY (2001) Fundamental studies of cavity-based flame
   holder concepts for supersonic combustors. J Propul Power 17(1):146–154

5. Ali MC, Job K (2008) Performance of Aft-ramp cavities for flame stabilization in supersonic flows. J Propul Power 24:635–637
6. Vikramaditya NS, Kurian J (2009) Effect of aft wall slope on cavity pressure oscillations in supersonic flows. Aeronaut J 113:291–300
7. Micka DJ, Driscoll JF (2009) Combustion characteristics of a dual-mode scramjet combustor with cavity flameholder. Proc Combust Inst 32:2397–2404
8. Webb N, Samimy M (2016) Supersonic cavity flow control for scramjet applications. In: 8th AIAA flow control conference, Washington, D.C
9. Malhotra A, Vaidyanathan A (2016) Aft wall offset effects on open cavities in confined supersonic flow. Exper Thermal Fluid Sci 74:411–428
10. Perng SW, Dolling DS (2001) Suppression of pressure oscillations in high-mach-number turbulent, cavity flow. J Aircraft 38(2):248–256
11. Dudley JG, Ukeiley L (2014) Passively controlled supersonic cavity flow using a span wise cylinder. Exp Fluids 55:1810

Mixing Analysis of Combined Aeroramp/Strut Injectors in Supersonic Flow

Nikhil Hemanth, Amit Thakur, Corin Segal, Abhay Hervatte, and K. V. Shreyas

Abstract Scramjet engine is the most promising air breathing propulsion system in the hypersonic flight regime. Combustion in a scramjet engine, however, is difficult to achieve due to flow residence times being comparable to chemical times. For our study, 3-D RANS CFD analysis of a strut flame holder of a scramjet engine combustor was carried out. The first part of the analysis focuses on the validation of CFD gas dynamics results with earlier experimental data in literature. The air enters the combustor at Mach 2 with a stagnation temperature of 612 K and a stagnation pressure of 7.82 atm. Various flow properties like velocity profile, wall static pressure and density gradient were in good agreement with experimental results. The next part of the analysis involves a strut mounted across the walls of the combustor with hydrogen fuel injector jets forming an aerodynamic ramp on both the upper and lower surfaces. The location of the injectors relative to the strut base and dynamic pressure ratio were varied and the observations presented.

Keywords Scramjet · Aeroramp injector · Strut

1 Introduction

There has been extensive research carried out since the 1960s to fully understand and efficiently implement fuel injection and mixing in hypersonic flow. Ramp, step and struts have been extensively used for flame holding along with other physically intrusive techniques to promote fuel air mixing. Extensive numerical and experimental investigations have been performed with the strut flame holder spanning the length of the combustor. One such investigation performed at Georgia Tech involved fuel injection from the base of the strut and validation of numerical code with experiments at

N. Hemanth · C. Segal
University of Florida, Gainesville, FL, USA

A. Thakur (✉) · A. Hervatte · K. V. Shreyas
PES University, Bangalore, KA, India
e-mail: amit.thakur.amt@gmail.com

409

DLR wind tunnel facility in Germany [1]. Other Large Eddy Simulation (LES) studies have also been performed on the same configuration [2, 3]. Besides non-reacting flow, they also performed combustion analysis and enhanced the understanding of reacting flow beyond the available experimental data.

According to Fuller [4], a physically intrusive structure in supersonic flow will necessarily create hot spots, with thermal loads at specific locations exceeding the temperature limits of practical materials. Also, there are added problems of drag and loss in thrust with such physically intrusive structures [5]. In order to prevent the drawbacks of physically intrusive structures, Cox et al. [6] came up with a novel injector concept called the 'Aerodynamic ramp' or simply 'Aeroramp'. This injection technique initially involved a three by three array of closely spaced flush walled jets with a yaw angle given to each row. The objective was to create individual fuel vortices as a result of interaction between the skewed injection of one hole with that of the downstream hole. These individual fuel vortices are called skew induced vortices and along with shock induced vortex generation enhance mixing significantly [4].

Due to the absence of physically intrusive structures in the supersonic flow, hot spots and hence high thermal loading at specific locations is avoided. There is also lower associated stagnation pressure loss with this injection technique. Results of both numerical and experimental analysis performed by Fuller at the US Airforce research laboratory show that the Aeroramp injection technique achieved better mixing in the near field as compared to a physical ramp, increasing the jet-air momentum ratio enhanced the mixing performance in both the near as well as the far field. The total pressure loss incurred by the Aeroramp in all the cases was found to be lower than that of the physical ramp. It was also found that the total pressure loss decreased with increasing momentum ratio. Once the Aeroramp injection configuration proved to be a viable alternative to fuel injection in supersonic flow, several studies were performed to optimize it. This optimization was done to establish the parameters in terms of number, size, orientation and spacing of the Aeroramp holes.

Improvement to the design was done experimentally in Virginia Tech supersonic wind tunnel [7]. The study was a comparison of the mixing performance of a four flush walled hole Aeroramp injector with a single, low downstream angled hole in a cross-stream flow of Mach 2.4. It was found that eliminating the centre row of holes from the original nine flush walled holes and increasing the toe-in angle enhanced axial vortex formation. This axial vortex prevented the development of a secondary fuel core near the wall by lifting the entire plume off the wall, thus eliminating the possibility of hot spots at locations on the wall during reactive flow. Concurrently, studies were also performed to determine suitable toe-in angles and jet to freestream momentum flux ratios for injection [8]. It was found that increased momentum ratio improved core penetration of the fuel plume into the freestream. However, it also results in the formation of stronger bow shocks, leading to higher stagnation pressure loss. Increasing the toe-in angle increased the injected plume area but decreased its penetration into the freestream [4]. From the studies by Jacobsen, it was found that the 15° toe-in angle array with 30° transverse injection resulted in a minimised overall total pressure loss associated with the injector shock structure [8].

The toe-in angle is defined as the angle formed by the axis passing through the centre of the hole on the streamwise plane with the freestream. In the two row holes of the Improved Aerodynamic ramp study [7], this was taken as 15° for the front row and 30° for the rear row. The transverse injection angle is the angle at which the fuel is injected into a horizontally moving freestream. These angles are 20° and 40° respectively for the front and rear set of holes. The jet to freestream momentum flux ratio is defined as:

$$q = \frac{\left(\rho \times u^2\right)_j}{\left(\rho \times u^2\right)_\infty} = \frac{\left(\gamma \times P \times M^2\right)_j}{\left(\gamma \times P \times M^2\right)_\infty} \tag{1}$$

Combustion experiments with the Aeroramp were also performed with the integration of a plasma torch as a flame holder [9]. Dual mode ramjet combustion experiments with the Aeroramp configuration have shown this method of injection to be viable of mixing and stable combustion [10]. The idea was further evolved at Beijing University where Aeroramp injector was scaled down, non-reacting and combustion experiments were performed. A jet of hot exhaust gases at 3000 K was injected downstream of the Aeroramp to serve as a flame holder [11], a more detailed analysis of the flow field was done using CFD [12].

In present study, the aero-ramp fuel injectors were mounted on the upper and lower surfaces of the strut to improve the transverse penetration and mixing of fuel and air. The interaction of aero-ramp vortices with the recirculation zone behind the strut and its influence on the mixing process was investigated for different conditions.

2 Numerical Methodology

2.1 Geometry

The injection technique in the current work consists of two components: a strut which acts as the flame holder and spans the entire width of the combustor, the Aeroramp injection configuration on the upper and lower faces of the strut.

2.1.1 Strut Without Aeroramp Injectors

The DLR model of combustor used for the current work was obtained from literature [1] and is shown in Fig. 1. It has a length of 340 mm, width of 40 mm and a height of 50 mm at the inlet. The strut mounted across the walls of the combustor has a half angle of 6°. A 3° diverging slope is applied on the top wall of combustor to compensate for the boundary layer growth and effect of heat release on slowing down of supersonic flow.
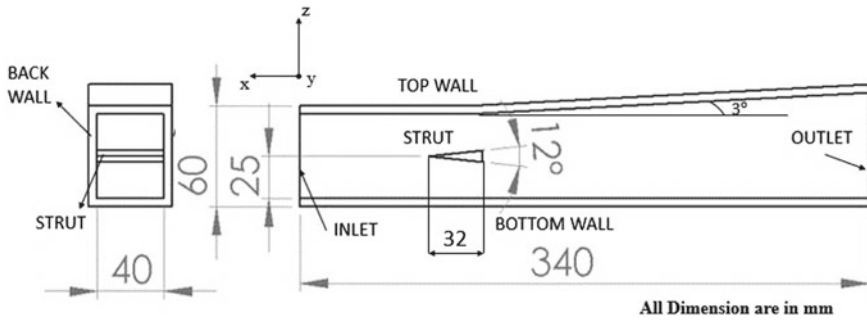
Fig. 1 Combustor geometry with strut flame holder

2.1.2 Strut with Aeroramp Injectors

The analysis deals with injecting fuel (H_2) from the top and bottom surfaces of the strut. In Fig. 2a, the isometric view of Aeroramp configuration on the upper face of the strut can be seen. An identical Aeroramp configuration is present on the lower face of the strut.

There are four injectors on the top surface and four on the bottom, making it a total of eight injectors. The injectors are placed in 2 rows. The front row of injectors is inclined at 29° with respect to the strut surface (35° with horizontal) and a toe-in angle of 20°. The back row of injectors is at a higher inclination of 49° with respect to the strut surface (55° with horizontal) and having a toe-in angle of 35°. The toe-in angles are indicated in Fig. 2b and transverse injection angles in Fig. 2c.

The location of Aeroramp injector with reference to the strut base was one of the parameters varied during the study, the end of the downstream injector row being 3 mm and 9 mm from the strut base respectively (Fig. 2b). When normalised with the length of the strut (32 mm), this corresponds to 0.09 and 0.28 for 3 mm and 9 mm from strut base respectively. Further increase in this distance would lead to a prohibitively small space for inclusion of the injector tubes. The holes have a jet diameter of 1 mm (d_j), with the equivalent diameter for four holes being 2 mm ($d_{eq} = 2d_j$). The front and back injectors were placed 8 mm ($4d_{eq}$) apart in the stream-wise direction with transverse spacing of 4 mm ($2d_{eq}$).

2.2 Mesh

A structured multi-block mesh was created using ICEM. The original mesh size was 3.4 million cells. The mesh was highly refined near the strut and combustor walls, giving y^+ less than 2, enough to capture the boundary layer gradients. The mesh was refined around the strut and its wake, with a cell size of approximately 0.2 mm and a moderate growth rate downstream of the strut. A finer mesh was obtained using
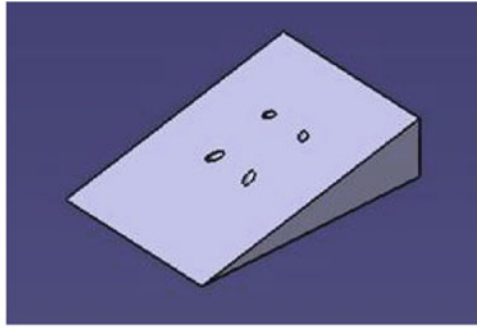
(a) Isometric view
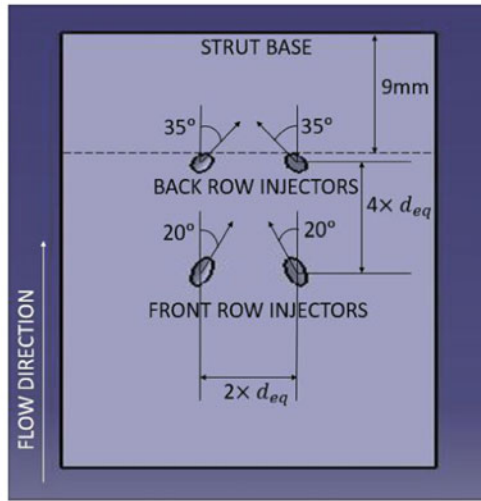
(b) Top view
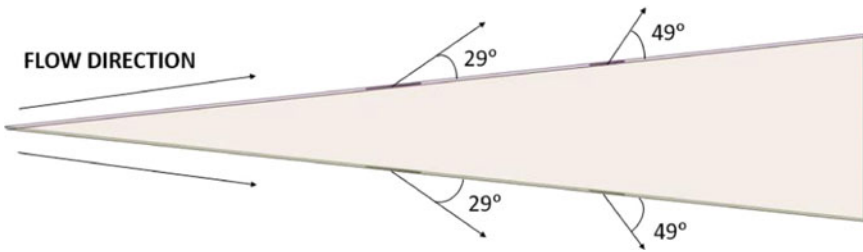
(c) Side view

Fig. 2 Strut geometry with fuel injectors placed 9 mm from base **a** isometric view **b** top view **c** side view

Adaptive Mesh Refinement (AMR) which increased the cell count to 7.7 million. The 3.4 million cell mesh was able to capture the flow field details accurately and used in the analysis.

2.3 Solver Setup

2.3.1 Governing Equations

The numerical analysis in this study was performed using the Ansys Fluent 17.2, which solves the Reynolds Averaged Navier Stokes Equations (RANS) for the flow field. The RANS equations are as follows:

Continuity:

$$\frac{\partial \rho}{\partial t} + \frac{\partial}{\partial x_i}(\rho u_i) = 0 \tag{2}$$

Momentum:

$$\frac{\partial}{\partial t}(\rho u_i) + \frac{\partial}{\partial x_j}(\rho u_i u_j) = -\frac{\partial p}{\partial x_i} + \frac{\partial}{\partial x_j}\left[\mu\left(\frac{\partial u_i}{\partial x_j} + \frac{\partial u_j}{\partial x_i}\right)\right] + \frac{\partial}{\partial x_j}\left(-\rho \overline{u_i' u_j'}\right) \tag{3}$$

Energy:

$$\frac{\partial}{\partial t}(\rho E) + \nabla \cdot (\vec{v}(\rho E + p)) = \nabla \cdot \left(k_{eff} \nabla T - \sum_j h_j \vec{J}_j + (\bar{\tau}_{eff} \cdot \vec{v})\right) \tag{4}$$

The fluctuating component is given by:

$$\frac{\partial}{\partial x_j}\left(-\rho \overline{u_i' u_j'}\right) \tag{5}$$

The k-ω SST turbulence model is used to calculate the Reynolds stresses. It is known to be reasonably accurate for a wide class of flows involving adverse pressure gradient and shock induced flow separation. It was also shown to capture species concentration gradients in a subsonic recirculation region behind a step in supersonic flow [13].

Species transport equation:

$$\frac{\partial}{\partial t}(\rho Y_i) + \nabla \cdot (\rho \vec{v} Y_i) = -\nabla \cdot \vec{J_i} + R_i \tag{6}$$

where R_i is net rate of production of species '*i*' by chemical reaction.

The transport of enthalpy due to species diffusion is given by $\nabla \cdot \left[\sum_{i=1}^{n} h_i \vec{J_i} \right]$ and included in the Energy equation.

2.3.2 Boundary Conditions

Air enters the combustor inlet at Mach 2 with a stagnation temperature and pressure of 612 K and 782.45 kPa respectively. Mach 2 corresponds to 732 m/s at 340 K static temperature. The turbulence intensity was set to 5%. The outlet was set as a pressure outlet with non-reflecting boundary condition in lieu of supersonic flow. The strut surface and walls were set as stationary adiabatic walls with no-slip condition. Vertical symmetry was used to model only half of combustor geometry. RANS CFD analysis was performed using $k-\omega$ SST turbulence model and compressibility correction enabled. The flow and turbulence parameters were set to vary as 2nd order upwind to maintain a balance between accuracy and the computational resources required. The Courant number was initialized to a sufficiently low value of 5, which was changed by the solver to maintain convergence.

Hydrogen was injected from all 8 holes, with injection parameters given in Table 1. Three cases were analyzed, two with the location of Aeroramp injectors from strut base varied from 3 to 9 mm and dynamic pressure ratio held constant at q = 1.9. The other case involved changing the dynamic pressure ratio from 1.9 to 3.5, with the location of Aeroramp injectors held constant at 9 mm from strut base. The values of static pressure (P) and Mach number (M) for the freestream in dynamic pressure ratio calculation (Eq. 1) are taken after the oblique shock formed at the strut tip.

Fuel-air mixing in cold flow is the sole focus of this study. Hence, volumetric combustion model used for reactive analysis is disabled in the current work. It must be noted, however, that the results obtained from cold flow analysis will only show a part of the flow physics and mixing involved in the combustor, phenomenon such as dilation encountered with actual reactive flows will change the results observed with cold flow analysis alone. Combustion experiments performed with dual injectors have shown that there would be augmentation of mixing due to "blockage effect", where front row of injectors blocks the flow leading to back injectors, thus allowing the back injectors to achieve better penetration and also resulting in stronger chemical reactions [14, 15]. Hence, further reacting flow analysis should be performed to fully establish the actual flow behaviour occurring in the scramjet combustor.

Table 1 H_2 injection parameters for strut with Aeroramp injection configuration

Location of injectors (from strut base)	Dynamic pressure ratio (q)
3 mm	1.9
9 mm	1.9
9 mm	3.5

3 Results and Discussion

3.1 Mesh Independence and Validation

The gas dynamics of flow past the strut is shown in Fig. 3. Oblique shocks are formed at the strut tip, these shocks reflect toward the centre line after impacting the walls. The shock reflections are not entirely symmetric about the centreline because of the 3° divergence on the upper wall. At the base of the strut, the flow separates leading to the formation of a recirculation region behind the strut, along with expansion fans at the rear edges.
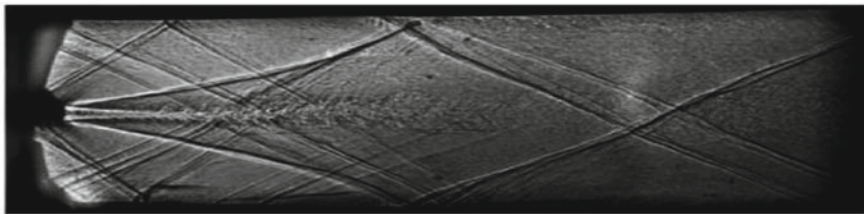
(a) Experimental Schlieren [1]
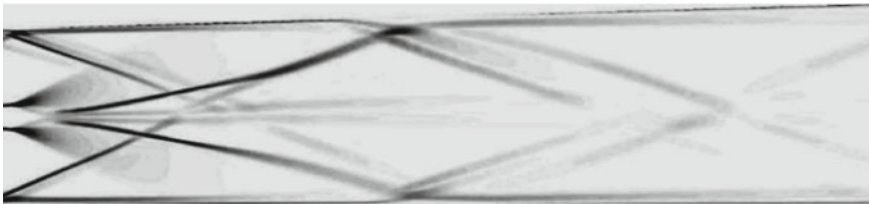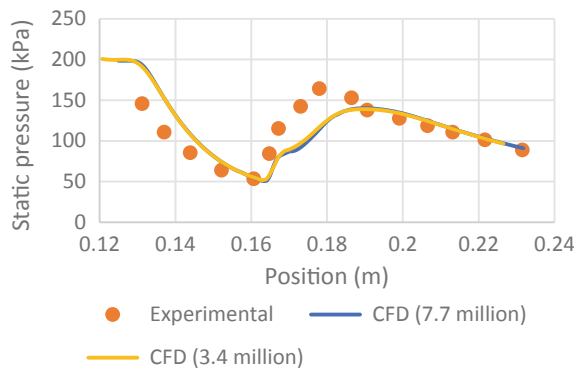
(b) CFD Schlieren

(c) Static pressure along bottom wall of combustor.

Fig. 3 Gas dynamics of flow around strut flame holder without injection **a** Experimental Schlieren [1] **b** CFD Schlieren **c** static pressure along bottom wall of combustor

Two shear layers are formed which separate the recirculation region and the main supersonic flow; they are pushed towards the centre by the expansion fans. As they curve back into the main flow, shock waves are formed. These shock waves reflect against the walls and interact with the boundary layer, which separates at the shock-boundary layer interaction zone due to adverse pressure gradient produced by the shock. A smaller recirculation zone can be seen where the shock reflects off the upper wall due to the 3° divergence angle.

Figure 3 also shows the comparison of the CFD density gradient contours with the experimental schlieren image obtained from [1]. The gas dynamics flow details in the CFD results match well with the schlieren image. The turbulent region behind the strut appears to be smoothened because time averaging was employed in the RANS model. Lower wall static pressure variation obtained downstream of the strut base from [1] and the CFD results were compared as shown in Fig. 3c. The initial decrease in pressure can be attributed to the expansion fan at the strut base. Later, the pressure increases due to the shock wave originating at the shear layer reflecting off the lower wall. The CFD results are in reasonable agreement with the experimental static pressure decrease due to the expansion fan, the minima being captured well in CFD. However, it predicts a weaker oblique shock and hence a lower pressure rise compared to the experiment.

The data for velocity validation was obtained from [1]. Here, three velocity profiles at distances of 11 mm, 58 mm and 166 mm from the base of strut and on symmetry plane were plotted against experimental values (Fig. 4). The strut length was 32 mm. A velocity deficit is observed in the recirculation region, which gradually reduces as we move away from the strut. In general, the velocity profiles between CFD and experiment are in good agreement. At x = 11 mm, the maximum velocity difference in recirculation region is 16%, while at other locations it is within 7%.

Both the 3.4 and 7.7 million cell mesh results are surprisingly close to each other, except x = 11 mm location, where the 3.4 million mesh data is closer to the experimental results than the 7.7 million mesh data. The wall static pressure variation also overlaps for the two meshes (Fig. 3c). Hence, the 3.4 million mesh was used in subsequent analysis.

3.2   Strut with Aeroramp Injector

3.2.1   Gas Dynamics of Flow Field

The flow field that results due to injection into supersonic cross-stream involves gas dynamics details that play a significant role in the overall mixing of fuel with air. In order to understand these details, Schlieren images are taken, giving the side view of strut and associated flow field for the three injection cases (Fig. 5), along with streamlines image giving the isometric view of fuel injected from the Aeroramp holes (Fig. 6).

Fig. 4 Velocity profiles at
a 11 mm **b** 58 mm **c** 166 mm
behind the strut on the
symmetry plane
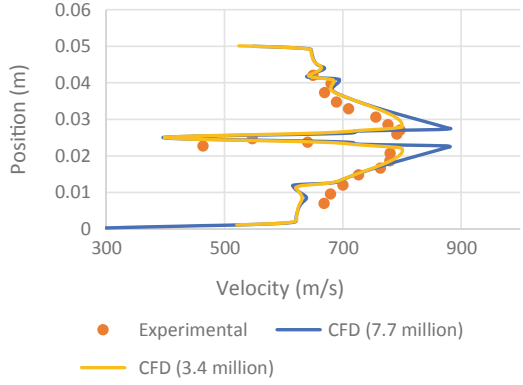
(a) Velocity profile at 11mm
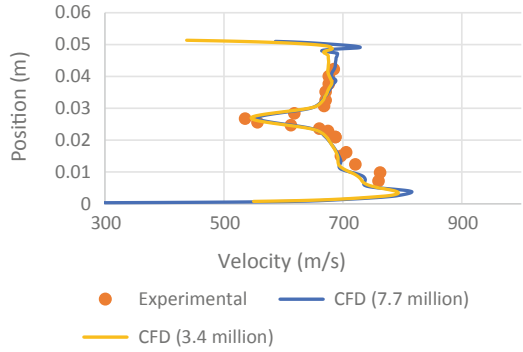
(b) Velocity profile at 58mm
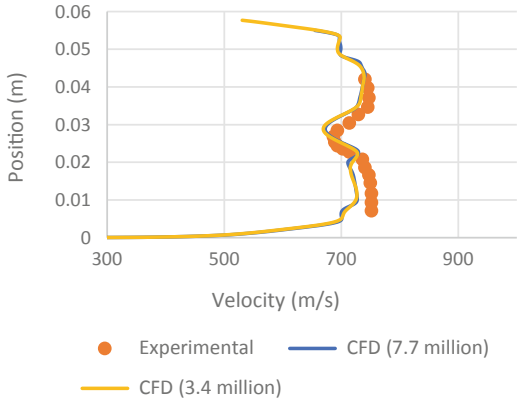
(c) Velocity profile at 166mm

Fig. 5 CFD Schlieren images for various fuel injection configurations from strut upper and lower surfaces **a** 3 mm, q = 1.9 **b** 9 mm, q = 1.9 **c** 9 mm, q = 3.5
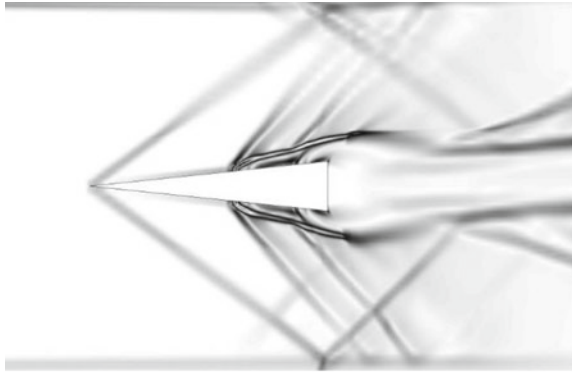
(a) 3mm, q = 1.9
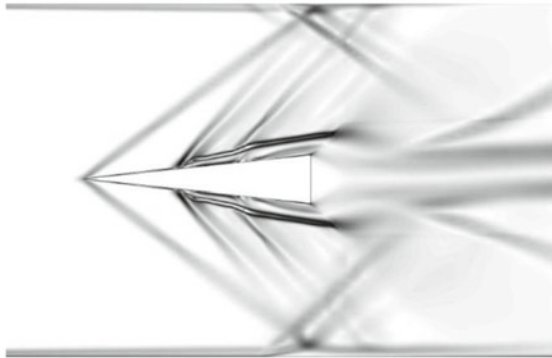
(b) 9mm, q = 1.9
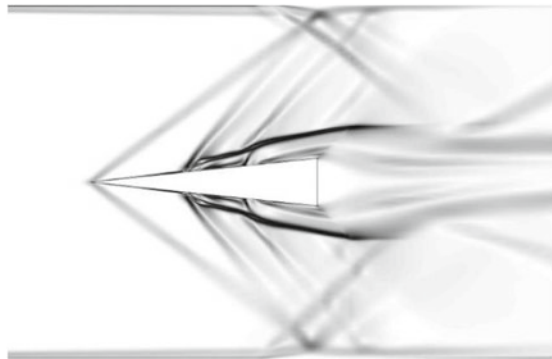
(c) 9mm, q = 3.5
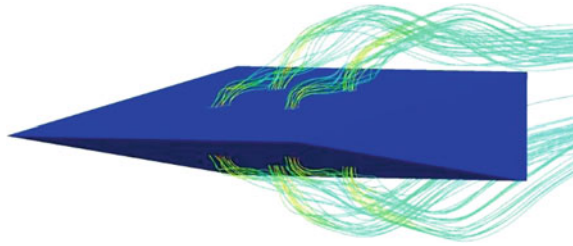
The CFD Schlieren images are given in Fig. 5 for strut with Aeroramp injectors. Schlieren is the first derivative of the density in the flow field. Hence the gradient of density is shown in these images in a vertical plane cutting through the fuel injectors. The region around the strut is shown to explain the effects of injection and the flow details associated with it. The region further downstream has some differences with that seen without injection. The reflected shocks originating at strut tip are at greater angles than that seen with just the strut, they get strengthened from the bow shocks emanating due to the injector jets. However, the shocks originating at the shear layer are weaker in the case with injection; their strength is controlled by the weaker expansion fan due to lower Mach number flow approaching the strut base.

The bow shocks ahead of the fuel jets are visible, with the bow shock formed as a result of front injectors stronger than the rear. This shields the rear jets and "blocks" the main flow to some extent, allowing better penetration of the rear jets into the core flow. The strength of these bow shocks is directly related to dynamic pressure ratio; higher the dynamic pressure ratio of injection, stronger the bow shocks associated with each injector. The fuel jets after injection undergo expansion due to the pressure gradient and subsequently lead to a Mach disk downstream. When the injector holes are 9 mm from the base of strut, for q = 3.5 (Fig. 5c), the Mach number at the strut base is lower compared to q = 1.9 (Fig. 5b) because of stronger bow shocks. This results in a weaker expansion fan and less turning of flow downstream of the strut base. Hence, the recirculation zone behind the strut is larger for q = 3.5. It has implications for fuel-air mixing, as discussed later.

The streamlines of hydrogen jets are shown for 9 mm, q = 3.5 in Fig. 6, with an isometric view encompassing the recirculation region at the strut base. The streamlines give the direction of fuel jets after injection, the effect of the Aeroramp can be seen in these images. The "blockage effect" of the front row of injectors allows the back row to bump up the fuel stream deeper into the core flow. As a result, the penetration of the fuel into the freestream is improved in the near field. At the strut base, the expansion fan forces the fuel vortices to turn back into the recirculation region, hence improving its mixing with air.

An important constraint in the development of combustor is the overall stagnation pressure loss incurred from inlet to exit. The flame holder and the fuel injection technique play a crucial role in this context. The stagnation pressure loss for various cases is given in Table 2.

Table 2 Overall stagnation pressure loss (%) for various cases

Case	Stagnation pressure loss (%)
Only strut (without injection)	21
3 mm, q = 1.9	22.7
9 mm, q = 1.9	21
9 mm, q = 3.5	20.6

Since the number of fuel injector holes is less, the injection process causes only a minor increase in mass-averaged stagnation pressure loss across the combustor; the maximum increase is 1.7% among the aero-ramp cases compared to the strut only case. An apparent anomaly observed in the table is that the loss is 0.4% lesser for the 9 mm, q = 3.5 case than loss without injection. As discussed earlier, the bow shocks due to fuel injection increase the losses, while the weaker shocks originating at the shear layer reduce the losses. For the case under discussion, the net effect of these two shock structures is a reduction in overall loss.

3.2.2 Equivalence Ratio Variation

The Equivalence ratio contours in Fig. 7 give a good picture of the mixing process from combustion point of view. Although combustion runs are not performed here, the equivalence ratio depicts what part of the fuel-air mixture in a plane is combustible. The outer black line in each image corresponds to Lower Flammability Limit (LFL) and the inner black line corresponds to Upper Flammability Limit (UFL). For the given airflow conditions, these values of LFL and UFL correspond to equivalence ratios of 0.1 and 2.1 respectively. Only the region between these limits is combustible; the region within the UFL line is very fuel rich and not combustible and the region outside the LFL line is very fuel lean and hence not combustible. This combustible region is compared among the three cases and along four planes downstream of strut base in the recirculation region, as most of the mixing occurs here.

Figure 7 shows the equivalence ratio contours for the three injection cases at four locations downstream of the strut base. The distance x is normalized by strut length L. At $x/L = 0.5$ given by Fig. 7a, for 3 mm, q = 1.9, the Aeroramp vortices are forced to turn by a sharp angle towards the recirculation zone due to the expansion fan at the strut base. Thus, there is some interaction of the Aeroramp vortices with the strut wake vortex. For the 9 mm, q = 1.9 case, the strut wake vortices are shorter due to the stronger expansion fan as discussed earlier. Hence, in contrast to the 3 mm case, the Aeroramp vortices have a more limited interaction with the strut wake vortices. In the 9 mm, q = 3.5 case, the recirculation vortex is larger, resulting in a stronger interaction and enhanced mixing with the Aeroramp vortices. There is also higher penetration in the vertical and lateral directions in this case compared to the previous two cases.

At $x/L = 1$ given by Fig. 7b, for 3 mm, q = 1.9, the orientation of these vortices is changed as they are pulled inwards by the significantly stronger recirculation zone

(a) x/L = 0.5
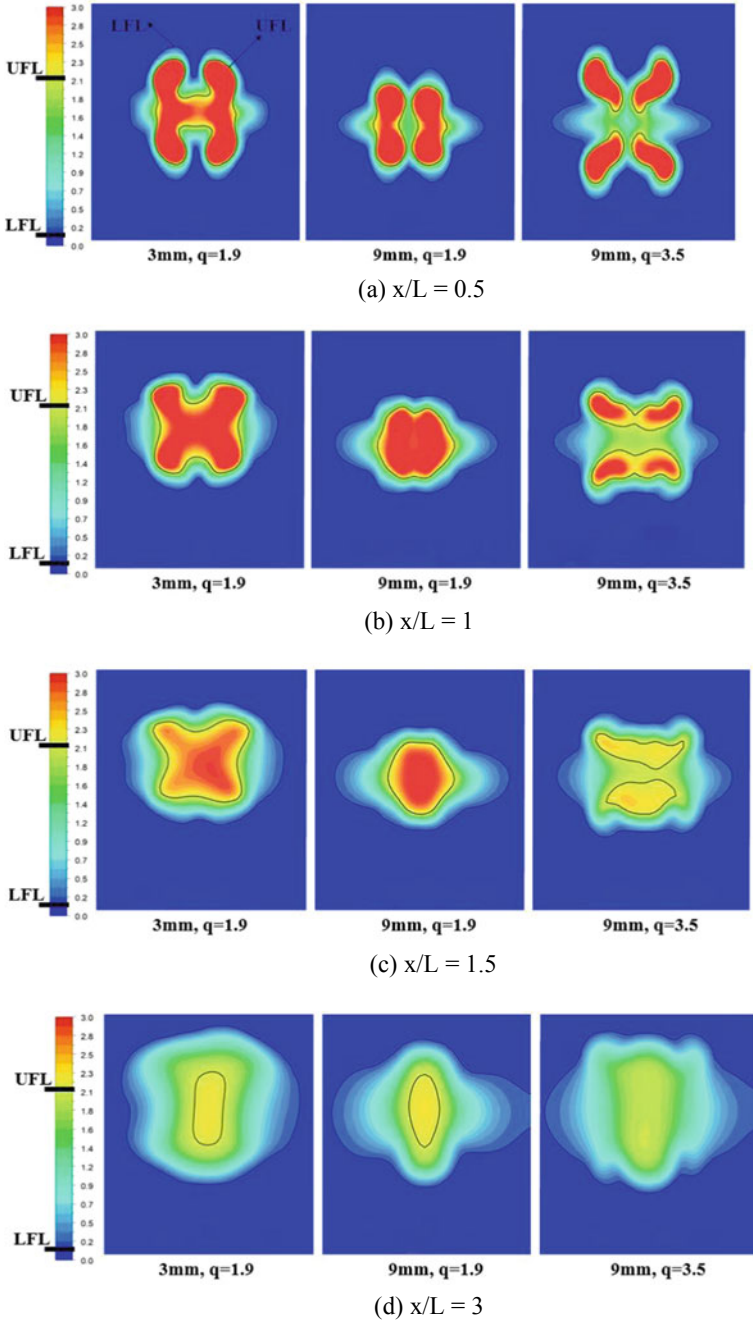
(b) x/L = 1

(c) x/L = 1.5

(d) x/L = 3

Fig. 7 Equivalence ratio contours for various fuel injection configurations at **a** x/L = 0.5 **b** x/L = 1 **c** x/L = 1.5 **d** x/L = 3

vortex. The orientation of the jet vortices is maintained for the 9 mm, q = 1.9 due to limited interaction with the recirculation vortex, hence causing a lateral bulge in the equivalence ratio contours. In the 9 mm, q = 3.5 case, the interaction is so significant that the Aeroramp vortices are flattened and each vortex begins interacting with the vortex adjacent to it in the lateral direction.

At $x/L = 1.5$ given by Fig. 7c, for 3 mm, q = 1.9, the Aeroramp vortices have merged together in an 'X' like pattern and for 9 mm, q = 1.9, all the Aeroramp vortices have merged into a single fuel rich blob. For the 9 mm, q = 3.5 case, the interaction with the strut wake vortex and adjacent vortices have resulted in the fuel richness dropping more prominently (from bright red to light yellow) than that seen in the other two cases.

At $x/L = 3$ given by Fig. 7d, we can see that the fuel richness has dropped rapidly to values below the UFL in 3 mm, q = 1.9 and 9 mm, q = 1.9 cases. There is still a central fuel rich region in these two cases that is not combustible. However, in the 9 mm, q = 3.5 case, there is no UFL as the mixing of fuel and air has been so extensive that the entire region within the LFL line is combustible.

This concludes that the best-case scenario is injecting at a higher dynamic pressure ratio (q = 3.5) and away from the strut base (9 mm). The fuel penetrates the incoming air better in both lateral and vertical directions and stays away from the injection surface. Fuel-air mixing is also enhanced around and behind the strut. The combustible area is higher at all locations for this case compared to the other two cases. To add to these advantages, the overall stagnation pressure loss is also lower for the 9 mm, q = 3.5 case than in the other two cases.

In Fig. 7, the region within the UFL line is bright red, signifying a very fuel rich mixture. Although the maximum equivalence ratio for these contours has been truncated at 3, the equivalence ratios in these fuel rich regions go well beyond 3.

The graph in Fig. 8 gives the maximum equivalence ratio variation from the strut base up to $x/L = 4$. The 9 mm location cases show lower maximum equivalence ratio compared to 3 mm case, since the Aeroramp vortices get more distance along the strut length to mix with air. While comparing the 9 mm, q = 1.9 and 9 mm, q = 3.5 cases, an interesting observation is that although more fuel is injected for the 9 mm, q = 3.5 case at higher dynamic pressure ratio, enhanced mixing with the larger strut wake vortex ensures that the local maximum equivalence ratio is lower than the 9 mm, q = 1.9 case.

4 Conclusion

The current study explores a novel strut-based fuel injection scheme for a scramjet combustor, incorporating an aerodynamic ramp fuel injector on the upper and lower strut surfaces. As the first step, the gas dynamics of flow past the strut using RANS CFD analysis were validated with DLR experimental data available in literature. The velocity profiles behind the strut, lower wall static pressure and density gradients agreed well with experiment.
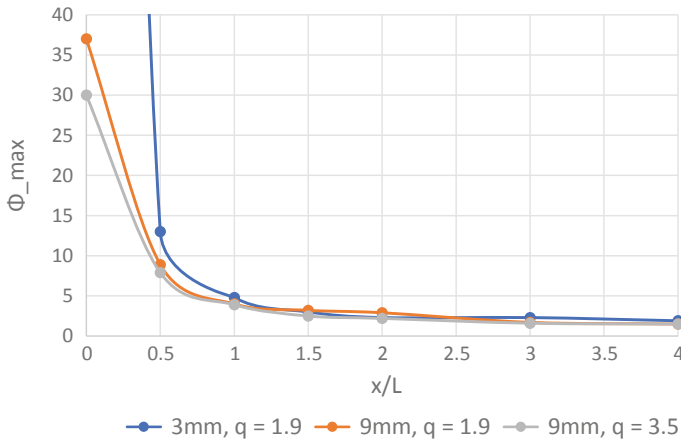
Fig. 8 Maximum equivalence ratio variation as a function of distance behind the strut for various fuel injection configurations

The Aeroramp injectors were incorporated on the strut surface to increase the lateral fuel penetration into the flow and improve mixing by Aeroramp vortices in the near field up to strut base. These vortices subsequently entrain into the larger strut wake recirculation vortex and further enhance fuel-air mixing.

The location of Aeroramp injectors with respect to strut base (3 mm, 9 mm) and dynamic pressure ratio (q = 1.9, 3.5) were varied. The fuel injected was hydrogen, only non-reacting flow runs were performed. Numerical schlieren, streamlines and equivalence ratio contours in various transverse planes behind the strut were obtained. The results indicate that it is beneficial to inject fuel away from the strut base and at a higher dynamic pressure ratio to achieve better fuel-air mixing and lower equivalence ratios downstream of the strut, which is more amenable to combustion. Fuel-air mixing is governed by the interaction of Aeroramp vortices with the larger strut wake recirculation vortex; the strength of expansion fan at strut base plays a key role in facilitating this interaction.

References

1. Genin F, Menon S (2010) Simulation of turbulent mixing behind a strut injector in supersonic flow. AIAA J 48(3):526–539
2. Berglund M, Fureby C (2007) LES of supersonic combustion in a scramjet engine model. Proc Combust Inst 31:2497–2504
3. Changmin Cao, Taohong Ye, Majie Zhao (2015) Large eddy simulation of hydrogen/air scramjet combustion using tabulated thermo-chemistry approach. Chin J Aeronaut 28(5):1316–1327
4. Fuller RP, Wu PK, Nejad AS, Schetz JA (1998) Comparison of physical and aerodynamic ramps as fuel injectors in supersonic flow. J Propul Power 14(2):135–145
5. Segal C (2009) The scramjet engine: processes and characteristics. Cambridge University Press

6. Cox SK, Fuller RP, Schetz JA, Walters RW (1994) Vortical interactions generated by an injector array to enhance mixing in supersonic flow. In: AIAA Paper, 94-0708

7. Jacobsen LS, Gallimore SD, Schetz JA, O'Brien WF, Goss LP (2003) Improved aerodynamic-ramp injector in supersonic flow. J Propul Power 19(4):663–673

8. Jacobsen LS, Schetz JA, Ng WF (2000) Flowfield near a mulitiport injector array in a supersonic flow. J Propul Power 16(2):216–226

9. Jacobsen LS, Gallimore SD, Schetz JA, O'Brien WF (2003) Integration of an aeroramp injector/plasma igniter for hydrocarbon scramjets. J Propul Power 19(2):170–182

10. Bonanos AM, Schetz JA, O'Brien WF (2008) Dual-mode combustion experiments with an integrated aeroramp-injector/plasma-torch igniter. J Propul Power 24(2):267–273

11. Baoxi W, Chen B, Yan M, Shi X, Zhang Y, Xu Xu (2012) Operational sensitivities of an integrated aerodynamic ramp injector/gas portfire flame holder in a supersonic combustor. Acta Astronaut 81:102–110

12. Chen B, Xu Xu, Baoxi W, Zhang Y (2017) Numerical simulations of turbulent flows in aeroramp injector/gas-pilot flame scramjet. Chin J Aeronaut 30(4):1373–1390

13. Thakur A, Sinha A, Roy AS, Ghosh D, Ali MS, Poptani S (2017) CFD analysis and validation of mixing and combustion behind a step flame holder in supersonic flow. In: 1st National aerospace propulsion conference, NAPC-2017-024

14. Lee SH (2006) Characteristics of dual transverse injection in scramjet combustor, Part 2: combustion. J Propul Power 22(5):1020–1026

15. Lee SH (2006) Characteristics of dual transverse injection in scramjet combustor, Part 1: mixing. J Propul Power 22(5):1012–1019

Effect of Swirl and Wall Heat Transfer on the Performance of Arcjet Thrusters Using Numerical Modeling

Deepak Akhare, Hari Prasad Nandyala, Amit Kumar, and T. Jayachandran

Abstract To sustain the arc in the arcjet, the swirl is thought to be necessary. This paper conducts a numerical study on various geometry and input conditions. The effect of swirl and wall temperature of a nozzle on the plasma flow, arc behavior, and performance parameter of low power arcjet has been studied. The physics behind the working of low power arcjet and behavior of swirl velocity has been plotted. Various aspect of swirl, which stabilizes the arc, is also discussed.

Keywords Arcjet · Swirl · Numerical modeling · Argon · Plasma

Nomenclature

A_{exit}	Exit area of the nozzle
B	Magnetic induction vector
$\bar{C}$	Mean velocity
B_θ	Azimuthal component of magnetic induction vector
F	Thrust
I	Electric current
I_{sp}	Specific impulse
J	Current density vector
P_{exit}	Pressure at exit of the nozzle
Q_{ij}	Collision cross section for i, j species encounter

D. Akhare (✉) · H. P. Nandyala · A. Kumar · T. Jayachandran
Department of Aerospace Engineering, Indian Institute of Technology Madras, Chennai, India
e-mail: akharedeepak@gmail.com

H. P. Nandyala
e-mail: hari25.astro@gmail.com

A. Kumar
e-mail: amitk@ae.iitm.ac.in

T. Jayachandran
e-mail: t_jayachandran@ae.iitm.ac.in

R_{gas}	Characteristic gas constant
U_{exit}	Velocity of gas at exit of the nozzle
T	Gas Temperature
V	Velocity vector
a	Velocity of sound
e_t	Total energy
h	Plank's constant
h_t	Total Enthalpy
$j_{r,}$	Radial current density vector
j_z	Axial current density vector
k	Thermal conductivity
k_{Boltz}	Boltzmann constant
$\dot{m}$	Mass flow rate
m_e	Mass of electron
n_e, n_n	Number density of electrons and neutral atoms
$\dot{n}_e$	Production rate of electron
n_n	Number density of neutral atoms
p	Pressure
v_r	Radial velocity
v_z	Axial velocity
v_θ	Azimuthal velocity
y_e	Mass fraction of electron
r, z, θ	Radial, axial, and azimuthal coordinates
ρ	Density
$\overline{\overline{\tau}}$	Viscous stresses
σ	Electrical conductivity
α	Degree of ionization
μ	Coefficient of viscosity
μ_0	Magnetic permeability of free space
ϵ_0	Permittivity of free space
ε_i	Ionization energy

1 Introduction

Arcjet thrusters are used in space propulsion, due to their better specific impulse. Instead of using chemical energy as conventional rockets do, arcjets use electrical energy in the form of dc arc to give energy to its propellants. So, a large amount of energy can be supplied to the propellant, leading to an increase in its specific impulse. The only limitation on the addition of heat will be the temperature up to which a material can stand. The arcjets can go up to 2000s specific impulse.

In arcjet thrusters, the propellant gas is injected from the upstream end and passed through a converging–diverging nozzle. The electrical energy is used to create an arc

in the flow between the cathode tip present in the convergent section and anode wall as a diverging section of the nozzle. The arc is passed through the constrictor. The propellant gets heated by the dc arc present in the constrictor region up to an order of 10^4K. This high-temperature gas is then expanded through a diverging section of a nozzle. Electrical energy is thus converted into kinetic energy, thereby producing thrust.

According to a literature survey [1], it is thought that if swirl is introduced in the constrictor, it will prevent the kinking of the arc by introducing a radial pressure gradient, thereby stabilizing the arc in the constrictor region. A further study had been done by [2] on the behavior of swirl in arcjet thrusters. It showed that swirl injection was dependent on mass flow rate and distance from the inlet plenum to the beginning of the converging section. Further [3] showed a significant reduction in discharge coefficient and vacuum thrust efficiency due to swirl may occur, but specific impulse will not be affected significantly. But, there is no existing literature on the effect of the swirl on the performance of arcjet thrusters.

One can use different material and cooling system for the nozzle of the arcjet. So, the temperature difference on the inner wall of the anode will be affected. The effect of the anode wall temperature on the position of arc and performance is also not clearly known.

In this paper, the modeling study is thus conducted to understand the effect of swirl and wall temperature on the performance of low power arcjet thruster.

2 Formulation

A model which describes all necessary processes occurring inside an arcjet for accounting the above objectives is formulated.

2.1 Assumptions

(a) The present model is only designed for argon as a propellant.
(b) The flow considered here is assumed to be steady, laminar, compressible, and axisymmetric.
(c) The grid considered here is 2 dimensional as the flow assumed is axisymmetric. So, the gradients in θ direction are made zero.
(d) This model neglects second-order ions in the plasma and only considers ionization-recombination reaction.

$$Ar + e^- \rightarrow Ar^+ + e^- + e^-$$

Thus, the plasma only contains Ar^+ and Ar atoms as heavy species.

(e) The plasma is electrically neutral, i.e., the number of ions and electrons will be the same ($n_e = n_i$).
(f) Plasma considered here is optically thin and is in local thermodynamic equilibrium (LTE).
(g) The convection velocity of all species in plasma is considered to be the same.
(h) Radiation loses have been neglected.
(i) The continuum model is valid everywhere in the domain except at the exit of the nozzle. The Knudsen number turns out to be $K_n \approx 0.0014$ at the constrictor.

As the model is axisymmetric, the derivatives with respect to θ are zero. i.e. $\frac{\partial}{\partial \theta} = 0$ and $B_z = 0$, $B_r = 0$, $E_\theta = 0$.

2.2 Governing Equation

With the above assumptions, the Governing equations in cylindrical coordinates (r, θ, z) can be written as follows:

Mass conservation equation

$$\frac{\partial \rho}{\partial t} + \frac{1}{r} \frac{\partial}{\partial r} (r \rho v_r) + \frac{\partial}{\partial z} (\rho v_z) = 0 \tag{1}$$

Electron conservation equation

$$\frac{\partial \rho y_e}{\partial t} + \frac{1}{r} \frac{\partial}{\partial r} (r \rho y_e v_r) + \frac{\partial}{\partial z} (\rho y_e v_z) = m_e \dot{n}_e \tag{2}$$

where the production rate of electrons given by

$$\dot{n}_e = \beta(T) \left(S_a n_n - n_e^2 \right) \tag{3}$$

where $\beta(T)$ represents Hinnov–Hirschberg recombination rate coefficient

Momentum conservation equation in the r-direction

$$\frac{\partial \rho v_r}{\partial t} + \frac{1}{r} \frac{\partial (r \rho v_r v_r)}{\partial r} + \frac{\partial (\rho v_r v_z)}{\partial z} - \frac{\rho v_\theta^2}{r}$$
$$= -\frac{\partial p}{\partial r} + \frac{1}{r} \frac{\partial (r \tau_{rr})}{\partial r} - \frac{\tau_{\theta \theta}}{r} + \frac{\partial \tau_{rz}}{\partial z} - j_z B_\theta \tag{4}$$

Momentum conservation equation in θ direction

$$\frac{\partial \rho v_\theta}{\partial t} + \frac{1}{r} \frac{\partial (r \rho v_\theta v_r)}{\partial r} + \frac{\partial (\rho v_\theta v_z)}{\partial z} + \frac{\rho v_\theta v_r}{r} = \frac{1}{r} \frac{\partial (r \tau_{\theta r})}{\partial r} + \frac{\tau_{r\theta}}{r} + \frac{\partial \tau_{\theta z}}{\partial z} \tag{5}$$

Momentum conservation equation in z-direction

$$\frac{\partial \rho v_z}{\partial t} + \frac{1}{r}\frac{\partial (r\rho v_z v_r)}{\partial r} + \frac{\partial (\rho v_z v_z)}{\partial z} = -\frac{\partial p}{\partial z} + \frac{1}{r}\frac{\partial (r\tau_{zr})}{\partial r} + \frac{\partial \tau_{zz}}{\partial z} + j_r B_\theta \quad (6)$$

In the above momentum conservation equation, the $\frac{\rho u_\theta^2}{r}$ and $\frac{\rho u_\theta u_r}{r}$ are centrifugal and Coriolis force, respectively, which are there due to the presence of velocity in the θ direction (swirl velocity). The $j_z B_\theta$ and $j_r B_\theta$ present in the source is the Lorentz force term.

Energy conservation equation

$$\frac{\partial \rho e_t}{\partial t} + \frac{1}{r}\frac{\partial}{\partial r}(r\rho h_t v_r) + \frac{\partial}{\partial z}(\rho h_t v_z)$$

$$= \frac{1}{r}\frac{\partial}{\partial r}\left(rk\frac{\partial T}{\partial r}\right) + \frac{\partial}{\partial z}\left(k\frac{\partial T}{\partial z}\right) + j_z E_z + j_r E_r$$

$$+ \frac{1}{r}\frac{\partial}{\partial r}(r\tau_{rr}v_r + r\tau_{r\theta}v_\theta + r\tau_{rz}v_z)$$

$$+ \frac{\partial}{\partial z}(\tau_{zr}v_r + \tau_{z\theta}v_\theta + \tau_{zz}v_z) - \dot{n}_e \varepsilon_i \quad (7)$$

The $j \cdot E = j_z E_z + j_r E_r$ present in energy equation accounts for Joule heating due to arc, which increases the enthalpy of the propellant.

Ideal gas equation and total energy is

$$P = \rho R_{\text{gas}} T, e_t = c_v T + \frac{v_r^2 + v_z^2 + v_\theta^2}{2}$$

Viscous stresses are

$$\tau_{rr} = \mu\left[2\frac{\partial v_r}{\partial r} - \frac{2}{3}\nabla \cdot V\right], \tau_{zz} = \mu\left[2\frac{\partial v_z}{\partial z} - \frac{2}{3}\nabla \cdot V\right]$$

$$\tau_{\theta\theta} = \mu\left[2\left(\frac{1}{r}\frac{\partial v_\theta}{\partial \theta} + \frac{v_r}{r}\right) - \frac{2}{3}\nabla \cdot V\right], \tau_{r\theta} = \mu\left(\frac{1}{r}\frac{\partial v_r}{\partial \theta} + \frac{\partial v_\theta}{\partial r} - \frac{v_\theta}{r}\right)$$

$$\tau_{rz} = \mu\left(\frac{\partial v_r}{\partial z} + \frac{\partial v_z}{\partial r}\right), \tau_{z\theta} = \mu\left(\frac{1}{r}\frac{\partial v_z}{\partial \theta} + \frac{\partial v_\theta}{\partial z}\right) \quad (8)$$

Steady-state magnetic induction equation given below is solved to get a magnetic field.

$$\frac{\partial}{\partial z}\left(\frac{1}{\mu_0 \cdot r \cdot \sigma}\left(\frac{\partial \psi}{\partial z}\right)\right) + \frac{\partial}{\partial r}\left(\frac{1}{\mu_0 \cdot r \cdot \sigma}\left(\frac{\partial \psi}{\partial r}\right)\right) = \frac{\partial}{\partial z}\left(\frac{v_z \psi}{r}\right) + \frac{\partial}{\partial r}\left(\frac{v_r \psi}{r}\right)$$

$$(9)$$

where $\psi = r B_\theta$

Current density is obtained from ohms law

$$J = \sigma(E + V \times B)$$

The electric field is obtained from

$$\nabla \times B = -\mu_0 \sigma(E)$$

where σ is electrical conductivity of partially ionized gas given by Spitzer Hammer [4].

$$\sigma = 2.5 \frac{n_e e^2}{m_e \bar{c}(n_e Q_{ei} + n_n Q_{en})} \tag{10}$$

Dynamic viscosity for argon plasma is calculated using the kinetic theory of gases, as given in Neiwood thesis [5].

$$\mu = \mu_n \frac{1-\alpha}{1 - \alpha + \alpha \frac{Q_{in}}{Q_{nn}}} + \mu_i \frac{\alpha}{(1-\alpha)\frac{Q_{in}}{Q_{ii}} + \alpha} \tag{11}$$

where

$$\mu_i = \frac{0.406(4\pi\epsilon_0)^2 \sqrt{m_i}(k_b T)^{\frac{5}{2}}}{e^4 \ln \Gamma}, \quad \mu_n = \frac{m_i \vec{C}_i}{2 Q_{nn}}$$

$$\Gamma = 1.24 \times 10^7 \sqrt{\frac{T^3}{n_e}}, \quad \bar{C} \sqrt{\frac{8 k_b T}{\pi m_e}}$$

The thermal conductivity of heavy particles is calculated from Euken's relation and thermal conductivity of electron is taken from Neiwood thesis [5].

$$k_i = \frac{15}{4} \frac{k_b \mu}{m_i}, k_e = 1.7142 \frac{k_b^2 T \sigma}{e^2} \tag{12}$$

$$k = k_i + k_e$$

For which the collision cross section of argon plasma is taken from [6].
Performance parameter calculation:
Thrust is given as

$$F = \dot{m} U_{\text{exit}} + P_{\text{exit}} A_{\text{exit}} \tag{13}$$

And the specific impulse is calculated as

$$I_{\mathrm{sp}} = \frac{F}{\dot{m} \times g}; \quad g = 9.81 \text{ m/s}^2 \tag{14}$$

3 Modeling Approach

The computational domain of arcjet thruster is shown in Fig. 1. The nozzle has a constrictor radius of 0.5 mm and constrictor length of 1 mm. The cathode tip half-angle is 30° and the cathode radius is 3 mm. The exit area to throat area ratio is 225 and the divergent angle is 20°. Here anther nozzle has also been considered with constrictor radius 0.75 mm. Exit area to throat area ratio of both the nozzle is kept constant.

A numerical code has been developed to solve the governing equations. The governing equations in the code are solved using a cell-centered finite volume method [7]. The nozzle with constrictor radius 0.5 mm and 0.75 mm will be referred to as Nozzle I and Nozzle II, respectively. Here an unstructured mesh is considered for modeling the Nozzle I with 183×20 grid cells and Nozzle II with 202×20 grid.

The convective fluxes are calculated using an all speed 2nd order in space AUSM+-(Advection Upstream Splitting Method) algorithm [8].

The flux is spat as

$$f_{1/2} = \dot{m}_{1/2} \vec{\psi}_{L/R} + p_{1/2}$$

where

$$\vec{\psi}_{L/R} = \begin{cases} \vec{\psi}_L & if \, \dot{m}_{1/2} > 0, \\ \vec{\psi}_R & otherwise \end{cases}$$

$$\dot{m} = \rho u, \vec{\psi} = \left[1, v_r, v_\theta, v_z, H, Y_e \right]$$

Algorithm for AUSM is as follows:

$$M_{L/R} = \frac{v_{L/R}}{a_{1/2}}, a_{1/2} = \frac{a_L + a_R}{2}$$

$$\bar{M}^2 = \frac{v_L^2 + v_R^2}{2a_{1/2}^2}$$

$$M_o^2 = min\left(1, max\left(\bar{M}^2, M_\infty^2\right)\right) \in [0, 1]$$

$$f_a(M_0) = M_0(2 - M_0) \in [0, 1]$$

$$M_{1/2} = \mathcal{M}_{(4)}^+(M_L) + \mathcal{M}_{(4)}^-(M_R) - \frac{K_p}{f_a} max\left(1 - \sigma \bar{M}^2, 0\right) \frac{p_R - p_L}{\rho_{1/2} a_{1/2}^2}, \rho_{1/2} = \frac{(\rho_L + \rho_R)}{2}$$

where $0 \leq K_p \leq 1$ and $\sigma \leq 1$.

Then the mass and pressure fluxes are readily defined,

$$\dot{m}_{1/2} = a_{1/2} M_{1/2} \begin{cases} \rho_L \ if \ M_{1/2} > 0, \\ \rho_R \ \ otherwise \end{cases}$$

$$p_{1/2} = \sqrt{(5)}^{+}(M_L) p_L + \sqrt{(5)}^{-}(M_R) p_R - K_u \sqrt{(5)}^{+} \sqrt{(5)}^{-} (\rho_L + \rho_R)(f_a a_{1/2})(u_R - u_L)$$

Using the parameters with $0 \leq K_u \leq 1$

$$\alpha = \frac{3}{16}(-4 + 5 f_a^2) \in \left[-\frac{3}{4}, \frac{3}{16}\right], \beta = \frac{1}{8}$$

Finally, the whole flux is

$$f_{1/2} = \dot{m}_{1/2} \begin{cases} \vec{\psi}_L \ if \ M_{1/2} > 0, \\ \vec{\psi}_R \ \ otherwise \end{cases} + p_{1/2}$$

In all calculations $K_p = 1$, $K_u = 0.75$, $\sigma = 1$

The viscous fluxes are obtained from the Central Difference Scheme. Gradient terms are computed based on the least square residual method. The marching in time is done using the Runge-Kutta 4th order method. The solution is obtained by running the unsteady code until it reaches a steady-state.

The electromagnetic field is considered to be in a steady-state at each time step. The steady-state Maxwell Equations solved together with the Ohm's law gives Magnetic induction equation. Gauss–Seidel iterative procedure is adopted for solving Magnetic induction equation to get a steady electromagnetic field.

The Lorentz forces and Joule heating calculated from the electromagnetic field are then added to the Navier–Stokes equation in the source term. The properties are calculated using temperature and pressure obtained from the conservative variable after solving the Navier–Stokes equation. Thus, a two-way coupling is established between Fluid solver and Electromagnetic Field solver.

3.1 Boundary Conditions

All simulations are carried at a constant mass flow rate of 60 mg/s at the inlet. The pressure gradient at the inlet (A-G) is set to zero. The axial component of velocity at the inlet is implicitly extrapolated from the interior values and the radial component of velocity is set to zero. While the swirl component of velocity at the inlet is either set to a parabolic distribution or to zero. Other properties are calculated using isentropic relation. The electron number density at the inlet is set to 1×10^6.

On the solid boundaries (A-B, D-E-F-G) no-slip condition is imposed and the gradient of electron number density is set to zero. The temperature along the anode (D-E-F-G) inner-surface is set to increase linearly from 500 K at the nozzle inlet (G) to 1800 K at the end of the constrictor (E), and then decrease linearly to 700 K at the nozzle exit (D). The temperature gradient at the cathode wall (A-B) is set to zero. At axis (B-C), an axisymmetric boundary condition is implemented. At exit (C-D) the flow is supersonic. All the variables are extrapolated from the interior variables.

The boundary conditions [1] for the magnetic induction equation, at the inlet (A-G), is $rB_\theta = -\frac{\mu_o I}{2\pi}$, where I is input current. B_θ is set to zero along the axis (B-C) (imposing symmetry) and along the exit plane (C-D) to prevent the current from blowing out of the thruster. The anode (D-E-F-G) considered here is a perfect conductor, thus the current streamlines enter the anode surface normal to it. Which is imposed by setting $(\nabla \times \boldsymbol{B}) \cdot \hat{t} = 0$ ($\hat{t}$ is the unit tangent vector along the anode and cathode surface).

3.2 Validation

The Computational fluid dynamics code for modeling of arcjet thruster was written in FORTRAN language. The CFD code was validated against standard compressible benchmarks like CD nozzle flow. The CFD code was then used to simulate the experiments of a hydrazine arcjet by Bufton and Burton [9]. The thruster has an area ratio of 225 and divergent angle of 20°, with constrictor diameter of 0.64 mm. With an input arc current of 10 A, the gas is injected at 500 K with a mass flow rate of 50 mg/s. In the experiments, the radial profiles of axial velocity of gas mixture plasma at 1.0 mm downstream from the exit plane were measured. One can note from the paper presented on numerical simulations on arcjet (Nandyala et al. 2017) that the predicted axial velocity profile is in good agreement with the corresponding experimental data and predicted radial distributions of the heavy-species temperature at the arcjet exit plane with the corresponding experimental data of Bufton and Burton.

The code was modified to include swirl component of the velocity for simulating argon as a propellant on geometry used in experiments in BUAA by Wang et al. (2009). A grid-independent study has been done with 1000, 2000, 4000, 8000 grid cells. A grid with 4000 cells was considered for further study as the difference in mass flow rate for 4000 cells and 8000 cells is less than 0.1%. It was also ensured that the mass flow rate across each section is preserved. Present CFD simulations show that the arcjet thruster has a specific impulse of 225 s with a predicted voltage of 30.9 V when the mass flow rate is 72.8 mg/s and the total current I = 10 A. The simulation result of temperature distribution along the axis as shown in Fig. 2 is in good agreement with the results of Wang [11]. The maximum temperature captured at the cathode tip position is almost similar and follows the same trend along the axis. Other flow field variables presented in the paper by Wang [11] are also in a good match with the present computed results.

4   Results and Discussion

The simulation is first carried on the base case with base arcjet thruster dimensions as given in Fig. 1a. The mesh distribution is shown in Fig. 1b. The input current is 10 A. The argon gas is injected into the thruster at a constant mass flow rate of 60 mg/s and at temperature 500 K. The outer wall of the nozzle was fully considered as an anode.

Modeling results show that the arc is present in the constrictor region flowing from the cathode tip to the anode wall. As Fig. 3a shows, the heating mainly happens in the constrictor region. The cold flow coming from the convergent section of the nozzle absorbs heat in the constrictor region. The highest temperature is present at the cathode tip above 15000 K.

Figure 3b shows the arc attachment point that is ahead of the constrictor end in the divergent section, which can also be visualized in Fig. 3a. The magnetic field distribution (B_θ / B_0) in Fig. 3a mostly resembles the current. 90% of the current is flowing through those color counters. Figure 3a shows that the arc starts from cathode tip passing through a narrow gap of the constrictor, attaching ahead of the constrictor exit to the divergent section of the nozzle. The arc gets diffused while coming out of the constrictor. Figure 3c shows the curves of Mach number and temperature for the base case. As the Joule heating is concentrated mainly in the constrictor along the axis, the temperature is higher in the central core of the constrictor and it drops rapidly

(a)   Geometric dimensions

(b) grid (183 X 20)
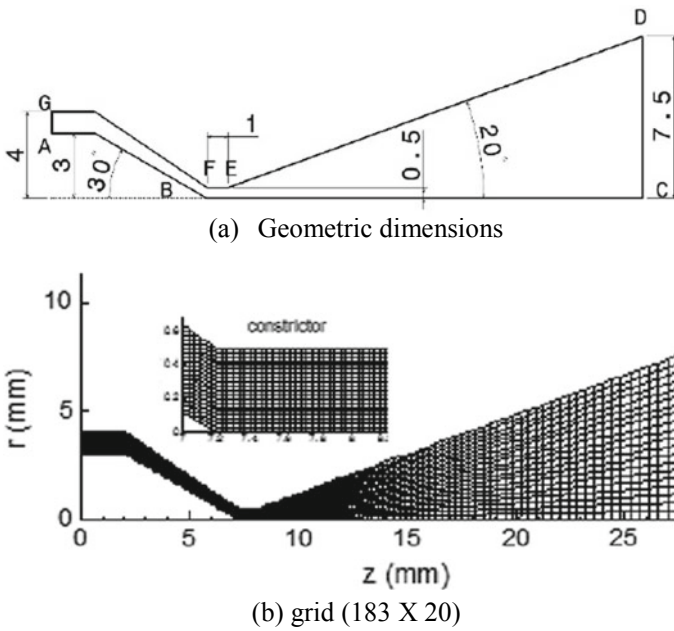
Fig. 1 Computational domain
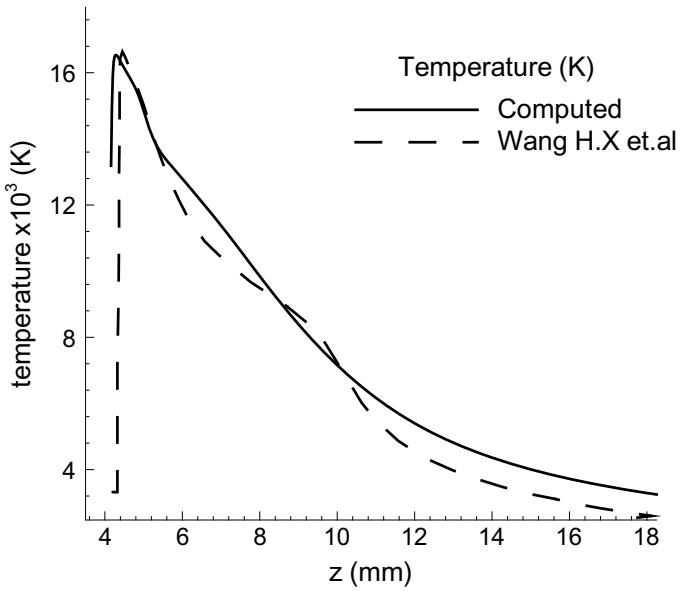
(a) temperature distribution along the axis
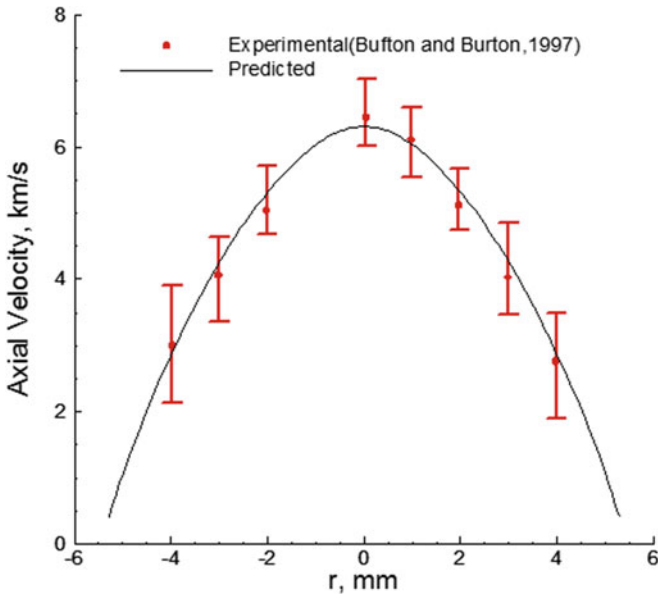
(b) axial velocity at the exit plane

Fig. 2 Comparison of experimental and numerical distribution along the axis
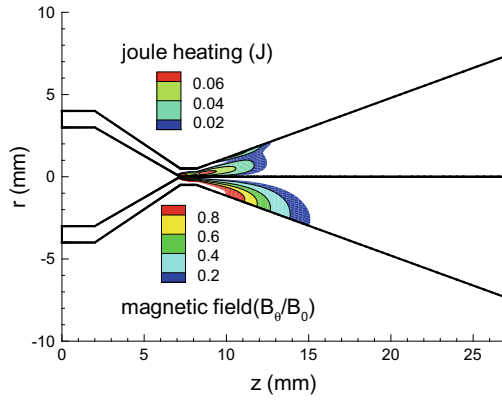
(a) Computed distribution of joule heating J and normalized magnetic field
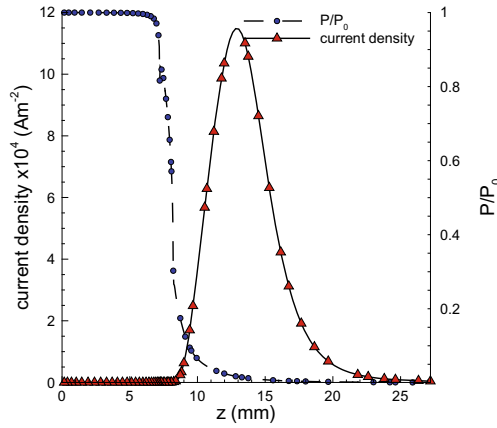
(b) Distribution of anode wall static pressure ratio and current density Am^{-2}
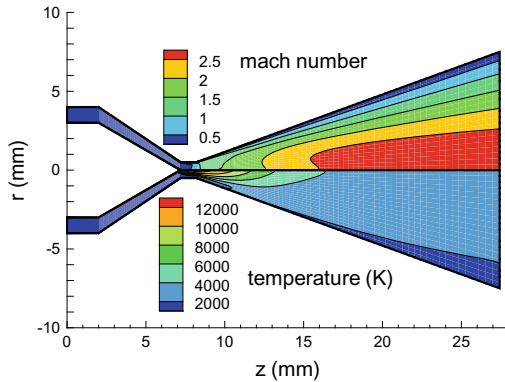
(c) Computed distribution of mach number and temperature K

Fig. 3 Computed distribution of base geometry

along the radial direction. The temperature of the gas gradually decreases with an increase in local Mach number along the divergent section due to the expansion of propellant.

4.1 Effect of Swirl

Figure 4 shows the distribution of swirl in the arcjet. The swirl component of the velocity given at the inlet accelerates as it approaches the constrictor as the angular momentum is conserved. The swirl velocity grows more than 50 m/s for 20 m/s inlet swirl velocity. The profile of the swirl component of the velocity is shown in Fig. 5 at the constrictor inlet for different swirl input velocities. The swirl velocity increases along the radial direction and again decreases due to the presence of the wall. Further, the swirl velocity decelerates in the divergent section. The maximum swirl velocity is observed at the constrictor inlet.

Figure 6a and b shows that the increase in swirl velocity at constrictor inlet results in the increase of pressure near the constrictor walls. By the previous understanding, the pressure gradient created by swirl is positive $\left(\frac{\partial P}{\partial r} > 0\right)$ and supposed to sustain the arc, but both plots show that the pressure near constrictor wall region is well below as compared to the pressure at the axis of the constrictor for swirl velocities lower than 50 m/s for nozzle I and 20 m/s for nozzle II, even though the swirl velocities are more than 120 m/s at constrictor inlet. One can argue that for higher constrictor radius (0.75 mm) and higher inlet swirl velocity, the pressure at wall will be more at center, but this positive pressure gradient is only present at constrictor inlet and as one progress further down the constrictor, this pressure gradient will disappear as shown in Fig. 7a and b.

Figure 7a and b are showing the radial variation of pressure at end of the constrictor. Both plots show that the introduction of swirl velocities has a negligible

Fig. 4 Distribution of swirl and axial component of velocity in arcjet

effect on pressure distribution at the end of the constrictor. The purpose of the swirl introduction is to create a lower pressure zone at the axis of the constrictor. But the presence of arc causes higher temperature region at the axis of the constrictor resulting in a higher pressure zone at the center line, which counters the purpose of swirl introduction.

This phenomenon described above can be further extended to the possibility that the pressure gradients created by swirl may not be strong enough to prevent the kinking of the arc.

Figure 8a and b shows the steep temperature gradients across the constrictor. The sharp changes in temperature along radial direction show the presence of hot flow at the axis of the constrictor and cold flow near the constrictor wall region. The temperature is observed highest at the cathode tip above 15000 K. The swirl results in enhancement of pressure near the wall squeeze the hot flow leading into increase in maximum temperature at the cathode tip. The introduction of swirl velocity shows negligible effects on the radial variation of temperature as profile across the radius remains almost intact.

Figure 9a and b shows that the current flows from the center of the constrictor, which explains the high-temperature zone in the core of the constrictor. As the temperature at cathode tip increases with increase in input swirl velocities, the electrical conductivity also increases, which further leads to an increase in current density.

The results above show that the effect of a change in input swirl velocity has an almost negligible effect on flow parameters like temperature and current density.

Figure 10 concludes the effect of input swirl velocity on specific impulse and thrust for two different geometric configurations. The variation in geometry has been done in terms of constrictor radius (CR), which is the most sensitive geometric parameter shown by [12]. The magnitude of swirl velocity at inlet has been varied as 0 m/s,

Fig. 6 Pressure distribution along radial direction at constrictor inlet for different input swirl velocity
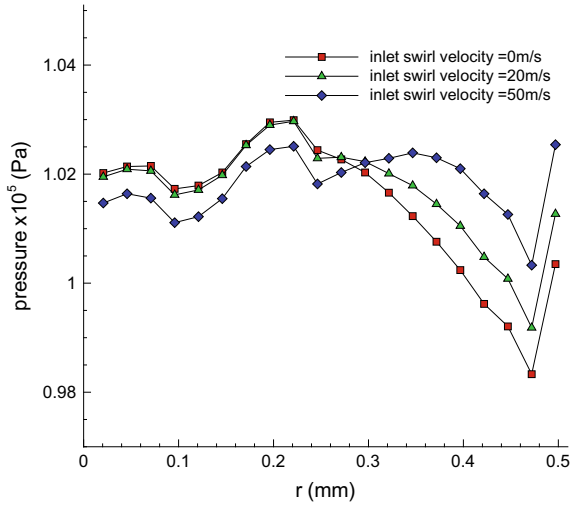
(a) Constrictor radius = 0.5mm
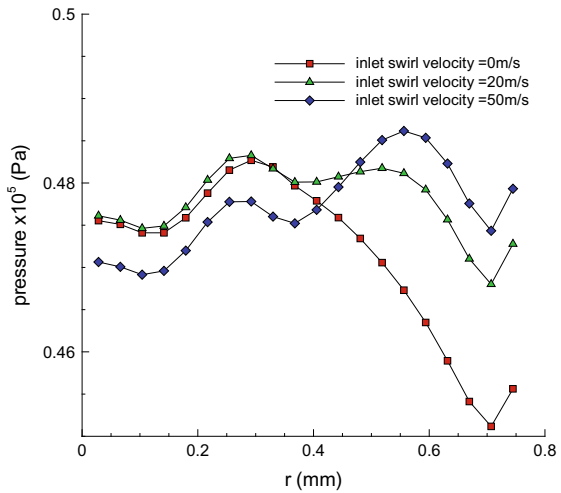
(b) Constrictor radius = 0.75mm

20 m/s, 50 m/s and 100 m/s, respectively. The change in swirl velocity has almost no significant effect on thrust and specific impulse.

4.2   Effect of Anode Wall Temperature

Here the study on the effect of nozzle wall temperature on the arc is done. The temperature at the anode surface is linearly increased from 500 K at nozzle inlet to

Fig. 7 Pressure distribution
along radial direction at
constrictor exit for different
input swirl velocity
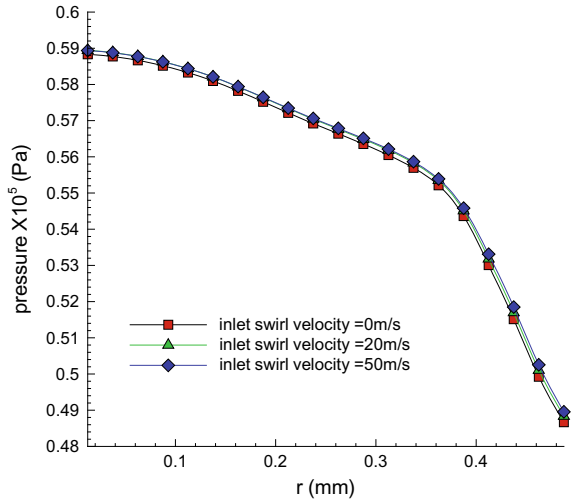
(a) Constrictor radius = 0.5mm
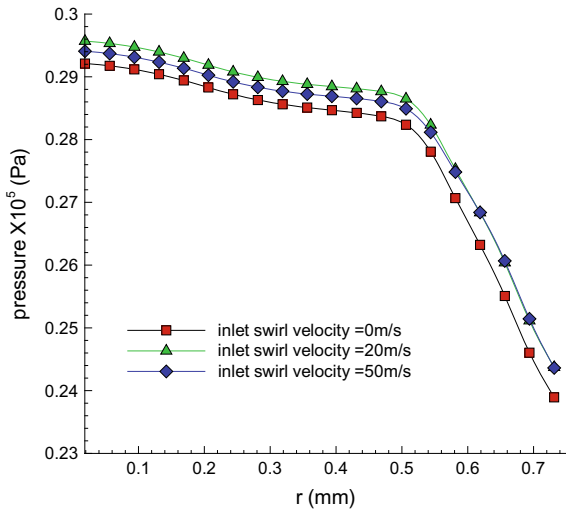
(b) Constrictor radius = 0.75mm

a particular temperature Tmax at the exit of the constrictor and linearly decreased to
700 K at the exit of the nozzle. In this study, the Tmax (the maximum temperature
at the anode wall) is varied as 1000, 1500, 2000, 2500, and 3000 K.

Figure 11 shows the profile of current density on the anode wall for a different
maximum temperature at the anode wall. It can clearly be seen in Figs. 11 and 12
that as the temperature on the anode wall increases the arc span (distance between
cathode tip to maximum current density point on anode wall) decreases with increase
in maximum current density. As the maximum temperature on the anode wall is
increased, the electrical conductivity increases, which decreases the width and arc

Fig. 8 Temperature
distribution along radial
direction at constrictor inlet
for different input swirl
velocity
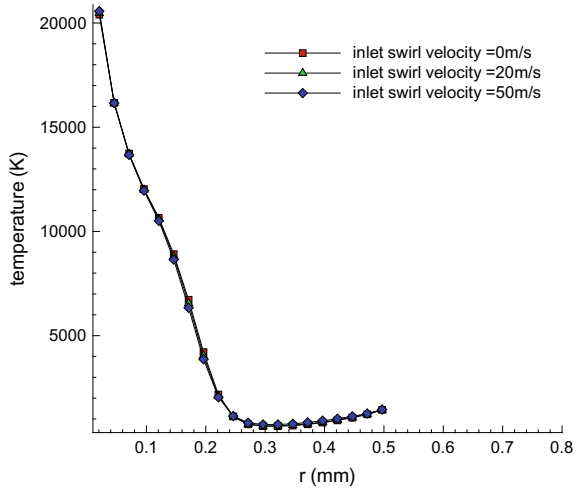
(a) Constrictor radius = 0.5mm
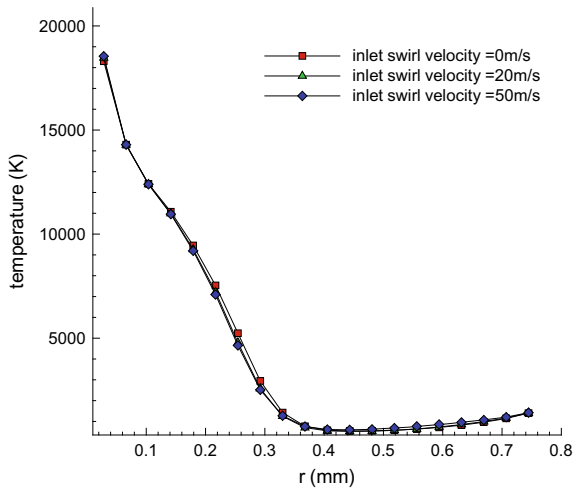
(b) Constrictor radius = 0.75mm

span of the arc. As the current is constant for all the cases, the maximum current
density will increase.

Figure 13 concludes the effect of anode wall temperature on the specific impulse
and trust. It shows the specific impulse and thrust increases with increasing the
anode maximum temperature. The increase in specific impulse and thrust is due to
an increase in Joule heating, due to the increase in current density. Even though the
arc span is decreasing with an increase in wall temperature, the voltage is increased
as power consumption is increasing with a constant current.

Fig. 9 Current density
distribution along radial
direction at constrictor inlet
for different input swirl
velocity
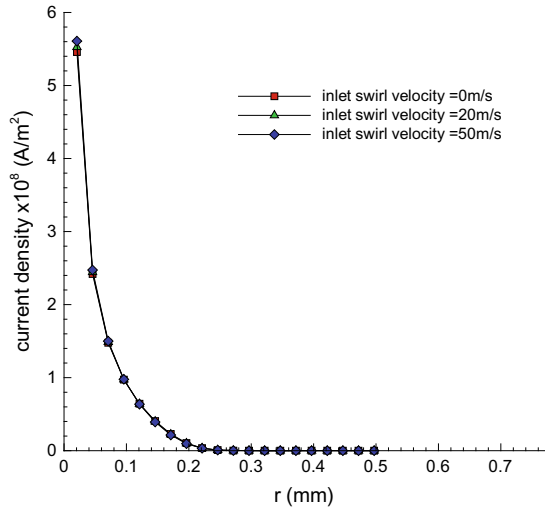
(a)   Constrictor radius = 0.5mm
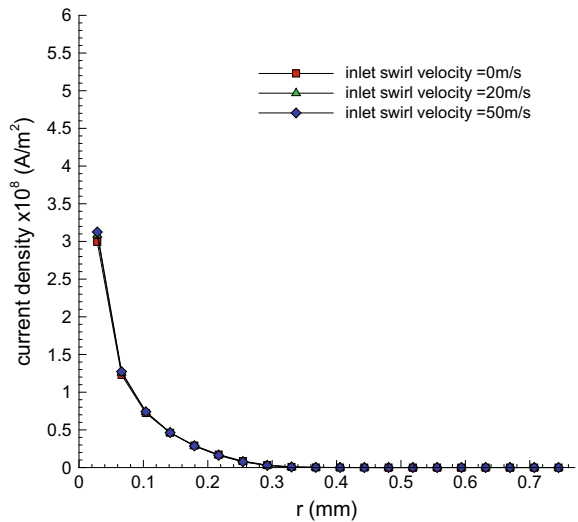
(b)   Constrictor radius = 0.75mm

5   Conclusions

The swirl generated in the constrictor of nozzle I with input swirl velocity less than
50 m/s and nozzle II with swirl velocity less than 20 m/s will not create a low-pressure
zone at the center of the constrictor. So, the sustainability of the arc by swirl within
the considered geometry cannot be promised.

Fig. 10 Specific impulse and thrust for different input swirl velocities and different geometry with constrictor radius (CR) 0.5 and 0.75 mm
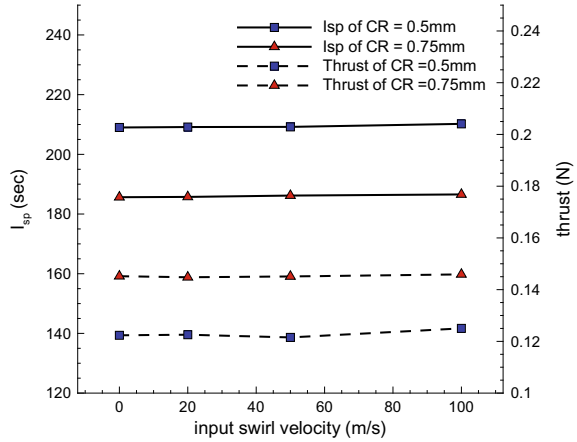
Fig. 11 Profile of current density along the anode wall for different maximum temperature on the anode wall
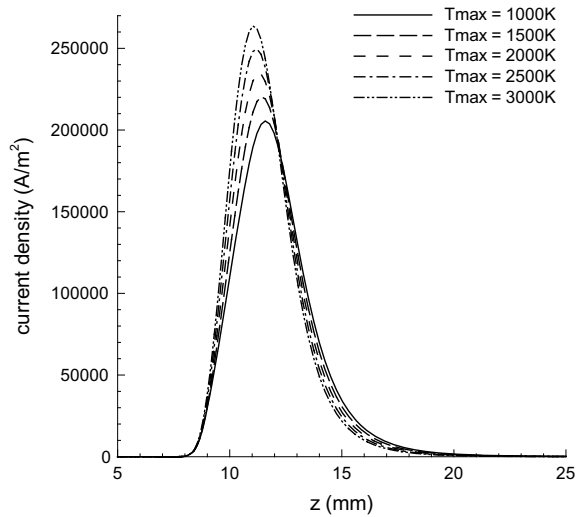
There is a negligible effect of swirl on the performance parameter of arcjet. Hardly any change in thrust or specific impulse is observed.

The higher anode wall temperature will enhance both the specific impulse and thrust for a given geometry. The only limitation is on the material.
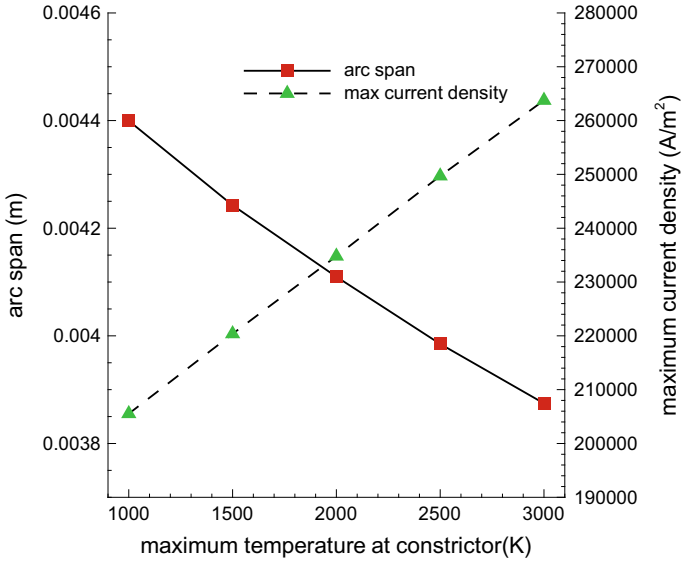
Fig. 12 Arc span and maximum current density on anode wall for different temperature profile on anode wall
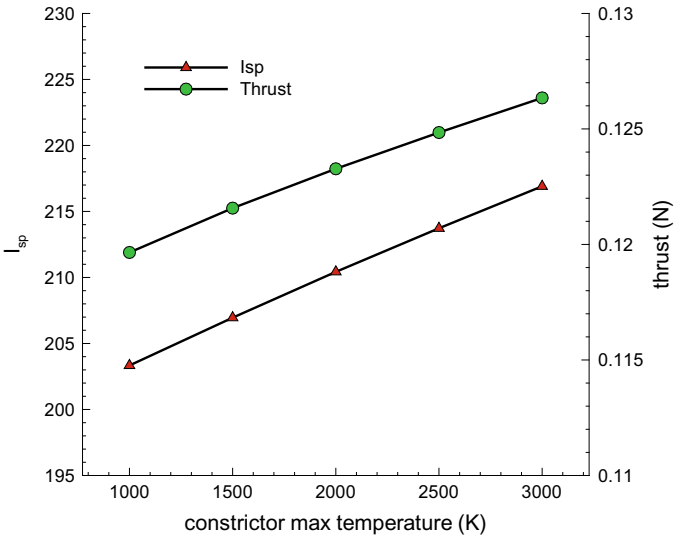
Fig. 13 Specific impulse and thrust for different temperature profile on anode wall

References

1. Jahn RG (2006) Physics of Electric Propulsion
2. Babu V, Aithal SM, Subramaniam VV (1993) On the effects of swirl in arcjet thruster flows. In: International electric propulsion conference
3. Dutton JC (1987) Swirling supersonic nozzle flow. J Propul Power 3:342–349. https://doi.org/10.2514/3.22996
4. Nguyen-kuok S Theory of Low-temperature plasma physics. n.d
5. Niewood EH (1989) Master of science
6. Oikamoto L, Nishida M, Tanaka K-I (1991) Numerical studies of the flow field in a low power DC Arcjet thruster using Navier-Stokes equations. In: International electric propulsion conference, p 112
7. Blazek J (2001) Computational fluid dynamics: principles of grid generation https://doi.org/10.1016/B978-008044506-9/50013-8
8. Liou MS (2006) A sequel to AUSM, Part II: AUSM + -up for all speeds. J Comput Phys 214:137–170. https://doi.org/10.1016/j.jcp.2005.09.020
9. Bufton SA, Burton RL (1997) Velocity and temperature measurements in a low-power hydrazine arcjet. J Propul Power 13:768–774. https://doi.org/10.2514/2.5231
10. Hari Prasad N, Amit K, Jayachandran T, Peeraiah P (2017) Numerical modeling of arcjet thruster : effect of design & operating parameters on arc heating. In: International electric propulsion conference, Georgia, p 532
11. Wang HX, Chen X, Pan W (2009) Two-dimensional LTE modeling of a low-power argon arcjet thruster, 1–10
12. Nandyala Hari Prasad, Akhare D, Kumar A, Jayachandran T (2018) Numerical modeling and parametric study of low power argon arcjet thrusters. In: Proceedings of the 2nd national aero propulsion conference NAPC-2018 Dec 17–19, 2018, IIT Kharagpur, West Bengal, pp 1–8

Analytically Modeling a Dual-Mode Scramjet with Fuel Flow Rate as the Controlling Parameter

Sushmitha Janakiram and T. M. Muruganandam

Abstract Hypersonic airbreathing propulsion has applications in defence and space accessibility. The objective of this study is to analytically model a Dual-Mode Scramjet with fuel flow rate as the controlling parameter at a design Mach number of 6 with Kerosene as fuel. The components of the scramjet were modeled individually and integrated through a one-dimensional analysis. The location of the fuel injectors determines the axial distribution of stagnation temperature in the combustor. This is necessary to evaluate the location of thermal choking. The combustor-isolator model can accommodate supersonic and subsonic combustion with the intermediate mode involving a Normal shock in the combustor. An algorithm was developed to determine the axial location of this Normal shock. On mapping the fuel flow rate to the thrust and integrating it with the Drag model, the flight profile of the vehicle can be simulated. Finally, the feasibility of controlling the trajectory (Mach number and Altitude) of a DMR-powered vehicle with the fuel flow rate as the input parameter is assessed analytically.

Keywords Scramjet · Hypersonics · Dual-Mode ramjet

1 Introduction

Airbreathing propulsion is remarkable which , unlike rocket engines that are required to carry the oxidants, employs the enveloping atmosphere in order to propel aerospace vehicles at sustained speeds. The primary objective of all airbreathing engines is to convert the energy derived from fuel into useful work done on a vehicle. Hypersonic Airbreathing Propulsion (HAP) is particularly noteworthy for the simplicity associated with its engine configuration, lacking any rotating machinery, and purely

S. Janakiram (✉) · T. M. Muruganandam
Indian Institute of Technology Madras, Chennai, India
e-mail: sush.jalways@gmail.com

T. M. Muruganandam
e-mail: murgi@ae.iitm.ac.in

Fig. 1 Geometric configuration of the concept engine

employing the principles of gas dynamics for its functioning. A typical scramjet consists of the following major components: Inlet, Isolator, Combustor, and Nozzle (Fig. 1). Since the efficiencies of ramjets and scramjets are limited to a given range of operation, there have been attempts to extend the range of Mach number of operation of the order of 3–10 which would require a combination of ramjet, scramjet, and rocket facilities. Of the various possible combinations, the Dual-Mode Combustion Ramjet (DCR) is considered favorable for the Mach number range of 4–8. Dual-mode scramjets are especially promising because they integrate the advantageous capabilities of both ramjets and scramjets into a single configuration [1].

In order to avoid carrying two different engines to meet the flight requirements over the broad range of operating conditions, the "no throat" scramjet engine geometry is operated at both ramjet and scramjet modes. A typical ramjet comprises two physical throats: one at the inlet and the other at the nozzle. The absence of a physical throat in the scramjet engine configuration is compensated by a thermal throat when operated at ramjet mode. The location of this thermal throat is a function of the combustor area variation and stagnation temperature distribution due to combustion in the combustor. The inlet configuration design and on-design operating conditions go hand in hand. For a ramjet or a scramjet, the design Mach number is fixed depending on the shock reflection configuration deemed necessary for the most optimal performance. For the Dual-mode scramjet under consideration, the design freestream Mach number was fixed at 6 and the inlet was designed so as to satisfy the shock on lip condition. That is, the oblique shock formed at the compression ramp is focused on the cowl lip. Typically, the design of all of the engine components is optimized to produce maximum thrust at the design-condition. The two prominent off-design conditions exist when operated at a freestream Mach number above and below the design Mach number. When the engine is operated at a Mach number above the design Mach number, the oblique shock formed at the compression ramp intersects the cowl downstream to the lip, resulting in a series of oblique shock reflections (Fig. 3). When the engine is operated at a Mach number below the design Mach number, the oblique shock formed at the compression ramp is upstream to the cowl lip. However, since the oblique shock formed is a weak shock, the flow is supersonic downstream to the shock. Hence, in order to turn the flow, another oblique shock is formed at the cowl lip which eventually intersects the compression ramp, once again resulting in a series of oblique shock reflections (Fig. 4).

As the vehicle accelerates from subsonic to supersonic speeds, the flow through the compression system evolves. At low subsonic speeds, the flow is subsonic throughout the inlet. The inlet eventually transits to subcritical state followed by the supercritical state [2]. The inlet is said to unstart when it transits to the undesirable subcritical state from the preferred supercritical state. Unstart is an extremely unsteady and a violent phenomenon and sufficient measures have to be taken to avoid it.

The present study is aimed toward mapping the fuel flow rate to the thrust generated by the Dual-Mode scramjet engine for the given freestream conditions which on integrating with the Drag model would facilitate analytical assessment of the feasibility of controlling the vehicle's trajectory (Mach Number and altitude).

2 Design of Scramjet Components

The individual components of the scramjet engine were designed and the flow was modeled in each of these components to accommodate different modes of operation. These components were eventually integrated in order to evaluate the overall performance of the engine for different freestream conditions and fuel flow rates. The current study focuses on modeling the flow through a scramjet with rectangular cross-section as shown in Fig. 1 whose dimensions are tabulated in Table 1.

2.1 Inlet

The inlet was designed so as to satisfy the shock on lip condition at the design Mach number ($M_\infty = 6$) (Fig. 2). The freestream conditions were evaluated assuming an

Table 1 Dimensions of geometric parameters of the concept engine

Geometric parameter	Symbol	Value
Compression ramp length	L_r	168.00 cm
Compression ramp angle	α	11°
Cowl length	L_c	46.62 cm
Isolator length	L_{iso}	92.83 cm
Combustor length	L	200.00 cm
Nozzle length	L_{noz}	150.00 cm
Height of the inlet throat	H_{th}	7.00 cm
Height of combustor exit	H_4	19.00 cm
Height of Nozzle exit	H_e	47.50 cm
Width of combustor and isolator	w	10.00 cm

Fig. 2 Inlet operation at design Mach number (shock on lip condition)

Fig. 3 Shock reflection configuration in the inlet when the Freestream Mach no. is above the design Mach no

Fig. 4 Shock reflection configuration in the inlet when the Freestream Mach number is below the design Mach number

altitude of operation of 20 km by employing the standard atmospheric model. Basic principles of gas dynamics and shockwave relations were employed in the algorithm to evaluate the flow conditions at the inlet throat to be fed to the isolator model for further analysis.

2.2 Isolator

Isolator is known to contain normal shock trains when operated at ramjet mode and oblique shock trains when operated at scramjet mode. Accurately modeling the flow behavior inside the isolator would be an extremely tedious task. Hence, the isolator was treated as a black body and a control volume analysis was carried out. The primary objective here is to estimate the burner entry Mach number, M_i for an imposed back pressure, p_3, given that, we know, the isolator entry Mach number, M_{th} and the pressure at the isolator entrance, p_{th}. By applying the principle

of conservation of mass, momentum and energy across this control volume, we have [2]

$$M_i = \left\{ \frac{\gamma_b^2 M_{th}^2 \left(1 + \frac{\gamma_b - 1}{2} M_{th}^2\right)}{1 + \gamma_b M_{th}^2 - \frac{p_3}{p_{th}}} - \left(\frac{\gamma_b - 1}{2}\right) \right\}$$ (1)

Knowing M_{th} and p_i/p_{th}, M_i can be evaluated from Eq. 1. Rearranging Eq. 1, gives

$$\frac{p_i}{p_{th}} = 1 + \gamma_b M_{th}^2 - \gamma_b M_{th} M_i \sqrt{\frac{1 + \frac{\gamma_b - 1}{2} M_{th}^2}{1 + \frac{\gamma_b - 1}{2} M_i^2}}$$ (2)

Hence, Eq. 2 can be used to evaluate the back pressure. A pressure matching algorithm was developed in order to integrate the isolator and combustor models and determine the isolator exit Mach number when the engine is being operated in scramjet mode.

We know that the information of Mach number distribution is necessary in order to determine the pressure levels in the combustor. These pressure levels in turn impose the back pressure experienced by the isolator. This back pressure information is required to determine Mach number at the isolator exit. The Mach number at the isolator exit in turn determines the Mach number distribution in the combustor. Hence, we are caught in a loop. In order to break this loop, the pressure values at the isolator exit and combustor entry can be determined by iterating different values of isolator exit Mach numbers and the Mach number at which these pressure values match would be the isolator exit Mach number (M_i). However, this iteration technique wouldn't work, because, the isolator model involving Eq. 2 is redundant, since, no other information with respect to compression efficiency or entropy losses due to the presence of shock trains is taken into account. Hence, when solved for M_i using the iteration described above, the result would be isolator exit Mach number being equal to isolator entry Mach number. Therefore, in order to account for losses, a compression efficiency of $\eta_c = 0.85$ was assumed. The isolator was assumed to undergo an adiabatic compression process. The following iteration was carried out in order to determine the isolator exit Mach number:

1. Assume a value for Mi.
2. Determine the corresponding static temperature ratio, across the isolator.

$$\phi = T_i/T_{th}$$ (3a)

3. Estimate the static pressure ratio across the isolator assuming an adiabatic compression process, for a given η_c.

$$\frac{p_i}{p_{th}} = \left(\frac{\phi}{\phi(1 - \eta_c) + \eta_c}\right)^{\left(\frac{\gamma}{\gamma - 1}\right)} \tag{3b}$$

4. Knowing pth, pi can be determined.

$$p_i = p_{th} \cdot \frac{p_i}{p_{th}} \tag{3c}$$

We can see that, the set of equations, 1 and 3 form a system of two equations in two unknown variables, p_i and M_i and hence, can be solved for. However, since the set of equations are non-linear, multiple solutions are possible. Also, the isolator entry Mach number, M_{th} would be one of the solutions. Hence, the supersonic solution below M_{th} is the required solution. When, M_{th} is the only solution, it implies that the engine is being operated at ramjet mode. The strategy to determine isolator exit conditions at ramjet mode is described in the following section.

2.3 Combustor

The combustion in the combustor is modeled with kerosene as fuel. The chemical combustion of Kerosene is modeled along the lines of Dodecane whose chemical reaction for combustion is given by

$$C_{12}H_{26}(l) + 18.5(O_2(g) + \frac{79}{21}N_2(g)) \Rightarrow 12CO_2(g) + 13H_2O(g) + 18.5 \times \frac{79}{21}N_2(g) \tag{4}$$
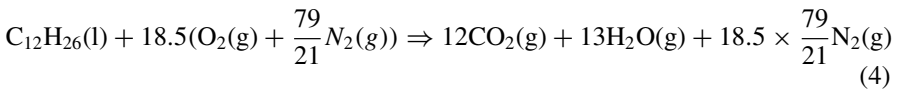
Assuming complete combustion in the combustor, the stagnation temperature ratio across the combustor is given by

$$\delta \dot{Q} = (LHV) \times \dot{m}_f \tag{5a}$$

$$\delta \dot{q} = \frac{\delta \dot{Q}}{\dot{m}_{th}} \tag{5b}$$

$$T_{04} = \frac{\delta \dot{q}}{C_p} + T_{03} \tag{5c}$$

$$\tau_b = \frac{T_{04}}{T_{03}} \tag{5d}$$

A lognormal heat-release distribution was assumed in the combustor, which is given by, [3]

$$Q_{nd} = A\sigma^{-1}(\frac{x}{L_f})^{-1}(2\pi)^{-1/2}exp\{-[ln(x/L_f) - \mu]^2/(2\sigma^2)\} \qquad (6)$$

Here, $Q_{nd} = q_F L_f / LHV$ where q_F is the heat added per unit length, per unit mass of the fuel alone. Also, the parameters corresponding to the lognormal distribution are given by $A = \tau b$, $\mu = -1.9$ and $\sigma = 0.8$. Here, A, μ, and σ are the parameters associated with the lognormal distribution. Hence, assuming the flow through the combustor to be frictionless flow without any mass addition, with however, change in both cross-sectional area and stagnation temperature, the ordinary differential equation governing the axial variation of Mach number is given by [2]

$$\frac{dM}{dx} = M\Big(\frac{1 + \frac{\gamma-1}{2}M^2}{1 - M^2}\Big)\Big\{ -\Big(\frac{1}{A}\frac{dA}{dx}\Big) + \frac{(1 + \gamma M^2)}{2}\Big(\frac{1}{T_0}\frac{dT_0}{dx}\Big)\Big\} \qquad (7)$$

When a dual-mode combustion system is operating in ramjet mode, the absence of a physical throat between the combustor and the nozzle necessitates the need for a choked thermal throat which can be established by a particular combination of axial distribution of the Area and stagnation temperature. The axial location of thermal choking ($M = 1$) is determined using the following equation, [2]

$$\Big(\frac{1}{A}\frac{dA}{dx}\Big)_* - \frac{(1 + \gamma)}{2}\Big(\frac{1}{T_0}\frac{dT_0}{dx}\Big)_* = 0 \qquad (8)$$

Also, since, Eq. 7 becomes indeterminate at the critical point, l'Hospital's rule is employed to address the singularity while estimating the axial distribution of Mach number in the combustor which in turn is used to determine the other flow properties (Eq. 9) [2].

Taking into consideration, thermal choking and mode of operation of the engine, the following four cases arise when the engine is operated at different freestream Mach numbers and fuel flow rates. The foregoing discussion is about how each case is addressed and Eq. 7 is integrated accordingly in order to estimate the axial distribution of Mach number in the combustor.

2.3.1 Case 1: Scramjet Mode with Thermal Choking

This mode is not a purely scramjet mode. This case arises when the engine is operated at an intermediate mode between that of a scramjet mode and a ramjet mode. This mode is characterized by the presence of a Normal shock in the combustor. Downstream to the normal shock, flow is subsonic followed by the choked thermal throat. An algorithm was developed to determine the axial location of this normal shock and subsequently evaluate the axial distribution of Mach number.

2.3.2   Case 2: Scramjet Mode Without Thermal Choking

The Mach number at the combustor inlet, M_i is determined from the pressure matching algorithm discussed in the isolator section. Equation 7 is marched downstream with M_i being the initial condition.

2.3.3   Case 3: Ramjet Mode with Thermal Choking

This is the default case which involves the evaluation of the location of thermal choking and marching upstream in order to determine the combustor inlet Mach number and the subsequent axial distribution of the Mach number.

2.3.4   Case 4: Ramjet Mode Without Thermal Choking

The pressure matching algorithm across the isolator works only for scramjet mode. Hence, the absence of thermal choking rules out the possibility of marching upstream to determine the burner entry conditions. Hence, normal shock relation is employed. Ramjet mode of operation involves the presence of a normal shock in the isolator. With the isolator entry Mach number, M_{th} known, and with area of the isolator being constant, it is assumed that the Mach number upstream to the Mach number remains uniform up to the inlet throat and the Mach number downstream to the normal shock remains uniform up to the combustor inlet. This subsonic Mach number downstream to the normal shock corresponding to isolator entry Mach number is marched downstream and the axial distribution of the Mach number is accordingly evaluated.

$$T(x) = T_{th}.\frac{T_0(x)}{T_{0th}}\left[\frac{1+\left(\frac{\gamma-1}{2}\right)M_{th}^2}{1+\left(\frac{\gamma-1}{2}\right)M(x)^2}\right] \tag{9a}$$

$$p(x) = p_{th}.\frac{A_{th}}{A_c(x)}.\frac{M_{th}}{M(x)}\sqrt{\frac{T(x)}{T_{th}}} \tag{9b}$$

$$p_0(x) = p_{0th}.\frac{p(x)}{p_{th}}\left[\frac{T_{th}}{T(x)}\frac{T_0(x)}{T_{0th}}\right]\left(\frac{\gamma}{\gamma-1}\right) \tag{9c}$$

$$u(x) = u_{th}.\frac{M(x)}{M_{th}}\sqrt{\frac{T(x)}{T_{th}}} \tag{9d}$$

2.4 Nozzle

The nozzle exit conditions were evaluated on determining the mode of operation of the nozzle based on the nozzle entry and ambient conditions. The effects of friction and boundary layer interactions were neglected in the analysis.

3 Analysis and Results

We now have a working model, which can be used to evaluate various performance parameters and flow properties associated with the engine for a wide range of freestream conditions and fuel flow rates.

3.1 Location of Normal Shock in the Combustor

As discussed earlier, this situation of a normal shock being situated in the combustor arises when the engine is operated in an intermediate mode with flow at the combustor inlet being supersonic and the flow upstream to the thermal choking location being subsonic. In order to determine the Normal shock location, thermal choking constraint was evoked. In the one-dimensional analysis that has been carried out, we know that the axial gradient of the Mach number in the combustor (Eq. 7) has a singularity at sonic velocity. Hence, on considering the gradient corresponding to the subsonic solution at the sonic point, a subsonic initial condition is generated just upstream to the location of thermal choking. Equation 7 is marched upstream from this initial condition. This generates the "upstream" curve shown in Fig. 5. The supersonic combustor inlet Mach number (M_i) evaluated from the pressure matching
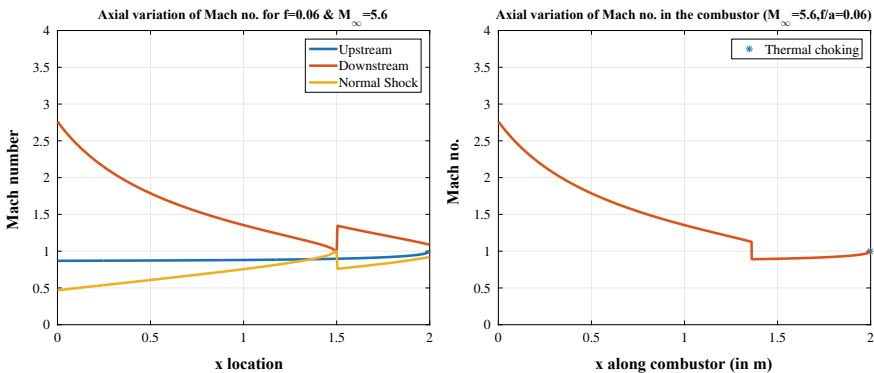

Fig. 5 Evaluation of Normal shock location for $M_\infty = 5.6$ and $f/a = 0.06$
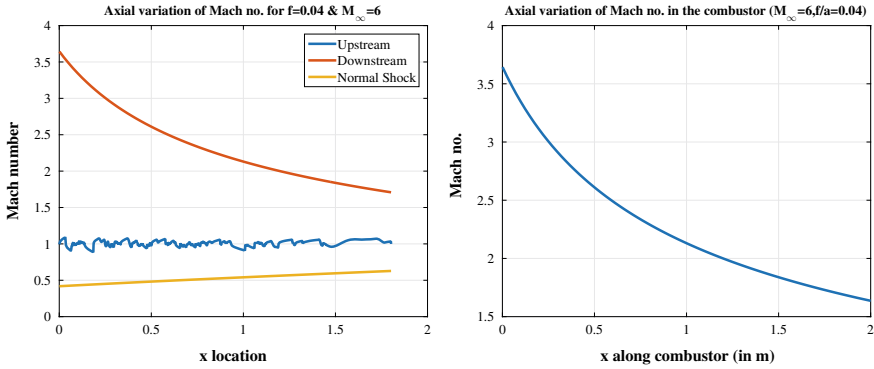
Fig. 6 Evaluation of Normal shock location for $M_\infty = 6$ and $f/a = 0.04$

algorithm is used as an initial condition and once again, Eq. 7 is integrated downstream along the length of the combustor up to the location of thermal choking. This generates the "downstream" curve shown in Fig. 5. The supersonic Mach numbers in the "downstream" segment of the curve are filtered out. A hypothetical Normal shock is assumed to exist at each of these supersonic Mach numbers and the corresponding subsonic Mach numbers are plotted as the "Normal shock" curve in Fig. 5. If at all a normal shock exists, it does so at the first point upstream where "Normal shock" curve and the "upstream" curve intersect. Hence, the Axial distribution of Mach number in such a situation is obtained by integrating the "Downstream" curve, upstream to the normal shock and the "upstream" curve, downstream to the normal shock. Once the Mach number distribution is evaluated, all the other parameters can be subsequently estimated as explained earlier.

Also, if the curves, "Normal shock" and "upstream" do not intersect, as shown in Fig. 6, it corresponds to "Case 2: Scramjet mode without thermal choking" described in the previous section. That is, the flow in the combustor is completely supersonic with the engine being operated at a "scramjet mode."

Using the algorithm that has been developed, this case was predicted for a very narrow range of freestream Mach numbers, 5.6–6.2 for the range of fuel-to-air ratios, 0.055–0.070.

3.2 Thrust, Specific Impulse and the Drag Model

Once the flow properties at the nozzle exit, the Mach number, static pressure, density and temperature, in particular, are evaluated, the thrust generated by the engine can be estimated. The thrust equation is given by

$$T = \dot{m}_e v_e - \dot{m}_0 v_0 + (p_e - p_0)A_e \tag{10}$$

Table 2 Thrust, T generated by the engine for a wide range of freestream Mach numbers and fuel-to-air ratios

Freestream Mach No.	Thrust, T (in N) evaluated at various Fuel-to-air ratios, f/a								Drag (in N)
	0.04	0.045	0.05	0.055	0.06	0.065	0.07	0.075	
3	8332.36	4443	2003.39	2230.5	5211.36	5475.83	5587.86	5587.86	989.02
4	7151.62	2520.2	11922.28	8044.65	8390.38	9340.9	8847.58	8847.58	1516.44
5	3197.89	3717.89	4192.02	15677.03	14561.71	5627.34	21554.6	21554.6	2138.6
6	2443.28	2784.87	3131.02	3481.79	3839.38	4205.55	13805.47	13805.47	2855.05
7	5603.36	6462.52	7330.35	8207.44	9094.09	9992.2	10353.11	10353.11	3665.59
8	3530	4045.26	4564.58	5088.09	5615.43	6145.86	6358.79	6358.79	4570.18
9	4227.03	4859.78	5498.77	6140.48	6783.81	7434.45	7695.36	7695.36	5568.9

The specific impulse is given by

$$I_{sp} = \frac{T}{\dot{m}_f g} \tag{11}$$

The total Drag experienced by the vehicle, which is a combination of the pressure drag, wave drag, and skin friction drag was estimated using empirical relations [4].

Tables 2 and 3 show the mapping of Specific Impulse and Thrust, respectively, to the fuel flow rate for a wide range of freestream Mach numbers. Table 4 also shows a comparison between drag evaluated from the Drag model and thrust at different freestream Mach numbers. Table 4 shows the distribution of combustor exit Mach number evaluated at different fuel-to-air (f/a) ratios for a given range of freestream Mach numbers. Similarly, Table 5 shows the distribution of combustor exit Mach number evaluated at different fuel-to-air (f/a) ratios over the same range of freestream Mach numbers. Table 6 shows the distribution of inlet throat Mach numbers and Isolator exit Mach numbers as a function of the freestream Mach number.

Table 3 Specific impulse, I_{sp} generated by the engine for a wide range of freestream Mach numbers and fuel-to-air ratios

Freestream Mach No.	Specific Impulse, I_{sp} (in s) evaluated at various Fuel-to-air ratios, f/a							
	0.04	0.045	0.05	0.055	0.06	0.065	0.07	0.075
3	9875.05	4680.53	1899.45	1922.52	4117.47	3993.63	3953.69	3953.69
4	5123.23	1604.8	6832.64	4191.25	4007.09	4117.89	3783.98	3783.98
5	1262.93	1305.15	1324.44	4502.75	3833.88	1367.63	5082.09	5082.09
6	1045.75	1059.52	1072.09	1083.82	1095.54	1107.71	3527.71	3527.71
7	876.36	898.43	917.17	933.56	948.21	961.71	966.7	966.7
8	816.51	831.72	844.65	855.93	865.92	874.81	878.1	878.1
9	745.7	762.06	776.04	787.82	797.83	807.09	810.48	810.48

Table 4 Mach number at the combustor exit, M_4 evaluated for a wide range of freestream Mach numbers and fuel-to-air ratios

Freestream Mach No.	M_4 evaluated at various Fuel-to-air ratios, f/a							
	0.04	0.045	0.05	0.055	0.06	0.065	0.07	0.075
3	0.3681	0.9279	1.0096	1.3702	0.9537	0.927	0.9117	0.9117
4	0.7652	1.0526	0.472	0.8709	0.8934	0.763	0.9401	0.9401
5	1.0598	1.1215	1.0212	0.7153	0.9498	1.085	0.5481	0.5481
6	1.6361	1.5186	1.4107	1.3078	1.2054	1.086	0.9332	0.9332
7	1.8144	1.7042	1.6047	1.5134	1.428	1.347	1.3146	1.3146
8	2.2815	2.1545	2.0421	1.9414	1.8501	1.766	1.7341	1.7341
9	2.5812	2.4464	2.328	2.2216	2.1249	2.0377	2.0048	2.0048

Table 5 Mach number at the nozzle exit, M_e evaluated for a wide range of freestream Mach numbers and fuel-to-air ratios

Freestream Mach No.	M_e evaluated at various Fuel-to-air ratios, f/a							
	0.04	0.045	0.05	0.055	0.06	0.065	0.07	0.075
3	0.1378	0.2409	2.3437	2.4382	0.2416	0.2408	0.2402	0.2402
4	0.2284	2.3459	0.1692	0.2381	0.2394	0.2281	0.2412	0.2412
5	2.3465	2.3551	2.344	0.2217	0.2415	2.3494	0.189	0.189
6	2.5906	2.5168	2.4579	2.411	2.3752	2.3495	0.241	0.241
7	2.718	2.6373	2.57	2.5137	2.4667	2.4277	2.4138	2.4138
8	3.1116	2.998	2.9011	2.8177	2.7453	2.6818	2.6586	2.6586
9	3.3932	3.2645	3.1541	3.0576	2.9722	2.8974	2.8698	2.8698

Table 6 Inlet throat and isolator exit Mach numbers evaluated for a range of Freestream Mach numbers

Freestream Mach no.	Inlet throat Mach no.	Isolator exit Mach no.
3	1.4094	0.7305
4	2.3782	1.9396
5	2.878	2.4923
6	4.0204	3.6433
7	3.6368	3.2647
8	4.7675	4.3702
9	5.0997	4.6907

Figure 9 shows the variation of the specific Impulse, I_{sp} as a function of the freestream Mach number, M_∞ for a wide range of fuel-to-air ratios. While there is a close resemblance in the I_{sp} trends when compared to the typically expected propulsion performance corresponding to the range of scramjet mode, there is some anomaly in the ramjet mode.
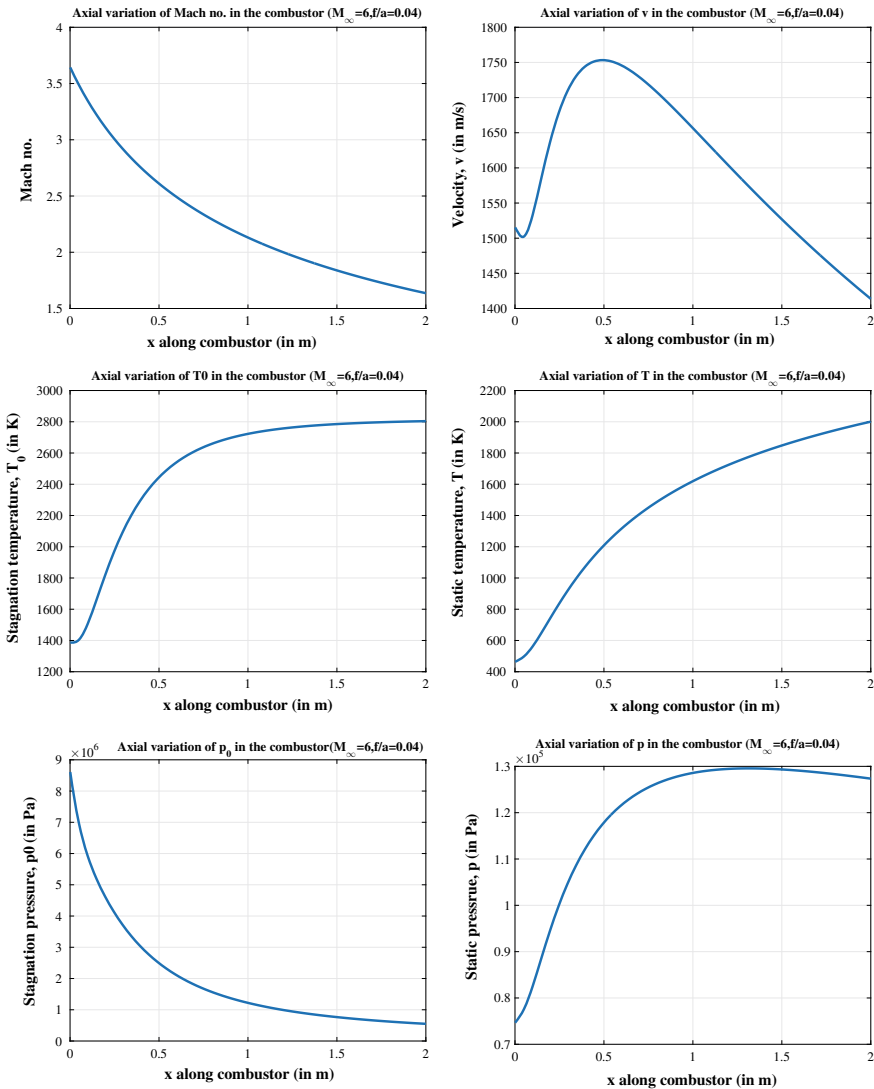

Fig. 7 Axial variation of flow properties for $M_\infty = 6$ and f/a $= 0.04$ (Fuel lean case)

3.3 Axial Distribution of Flow Properties in the Combustor

The axial distribution of the flow properties in the combustor, like, Mach number, static temperature, static pressure, and so on are plotted at design Mach number for the fuel rich (f/a = 0.07) and fuel lean (f/a = 0.04) cases in Figs. 7 and 8.
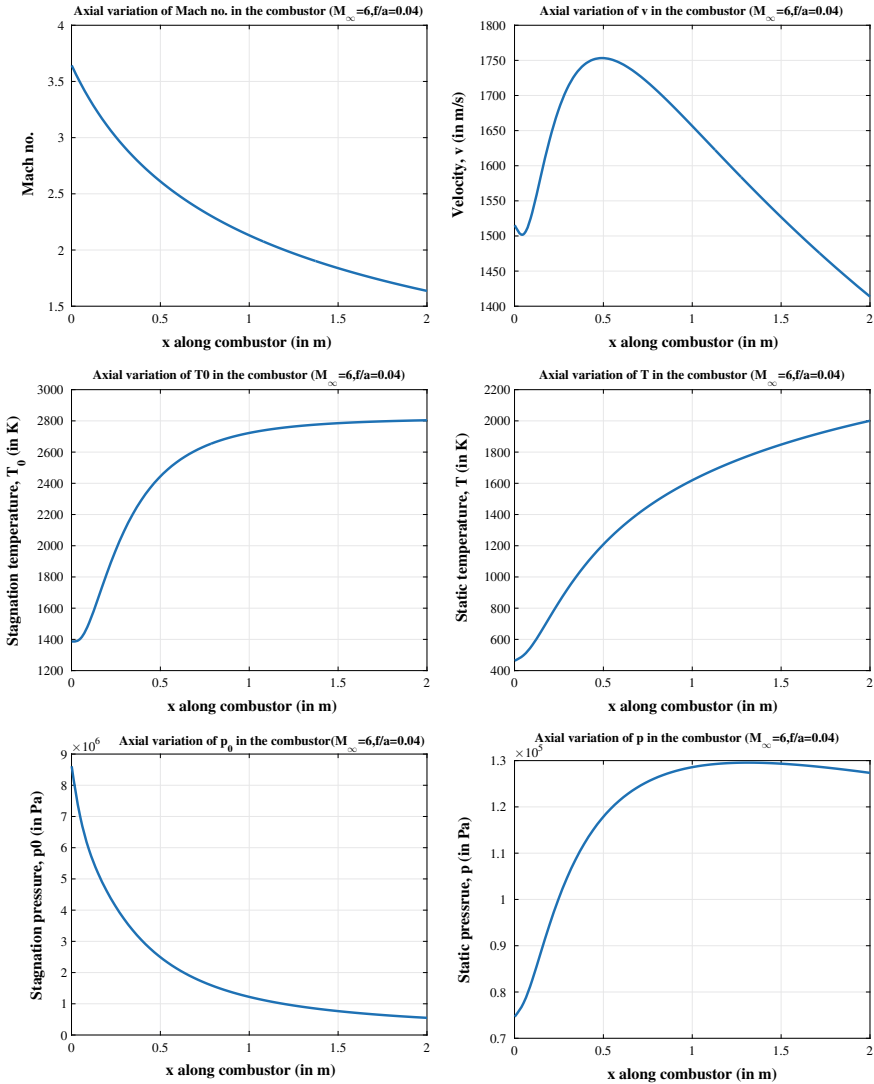
Fig. 8 Axial variation of flow properties for $M_\infty = 6$ and f/a = 0.07 (Fuel rich case)

4 Conclusions

From the foregoing analysis, it can be concluded that the current one-dimensional model predicts the performance of the engine to a reasonably agreeable degree. The strategies adopted in integrating the components, predicting the modes of operation and executing the algorithm would still be applicable even if sophisticated models were to be developed corresponding to each of the components. In Fig. 9 which shows the propulsion performance of the vehicle, the I_{sp} curve is bifurcated into two segments. While the bottom segment is in accordance with the trends expected of hydrocarbon based ramjets and scramjets [Fig. 1.1, [1]], the appearance of the upper segment calls for a detailed dynamical analysis. The presence of normal shocks in the combustor was predicted by the algorithm in the expected range of freestream Mach number (5.6–6.2) which can be interpreted as an intermediate mode between that of the scramjet mode and the ramjet mode. While the variation of flow properties in the combustor, in the scramjet mode (Mach numbers greater than or equal to 6) are reasonably smooth in accordance with the stagnation temperature distribution assumed for the combustor model; numerous cases of random oscillations were observed close to sonic speeds in ramjet mode of operation for most of the cases. This must be due to the singularity associated with the axial gradient of the Mach number at sonic speeds. While the drag levels estimated are considerably low in comparison with the thrust levels at ramjet mode, they fall well within the minimum and the maximum margins at the scramjet mode allowing for acceleration and deceleration.
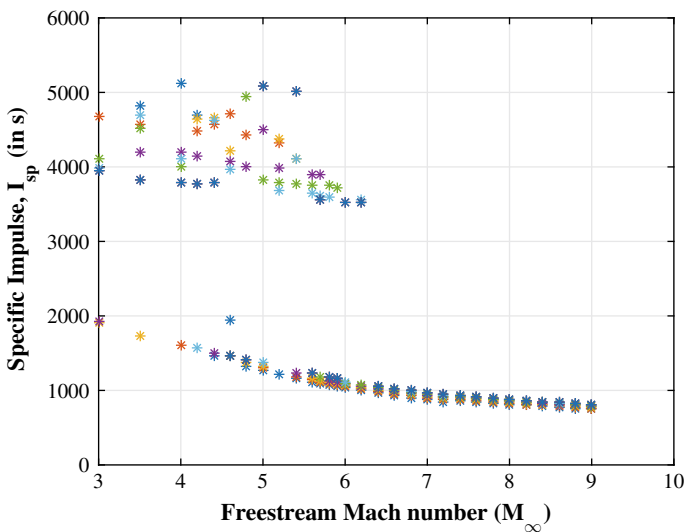

Fig. 9 Variation of I_{sp} with M_∞ for a wide range of fuel flow rates (f/a $= 0.04 - 0.07$)

While the current analysis has incorporated simple one-dimensional tools, a much more rigorous analysis can be carried out by accounting for boundary layer effects, shock–boundary layer interactions, flow separation, modeling the chemical kinetics of combustion and taking into consideration the commonly faced challenges in scramjet engines associated with combustion like ignition delay, low residence time, mixing efficiency, incomplete combustion, modeling the high-temperature gas dynamics, and so on. Eventually, we would be having the analytical tools that would enable confident control over the engine design and reliably predict the actual behavior of the vehicle.

References

1. Segal C (2009) The Scramjet engine: processes and characteristics
2. Heiser WH, Pratt DT (1994) Hypersonic airbreathing propulsion
3. Yoon Y, Donbar JM, Huh H, Driscoll JF (1996) measured supersonic flame properties: heat-release patterns, pressure losses, thermal choking limits. J Propuls Power
4. Hoerner SF (1965) Fluid-dynamic drag

Effect of Activated Charcoal on the Performance of Hybrid Rocket Motor

Nitesh Kumar, Mengu Dinesh, and Rajiv Kumar

Abstract In the present study, attempts were made to study the effect of activated charcoal (AC) on performance of hybrid rocket motor with polyvinyl chloride–dioctyl phthalate (PVC–DOP) as solid fuel. Activated charcoal at 1, 2 and 5% mass fractions was added to PVC–DOP. The regression rate and combustion efficiency of the PVC–DOP/AC fuel combinations were determined using laboratory-scale hybrid rocket motor with gaseous oxygen as oxidizer. The results showed that among the fuel combinations studied, PVC–DOP with 1% AC exhibited the highest improvement in regression rate as well as combustion efficiency. The excessive char formation was observed as the mass fraction of AC increases and this causes the reduction in performance of hybrid rocket. Additionally, the mechanical properties were studied and TGA analysis was also conducted for the PVC–DOP/AC fuel samples.

Keywords Hybrid rocket · Regression rate · Combustion efficiency · Activated charcoal · PVC–DOP solid fuel

1 Introduction

Hybrid rocket is the combination of solid and liquid rocket engine, where the fuel and the oxidizer are stored in two different phases. Due to this distinctive feature, hybrid rocket possesses some advantages over the solid and liquid rockets. Hybrid rockets are safer, cost-effective and easier to handle during transportation. They can throttle which is not possible in solid rockets. Apart from this, since the propellant constituent is in solid phase, the complexities in designing the pump feed system are

N. Kumar · M. Dinesh · R. Kumar (✉)
Department of Space Engineering and Rocketry, Birla Institute of Technology, Mesra, Ranchi, India
e-mail: rajiv@bitmesra.ac.in

N. Kumar
e-mail: aerospace547@gmail.com

M. Dinesh
e-mail: dinesh18793@gmail.com

lesser than liquid rockets. Despite of these advantages, yet, hybrid rocket is not being used in practical applications due to its lower regression rate and poor combustion efficiency relative to solid and liquid rocket engines. Furthermore, the shift in O/F ratio with time and sliver losses are creating more complications in designing the hybrid rocket [1, 2].

In general, the polymers such as hydroxyl-terminated polybutadiene (HTPB), polyethylene (PE), polymethylmethacrylate (PMMA) and polyvinyl chloride (PVC) are frequently used as solid fuels in conventional hybrid rockets [2]. Over the past several decades, various methods [3, 4] have been developed to improve the regression rate of solid fuels in hybrid rocket motor. Some of these methods are adding energetic metals (aluminium, boron, magnesium etc.), metal hydrates and oxidizer particulates (ammonium particles) as additives to solid fuel and using different oxidizer injection techniques and creating turbulence inside the combustion chamber. Karabeyoglu [5, 6] reported that the paraffin-wax-based fuels can regress 3–5 times faster than the conventional polymeric-based fuels. However, the inherent nature of poor mechanical properties restricts the utilization of wax-based fuels in practical applications. In solid propellants, using activated charcoal as burn rate modifier is an effective method to enhance the burn rate [7]. Also, activated charcoal has been used as an additive to solid fuels in hybrid rocket research [8]. The activated charcoal enhances heat to the fuel surface through radiative heat transfer mode [2].

It has been reported in the literature that the activated charcoal is used as the burn rate enhancer in solid propellants [7]. The results showed an increase in the regression rate by 100% and the pressure index of combustion is 0.65. Following these results, it is expected that the use of activated charcoal can enhance the performance of hybrid rocket motor. Also, there is no abundant data available regarding the effect of the mass fraction of activated charcoal on performance of hybrid rocket. Thus, in the present study an attempt has been made to study the effect of activated charcoal on performance of laboratory-scale hybrid rocket with PVC–DOP as a solid fuel. Apart from this, thermal decomposition and mechanical properties of PVC–DOP/AC fuel combinations were also studied.

2 Experimental Procedures

In the present study, the combination of PVC–DOP (50:50) was used as fuel. In PVC–DOP combination, PVC is a plastisol (amorphous phase) and DOP is a plasticizer (liquid phase). Activated charcoal at 1, 2 and 5% mass fractions was added as additive to the PVC–DOP fuel. The properties of PVC–DOP/AC are given in Table 1.

Table 1 Properties of fuel constituents

Ingredient	Chemical formula	Density (kg/m^3)
PVC	$C_{2000}H_{3000}Cl_{1000}$	1380
DOP	$C_{24}H_{38}O_4$	980
AC	C	2100

2.1 Preparation of Fuel Grain

In the present study, solid fuel is a combination of PVC and DOP in the ratio 50:50. Prior to blending the DOP with PVC powder, DOP should be dehumidified to remove the moisture. Then, the PVC is added to DOP and this combination is mixed using a sigma blade mixer (4 kg capacity) under ambient conditions for 3–4 h. After this, activated charcoal is added to the slurry and stirred till they blend without any lumps. Further, this slurry is used to prepare the fuel grains using mould and mandrel setup. Once the slurry is casted in the mould, it should be kept in vacuum chamber to remove the trapped air. Later, the mould is kept in the oven for curing process at 125 °C for 4 h. A well-structured grain is formed after curing. Prior to casting the fuel grains, grease was applied to avoid sticking to the mould and mandrel. The dimensions of the fuel grain are given in Table 2. Figure 1 presents X-ray photographs of the PVC fuels grains prepared in the present study. It can be observed from Fig. 2 that the fuel grain is void-free.

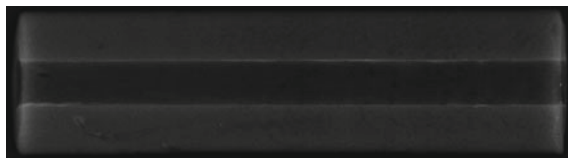| Table 2 Dimensions of the hybrid rocket motor		
Fuel grain length	188 mm
Motor length	240 mm
Port diameter	15 mm
Outer diameter	50 mm
Throat diameter	10 mm
Exit diameter	24 mm

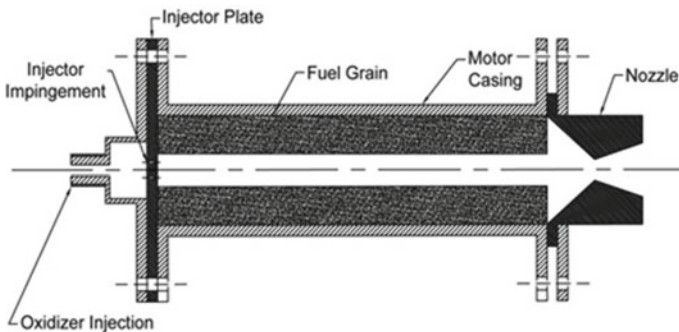**Fig. 1** X-ray photographs of PVC–DOP fuel grains

Fig. 2 Laboratory-scale hybrid rocket motor

2.2 Experimental Setup

The geometrical representation of the laboratory-scale hybrid rocket motor is shown in Fig. 2. It has shower head injector, motor case with fuel grain and C-D nozzle made of high-density graphite covered with mild steel casing. The dimensions of the motor and fuel grains are given in Table 2. The experiments on hybrid rocket motor were conducted using the experimental facility shown in Fig. 3. This experimental facility is similar to the one used in Ref. [12]. In Fig. 3, experimental setup consists of two commercially available gaseous oxygen cylinders, weighing balance, oxidizer feed system, electrical systems and test bed. The gaseous oxygen was supplied to the motor at the rate of 30 g/s. The oxidizer mass flow rate was measured by taking the weight of the oxygen cylinders before and after the combustion over the intended time. The oxidizer flow was controlled using the solenoid valve which is connected to sequential timer. This sequential timer controls the time required to open and close the solenoid valve. The ignition of the motor was achieved by igniting the solid propellant bead embedded with nichrome wire. This nichrome wire is connected to the electrical wire which is then inserted into chamber through the nozzle in such way that the propellant bead is at injector end. A 12 V DC power was supplied through the electrical wire to ignite the solid propellant bead. Once the propellant bead is ignited, the solenoid valve will open to inject the oxidizer. The entire sequence was controlled using the sequential timer.

In the current experimental study, regression rate (r) is deduced using the interrupted test in weight loss method. A detail explanation of this method can be found in Ref. [10]. In this method, the mass of the fuel (m_f) consumed during combustion
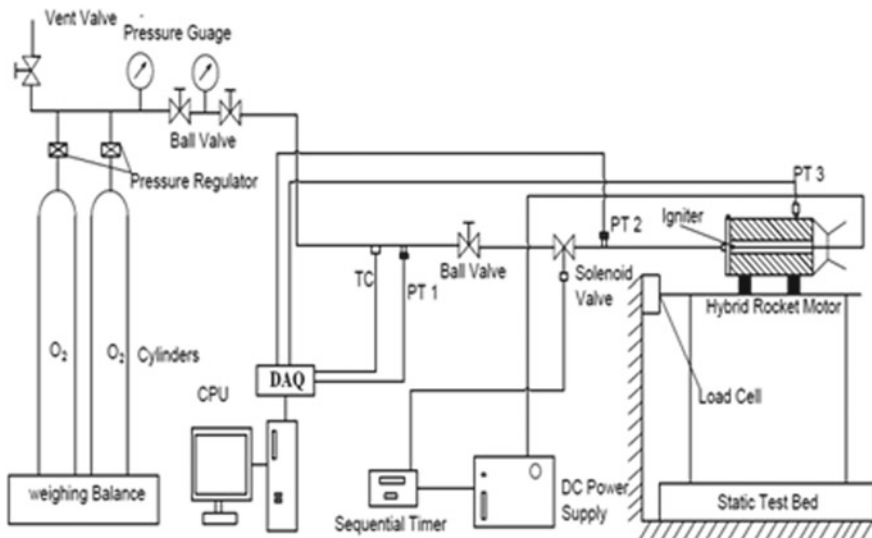

Fig. 3 Hybrid rocket experimental facility

is determined by measuring the weight of the motor before and after combustion. This mass lost in the motor will be measured at regular intervals of time (t_b) by interrupting the combustion. Using the known mass of the fuel consumed at each interval, the final diameter of the fuel grain will be measured using Eq. (1). Further, this final diameter will be helpful to calculate the regression rate and oxidizer mass flux (G_{ox}) using the Eqs. (2) and (3).

$$d_f = \sqrt{\frac{4m_f}{\pi \rho_f L} + d_i^2} \tag{1}$$

$$\dot{r} = \frac{(d_f - d_i)}{2t_b} \tag{2}$$

$$G_{ox} = \frac{\dot{m}_{ox}}{A_p} \tag{3}$$

The combustion efficiency is determined using Eq. (4). The experimental characteristic velocity $\left(C_{ex}^*\right)$ is calculated with the help of Eq. (5). In Eq. (5) the average chamber pressure is measured using piezoresistive pressure transducer at the sampling rate of 2 kHz. This pressure transducer is connected at the nozzle end of the motor, as shown in Fig. 3. The response of pressure transducer is recorded using NI-9215 module and Lab-View signal express software. The theoretical characteristic velocity $\left(C_{th}^*\right)$ is determined using NASA SP-2713 chemical equilibrium software [11] at corresponding chamber pressure and O/F ratio.

$$\eta = \frac{C_{ex}^*}{C_{th}^*} \tag{4}$$

$$C_{ex}^* = \frac{P_c A_t}{\dot{m}_t} \tag{5}$$

The thermal degradation studies of PVC–DOP/AC fuel formations are conducted using simultaneous thermal analyser (STA). The experiments are conducted under the nitrogen atmosphere at the heating rate of $10°K \min^{-1}$. In addition to this, the effect of activated charcoal on the mechanical properties of PVC–DOP fuel formations is also studied. The mechanical properties are determined using UTM-3655, INSTRON instrument at the strain rate of 5 mm/min under the ambient conditions.

3 Results and Discussions

3.1 Studies on Regression Rate

Regression rates for the PVC–DOP/AC fuel combinations were determined with the help of experimental facility shown in Fig. 3. The regression rate data reduction method is illustrated in experimental procedure section (using Eqs. 1–3). Gaseous oxygen is used as the oxidizer and its flow rate is maintained around 30 g/s for the entire experiments. In case of interrupted test method, the hybrid rocket requires a series of four interruptions during combustion with a burn time interval of 2 s. Figure 4 presents the regression rates for the fuel combinations studied in the present study. It can be seen from Fig. 4 that the regression rate is significantly enhanced compared to the PVC–DOP fuel alone. Among the PVC–DOP/AC fuel combinations, PVC–DOP/AC1% has given the better regression rates. However, there is no substantial difference observed in regression rate among the PVC–DOP/AC fuel formulations. The mass flux index for all the PVC–DOP/AC fuel formulations is less than 0.5.

In Fig. 4, the regression rate above the 90 kg/m^2 s is observed to be higher for the PVC–DOP/AC5% compared to other fuel combinations. As the oxidizer mass flux drops below the 90 kg/m^2 s, the regression rate for the PVC–DOP/AC5% decreased. The reason for this is explained as follows. After extinction of the combustion, the fuel grains were cut and the fuel surface was observed. The soot formation is observed over the fuel surface in case of all the PVC–DOP/AC fuel grains. For the PVC–DOP fuels with 2 and 5% AC mass fraction, the soot formation is much higher than with 1% AC. The cut sections of the fuel grains indicating soot layer are shown in Fig. 5 for the PVC–DOP/AC5% fuel. The soot formed might be due to the increase in the carbon content in the fuel with the addition of AC. In addition to this, the PVC itself

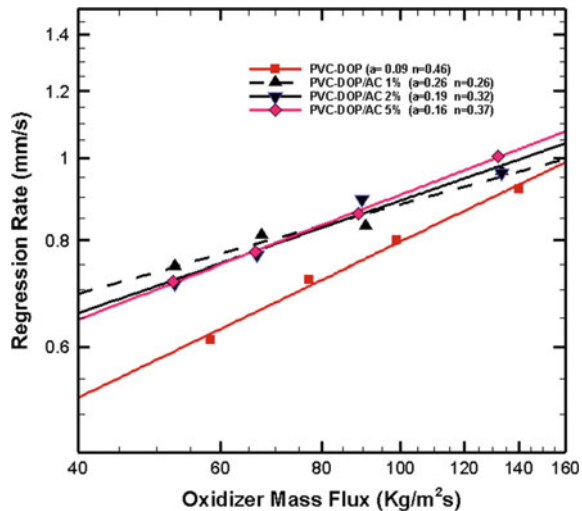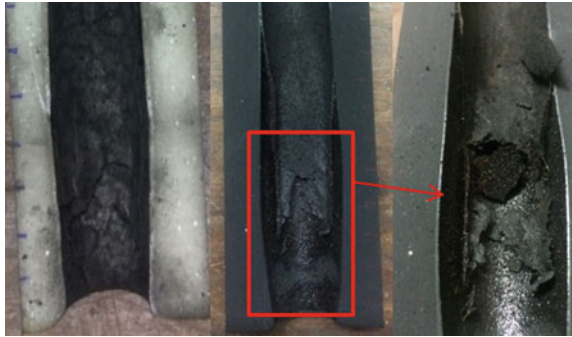**Fig. 4** Regression rate versus oxidizer mass flux of PVC–DOP/AC fuel formulations

is a carbon-rich material. Hence, the soot formation is intensifying as the carbon AC mass fraction increases and more number of carbon atoms in the PVC also aids to form the more soot during combustion along with AC. This soot layer on the fuel surface acts as ablative surface which inhibits the pyrolysis process over the fuel surface. Due to this, the regression rate is decreasing with increasing AC mass fraction as the time progress during combustion. Thus, if one wants to use the AC in PVC–DOP fuels, <1% AC mass fraction is preferable.

3.2 Studies on Combustion Efficiency

In the earlier section, a significant improvement in regression rate was observed with the addition of AC to PVC–DOP. Furthermore, it would be interesting to observe the combustion efficiencies of the PVC–DOP/AC fuel formulations. Therefore, in this section experiments were carried out to study the combustion efficiencies of all the fuel formulations. The oxidizer mass flow rate is maintained at 30 g/s. The burn time for these experiments was 6 s. The pressure transducer (GE make, UNIK 5000 model) was used to record the chamber pressure through NI DAQ system. The average chamber pressure was used to calculate the experimental characteristic velocity (see Eq. 4). The combustion efficiency is determined using Eq. (5). The combustion efficiencies for the PVC–DOP/AC fuel formulation are presented in Table 3. It is given in Table 3 that the highest improvement is obtained for the PVC–DOP/AC1% fuel formulation. The improvement was around 21% compared to base

Table 3 Combustion efficiencies of PVC–DOP/AC fuel formulations

Fuel composition	O/F	η (%)
PVC–DOP	4.1	60
PVC–DOP/AC1%	2.64	73
PVC–DOP/AC2%	2.72	66
PVC–DOP/AC5%	2.6	63

Table 4 Mechanical properties of PVC–DOP/AC fuel formulations

Fuel composition	Maximum tensile strength (MPa)	Percentage elongation (%)
PVC–DOP	0.24	27.31
PVC–DOP/AC1%	0.44	25
PVC–DOP/AC2%	0.24	18.25
PVC–DOP/AC5%	0.11	14.5

fuel. The decrease in combustion efficiency is observed with increase in AC mass fraction in PVC–DOP. This might be due to the soot formation as shown in Fig. 5.

3.3 Studies on Mechanical Properties

In this section, the effect of addition of activated charcoal on mechanical properties of PVC–DOP fuel is investigated. The mechanical properties such as tensile strength and percentage elongation are determined using INSTRON UTM-3655 instrument at 5 mm/min strain rate. The mechanical properties for the PVC–DOP/AC fuel samples are given in Table 4. It is observed from Table 4 that the mechanical properties are decreasing with increasing AC mass fraction in PVC–DOP fuel. It is also seen that at higher AC mass fraction the mechanical properties were significantly dropped and it was around two times lower than the origin fuel. Among the PVC–DOP/AC fuels, the percentage elongation for the PVC–DOP/AC1% is 25% and it is within the range (6–25%) that required to be used in practical applications [12].

3.4 TGA/DTG Studies

It was realized from the above studies that the PVC–DOP/AC1% is best fuel among the PVC–DOP/AC formulations. Thus, an attempt has been made to observe the degradation behaviour of the PVC–DOP/AC1% fuel sample using TGA/DTG curves. The TGA and DTG for the PVC–DOP and PVC–DOP/AC1% fuel formulation are presented in Figs. 6 and 7.

It can be seen from Fig. 6 that the degradation takes place at two different steps. The first step corresponds to the degradation of the DOP and the second step corresponds to PVC. The peak degradation temperatures at two steps are indicated on DTG curves in Fig. 7. The peak temperature for pure PVC is around 298 °C. With the addition of 1% AC the peak degradation temperature of PVC reduced significantly and it was around 272 °C. Thus, the addition of AC significantly increases the regression rate of PVC–DOP (see Fig. 4).

The temperature ranges and mass loss are given in Table 5 for the corresponding TGA curves in Fig. 5. From Table 5 it can be observed that the phase change of the

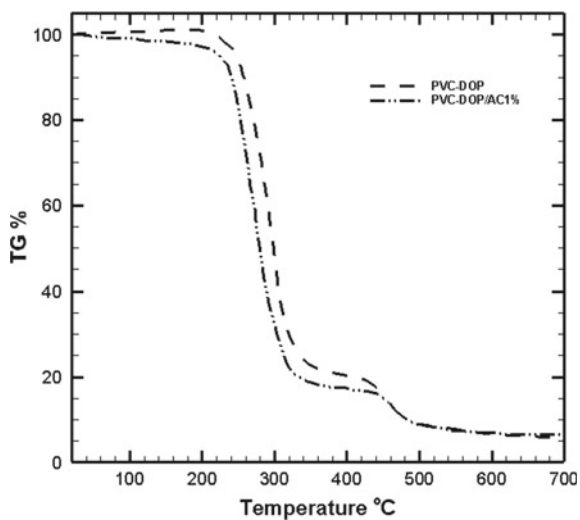**Fig. 6** TGA curves for PVC–DOP/AC fuel formulations
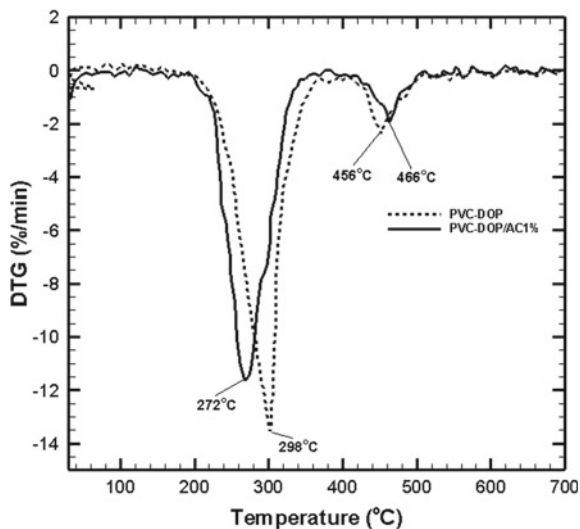

Fig. 7 DTG curves for PVC–DOP/AC fuel formulations

Table 5 TGA results for the PVC–DOP/AC fuel formulations

Fuel sample	T_{S1}(°C)	M_1 (%)	T_{S2} (°C)	M_2 (%)	M_R (%)
PVC–DOP	205–380	80	380–698	14	6
PVC–DOP/AC1%	180–358	76	358–699	11	12

PVC started earlier (at 180 °C) with the addition of 1% AC. However, the residual mass at 700 °C is higher for the PVC–DOP/AC1% fuel. This might be due to the soot left after total degradation of the fuel sample. It has been already described earlier that the soot formation is the reason for decrease in regression at higher mass fractions of AC in PVC–DOP fuels. This residual mass may be increased further with the increase of AC mass fraction.

4   Conclusions

The effect of activated charcoal on regression rate and combustion efficiency of the PVC–DOP-based polymeric fuel was investigated. Activated charcoal was added to the solid fuel at 1, 2 and 5% mass fractions. Additionally, mechanical properties and thermal characterization for these fuel formulations were also studied. The important conclusions from the current study are as follows:

1. The addition of activated charcoal enhances the regression rate by around 25% compared to pure PVC–DOP fuel.
2. At lower oxidizer mass flux, the regression rate for PVC–DOP/AC1% is better than other fuel combinations.
3. The formation of excess soot during combustion resulted in decrease in the regression rate with increase in AC mass fraction.
4. The combustion efficiency for the PVC–DOP/AC1% is higher among PVC–DOP/AC fuel formulations. This improvement was around 25% greater than the PVC–DOP alone.
5. The mechanical properties decreased with increasing AC mass fraction in PVC–DOP.

References

1. Sutton GP, Biblarz O (2000) Hybrid propellant rockets. In: Rocket propulsion elements. Wiley-VCH, Weinheim
2. Altman D, Holzman A (2006) Overview and history of hybrid rocket propulsion. In: Fundamentals of hybrid rocket combustion and propulsion. American Institute of Aeronautical and Astronautics, Inc., Raston, VA
3. Mazzetti A, Merotto L, Pinarello G (2014) Paraffin-based hybrid rocket engines applications: a review and a market perspective. Acta Astronaut 126:286–297
4. Veale K, Adali S, Pitot J, Brooks M (2017) A review of the performance and structural considerations of paraffin wax hybrid rocket fuels with additives. Acta Astronaut 141:196–208
5. Karabeyoglu A, Cantwell BJ, Altman D (2001) Development and testing of paraffin based hybrid rocket fuels. In: AIAA Paper 2001, p 4503
6. Karabeyoglu A, Zilliac G, Cantwell BJ, Dezilwa S, Castellucci P (2004) Scale-up tests of high regression rate paraffin-based hybrid rocket fuels. J Propuls Power 20(6):1037–1045
7. Sumit V, Ramakrishna PA (2010) Activated charcoal—a novel burn rate enhancer of aluminized composite propellant. Combust Flame 157:1201–1210

8. Yash P, Kalpit K, Dash PK (2011) Regression rate study of PVC/HTPB hybrid rocket fuels. Int J Mech Ind Eng 1(1)
9. Chatterjee AK, Mate RS, Joshi PC (1975) Port size effects on the combustion of PVC Plastisol-O_2 (gas) system. J Spacecraft 12(11):699–700
10. Kumar R, Ramakrishna PA (2013) Issues related to the measurement of regression rate of the fast burning hybrid fuels. J Propuls Power 29(5):1114–1121
11. Gordan S, McBride BJ (1971) Technical Report No. NASA-SP-273 NASA Lewis Centre, Washington
12. Dinesh M, Kumar R (2018) Development of EVA-SEBS Based Wax Fuel for Hybrid Rocket Applications. Acta Astronaut 152:325–334

Structures and Materials

Structural Health Assessment of Gas Turbine Engine Carcass

Dilip Kumar and Sanjay G. Barad

Abstract Gas turbine engine carcass is one of the major structures that supports/houses the main engine rotors, stator blade rings, interface features to mount the engine onto the airframe and accessories, viz., gearbox, electronic control units, pipelines, actuators, and so on. All the reaction forces generated by the engine are finally grounded to the airframe through this engine carcass. Specific to aero engines, designers make every effort to reduce the weight of this engine carcass so as to maximize thrust to weight ratio of the engine while maintaining the stiffness requirement. The present paper deals with an integrated approach for health assessment of the engine carcass. The theoretical and experimental studies undertaken for the engine carcass and rotor for enhancing the diagnostic reliability have been put forward. The requisite instrumentation and signal processing to assess the health have also been included. The decision-making for furthering of the test and remedial measures are also brought out.

Keywords Condition monitoring · Gas turbine · Rotor dynamics

Nomenclature

HP	High pressure spool
LP	Low pressure spool
NL	LP spool speed
NH	HP spool speed
EMA	Experimental modal analysis
[H(f)]	Matrix of frequency responses

D. Kumar (✉) · S. G. Barad
Gas Turbine Research Establishment, Defense Research and Development Organization, Bangalore, India
e-mail: dilipkumar@gtre.drdo.in

S. G. Barad
e-mail: baradsg@gtre.drdo.in

Q_r Modal scaling constant
r   Mode number
s_r Pole of mode number r
$\{\varphi\}_r$ Mode shape vector for mode r
n Number of modes
ω Frequency in rad/sec
FRF   Frequency response function

1 Introduction

Structural health, or equivalently, the state of damage can be established either directly or indirectly. The *direct* approach checks for the damage type (e.g. cracks, corrosion or delamination) by applying an appropriate inspection technique. These techniques, based on physical phenomena, have a very local and direct character. The established inspection techniques vary from visual inspection by the naked eye to passing the structure through a fully automated inspection gantry. In the *indirect* approach, structural performance or rather dynamic structural behavior is measured and compared with the supposedly known global response characteristics of the undamaged structure. If the effect of certain damages on structural response characteristics is known, this approach provides an indirect measure of damage and of structural health. Obviously in both the direct and indirect approaches, the sensitivity and the reliability of inspection are important quantitative performance measures [1]. They are determined, on the one hand, by the laws of physics, but on the other, in practice also, by the hardware and software quality of the inspection equipment and, last but not the least, by the equipment operator: the inspector. In this connection human factors such as loss of alertness in case of rare occurrences of damage and inspector fatigue in case of long and tedious inspections are important reasons to consider a smarter solution to inspection as an element of structural health monitoring.

Most of the time these two measures are done in parallel. However, the direct technique is limited by factors like accessibility and space constraints. On the other hand, the indirect methods do not have such limitations. The modal parameters, viz., frequencies, damping, mode shapes, stiffness, and so on, when accrued from the measured responses coupled with advanced signal processing and trending does help in assessing the structural health. The deviation in modal response can be attributed to issues in terms of loss of fits, cracks in the carcass, loss of clamping forces in bolted joints at the flanges, thermal expansions, loss of spigot fits, and so on.

On the engine level such observations can be made with carcass assembly or rotor assembly or both. On the rotor assembly this is dictated by shift in critical speeds, rotor amplitude response, and rotor phase response. While on the structural assembly, this is dictated by shift in resonances, damping, and vibration responses. In fact, one could observe this as an integrated response characteristic of the rotor

structure interaction. A regular trending of these modal responses is must to enable early detection of deviations in modal responses in order to avoid engine failures.

To date, the most successful application of structural health monitoring technology has been for the monitoring of rotating machinery [2]. The rotating machinery application is normally a pattern recognition-based method applied to time histories coupled with advanced spectral technique for feature extraction.

2 Engine Dynamics

Aero gas turbine design is driven by severe constraints of maximizing the thrust to weight ratio. This is achieved by keeping the turbine entry temperature as high as possible and reducing the weight which in turn demands for reducing the engine diameter and increasing the rotor speed [3]. These constraints imposed do pose challenges for designing of the engine carcass and rotor systems. Many unique features in the carcass design that support the rotor does stem from the understanding of proper spatial relationship against the thrust, pressure, and inertial loads.

For a typical twin spool engine, the engine carcass comprises a fan casing, intermediate casing, compressor casing, combustor, high pressure turbine casing, front mount frame, rear mounting frame, low pressure turbine casing, and the exhaust. The rotor system is supported by the ball/roller bearings at specific locations. Normally, the low-pressure spool is supported by three bearings, while the high-pressure spool is supported by two bearings. The schematic in Fig. 1 shows an engine carcass with the rotor system.

Being a high-speed flexible rotor system, the system has to cross several critical on the way to attaining its maximum design speed. At the design stage every effort is made to place the rotor critical away from the operating speed regime. The HP spool has normally a large diameter and hence no flexing of this HP shaft is observed. This rotor normally has stick/bounce modes with no flexing of shaft. However, the LP shaft is rather slender and one can observe encountering of flex criticals during critical speed crossover. Very often a strong modal coupling exists between the engine carcass
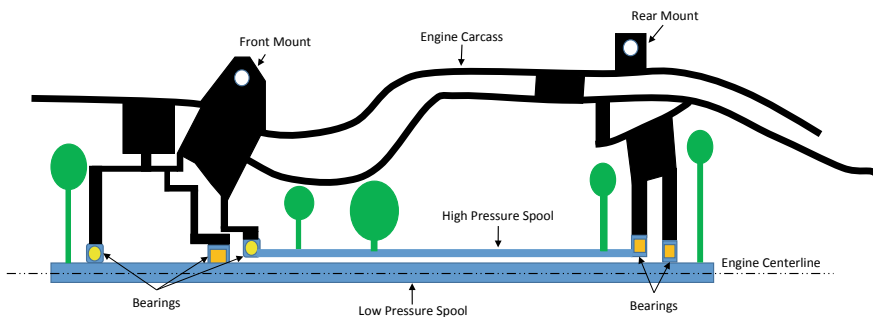

Fig. 1 Schematic of engine carcass

and rotor because of flexible casings. The carcass does participate significantly in the vibration response characteristics. This leads to high vibration responses due to resonances of carcass, which in turn influences the stiffness characteristics of the support structure and hence the rotor response behavior.

3   Dynamic Characterization

The dynamic characterization of an engine system has two distinct systems which may show a good coupling between them in most of the cases. The two components are:

1. The engine rotor system
2. The engine carcass.

The dynamic characterization involves both of these systems and at a refined stage do demand for an integrated analysis. The carcass dynamic analysis does demand for estimation of natural frequencies and assessment of stiffness of the bearing support planes. However, the rotor dynamic analysis demands for the estimation of critical speeds and response predictions for unbalance loads. These are done using FEM in majority of the cases or some in-house validated codes developed over a period of time.

$$[H(f)] = \sum_{r=1}^{n} \frac{Q_r \{\varphi\}_r \{\varphi\}_r^T}{j\omega - s_r} + \frac{Q_r^* \{\varphi^*\}_r \{\varphi^*\}_r^T}{j\omega - s_r^*} \tag{1}$$

On the experimental side, the modal characterization is undertaken by a conventional experimental modal analysis technique. The EMA is a standard technique to know the frequency response function—FRF of the test object. The process involves exciting the structure with a known input, viz., impulse, sine sweep, random, burst random, chirp, and so on, and measure the response using a sensor, like accelerometer, laser vibration measuring system, optical sensor, and so on. The ratio of this measurable output (response) and input (force) does give us the FRF of the test component. This FRF can be displayed as inertance/dynamic mass or mobility/impedance or compliance/dynamic stiffness. Figure 2 shows a typical transfer function plot for an engine carcass indicating various modal frequencies. The modal information is embedded into this set of transfer function and one can extract the modal parameters like frequency, damping and mode shape information from this. Equation (1) is a relation in frequency domain housing all the information [4].

The modal information can be extracted from this by several parameter extraction methods, viz., Prony residue method, least square complex exponential, polyreference time domain method, and so on. The details about this EMA procedure are available in the open literature to a great detail.
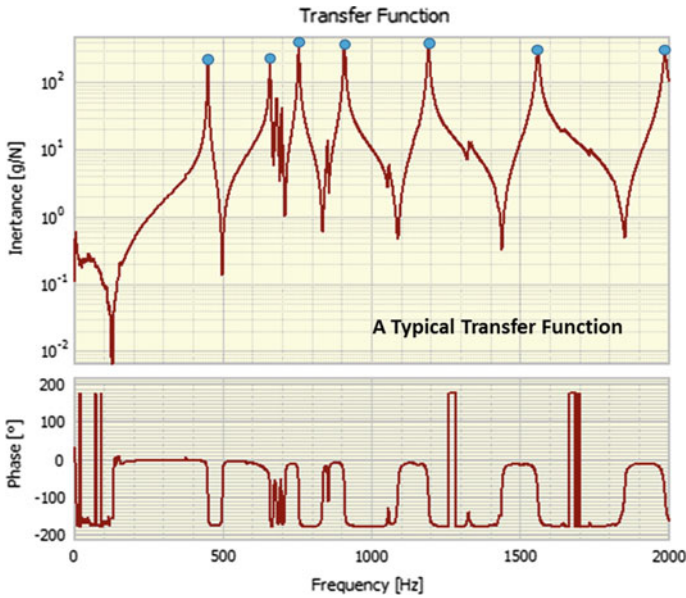
Fig. 2 A typical frequency response function plot for an engine carcass

The fundamental idea behind establishing the modal parameters is that these modal parameters are functions of the physical properties of the system (mass, stiffness, and damping) and any changes in these properties could cause variations in modal parameters. The dynamic characteristics can be represented by a spatial model or a response model or a modal model.

In the present work, the integrated engine carcass is characterized for modal parameters using an experimental modal analysis technique. The excitation was through an instrumented impact hammer and the response was measured using an accelerometer. Table 1 gives the modal frequencies ascertained at various stages of investigation. This transfer function for the base configuration forms a basis for assessing the health of carcass. This is because frequency is a global modal parameter and dictates the health of the structure in terms of stiffness. This characterization/assessment is done in a laboratory condition.

However, the dynamic characterization on the engine level is undertaken by ascertaining the shaft critical speeds and the amplitude response levels. In the present configuration, it was not feasible to undertake phase tracking due to space constraints for mounting the speed measuring probe. This phase track plot along with the amplitude response, popularly known as Bode plot, is conventionally used to confirm the critical speed experimentally. However, the critical speeds were confirmed through correlation between the theoretical studies and measured vibration amplitude response. Table 2 gives the theoretical estimation and experimentally established critical speeds. A good correlation exists between the two. This information is normally represented on a Campbell diagram [5] to study the interference with the rotor

Table 1 Natural frequencies of the carcass at various stages

Base configuration (Hz)	Damaged configuration (Hz)	Frequency change (Hz)	After rectification (Hz)
620	587	−33	611
666	648	−18	684
690	–	–	699
753	745	−8	751
797	756	−41	788
855	776	−79	876
967	–	–	958
1080	1041	−39	1064
1140	1122	−18	1124
1191	1179	−12	1204

Table 2 Placement of critical speeds. *Note* All critical speeds are normalized with lowest critical speed estimated

LP synchronous critical (Theoretical)	LP synchronous critical (Expt'al)	HP synchronous critical (Theoretical)	HP synchronous critical (Expt'al)
1.00—B	1.00—B	1.00—F	–
1.33—B	1.20—B	–	–
2.33—F	2.25—F	1.57—B	–
2.40—F	2.36—F	1.86—F	1.77—F
2.50—B	–	2.96—B	–
–	–	–	3.76—F
3.00—B	3.00—B	4.06—B	4.06—B
3.20—F	–	5.80—B	–
3.83—B	–	**F—implies forward whirl**	
4.67—F	–	**B—implies Backward whirl**	

speeds and its harmonics with the natural frequencies of the engine carcass and critical speeds. Figure 3 gives the HP and LP spool speed relationship and the observed critical crossovers at different speed regimes. The data represented is normalized with the lowest critical estimated theoretically. These critical speeds are LP excited and HP excited and are called as LP synchronous and HP synchronous critical speeds, respectively. Practically, they are the same rotor system modes and do get excited by HP rotor orders and LP rotor orders. However, a slight variation in these critical speeds for the same mode is observed due to gyroscopic and thermal effects.

As observed during the testing the backward whirls also gets excited because of tighter seal clearances which lead to further increased seal rubs and excitation of rotor critical. This is very common in the small gas turbine engines with high-speed operations. In many cases this can lead to instabilities in rotor systems due to rubs.
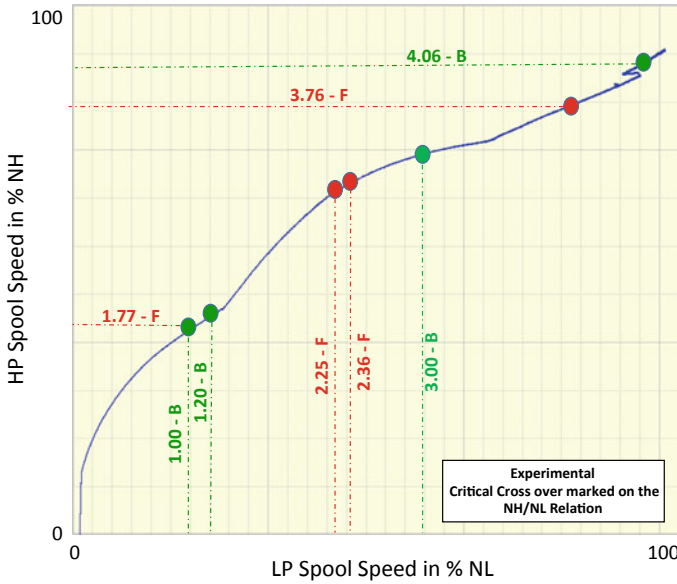
Fig. 3 LP and HP synchronous critical crossover during the engine operation represented on LP–HP speed relationship

4 Condition Monitoring

Being a developmental engine a comprehensive instrumentation is undertaken to understand the dynamic behavior and establishing the correlation with the theoretical models. The process involves assessment of mechanical health as well as performance targets. The carcass dynamics has much less influence on performance behavior except for the minor dimensional changes due to thermal effects. However, the mechanical health assessment is significantly governed by the carcass dynamics.

In order to assess this mechanical health, the vibration signatures from various locations on the engine, viz., casings, bearings, gearbox, mounts, and so on, are acquired and analyzed. The feature vectors extracted from this data are trended to observe any deviation in the dynamic behavior. For the present case, the first-order LP response for a specific location on the engine has been trended, refer Fig. 4. A clear shift in the critical speeds and significant deviation in the amplitude response was an indication of a significant distress in the system. This large deviation in the response was attributed to various causes, viz., loss of rotor support stiffness, excessive rub of the rotor with seals/stators, and loss of fit of the rotor stack.

Vibration spectrogram analysis further confirmed that the most probable cause is loss of support structure stiffness that resulted in shift of critical speeds and increase in vibration response.

With this assessment of the condition, the engine was subjected for inspection and modal survey. Experimental modal analysis—EMA undertaken on the engine carcass
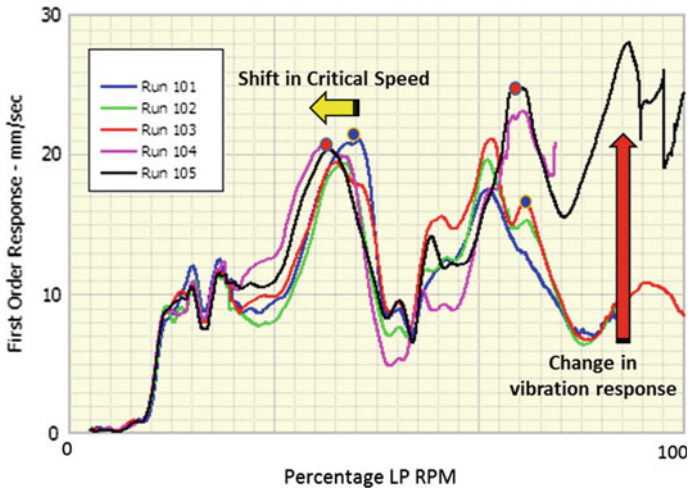
Fig. 4 Trending of first-order vibration response

that supports the engine rotor system revealed a significant shift in the frequencies when compared with the base transfer function. Table 1 gives the variation in these frequencies in free condition. With this confirmation the carcass was subjected to fluorescent dye penetrant test for detection of any cracks in the structure.

Fluorescent dye penetrant test revealed through cracks the LP casing stator-casing interface (weld location) in total of 13 locations. This confirmed the findings, refer Fig. 5.

Fig. 5 Detection of cracks through fluorescent dye penetrant test
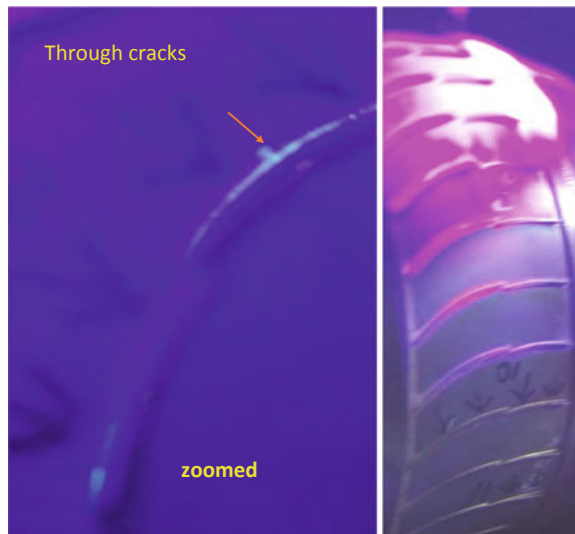
The shift in critical and increase in amplitude response was as a result of this change in stiffness of the bearing support due to cracks at the stator-casing weld interface.

5 Rectification and Implementation of Remedy

With the confirmation of distress in the carcass, the rectification of the weld was undertaken. Repeat EMA undertaken on this rectified (high temperature brazing) carcass revealed that the modal frequencies have been restored to the base configuration, refer Table 1. The engine was rebuilt with this carcass. Figure 6 indicates the vibration response before and after rectification.

The figure shows a significant reduction in the vibration response at higher speeds. The reason for this is a significant shift in the critical to higher speed. Refer point A, B, C, and D in the figure. The critical speed D has shifted to much higher speed, refer Fig. 6. This shift in the critical after rectification is due to an increase in the bearing plane stiffness.
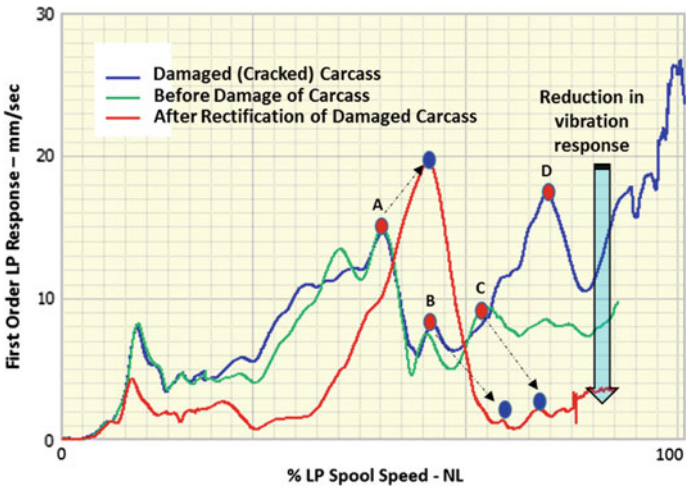
Fig. 6 First-order vibration response for various stages of testing

6   Conclusions

The case study indicates that monitoring of modal parameters, viz., critical speeds, resonant responses, instability frequencies, is a well-established procedure for health assessment of the engine carcass and rotor systems. Damages that are in the load path contribute significantly to the changes in modal parameters. Noticeable change in the frequencies for the initial few carcass modes does indicate a confirmed structural abnormality.

Apart from monitoring the modal frequencies of the carcass, the shift in the rotor critical needs to be monitored as this is a direct indication of loss of stiffness of support structure.

Other parameters like lubrication temperatures, pressure, and internal pressure balance may be fused with the vibration parameters to enhance the diagnostic reliability. Specific to carcass damage, the performance parameters may not show any quantitative change, viz., efficiency, pressure ratios, and so on.

In normal cases of structural health monitoring of aircraft wings, pressure vessels, and so on, the instrumentation can be more comprehensive. This can be tuned to localize a fault and also to a great extent undertake prognostic studies. However, in case of engine carcass practically, always all the modal parameters may not be available for decision making. This is because of severe space constraints and limited accessibility for instrumentation to measure the responses. These deficiencies can be overcome by having theoretical studies and baseline response for a given system.

At the production stage these modal parameters can be used or tuned for an acceptance test as one of the technique. This can be automated and implemented in the production line at the final stage of component pass-out.

As a good practice, the vibration data should be acquired for the base configuration and stored at the time of acceptance testing and commissioning.

Various techniques like intentional unbalance response test, synchronous perturbation test, non-synchronous perturbation test, and experimental modal test can be conducted on the rotor system (carcass + rotor) to establish the steady-state behavior during partial and full load, and transient condition during start-up and shutdown. This process provides a valuable data for health assessment of the system in future testing.

References

1. Staszewski WJ, Boller C, Tomlinson GR (2003) Health monitoring of aerospace structures—smart sensor technologies and signal processing. Wiley. ISBN 0-470-84340-3
2. Deraemaeker A, Worden K (2010) New trends in vibration based structural health monitoring. In: CISM—International Center for Mechanical Sciences, Courses and Lectures, vol 520. Springer Wien, New York
3. Kerrebrock JF Aircraft engines and gas turbines. MIT Press. ISBN 0-262-11162-4
4. Ewins DJ (2002) Modal testing: theory, practice and application. Research Studies Press Ltd, 2nd edn, United Kingdom. ISBN 0-86380-218-4
5. Genta G (2005) Dynamics of rotating systems. Mechanical Engineering Series. Springer. ISBN 0-387-20936-0

Methods of Simulation of Bird-Strikes on Critical Aero Structures with Some Test Cases and Conceptualization of an Alternative Technique for the High-Speed Measurement

Rajappa Banger, Praveen Kumar, Rajesh Sundrani, Anil Mahobia, Niranjan Sarangi, and P. Ramesh

Abstract The structural integrity evaluation of the aero structures and components is of paramount importance not just to validate the design and manufacturing processes, but it is also mandatory to prove the satisfactory compliance of design objectives laid down with respect to the performance and functioning. The paper depicts the methods employed for simulating the bird-strikes on the aero structures (of both military and civilian aircrafts) in the state-of-the-art test facility developed for conducting such tests along with some test cases and conceptualizing a new technique for the high (linear) speed measurement of the bird.

Keywords Bird strike · Test · Camera · Speed

1 Introduction

Whenever the birds and aircraft occupy the same space and time, the bird-strikes on the critical aero structures and components such as windshields, canopies, nacelles and the gas turbine engines (typically the fan blades) sometimes lead to the catastrophic failures and hence possess a serious threat to the safety of the man and machine.

Bird-strikes are a concern for both civil and military aircrafts. The external surfaces of an aircraft, which include windshields, nacelles, canopies, wind leading edges, engines, are susceptible to bird-strikes. The first known collision between wildlife and an aircraft occurred in Ohio in 1908 when Orville Wright struck and killed a bird near Dayton [1].

The bird-strikes on civil and military aircrafts are reported into a National Wildlife Strike Database. A significant bird-strike, while rare, can be very costly. The USAF

R. Banger · P. Kumar · R. Sundrani (✉) · A. Mahobia · N. Sarangi · P. Ramesh
Gas Turbine Research Establishment, Bangalore, India
e-mail: rajeshsundrani@gtre.drdo.in

N. Sarangi
e-mail: niranjansarangi@gtre.drdo.in

experiences about 3000 bird-strikes per year, and these bird-strikes result in a loss of about 1–2 aircraft per year and a loss of about 1–2 aircrew members every 3–5 years. The USAF costs for bird-strike damage are about 50 million US dollars per year; however, the above numbers are for average years, and the costs in dollars are much larger in the years where one of the lost aircraft was a large aircraft (B-1 in 1987, E-3 AWACS in 1995) [2]. Moreover, population development of large flocking birds has increased dramatically in many parts of the world. Many researchers focused their research on this problem, and most of the aeronautical companies build new airplane according to these requirements, even if yet neither design/construction standards nor operational practice has changed to react to the new threat due to possible bird-strike. Nowadays, the aircraft companies invest money in the crashworthiness, and the bird-strike has become a design requirement. Certification standards, which include verification of the structural integrity of airframes and engines, are established by FAA [3] and EASA [4]. The military and civil bird-strike statistics demonstrate the vulnerability of forward-facing areas to bird-strike. It is important, therefore, that all the implications of bird impact are considered at the design stage of the aircraft.

2   Experimental Method

Simulating the bird impact is a complex and challenging task. Figure 1 illustrates the schematic layout of the Bird Ingestion Test Facility employed for carrying out the impact test. Both dummy as well as real birds are used for carrying out the tests.

The facility has an air reservoir with a long gun barrel separated by a breach unit which can be either a diaphragm or a quick opening valve. At the end of the gun barrel there is a projectile holder catching unit. The projectile that has to be launched is centralized in the canister through suitable packing material. It is introduced into the gun by a projectile holder. The gun is charged with a compressed air and when the breach unit is triggered, the projectile is accelerated to the desired velocity depending upon the projectile mass and compressed air pressure. The gun is calibrated for projectile velocity with respect to the compressed air pressure.

An exhaustive amount of research has been carried out for the characterization of artificial birds used for simulation of impact tests. Typically, the artificial bird is prepared using gelatine, micro balloon and water. This method of bird preparation is generally accepted by certifying agencies and aerospace houses. The main parameters of the bird to be simulated are density and weight. The density of the bird to be

Fig. 1 Layout of facility

SCHEMATIC LAYOUT OF AIR GUN
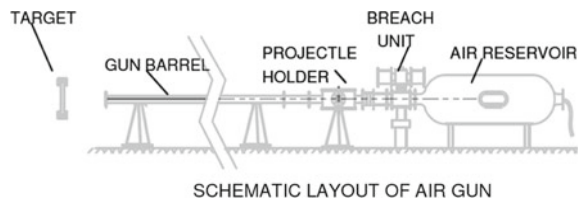
simulated is the most debated issue, and recently, the density of about 0.94 g/cc has found great acceptance. Dummy birds made of gelatine are being used worldwide for the reasons of accuracy, repeatability, shape, size and ease of handling. It has been proven that gelatine birds show characteristics that are closest to the real birds. Figure 2 shows the test facility located at GTRE and Fig. 3 shows an artificial bird made of gelatine.

The velocity of the projectile is calculated by capturing high-speed images of projectile with respect to time. High-speed video camera capable of capturing 10,000 frames per second with record/playback systems is employed for motion analysis. The test velocity is calculated based upon the distance travelled by the projectile and time taken for travel. The test article is illuminated by quartz and arc lamps. The high-speed motion analysis software can replay the recorded event frame by frame for detailed analysis of projectile motion and its engagement with the target.
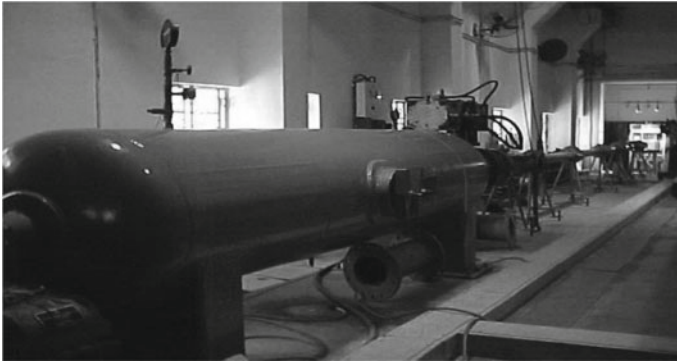
Fig. 2 Bird ingestion test facility

Fig. 3 Artificial bird
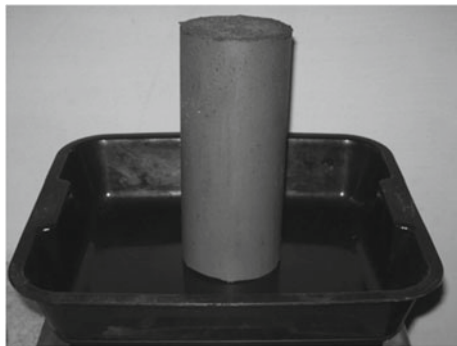
Fig. 4 SATCOM Radome on aircraft [5]

3 Case Study No. 1

3.1 Bird-Strike Test on SATCOM Radome of AEWCS

About the Test Specimen: SATCOM Radome is a module of AEW&C system which has been conceived, designed and developed by Centre for Air Borne Systems (CABS), a premier establishment of Defence Research and Development Organisation (DRDO). The SATCOM Radome is installed on the top of the fuselage that houses the antenna. The Radome is made of composite material and designed such that it is transparent to radar signals and has enough strength to withstand air loads and impact loads of bird hit during flight. The position of SATCOM Radome on aircraft is shown in Fig. 4. The SATCOM Radome has to undergo several tests including bird-strike as part of the qualification test for fitment on the aircraft.

3.2 Test Objective and Acceptance Criteria

The primary objective of the test is to determine whether the SATCOM Radome design is conforming to the requirements of FAR 25.571 (e) (1). As per FAR 25.571(e) (1) regulations, the airplane must be capable of successfully completing a flight during which structural damage might occur as a result of impact with a 4 lb (1800 g) bird when velocity of the airplane relative to the bird along the airplane's flight path is equal to 131 m/s at a height of 2400 m from sea level.

SATCOM Radome should withstand the 4 lb (1820 g) bird at a velocity of 131 m/s. The acceptance criteria are bird should not penetrate the Radome and there should be no detachment of the Radome from the fixture.

The test procedure was mutually agreed upon between CABS and GTRE before conducting the test.

3.3   Test Details and Result

EMB 145 AEW&C India SATCOM Radome is utilized for the test. The test hardware was mounted on a supporting structure. It was installed on the fixture with an interface using the same bolts used for final assembly on the AEW&C aircraft to simulate actual operational condition for the test. The test fixture and the Radome were fixed with the bedplate in the test facility.

The position and orientation of the Radome is as follows:

- The Radome was oriented at an angle of 0° to the air gun.
- Birds hit the Radome at 350 mm from the horizontal base of the Radome.
- The distance between gun barrel end (where bird comes out) and bulls eye (hitting point on the Radome) was 905 mm.
- Assembly of the test hardware is shown in Fig. 5.

Bird to hit the test hardware at the required speed was placed in the cylindrical canister that was placed in the air barrel to accelerate to the required speed, as shown in Fig. 6.
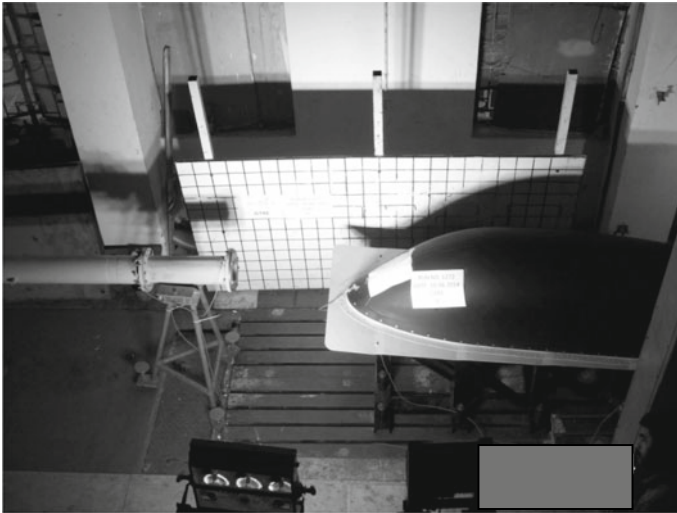
Fig. 5 Assembled Radome

Fig. 6 Bird inside canister

The test hardware was aligned at an angle of 0° to the air gun. The room temperature and relative humidity (RH) at test facility were recorded and bird weight was noted. The bird was housed in a canister and was assembled in the gun barrel. The reservoir was pressurized to around 3 bar pressure to achieve minimum impact velocity 131 m/s. A rupture disc of 33.25 psi (2.29 bar) rating was used for providing the impact velocity to the bird. A solenoid valve was energized to trigger the projectile lunch at the SATCOM Radome. The bird stroke the bull's eye (target) on the Radome at the specified velocity while the canister was retained in the gun barrel. The entire bird impact was captured by high-speed camera having the sampling rate of 7000 frames per second, and photographs of the test specimen before and after the test were taken. Figures 7 and 8 show the test component before and after the test, respectively.

3.4   Camera Results

Velocity measurement was done with high-speed camera by counting the frames for given distance. Images were captured during the test using high-speed camera at the rate of 7000 frames per second as shown in Fig. 9 during impact at 132.3 m/s with 1825 g bird.

3.5   Test Conclusion

- SATCOM Radome is capable of withstanding 1825 g bird impact at 132.3 m/s.
- A dent was produced on the Radome at the place of impact.
- Fasteners found intact with the fixture.

Fig. 7 Radome before test
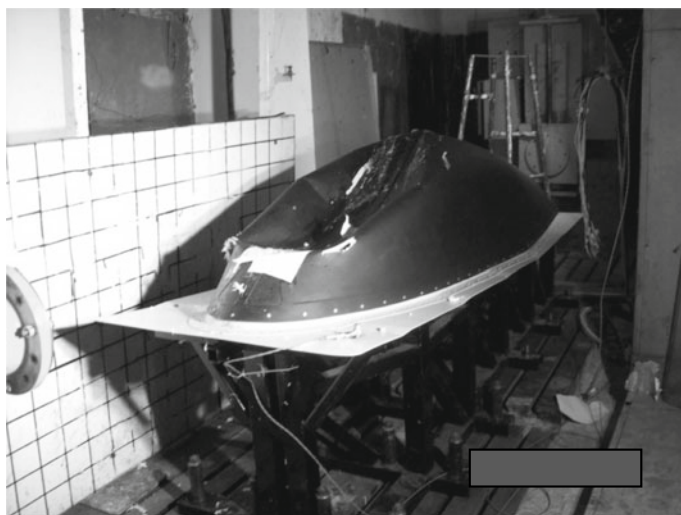
Fig. 8 Radome after test

Fig. 9 High-speed camera images
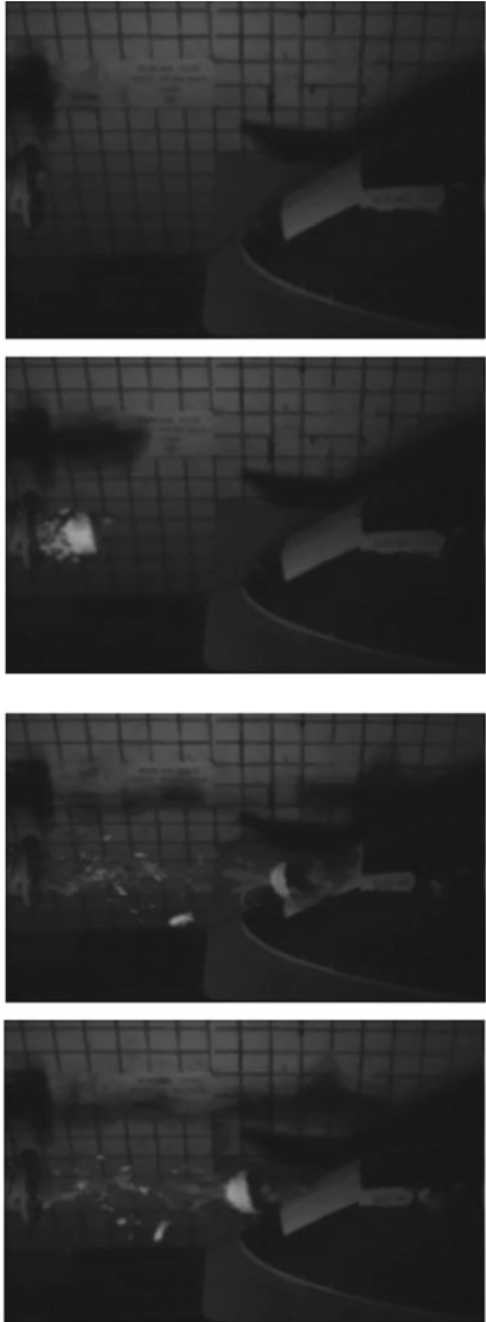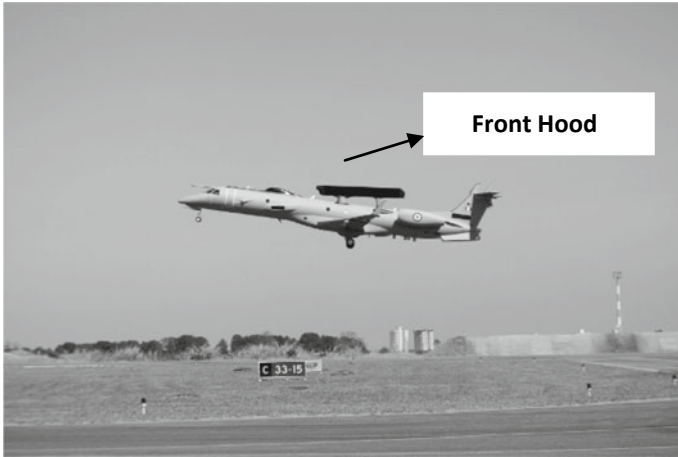
Fig. 10 Front hood on the aircraft [5]

4 Case Study No. 2

4.1 Bird-Strike Test on Front Hood of AEWCS

About the Test Specimen: AEW&C system has many subsystems like SATCOM, ESM, CSM, PR-SSR housed inside AAAU. The front hood provides regulated air intake for cooling of AAAU electronic components. The front hood is made of composite material and designed such that it has enough strength to withstand air loads and impact loads of bird hit during flight. Therefore AAAU front hood has to undergo several tests including bird-strike as part of the qualification test for fitment on the aircraft. The position of AAAU front hood on the aircraft is shown in Fig. 10.

4.2 Test Objective and Acceptance Criteria

The primary objective of the test was to determine whether the front hood design is adequate to withstand the requirements of FAR (same as Case Study No. 1).

Front hood should withstand the 4 lb (1800 g) bird at a velocity of 131 m/s. The acceptance criteria are bird should not penetrate the front hood and there should be no fragments and detachment of the front hood.

The test procedure was mutually agreed upon between CABS and GTRE before conducting the test.

4.3 Test Details and Result

The test hardware was mounted on a supporting structure as shown in Fig. 11. It was installed on the fixture with an interface using the same bolts used for final assembly on the AEW&C aircraft to simulate actual operational condition for the test. The test fixture along with the front hood was fixed with the bedplate in the test facility.

The position and orientation of the front hood is as follows:

- The front hood was oriented at an angle of −6° to the air gun.
- Angle of attack was 0°.
- Impact location was 380 mm from the base of the front hood.
- The distance between gun barrel end (where bird comes out) and bulls eye (hitting point on the front hood) was 1000 mm.
- Assembly of the test hardware is shown in Fig. 11.

Bird to hit the test hardware at the required speed was placed in the cylindrical canister which was placed in the air barrel to accelerate to the required speed as shown in Fig. 12.

The test hardware was aligned at an angle of −6° to the air gun. The room temperature and relative humidity (RH) at test facility were recorded and bird weight was noted. The bird was housed in a canister and was assembled in the gun barrel. The reservoir was pressurized to around 3 bar pressure to achieve minimum impact velocity of 131 m/s. A rupture disc of 33.25 psi (2.29 bar) rating was used for providing the impact velocity to the bird. A solenoid valve was energized to trigger the projectile launch at the front hood. The bird stroke the bull's eye (target) on the front hood at the specified velocity while the canister was retained in the gun barrel. The entire bird impact was captured by high-speed camera having the frame rate of

Fig. 11 Assembled front hood

Fig. 12 Bird inside the canister

10,000 frames per second and photographs of the test specimen before and after the test were taken. Figures 13 and 14 show the test component before and after the test, respectively.
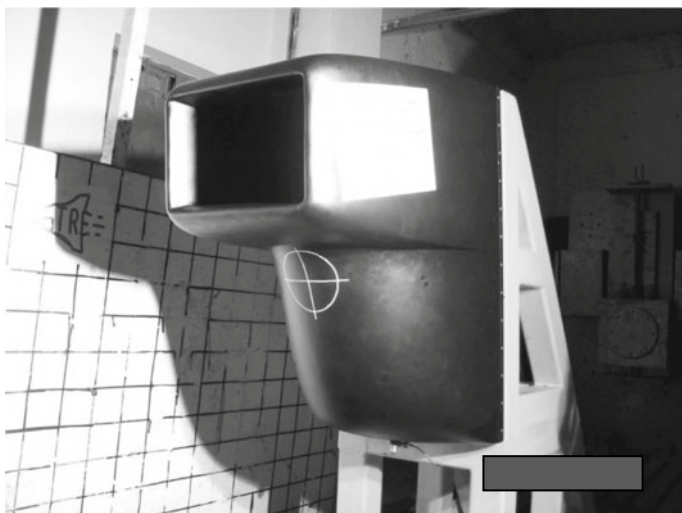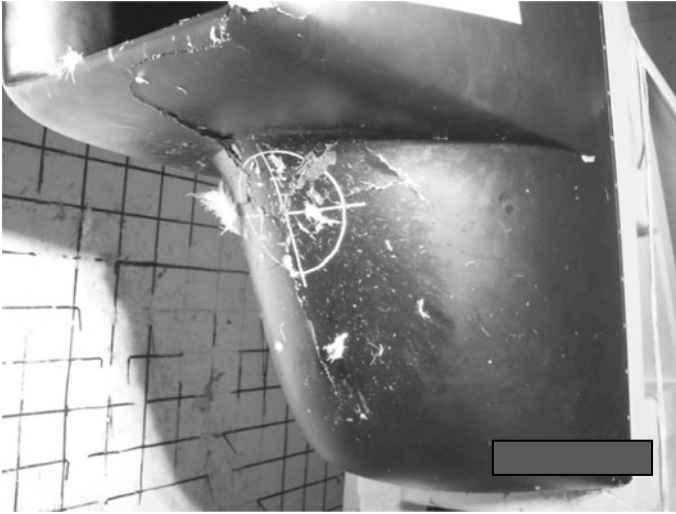

Fig. 13 Front hood before test

Fig. 14 Front hood after test

4.4 Camera Results

Velocity measurement was done with high-speed camera by counting the frames for given distance. Images were captured during the test using high-speed camera with the rate of 10,000 frames per second as shown in Fig. 15 during impact at 131.1 m/s with 1811.5 g bird.

4.5 Test Conclusion

- AAAU front hood is capable of withstanding 1811.5 g bird impact at 131.1 m/s.
- A crack was produced on the front hood at the place of impact.
- Fasteners were found intact with the fixture.

5 Conceptualization of a New Technique for High Linear Speed Measurement Through Accelerometers

For the measurement of speed with which the bird is impacting the test component, a high-speed camera is being used in the test facility. This camera has the feature to capture up to 10,000 frames per second and the speed is measured through the captured frames. In order to validate the speed of the bird-strike as measured by

Fig. 15 High-speed camera images
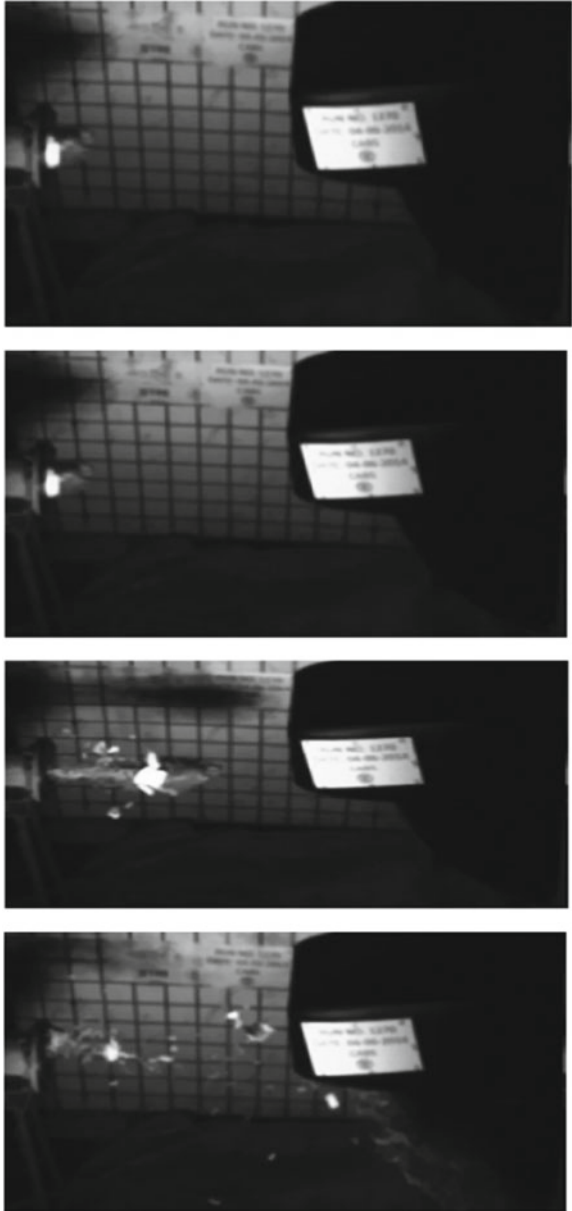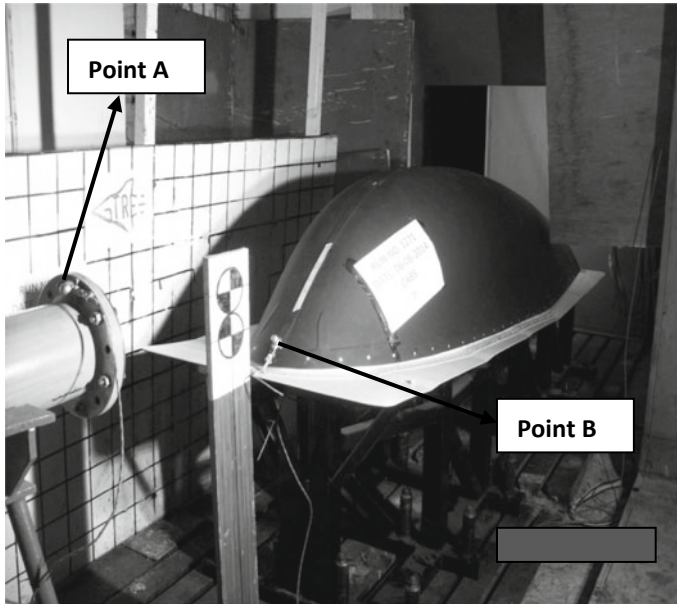
Fig. 16 Accelerometer arrangement

the camera, an alternative technique was evolved and applied using accelerometers. Accelerometer is a transducer which converts the input mechanical force into the electrical charge/voltage. The outputs generated by the accelerometers were acquired through a data acquisition device in high sampling rate mode of the order of 50,000 samples per second. Figure 16 depicts the arrangement of accelerometers in the test facility for the Test Case No. 1.

Point A and Point B are the locations of accelerometers at the gun barrel end and test component, respectively. Once the canister containing the bird stroke the arrester at the gun barrel end, first pulse was generated, and when the bird stroke the target, second pulse was generated as shown in Fig. 17.

The distance between Point A and Point B is fixed, that is, 0.904 m. The time difference between the two pulses was measured as 6.834 ms. With these values, the speed (distance/time) of the bird was calculated as 132.28 m/s.

Similar experiment was carried out for Test Case No. 2 for which the data obtained is shown in Fig. 18 and the speed of the bird was calculated as 131.1 m/s.

Table 1 depicts the comparison between the speeds measured through camera and accelerometer for both the test cases and verifies that the speeds measured by accelerometer technique is very much in-line with the speeds measured by the camera.
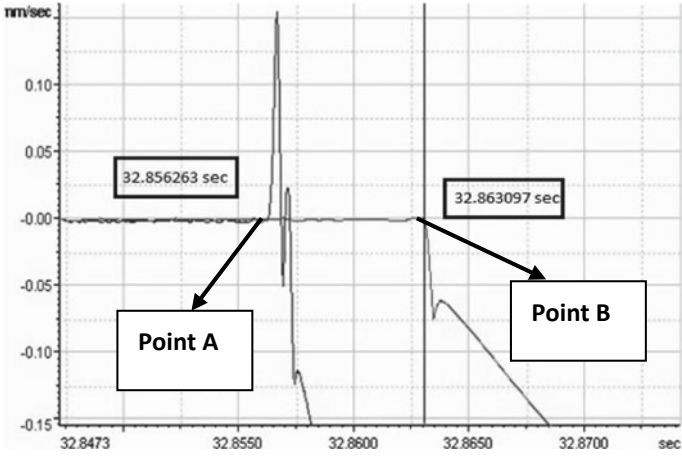
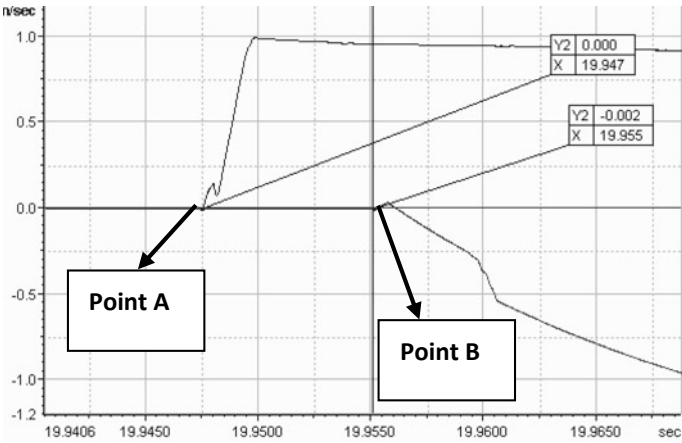**Fig. 17** Captured pulses (Test Case No. 1)

Fig. 18 Captured pulses (Test Case No. 2)

	Test case no.	Speed $_{Camera}$	Speed Accelerometer	Variation (%)
Table 1 Speed comparison between both measurements	1	132.3	132.28	0.015
	2	131.1	131.1	0

6 Conclusions

The ever-demanding need to better the performance of the aero structures is a huge challenge for the design engineers. It is equally challenging for the test engineers to develop customized test facilities and test such complex components under the simulated ambient conditions.

The subject test facility has been used to carry out numerous tests related to in-house engine development programme as well as external projects of national importance.

Bird impact tests on aero structures present a complex combination of structural and aerodynamics-related issues which demands extensive research work in the field of bird simulation and understanding of the bird-structure engagement.

References

1. Lebow EF (1989) Cal Rodgers and the Vin Fiz "The First Transcontinental Flight". Smithsonian Institution Press, Washington D.C.
2. Speelman III RJ, Kelley ME, McCarty RE, Short JJ (1999) Coping strategies for the aircraft birdstrike problem: resisting ımpacts, avoiding collisions, and … Bird Strike Committee-USA/Canada. In: First joint annual meeting, Vancouver, BC
3. Federal Aviation Regulation FAR 33.76. Bird ingestion. FAA 9 (2007)
4. Certification Specifications CS 25.571. Damage tolerance and fatigue evaluation of structures. EASA certification specifications for large aeroplane, 9 (2003)
5. Photo Courtesy. https://www.airforce-technology.com/news/newsindia-emb-145-aewc-embraer/

Experimental Evaluation of Elastic Ring Squeeze Film Dampers for Small Gas Turbine Engine

S. Thennavarajan, Sadanand Kulkarni, L. P. Manikandan, Soumendu Jana, Ajit Kumar, and Iqbal Momin

Abstract Squeeze film dampers play a vital role in absorbing vibration energy in a rotor bearing system. The damper under study has an elastic ring with pedestals between bearing and stator dividing oil cavity into small oil pockets. This arrangement is different from conventional squeeze film damper where a single annular oil film is formed. This provides the required support stiffness as well as damping to the rotor. These types of dampers are called elastic ring squeeze film dampers (ERSFD) which are mainly used in high-speed small gas turbine engines by virtue of its compact design. There are very few literatures available to evaluate the damping offered by these SFDs. The main objective of this work is to determine the damping offered by ERSFD experimentally. For this study the rotor is designed to simulate the dynamics of a typical gas turbine engine. The rotor has to cross two rigid critical speeds within 18,000 rpm. The rotor response is measured under undamped (UND-without oil supply) and damped (D-with oil supply) conditions to evaluate the damper performance. The performance data is generated at three different oil temperatures (40, 70 and 100 °C) under unbalanced load ranging from 2 to 8 g at 58.5 mm radius (UBR). This experimentation and performance analysis shows enhanced damping at critical speeds leading to the reduction in rotor vibrations after introducing ERSFD. The

S. Thennavarajan (✉) · S. Kulkarni · L. P. Manikandan · S. Jana
Propulsion Division, CSIR-National Aerospace Laboratories, Bangalore 560017, India
e-mail: thenan@nal.res.in

S. Kulkarni
e-mail: sadanandsk@nal.res.in

L. P. Manikandan
e-mail: lpmanikandan@nal.res.in

S. Jana
e-mail: sjana@nal.res.in

A. Kumar · I. Momin
Gas Turbine Research Establishment (GTRE), DRDO, Bangalore 560093, India
e-mail: ajitkumar@gtre.drdo.in

I. Momin
e-mail: igbamobin@gtre.drdo.in

experimental data is further processed to calculate the amount of damping offered by ERSFD using rotor dynamic relations.

Keywords Small gas turbine engine · Rotor dynamics · Elastic ring squeeze film damper · Damping characterization

1 Introduction

Vibration problem in case of high-speed rotors is a common phenomenon. In most of the high-speed systems, it is required to cross one or more critical speeds to reach the operating speed. Synchronous vibrations can be reduced by proper balancing of the rotor system. Use of squeeze film dampers is one of the common techniques to reduce the rotor vibrations while passing critical speeds [1]. In conventional squeeze film dampers, the outer race of the bearing is held in the squirrel cage to give the required stiffness in the bearing plane and also to allow the specified deflection for squeeze film damper to be effective. In case of small rotors, such as small gas turbines, it is difficult to accommodate the squirrel cage due to space constraint. Also the weight reduction is the priority in any flying applications. In order to address these issues, a novel type of squeeze film dampers with elastic ring are used [2]. The schematic of the typical ERSFD is shown in Fig. 1. It consists of bearing outer sleeve and damper housing separated by elastic ring forming various cavities which are filled with oil. The elastic ring has alternate pedestals on both ID and OD which will closely fit with the bearing sleeve and damper housing, forming equispaced oil pockets. The region between the pedestals has the oil holes which allow the oil to flow between different pockets. During high vibrations the oil layer in these pockets gets squeezed and part of the oil will flow through the orifices, resulting in energy loss and reduction in vibration amplitude [3].
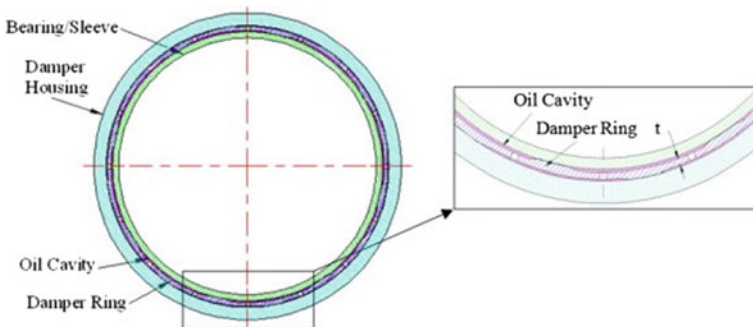

Fig. 1 Elastic ring squeeze film damper

Table 1 Configurations of ERSFD (Figs. 12 and 13)

Set	Thickness (mm)	No. of rows	No. of holes per row	Width (mm)	Remarks
1	0.9	2	16	15.5	Undamped-baseline
2	0.9	2	16	15.5	Damped

2 Methodology

The performance of the ERSFD is crucial, especially when the rotor crosses its critical speed region. For experimental evaluation it is proposed to use the existing fatigue test rig in CSIR-NAL, which can go up to 25,000 rpm. The shaft system is designed such that the rotor crosses both the rigid critical speeds within 20,000 rpm simulating actual dynamics of the engine. The bearing selected for this has the capability to go up to 25,000 rpm with grease as well as with oil lubrication. The bearing housing is designed such that it can accommodate the ERSFD mechanism. The support stiffness in the ERSFD plane is kept around 10 MN/m as in the case of typical small gas turbine [3, 4]. The rotor is rotated with and without supply of oil to ERSFD and the rotor vibration data is acquired using dedicated data acquisition system. Reduction in the rotor vibration levels with ERSFD at given speeds depicts the effectiveness of the ERSFD.

For parametric studies the UND and D performances are compared under varied unbalance conditions. Table 1 gives the details of ERSFD configurations used for experimentation and Table 2 shows the parametric variation for this study.

3 Rotor Dynamic Analysis

The effectiveness of ERSFD is to be studied at critical speeds; the rotor is designed such that first two critical speeds fall within 20,000 rpm. For the analysis assumed stiffness in the bearing plane is in the range of 10–12 MN/m. It is equal to the elastic ring stiffness as all other parts in bearing plane have much higher stiffness.

The 3D model of the rotor system is shown in Figs. 2 and 3 and the Campbell diagram for the designed rotor system is shown in Fig. 4 and the corresponding modes shapes are shown in Figs. 5 and 6. The estimated rotor response for G2.5 level of unbalance (RUB) and with 8 g unbalance is determined and the same is shown in Figs. 7 and 8. From response analysis it is observed that the amplitude of vibration is considerably higher at second critical (17,926 rpm) speed compared to the first critical speed (10,539 rpm) [5, 6].
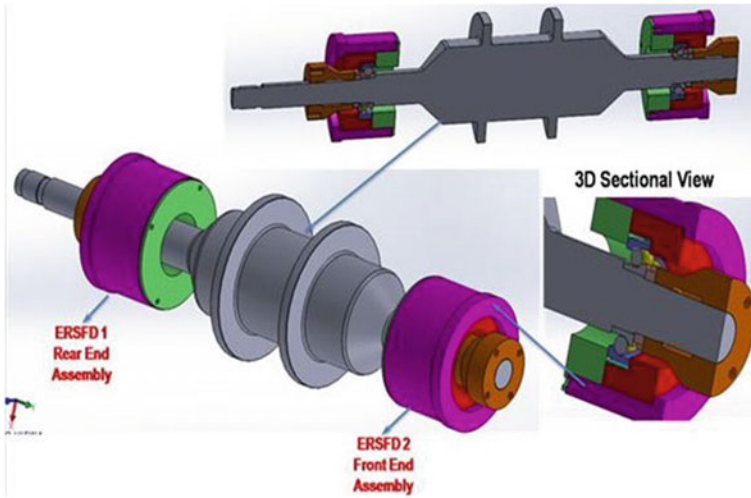
Table 2 Unbalance and viscosity variation

Temperature variation in viscosity change	Ring 1	Unbalance mass variation in grams [$*10^{-4}$ kg m]									
		RUB [0]		2 [1.17]		4 [2.34]		6 [3.51]		8 [4.68]	
		IP	OP	IP	OP	IP	OP	IP	OP	IP	OP
40		T1	T1	T1	T1	T1	T1	T1	T1	T1	T1
		T2	T2	T2	T2	T2	T2	T2	T2	T2	T2
70		T1	T1	T1	T1	T1	T1	T1	T1	T1	T1
		T2	T2	T2	T2	T2	T2	T2	T2	T2	T2
100		T1	T1	T1	T1	T1	T1	T1	T1	T1	T1
		T2	T2	T2	T2	T2	T2	T2	T2	T2	T2

Fig. 2 3D model of typical SGT engine rotor with dual ERSFD
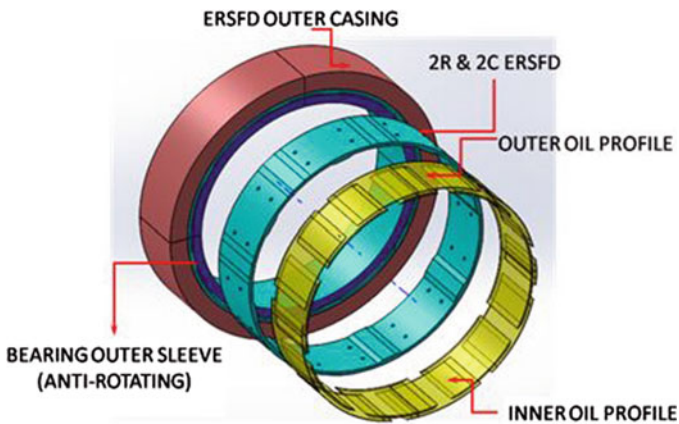
Fig. 3 Exploded view of ERSFD components

4 Proposed Test Rig Configuration

Schematic of the fatigue test rig in which the ERSFD is tested is shown in Fig. 9. The specifications of the test rig are given in Table 3. The test rig consists of test rotor supported on two bearings and driven by motor through multiplier. The ERSFDs are introduced between the bearings and the support structure. The rotor is provided with the two flanges to introduce the desired level of UB force on the bearings. Lubricant
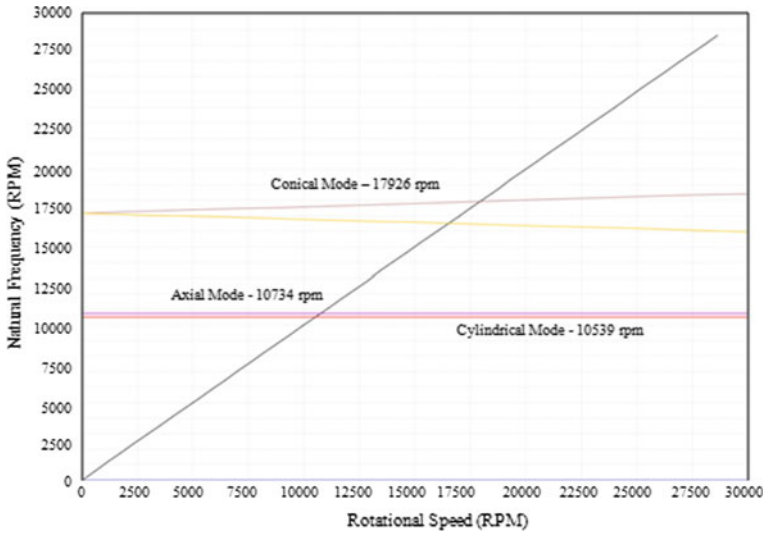
Fig. 4 Campbell diagram for the designed rotor bearing system

Fig. 5 Cylindrical mode—I
at 10,539 rpm
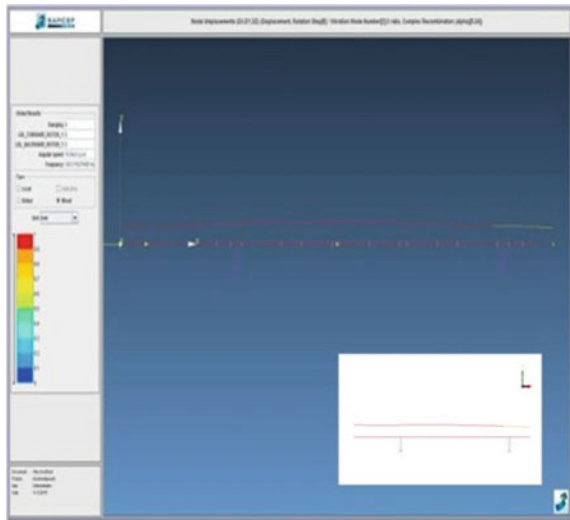
to the test bearing is supplied by oil jet provided at the appropriate location. The part of the oil after lubricating the bearing enters the ERSFD region through the annular space provided around the bearing. This oil film gets compressed to provide the required damping.

Fig. 6 Conical mode—II at 17,926 rpm
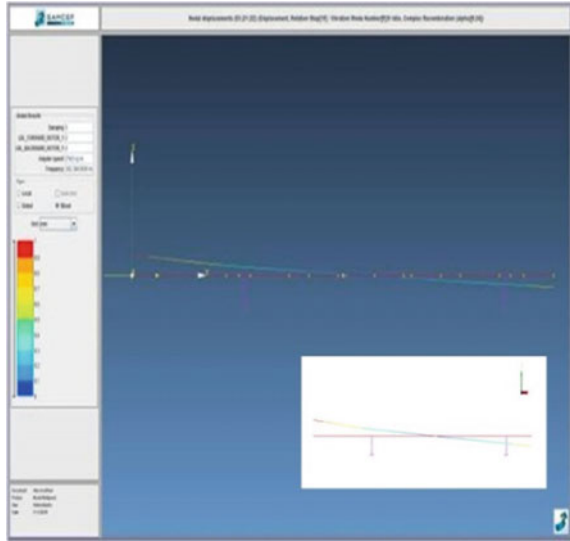
4.1 Fatigue Test Rig for ERSFD Testing

In this fatigue test rig the rolling element bearings are subjected to actual engine running conditions in terms of applied load (radial and axial), inlet lubricating oil temperature, lubricant flow rate and shaft speed. The performance of the bearings as well as the lubricants is monitored in terms of metal temperature, vibration, motor power consumption and metallic particles in the used lubricant. The rig is designed such that the two test bearings can be tested at the same time. Test section of the test rig and the associated lubrication systems have been suitably designed and modified to accommodate ERSFD with rotor system.

The rotor shaft disks have provision to add unbalance radial load. The test bearing section and drive section are lubricated with different types of lubricants supplied by separated lubrication systems. Provisions are made to avoid mixing of oils. The bearing fatigue test rig and its associated sub-systems are shown in Fig. 10.

4.2 Rotor System for ERSFD Testing

The shaft system used for testing of ERSFD consists of

- Test shaft—1 no.
- High-speed test bearings—2 nos.
- Test bearing adaptors—2 nos. (each side)
- Bearing sleeve—2 nos.
- Bearing lock nut—2 nos. (each side)

Unbalance Masses (RUB) in-phase

Unbalance Masses (RUB) out-of-phase
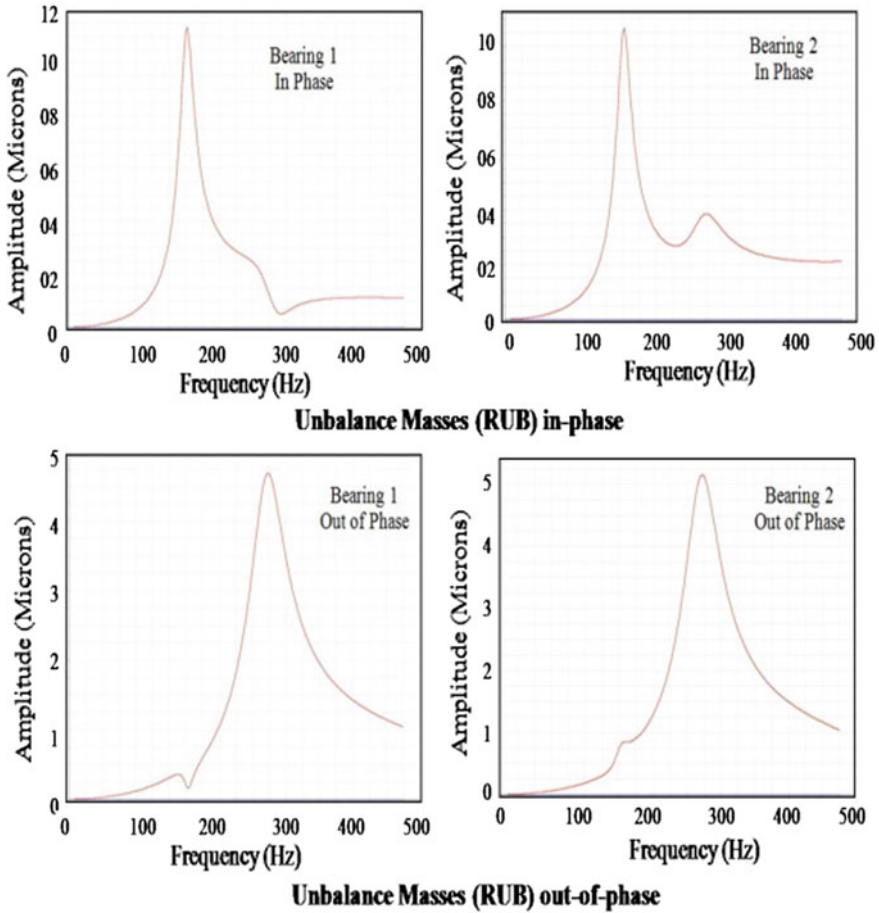
Fig. 7 Response of the rotor with RUB

- ERSFD rings—2 nos.
- UB addition—Rotor dual-disk having provision of six holes per side
- Lubrication jet nozzles—2 nos.
- Drive end flexible coupling—1 no. (Teflon)

The test rotor and its related components are fabricated with high precision and dimensional tolerances to meet the required fit with bearings and other components. The photograph of fabricated rotor system components is shown in Fig. 11.

Unbalance Masses (8 gms) in-phase

Unbalance masses (8 gms) out-of-phase
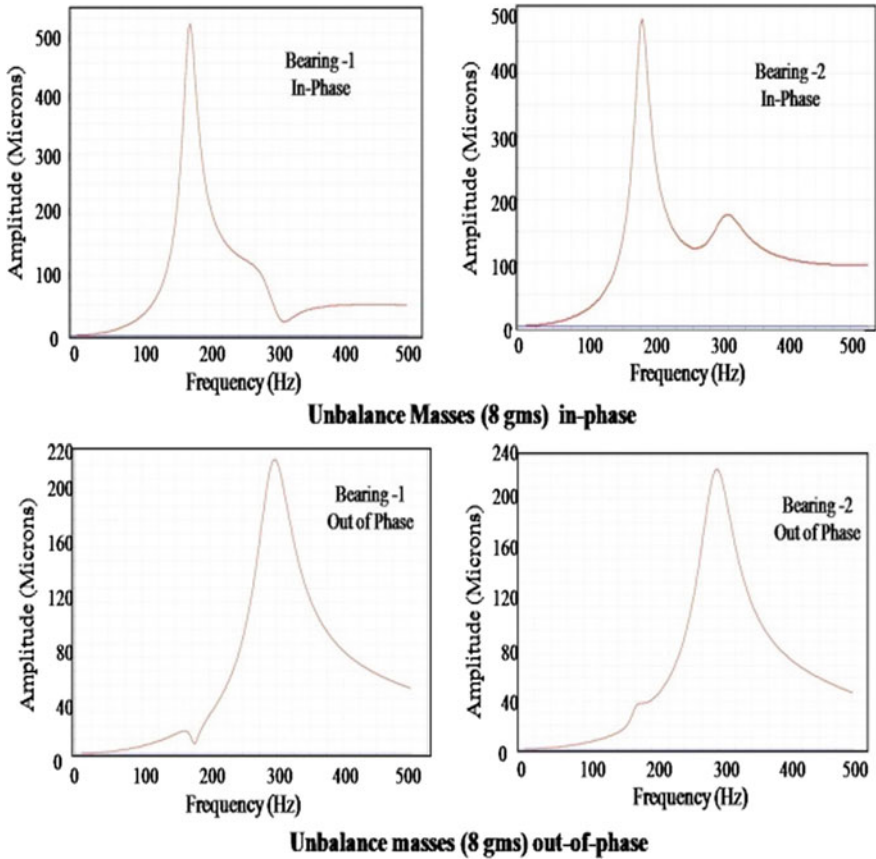
Fig. 8 Response of the rotor with 8 g UB

4.3 Dynamic Signal Processing (ADRE 408 DSP)

ADRE-Sxp Software and the 408 DSPI (dynamic signal processing instrument) are used for dynamic signal processing and data acquisition. These are specifically used for real-time parallel signal processing and presentation. The specified test rig has many safety features and automated cutoff switches for normal and fatigue test-related activities. This testing with ERSFD is highly dynamic in nature and requires a more data collection to predict dynamics. Hence the ADRE system is used in parallel to collect real-time dynamic parameters using eddy probes for displacement in X, Y of dual-disk and speed pickup at mid-span, as shown in Fig. 9. The errors observed in real-time plots due to oil deposition in tip of speed pick up and keyphasor are solved by supplying high-pressure air jets.
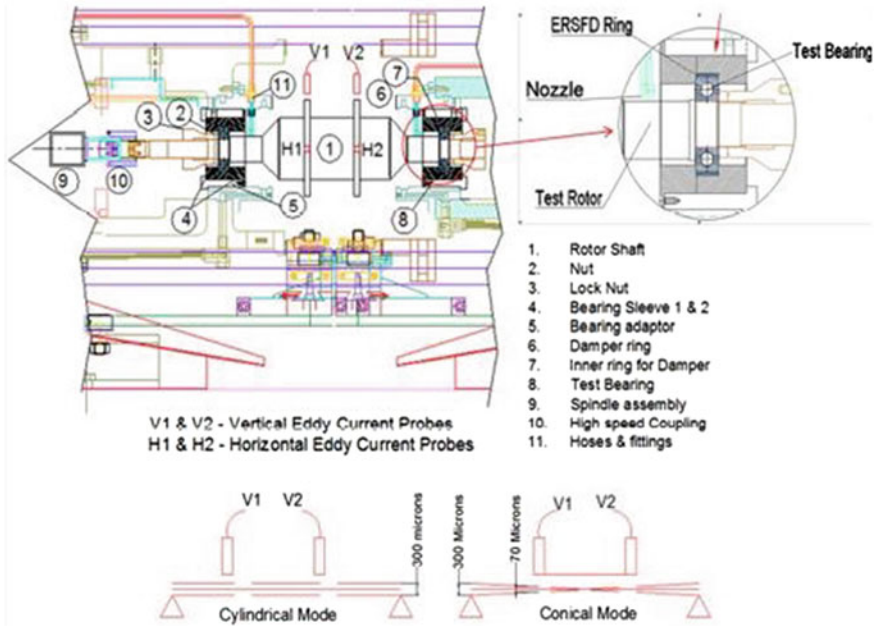
Fig. 9 Schematic of the ERSFD test rig

Table 3 Test rig specifications

Sl. no.	Parameter	Specification
1	Speed	Up to 25,000 rpm (accuracy 0.1%)
2	Load	Up to 200 KN (axial and radial) (accuracy 0.1%)
3	Temperature	0–150 °C (accuracy 0.1%)
4	Oil flow	Up to 12 lpm
5	Bearing size	Up to Ø300 mm of outer race

4.4 ERSFD and Bearing Metal Temperature

The specially made set of k-type flexible temperature sensors has been used to measure ERSFD/bearing metal temperature and connected with rig data acquisition system. Two sensors on each side of the bearing adaptors downstream are mounted approximately 30° apart. This temperature signature in ERSFD/bearing metal will provide energy dissipation and temperature influence in ERSFD performance. Also, it will aid in providing real-time signature due to friction between the components or sudden failure due to any other means.

Fig. 10 Aero-engine bearing fatigue test rig for ERSFD testing

Fig. 11 ERSFD test rig and rotor system components

4.5 *Sensor and Probe Calibration*

The sensors used in the test rig are calibrated to avoid zero set error. The eddy current sensors are calibrated using the following technique. It consists of a power supply, dial gauge, eddy current sensor and multimeter. A piece of ERSFD/bearing strip is mounted in such a way that it faces the eddy current probe. When the strip is moved by adjusting screw toward eddy current probe the gap is reduced or increased and displacement measured by dial gauge. The parallely connected multimeter displays the gap voltage which is sensed by the eddy current probe. The initial gap voltage is noted from the multimeter. Then the position of the sample is moved from a known distance using dial gauge and for different number of steps, the corresponding

Table 4 Supply lubrication parameters

Lubricant oil	MIL-PRF-23699 (OX-27)
No. of injector	2
Hole diameter each (mm)	2
Oil flow rate (l/min)	1.5/per bearing
Inlet oil temperature (°C)	40, 70 and 100

displacement is measured through the dial gauge and noted. The diameter of the eddy current probe used is 8 mm with a sensitivity of 8.07 mV = 1 μm.

4.6 Lubrication Supply and Calibration

The lubricant flow rate, number of nozzles, nozzle diameter and inlet oil temperature as specified for test bearing and ERSFD are given in Table 4. The same has been followed during the damper performance testing of damped bearing support [7].

The lubricant flow rate is calibrated before testing. The test bearing lubricating oil inlet and outlet temperature is continuously monitored using k-type thermocouple sensors.

4.7 Balancing and Integration with Test Rig

1st Stage—Assembly of rotor system balancing along with its rotating parts, like bearing inner race and lock nuts, except ERSFD components, as shown in Fig. 12. The fabricated individual components as well as the rotor system are dynamically balanced with G2.5 grade (ISO 1940). This balancing was made by material removal on dia 90 mm of each plane on either side. The maximum allowable unbalance was maintained well within the limit of 24 mmg/plane. This has been taken as a reference data generation for residual unbalance (RUB) condition during the test. Then the unbalance level is added in 2 g steps till 8 g.

2nd Stage—Once the rotor system balancing is over, the next stage assembly is carried out along with the dual ERSFD components, which will be accommodated with grease-filled angular contact bearing. This assembly is shown in Fig. 13 and is used to generate standard data set without lubrication oil supply (undamped). Here the elastic ring stiffness alone holds the rotor to its center axis and supports.

3rd stage—To find real damping effect, the third stage assembly was carried out along with the dual ERSFD components, which will be accommodated with oil lubricated angular contact bearing. This assembly is shown in Fig. 13 and is used to generate real damping performance data set with oil supply (damped). Here in this configuration the elastic ring stiffness and the hydrodynamic oil stiffness both together hold the rotor to its center axis and support well within the limit of vibration.
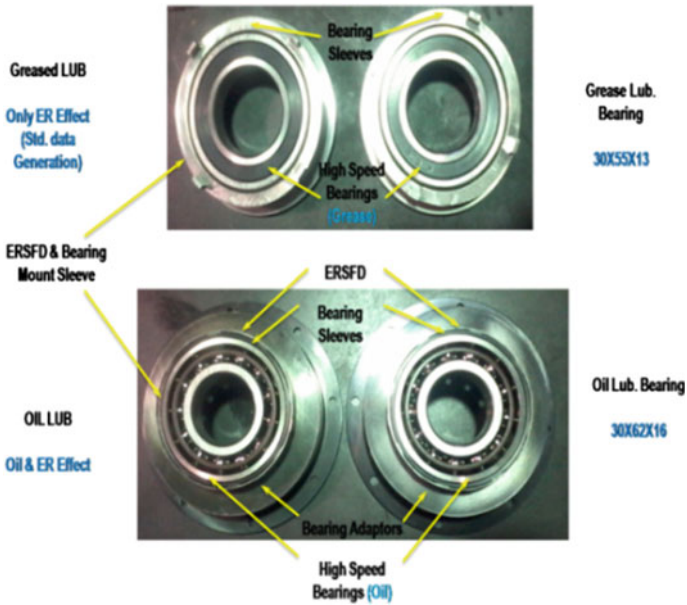
Fig. 12 Dynamic balancing of rotor

Fig. 13 Oil and greased bearing with ERSFD assembly

5 Test and Data Generation

The fabricated components are inspected and assembled into the test rig (Figs. 12 and 13). The test rig is instrumented with the eddy probe and speed sensors along with other rig sensors like accelerometer and thermocouples. The photograph of the test rotor assembled in the test rig is shown in Fig. 14. The testing was carried out with baseline configuration. In baseline configuration the rotor is tested with and without oil to the ERSFD for different unbalance levels and inlet oil temperatures.

The unbalance level is varied from residual to 8 g in steps of 2 g (at UBR 58.5 mm) and inlet oil temperature was maintained at 40, 70 and 100 °C. In case of 2 g unbalance mass addition, 1 g mass is added to each side of the flanges on shaft. Subsequently, every time 1 g mass is added on each flange to increase the unbalance level. Table 2 shows various test performed with IP and OP conditions for both coast-up and coast-down conditions.

5.1 Baseline Data Generation for Damping Effect Analysis

The baseline configuration consists of testing ERSFD with and without oil to check its effectiveness. The rotor response over desired speed range at various unbalance levels and oil temperature was recorded. Each experiment is repeated for the confirmation of the results obtained. A typical IP and OP response comparisons with (D) and without oil (UND) in ERSFD at 40, 70 and 100 °C inlet oil temperature with RUB, 2, 4, 6 and 8 g UB are shown in Figs. 15a, 16, 17 and 18b (for IP and OP), respectively.
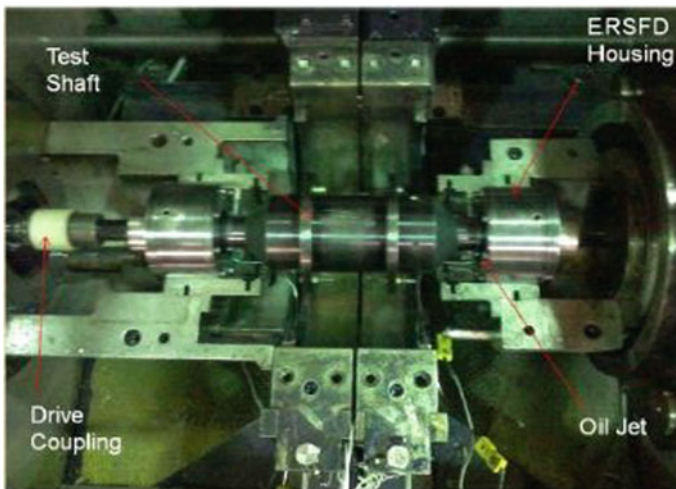
Fig. 14 ERSFD rotor assembled in test rig
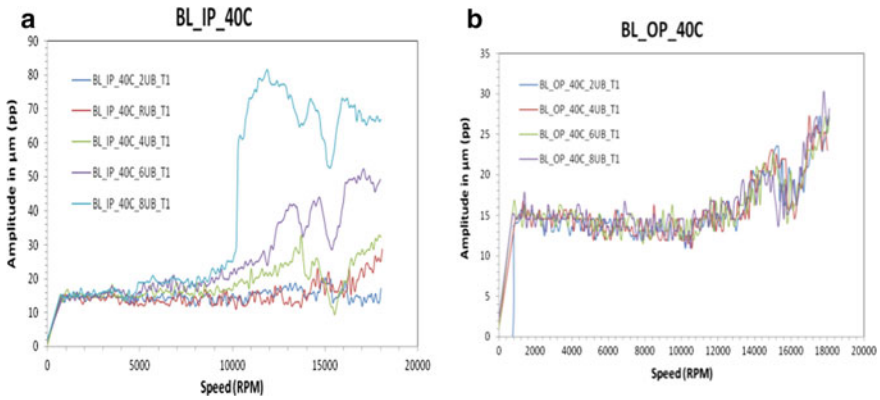
Fig. 15 **a** Data comparison with 40 °C heat and UB effect on ERSFD ring—D(IP) **b** Data comparison with 40 °C heat and UB effect on ERSFD ring—D(OP)
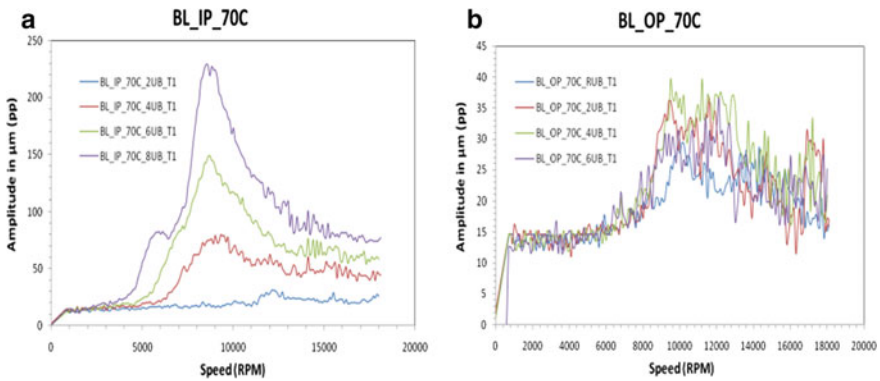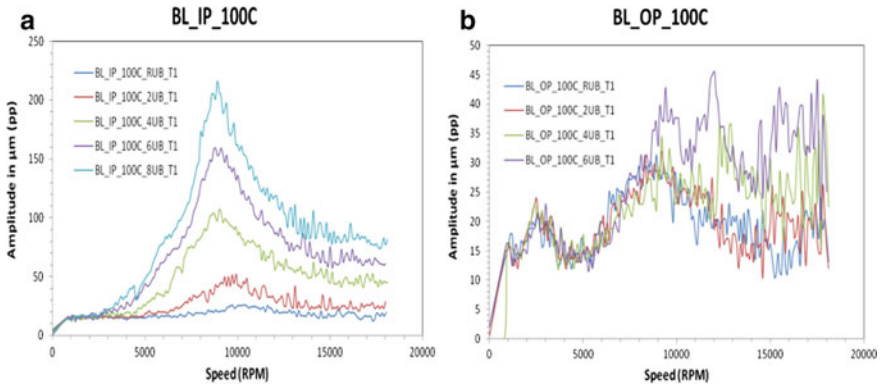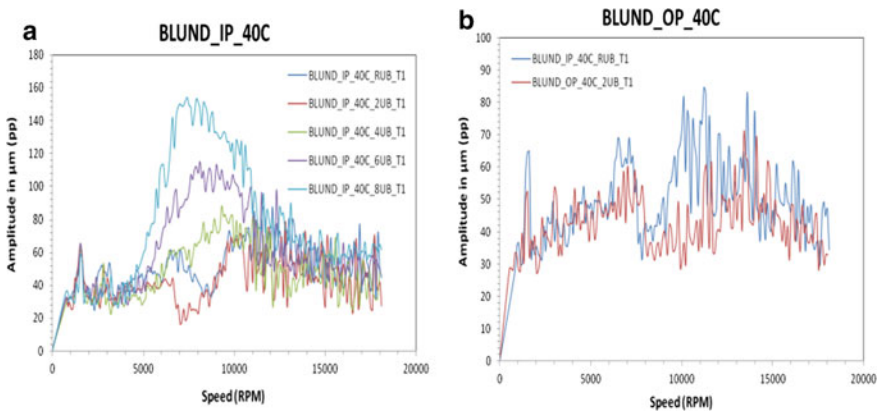

Fig. 16 **a** Data comparison with 70 °C heat and UB effect on ERSFD ring—D(IP) **b** Data comparison with 70 °C heat and UB effect on ERSFD ring—D(OP)

In order to generate baseline data, the elastic ring squeeze film damper system with greased bearing is pre-heated to temperature of 40 °C. Once the desired temperature is reached they are tested without oil in dry condition. In case of damped tests, the system is supplied with oil at different temperatures with flow rate of 3 lpm and the temperature change leads to variation in supply oil viscosity. All the damped and undamped tests are carried out in similar manner.

The above comparisons show that in damped conditions, both temperature and unbalance ranges in IP and OP conditions are tested. But in case of IP UND condition at 8 g, 40 °C rotor attained max amplitude of vibration, which is shown in Fig. 18a. Also in OP case with 2 g UNB rotor attains max vibration, beyond which it makes metal to metal contact and testing is not possible (Fig. 18b). It is also observed that the damping provided by the ERSFD is significant to reduce vibration levels within

Fig. 17 **a** Data comparison with 100 °C heat and UB effect on ERSFD ring—D(IP) **b** Data comparison with 100 °C heat and UB effect on ERSFD ring—D(OP)

Fig. 18 **a** Data comparison with 40 °C heat and UB effect on ERSFD ring—UND(IP) **b** Data comparison with 40 °C heat and UB effect on ERSFD ring—UND(OP)

the allowable limits while crossing the critical speeds. In addition it is observed that as the temperature increases the damping provided by the ERSFD reduces. From the above evaluation, it may be noted that the response in OP condition appears to be lesser compared to IP. It is because in OP cases amplitude varies with the measurement location. Here the measurement location lies in between node point and bearing planes (ERSFD planes).

Figure 19 clearly shows that UND system amplifies vibration in abrupt mode at low load itself. The D shows smooth change over to critical speeds with suppressed vibration at high loads [8].
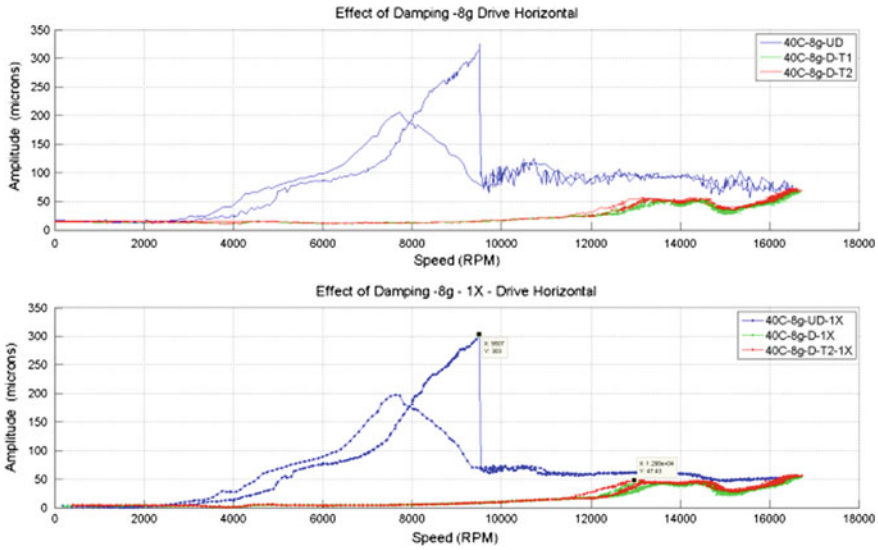
Fig. 19 Bode plot for D and UND at 40 °C and 8 g

5.2 Rig Response Parameters and Post Experimentation Component Check

The performance of the damper is evaluated mainly in terms of ERSFD/bearing housing vibration, rotor variation and metal temperature. The test bearing/ERSFD metal temperature is measured using two thermocouples placed at 30° apart on each bearing outer race at the bottom stream. The test bearing housing vibrations in two directions (X, Y) are measured using accelerometers on each bearing housing. In addition to that, total power consumption by the drive motor during testing has been monitored.

The above said response parameters are monitored and recorded during testing through computer-controlled data acquisition system. The elastic ring components are visually inspected after the scheduled tests. Components used for D and UND conditions are shown in Fig. 20. It clearly shows that the metal to metal contacts were established between outer pedestals to housing inner surface and the inner pedestals to bearing outer sleeve surfaces. Also the oil cavity surfaces between pedestals experienced elastic deformation in the elastic centering ring. These occurred during effective D and UND due to highly UNB response on the SGT rotor system. The clearcut contact surfaces of projected inner, outer pedestals and oil cavities with orifices are shown in Figs. 21 and 22.
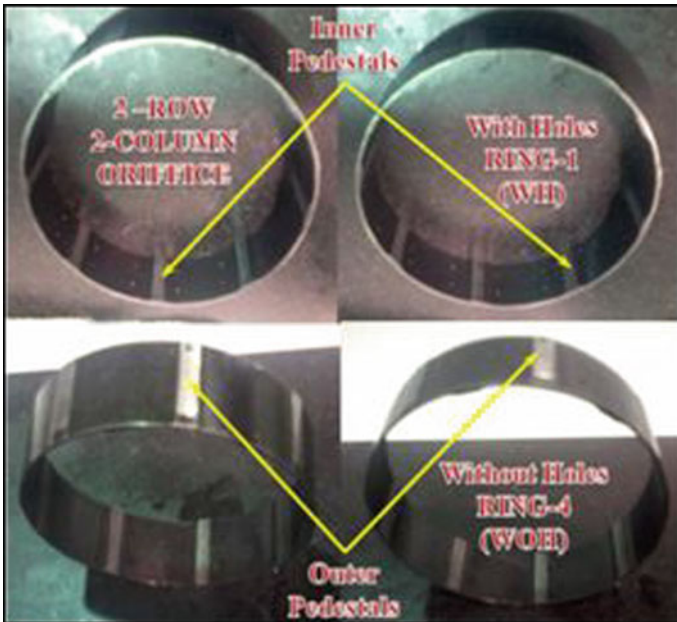
Fig. 20 D and UND component disassembly

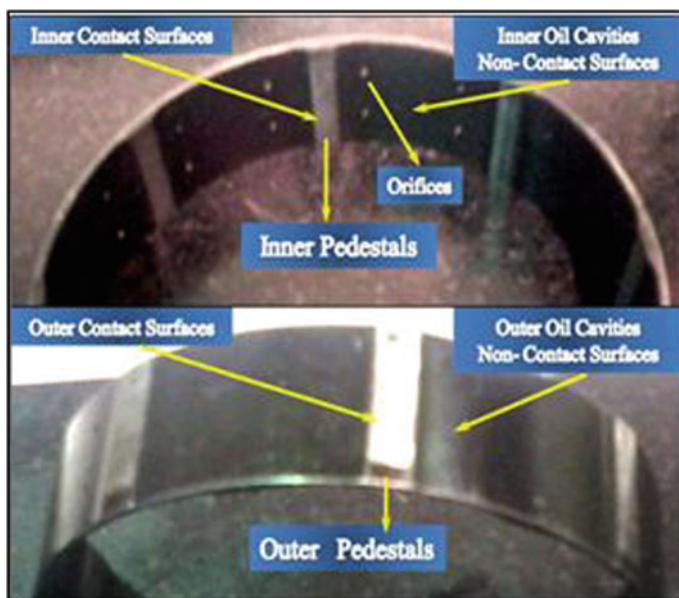**Fig. 21** Contact pedestals of ERSFD

Fig. 22 Pedestals and non-contact surfaces of ERSFD

6 Conclusion

Damped and undamped configurations of ERSFD have been evaluated experimentally. The damping provided by the ERSFD is sufficiently high to reduce the response of the rotor at critical speeds considerably. Experimental results indicate that as the heat and UNB reduces the damping increases. Experimentally determined damping parameters are used as an input for the rotor dynamic analysis of the small gas turbine engine rotor for accurate prediction of its response. Study indicates that two rigid critical speeds can be crossed using these elastic ring squeeze film dampers.

References

1. Gunter EJ (1977) Design of non-linear squeeze film dampers for aircraft engines. J Lubric Technol 99(1): 57–64
2. Leontiev MK, Tereshko AG Research of characteristics of elastic rings mounted in rotor bearings of gas-turbine engines, Technical Report, Engineering & Consulting centre, Alfa Transit, Moscow Aviation Institute, Moscow

3. Thennavarajan S, Jeyaraj P, Manikandan LP, Kulkarni SS, Jana S (2016) FSI and modal analysis of elastic ring squeeze film damper for small gas turbine engines. In: COMSOL conference, No: 54821, Bangalore, pp 1–6
4. Leontiev MK, Tereshko AG Investigation of influence of rotor supports elastic elements characteristics on gas turbine engines, Technical Report, Moscow Aviation Institute, A. Lyulka Scientific and Technical Center, Moscow
5. San Andrés L (1996) Theoretical and experimental comparisons for damping coefficients of a short length open-end squeeze film damper. ASME J Eng Gas Turbines Power 118: 810–815
6. Kulkarni SS, Murugesh S, Manikandan LP, Thennavarajan S, Jana S (2017) Development of rotor bearing system for a typical small gas turbine engine. In: 13th International conference on vibration problems, ICOVP, IITG, Guwahati
7. Hamrock (2004) Fundamentals of fluid film lubrication, Marcel Dekker
8. Rao SS Mechanical vibrations, Fifth edn, University of Miami

Effecting Critical Frequency Shift in Rotors Using Active Magnetic Bearings

Balaji Sankar, Pramod Manjunath, A. Hemanth Kumar, Shah Brijeshkumar, A. S. Sekhar, and Soumendu Jana

Abstract Low stiffness bearings are useful to reduce the force transmitted from the vibrating rotor to the surrounding support structure. However, having low stiffness requires us to cross the low rigid body critical frequency while accelerating to operating rpm. In this work the stiffness of the bearing is changed online during operation by using an active magnetic bearing instead of a conventional constant stiffness rolling element bearing. This methodology is shown for a rigid rotor using both simulation and experimental techniques. During acceleration phase, a high stiffness is maintained, which gives us high critical frequency. After acceleration to operating rpm, the stiffness of the bearing is reduced at run time so that the bearing again becomes a soft support. In this work, a thrust magnetic bearing of variable stiffness is used to show that by changing the stiffness at run time, we can avoid crossing the rigid body critical frequency and hence reduce the amplitude of resonant vibrations.

Keywords Active magnetic bearings · Magnetic levitation · Critical frequency shift · Resonance

B. Sankar (✉) · S. Brijeshkumar · S. Jana
CSIR-NAL, Bangalore, India
e-mail: balajis_dd@nal.res.in

S. Brijeshkumar
e-mail: shahbrij@nal.res.in

S. Jana
e-mail: sjana@nal.res.in

P. Manjunath · A. Hemanth Kumar
BMSIT College of Engineering, Bangalore, India
e-mail: pramodmanjunath1996@gmail.com

A. Hemanth Kumar
e-mail: hemanth96mani@gmail.com

A. S. Sekhar
IIT Madras, Chennai, India
e-mail: as_sekhar@iitm.ac.in

1   Introduction

Active magnetic bearings are increasingly being considered for ground-based power applications where weight is not a major concern. Bleuler [1] reported gas turbines and natural gas compressors using AMBs for supporting their main rotors. AMBs are also being used for air cycle machines, fly wheel energy storage systems, turbo molecular pumps, laser pumps, blood pumps, liquid sodium pumps and beverage pumps. High-speed machining spindles of over 180,000 rpm have been developed with AMBs as early as 1998 [2].

AMBs have multiple advantages over conventional rolling element bearings. They support the rotor without any mechanical contact with the rotor and hence reduce the wear and tear of the rotor considerably. They eliminate the need for lubrication systems. They have controllable damping and stiffness characteristics. They do not limit the speed of the rotor and have been shown to operate at surface speed of 300 m/s [3]. They reduce the power wastage due to friction by over one-tenths [4] and offer inbuilt rotor condition monitoring capabilities.

The controllable stiffness offered by the active magnetic bearing is used to shift the critical frequency of the rotor in this work. Using a rigid rotor simulation model, the transient response of the rotor as the rotor rpm ($1\times$ excitation frequency) crosses the critical frequency (ω_{Low}) is shown for a low stiffness support (K_{Low}). This response shows the resonant peak in vibration response at the critical frequency. The stiffness of the rotor is then increased to a high value $\left(K_{High}\right)$ such that the new critical frequency $\left(\omega_{High}\right)$ is higher than the operating speed $\left(\omega_{Op}\right)$ of the shaft. After the shaft has crossed ω_{Op} during acceleration, the stiffness again reduced from K_{High} to K_{Low}. Thus the bearing returns to its low stiffness condition and hence reduces the forces transmitted from the rotor to the support structure.

Experimentally, the same process is repeated with a thrust active magnetic bearing that supports a 2 kg weight in the vertical direction. The stiffness is changed back to a low value after crossing the critical frequency corresponding to the lower stiffness. By comparing the vibration response of the suspended plate, it is obvious that the online variation of stiffness using the AMB reduces the amplitude of resonant vibrations.

2   Simulation Methodology

For purposes of demonstrating the concept using simulation, a rigid rotor supported on AMB is considered. The mass of the shaft on a single AMB is treated as a point mass on which the disturbance force at $1\times$ frequency is applied. A simplified magnet circuit model is used to derive the force exerted by the electromagnet and to obtain the transfer function of the system. A PD controller is used to stabilize the mass at the reference location. The gains to be used in the PD controller are calculated using root locus technique. After fixing the bottom bias current of the AMB, the top bias current is calculated to compensate for the weight of the shaft. Equal bias currents are used

Table 1 Parameters of the AMB used in simulation

Parameter	Value
Magnet constant	2.46E-06
Shaft mass on AMB	2.00 kg
Number of turns	140
Initial air gap	1 mm
Single pole area	4 sq cm
Bottom bias current	0.50 A
Downward magnetic force	2.46 N
Top bias current	1.50 A
$\left(\frac{\partial F}{\partial x}\right)_t$	−88332 N/m
$\left(\frac{\partial F}{\partial x}\right)_r = \left(\frac{\partial F}{\partial x}\right)_l = \left(\frac{\partial F}{\partial x}\right)_b$	−9852 N/m
$\left(\frac{\partial F}{\partial i}\right)_t$	29.5 N/Ampere
$\left(\frac{\partial F}{\partial i}\right)_r = \left(\frac{\partial F}{\partial i}\right)_l = \left(\frac{\partial F}{\partial i}\right)_b$	9.85 N/Ampere

for left and right actuators of the AMB. The architecture used for the control is the common differential mode driving architecture. In this scheme, the control current from the PD controller is added to the top actuator bias current and subtracted from the bottom bias current. The arrangement of the horizontal and vertical actuators of the AMB around the rigid rotor is shown in [5]. The force derivatives for horizontal and vertical actuators and other parameters of the magnetic bearing used in the simulation model are given in Table 1.

The full methodology used in obtaining the magnet constant, controller architecture design, proportional and derivative gains for stable levitation is given in detail in [1] and presented by the author for this configuration previously in [6] and [7].

3 Simulation Results

For the proportional gains ($K_{horizontal} = 1.2$ and $K_{vertical} = 1.8$) chosen for this work, the natural frequencies of the rotor in the AMB are 63.3 Hz in the horizontal direction and 79.8 Hz in the vertical direction. The frequency response of the point mass for the two gain values is shown in Fig. 1. The blue curve shows the response in the horizontal direction corresponding to a gain of $K_{horizontal} = 1.2$. Since this stiffness is relatively low, its vibration amplitude is higher than the amplitude shown in frequency response of the vertical (shown in red color). Both the responses were obtained by doing a time-domain simulation of the bearing in which it was excited by a range of frequencies, and the peak response for each frequency of excitation was recorded.

In order to better illustrate the concept of reducing peak vibration amplitude by varying stiffness, only one axis (vertical) of the bearing is considered for further discussions. The stiffness and natural of the bearing in each direction can be changed
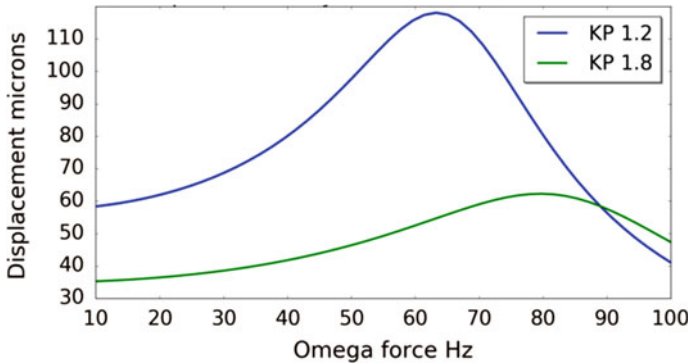
Fig. 1 Frequency response for gain 1.2 (resonating at 63.26 Hz) and for gain 1.8 (resonating at 79.8 Hz)

by appropriate change in the proportional gain of the PD controller. The variation in natural frequency with proportional gain is shown in Fig. 2.

In this illustrative example, we desire to keep the stiffness low at a gain of 1.2 and our operating frequency is $\omega_{Op} = 100 Hz$, to which we desire to accelerate in 10 s. While accelerating from low speed to ω_{Op}, we do not wish to have the high resonant vibrations corresponding to the low gain (shown in blue) at 4 s or the resonant vibrations corresponding to high gain at 5 s (shown in red) in Fig. 3. For this purpose, we maintain a gain of $K_{high} = 1.8$ for 4.5 s and then switch over to the lower gain of $K_{low} = 1.2$. By this switching of gain at 4.5 s, we avoid the resonant peaks of both low and high gain as shown in Fig. 4.

As can be seen at 4.5 s in Fig. 4, there is a sharp peak when the gain abruptly changes from a higher value to a lower value. The sudden lower gain allows the plate to fall and then the controller recovers and maintains the stable levitation of plate.
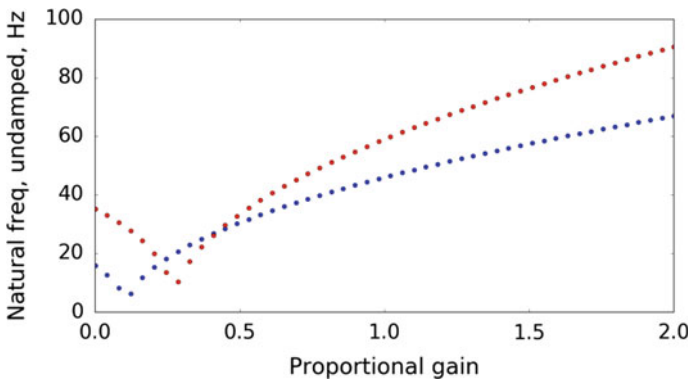
Fig. 2 Variation of natural frequency with proportional gain of the PD controller (red = 1.8 gain, blue = 1.2 gain)
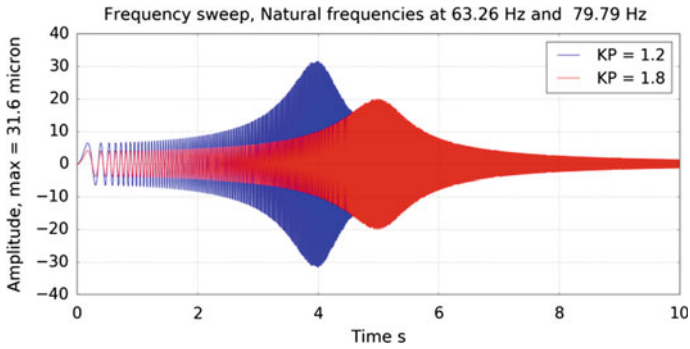
Fig. 3 Amplitude of vibration as the $1\times$ excitation frequency is increased as function of time
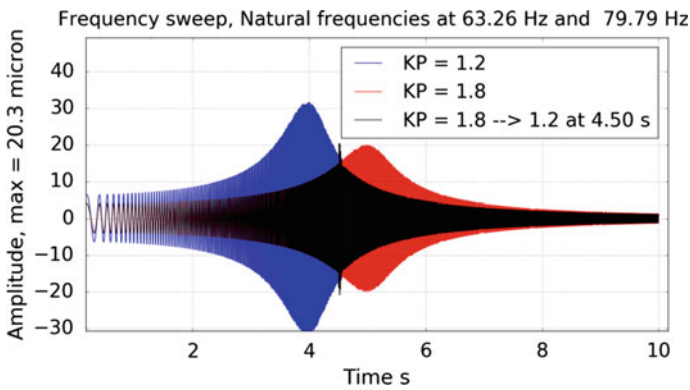
Fig. 4 Avoiding of resonant peaks: The stiffness is changed from a high value of $KH = 1.8$ to a low value of $KL = 1.2$ after crossing the lower natural frequency $\omega_L = 63.26$ Hz during the acceleration phase

4 Experimental Methodology

The schematic of the experimental setup used to demonstrate the concept and the actual setup is shown in Figs. 5 and 6. The flapping plate is loaded at mid span by mild steel pieces and is supported at the right end by a pin joint and at the left end by the AMB. The top and bottom actuators of the AMB are supplied by the power amplifiers and the control signal to the amplifiers is given by the controller through a digital to analog controller. An eddy current sensor is used to give feedback about the position of the plate to the controller. A signal generator capable of generating sine waveform of gradually increasing frequency is connected to the power amplifier of the excitation actuator.
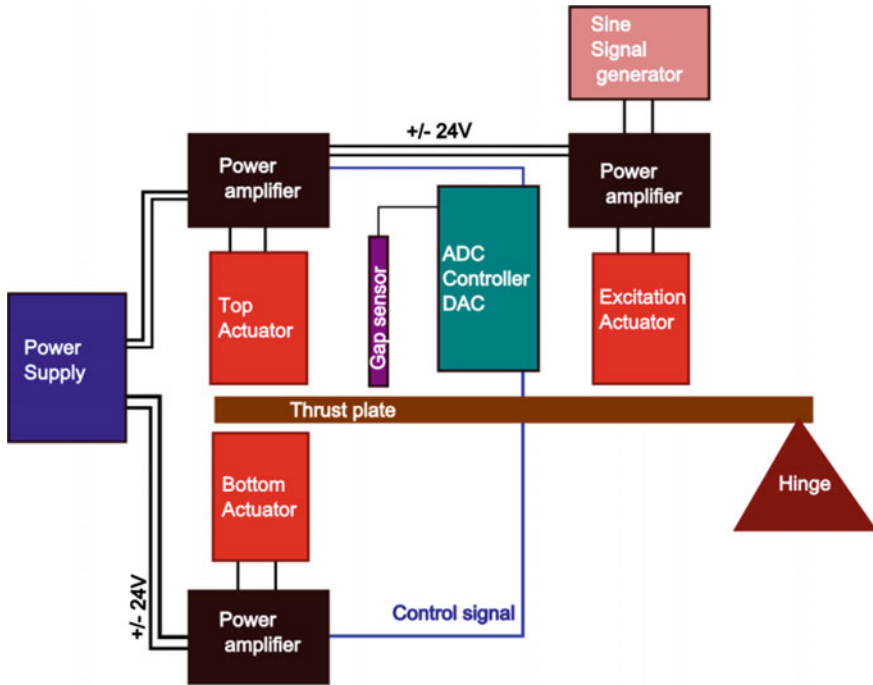
Fig. 5 Schematic of the experimental setup
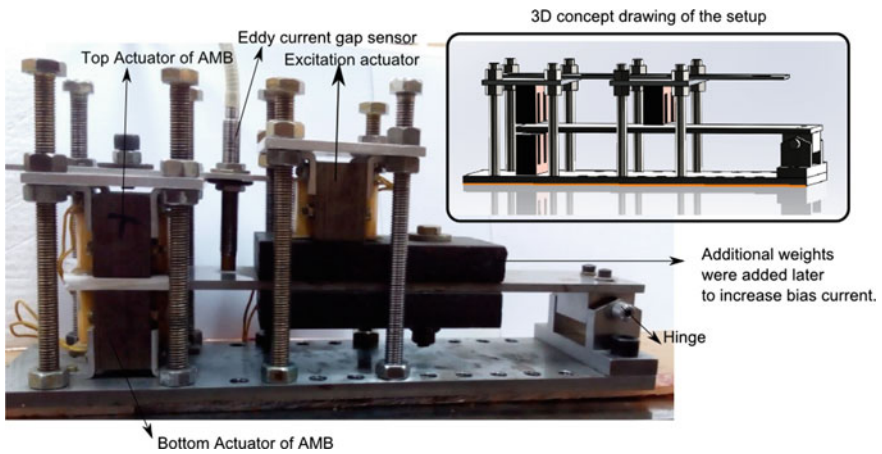
Fig. 6 Front view of the experimental setup showing hinge at the right end and the AMB at the left end. The excitation force is applied by the third excitation actuator in the middle

5 Experimental Results

The initial gap between the actuator and the plate when the plate is at BDC is 1 mm. At ideal levitation case, gap has to be 0.5 mm on both sides of the plate after levitation. However, due to experimental difficulties in setting the bias current, a lower gap exists at the bottom than at the top. The eddy current sensor used to measure the gap gives output in terms of voltage and has a sensitivity of 6.3 volts per mm. Initially plate is at rest at BDC. The controller increases top control current to bring the plate to reference location. However, during the overshoot beyond reference gap, the bottom control current is increased to pull the plate down and top current is dipped, as can be seen in the initial levitation graph shown in Fig. 7.

When the levitated plate is excited at a gradually increasing frequency for a gain of 1.2, the peak in the gap signal is observed at 26.1 Hz. The gradually increasing frequency of excitation signal is shown in Fig. 8a. The resonant peak in gap signal demands increase in the top actuator control voltage, which can be seen to increase at 3.5 s in Fig. 8b. The top and bottom control signals are shown in Fig. 8c, d. Similar gap variation plot has been shown for a gain of 1.9 in Fig. 9a. For this higher value of gain, the resonant peak occurs at a higher frequency of 44.9 Hz at 5.5 s. For this higher value of stiffness, the amplitude of vibration has reduced. Also the beam can be seen oscillating around a higher mean value compared to the lower gain case, which again matches the higher stiffness requirement. The top and bottom control signals for this constant gain are shown in Fig. 9b, c.

When the gain is changed from higher stiffness to a lower stiffness after crossing the resonant frequency of lower stiffness, we avoid both the resonant peaks and have lower amplitude of vibration as shown in Fig. 10a. As the stiffness reduces, there is
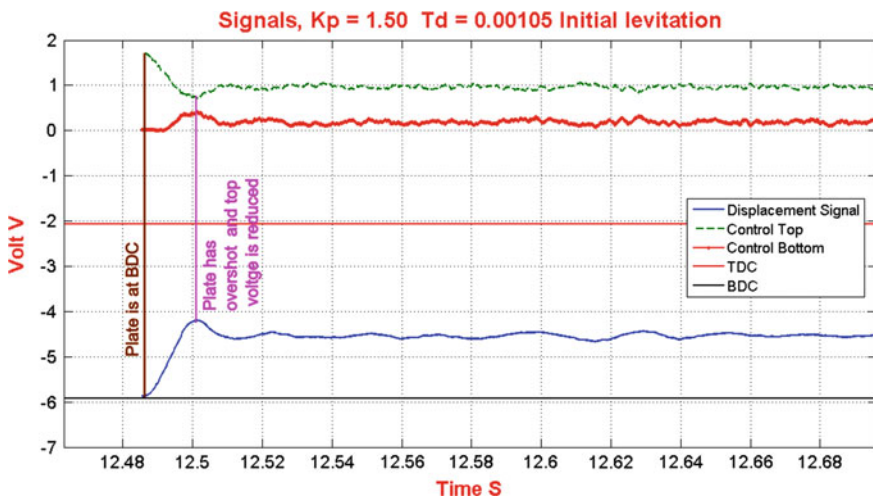

Fig. 7 Initial levitation of the plate at the left end in the AMB [8]
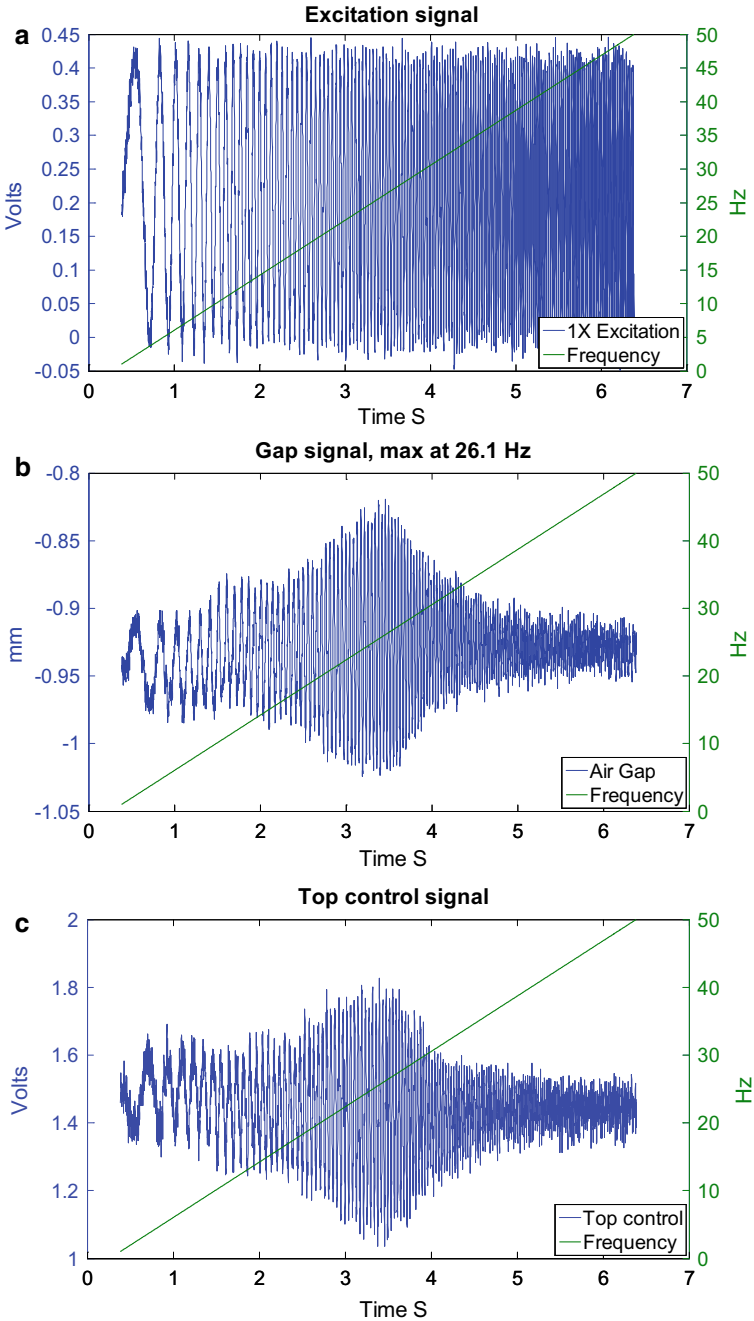
Fig. 8 a Excitation signal applied to all three cases **b** Gain 1.2, gap variation when crossing resonant frequency **c** Gain 1.2, top control voltage variation when crossing resonant frequency **d** Gain 1.2, bottom control voltage variation when crossing resonant frequency
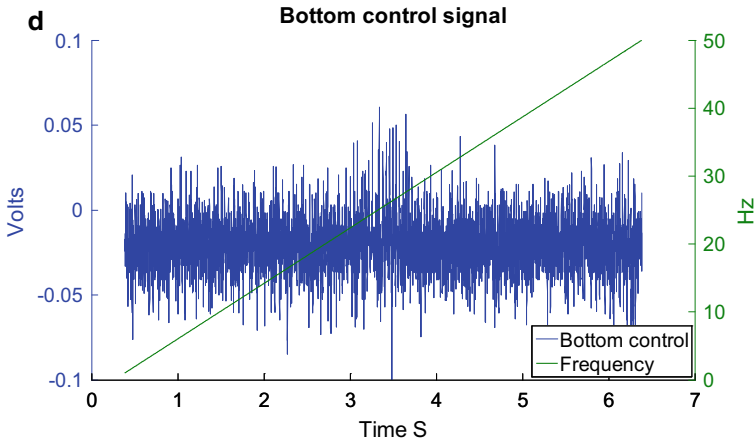
Fig. 8 (continued)

a marked drop in the plate position and reduction in the amplitude of both bottom and top control signal, as can be seen in Fig. 10b, c. The mean value of the top signal has also increased.

6 Conclusion

Lower stiffness bearings allow the rotor to vibrate at higher amplitude and reduce the forces transmitted to the surrounding structure. Magnetic bearings offer capability to change the stiffness of the bearing during run time. In this work it has been shown that there is a reduction in amplitude of vibration by maintaining high stiffness during acceleration phase and then switching over to a low stiffness during steady-state operation. In the experimental results, there is a reduction in the mean height of the levitated plate when the stiffness reduces. This will be compensated in next phase by appropriately changing the nominal force characteristics when the stiffness is changed. Also there is a sudden momentary drop in the plate position when the gain changes abruptly. A gradual reduction in the gain will be attempted to reduce the magnitude of the drop in the next phase.
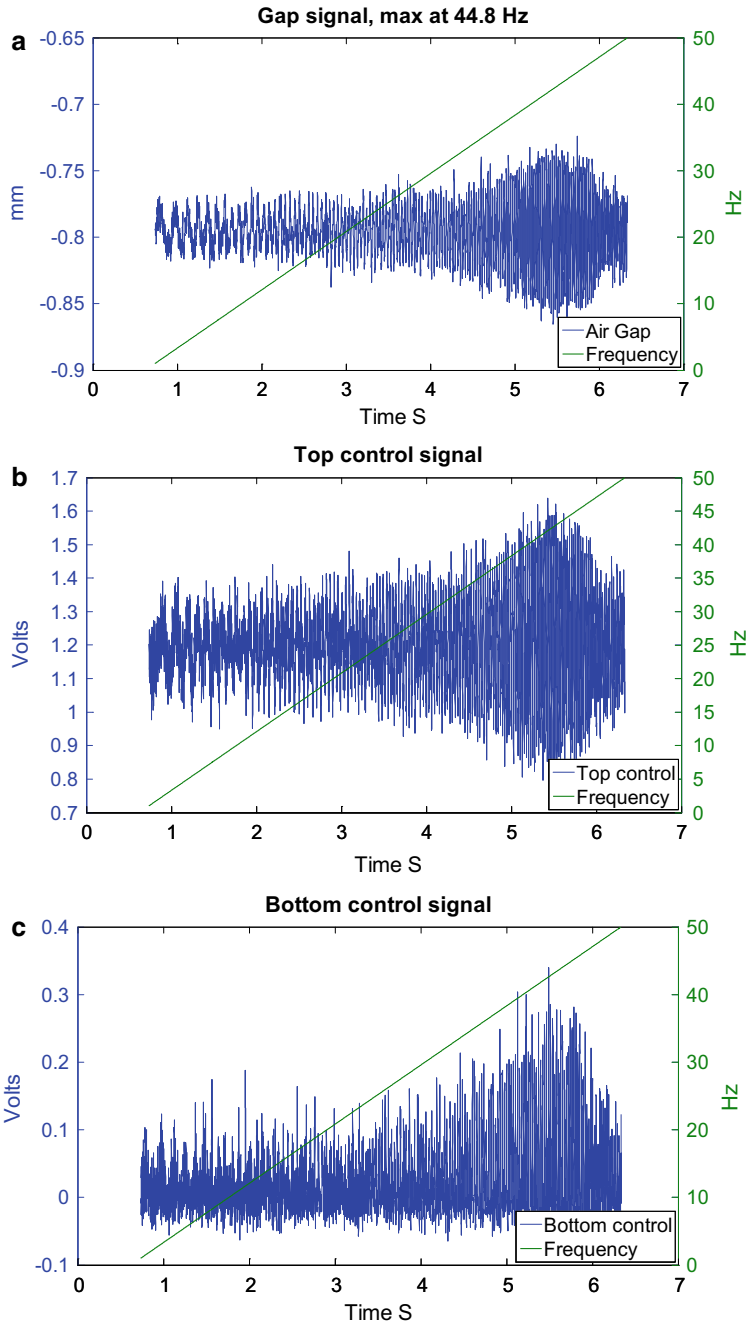
Fig. 9 **a** Gain 1.9, gap variation when crossing resonant frequency **b** Gain 1.9, top control voltage variation when crossing resonant frequency **c** Gain 1.9, bottom control voltage variation when crossing resonant frequency
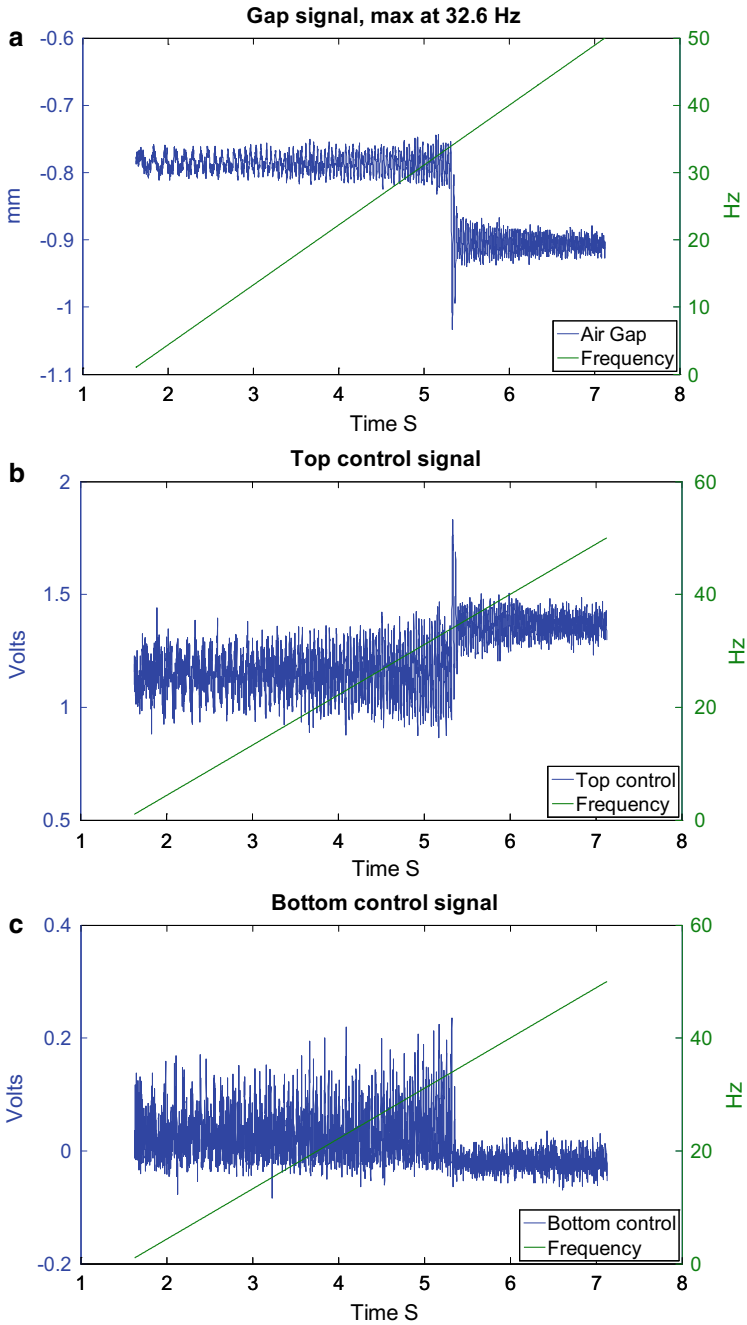
Fig. 10 a Gap response of the AMB when the gain is changed from 1.9 to 1.2 **b** Gain change from 1.9 to 1.2, top control voltage variation with frequency **c** Gain change from 1.9 to 1.2, bottom control voltage variation with frequency

References

1. Bleuler H, Cole M, Keogh P, Larsonneur R, Maslen E, Okada Y, Schweitzer G, Traxler A (2009) Magnetic bearings: theory, design, and application to rotating machinery. Springer Science & Business Media
2. Autila M, Lantto E, Arkkio A (1998) Determination of forces and linearized parameters of radial active magnetic bearings by finite element technique. IEEE Trans Magn 34(3): 684–694
3. Wadhvani VA (2011) Feedback control of a permanent magnet biased, homopolar magnetic bearing system. PhD diss., Texas A & M University
4. Studer PA, Allaire EH, Sortore CK (1991) Low power magnetic bearing design for high speed rotating machinery. In: International symposium on magnetic suspension technology, Hampton, Virginia
5. Brijeshkumar, Sankar B, Santosh kumar, Jana S, Giridhara RK (2018) Demonstration of magnetic bearing in high speed applications. In: NAPC 2018, IIT Kharagpur
6. Sankar B, Brijeshkumar, Jana S (2016) Analysis of active magnetic thrust bearing under varying load condition. In: National symposium on rotor dynamics, NIT Rourkela
7. Sankar B, Sekhar AS, Jana S (2017) Development of magnetic bearing model, controller and synchronous signal suppression. In: National symposium on rotor dynamics, IIT Patna
8. Sankar B, Sekhar AS, Brijeshkumar, Jana S (2018) Vibration characteristics of a thrust plate supported on active magnetic bearing. In: VETOMAC 2018, Lisbon, Portugal

Aramid Fiber Composite Layers for Fan Blade Containment in a Gas Turbine System: Some Experimental Studies

M. R. Bhat, Dineshkumar Harur Sampath, Sumit Khatri, and K. Umesh

Abstract The objective of this study is to investigate the suitability of Aramid fiber polymer composite as reinforcement for blade containment in a gas turbine system. The preliminary experimental study is focused on optimization of Aramid fiber epoxy laminate composite in terms of number of layers and fiber orientation with respect to energy-absorbing capability. Acoustic energy attenuation study has been performed along different directions of laminates to gauge the effect of fiber orientation and number of layers on stress wave attenuation. NDE measurements and standard destructive tests were performed on sets of samples with varied number of layers and orientation of Aramid fibers. Energy-absorption characteristics of the Aramid fiber epoxy composite laminates along with these variables were investigated. This experimental study has yielded some interesting and encouraging results.

Keywords Aramid fibers · FBO · Containment · NDE

1 Introduction

Over many decades now, optimally designed composite structures have enabled major weight reduction in aircraft with added strength and superior durability for longer lifespan. Being lighter than metal airplanes of the same class, aircraft made using composite materials extensively have lower fuel costs compared to traditional ones. Composites are also relatively less prone to corrosion. High-strength-woven fabrics were considered ideal candidate materials for use in structural systems where high-energy absorption is required. Their high strength-to-weight ratio and the ability to resist high-speed fragment impacts are expected to enable them to be very efficient compared to metals. In other words, when subjected to localized high-velocity impact

M. R. Bhat (✉) · D. Harur Sampath · S. Khatri · K. Umesh
Department of Aerospace Engineering, Indian Institute of Science, Bengaluru, Karnataka 560012, India
e-mail: mrb@iisc.ac.in

D. Harur Sampath
e-mail: dineshkumar@iisc.ac.in

loads these materials can dissipate energy through multiple paths in the formation of matrix cracking, multiple delaminations, fiber breakage, and so on. One of the more widely sought applications for woven fabrics is in propulsion engine containment systems [1–6]. Designing the containment system consists of determining the type of fabric, the number of fabric layers and fiber orientation. However, instead of using dry fabric, layers of an Aramid fiber-reinforced polymer composite material perhaps can be highly effective due to the high strength per unit density of such fiber composites and their superior energy-absorbing capabilities. This paper discusses the experimental investigations carried out using non-destructive evaluation (NDE) tools and standard destructive tests to study the energy-absorbing capability with change in number of layers and fiber orientation in Aramid fiber-reinforced epoxy composites.

2   Experimental Details

Aramid/epoxy composite laminates were fabricated by hand layup and vacuum bagging method. The numbers of layers were varied while keeping the thickness same according to the areal density of the fabric. For this, Aramid-woven fabrics with five different areal density (grams per square meter—GSM) have been tried. The experimental study is focused on optimization of Aramid laminate composite on the basis of the number of layers and orientation.

Ultrasonic C-scans were carried out on all the fabricated laminates before specimen preparation to check the porosity levels and for quality control. Ultrasonic testing (UT) uses high-frequency sound energy to conduct examinations and make measurements. Ultrasonic inspection can be used for flaw detection/evaluation, dimensional measurements, material characterization, and more. For example, Fig. 1 shows a typical C-scan of one of the laminates without any significant gross defect.

2.1   Acoustic Wave Propagation to Study Energy Absorption in the Laminates

High-frequency acoustic waves were made to propagate in the Aramid/epoxy laminates and the energy-absorbing characteristics of the laminates were compared for varied number of layers and fiber orientation in the laminates. In this case, acoustic waves were generated with the help of breaking standard lead pencil on the surface of the laminate. In this process, acoustic waves from a localized source travel as stress waves in all directions in the laminate and get picked up by piezoelectric sensors placed at definite locations at known distances. In this way, wave attenuation along different angles can be recorded and compared (Fig. 2).

Figure 3 shows the average acoustic energy attenuation for the Aramid/epoxy
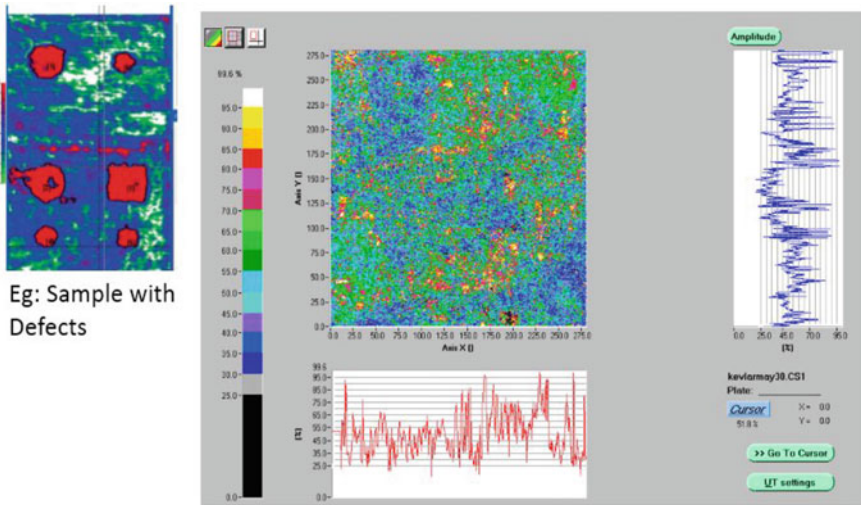
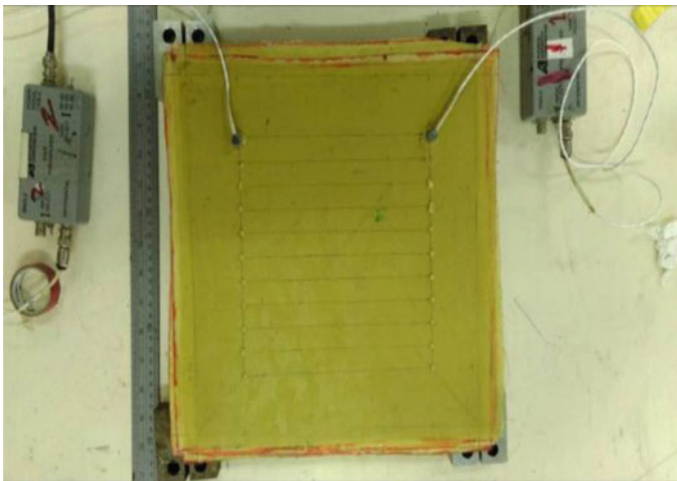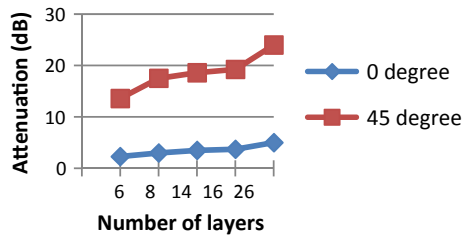**Fig. 1** C-Scan image of a multilayered aramid/epoxy laminate

Fig. 2 Acoustic wave attenuation study on laminate

Fig. 3 Acoustic energy attenuation in aramid/epoxy laminates

laminates along 0° and 45° orientations. Both the graphs show the similar trend that the 45° direction exhibited much higher acoustic energy attenuation compared to along the fiber direction in the laminates. Furthermore, thin fabric with more number of layers showed superior acoustic energy attenuation than thick fabric with less number of layers for same laminate thickness.

2.2 Tensile Testing (ASTM—D3039)

Standard tensile tests were performed on sets of samples cut out from each of the Aramid/epoxy laminates with different number of layers and different fiber orientation. Stress–strain behavior of these laminates along 0° and 45° fiber-oriented specimens was recorded. Toughness is measured as the area under these stress–strain curves, which represent the ability of material to absorb energy up to fracture. It can be an indirect measure of the impact loading that a structure can withstand before failure.

Figure 4a presents a typical stress–strain curve for specimens with different fiber orientation, and Figure 4b shows the energy absorbed by them. Following the trend observed by NDE measurements in terms of acoustic wave attenuation, these tests also showed that energy absorbed is much higher when loading is at 45° compared to its specimens loaded along the fiber direction, though the stress to failure was much less. Further, laminates with thinner fabric with more number of layers showed superior energy absorption than thicker fabric with less number of layers for same laminate thickness. Percentage elongation for specimens loaded along the fiber direction was in the range of 3–4% and when loaded along 45° was as high as 30–40% (Fig. 4a).

Further, it was observed that final failure of specimens when loaded along the fiber direction was more by gross fiber failure with much lesser failure strain where as when stressed along 45°, the failure occurs layer by layer and in the process much higher energy being absorbed by multiple interfaces, as shown in Fig. 5.

2.3 Flexural Testing (ASTM—D790)

Three-point bend flexural tests were carried out on samples cut off from the laminates (Fig. 6a). These tests provide information about the inter-laminar properties and different failure mechanisms involved in energy absorption before final failure (Fig. 6b).

Flexural testing of specimens cut along the fiber direction showed progressive, step by step failure. However, 45° specimens did not fail even until the maximum deflection limit was reached. Flexural modulus obtained for different samples are as shown in Fig. 7.
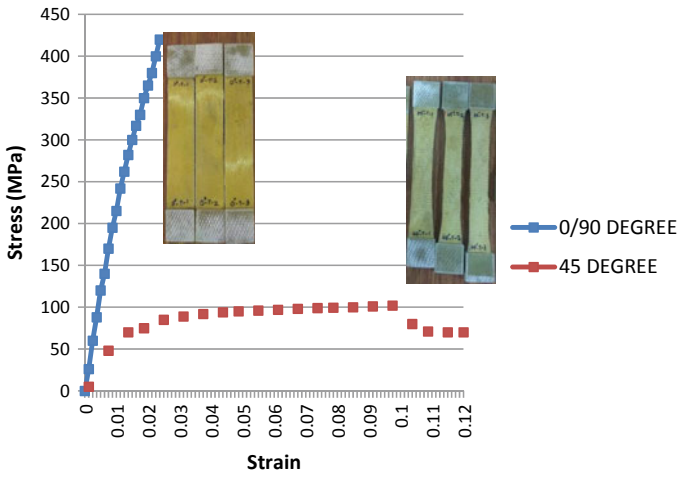
(a)
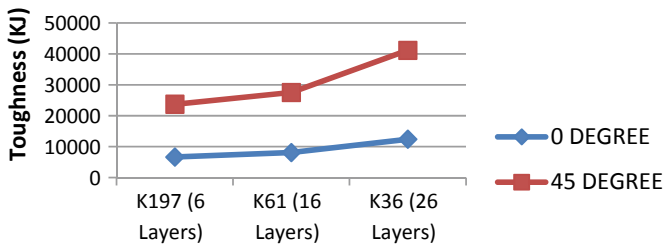
**K36=Kevlar plain weave 36GSM; K61=Kevlar plain weave
61GSM; K36=Kevlar plain weave 36GSM**

(b)

Fig. 4 Stress-strain curves and toughness values from tensile tests

Fig. 5 Change in failure modes in multilayer-composite specimens with fiber orientation

2.4 Low-Velocity Impact Test (Drop Test)

A special low-weight frame has been designed, fabricated, and set up for the low-velocity impact tests (Fig. 8). Aramid/epoxy laminate specimens prepared using
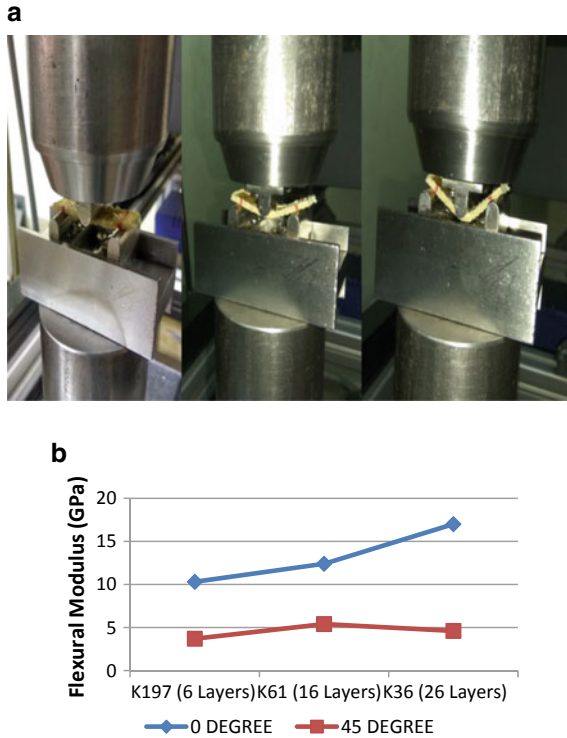
a

b

Fig. 6 **a** Flexural test on aramid-epoxy specimens **b** Flexural Modulus variation

different aerial density fabrics and with different fiber orientation were tested for energy absorption.

A mass of 10 kg was dropped from a height of 31.5 cm to make an impact energy of approximately 31 Joules on the specimen. The energy absorbed by the set of laminates is presented in Table 1.

It can be observed that energy absorbed by the laminates of same thickness with higher number of layers exhibits higher energy-absorbing capability compared to lesser number of layers of higher GSM fibers.

3 Summary and Conclusions

Energy-absorption characteristics of Aramid-woven fabric-reinforced epoxy composite laminates have been studied with respect to change in number of layers as well as change in fiber orientation.
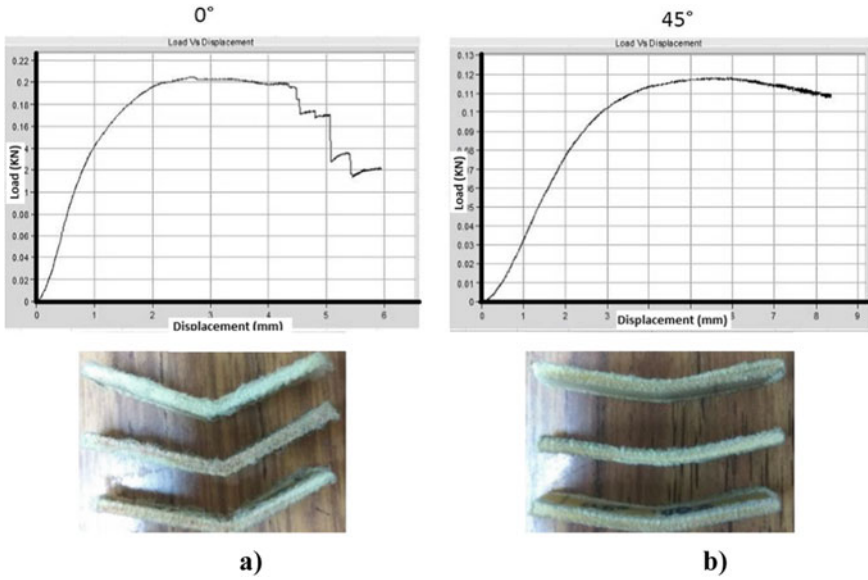
Fig. 7 Load versus displacement plots for specimens; **a** along fibers **b** at 45°
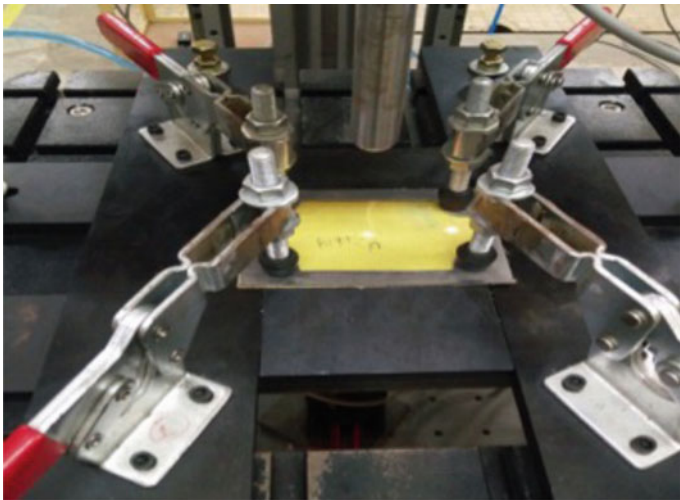

Fig. 8 Low-velocity drop weight impact test set up

Table 1 Energy absorbed by Aramid/epoxy laminates with different number of layers

Fabric layers	6	8	14	16	26
Energy absorbed (J)	6.31	6.35	7.29	7.36	8.81

NDE measurements in the form of acoustic wave attenuation and energy absorption during standard mechanical tests were compared for different sets of composite laminates.

The results of these preliminary experimental investigations show that higher number of layers of lower GSM Aramid-woven fibers for a pre-defined thickness of composite laminates exhibits higher energy-absorption capability compared to lesser number of layers of higher GSM-woven fabric reinforcement.

Further, the laminates have better energy-absorption capability when loaded at 45° to the fiber direction compared to when loaded along the fiber direction.

For the case of low-velocity impact loading also, energy-absorbing capability increases with higher number of layers for a given thickness.

Investigations are under progress to study the behavior of these composite laminates with varied number of layers and fiber orientation when subjected to high-velocity impact loading conditions.

Fan blade-out events in a turbine system are rather in the high-velocity impact category and hence experimental investigations simulating the high-velocity impact on these laminates are under progress. However, the preliminary experiments presented above through standard mechanical property evaluation and low-velocity impact loading have provided us with basic information to correlate energy-absorbing capability of multi-layered Aramid/epoxy composite material with regard to number of layers and fiber orientation.

References

1. Naik D, Sankaran S, Mobasher B, Rajan SD, Pereira JM (2009) Development of reliable modeling methodologies for fan blade out containment analysis part I: experimental studies. Int J Impact Eng 36(1):1–11
2. Stahlecker Z, Mobasher B, Rajan SD, Pereira JM (2009) Development of reliable modeling methodologies for engine fan blade out containment analysis. Part II: finite element analysis. Intl J Impact Eng 36(3):447–459
3. Nilakantan G, Keefe M, Bogetti TA, Adkinson R, Gillespie JW Jr (2010) On the finite element analysis of woven fabric impact using multiscale modeling techniques. Int J Solids Struct 47(17):2300–2315
4. Bresciani LM, Manes A, Ruggiero A, Lannitti G, Giglio M (2016) Experimental tests and numerical modelling of ballistic impacts against kevlar 29 plain-woven fabrics with an epoxy matrix: macrohomogeneous and meso-heterogeneous approaches. Compos B Eng 88:114–130
5. Carney KS, Pereira JM, Revilock DM, Matheny P (2009) Jet engine fan blade containment using an alternate geometry. Int J Impact Eng 36:720–728
6. Hai-jun Xuan, Rong-ren Wu (2006) Aeroengine turbine blade containment tests using high-speed rotor spin testing facility. Aerosp Sci Technol 10:501–508